SELCUK UNIVERSITY
FACULTY OF TECHNOLOGY

ICENTE'23

INTERNATIONAL CONFERENCE ON ENGINEERING TECHNOLOGIES

November 23-25, 2023

Konya/TURKEY

PROCEEDINGS BOOK

Editor
Prof. Dr Sakir TASDEMIR

E-ISBN: 978-975-448-240-9

International Conference on Engineering Technologies

7th International Conference, ICENTE
Konya, Turkey, November 23-25, 2023

Proceedings Book

Editor
Sakir TASDEMIR

International Conference on Engineering Technologies, **ICENTE'23**
Konya, Turkey, November 23-25, 2023

7TH INTERNATIONAL CONFERENCE ON ENGINEERING TECHNOLOGIES

23-25 NOVEMBER 2023

Editör
Şakir TAŞDEMİR

EBOOK ISBN: 978-975-448-240-9

EDITOR :

Prof. Dr. Sakir TASDEMIR
Selcuk University, Turkey
Depertmant of Computer Engineering, Faculty of Technology
Alaeddin Keykubat Campus, 42031, Konya, TURKEY
stasdemir@selcuk.edu.tr

PREFACE

International Conference on Engineering Technologies (ICENTE'23) was organized in Konya, Turkey on 23-25 November 2023.

The main objective of ICENTE'23 is to present the latest research and results of scientists related to Biomedical, Computer, Electrics & Electronics, Mechanical, Mechatronics, Metallurgy & Materials and Civil Engineering fields. This conference provides opportunities for the delegates from different areas in order to exchange new ideas and application experiences, to establish business or research relations and to find global partners for future collaborations.

All paper submissions have been double blind and peer reviewed and evaluated based on originality, technical and/or research content/depth, correctness, relevance to conference, contributions, and readability. Selected papers presented in the conference that match with the topics of the journals will be published in the following journals:

- Artificial Intelligence Studies (AIS)
- Gazi Journal of Engineering Sciences (GJES)
- International Journal of Applied Mathematics, Electronics and Computers (IJAMEC)
- International Journal of Automotive Engineering and Technologies (IJAET)
- International Journal of Energy Applications and Technology (IJEAT)
- MANAS Journal of Engineering (MJEN)
- New Trends in Computer Sciences
- Open Journal of Nano (OJN)
- Selcuk University Journal of Engineering Sciences (SUJES)
- Intelligent Methods in Engineering Sciences (IMIENS)

At this conference, there are 177 paper submissions. Each paper proposal was evaluated by two reviewers. and finally, 115 papers were presented at the conference from 6 different countries with 58 local and foreign universities and organizations participating,

In particular, we would like to thank Prof. Dr. Metin AKSOY, Rector of Selcuk University, conference scientific committee, session chairs, invited speakers, referees, technical team, participants, and all our colleagues who have contributed. They have made a crucial contribution to the success of this conference. Our thanks also go to our colleagues in our conference office.

Prof. Dr. Sakir TASDEMIR
Editor

PROGRAMME COMMITTEES

HONORARY CHAIR :

Metin Aksoy, Rector of Selcuk University, Turkey

GENERAL CHAIRS :

Sakir Tasdemir, Selcuk University, Turkey

SECTION EDITORS :

Adem Golcuk, Selcuk University, Turkey
Ali Yasar, Selcuk University, Turkey
Eyub Canli, Selcuk University – Turkey
Fatih Basciftci, Selcuk University, Turkey
Gokhan Arici, Selcuk University, Turkey
Ilkay Cinar, Selcuk University, Turkey
Ismail Saritas, Selcuk University, Turkey
Mehmet Cunkas, Selcuk University, Turkey
Murat Ciniviz, Selcuk University, Turkey
Mustafa Acarer, Selcuk University, Turkey
Mustafa Altin, Konya Technical University, Turkey
Nurettin Dogan, Selcuk University, Turkey
Suleyman Neseli, Selcuk University, Turkey
Yunus Emre Acar, Selcuk University, Turkey

INTERNATIONAL ADVISORY BOARD :

Abdullah Erdal Tumer, Kirgizistan Turkiye Manas University, Kyrgyzstan
Ahmet Yonetken, Afyon Kocatepe University, Turkey
Ahmet Fenercioglu, Gaziosmanpasa University, Turkey
Ahmet Afsin Kulaksiz, Konya Technical University, Turkey
Alexander Sudnitson, Tallinn University of Technology, Estonia
Alina Ivan Dramogir, Gheorghe Asachitechnical University Of Iasi, Romania
Almoataz Youssef Abdelaziz, Ain Shams University, Egypt
Amar Ramdane Cherif, University of Versailles, France
Anca Loana Andreescu, Academy of Economic Studies, Bulgaria
Anne Villems, University of Tartu, Estonia
Antonella Reitano, University of Calabria, Italy
Antonio Mendes, Universidade De Coimbra, Portugal
Arif Gok, Amasya Teknoloji Faculty, Turkey
Aristomenis Antoniadis, Technical University Of Crete, Greece
Artan Luma, South East European University, Macedonia
Bahattin Karakaya, Istanbul University, Turkey
Biagio Lenzitti, University of Palermo, Italy
Binod Kumar, Jspm Jayawant Institute Of Computer Applications Pune, India
Boris Akanaev, Kazak National University, Kazakhistan
Domenico Tegolo, Universita Degli Studi Di Palermo, Italy
Eisha Akanksha, Mvj College of Engineering, India
Elinda Kajo Mece, Polytechnic University of Tirana, Romania
Engin Ozdemir, Kocaeli University, Turkey
Erol Turkes, Kirklareli University, Turkey
Ertugrul Durak, Suleyman Demirel University, Turkey
Gabriel Luna Sandoval, Sonora State University, Mexico
Hamit Saruhan, Duzce University, Turkey
Hamza Bensouilah, Laboratoire de Mecanique et Structures, Algeria

Hasan Gokkaya, Karabuk University, Turkey
Howard Duncan, Dublin City University, Ireland
Huse Fatkic, University Of Sarajevo, Bosnia & Herzegovina
Ihsan Korkut, Gazi University, Turkey
Ismail Sahin, Gazi University, Turkey
Ivan Jelinek, Czech Technical University, Czech Republic
Jaharah A Ghani, National University of Malaysia, Malaysia
Jan Vom Brocke, University of Liechtenstein, Liechtenstein
Janis Grundspenkis, Riga Technical University, Latvia
Janusz Jablonowski, Warsaw University, Poland
Jiri Srba, Aalborg University, Denmark
Kadir Gok, Manisa Celal Bayar University, Turkey
Karl Jones, Liverpool John Moores University, United Kingdom
Laurentiu Cristian Deaconu, University of Pitesti, Romania
M Ugras Cuma, Cukurova University, Turkey
Mahdi Shahbakhti, Michigan Technology University, United States
Mahmut Sami Donduren, Konya Technical University, Turkey
Majida Ali Abed Meshari, Tikrit University, Iraq
Marco Porta, University of Pavia, Italy
Mehmet Akbaba, Karabuk University, Turkey
Mehmet Cengiz Kayacan, Suleyman Demirel University, Turkey
Mehmet Turan Demirci, Selcuk University, Turkey
Mesut Gunduz, Konya Teknik University, Turkey
Mirjana Ivanovic, University of Novi Sad, Serbia
Miroslav Neslusan, University of Zilina, Slovakia
Muciz Ozcan, Necmettin Erbakan University, Turkey
Muhammad Zia Ur Rehman, National Defence University, Pakistan
Musa Hakan Arslan, Konya Technical University, Turkey
Mustafa Altin, Konya Technical University, Turkey
Mustafa Tolga Cogurcu, Konya Technical University, Turkey
Natasa Hoic Bozic, Universityof Rijeka, Croatia
Nihat Yildirim, Gaziantep University, Turkey
Nikolaos Blasis, Technical University of Crete, Greece
Novruz Allahverdi, Kto Karatay University, Turkey
Osman Nuri Celik, Konya Technical University, Turkey
Pantha Ghosal, University of Technology Sydney, Australia
Pino Caballero Gil, University Of La Laguna, Spain
Rita Ismailova, Kyrgyz Turkish Manas University, Kyrgyzstan
Silyan Sibinov Arsov, Rousse University, Bulgaria
Spiridon Cretu, Gheorghe Asachitechnical University Of Iasi, Romania
Stavros Nikolopoulos, University of Ioannina, Greece
Stavros Christodoulakis, Technical University of Crete, Greece
Tatjana Dulinskiene, Kaunas University of Technology, Lithuania
Tayfun Findik, Gazi University, Turkey
Temel Kayikcioglu, Karadeniz Technical University, Turkey
Thomas Engel, University of Luxembourg, Luxembourg
Tugce Demirdelen, Adana Science Technology University, Turkey
Ulku Sultan Keskin, Konya Technical University, Turkey
Ulvi Seker, Gazi University, Turkey
Umit Ayata, Ataturk University, Turkey
Yuri Pavlov, Bulgarian Academy of Sciences, Bulgaria
Yusuf Uzun, Necmettin Erbakan University, Turkey
Zarifa Jabrayilova, Institute of Information Technology Anas, Azerbaijan

ORGANIZING COMMITTEE :

Abdullah Engin Ozcelik, Selcuk University, Turkey
Angel Smrikarov, Rousse University, Bulgaria
Ilker Ali Ozkan, Selcuk University, Turkey
Lilia Georgieva, Heriot Watt University, United Kingdom
Murat Koklu, Selcuk University, Turkey
Polyxeni Arapi, Technical University of Greece, Greece
Silyan Sibinov Arsov, Rousse University, Bulgaria

TECHNICAL COMMITTEE :

Abdulkadir Saday, Selcuk University, Turkey
Musa Dogan, Selcuk University, Turkey
Yusuf Eryesil, Selcuk University, Turkey

CONTENTS

Using MATLAB Toolboxes in Biomedical Image Processing

Y. NUHOĞLU[1], Y. ADWAN[2] AND A. ATASOY[3]

[1] Karadeniz Technical University, Trabzon/Turkey, yasinnuhoglu@odu.edu.tr
[2]Karadeniz Technical University, Trabzon/Turkey, monder1999@windowslive.com
[3]Karadeniz Technical University, Trabzon/Turkey, ayten@ktu.edu.tr

***Abstract* - MATLAB and the Computer Vision Toolbox provision a large range of improved image processing functions and correlative tools for developing and to investigate digital images. Correlative tools enable morphological operations for instance spatial image transformations, edge find and noise elimination, related area processing, filtering, FFT, DCT fundamental statistics, graph fitting and Radon Transform to be performed. Making graphic objects semi-transparent is a convenient technique in 3D visualization that provides more knowledge about the spatial intercourses of diverse constructions. The toolbox functions applied in MATLAB have also been used to improve customized algorithms.**

***Keywords* - MATLAB, biomedical image processing, toolbox.**

I. INTRODUCTION

Technological advances in biomedical imaging over the past centenary have formed unprecedented chances for diagnosis, without requiring any contact, and have established biomedical imaging as an integral part of healthcare systems nowadays. One of the most important zones of invention symbolizing these developments is the interdisciplinary area of biomedical image processing. Biomedical image processing is a highly complex, interdisciplinary area that involves countless scientific disciplines, from computer science and mathematics to medicine and physics. This area of fast improving deals with a multitude of processes, from crude data collection to numerical image communication, which supports the entire data flux in new biomedical imaging systems. Today, these systems present progressively higher decisions in spatial and density sizes, besides faster acquiring times, bring about a large quantity of superior-quality crude image data that should be agreeably processed and interpreted to reach right diagnostic conclusions [1].

Biomedical image processing includes the use and research of 3D image datasets of the human body, most frequently obtained from a Computed Tomography (CT) or Magnetic Resonance Imaging (MRI) scanner, for research purposes or to lead medical interpositions like diagnosing pathologies or planning surgery. Biomedical image processing is performed by radiologists, engineers, and clinicians to better understand the anatomy of individual sufferers or population groups. The basic utility of biomedical image processing is that it allows the internal anatomy to be investigated in depth and in a way that does not disturb its integrity. 3D models of anatomies of relevance can be invented and studied to develop cure results for the sufferer, improve advanced medical devices and medicament delivery systems, or obtain more notified diagnoses. In recent years, it has become one of the main tools used for medical advances. The ever-improving imaging quality, combined with advanced software tools, facilitates accurate digital reproduction of anatomical structures at various scales, as well as greatly varying features, including bone and soft tissues [2].

MATLAB is an up-level technical tongue and correlative circumference for data analysis and mathematical computational functions like signal processing, optimization, fractional differential equation solving, etc. It makes correlative tools including threshold, interaction, fourier analysis, filtering, fundamental statistics, graph fitting, matrix analysis, 2D and 3D drawing functions. It allows image manipulation operations, noise reduction and image enhancement, image transformations, color map orientation, color space transformations, region of interest processing, and geometric operations to be performed [3]. Toolbox functions applied in the MATLAB tongue can be used to improve customized algorithms [4].

II. MATLAB TOOLBOXES USED IN BIOMEDICAL IMAGE PROCESSING

The biomedical imaging toolbox provisions applications, functions, and workflows for designing and testing diagnostic imaging practices. It performs 3D processing and visualization of radiology images, multimodal recording, and segmentation and labeling. The toolbox allows training of predefined deep learning networks (with the Deep Learning Toolbox). It can import, pre-process, and analyze radiology images from a variety of imaging modalities, including projected X-ray imaging, computed tomography (CT), magnetic resonance imaging (MRI), ultrasound, and nuclear medicine (PET, SPECT). The Medical Image Labeler application allows semi-automatic 2D and 3D labeling for use in artificial intelligence workflows. Multimodal recordings of medical images, including 2D images, 3D surfaces, and 3D volumes, can be performed. The toolbox provisions an integrated medium for head-to-head computer-aided diagnostics and medical image analysis.

A. Important Toolbox Functions in Biomedical Imaging

- medicalImage: The 2-D biomedical image shows pixel data and file metadata.
- extractFrame: Extracts pixel data for a frame of a series of 2D biomedical images.
- montage: It displays medical image sections or frames as montages in sufferer harmonizes.
- implay: Displays a series of 2D medical images in the Video Viewer application.
- medicalVolume: The 3D medical image shows voxel data and spatial reference knowledge.
- extractSlice: Extracts voxels and spatial details for a cross-section medical volume.
- replaceSlice: A cross-section acts as a change in voxel values for the medical volume.
- resample: Resamples the volume of the medical image in different sufferer harmonize systems.
- sliceCorners: It extracts the harmonizes of the corner voxels for a slice of medicinal volume.
- sliceLimits: Extracts the X-, Y-, Z-limits for a cross-section medical volume.
- sliceViewer: Browse slices of the medical image volume in sufferer harmonizes.
- volshow: Performs imaging in sufferer harmonizes of the medical volume.
- isnrrd: Checks if the file is a valid NRRD file.
- nrrdinfo: It reads metadata from the NRRD file.
- nrrdread: It reads image data and metadata from the NRRD file.

B. 3D Medical Image Volumes: Import and Spatial Referencing Definition

The medicalVolume object transposes volumetric image data from the NIfTI, DICOM and NRRD file formats. The medicalVolume object stores pixel data and spatial reference information for an image. By using medicalVolume's properties and object functions, pixel data, spatial reference and density scaling information can be accessed for the associated image volume. For example, using the extractSlice function, an image section can be extracted in coronal, sagittal, or transverse anatomical planes.

The medicalref3d object describes spatial references for the 3D medical image volume. The medicalref3d object defines the mapping among the internal image harmonize system, the patient harmonize system, and the left/right, anterior/posterior, inferior/upward anatomical axes.

C. 2D Medical Images and Image Series: Importing and Extracting Frames

The medicalImage object imports image data from DICOM files that contain a time-related 2D image or a series of 2D images. By using the medicalImage object, it is possible to access pixel data and metadata attributes such as pixel pitch (in millimeters), frame times, and image window values. A frame of an image time series is extracted using the extractFrame object function.

D. Pre-Processing and Augmentation Processes for Noise Removal and Random Increments Application Process in Medical Image Data

To reduce speckle noise, the specklefilt function is used in 2D images such as ultrasound data. This function reduces noise using the speckle-reducing anisotropic diffusion (SRAD) algorithm.

The jitterIntensity function is used to randomly adjust the intensity of grayscale images and image volumes. This function changes the intensity of the images by making random increases.

III. METHOD

A. Code to Download Image Volume Data

The sample code in Figure 1 uses a chest CT volume saved as an index. The volume is part of a data set that includes a three-dimensional CT scan.

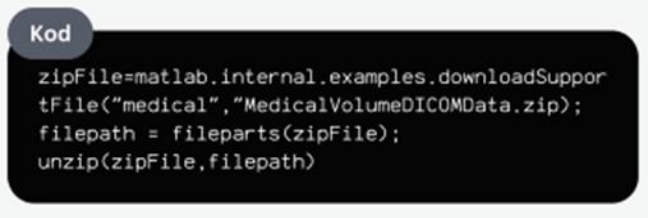

Figure 1: A sample image volume data download code

B. Image Reading

The medicalVolume object retrieves data from the DICOM, NIfTI, and NRRD medical image file formats. DICOM volumes can be stored as a only file or as a directory to comprise separate files for each 2D section. The medicalVolume object spontaneously defines the file format and extracts image data, spatial knowledge, and modality from the file metadata. In the following code, the data source is determined to be the download directory of the chest CT scan.

```
medVol = medicalVolume(dataFolder)
```

The VolumeGeometry feature comprises the medicalref3d object, which describes the spatial referencing for the image volume. This referencing involves the mapping among the internal and sufferer harmonize systems. The main harmonize system is defined by the columns, rows and slices of the Voxel sequence and has coordinates in voxel units. Voxel units represent the volumetric characteristics of the image. The patient harmonize system, on the other hand, is defined in terms of the patient's anatomical axes and is expressed in real-world units (e.g., millimeters). This harmonize system is used to determine the anatomical position of the image.

```
R = medVol.VolumeGeometry
```

C. 2D Visualization

When the code sliceViewer(medVol) title('CT Volume, Transverse Slices') is written into MATLAB, a 2D image appears. The example in Figure 2 is a 2D image that can be viewed from several places by changing the coordinates.

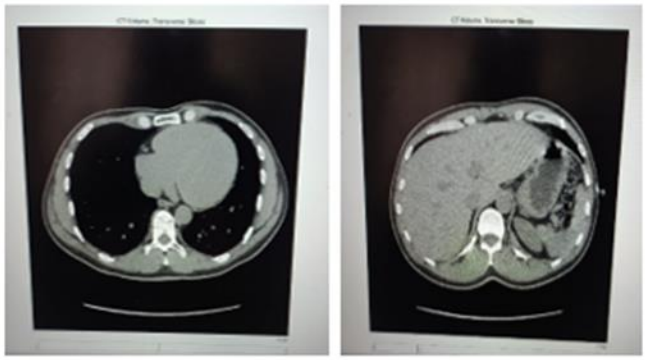

Figure 2: An example 2D scene

D. 3D Visualization

It represents the CT volume as a 3D object using the volshow function. The volshow function sets the conversion property of the volume object using the spatial details in medVol and displays the volume in the patients harmonize system. The volume image is customized by adjusting the features of the volume object. A special transparency map and color map are determined, highlighting the rib cage. Alpha and color values were determined based on the CT-bone rendering style in the biomedical image labeler application. Density values were adjusted for this volume by trial and error.

```
Kod
alpha = [0 0 0.72 0.72];
color = [0 0 0; 231 208 141; 231 208 141; 255 255 255]/255;
intensity = [-3024 50 1400 1499];
queryPoints = linspace(min(intensity),max(intensity),256);
alphamap = interp1(intensity,alpha,queryPoints)';
colormap = interp1(intensity,color,queryPoints);
vol = volshow(medVol,Colormap=colormap,Alphamap=alphamap);
```

Figure 3: An example code for using the volshow function in 3D rendering

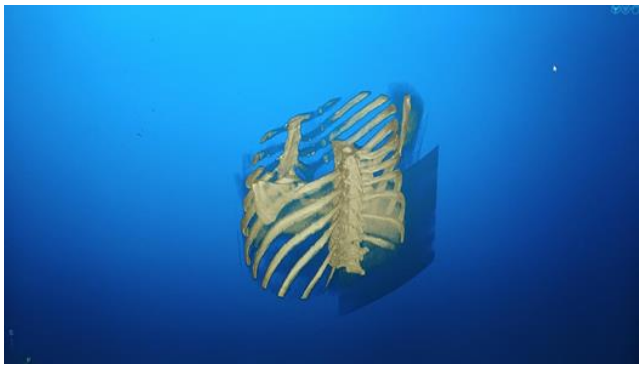

Figure 4: An example 3D image

E. Writing (saving) processed data to a new NIfTI file

By writing the processed image data to a new NIfTI file using the write object function, this function only aids writing medical volume data in the NIfTI file format [5].

```
Kod
niftiFilename = "LungCT01.nii";
write(medVol,niftiFilename)
```

Figure 5: Code for writing (saving) processed data to a new NIfTI file

IV. VESSEL SEGMENTATION PROCESS BY CLASSIFICATION OF EIGENVALUES USING BIOMEDICAL IMAGING TOOLBOX

1) First, an image (angi.jpg) and its labels (angi_label.bmp) to be used as the training data set were loaded.
2) Eigenvalue calculation was made using the vesselness2D function. This step is used to extract features from the image. Feature vectors were created.
3) The training data is organized as feature vectors (X) and labels (Y). In this step, labels corresponding to each feature vector were determined.
4) The K-NN model was created and trained. Using the fitcknn function, a KNN model was created on feature vectors and labels.
5) The image (angio_test.jpg) to be used as test data has been uploaded.
6) Eigenvalue calculations were made on the test data and feature vectors were created.
7) Segmentation was made using the KNN model. The predict function makes predictions using the feature vectors of the test data. It took about 10 minutes to train the model.

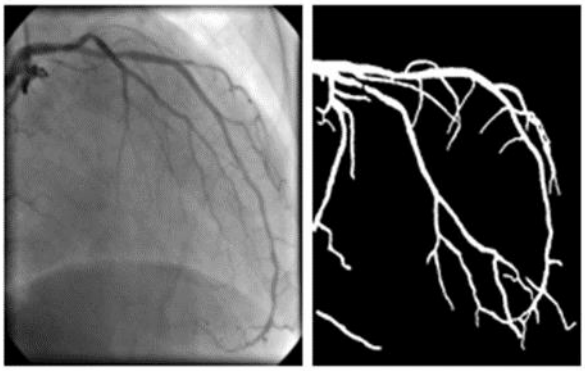

Figure 6: Training image (anjiyo_test.jpg)(left) and labels (anjiyo_label.bmp)(right)

V. CONCLUSION

Segmentation results have been reshaped based on image sizes (size(testData, 1), size(testData, 2),[]). The original image and segmentation result are shown side by side using the imshow and subplot functions.

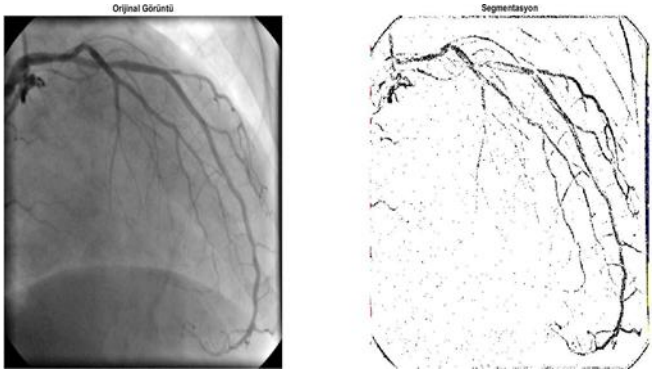

Figure 7: Original image (left) and segmentation (right)

If we want to invert the colors, we can add to our code;

segmentation(segmentation == 0) = 255;

segmentation(segmentation == 1) = 0;

We add these two functions to our code and the white places are converted to black.

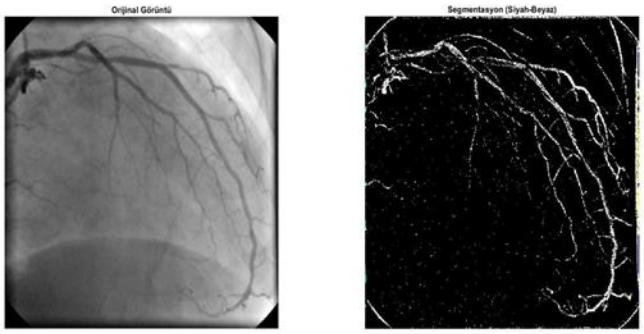

Figure 8: Original image (left) and segmentation (black and white) (right)

Using the biomedical imaging toolbox, the eigenvalues (single or multi-resolution) calculated on the image were trained with a classifier (k-NN, SVM, Neural Network, Bayes, LDA, etc.) using the training image (angiography.jpg) and labels (anjiyo_label.bmp) and segmentation of the vessel area of interest.

MATLAB provides functions and correlative tools for improving and to investigate digital images and advance image processing algorithms. MATLAB visualization tools allow the knowledge included in X-ray and CT image data to be represented owing to histograms, pixel zones, transparent covering, and tissue-mapped images to surfaces [6].

REFERENCES

[1] Patyuchenko, A., "Medical Image Processing: From Formation to Interpretation," Ahead of What's Possible is a trademark of Analog Devices, 2019.

[2] Synopsys. "Medical Image Processing". Retrieved : 17.06.2023. www.synopsys.com/glossary/what-is-medical-image-processing.

[3] B. Hahn. D.T. Valentine, Essential MATLAB for Engineers and Scientists, Elsevier (Third edition), 2007.

[4] E.G. Bistriceanu - Principiile Matematematice şi Fizice ale Tomografiei Computerizate, Matrix ROM, Bucureşti, 1996.

[5] Mathworks."Medical Imaging Toolbox". Retrieved: 17.06.2023. www.mathworks.com/help/medical-imaging.

[6] Seletchi, E.D., "Medıcal Image Processıng Usıng Matlab," Journal of Informatıon Systems & Operatıons Management, No.2, July, Bucharest/Romania , 2008.

Performance Evaluation of Graph Cut and Snake Algorithms on Skin Lesion Segmentation

S. GÜL[1] and G. ÇETİNEL[2]

[1] Sakarya University, Sakarya/Turkey, gulsevda@sakarya.edu.tr
[2]Sakarya University, Sakarya/Turkey, gcetinel@sakarya.edu.tr

***Abstract* - This study aimed to detect skin lesions and determine the lesion area using images taken by the dermatoscopy device, widely used by experts in skin cancer imaging. For this purpose, first of all, the hairs on the skin were removed with the Frangi filter based on the fast marsh method, and then the lesion area was determined by graph cut and snake segmentation methods. The segmentation results were compared with the binary ground truth images over five metrics. Simulation results showed that both graph cut and snake algorithms provided successful results in skin lesion segmentation. However, the snake algorithm provided a superior performance with approximately 92% accuracy, 99% sensitivity, 89% specificity, 78% Jaccard index (JI) and 87% Dice coefficient values.**

***Keywords* - Skin cancer, segmentation, Graph cut, Snake algorithm.**

I. INTRODUCTION

SKIN cancer can be defined as the uncontrolled growth of abnormal cells caused by exposure to ultraviolet rays from the sun [1]. Light skin color, sunburn, genetic background, and weak immunity are other risk factors that contribute to skin cancer formation. The most common types of skin cancer are Basal Cell Carcinoma (BCC), Squamous Cell Carcinoma (SCC), melanoma, and Merkel Cell Carcinoma (MCC). The most dangerous of these is melanoma [2]. In 2020, according to data from the International Agency for Research on Cancer (IARC), an estimated 19.3 million new cancer cases (18.1 million excluding non-melanoma skin cancer) were detected worldwide. In 2020, there were approximately 10 million cancer deaths (9.9 million excluding non-melanoma skin cancer). The incidence of skin cancer is about two times higher in men than in women. Although the incidence of melanoma-type skin cancer is low, it is one of the leading causes of death in skin cancer cases [3].

Manual detection of skin cancer by an expert is a time-consuming process. In addition, differences in interpretation between experts affect the accuracy of diagnosis. Software-based decision support systems for skin cancer diagnosis are being developed to reduce time loss and increase diagnostic accuracy. Some of the most recent studies can be summarized as follows.

The study by Nagayalanka and Ghanta aims to classify skin cancer into three categories: benign, malignant, and normal, using dermoscopic images. In the study, the Fuzzy C-Means (FCM) algorithm was used for segmentation. Features were extracted from the segmented images using Local Vector Pattern (LVP) and Local Binary Pattern (LBP) techniques. A fuzzy Classifier (FC) was used to classify the LVP and LBP features, and an accuracy of approximately 90% was obtained. [4]. Ranpreet et al. used an end-to-end atrous spatial pyramid pool-based Convolutional Neural Network (CNN) as a novel approach for automatic lesion segmentation in open-access dermoscopic images. Accuracy, Jaccard Index (JI), and boundary F1 contour matching index (BF-Score) metrics were calculated to evaluate the segmentation process. Promising results were obtained in the study [5]. In [6], Cascade Knowledge Diffusion Network (CKDNet) was used for skin cancer segmentation and classification. Two new complexity modules, Entangle-Cls and Entangle-Seg, were created. Accuracy, precision, JI, and Dice coefficient metrics were used to evaluate the segmentation results. In the study, an accuracy rate of approximately 93% was achieved. Liu et al. applied noise reduction, segmentation, morphology, feature extraction, feature selection, and classification algorithms to images from open-access databases. The Otsu thresholding method was used in the segmentation step. Twenty different features were extracted from the images with lesion areas, and feature selection was performed using the Thermal Exchange Optimization Algorithm (TEOA). The extracted features were classified using Support Vector Machines (SVM) [7]. In another study, four basic steps were followed. In the first step, noise reduction and contrast enhancement were applied to open-access dermoscopic images.

After these processes, the Kernel-Based Fuzzy C-Means (KFCM) segmentation method was used to identify the region of interest. Accuracy, precision, and sensitivity criteria were used to compare the segmentation result with the manually segmented image. A feature extraction and selection step based on the Improved Neural Network Algorithm (INNA) was performed, and SVM classification was performed in the last step. The study provided a superior performance compared to the methods it was compared with [8]. Adekanmi et al. created images with the same scale and resolution by cropping and resizing from open-access skin cancer images and performed image normalization with the pixel mean value and standard deviation of the obtained images. After this step, which can be

considered as a pre-processing step, skin cancer was detected using probabilistic deep networks. In the presented study, an accuracy of 97% was achieved [9]. Finally, in the study presented in [10], melanoma skin cancer images from an open-access database were segmented with U-net, a deep learning-based convolutional neural network model. The maximum accuracy value obtained with a post-processing step applied at the output of the deep network is just over 96%.

A general review of the literature shows that dermatoscope images from PH2, ISBI, ISIC, DermIS, DermQuest, DermNet, and MED-NODE open databases are commonly used in studies on skin cancer. The studies aim to determine the boundaries of skin lesions in the most accurate way and/or to classify the lesions according to their types. However, the determination of lesion boundaries is a very challenging process, especially when the lesion boundaries are not evident, when there are hairs, blisters, or vascularization on the lesion, and when there is an artifact in the image. Accurate detection and delineation of skin lesions are critical in the diagnosis and treatment process. In this study, skin lesion images from the open-access database created by The International Skin Imaging Collaboration (ISIC) were used. The study aims to detect skin lesions in the images available in the database and to determine the lesion area accurately, even in challenging situations. In order to evaluate the performance of the proposed work, accurate reference binary masks from the database and automatic segmentation results are compared using five different metrics.

The study is organized as follows. Section II describes the database and the methods used. Section III presents the results of simulations to evaluate the performance of the proposed methods. Finally, Section IV contains discussions and future work.

II. Material and Method

In this section, the methods applied for the defined purpose are explained. The flow of the proposed system is shown in Figure 1.

A. Database

In this study, skin cancer images from the ISIC 2016 database were used [11]. The database contains 900 dermoscopic lesion images in JPEG format and two-level image masks in PNG format.

B. Remove Hair

In dermoscopic images, the hairs on the lesion make it challenging to determine lesion boundaries and to examine tissue characteristics. In such cases, the performance of the segmentation step is also degraded. Therefore, the first step in the presented work is to remove the hair. For this purpose, the Frangi filter and the Fast March Method (FMM) are used. In the Frangi filter, the sigma value varies between 0.5-2.5 with a step interval of 0.5. The input image resolution used in the Hessian matrix calculation and the output image intensity value of the filter are one, and the dark background is selected. FMM was used to remove the hairy regions identified by the Frangi filter from the image. In FMM, an image smoothing estimator gradually paints the inside of the region by filling in each pixel starting from the boundary region. The FMM is calculated as a weighted average over a small known neighborhood around the pixels to be inpainted. When a hairy pixel is colored, the FMM is used to move to the next closest pixel [12]. Since simulations have shown that the FMM algorithm is faster and more efficient than other methods, this method was preferred in this study. Figure 2 (a) shows the original image, (b) the Frangi-filtered image, and (c) the FMM-applied image.

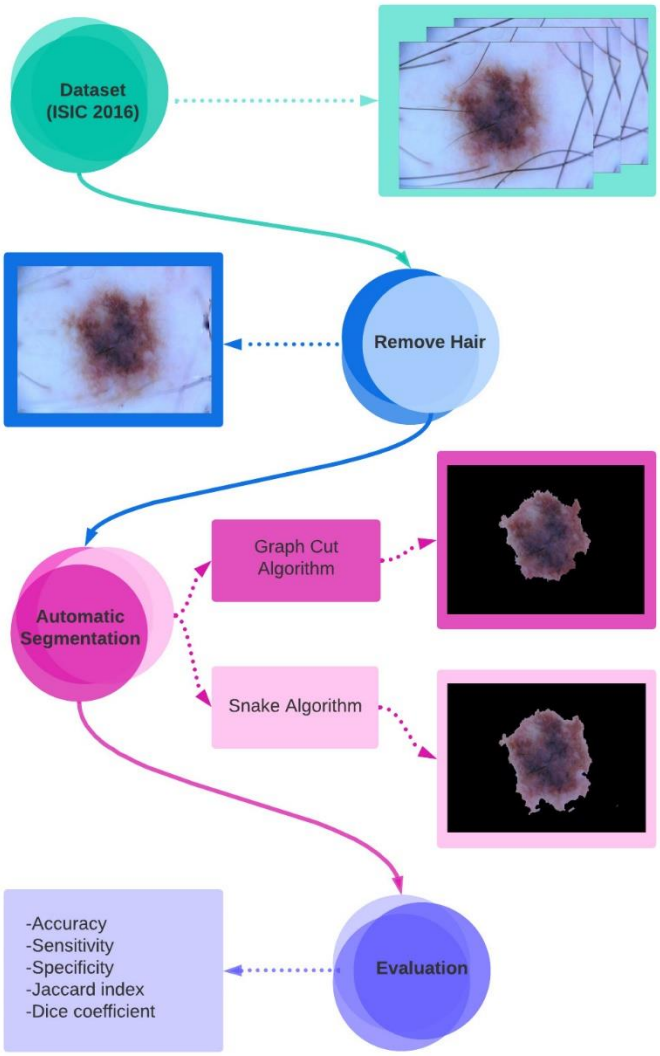

Figure 1: Flow of the proposed system

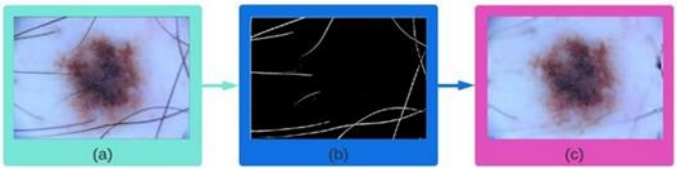

Figure 2: (a) Original image, (b) Frangi filtered image, (c) FMM applied image

C. Segmentation

The segmentation step aims to identify the lesion area with the highest accuracy. For this purpose, two different segmentation methods were used. These are the Graph Cut (GC) and Snake (Snake) methods. Details of the methods are given below.

Graphical cutting algorithm: GC is an image segmentation method based on graphical cuts. This method uses the Gaussian Mixture Model (GMM) to estimate the color distribution of the target object and the background, starting with a user-specified boundary around the structure to be segmented. The GC algorithm takes two inputs: a set of background pixels T_B and a set of foreground pixels T_F. Initially, T_B and T_F are selected by drawing a boundary around the lesion of interest. Every pixel outside this boundary is considered a background pixel, and every pixel inside the boundary is considered a foreground pixel. In this study, the boundary detection was done automatically by selecting the upper left corner *(0.1 × w, 0.1 × h)* and the lower right corner *(0.9 × w, 0.9 × h).* Here, w and h are the width and height of the image, respectively. In some dermoscopic images, the lesion area may extend to one of the corners or edges. In these cases, the GC algorithm can consider part of the lesion area as background.

Given the input image, the algorithm first labels foreground and background pixels and develops two GMMs, one for foreground and one for background, each containing five Gaussians. The GC then constructs a weighted directed graph where pixels in the image are considered as nodes. Two additional nodes are added to the graph: a source node and a sink node. Foreground pixels are connected to the source node, while background pixels are connected to the sink node. The weights (D) for the edges between the source or sink node and the pixels are determined by the probability that a pixel is a foreground or background pixel. Given a pixel vector z_n in RGB color space, α is the segmentation result of label vectors (0 represents the background and the foreground). θ is the histogram showing the pixel value distribution of the foreground and background labels, and k_n is an additional vector that assigns a single GMM component to each pixel (either from the background or foreground, depending on whether α=0 or 1). Accordingly, the data term U for the color GMM model is defined by (1):

$$U(a,k,\theta,z) = \sum_n D(\boldsymbol{\alpha}_n, \boldsymbol{k}_n, \theta, \boldsymbol{z}_n) \quad (1)$$

The weights of edges between pixels are assigned based on pixel color similarity. If the difference in pixel color is huge, the edge between these pixels will receive a low weight/cost. The smoothness term *V* is given in (2).

$$V(\alpha,z) = \gamma \sum_{(m,n)\in C} dis(m,n)^{-1}[a_n \neq a_m] e^{-\beta\|z_m - z_n\|^2} \quad (2)$$

Where *C* is the set of neighboring pixel pairs γ and β fixed and *dis*(.) is the Euclidean distance of neighboring pixels. Once *V* is calculated, the graph is divided into two separate source and sink nodes such that the minimum cost function (*E*) given by (3) is satisfied. After splitting, pixels connected to the source node are labeled as foreground, and pixels connected to the sink node are labeled as background. The whole process continues until the classification converges [12].

$$E(a,k,\theta,z) = U(a,k,\theta,z) + V(\alpha,z) \quad (3)$$

Snake algorithm: A contour extraction method based on the concept of active contours, which can be defined as energy-minimizing curves. The snake model is a controlled continuum curve under the influence of image forces. Image forces push the snake towards salient image features, while internal energy forces try to impose a piecewise regularity constraint. The active contour geometry is a curve with an arc length as a parameter. $v(s) = (x(s), y(s))$ is represented by the curve. The energy equation for the contour is defined by (4),

$$E_{snake} = \int_0^1 \left[E_{internal}\big(v(s)\big) + E_{external}(v(s))\right] ds \quad (4)$$

Here, *internal* represents the internal energy of the contour due to curvature or discontinuity, while *external* represents image forces such as lines and edges. The internal energy is given in (5).

$$E_{internal} = \alpha(s)|v(s)|^2 + \beta(s)|v_{ss}(s)|^2 \quad (5)$$

In the equation, the lower indices indicate the derivative concerning *s*. The first-order continuity term will have larger values when there is a gap in the curve, while the second-order curvature term will be more extensive where the curve curves rapidly. At a point α and β values determine how much the contour is allowed to stretch or curl at that point. At one point, α discontinuity if the value is zero, β If the value is zero, a corner can be formed. The external energy consists of the edge strength of the image and is expressed by equation (6).

$$E_{external} = \gamma|\nabla G_\sigma * I(v_{n,k})| \quad (6)$$

Here vn,k is the current search position (n=0,…,N−1, k=0,…,M−1). γ is the energy rate constant, and $Eharici$is an empirically determined value by the Canny edge detector. σ is calculated with the value. The segmentation process is completed by performing the specified number of iterations [13].

III. Results

The study aims to apply two different segmentation algorithms to skin cancer images taken with a dermatoscopy to determine the lesion area most accurately and thus to provide a system that supports experts in the diagnosis phase. In the study, the lesion is visualized more accurately, and the performance of the segmentation step is improved by removing the hairy parts before the segmentation step.

GC and snake algorithms were preferred in the segmentation step. The reason for choosing these methods is that they can provide successful results in region-based segmentation by working with an automatically selected starting point. In this way, there is no need for any intervention by the expert when determining the lesion region.

In order to evaluate the performance of the proposed system, the automatic segmentation results obtained by both methods are compared with the real reference masks in the database using five metrics. These metrics were determined after a detailed literature analysis. The metrics used are accuracy

(ACC), sensitivity (SN), specificity (SP), Jaccard index (JI), and Dice coefficient. The equations for the metrics are given below respectively.

$$ACC = \frac{TP+TN}{TP+TN+FP+FN} \quad (7)$$

$$SN = \frac{TP}{TP+FN} \quad (8)$$

$$SP = \frac{TN}{FP+TN} \quad (9)$$

$$JI = \frac{TP}{TP+FP+FN} \quad (10)$$

$$Dice = \frac{2*JI}{1+JI} \quad (11)$$

The equations TP, TN, FP, and FN represent true positive, true negative, false positive, and false negative numbers, respectively.

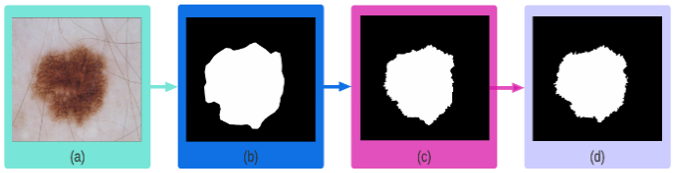

Figure 3: (a) Original image, (b) Binary mask image, (c) GC algorithm, and (d) Snake algorithm results.

Figure 3 (a) shows the original skin cancer image, (b) shows the real reference binary mask image from the database, and (c) and (d) shows the binary mask images resulting from the GC and snake algorithms, respectively. The performances of the GC and snake methods for the images from the ISIC 2016 database are given in Table I. When the table is analyzed, it is seen that the snake algorithm provides higher accuracy and precision than the GC algorithm. In addition, the JI and Dice values, which represent the overlap between manual and automatic segmentation results, are closer to 1, the best value in the snake algorithm.

Table 1: Performance Evaluation

Metrikler	**Segmentasyon**	
	GC algorithm	***Snake algorithm***
ACC	0,9013	0,9231
SN	0,9385	0,9980
SP	0,9006	0,8948
JI	0,7297	0,7813
Dice	0,8226	0,8708

IV. Discussions and Future Work

In the proposed study, GC and snake algorithms are applied to the images taken from the ISIC 2016 database after removing the hairy parts to detect the skin lesion regions most accurately. The segmentation results were evaluated by determining the five most commonly used metrics. The results showed that the snake algorithm gave successful results.

Future studies aim to develop an end-to-end decision support system by using open databases and skin lesion images obtained within the scope of data usage permission. The decision support system aims to provide experts with a non-invasive diagnosis process from acquiring the skin lesion image until the report stage.

Acknowledgements: The study is supported by The Scientific and Technical Research Council of Turkey (TUBITAK) through The Research Support Programs Directorate (ARDEB) with project number of 122E629.

References

[1] Duggani, K. and Nath, M. K. "A Technical Review Report on Deep Learning Approach for Skin Cancer Detection and Segmentation," Lecture Notes on Data Engineering and Communications Technologies, vol 54. Springer, Singapore, 2021.

[2] Sarnoff, D. S, "What is skin cancer?", "https://www.skincancer.org/skin-cancer-information/", Avaliable: 10.01.2021.

[3] Sung, H. *et al.*, "Global Cancer Statistics 2020: GLOBOCAN Estimates of Incidence and Mortality Worldwide for 36 Cancers in 185 Countries," *CA. Cancer J. Clin.*, vol. 71, no. 3, pp. 209–249, 2021.

[4] Durgarao, N. and Sudhavani, G. "Diagnosing skin cancer via C-means segmentation with enhanced fuzzy optimization," IET Image Process., vol. 15, no. 10, pp. 2266–2280, 2021.

[5] Kaur, R., Gholamhosseini, H., Kaur, R., Gholamhosseini, H. and Sinha, R., "Automatic Lesion Segmentation Using Atrous Convolutional Deep Neural Networks in Dermoscopic Skin Cancer Images Automatic Lesion Segmentation Using Atrous Convolutional Deep Neural Networks in Dermoscopic Skin Cancer Images," 2021.

[6] Jin, Q., Cui, H., Sun, C., Meng, Z. and Su, R., "Cascade knowledge diffusion network for skin lesion diagnosis and segmentation," Appl. Soft Comput., vol. 99, p. 106881, 2021.

[7] Wei, L., Pan, S. X., Nanehkaran, Y. A. and Rajinikanth, V., "An Optimized Method for Skin Cancer Diagnosis Using Modified Thermal Exchange Optimization Algorithm," Comput. Math. Methods Med., vol. 2021, 2021.

[8] Huaping, J., Junlong, Z. and Norouzzadeh Gil Molk, A., "Skin Cancer Detection Using Kernel Fuzzy C-Means and Improved Neural Network Optimization Algorithm," Comput. Intell. Neurosci., vol. 2021, 2021.

[9] Adegun, A., Viriri, S. and Yousaf, M., "A probabilistic-based deep learning model for skin lesion segmentation," Appl. Sci., vol. 11, no. 7, 2021.

[10] Araújo, R. L., Rabelo, R. A. L., and Rodrigues, J. J. P. C., e. Silva, R. R. V., "Automatic segmentation of melanoma skin cancer using transfer learning and fine-tuning," Multimed. Syst., 2020.

[11] Gutman, D., Codella, N. C. F., Celebi, E., Helba, B., Marchetti, M., Mishra, N., Halpern, A., "Skin Lesion Analysis toward Melanoma Detection: A Challenge at the International Symposium on Biomedical Imaging (ISBI) 2016, hosted by the International Skin Imaging Collaboration (ISIC)", 2016.

[12] Jaisakthi, S. M., Mirunalini, P. and Aravindan, C., "Automated skin lesion segmentation of dermoscopic images using GrabCut and kmeans algorithms," *IET Comput. Vis.*, vol. 12, no. 8, pp. 1088–1095, 2018.

[13] Joong Kang, D., "A fast and stable snake algorithm for medical images," *Pattern Recognit. Lett.*, vol. 20, no. 5, pp. 507–512, 1999.

Analysis of the Wing Structure of the Coenonympha Pamphilius Butterfly Species using Atomic Force Microscopy

RASHID DALLAEV[1], ŞTEFAN ŢĂLU[2], TATIANA PISARENKO[1] and VLADIMÍR HOLCMAN[1]

[1] Brno University of Technology, Faculty of Electrical Engineering and Communication, Department of Physics, Technická 2848/8, 61600 Brno, Czech Republic, xdalla03@vut.cz; 177722@vut.cz; holcman@vut.cz

[2] The Technical University of Cluj-Napoca, The Directorate of Research, Development and Innovation Management (DMCDI), 15 C-tin Daicoviciu St., Cluj-Napoca, 400020, Cluj county, Romania, stefan_ta@yahoo.com; stefan.talu@auto.utcluj.ro

***Abstract* - This article shortly describes the structure of the butterflies' wings scales, their variations and properties. Experimental data obtained herein using an atomic force microscope (AFM) instrument sheds some light on the Coenonympha pamphilius scaly wing structure. Coenonympha pamphilus is the smallest butterfly of Satyrinae subfamily and is otherwise known as the 'small heath'. The study of the butterflies' wings structure is important for creation/improvement of photonic crystals which are commonly used in the field of optoelectronics.**

***Keywords* - Atomic force microscopy, butterflies' wings, Coenonympha pamphilius, scanning electron microscopy, surface morphology.**

I. Introduction

More than 150 million years ago and to this day, representatives of this order of insects live on our planet. 160,000 species of butterflies are distributed from cold tundras to hot deserts. Their life cycle is short (a few days), but there are specimens of centenarians Brixton Butterfly that can live up to 10 months. Butterfly wingspan varies from 3 mm to 30 cm (Thysania agrippina). These small insects can reach speeds of 19-50 km/h in flight.

The scales of these insects are basically modified hairs that underwent an evolutionary change, becoming shorter and flatter. The scales have different colors, and their combination creates a bizarre pattern. Recent studies of butterflies' coloration have revealed many optical mechanisms that greatly alter the composition of incident light and reflect bright colors. Pigments are usually the main means of creating color [1]. The fine structure of the scales often creates structural coloration. For example, the bottom plate of the flakes acts generally as a thin-film reflector [2,3]. The stacked lamellas then act as optical multi-layers that create fascinating blue-metallic reflections of the butterflies [4,5]. The physics of wing coloration has been extensively studied and has proven to be quite complex where angle-dependent iridescence is involved due to the unique type of flattened scales [6]. The complex coloration of the wings must be critical for visual signaling, but information on their vision is limited [7].

Butterfly wings are covered with scales of submicron sizes arranged in regular rows across the wing in an overlapping manner. Scales are either pigmentary or optical:

• Pigmentary scales contain pigment (dye), each scale contains only one pigment. Melanin is produced by the butterfly itself and gives the scales black and brown colors. Multi-colored coloring can depend both on the distribution of pigments in scales (pigment grains) and the temperature factor affecting the pupae. It is obtained from substances that were part of the caterpillar's diet.

• Optical flakes are cone-shaped traps for light. White light is refracted in thin scales into individual colored rays of the spectrum. Sunlight falling into a cone-shaped trap is partially absorbed and reflected by it, there is no pigment in them. There are instances where there are no scales on the wings at all and in such case the wings seem completely transparent (for example, the glasswing butterfly).

Scales are equally spaced grooves or pits that separate white light into all its color components, but at a certain angle. Weakening interference destroys all colors except for the desired color, which is intense due to amplifying interference. These flakes are called "submicrometer photonic structures" because they can affect light waves. The deep black that adorns the edges of the butterfly's wings is not the result of black pigment, but of photonic structures that trap light [8].

Butterfly wing scale ultrastructures can take many forms, often resulting in striking coloration in many butterflies due to light interference. The multitude of color mechanisms is amazing, but often only individual mechanisms are described for specific animals. The intriguing use of order and disorder in coupled photonic structures in butterfly wing scales could inspire new optical materials as well as research to develop these nanostructures in vivo [9].

Butterfly wings work wonders with light: from one angle they look one way, and from another they look different. Physicists from China and Malaysia have found that small differences in the structure of the wings determine the variety of their visible shades in various swallowtails. The results of the study are published in the journal Optical Materials

Express [10]. The wings of the swallowtail Blume (Papilio blumei) are green when viewed from above, those of its "cousin" P. peranthus are yellow-green, and those of the sailboat Ulysses (P. ulysses) are turquoise. By measuring the wavelengths reflected from the wing at different viewing angles, the researchers found that the differences in the color of the wings of butterflies are due to differences in the structure - for example, P. ulysses has 7 cuticular layers, and P. peranthus has 8. The cross section of the wings under the scanning electron microscope shows that the cuticular layers of cells with hard shells alternate with air layers, in which cuticular cells also come across. In general, the flakes acquire a crystalline structure, similar to that in a distributed Bragg reflector - a multilayer "mirror" with a variable refractive index [9]. The scanning electron microscopy (SEM) image of P. blumei scale is given in Figure 1.

Figure 1: The scale of P. blumei consists of 7 cuticular layers [9].

II. Experimental Data

The topographic structure of the Coenonympha pamphilius butterfly was observed using atomic force microscopy (AFM) and the results are provided in Figure 2. For data acquisition, an atomic force microscope NTEGRA (NT-MDT production) was used for the surface topography study in semi contact mode with phase imaging, with a Silicon cantilever NSG01 type cantilever, having the tip radius of curvature of 10 nm. When the cantilever is vibrating, the effect of force gradients affects its frequency shift and provides the possibility of non-contact scanning measurement. When the vibrating tip contacts the sample, it is affected to some degree by adhesive, repulsive, and even capillary forces. The interaction between the sample– and the tip then leads to a change in both frequency and phase shift [10,11]. For example, sample inhomogeneity leads to an inhomogeneous change in phase shift (hence the name phase imaging mode). The resolution is mainly affected by the material of the cantilever used for the measurement, the size of the tip, and the speed of the scan.

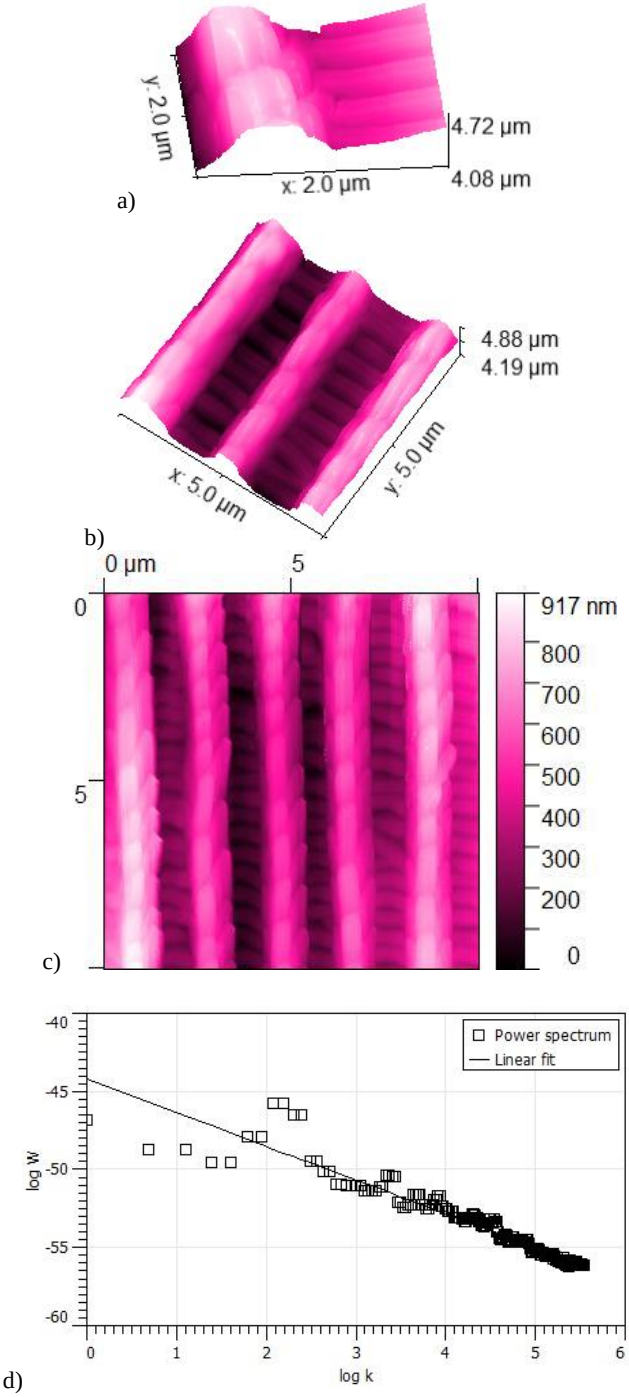

Figure 2: AFM of the Coenonympha pamphilius wing scale: a) 3D image 2x2 µm^2; b) 3D image 5x5 µm^2; c) 2D image 10x10 µm^2; d) Power spectral density (PSD) graph from the c)-image.

According to AFM investigations, butterfly scales frequently include complex nanostructures, such as ridges, grooves, and nanoscale protrusions. These elements are essential for

producing the vibrant hues and visual illusions seen in butterfly wings.

Surface topography were quantified by measuring five locations on regions of each sample. The basic properties of the height values distribution of the surface samples were computed according the Ref. [12] and is given in Table 1. Statistical analyses were performed using the GraphPad InStat version 3.20 computer software package (GraphPad, San Diego, CA, USA).

Table 1: The basic properties of the height values for scanning square areas of 10 µm x 10 µm.

The basic properties of the height values distribution of the surface samples	Sample Values	p values * Values
Mean roughness (Sa) [µm]	0.306±0.011	0.016
Rms roughness (Sq) [µm]	0.391±0.014	0.021
Skew (Ssk) [-]	0.655±0.014	0.025
Kurtosis (Sku) [-]	0.540±0.012	0.022
Maximum peak height (Sp) [µm]	2.231±0.043	0.011
Maximum pit depth (Sv) [µm]	0.885±0.018	0.022
Maximum height (Sz) [µm]	3.116±0.056	0.027
Inclination θ [°]	0.8±0.1	0.012
Inclination φ [°]	-66.58±0.8	0.014

* Statistically significant difference: $p < 0.05$.

In Fig. 3 is shown the height distribution function for a scanning square area of 10 µm x 10 µm (where p is the corresponding quantity), computed as non-cumulative.

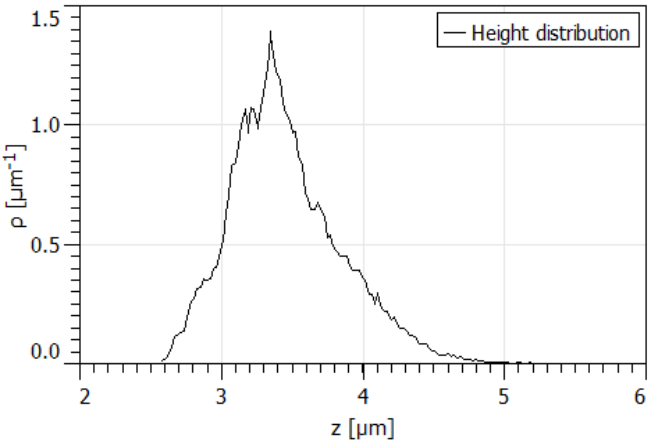

Figure 3: The height distribution function for a scanning square area of 10 µm x 10 µm.

In Fig. 4 is shown the distribution of angles for a scanning square area of 10 µm x 10 µm (where p is the corresponding quantity), computed as non-cumulative.

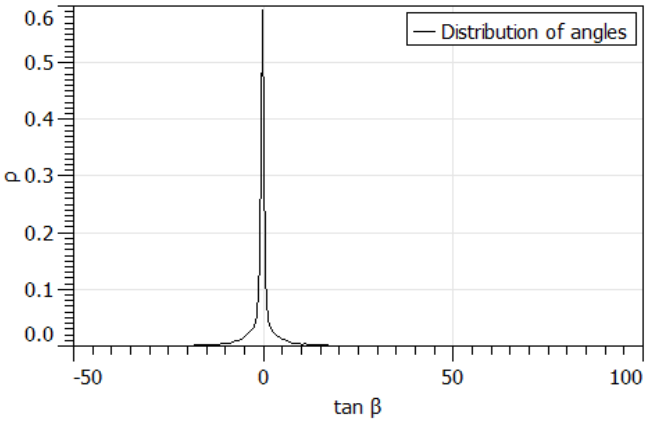

Figure 4: The distribution of angles for a scanning square area of 10 µm x 10 µm.

In Fig. 5 are shown the graphical representations of the autocorrelation function (ACF), the height-height correlation function (HHCF), the radial power spectral density function (PSDF) based on the linear interpolation type, for samples of fig. 1c, in vertical direction: a) ACF curve; b) HHCF curve; c) radial PSDF curve.

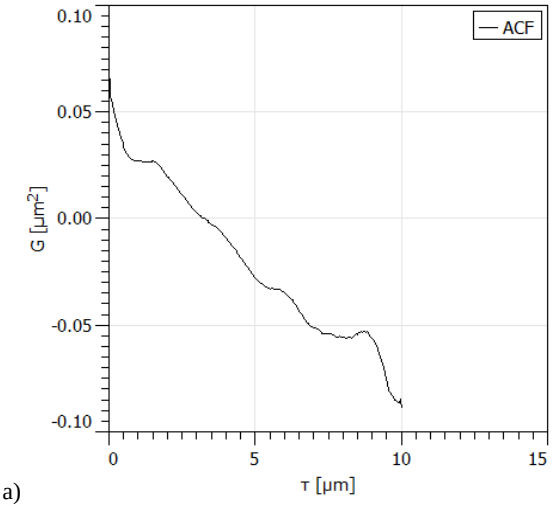

a)

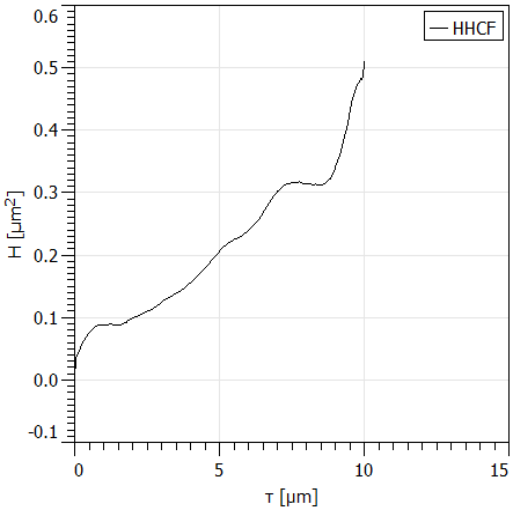

b)

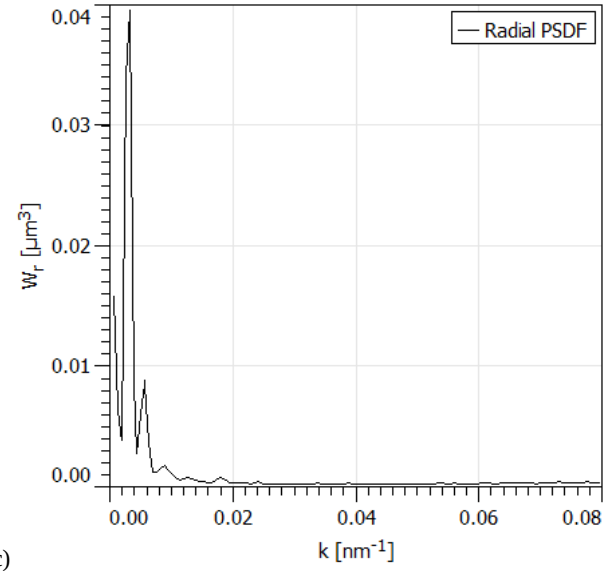

c)

Figure 5: The ACF, HHCF, PSDF curves for a scanning square area of 10 µm x 10 µm.

In Fig. 6 are shown the graphical representations of the angular spectrum, and radial autocorrelation function, for sample of fig. 1c,: a) angular spectrum curve; b) radial ACF curve.

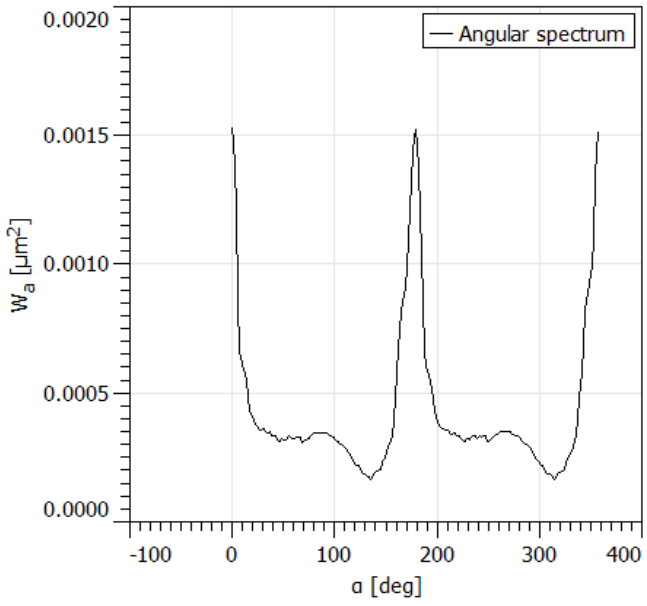

a)

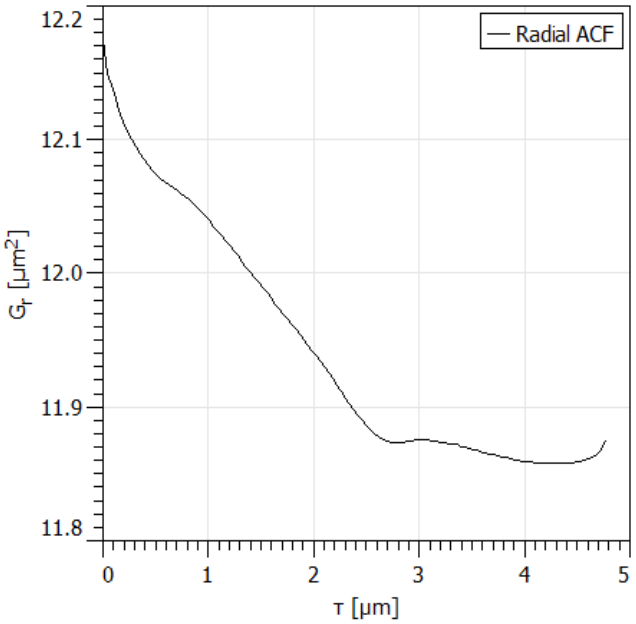

b)

Figure 6: a) The angular spectrum, b) Radial ACF curves for a scanning square area of 10 µm x 10 µm.

Researchers can learn more about the processes underlying the vivid colors and light manipulation in butterflies by studying the topography of scales at the nanoscale. The intricacy of a geometric design or pattern is described mathematically using the idea of fractal dimension [13,14]. Fractal geometry can be used to investigate the complicated patterns and structures that are frequently found on butterfly wings. It is believed that the fractal structure of butterfly wings contributes to a number of biological functions, such as thermoregulation, mate choice, and camouflage. Butterfly wings include intricate patterns and structures that aid in body temperature regulation, blending into their surroundings, and attracting mates. It's crucial to remember that while the idea of fractal dimension offers a numerical gauge of complexity, it doesn't encompass all facets of the complex structures and patterns observed on butterfly wings. These patterns are a product of genetic and environmental influences, and they add to the overall appeal and usefulness of these amazing insects.

III. Conclusion

In this paper, the nature and properties of butterflies' wing was briefly discussed. The experimental part consists of the topographical study of the wings with the use of the AFM method. AFM images revealed the intricate characteristics of Coenonympha pamphilius wing scaly structure, and the surface morphology highlighted the complex wing patterns as well as their effect on the biological functions of butterflies.

Acknowledgment

Research described in the paper was financially supported by the Internal Grant Agency of Brno University of Technology, grant No. FEKT-S-23-8228.

REFERENCES

[1] B. Wijnen, H.L. Leertouwer, and D.G. Stavenga, "Colors and pterin pigmentation of pierid butterfly wings". J. Insect. Physiol., vol. 53, pp. 1206–17, 2007.

[2] D.G. Stavenga, "Thin film and multilayer optics cause structural colors of many insects and birds". Mater. Today Proc., vol. 1S, pp. 109–21, 2014.

[3] B.R. Wasik, S.F. Liew, D.A. Lilien, A.J. Dinwiddie, H. Noh, H. Cao, A. Monteiro, "Artificial selection for structural color on butterfly wings and comparison with natural evolution", Proc. Natl. Acad. Sci. USA., vol. 111, pp. 12109–14, 2014.

[4] B.D. Wilts, H.L. Leertouwer, and D.G. Stavenga, "Imaging scatterometry and microspectrophotometry of lycaenid butterfly wing scales with perforated multilayers". J.R.Soc.Interface., vol. 6, pp. S185–92, 2009.

[5] L.P. Biro, K. Kertesz, Z. Vertesy, G.I. Mark, Z. Balint, V. Lousse, and J. Vigneron, "Living photonic crystals: butterfly scales - Nanostructure and optical properties". Mater. Sci. Eng. C. vol. 27, pp. 941–946, 2007.

[6] D.G. Stavenga, M.A. Giraldo, and H.L. Leertouwer, "Butterfly wing colors: glass scales of Graphium sarpedon cause polarized iridescence and enhance blue/green pigment coloration of the wing membrane". J. Exp. Biol. vol. 213, pp. 1731–1739, 2010. DOI: 10.1242/jeb.041434

[7] E. Eguchi, K. Watanabe, T. Hariyama, and K. Yamamoto, "A comparison of electrophysiologically determined spectral responses in 35 species of lepidoptera". J. Insect Physiol. vol. 28, pp. 675–682, 1982. DOI: 10.1016/0022-1910(82)90145-7.

[8] D. Bergman, "Problems of the theory of sexual selection and neo-Darwinism" Journal of Creation, vol. 18, pp. 112–119, 2004. [Lerner E.D., Blue butterflies // The Industrial Physicist, Briefs, April, 2004].

[9] B.D. Wilts, M.A. Giraldo, and D.G. Stavenga, "Unique wing scale photonics of male Rajah Brooke's birdwing butterflies". Front. Zool., vol. 13, 36, 2016. DOI: 10.1186/s12983-016-0168-7.

[10] P. Kaspar, D. Sobola, P. Sedlak, V. Holcman, and L. Grmela, "Analysis of color shift on butterfly wings by Fourier transform of images from atomic force microscopy". Microsc. Res. Tech., vol. 82, pp. 2007-2013, 2019.

[11] Ş. Ţălu, Micro and nanoscale characterization of three dimensional surfaces. Basics and applications. Napoca Star Publishing House, Cluj-Napoca, Romania, 2015.

[12] Gwyddion 2.62 software (Copyright © 2004-2007, 2009-2014 Petr Klapetek, David Nečas, Christopher Anderson). Available from: http://gwyddion.net (last accessed August 5th, 2023).

[13] Ş. Ţălu, I.A. Morozov, D. Sobola, and P. Škarvada, "Multifractal characterization of butterfly wings scales". Bulletin of Mathematical Biology, vol. 80, no. 11, pp. 2856–2870, 2018. DOI: 10.1007/s11538-018-0490-7.

[14] Z. Garczyk, S. Stach, Ş. Ţălu, D. Sobola, and Z. Wróbel, "Stereometric parameters of butterfly wings". Journal of Biomimetics, Biomaterials and Biomedical Engineering, vol. 31, no. 1, pp. 1-10, 2017. DOI: 10.4028/www.scientific.net/JBBBE.31.1.

The Eye Structure of the Coenonympha Pamphilius Butterfly Species studied by Atomic Force Microscopy

RASHID DALLAEV[1], ŞTEFAN ŢĂLU[2], TATIANA PISARENKO[1], PETR SADOVSKÝ and DINARA SOBOLA[1]

[1] Brno University of Technology, Faculty of Electrical Engineering and Communication, Department of Physics, Technická 2848/8, 61600 Brno, Czech Republic, xdalla03@vut.cz; 177722@vut.cz; petrsad@vut.cz; sobola@vut.cz

[2] The Technical University of Cluj-Napoca, The Directorate of Research, Development and Innovation Management (DMCDI), 15 C-tin Daicoviciu St., Cluj-Napoca, 400020, Cluj county, Romania, stefan_ta@yahoo.com; stefan.talu@auto.utcluj.ro

Abstract **- Butterflies have color vision which they utilize in the search for flowers. There are typically around six difference classes of photoreceptors with specific spectral sensitivities. This paper goes over a typical butterflies' eyes structure as well as their properties. The experimental data obtained using an atomic force microscope was used to investigate the surface characteristics of an eye of Coenonympha pamphilus butterfly species. Coenonympha pamphilus which is also known colloquially as the 'small heath' is the smallest butterfly within Satyrinae subfamily.**

Keywords **- Atomic force microscopy, Coenonympha pamphilius, eye structure, surface morphology.**

I. Introduction

Compound eyes of butterflies are located on the sides of the head and consist of ocelli - ommatidia. Their number can reach several hundreds and even thousands. Each ommatidium consists of an optic and a sensory division. The optical section of the ommatidium consists of a chitinous transparent facet in the form of a hexagon and a crystal cone located under it, which is formed by four elongated transparent cells. The crystal cone is surrounded by pigment cells along the periphery. The sensory part of the ommatidium consists of 4-12 visual retinal cells arranged radially. In the center of the contact of the retinal cells, a visual rod is formed - the rhabdom. The central processes of the visual cells pass into the optic nerve. The retinal cells are also surrounded by pigment cells. Thus, each ommatidium is enclosed in a two-tiered pigment cup, which isolates it from neighboring ommatidia [1]. The structure of a complex compound eye is given in Figure 1.

The convex eyes of butterflies (round or oval) have a complex facet structure. They are located on the sides of the head, composed of individual hexagonal lenses, which can number up to 27,000 ommatidia, transmitting a mosaic image. In some individuals, behind the base of the antennae, near the upper edge of the compound eyes, there may be simple parietal ocelli.

Animals with complex compound eyes are able to increase the diameter of individual eyes to allow more light to enter, as well as reduce their length so that the photon does not have to travel too long to reach the sensitive pigment [2].

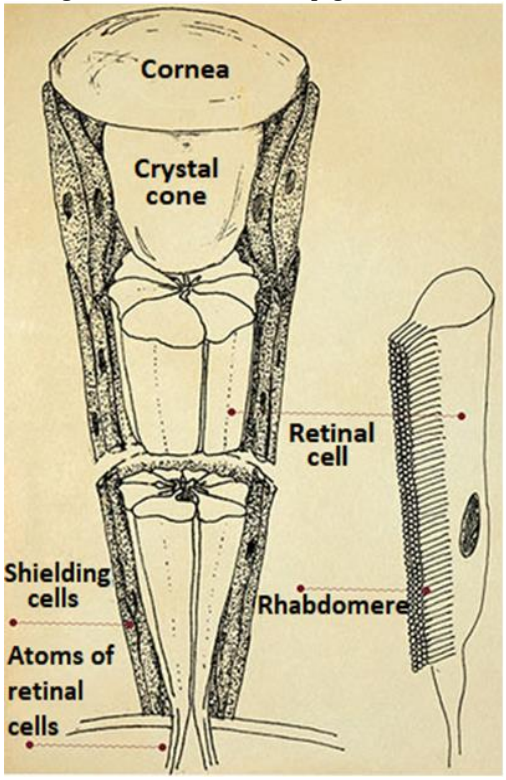

Figure 1: The complex compound eye of an insect consists of separate units - facets (ommatidia). Each ommatidium is a multi-cellular formation that includes dioptric structures (cornea and crystalline cone), photoreceptors - retinal cells with a photosensitive pigment rhodopsin, as well as shielding cells with light-absorbing pigments. Rhodopsin is located in the membrane of many microscopic tubes-villi that make up the rhabdomer. A figure of N. Kryukova. (IS&EZh SB RAS, Novosibirsk).

In different orders of insects, stemma may differ from each other in structure. These differences are possibly associated with their origin from different morphological structures. Thus, the number of neurons in one eye can range from several units to several thousand. Naturally, this affects the perception of the surrounding world by insects: if some of them can only see the movement of light and dark spots, others are able to recognize the size, shape and color of objects [3].

Butterflies and moths often have complex color vision [4, 5]. Their color vision appears to have evolved from an inherited tricolor system based on photoreceptors sensitive to ultraviolet, blue, and green [6,7].

Ommatidium consists of three types of cells that form the optical, sensitive and pigment part. Diurnal insects have the so-called appositional vision. Nocturnal and crepuscular insects have super-positional vision, which is associated with morphological and physiological differences in their ommatidia. In the superposition eye, the sensitive part is more remote from the optical part, and the pigment cells isolate mainly the optical part. Due to this, two types of rays penetrate to the visual stick - straight and oblique; the former enter the ommatidium through its lens, and the latter from neighboring ommatidium, which enhances the light effect [8].

II. Experimental Data

The topographic structure was observed using atomic force microscopy (AFM) and the results are provided in Figure 2. An atomic force microscope NTEGRA (NT-MDT production) was used for data collection in semi contact mode with phase imaging, with a Silicon cantilever NSG01 type cantilever, having the tip radius of curvature of 10 nm. When the cantilever vibrates, the force gradient affects the frequency shift, allowing non-contact scanning measurements. When the vibrating tip contacts the sample, adhesive, repulsive, and even capillary forces act to some extent. The interaction between the sample and the needle changes both the frequency and the phase shift. For example, sample inhomogeneity leads to inhomogeneous changes in phase shift (hence the term "phase imaging mode"). Resolution depends primarily on the cantilever material used for the measurement, the tip size, and the scan speed [9,10].

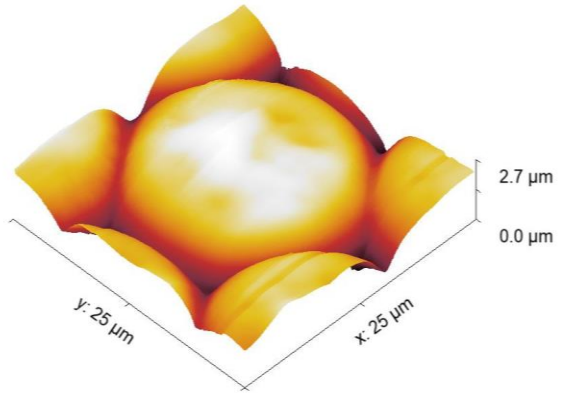

a)

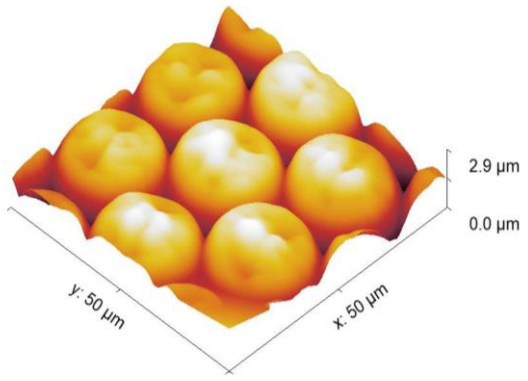

b)

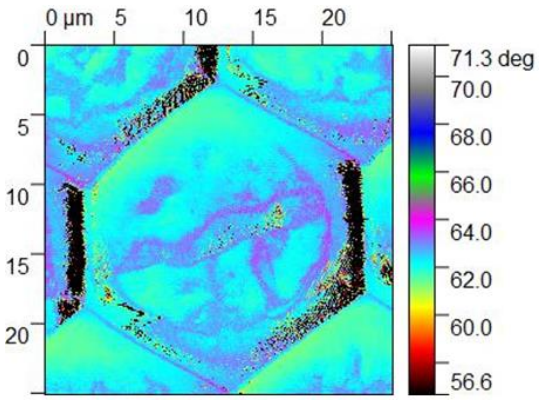

c)

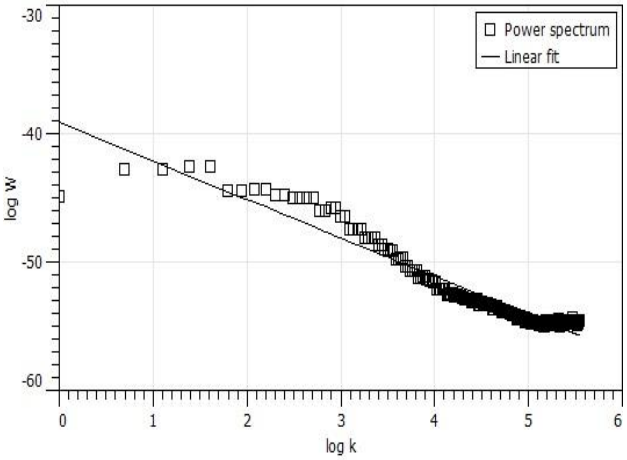

d)

Figure 2: AFM of the Coenonympha pamphilius eyes: a) 3D image 25x25 µm^2; b) 3D image 50x50 µm^2; c) phase-distribution of the area from a)-image; d) Power spectral density (PSD) graph from the b)-image.

Figure 2's photos illustrate the intricate 3D anatomy of the ocular surface using a day butterfly.

Surface topography were quantified by measuring four locations on regions of each sample. The basic properties of the height values distribution of the surface samples were computed according the Ref. [11] and is given in Table 1.

The GraphPad InStat version 3.20 computer software package (GraphPad, San Diego, CA, USA) was used for statistical analyses.

Table 1: The basic properties of the height values for scanning square areas of 50 µm x 50 µm.

The basic properties of the height values distribution of the surface samples	Sample Values	p values * Values
Mean roughness (Sa) [µm]	0.955±0.018	0.018
Rms roughness (Sq) [µm]	1.148±0.021	0.022
Skew (Ssk) [-]	-0.067±0.009	0.023
Kurtosis (Sku) [-]	-0.733±0.015	0.025
Maximum peak height (Sp) [µm]	2.538±0.047	0.027
Maximum pit depth (Sv) [µm]	2.232±0.045	0.026
Maximum height (Sz) [µm]	4.769±0.072	0.027
Inclination θ [°]	4.06±0.4	0.018
Inclination φ [°]	-147.83±1.2	0.023

* Statistically significant difference: $p < 0.05$.

In Fig. 3 is shown the height distribution and cumulative height distribution function for a scanning square area of 50 µm x 50 µm (where p and D are the corresponding quantities).

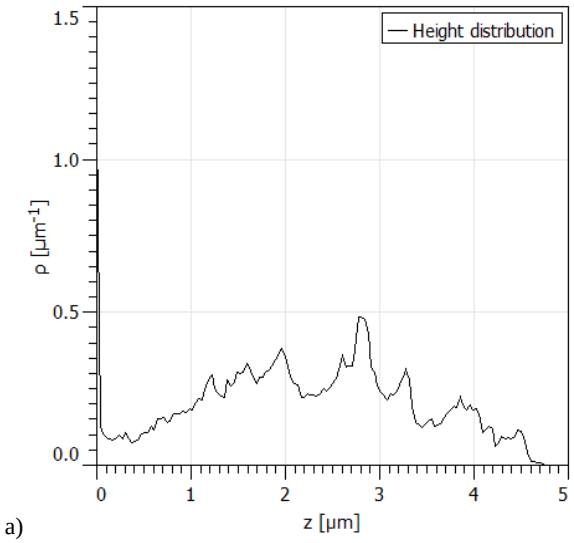

a)

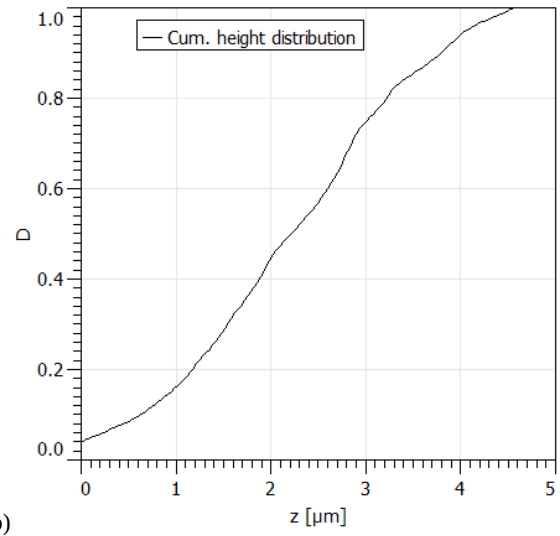

b)

Figure 3: a) The height distribution function, and b) cumulative height distribution, for a scanning square area of 50 µm x 50 µm.

In Fig. 4 is shown the distribution of angles for a scanning square area of 50 µm x 50 µm (where p is the corresponding quantity), computed as non-cumulative.

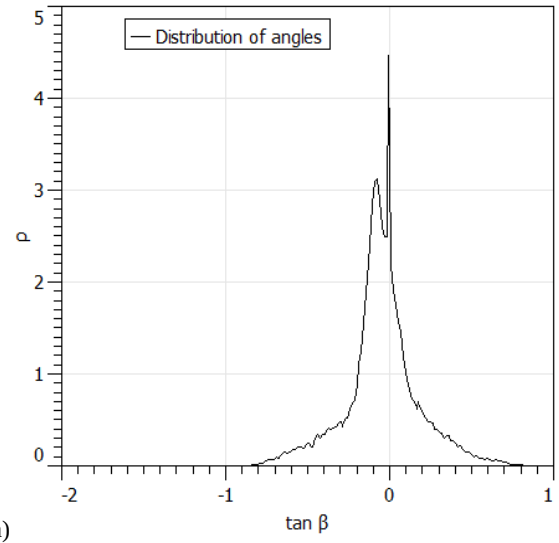

a)

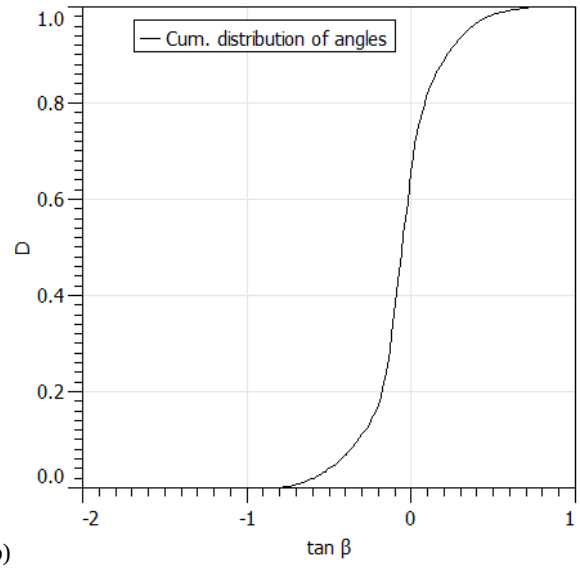

b)

Figure 4: a) The distribution of angles, and b) cumulative distribution of angles, for a scanning square area of 50 µm x 50 µm.

In Fig. 5 are shown the graphical representations of the autocorrelation function (ACF), the height-height correlation function (HHCF), the radial power spectral density function (PSDF) based on the linear interpolation type, for samples of fig. 2b, in vertical direction.: a) ACF curve; b) HHCF curve; c) radial PSDF curve.

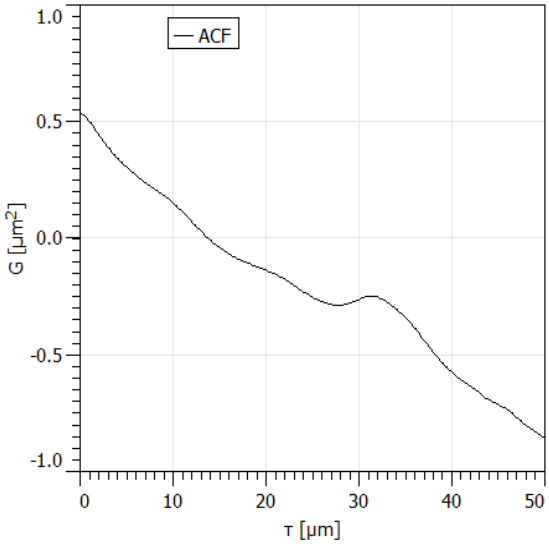

a)

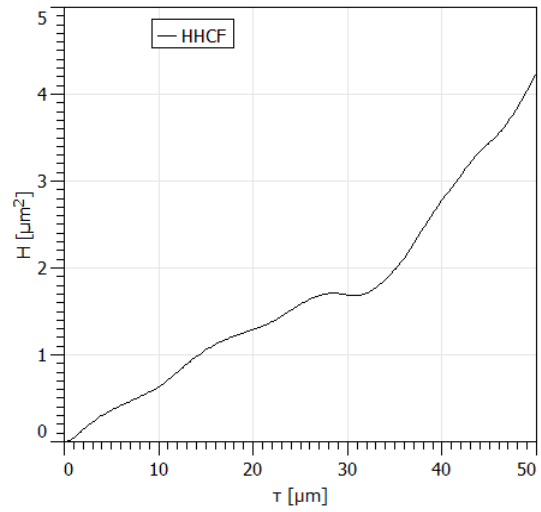

b)

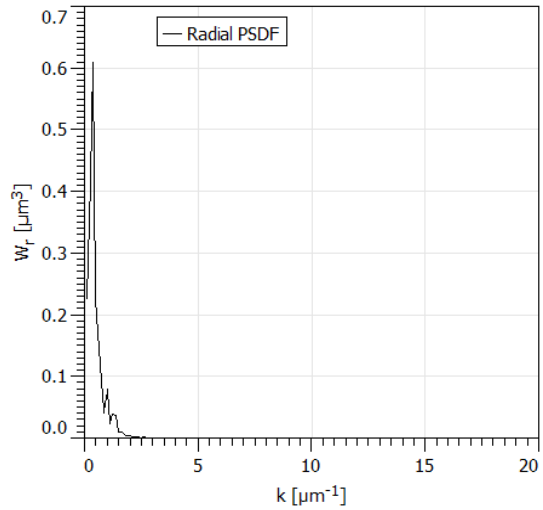

c)

Figure 5: The ACF, HHCF, PSDF curves for a scanning square area of 50 µm x 50 µm.

In Fig. 6 are shown the graphs of the angular spectrum, and radial autocorrelation function, for sample of fig. 2b: a) angular spectrum curve; b) radial ACF curve.

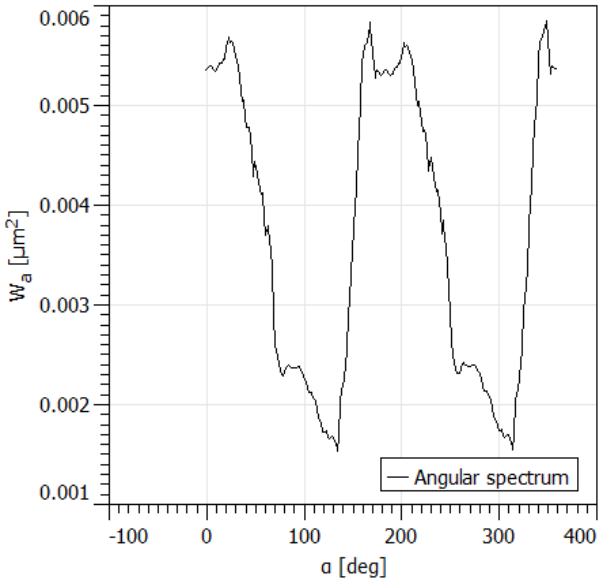

a)

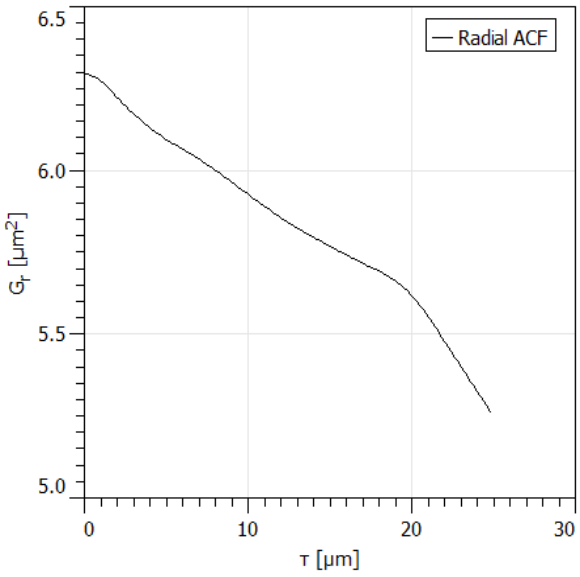

b)

Figure 6: a) The angular spectrum, b) Radial ACF curves for a scanning square area of 50 µm x 50 µm.

In Fig. 7 is shown the range distribution (a plot of the growth of value range depending on the lateral distance).

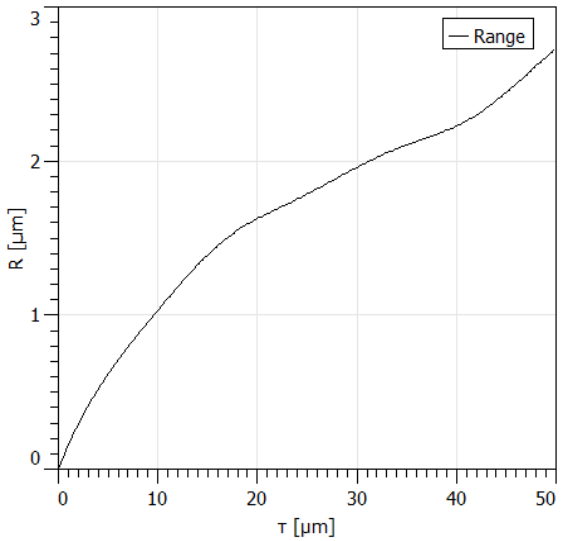

Figure 7: The range distribution curve for a scanning square area of 50 µm x 50 µm.

III. Conclusion

This paper provided a short overview of butterflies' eye structure. The experimental part included a surface analysis of the eyes using the AFM method that revealed the intricate and fascinating patterns of Coenonympha pamphilius eye structure. The results obtained lay a decent ground for future research.

Acknowledgment

Research described in the paper was financially supported by the Internal Grant Agency of Brno University of Technology, grant No. FEKT-S-23-8228.

References

[1] I.Kh. Sharova, "Zoology of invertebrates: Proc. For stud. higher textbook establishments". - M .: Humanit. Ed. center VLADOS, 2002. - 592 pages. ISBN 5-691-00332-1.

[2] S.S. Sponberg, J.P. Dyhr, R.W. Hall, and T.L. Daniel, "Luminance-dependent visual processing enables moth flight in low light", Science, vol. 348, pp. 1245–1248, 2015.

[3] V.C. Glupov, "From the point of view of an insect", Science first hand, no. 2, 2013. URL: https://cyberleninka.ru/article/n/s-tochki-zreniya-nasekomogo.

[4] A. Kelber, M. Pfaff, "True colour vision in the orchard butterfly, Papilio aegeus", Naturwissenschaften, vol. 86, pp. 221–224, 1999.

[5] M. Kinoshita, N. Shimada, K. Arikawa, "Colour vision of the foraging swallowtail butterfly Papilio xuthus", J. Exp. Biol., vol. 202, pp. 95–102, 1999.

[6] D. Peitsch, A. Fietz, H. Hertel, J. Desouza, D.F. Ventura, and R. Menzel, "The spectral input systems of hymenopteran insects and their receptor-based colour vision". J. Comp. Physiol. A, vol. 170, pp. 23–40, 1992. DOI: 10.1007/BF00190398

[7] J.T. Lin, "Identification of photoreceptor locations in the compound eye of Coccinella septempunctata Linnaeus (Coleoptera, Coccinellidae)". J. Insect Physiol., vol. 39, pp. 555–562, 1993.

[8] Online source (last accessed August 5th, 2023). URL: https://studbooks.net/1362779/meditsina/zrenie_nasekomyh_superpozitsionnoe_zrenie_nochnyh_sumerechnyh_nasekomyh

[9] D. Sobola, Ş. Ţălu, S. Shahram, G. Lubomír, "Influence of scanning rate on quality of AFM image: study of surface statistical metrics". Microsc. Res. Tech., vol. 80, no. 12, pp. 1328-1336, 2017. DOI: 10.1002/jemt.22945.

[10] Ş. Ţălu, Micro and nanoscale characterization of three dimensional surfaces. Basics and applications. Napoca Star Publishing House, Cluj-Napoca, Romania, 2015.

[11] Gwyddion 2.62 software (Copyright 2004-2007, 2009-2014 P. Klapetek, D. Nečas, C. Anderson). Available from: http://gwyddion.net (last accessed August 5th, 2023).

IMPLEMENTATION OF SECURE VOTING SYSTEM USING BLOCKCHAIN

Omar Ahmed Salad
Graduate school of science
Master Degree of Cybersecurity
Uskudar University
Street. No:04 PK:34672 Uskudar / Istanbul

***Abstract*__ To implement secure voting system using blockchain technology is ensure to make the current voting process to take place in an honest, accurate and highly secure way to trust all the participants include candidates and voters. This system stores the details of candidates and voters in blockchains which provides transparency into election result by allowing voters independently vote while protecting each voter's right to privacy and protect the integrity of your vote by preventing voters from being able to vote multiple times. The blockchain is a new technology that is decentralized, distributed, and has strong cryptographic foundations. It has the potential to enhance numerous sectors in various ways. The current security challenges with voting could be resolved by incorporating blockchain technology into the process, however, I build electronic voting system based on blockchain technology that will reduce voting fraud and make the voting process quick, safe, and effective.**

Keywords*: Blockchain, Electronic voting, Decentralized, Security*

i. INTRODUCTION

The internet is the greatest invention that humankind has ever made. However, there are several shortcomings with the internet. Think of a circumstance where you are depositing money or casting a vote, there is a single point of authority and security challenges, and we are expected to trust him or her with our information, money, or vote. A single point of control or failure is the current system's limitations. The Authority might or might not be dishonest or corrupt. The solution of this problem is to employ decentralized and distributed system where the consensus of the users and peers is used to evaluate the transactions, votes, and data. Voting fraud is a concern on several fronts, including fake voters and fraud in the pooling booths. Consequently, the need for the creation of a secure, decentralized, fraud-free voting system arose. Blockchain-based decentralized voting systems can also resolve all the problems with current voting methods.

A blockchain is a collection of blocks connected with chains using cryptography. Blockchain is the one of the best emerging technologies with the strong cryptographic foundations that allow apps to take advantage of these capabilities to produce resilient security solutions. In this case, the data is broken up into blocks and connected via links. Each block has a hash value that identifies it, and the link between them is created by putting the previous block's hash in the current block. In summary, a block consists of the data section, hash, and previous hash.

The chain of blocks that has been formed no longer gets kept in a single machine. Each user of the blockchain, also known as the Distributed Ledger, has their own copy. When someone tries to alter the data, the hash value is altered, the link is broken, and the hash value is altered. The attacker must modify and recalculate the hashes of succeeding blocks in order for the attack to succeed. Users curate each block once it is made depending on their consensus, and each block can either be accepted or rejected. Consequently, security, immutability, and transparency are provided by blockchains. However, blockchain can be studied as a database that can be analyzed as a distributed database with many users. Each user received a portion of the essential.

A. Key features of Blockchain

- High availability
- Verifiability
- Transparency
- Immutability
- Distributed ledger
- Decentralized

- Enhanced security

My research focuses on looking at important topics including end-to-end verification, voter anonymity, and vote secrecy. These issues serve as the cornerstone of an effective voting system that protects the fairness of the electoral process and makes use of the open source Ethereum blockchain technology. The system generates a strong cryptographic hash for each vote transaction based on information specific to a voter in order to protect the anonymity and integrity of a vote. In order to assist verification, this hash is also sent to the voter over encrypted channels. Therefore, the system complies with the fundamental requirements of an electronic voting system and all these features serve the implementation of secure voting system.

ii. RELATED WORK

A. Survey Existing Voting systems

[1] "Security analysis of India's electronic voting machines" Election is a highly essential event in a modern democracy; however, many people don't trust their election system, which is a concern for the democracy. Even India, the U.S., and Japan have defective electoral systems. Vote rigging, EVM hacking, election manipulation, and polling booth capturing are difficulties with the existing voting system. In this study, we investigate challenges in electoral voting systems and suggest E-voting to fix them. This article evaluates blockchain as a service for distributed electronic voting systems.

The article discusses prominent blockchain frameworks that offer blockchain as a service and an electronic E-voting system based on blockchain that addresses all restrictions and preserves participant anonymity while remaining available to public inspection.

In this paper [1], it has highlighted about the major problem in voting security in India Presidential Elections, EVM's were likely to be intercepted and votes were tampered.

The study found that this old voting equipment is not only more prone to failures and crashes

but is also notoriously easy to hack and tamper with.

[2] "A conceptual secure blockchain-based electronic voting system" Blockchain allows for new digital services to securely make transaction along with hidden identities and ownership, while research is still evolving, it has primarily focused on technological and legal difficulties instead of using this innovative concept to create enhanced digital services. In this article, we will use Blockchain to develop a new electronic voting system for municipal or national elections. The secure, dependable, and anonymous Blockchain-based system will enhance voting turnout and faith in governments.

Ayed, Ahmed, et al. [2] suggested a Blockchain-based electronic voting system. Decentralized, trust-free system. Any registered voter can vote online with any device. The Blockchain will be publicly verifiable and uncorrectable. Rifa and Budi concluded that using hash values to record vote results from each linked polling station makes the system more secure and digital signatures make it more dependable.

[3] "Blockchain Based E-voting recording system design" Digital technology now helps many people, unlike the election system, it employs many research papers extensively. Traditional elections threaten security and transparency (offline). General elections are still managed by one body. With an organization that has full control over the database and system, it's conceivable to tamper with the database. Blockchain technology is a solution because it's decentralized and owned by many users. The decentralized Bitcoin Bank uses blockchain. Blockchain can reduce one source of database manipulation cheating in e-voting systems.

This research discusses the recording of voting result using blockchain algorithm from every place of election. Unlike Bitcoin with its Proof of Work, this paper proposed a method based on a predetermined turn on the system for each node in the built of blockchain. The use of the sequence proposed in the blockchain creation process in this system considers that in an electoral system not required for mining as in the Bitcoin system because the voter data and numbers are clear and are not allowed to select more than once, the proposed sequence

ensures that all nodes Which is legally connected and can avoid collision in transportation [3].

[4] "Platform-independent Secure Blockchain-Based Voting System" Cryptography is used to secure voting systems to boost their use. All participants in electronic voting systems should trust the third party's public bulletin board for posting and auditing voting results. Recently, several blockchain-based solutions have been proposed. These systems are impracticable because to the limited voter and candidate numbers supported and their security architecture, which depends on the underlying blockchain protocol and is vulnerable to attacks (e.g., force-abstention attacks). we propose a platform-independent secure and verifiable voting system that can be deployed on any blockchain that supports smart contract execution. Verifiability is given by the blockchain platform, but cryptographic techniques like Paillier encryption, proof-of-knowledge, and linkable ring signature provide system security and user privacy independent of the blockchain platform's security and privacy characteristics. We test the correctness and coercion resistance of our voting mechanism. We deploy and analyze our voting system using Hyperledger Fabric.

Bin, Joseph, et al. concluded that the current blockchain voting system cannot provide comprehensive security features, and most of them are platform-dependent. We proposed a blockchain-based voting system that guarantees voters' privacy and voting correctness by homomorphic encryption, linkable ring signature, and PoKs between the voter and blockchain [4].

[5] "Decentralized Voting Platform Based on Ethereum Blockchain" Voters have always questioned and perceived differently the results of centralized voting events. Most E-Voting systems are centralized; therefore, voters must trust the organizational authority for the results' integrity. In this paper, we propose a decentralized trustless voting mechanism based on Blockchain technology. This approach ensures data accuracy and transparency and allows only one vote per cell phone number every poll, with privacy guaranteed. To do this, organizers will install transparent, consistent, and deterministic smart contracts on Ethereum Virtual Machine (EVM) for each vote event to run the voting rules. Without a third-party server, users are authenticated by their mobile phone numbers. The results demonstrated that the system is viable and may lead to optimum surroundings for such experiences.

David Khoury,Elie F. Kfoury, Ali Kassem, and Hamza Harb,2018 "Decentralized Voting Platform Based on Ethereum Blockchain", Department of Computer Science American University of Science and Technology, propose a novel approach for a decentralized trustless voting platform that relies on Block-chain technology to solve the trust issues. This approach ensures data accuracy and transparency and allows only one vote per cell phone number every poll, with privacy guaranteed. EVM is employed as the Blockchain runtime environment. [5]

[6] "Online Voting system using blockchain" Creating a new voting system while considering legal issues is difficult. Old systems and computer technologies have proven vulnerable to threats, increasing the demand for new technology. Block chain provides several advantages over current approaches. Our electronic voting system will test blockchain's features. We propose a new block chain-based decentralized electronic voting system that fixes all the existing system's flaws.

Vaibhav Anasune, Pradeep Choudhari, Madhura Kelapure, and Pranali Shirke Prasad Halgaonkar, "Online Voting: Voting System Using B-chain," 2019, paper presents a quick assessment on current voting methods. The study will assist develop a system that can tackle present and future issues and remove disadvantages from past systems. [6]

B. Disadvantages of existing Voting Systems

1. Centralized architecture for most systems
2. Attack prone
3. Not trustable
4. Non-transparent vote casting process

A democratic society must include the right to vote. Voting is a vital decision-making process, and security is crucial. Current voting systems include:

1. *Ballot system* - There was a paper-based voting method in place in India before to 2004. This approach is known as

a paper ballot system. The voters use it while it is set up in the polling site.

2. *Electronic voting system* - In order to overcome duplication and damage of ballot problems and Electronic Voting Machines Were introduced. It stores and assembles votes, used by poll workers.
3. *Current digital voting system*- There are currently a number of digital voting systems in operation in various nations.

C. Proposed Voting System

I 've proposed to design a voting system which integrated with blockchain technology. The proposed system has the following advantages as compared to the existing system as discussed on the last page.

- Authentication - only registered voters can only vote.
- Prevention of evidence deletion and transparency with privacy.
- Accuracy: Votes once cast are permanently recorded and cannot be modified or changed under any circumstances.
- Verifiability – the system is verifiable such that the number of votes is counted
- Users' can vote from anywhere in the world until he possess a citizenship of the country.
- The voting is stored in the blockchain which makes it tamper proof.
- As there's no standing in queue for casting vote that will save a lot of time and reduce the workload.

iii. METHODOLOGY

This project will be a web application with front end, back end and database. Registration of voters and candidates must be done in advance. Personal verification must be done before creating accounts. After verifying the identity document, the authorized person must verify the eligible users by proving a coin or token Using this coin or token each user can vote only once. The Blockchain verification process will ensure that dual use of this symbol is not possible. So, any user cannot vote multiple times. The blockchain-based e-voting system has been expanded. There is no central authority to conduct elections. Votes are cryptographically protected.

An app dedicated to electronic voting, or dApp, built into the Ethereum blockchain. A smart Ethereum contract was signed with Solidity to get the votes cast. User communication on the client side is designed to use Ethereum accounts for voting.

A. Flowchart of the project

Here is overall flowchart of the project.

1) Admin Block Diagram

The admin will manage the voters and candidates, the user will cast his vote, Only the voters who are registered will be eligible for voting**.**

Figure 3.1 admin flowchart

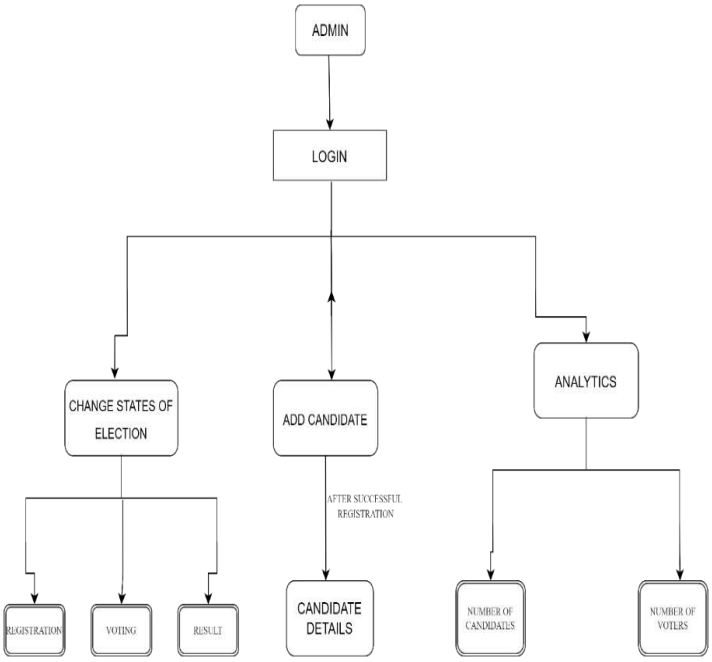

2) User Block Diagram

In the figure below is a User that registers himself to cast a vote to the political party and also has a capability to vote after successful registration.

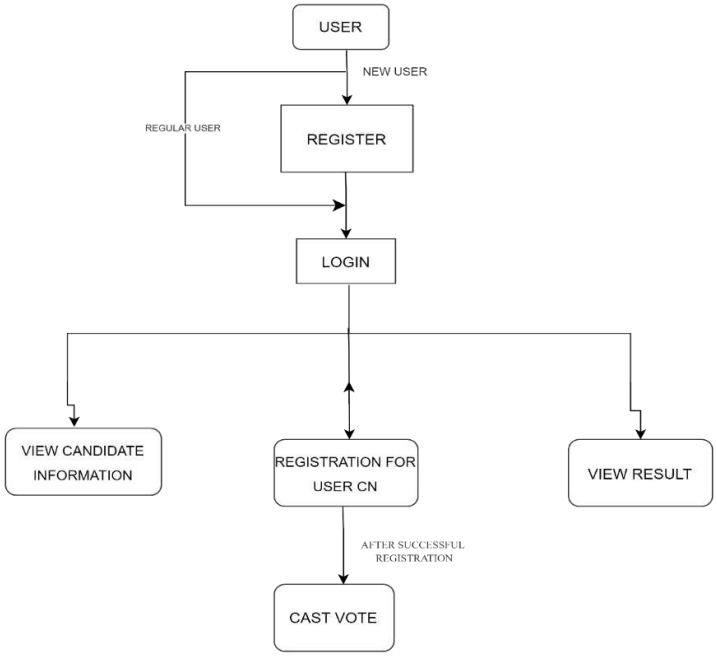

F-gure3.2 user flowchart

B. Modules

The project has been divided into many modules in which for every functionality we have designed modules. Any software consists of a number of systems, each of which has a number of subsystems, each of which has its own subsystems, and so on. Therefore, building a whole system at once that includes all necessary capabilities is a laborious task that, due to the process's immense complexity, may contain numerous faults. Effective modular design can be achieved if the partitioned modules are separately solvable, modifiable as well as compliable. Following are the two modules of the system:

1) ***Admin Module*:** the admin module will divide into 5 components:

Dashboard: it will contain various charts to display information such as number of candidates and number of voters

Add Candidates: in this feature admin can add candidates who are representing to the political party in the election.

Change State: in this feature admin can also updates the states of the election in the three phases registration, voting and result of the election.

Candidate details: in the candidate details, all candidates added by the admin will be displayed and admin can update the candidates' details if wrong entry made.

Analytics: in the section, admin will oversee the candidate votes and how many voters casted their vote to the political party

2) ***User Module**:* The User module will also divide into five components:

Dashboard: the user dashboard contains information about parties and their candidates. User can see all information of the candidates.

Voter registration: user will register himself by using his or her citizen number, then he will be able to cast his vote.

Voting area: After user is registered, the he will be redirected in this page, then he can cast his vote.

Result: in this component the user will be able to see the result of the election.

About: in this section, the user can read all steps to follow to cast a vote in the election. All phases election mentioned in this page to guide the new user.

C. Software requirements

- Operating system: window 7 and above operating systems.
- Development environment: Solidity programming, web Development (CSS, HTML, JAVA SCRIPT).
- Scripting language: Solidity programming language.
- Decentralized application: Ethereum framework i.e., Truffle and Ganache.
- Browser: google chrome.
- Adds-on in browser: MetaMask.
- Software: visual studio or similar IDE.

D. User requirements

The program works by considering the input from the user as he/she need to prove his identity.

- Browser: Google Chrome

- Adds-on Browser: MetaMask and Internet connectivity.

iv. RESULTS

In this project I used React.js for developing front-end and solidity to write smart contracts. I used MetaMask wallet for performing transactions using Ether. The application is working and is deployed on personal Blockchain called Ganache. the transactions in the application are immutable, transparent and are completely secured.

Figure 1 HomePage

This is the Homepage of the Electronic Voting web application where there are User Login and Admin Login.

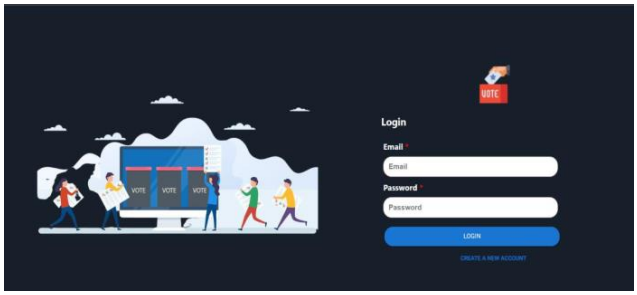

Figure 2 User Login

User need to create his account by providing his Email Id and a unique Password.

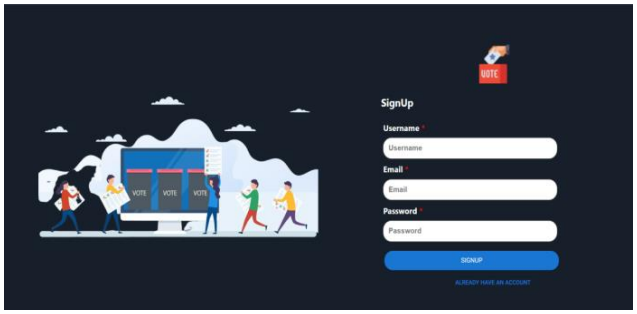

Figure 3 Sign Up

If a user is new to the website, he/she must create a new account by providing Username, Email Id and password. If Email Id already exists then the website will not allow user to create the account.

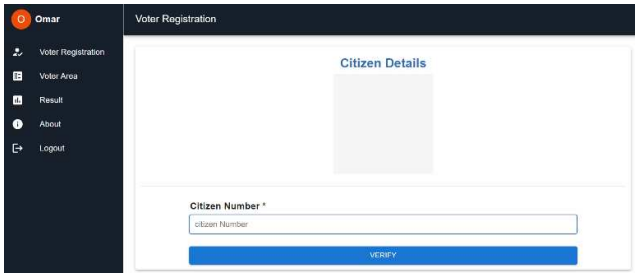

Figure 4 User Dashboard

Once the User login successfully the User will be redirected to User Dashboard, after that User need to provide his/her citizen details to be eligible for voting. The admin will check age from Citizen Details and may allow the user to cast the vote if eligible else will be rejected as well.

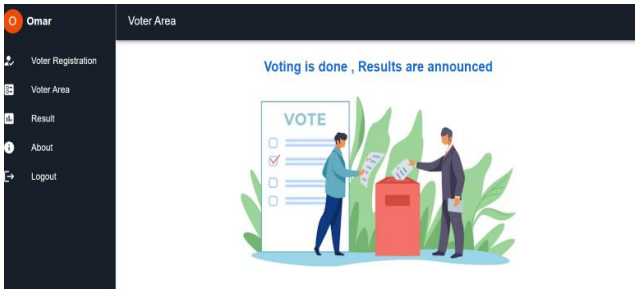

Figure 5 Voter Area

This is the area where User will cast his vote once the time has come for Elections. The candidates who are participating in election will be displayed here.

Figure 6 Result of Voting

The Result page is where the candidate who won in the Election will be displayed and also shows how many votes each Candidate got in the Election.

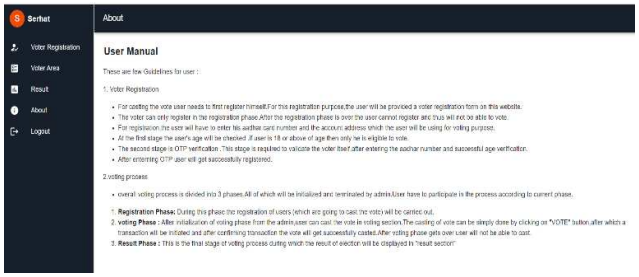

Figure 7 About page

This is the Page for User refrence where is given a clear idea for the user how election process carry on.

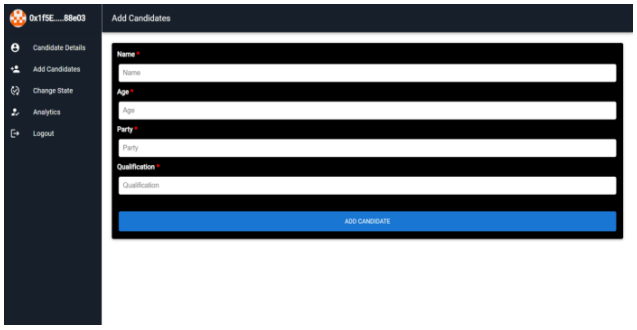

Figure 8 Add candidate

This is the Admin dashboard where the new candidates from the Parties will be added by the Admin by filling up the above informations.

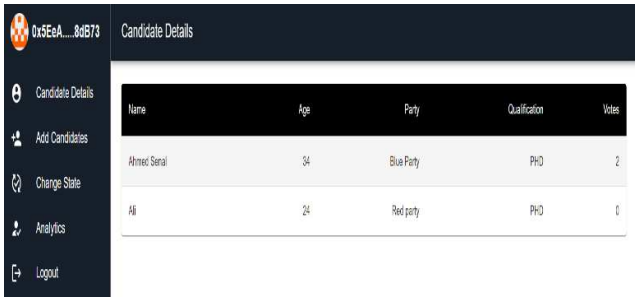

Figure 9 Candidate Details

Once the Admin added a Candidate, the Candidate details will be shown in the candidate Details page.

The attributes are the Name, Age, Party Name, Qualifications and No of votes he found.

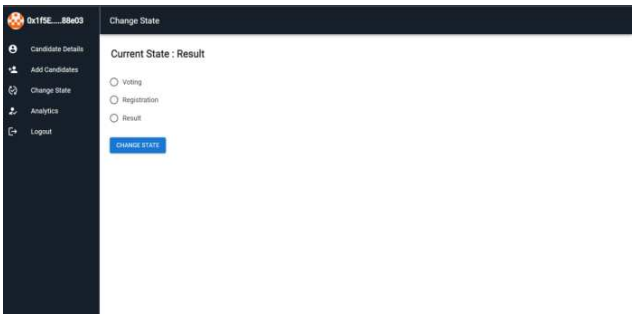

Figure 10 Change State

This is the area where the Admin will change the Phase of Election to Registration, Voting and Result state.

If the state is Registration means the Admin is adding the eligible candidates for Election where the User can see the Candidate details and aslo can see vote button.

If the state is Voting implies that the users can cast their vote and keep in mind that a user can cast vote once in the Election.

If the state is Result means that the Election is completed and the results are announced where user or voters can see the result from user result page.

Figure 11 Analytics of Voting

This is the page which describes the totol number of candidates and totl votes casted as of now.

The graph show shows how got more votes with the particular time.

v. CONCLUSION

Any democracy needs an honest and trustworthy voting process. A strong democracy depends on reliable elections, thus voters must have faith in the electoral process, however, this project has been developed to a Blockchian-based electronic voting system that utilizes smart contract to enable secure and cost-efficient while guaranteeing voters privacy. It outlines the

systems design and architecture, implementation of the project and the security analysis of the system.

Traditional paper-based elections, however, do not offer credibility. In contemporary culture, the idea of modifying digital voting technologies to simplify, speed up, and reduce the cost of the public political process is appealing.

Making the voting process quick and inexpensive normalizes it in the eyes of the electorate, lowers the power barrier between the electorate and the elected officials, and exerts some pressure on them. Additionally, it makes way for a more direct form of democracy by enabling citizens to voice their opinions on particular proposals and bills.

User votes are cryptographically protected, once the votes have been saved they have not changed and there is evidence of disruption and the system maintains voter privacy and anonymity and also promotes the transparency. Finally system allows for quick result and publicly auditable.

REFERENCES

[1] Ohlin, Jens David. "Did Russian cyber interference in the 2016 election violate international
law." Tex. L. Rev. 95 (2016): 1579.

[2] Ayed, Ahmed Ben. "A conceptual secure blockchain-based electronic voting system."
International Journal of Network Security & Its Applications 9.3 (2017): 01-09.

[3] Hanifatunnisa, Rifa, and Budi Rahardjo. "Blockchain based e-voting recording system
design." 2017 11th International Conference on Telecommunication Systems Services and
Applications. IEEE, 2017.

[4] Yu, Bin, et al. "Platform-independent secure blockchain-based voting system."
International Conference on Information Security. Springer, Cham, 2018.

[5] David Khoury,Elie F. Kfoury, Ali Kassem and Hamza Harb,(2018), Decentralized Voting Platform Based on Ethereum Blockchain.

[6] Vaibhav Anasune, Pradeep Choudhari, Madhura Kelapure and Pranali Shirke Prasad Halgaonkar,"Online Voting: Voting System Using B-chain" ,(2019), Online Voting: Voting System Using Blockchain.

Breakdown Prediction with Machine Learning Methods

A.MURZAEVA[1], S.ILHAN OMURCA[2], B.OZSOY[3], K.Y.KOC[4], E.DENIZ[5], M.GUNDOGDU [6]

[1]IBSS Technology and Software, Istanbul/Turkey, azhar.murzaeva@ibss.com.tr
[2] Kocaeli University, Kocaeli/Turkey, silhan@gmail.com
[3]IBSS Technology and Software, Istanbul/Turkey, berk.ozsoy@ibss.com.tr
[4]IBSS Technology and Software, Istanbul/Turkey, kadiryunus.koc@ibss.com.tr
[5]IBSS Technology and Software, Istanbul/Turkey, enes.deniz@ibss.com.tr
[6]IBSS Technology and Software, Istanbul/Turkey, muhammed.gundogdu@ibss.com.tr

In factories, the cessation of manufacturing processes due to machine breakdowns is an undesirable situation for companies. It is crucial to swiftly understand and resolve the issue in case of a breakdown. However, this often takes considerable time, causing financial losses to companies. Artificial intelligence is being considered to predict machine failures in advance.

This study aims to design a system that anticipates breakdown situations in factory manufacturing lines. The goal is for this product to be sustainable and adaptable to changes in manufacturing lines, with the potential for application in similar product groups. This study involves innovative solutions such as a Predictive Maintenance System, enabling authorized personnel to monitor the operational status of machines. It encompasses alerting authorized personnel when machines are nearing breakdown conditions.

In the modeling processes, we use some fundamental models based on classical machine learning methods (Support Vector Machines (SVM), Decision Trees (DT), etc.) for classification purposes. Additionally, Bagging algorithms such as Random Forest and Boosting algorithms like XGBoost, Gradient Boosting, and AdaBoost were applied. These methods were utilized for testing and enhancing the fundamental models, aiming to achieve fast and robust models. Models with high performance were integrated into the system for practical use.

Keywords: breakdown prediction, machine learning in manufacturing, manufacturing production line breakdowns, predictive maintenance.

I. INTRODUCTION

In the manufacturing sector, the impact of errors arising from production processes on processes and costs is significant. After Industry 4.0, companies have been undergoing a process of automation, and as a result, they are working to reduce the costs and losses incurred due to breakdowns in the production process. These efforts aim to eliminate downtime and slowdowns caused by breakdowns in the manufacturing sector by making predictions about these breakdowns.

The big amount of data, collected by industrial systems, contains information about processes, events and alarms that occur along an industrial production line. Moreover, when processed and analyzed, these data can bring out valuable information and knowledge from manufacturing process and system dynamics. By applying analytic approaches based on data, it is possible to find interpretive results for strategic decision-making, providing advantages such as, maintenance cost reduction, machine fault reduction, repair stop reduction, spare parts inventory reduction, spare part life increasing, increased production, improvement in operator safety, repair verification, overall profit, among others [1].

Predictive maintenance approaches able to monitor equipment conditions for diagnostic and prognostic purposes can be grouped into three main categories: statistical approaches, artificial intelligence approaches and model-based approaches. As model-based approaches need mechanistic knowledge and theory of the equipment to be monitored, and statistical approaches require mathematical background, artificial intelligence approaches have been increasingly applied in PdM applications [2]. ML approaches have the ability to handle high dimensional and multivariate data, and to extract hidden relationships within data in complex and dynamic environments (such as, industrial environments) [3].

Predictive maintenance is one of the manufacturing areas that Industry 4.0 is introducing the use of computers and digitalization in [4, 5] and prognostics and health management (PHM) has become an obvious for smart industrial evolution; moreover, it provides a dependable solution for managing the health state of industrial equipment. Maintenance is vital since it extends the lifetime of an equipment. A system's lifespan can be prolonged by implementing maintenance. Maintenance should be scheduled ahead of time with a precise prediction of the machine failure for avoiding the accidents in production line and to reduce the economic loss. Predictive Maintenance (PdM) is widely employed in a variety of industries, including manufacturing [6, 7], car [8], and aerospace [9]. Engineering tools working well in anticipating the failure time of equipment in advance. Furthermore, PdM is supposed to foresees the failure precisely [10, 11]. Data flexibility is viewed by PdM as a significant concern that could impair algorithm performance for data driven modeling [12].

Using data from machine-attached sensors and training AI models with breakdown records, we aim to demonstrate that this project not only achieved a 48% efficiency rate in the first

quarter of 2020 but also experienced only approximately a 7% efficiency loss during the same period. The ultimate goal of this project is to predict breakdown situations with a 90% accuracy rate. Through the integration of AI technologies, we strive to attain the desired precision, achieve higher success rates, and expedite critical production processes.

In our study, we aimed to design a system that predicts possible failure scenarios in factory production lines for a Turkish company, which is a leading manufacturer in the consumer electronics and white goods industry. We applied Logistic Regression, Decision Tree, Support Vector Machine (SVM), Random Forest, Gradient Boosting, XGBoost (eXtreme Gradient Boosting), AdaBoost (Adaptive Boosting) algorithms, which are machine learning methods, for failure prediction. The main motivation of the study is to create a system that is sustainable, can adapt to changes in production lines, and has the potential to be applied to similar product groups. This work includes innovative solutions such as the Predictive Maintenance System, which allows authorized personnel to monitor the operational status of machines and alert them when machines are approaching failure.

II. Material and Methods

In this section, the applied machine learning methods and the dataset used are explained briefly.

2.1. Data Collection

The experiments are conducted on a real world dataset taken from a leading Turkish home and professional appliances manufacturing company. This dataset consists of data collected by the company from its production line between June 06, 2022, and July 28, 2022. There are a total of 31,662 records in the dataset. The data records include oil temperature and pressure information from six different hydraulic tanks on the production line. Additionally, it contains data on the operating cycles of 12 different stations, uncoil alarms, tox alarms, line alarms, product model numbers, and production quantities.

The dataset comprises 12 oil temperature and pressure features from six different hydraulic tanks. Furthermore, it includes information on the operating cycles of 17 different stations and represents product model numbers using the one-hot encoding method. According to the information provided by the company, it is noted that changes in the values of these selected features affect three different alarms: LINE, TOX, and UNCOIL. Since all UNCOIL alarm values are 0 (zero), this alarm information has been excluded from the model evaluation studies. Additionally, the company has shared that LINE alarm status is more critical and important that TOX and UNCOIL alarm statuses.

Throughout this study, it was noted that the data preprocessing steps involved removing non-alarm situations and organizing the data. Three different datasets were created based on different types of alarms: LINE or TOX alarm, only LINE alarm, and only TOX alarm. The proposed models were used to predict the LINE and TOX alarms occurring on the production line.

The feature information in Dataset-1 (DS1) corresponds to LINE or TOX alarms. Dataset-1 is the dataset where data records are marked as faulty if there is a fault indication in any of the LINE or TOX alarm values associated with the data. Dataset-2 (DS2) contains LINE alarms, and Dataset-3 (DS3) pertains to TOX alarms. An example of the data content is presented in Figure 2.1. The "LINE_ALARM" state in the figure is a label indicating whether there is a LINE alarm (a value of 1 means "alarm present," and 0 means "no alarm"). In other cases, the fault condition is similarly indicated.

	STATION_10_CYCLE_TIME	STATION_11_CYCLE_TIME	STATION_12_CYCLE_TIME	...	MODELNO_4	MODELNO_5	LINE_ALARM
0	-7328.409576	-6444.297581	-6534.090045	...	0	0	1
1	-7328.409576	-6444.297581	-6534.090045	...	0	0	0
2	-7328.409576	-6444.297581	-6534.090045	...	0	0	0
3	-7328.409576	-6444.297581	-6534.090045	...	0	0	0
4	-7328.409576	-6444.297581	-6534.090045	...	0	0	0
...	...	...	...	...	...	...	...
31657	-200.409576	526.702419	425.909955	...	0	0	0
31658	-125.409576	523.702419	422.909955	...	0	0	0
31659	-125.409576	523.702419	422.909955	...	0	0	0
31660	-254.409576	504.702419	392.909955	...	0	0	0
31661	-192.409576	493.702419	425.909955	...	0	0	0

31662 rows × 35 columns

Figure 2.1: Example values included in the dataset created based on LINE alarms.

2.2. Machine Learning Methods

2.2.1 Logistic Regression

Logistic regression is a binary classification algorithm that maps the input features to a predicted output variable. Due to its ease of implementation, it has been commonly used for several binary classification tasks, such as failure prediction. Logistic regression explores the relationship between one or more independent variables and predicts a dependent variable.

2.2.2 Decision Tree

Decision tree is one of the widely used algorithms both for classification and regression. The algorithm's popularity is increased due to its ability to represent information, produce easily explainable outputs, and be easily applicable. Among ensemble learning models, ensemble tree models constitute one of the most successful approaches.

2.2.3 Support Vector Machine

Support Vector Machine (SVM) is a binary classifier that separates two regions associated with two classes from an n-dimensional space with n features [13]. The n-dimensional hyperplane divides two regions so that it is farthest from the training vectors of the two classes called support vectors. SVM is employed for linear classification as well as nonlinear classification by using kernel methods. Kernel methods enable mapping input samples into linearly separable high-dimensional feature spaces. By using different kernel functions in an SVM, various classifiers with different decision boundaries can be constructed. In this study, a radial basis function (RBF) kernel is used for the classification tasks.

2.2.4. Random Forest

The Random Forest [14] is a bagging tree application that can achieve high prediction accuracy, deal with noise, and reduce the overfitting effect. Bagging and boosting are two main approaches in ensemble learning. Ensemble learning is one of the learning approaches in machine learning that aims to obtain better predictive performance by combining the predictions from base learners. In bagging, multiple classifiers are combined to get more accurate prediction results. Integrating multiple classifiers reduces variance, resulting in more accurate prediction results. Majority voting is a commonly used method to label test samples. In this method, each of the unlabeled samples is labeled due to the maximum number of votes from base classifiers.

2.2.5 Gradient Boosting

While Bagging trains multiple classifiers in parallel on different samples of the original data and combines the predictions, boosting has a structure of sequential classifiers, where each classifier corrects incorrect predictions made by previous ones. Gradient Boosting is a robust boosting algorithm that can solve problems with noisy data, complex dependencies such as heterogeneous features, and produce accurate classification results without a very large amount of data. In Gradient Boosting, decision trees are trained as weak learners on gradient-based functions and introduced into the ensemble model as "boosted" models.

2.2.6 Extreme Gradient Boosting

XGBoost [15] is a Gradient boosting algorithm based on decision trees. Boosting is one of the effective methods used to reduce the errors of machine learning prediction methods. XGboost is capable of creating more accurate classifier output by giving extra weights to data points that previous classifiers predicted incorrectly.

2.2.7 Adaboost

AdaBoost [16] was the first successful boosting approach, which was developed for binary classification. Adaboost forces the next base classifiers to focus on misclassified samples by changing the weights of misclassified samples in the training set [17].

III. EXPERIMENTS

3.1. Evaluation Measures

In training experiments, we aim to minimize the error between predicted and actual failures. For this aim, commonly used metrics are calculated: precision, recall, f-score, and accuracy. Figure 3.1 illustrates the confusion matrix, which is used to calculate alternative performance measures of a classification model.

		Predicted Failure	
		True	False
Actual Failure	True	TP	FN
	False	FP	TN

Figure 3.1. Confusion Matrix

According to confusion matrix, the following measures are calculated:

Precision = TP/ (TP+FP),

Recall = TP/ (TP+FN),

F-score=2*Precision*Recall/(Precision+Recall),

Accucary=(TP+TN)/(TP+FP+TN+FN).

3.2. Experimental Results

In the conducted experimental studies, as described in Section 2, three different datasets were utilized. When applying algorithms to datasets, some parameter adjustments are done to obtain optimal hypothesis.

Logistic regression was applied with a penalty term "l1" for DS1 and "l2" for both DS2 and DS3. To solve the optimization problem, "liblinear" was used for DS1, while "newton-cg" was used for DS2 and DS3. Gini is used as impurity measure in decision tree. "Max depth" defined to prevent overfitting in decision tree training is 8, 10 and 12 for DS1, DS2 and DS3 respectively. Radial basis function (RBF) kernel was used in SVM training for all datasets. For Random Forest algorithm "max features" parameter that expresses the size of random subsets of features when splitting a node are defined as 5 for both DS1 and DS3, as 1 for DS1. The numbers of trees are 190 for both DS1 and DS3, as 170 for DS2. For Gradient Boosting, as in the Random Forest, "max features" parameter defined as 19 for both DS2 and DS3, as 17 for DS3. The "min samples leaf" parameter that defines the minimum observations required in a leaf is determined 50, 70 and 40 respectively. XGboost is applied with 0.1 "learning rate" and 12 "max decision tree depth" for all datasets. The numbers of trees are 100 for DS1 and 190 for both DS2 and DS3. For Adaboost, the numbers of trees are 190, 180 and 200 for DS1, DS2 and DS3 respectively.

The evaluation results of the classifiers explained in section II on three datasets are summarized in Table 4.1.

Table 4.1 Experimental Results for Datasets

	Dataset-1				Dataset-2				Dataset-3			
	AC	PR	RE	F1	AC	PR	RE	F1	AC	PR	RE	F1
Logistic Regression	0.72	0.70	0.69	0.69	0.79	0.84	0.76	0.77	0.70	0.75	0.68	0.67
Decision Tree	0.75	0.75	0.74	0.74	0.84	0.84	0.82	0.82	0.79	0.80	0.80	0.80
XGBoost	0.78	0.78	0.77	0.78	0.86	0.86	0.85	0.85	0.84	0.84	0.84	0.84
Random Forest	0.86	0.76	0.75	0.76	0.94	0.87	0.85	0.86	0.92	0.85	0.84	0.84
Gradient Boosting	0.76	0.76	0.75	0.76	0.84	0.85	0.82	0.83	0.79	0.80	0.78	0.78
Ada Boost	0.76	0.75	0.74	0.74	0.83	0.85	0.82	0.83	0.78	0.78	0.76	0.77
Support Vector Machine	0.70	0.68	0.67	0.67	0.77	0.77	0.76	0.76	0.69	0.72	0.66	0.66

AC:Accuracy PR:Precision RE:Recall F1:F1 Score

When the table 4.1 examined, for DS1, Random Forest model has achieved the highest accuracy value, 0.86. The second-highest accuracy value, 0.78, has been obtained by the XGBoost model. For F1 score, the highest value, 0.78, has been provided by the XGBoost model. The second-highest F1 score, 0.76, has been obtained by both the Gradient Boosting and Random Forest models.

Similarly, for DS2, the Random Forest model has achieved the highest accuracy value, 0.94. The second-highest accuracy value, 0.86, has been obtained by the XGBoost model. On the other hand, the highest F1 score for DS2 has been obtained with the RF algorithm. However, it was only 0.1 times more

successful than XGboost.

As with other datasets, for DS3, the best prediction accuracy belongs to the RF algorithm with 0.92. XGboost was the algorithm that resulted in the 2nd highest degree of accuracy, as in the other 2 datasets. For the F1 score, both XGBoost and Random Forest models achieved the highest value with 0.84.

It was concluded that the results of Logistic Regression and SVM were close to each other, however, SVM was the classifier with the lowest prediction performance for all data sets. According to the F1 score, it was observed that the best predictive models in all data sets were XGBoost and Random Forest, with performance values close to each other. Considering the results obtained, it has been concluded that boosting algorithms give more accurate results than traditional machine learning algorithms in the predicting machine failure task.

IV. Conclusion

In this paper, a failure detection system developed by using a real-world manufacturing system data by using various machine learning methods, such as Logistic Regression, Decision Tree, SVM, Random Forest, Gradient Boosting, XGBoost, AdaBoost.

The datasets used in this study contain data collected over a specific period. Collecting and monitoring data over a longer period may provide access to more data, enhancing the reliability of machine failure predictions. As a result, three data sets have been created to detect three type failure alarms occurring on the production line. Considering the experimental results obtained with these data sets, the performance rates of the models vary between 75% and 84%.

In future studies, it is anticipated that increasing the data volume with additional data obtained from sensors may lead to higher prediction performances. According to the experimental results, it is planned to predict production errors with machine learning models such as Random Forest and XGBoost, using the data set containing LINE and TOX alarm labels (DS2). Another future direction of our study is to increase the accuracy by incorporating deep learning methods.

In conclusion, this study represents a significant step in predicting machine failures in industrial manufacturing processes. The findings obtained can provide a solid foundation for further research and applications in this field. Future research endeavors may support the widespread use of such predictive systems in industrial processes, enhance efficiency, and reduce costs. In future processes, we will utilize the results of the foundational models designed with machine learning. These models will be employed to test and enhance deep learning-based algorithms, which we believe will yield higher results in terms of speed and performance. We aim to achieve better results using LSTM, CNN, CNN-LSTM, and other deep learning methods. In addition, we plan to research the maintenance duration estimates.

V. Acknowledgment

This study is supported within the scope of project number 3215073 by TÜBİTAK.

References

[1] Peres, J., Sezer, V., Biswal, M. (2018). Leveraging Industrial Data for Strategic Decision-Making in Manufacturing: A Review. IEEE Transactions on Industrial Informatics, 14(8), 3674-3683.

[2] A.K.S. Jardine, "A review on machinery diagnostics and prognostics implementing condition-based maintenance," Mechanical Systems and Signal Processing, cilt. 20, sayı 7, Ekim 2006, ss. 1483-1510.

[3] Wuest, D. Weimer, C. Irgens, and K.-D. Thoben, "Machine learning in manufacturing: advantages, challenges, and applications," IEEE Transactions on Industrial Informatics, vol. 12, no. 6, pp. 23-45, 2016.

[4] Abidi, M.H.; Alkhalefah, H.; Umer, U. Fuzzy harmony search based optimal control Strategyfor wireless cyber physical system with industry 4.0. J. Intell. Manuf. 2021.

[5] Maddikunta, P.K.R.; Pham, Q.-V.; Prabadevi, B.; Deepa, N.; Dev, K.; Gadekallu, T.R.; Ruby,R.; Liyanage, M. Industry 5.0: A survey on enabling technologies and potential applications.J. Ind. Inf. Integr. 2021, 26, 100257.

[6] Baruah, P.; Chinnam, R.B. HMMs for diagnostics and prognostics in machining processes.Int. J. Prod. Res.2005, 43, 1275–1293.

[7] Prytz, R.; Nowaczyk, S.; Rögnvaldsson, T.; Byttner, S. Predicting the need for vehicle Com-pressor repairs using maintenance records and logged vehicle data. Eng. Appl. Artif. In Tell.2015, 41, 139–150.

[8] Aremu, O.O.; Hyland-Wood, D.; McAree, P.R. A Relative Entropy Weibull-SAX frame-work for health indices construction and health stage division in degradation modeling ofMultivariate time series asset data. Adv. Eng. Inform. 2019, 40, 121–134.

[9] Susto, G.A.; Schirru, A.; Pampuri, S.; McLoone, S.; Beghi, A. Machine Learning for Pre-dictive Maintenance: A Multiple Classifier Approach. IEEE Trans. Ind. Inform. 2015, 11,812–820

[10] Malhi, A.; Yan, R.; Gao, R.X. Prognosis of Defect Propagation Based on Recurrent NeuralNetworks. IEEE Trans. Instrum. Meas. 2011, 60, 703–711.

[11] Yuan, M.; Wu, Y.; Lin, L. Fault diagnosis and remaining useful life estimation of aero Engineusing LSTM neural network. In Proceedings of the 2016 IEEE International Conference onAircraft Utility Systems (AUS), Beijing, China, 10–12 October 2016; pp. 135–140.

[12] Li, Z., Wang, Y. & Wang, KS. Intelligent predictive maintenance for fault diagnosis andprognosis in machine centers: Industry 4.0 scenario. Adv. Manuf. 5, 377–387 (2017). https://doi.org/10.1007/s40436-017-0203-8.

[13] Christopher J. C. Burges. 1998. A Tutorial on Support Vector Machines for Pattern Recognition. Data Min. Knowl. Discov. 2, 2 (June 1998), 121-167.

[14] L. Breiman, "ST4_Method_Random_Forest," Mach. Learn., vol. 45, no. 1, pp. 5–32, 2001

[15] Friedman J., Greedy Function Approximation : A Gradient Boosting Machine Author (s): Jerome H . Friedman Source : The Annals of Statistics , Vol . 29 , No . 5 (Oct ., 2001), pp . 1189-1232 Published by : Institute of Mathematical Statistics Stable URL : http://www. Ann. Stat. 29, 1189–1232.

[16] Y. Freund and R. E. Schapire, "A desicion-theoretic generalization of online learning and an application to boosting," in Proc. Eur. Conf. Comput. Learning Theory, 1995, pp. 23–37.

[17] J. C. W. Chan and D. Paelinckx, "Evaluation of Random Forest and Adaboost tree-based ensemble classification and spectral band selection for ecotope mapping using airborne hyperspectral imagery,"Remote Sens. Environ., vol. 112, no. 6, pp. 2999–3011, 2008

A Software Package to Compute Equivalent Water Thickness Changes Directly from GRACE GGMs: ESKaD

E. Z. ÖZTÜRK[1] and R. A. ABBAK[1]

[1] Konya Technical University, Konya/Turkey, ezozturk@ktun.edu.tr
[1]Konya Technical University, Konya/Turkey, raabbak@ktun.edu.tr

Abstract **- In this study, ESKaD software, which estimates equivalent water thickness changes through global geopotential models published by GRACE (Gravity Recovery and Climate Experiment) data processing centers, is introduced. Then, the performance of the software was analyzed with auxiliary data on the test points determined in Konya basin. The numerical results show that the equivalent water thickness changes, which play a major role in the monitoring groundwater changes, have been successfully estimated. The software package which aims to satisfy the demands of users quickly and practically, offers an alternative calculation tool for scientific researches in disciplines such as geodesy, geophysics, hydrology, and etc.**

Keywords **- Equivalent water thickness; GRACE; Global Geopotential Models; Software package; Groundwater changes.**

I. INTRODUCTION

Due to the internal dynamics of the Earth (earthquakes, tectonic movements, groundwater exchange, etc.), the gravity field changes depending on the time parameter. Large earthquakes and hydrological signals are the two main factors affecting the long wavelength structure of the gravity field on a short time scale. With the satellite gravimetry technique, it is possible to obtain information about the low-frequency content and temporal changes of the gravity field by reducing high frequencies with satellites at certain altitudes. Since 2002, time-varying global geopotential models obtained from the GRACE (Gravity Recovery and Climate Experiment; Tapley et al., 2004) and GRACE Follow-On (GRACE-FO; Flechtner et al., 2014) satellite missions have been used to monitor water changes on the continents at the cm level. With the integration of GRACE/GRACE-FO global geopotential models and hydrological models published free of charge and online, it is possible to monitor mass redistributions (Akyılmaz et al., 2016; Öztürk et al., 2018a; 2018b; Godah et al., 2018; Öztürk et al., 2020; Öztürk 2020; Öztürk 2022) on the continents faster and at low cost. The Global Land Data Asimulation System (GLDAS) (Rodell et al., 2004) and the WaterGAP (Water- a Global Assessment and Prognosis) Global Hydrology Model (WGHM; Schmied et al., 2014; Döll et al., 2014; Schmied 2017) are two of the hydrological models that show high consistency with GRACE gravity models. These models reflect hydrological regimes on a global and regional scale. They also provide the surface density of soil moisture (SM), snow water equivalent (SWE), plant canopy surface water (CAN) and groundwater bodies (GWS). Integration of this density information with the equivalent water thickness (EWT) variations obtained by the GRACE mission provides groundwater variations, which are very important today.

In all technical and scientific studies that require the monitoring of groundwater changes, a suitable calculation tool is needed to obtain EWT changes quickly and directly. In the literature, there are software packages developed in different programming languages such as Python (Nielsen et al., 2012), MATLAB (Bucha and Janák 2013; Godah 2019), FORTRAN (Rapp 1982; Tscherning et al., 1983; Holmes and Pavlis 2006) and C/C++ (Öztürk and Abbak, 2020). However, the majority of existing software packages have been developed primarily for determining static gravity functions. Therefore, in order to calculate time-varying gravity functions using these software, users may need to perform a preprocessing or modify GRACE-based global geopotential models. In addition, the developed software packages do not allow users to determine temporal variations of the EWT from GRACE-based geopotential models, are not freely available with commercial software, or interactive online tools such as mascon solutions cannot be used without an internet connection.

In this study, an open source and user-friendly software called "ESKaD" was developed in C/C++ programming language. This software enables users to calculate GRACE EWT variations time series quickly and free of charge. In the following sections, the data and methodology used in the calculations, the features and components of the ESKaD software, and the results of the case study are presented respectively.

II. DATA AND METHOD

The ESKaD software uses Level 2, version 6 (Release-06, RL06) global geopotential models obtained from JPL (Jet Propulsion Laboratory), GFZ (GeoForschungs Zentrum) and CSR (Center for Space Research), the official data centers of the GRACE mission. These models, symbolized by $C_{lm}^{W}$and S_{lm}^{W}, are called global harmonic models and each model has harmonic coefficient degree (l) and harmonic coefficient order (m). In the RL06 GRACE data used in this study, the

maximum coefficient order is 90 for GFZ models, 60 for JPL models and 96 for CSR models. As a result of the redistribution of surface masses, the crust is subjected to loading and deforms. In order to model these changes, Love numbers calculated by Wang et al. (2012) are used in the software. These coefficients were calculated using the structural parameters of the Earth's crust from the Preliminary Reference Earth Model (PREM) of Dziewonski and Anderson (1981). In addition, the GRACE C_{20} coefficients, which represent the dynamic flattening of the Earth, are replaced by the Satellite Laser Ranging (SLR) C_{20} coefficients. The Earth Gravity Model EGM2008 (Pavlis et al., 2012) is used as the reference model in the software. In the case study to test the software, EWT variations obtained from the IGiK-TVGMF software (Godah, 2019) were used.

The spherical harmonic expansion of the surface densities (SM, SWE, CAN, GWS) divided by the density of water (ρ_w) gives the EWT:

$$\Delta EWT = \delta h_{Hyd}^{TWS}(\theta,\lambda) = \frac{1}{\rho_w}\sum_{l=m}^{\infty}\sum_{m=-1}^{l}(\delta\rho_{lm}^{SM} + \delta\rho_{lm}^{SWE}\delta\rho_{lm}^{CAN}\delta\rho_{lm}^{GWS})Y_{lm}(\theta,\lambda) \quad (1)$$

In the equation, θ, λ are the polar distance and geocentric longitude, and Y_{lm} (θ,λ) is the surface harmonic function. According to equation (1), EWT reflects the entire change in the first 200 cm layer at the surface and groundwater (Eshagh, 2020). ESKaD software calculates the EWT changes obtained from the difference of the GRACE-based global geopotential models with respect to the specified reference model (EGM2008). If the spherical harmonic coefficients of the GRACE global geopotential models are expressed as $C_{lm}^{W(GRACE)}$ and $S_{lm}^{W(GRACE)}$ and the spherical harmonic coefficients of the EGM2008 model are expressed as $C_{lm}^{(\mathrm{EGM2008})}, S_{lm}^{(\mathrm{EGM2008})}$, the coefficients ΔC_{lm}^{T}, ΔS_{lm}^{T}, which express the difference between them are obtained as follows:

$$\left.\begin{aligned} \Delta C_{lm}^{W} &= C_{lm}^{W(\mathrm{GRACE})} - C_{lm}^{W(\mathrm{EGM2008})} \\ \Delta S_{lm}^{W} &= S_{lm}^{W(\mathrm{GRACE})} - S_{lm}^{W(\mathrm{EGM2008})} \\ \Delta C_{lm}^{T} &= C_{lm}^{W(\mathrm{GRACE})} - C_{lm}^{U(GRACE)} - (C_{lm}^{W(\mathrm{EGM2008})} - C_{lm}^{U(\mathrm{EGM2008})}) \\ \Delta S_{lm}^{T} &= S_{lm}^{W(\mathrm{GRACE})} - S_{lm}^{U(GRACE)} - (S_{lm}^{W(\mathrm{EGM2008})} - S_{lm}^{U(\mathrm{EGM2008})}) \end{aligned}\right\} \quad (2)$$

$C_{lm}^{W(\mathrm{EGM2008})}$, $S_{lm}^{W(\mathrm{EGM2008})}$, $C_{lm}^{W(\mathrm{GRACE})}$ and $S_{lm}^{W(\mathrm{GRACE})}$ represent the spherical harmonic coefficients of the EGM2008 and GRACE global geopotential models, respectively. $C_{lm}^{U(\mathrm{GRACE})}$, $S_{lm}^{U(\mathrm{GRACE})}$, $C_{lm}^{U(\mathrm{EGM2008})}$ and $S_{lm}^{U(\mathrm{EGM2008})}$ represent the spherical harmonic coefficients of the normal gravity field of the monthly GRACE global geopotential models and the EGM2008 model, respectively. The EWT variations can be obtained from the spherical harmonic coefficients of the time-dependent gravity field variations by the following formula:

$$\Delta EWT_{(r,\varphi,\lambda)} = \frac{a\times\rho_{ave}}{3}\sum_{l=0}^{l_{max}}\sum_{m=0}^{l}P_{lm}(sin\varphi)\frac{2l+1}{1+k_l}(\Delta C_{lm}^{T}\mathrm{cosm}\lambda + \Delta S_{lm}^{T}\mathrm{sinm}\lambda) \quad (3)$$

r and φ are the geocentric radius and spherical latitude of the point for which the EWT change is calculated, respectively, and a is the major semi-axis of the reference ellipsoid. The k values shown in the formula are the *l-th* Love numbers calculated with the structural parameters of the Earth's surface from PREM. ρ_{ave} (5517 kg/m^3) is the average density of the Earth. P_{lm} is the fully normalized Legendre functions (1st kind) of degree l and order m. l_{max} is the maximum degree applied.

III. Overview of ESKaD Software

This chapter provides a comprehensive overview of the ESKaD software. The software is coded in the GNU C/C++ platform and is called ESKaD. ESKaD should be compiled on a Linux-based computer or server, or through Linux-like platforms (such as Cygwin) provided for other operating systems. The software consists of a main function and two sub-functions. The functions in the software are described in detail below. The flowchart of the software is given in Figure 1.

main: This is the main function that retrieves from the command line the geographical latitude and longitude values of the point where the EWT variations will be calculated, the file name indicating which GRACE model the calculations will be performed with, and the maximum expansion value of the spherical harmonics. If the user wants to estimate with a model other than the models obtained from the official GRACE data processing centers JPL, GFZ and CSR, the user can upload the data file of the model to the working folder and perform the calculation with that model. In order to replace its coefficients with SLR data, the function again gets the file name of the SLR data from the command line. Finally, in order to model the deformation due to loading caused by mass movements, the file with the Love numbers obtained from the PREM model should also be entered on the command line.

legendre: This function calculates Legendre functions of the first kind using the coefficient degree entered by the user and the global latitude obtained according to the geodetic coordinates. The calculation algorithm is based on Avşar and Üstün (2011).

help: This function provides general information about the use of the software. In particular, it indicates what kind of data the parameters require and what the default parameters are.

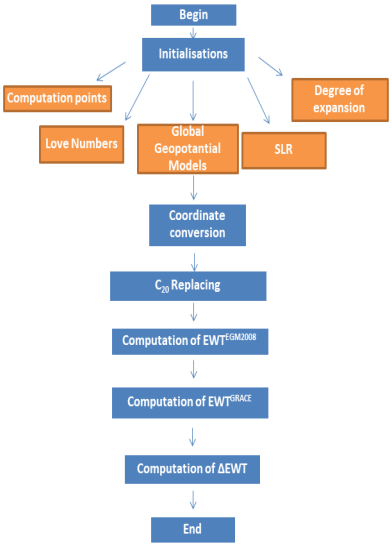

Figure 1: ESKaD software flow diagram

IV. Case Study

In this section, the developed ESKaD software is tested. The points selected for testing are points P1, P2 and P3 in Konya basin, shown in Figure 2 with geographic latitude and longitude values. Points P1, P2 and P3 are also the GSFC mascon grid centers and represent sub-regions in the 1°×1° frame. The EWT changes obtained from the IGiK-TVGMF software developed by Godah (2019) were used as control data. The IGiK-TVGMF software developed in MATLAB uses harmonic coefficients similar to the ESKaD software and most of the parameters used in the calculation are user-specified. For the test, CSR RL06 spherical harmonic coefficients were calculated to the 60th order using the DDK3 filter in both software and GRACE C_{20} values were replaced with SLR C_{20} values. Since GRACE-based global geopotential models do not contain gaps between 2004-2010, this period was chosen for the study.

The time series of EWT changes obtained from the software is shown in Figure 3. When the time series are analyzed, it is seen that ΔEWT^{ESKaD} and $\Delta EWT^{IGiK\text{-}TVGMF}$ values changed between -31.5 cm and +5.4 cm in the period of 2004-2011. It is seen that the interannual cycle of both variations during the study period is quite close to each other. However, as seen in the statistical results in Table 1, the standard deviation values obtained from the difference between $\Delta EWT^{IGiK\text{-}TVGMF}$ results and ΔEWT^{ESKaD} results are 6.5 cm for P1, 5.7 cm for P2 and 5.8 cm for P3. These values are acceptable for the 3°×3° spatial resolution of the GRACE/GRACE-FO data used in the software and prove that the ESKaD results are consistent with control data. In addition, while the normalized Legendre functions in the ΔEWT^{ESKaD} calculations are based on Avşar and Üstün (2011), the same functions in the $\Delta EWT^{IGiK\text{-}TVGMF}$ calculations are based on Borre (2008). The impact of this difference in methodology on the results should not be ignored (Öztürk and Abbak, 2020).

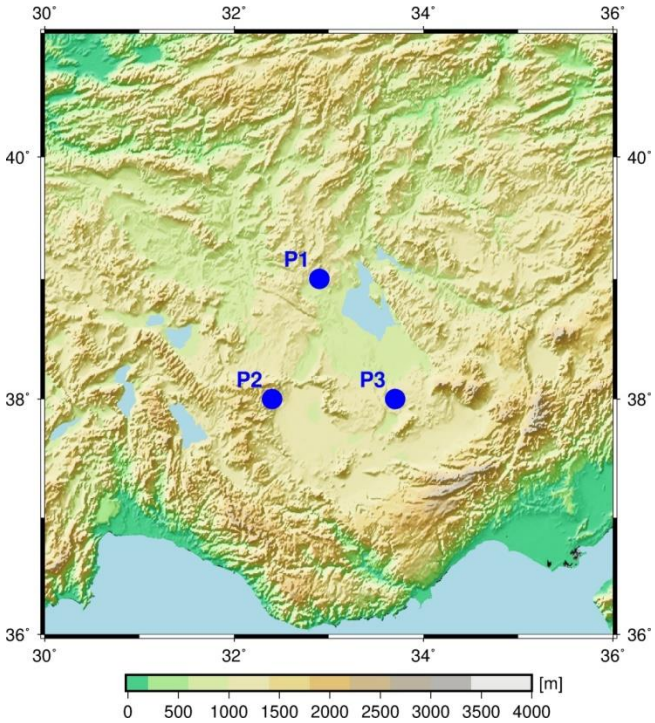

Figure 2: Test points P1 ($\varphi = 39°, \lambda = 32.9°$), P2 ($\varphi = 38°$, $\lambda = 32.4°$) and P3 ($\varphi = 38°$, $\lambda = 33.7°$) for ESKaD.

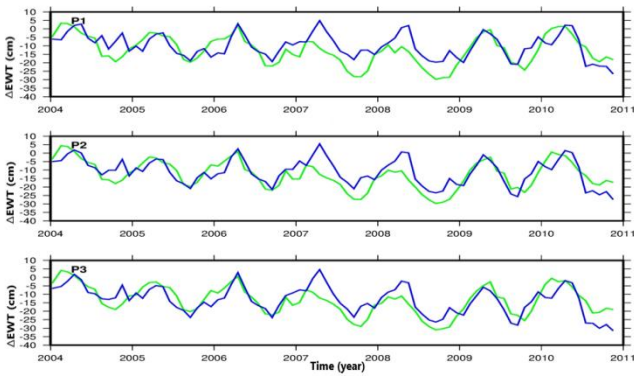

Figure 3: EWT changes obtained with ESKaD (blue) and IGiK-TVGMF (green) at test points P1, P2 and P3.

Table 1: Statistical results of ΔEWT^{ESKaD} and $\Delta EWT^{IGiK\text{-}TVGMF}$ differences at points P1, P2, P3 [cm].

	ΔEWT Differences (cm)	min	max	mean	std
P1	$\Delta EWT^{ESKAD} - \Delta EWT^{IGiK\text{-}TVGMF}$	-8.3	18.8	4.8	6.5
P2	$\Delta EWT^{ESKAD} - \Delta EWT^{IGiK\text{-}TVGMF}$	-7.9	16.6	4.4	5.7
P3	$\Delta EWT^{ESKAD} - \Delta EWT^{IGiK\text{-}TVGMF}$	-8.6	16.1	3.5	5.8

V. Discussion and Conclusion

In this study, ESKaD software developed in GNU C/C++ platform is presented to calculate EWT changes quickly, easily and free of charge. In order to test the results of the software, the analysis was carried out in the test region determined in the Konya closed basin and ESKaD EWT changes were compared with the EWT changes obtained from IGiK-TVGMF solutions. The standard deviation of

ΔEWT^{ESKaD} - $\Delta EWT^{IGiK\text{-}TVGMF}$ differences obtained at all three points is around ~6 cm, the changes are close to each other and the seasonal cycles are almost compatible with each other. Compared to other online or commercial counterparts, the software is very practical to use and provides fast results for those interested only in EWT variations and for academic studies. ESKaD also allows users to evaluate their results by adding their own analysis or plotting functions.

In the future, in addition to the C_{20} coefficients replaced with SLR coefficients in the software, the results can be further improved by making the same changes for the C_{30} coefficients (Velicogna et al., 2020). In addition, by adding parameters such as various filtering techniques, it is possible for the software to serve multidisciplinary uses with sub-functions. ESKaD source codes are published at https://github.com/ezozturk/ESKaD.

REFERENCES

[1] Akyılmaz, O., Üstün, A., Aydın, C., Arslan, N., Yağcı, O., Doğanalp, S., Güney, C., 2016. Yakın Yer Uyduları Yardımıyla Yüksek Çözünürlüklü Gravite Alanı Belirleme ve Bölgesel Kütle Değişimlerinin İzlenmesi, TÜBİTAK ARDEB 1001 Araştırma Projeleri, Proje No: 113Y155, Proje Sonuç Raporu, Ocak 2016.

[2] Avşar, N. B., Üstün, A., 2011. Genişletilmiş çift incelikli sayı formatı kullanılarak yüksek dereceli Legendre fonksiyonları ve türevlerinin hesabı. Harita Dergisi, 77(146), 18-26.

[3] Borre, K., 2004. Geoid undulations computed from EGM96. Aalborg University, April.

[4] Bucha, B., Janák, J., 2013. A MATLAB-based graphical user interface program for computing functionals of the geopotential up to ultra-high degrees and orders. Comput. Geosci., 56, 186–196.

[5] Döll, P., Schmied, H., Schuh, C., Portmann, F., Eicker, A., 2014. Global-scale assessment of groundwater depletion and related groundwater abstractions: Combining hydrological modeling with information from well observations and GRACE satellites. Water Resources Research, 50:5698–5720.

[6] Dziewonski, A. M., Anderson, D. L., 1981. Preliminary reference Earth model. Physics of the earth and planetary interiors, 25(4), 297-356.

[7] Eshagh, M., 2020. Satellite Gravimetry and the Solid Earth: Mathematical Foundations, Elsevier.

[8] Flechtner, F., Morton, P., Watkins, M., Webb, F., 2014. Status of the GRACE follow-on mission. In: Marti, U. (Ed.), Gravity, Geoid and Height Systems. International Association of Geodesy Symposia, 141. Springer, Cham.

[9] Godah, W., Szelachowska, M., Öztürk, E. Z., Krynski, J., 2018. On the contribution of physical height changes estimated with the use of GRACE satellite mission data to the modernization of a national vertical system. In AGU Fall meeting abstracts (Vol. 2018, pp. G13B-0525).

[10] Godah, W., 2019. IGiK–TVGMF: A MATLAB package for computing and analysing temporal variations of gravity/mass functionals from GRACE satellite based global geopotential models. Computers & Geosciences, 123:47–58.

[11] Holmes, S., A., Pavlis, N., K., 2006. A FORTRAN program for very-high-degree harmonic synthesis. Version 05/01, 2006.

[12] Nielsen, J., Tscherning, C. C., Jansson T. R. N., Forsberg, R., 2012. Development and user testing of a Python interface to the GRAVSOFT gravity field programs. Geodesy for Planet Earth Springer, Berlin, Heidelberg, 443-449.

[13] Öztürk, E. Z., Godah, W., Abbak, R. A., 2018a. Analysis of De-correlation filters performance for estimating temporal mass variations determined from GRACE-based GGMs over Konya basin. In FIG Congress 2018. Embracing our smart world where the continents connect: enhancing the geospatial maturity of societies. Technical Programme and Proceedings (pp. 1-16). FIG.

[14] Öztürk, E. Z., Godah, W., Abbak, R. A., 2018b. Evaluation of RL05 GRACE Based Global Geopotential Models on a Regional Scale: A case study of Turkey. In EGU General Assembly Conference Abstracts (p. 2141).

[15] Öztürk, E. Z., Abbak, R. A., 2019. Physical Height Changes Estimated by GRACE Data: A Case Study Over Greenland. XXIX International Symposium on "Modern Technologies, Education and Professional Practice in Geodesy and Related Fields".

[16] Öztürk, E. Z., Godah, W., Abbak, R. A., 2020. Estimation of physical height changes from GRACE satellite mission data and WGHM over Turkey. Acta Geodaetica et Geophysica, 55(2), 301-317.

[17] Öztürk, E. Z., Abbak, R. A., 2020. PHCSOFT: A Software package for computing physical height changes from GRACE based global geopotential models. Earth Science Informatics, 13(4), 1499-1505.

[18] Öztürk E. Z., 2020, Estimation and analysis of physical height changes using satellite gravimetry: case studies in Turkey and Greenland, PhD thesis, Konya Technical University Institute of Graduate Studies, Konya.

[19] Öztürk, E. Z. 2022, Evaluation of Water Storage Changes in Southeastern Anatolia, Turkey, using GRACE and GLDAS. Meteorology Hydrology and Water Management-Research and Operational Applications.

[20] Pavlis, N. K., Holmes, S. A., Kenyon, S. C., Factor, J. K., 2012. The development and evaluation of the Earth Gravitational Model 2008 (EGM2008). Journal of geophysical research: solid earth, 117(B4).

[21] Rapp, R. H., 1982. A Fortran Program for the Computation of Gravimetric Quantities from High Degree Spherical Harmonic Expansions. Report 334, Department of Geodetic Science and Surveying, The Ohio State University, Columbus.

[22] Rodell M., Houser P. R., Jambor U., Gottschalck J., Mitchell K., Meng C. J., Arsenault K., Cosgrove B., Radakovich J., Bosilovich M., Entin J.K., Walker J. P., Lohmann D., Toll D., 2004. The global land data assimilation system. Bull Am Meteorol Soc 85(3), 381–394.

[23] Schmied, H., 2017. Evaluation, modification and application of a global hydrological model. Frankfurt Hydrology Paper, 16.

[24] Schmied, H., Eisner, S., Franz, D., Wattenbach, M., Portmann, F., Flörke, M., Döll, P., 2014. Sensitivity of simulated global-scale freshwater uxes and storages to input data, hydrological model structure, human water use and calibration. Hydrology and Earth System Sciences, 18:3511–3538.

[25] Tapley, B. D., Bettadpur, S., Ries, J., Thompson, P. F., Watkins, M. M., 2004. GRACE measurements of mass variability in the earth system. Science 305, 503e505.

[26] Tscherning, C. C., Rapp, R. H., Goad, C., 1983. A comparison of methods for computing gravimetric quantities from high degree spherical harmonic expansions. Manuscripta Geod. 8, 249–272.

[27] Velicogna, I., Mohajerani, Y., A, G., Landerer, F., Mouginot, J., Noel, B., vd. 2020. Continuity of ice sheet mass loss in Greenland and Antarctica from the GRACE and GRACE Follow-On missions. Geophysical Research Letters, 47, e2020GL087291.

[28] Wang, H., Xiang, L., Jia, L., Jiang, L., Wang, Z., Hu, B., Gao, P., 2012. Load Love numbers and Green's functions for elastic Earth models PREM, iasp91, ak135, and modified models with refined crustal structure from Crust 2.0. Computers & Geosciences, 49, 190-199.

A Location Based Augmented Reality Application with Machine Learning Methods

K.KAPICI[1] and A.OZTURK[1,2]

[1] KTO Karatay University, Konya/Turkey, kapicikubraa@gmail.com
[1] KTO Karatay University, Konya/Turkey, ali.ozturk@karatay.edu.tr
[2] Havelsan A.S, Konya/Turkey, aliozturk@havelsan.com.tr

***Abstract* - Location-based augmented reality is a markerless technique which uses data from GPS, digital compass, etc. to determine the location of a mobile device. After making calculations by using the GPS and compass data, the application figures out where the mobile camera is looking and displays the relevant virtual information about the environment on the screen. In this study, a location-based augmented reality mobile application has been developed to inform users about the buildings of a university campus. The application determines which building it is by making angular calculations using the geographical position of the mobile device and the corner coordinates of the buildings. The application was then used within the campus to record the current latitude, longitude of the mobile device and the distance information of the buildings that were displayed on the device screen. The collected data were applied to Decision Tree, Random Forests, Support Vector Machines (SVM), and XGBoost algorithms with 3-fold cross validation and the results were compared. Based on the results obtained, the best performance belongs to the SVM algorithm with accuracy, precision, recall, and F1 Score values of 0.90, 0.91, 0.90, and 0.90, respectively. The use of machine learning algorithms within the application allows the detection of the buildings using only latitude, longitude of the mobile device and the building distance information, eliminating the need for angular calculations.**

***Keywords* – Location Based Agumented Reality, Augmented Reality, Machine Learning.**

I. INTRODUCTION

AUGMENTED reality is a technology created by enriching real-world objects with computer-generated data [1]. This technology adds additional information, graphics, or objects to users who view the real world through mobile devices or glasses, enabling interaction between the real and virtual worlds [2].

Location-based augmented reality is a technology that allows users to experience virtual content based on their current real-world location [3]. This system scans the user's surroundings using GPS or other location determination methods and displays location-specific virtual objects or information in the real world. Users can interactively experience this location-based augmented reality through smartphones or specialized devices. The challenges of GPS-based augmented reality applications involve the accurate positioning of physical objects and the stable attachment of virtual objects. Standard location services, such as those on iPhone or Android devices, may fall short in achieving high levels of accuracy. Therefore, developing a high-quality GPS-based AR application may require the use of specialized augmented reality SDKs and techniques and markerless technology. These SDK's are not free and may have integration difficulties into AR applications.

Location-based augmented reality technology is used in various fields [4]. It is commonly employed, particularly in tourist areas, to help tourists explore their surroundings more effectively and provide access to historical information. In education, it is used to teach students about historical or geographical locations in a more interactive manner. In the retail sector, it is used to provide store visitors with product information, promotions, and discounts. Lastly, in the automotive industry, it is used to enhance the driving experience by offering drivers directions and traffic information.

When augmented reality and machine learning are used together, the identification and functionality determination of objects become more effective. Machine learning can optimize the data collection and analysis processes for augmented reality, improving augmented reality to obtain real-time and more accurate results and expanding its use cases. The combined use of these technologies can enhance the user experience and further enhance data analysis processes.

A review of the literature reveals various location-based augmented reality studies conducted in different fields. As an example of a location-based augmented reality application, Pokemon GO, which became popular in 2016, can be cited. Pokemon Go is the first mobile augmented reality (AR) game. Existing augmented reality theories were used to make the user's adaptation to the game more efficient. A comprehensive framework was presented by considering different augmented reality criteria [5]. In another study [6], a mobile application was developed that provides information about important landmarks and handicraft locations in Istanbul to tourists visiting the city. It is an Android application with 2D map and augmented reality modes designed for offline use. The application provides location information over the internet through REST service calls and performs field distance calculations using the Haversine and Vicenty formulas. In a study that utilizes smartphone accelerometers, compasses, cameras, and augmented reality technologies, an examination was conducted for indoor navigation [7]. An application was developed that enables indoor navigation using only smartphone features without the need for additional hardware or components by utilizing signals emitted by Beacon Bluetooth devices. This application utilizes low-

power Bluetooth devices that employ the BLE communication protocol. An augmented reality prototype for the Roman baths in Ankara, developed in Unity, was created by overlaying images captured with a drone onto a 3D bath model created in Unity [8]. The application was tested using an Android-based tablet and a mobile phone. In another study [9], tourist attractions in Safranbolu's Old Bazaar were identified, 3D models were created, and spatial information was integrated to develop an Android application for tourism purposes. The application was built using internet-based applications such as SketchUp, Photoshop, Unity 3D, AR plugins, Android Studio, VRML, and Vuforia.

In this study, a location-based augmented reality application was designed using Unity and Vuforia, with the aim of providing users with information about campus buildings. An original algorithm was created for this purpose, which involved angle and distance calculations using GPS data, building corner coordinates, center coordinates, and angular calculation formulas. The current compass angle value of the mobile device was compared to the calculated angle range to determine which building was displayed on the screen. This way, a location-based augmented reality application was developed without the use of paid SDKs. Subsequently, Decision Trees, Random Forest, Support Vector Machine, and XGBoost algorithms were compared to find the best-performing machine learning algorithm, which was integrated into the application. This allowed building identification based solely on latitude, longitude, and distance data, eliminating the need for angular calculations.

II. Machine Learning Methods

A. Random Forest

Random Forest is a model created by combining multiple decision trees that can make predictions for classification or regression problems [10]. The algorithm trains each tree using a subset of the dataset and combines the independent decisions of these trees to obtain a final prediction. Random Forest can efficiently process large datasets and high-dimensional feature vectors. Additionally, it reduces the risk of overfitting and improves generalization by randomly selecting and training trees independently. It can determine the feature importance ranking, indicating which features contribute more to prediction performance. Random Forests can handle missing data and predict missing values for forecasting. They can achieve high accuracy in classification and regression problems and often produce reliable models. Feature selection, clustering, and separation can also be used for various machine learning tasks.

B. SVC (Support Vector Machine Classifier)

SVC (Support Vector Machine Classifier) is an algorithm used for classification problems in machine learning [11]. It creates a hyperplane of separation to classify data points. The algorithm utilizes support vectors to classify data points. Support Vector Machines can create both linear and non-linear separation hyperplanes. While Linear Support Vector Machines can classify as planes or lines, Non-linear Support Vector Machines allow flexible separation of more complex data sets using kernel functions. Support Vector Machines offer high classification accuracy, overfitting prevention, and generalization capabilities. However, they can be computationally intensive and have long training times, especially for large datasets and high-dimensional feature vectors.

C. Decision Tree

The Decision Tree is a commonly used algorithm in machine learning. It performs predictions by dividing and classifying a dataset using a tree structure. Each node represents a feature and a decision rule. Trees are constructed by selecting the best features and decision rules based on criteria such as data set, information gain, or Gini index. The Decision Tree is a simple and easy-to-understand model that can handle both categorical and numerical data. To reduce the risk of overfitting, decision trees can be pruned [12]. It is a widely used algorithm that can achieve successful results in classification and regression problems.

D. XGBOOST

XGBoost, short for "Extreme Gradient Boosting," is a machine learning algorithm and an enhanced version of the Gradient Boosting method [13]. XGBoost can work efficiently on large datasets and deliver high performance in classification and regression problems. The algorithm operates by creating consecutive trees, with each tree aiming to reduce the total error by correcting the errors of the previous trees. XGBoost can be configured through hyperparameters, allowing adjustments to the model's performance and generalization ability. It has a broad user base and is widely preferred due to its successful results in various machine learning competitions and real-world applications. As for the parameters, the gbtree, gblinear, and dart parameters were individually tested, and dart, which yielded the highest result, was chosen for use. XGBoost DART is an improved version of the XGBoost algorithm and is a tree-based learning algorithm. DART prevents overfitting models by using the dropout technique in tree creation and offers the advantage of faster learning with improved generalization capabilities.

III. Performance Metrics

Performance metrics used to evaluate machine learning performance include accuracy, precision, recall, and F1 score. When evaluating these metrics, there are four possibilities, namely True Positive (TP), False Positive (FP), True Negative (TN) and False Negative (FN) [14].

Accuracy is a metric that represents the ratio of correctly classified examples to the total examples. (1) is used for the calculation.

$$Accuracy = \frac{(\mathrm{TP} + \mathrm{FN})}{(\mathrm{TP} + FP + \mathrm{FN} + FN)} \quad (1)$$

Precision represents the ratio of true positive predictions

to the total number of positive predictions made. When calculating it, (2) is used.

$$Precision = \frac{\text{TP}}{(\text{TP} + FP)} \quad (2)$$

Recall, also known as sensitivity or true positive rate, signifies the ratio of true positive predictions to the total number of actual positive instances. When calculating it, (3) is employed.

$$Recall = \frac{\text{TP}}{(\text{TP} + FN)} \quad (3)$$

F1 score, on the other hand, represents a balanced average of precision and recall metrics and is used to assess a model's performance. When calculating it, (4) is utilized.

$$F1\ Score = 2 * \frac{(\text{Precision} * \text{Recall})}{(\text{Precision} + \text{Recall})} \quad (4)$$

These metrics are used to measure and compare the success of machine learning models from different perspectives.

IV. Method And Development Process In Location-Based Augmented Reality Application

In the study, Unity and Vuforia were utilized. Unity is a software tool commonly used as a game engine, and it is also employed in the development of interactive virtual reality applications. On the other hand, Vuforia is a software platform specifically focused on augmented reality technology. When Unity and Vuforia are used together, they provide a powerful toolkit for creating impressive augmented reality applications [15].

A. Acquisition Of Building Coordinates And Angular Calculations

The satellite images and locations (X, longitude, latitude) of the institution's buildings to be studied have been obtained. The satellite image of these buildings is shown in Figure 1.

These coordinates have been defined in the code for each building as front-right, back-right, front-left, and back-left. For angular calculations, angles, as shown in Figure 2, have been utilized.

During the calculations, a fixed point N (north) has been determined, and based on this point, along with the entered coordinates, building information is provided according to the corresponding data.

During the calculations, firstly, the coordinates of the buildings were entered. Then, the device's location (longitude, latitude) and heading angle information were obtained via GPS and displayed on the screen. Based on the received data, the identity of the nearest building to the coordinates was displayed on the screen.

Figure 1: Satellite Image of Institutional Buildings.

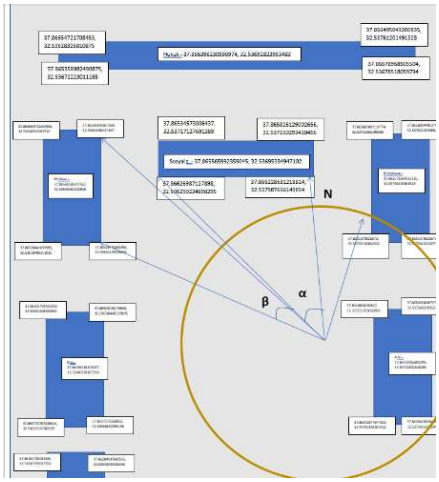

Figure 2: Angular Calculation.

Subsequently, the area where the institutional buildings are located was divided into four regions: inside, back, right-side, and left-side. The determination of the region was made with respect to the reference point. For example, if a person's latitude value is smaller than the reference latitude value, their position would be considered 'inside,' and the evaluation would proceed accordingly.

In these calculations, the Haversine formula was employed for distance calculation, as shown in (5).

$$d = 2r \arcsin\sqrt{\sin^2\left(\frac{\theta_2-\theta_1}{2}\right) + \cos(\theta_1)\cos(\theta_2)\sin^2\left(\frac{\lambda_2-\lambda_1}{2}\right)} \quad (5)$$

The Haversine formula is a mathematical formula used to calculate the direct distance between two points. This formula utilizes the latitude and longitude of two points and is calculated taking into account the radius of the Earth. The formula calculates the shortest distance between two points on a circle known as the great circle arc.

Another formula that is commonly used is the formula for calculating the magnitude of a vector. It represents the length of a vector from its starting point to its endpoint. The formula is shown in (6).

$$\|v\| = \sqrt{V_1^2 + V_2^2 + V_3^2 + \cdots + v_n^2} \quad (6)$$

One of the formulas used to find angles is the cosine angle formula, as shown in (7).

$$\cos(\Theta) = \frac{A \cdot B}{\|A\|\|B\|} \quad (7)$$

Where A and B are the vectors which were determined using the left and right corner coordinates of the buildings. These vectors were determined using the X-Y difference between the coordinates of the mobile device and the corner coordinates of the buildings relative to the north vector. The cosine of the angle between the A and B vectors were calculated according to (7). Then using arc cosine of this value, the angle is found. The building on the screen of the mobile device is determined by comparing this angle with the compass heading value of the mobile device.

V. EXPERIMENTAL RESULTS AND DISCUSSION

When the application is launched, it greets the user with a screen displaying information such as distance, latitude, and longitude, as shown in Figure 3. It also indicates which building is being shown to the camera.

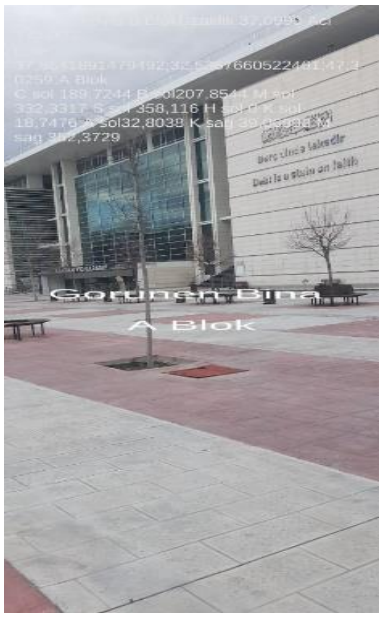

Figure 3: Application Screenshot.

The application was executed, and while navigating within the institutional buildings, a substantial amount of latitude, longitude, and distance data was collected and tabulated.

The obtained data was then used to train machine learning algorithms, including Random Forest, Decision Tree, XGBoost, and Support Vector Machine, using a 3-fold cross-validation method. Accuracy, precision, recall, and F1 score values were calculated, and the results are depicted in Figure 4.

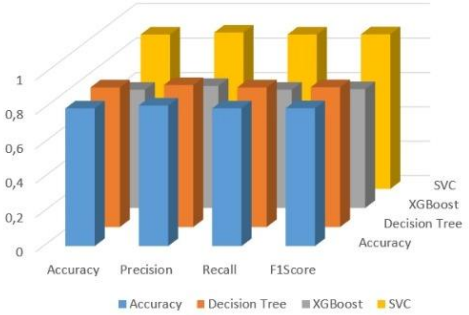

Figure 4: Evaluation Metrics Graph.

The results of the algorithms according to performance metrics are presented in Table 1. According to this data, the most successful algorithm is the Support Vector Machine (SVM), with an accuracy value of 0.898465, precision value of 0.909821, recall value of 0.898474, and an F1 score of 0.899661. On the other hand, the least successful algorithm is XGBoost. XGBoost has an accuracy value of 0.687974, precision value of 0.710125, recall value of 0.687977, and an F1 score of 0.691367.

Table 1: Results According to Performance Metrics Of Algorithms.

	Accuracy	Precision	Recall	F1 Score
Random Forest	0,80122	0,817848	0,801235	0,802026
Decision Tree	0,81227	0,826161	0,812283	0,813612
XGBoost	0,68797	0,710125	0,687977	0,691367
SVC	0,89847	0,909821	0,898474	0,899661

The confusion matrix for the most successful algorithm, the Support Vector Machine, according to these results, is shown in Figure 5.

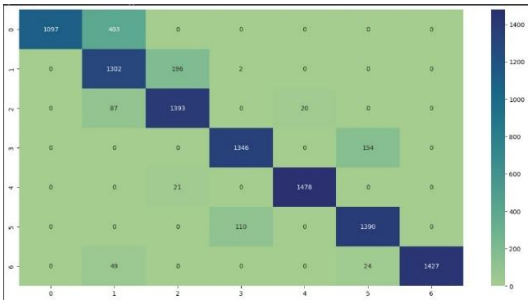

Figure 5: SVC confusion matris.

The use of machine learning algorithms within the application allows for the detection of the building solely based on the latitude, longitude, and building distance information from the mobile device. This eliminates the need for angular calculations traditionally required for building detection. The location-based augmented reality application which was developed in this study can be used in any institution having buildings in wide area. If the coordinates of the buildings were entered properly the application will work accordingly to inform users. The application was developed using an original algorithm without the use of commercial SDKs which is an important contribution of the study.

REFERENCES

[1] İçten, T. & Bal, G. (2017). Artırılmış Gerçeklik Üzerine Son Gelişmelerin ve Uygulamaların İncelenmesi . Gazi University Journal of Science Part C: Design and Technology , 5 (2) , 111-136

[2] Kleftodimos, A., Moustaka, M., Evagelou, A. Location-Based Augmented Reality for Cultural Heritage Education: Creating Educational, Gamified Location-Based AR Applications for the Prehistoric Lake Settlement of Dispilio. Digital 2023, 3(1), 18-45

[3] Altınpulluk, H. & Kesim, M. (2015, Şubat 4-6). Geçmişten günümüze artırılmış gerçeklik uygulamalarında gerçekleşen paradigma değişimleri [Sözlü bildiri]. Akademik Bilişim Kongresi, Anadolu Üniversitesi, Eskişehir, Türkiye.

[4] Gartner, G., Frank, A., & Retscher, G. (2003). Pedestrian navigation system for mixed indoor/outdoor environment. LBS and TeleCartography, 66, 161-167.

[5] Rauschnabel, P. A., Rossmann, A., & tom Dieck, M. C. (2017). An adoption framework for mobile augmented reality games: The case of Pokémon Go. Computers in Human Behavior, 76, 276-286.

[6] Bora, E. (2017). Mekanların konumsal veri ile harita üzerinde ve artırılmış gerçeklik kullanılarak üç boyutta gösterilmesi uygulaması örneği Tour İstanbul (Master's thesis, Bilişim Enstitüsü).

[7] Chawathe, S. S., 2009. Low-latency indoor localization using bluetooth beacons. In Intelligent Transportation Systems, ITSC'09, 12th International IEEE Conference on IEEE, 3- 7 October 2009, St. Louis, Missouri, 1- 7.

[8] Ünal, M. (2017). Kültürel Miras Alanları İçin Uzaktan Artırılmış Gerçeklik Sistemi.

[9] Polat, M. (2017). Coğrafi bilgi sistemleri yaklaşımı ile tasarlanan turistik amaçlı artırılmış gerçeklik uygulaması: Safranbolu örneği (Master's thesis, Fen Bilimleri Enstitüsü).

[10] Breiman, L. ((2001). "Random Forests", Machine Learning, 45:5–32.

[11] Cortes, C., & Vapnik, V. (1995). Suportt-vector networks. Machine Learning, 20(3): 273-297.

[12] Quinlan, J. R. (1993). C4.5: Programs for Machine Learning. Morgan Kaufmann Publisher.

[13] T. Chen, C. Guestrin. Xgboost: A scalable tree boosting system. In: Proceedings of the 22nd acm sigkdd international conference on knowledge discovery and data mining. 2016. p. 785-794.

[14] Abdullah A., (2020). Makine öğrenmesi sınıflandırma yöntemlerinde performans metrikleri ile test tekniklerinin farklı veri setleri üzerinde değerlendirilmesi. (Master's thesis Fen Bilimleri Enstitüsü)

[15] Orhan, İ., & Güler, A. (2021). Artırılmış Gerçeklik Uygulamaları İçin Unity ve Vuforia Kullanımı. Anadolu Üniversitesi Bilim Ve Teknoloji Dergisi- B Teorik Bilimler, 9(1), 67-74.

LANE TRACKING AND COLLISION AVOIDANCE USING DEEP LEARNING IN AUTONOMOUS VEHICLES

C.B. ŞAFAK [1] and A.OZTURK[1,2]

[1] KTO Karatay University, Konya/Turkey, belemirsafak@gmail.com
[1] KTO Karatay University, Konya/Turkey, ali.ozturk@karatay.edu.tr
[2] Havelsan A.S, Konya/Turkey, aliozturk@havelsan.com.tr

Abstract **- Autonomous cars can navigate their surroundings with little or no need for driver assistance. Autonomous cars allow disabled individuals to drive individually. Due to its benefits such as reducing human errors, fuel efficiency and comfortable driving, it is a technology that is always open to improvement. In this study, an autonomous vehicle simulation that automatically follows the lane and avoids obstacles while driving was made using a deep learning model. For this purpose, Webots which is a free and open source 3D simulation environment, was used. Four different tracks were created to increase the variety of objects on the route to be followed in the simulation environment. There are animals such as cats, dogs and foxes on the first track. The second track is a track where there are several people. The third track is a track with road construction work and various obstacles. The last track is a track with other vehicles. The vehicle with a camera on it was driven full laps on these four tracks without interruption. The drive lasted approximately 2 minutes, and data was collected from steering angle and camera images during the drive. The autonomous feature of the vehicle is given by a deep learning model. While training the model, three different optimizers were tried and different filters were applied. While evaluating the results, mean square error (MSE) and accuracy values were examined. Accuracy values were obtained as 95.31%, 95.01% and 95.26% for the "sgdm", "adam" and "rmsprop" optimizer parameters, respectively. The MSE values were 0.3673, 0.3976 and 0.3885, respectively. Autonomous vehicle driving was achieved with the deep learning model using the "sgdm" optimizer, which has the highest accuracy.**

Keywords **– Autonomous driving, collision avoidance, lane tracking, deep learning.**

I. INTRODUCTION

IN the modern era, artificial intelligence is used to solve many problems. Using artificial intelligence in cars is an important technology that will make human life easier. In this way, traffic accidents caused by humans can be eliminated, time spent in traffic can be reduced, and disabled people can drive. Many new solutions are being proposed for robot cars, also known as autonomous vehicles, which are formed by the combination of artificial intelligence and the car. In this study, we designed a self-driving, lane following and obstacle avoiding vehicle with deep learning.

In the literature, there are several studies on autonomous driving. Rathod [1] conducted a study examining the development of Google's autonomous driverless vehicle project. The study involved a test fleet of at least eight vehicles, including six Toyota Priuses, an Audi TT and a Lexus RX450h. Lombard prepared and vehicles Street, then the Golden Gate Bridge, the Pacific Coast Highway and Lake Tahoe. has been stated. The results of the Urban Challenge showed that an autonomous vehicle could navigate in traffic in the future.

Hofmann et al. [2] stated in their study that the idea of autonomous driving has almost become an existing reality thanks to lane keeping assist and adaptive cruise control systems in vehicles. For autonomous driving to be more efficient, they mentioned the importance of the data set that needs to be prepared. They emphasized that navigation systems will also contribute to the data set.

An autonomous car study based on deep learning in Udacity simulation environment by Lade et al. [3] has been done. While training the model, the more complex CNN A architecture with 11 layers and the simpler CNN B architecture with 7 layers were compared. The result was observed in a driving environment and they obtained 96.83% accuracy for model A and 76.67% accuracy for model B. In another study, Bhalla et al [4] aimed to build a deep learning model that enables driving in an autonomous car without any manual operation. As a result, the proposed modified CNN model achieved better results compared to Resnet50, DenseNet 201, VGG16, and VGG19.

Bhujbal and Pawar [5], aimed to train a convolutional neural network for autonomous driving using Udacity's Car Simulator Environment. The dataset was created and then NVIDIA's convolutional neural network model was used to predict the autonomous driving of the car. As a result, it was observed that the vehicle drove well on the easy track, but the expected results were not obtained on the difficult one.

Burnett et al [6] explained their Zeus' system architecture and proprietary algorithms. As a result, they were able to prepare the Zeus car for SAE AutoDrive competition after extensive testing. Stop sign detection and obstacle detection operated as expected without adjustments. They were able to create a system reliable enough to win the competition.

Lee et al. [7] wanted to show that autonomous driving can be safe in adverse driving conditions in order to increase

confidence in autonomous driving. They stated that in order to be able to drive in adverse driving conditions such as rain and wet conditions, algorithms should be able to use sensors such as laser scanners and cameras to detect roads with minimal error margin. They developed a sensor fusion algorithm that can work in bad weather conditions and demonstrated its operability at the 2014 Hyundai Motor Company's Autonomous Car Competition.

Rosyid et al [8] conducted a study targeting a self-driving vehicle avoiding potholes on the road. They observed how an autonomous vehicle avoids potholes in a driving simulator called AirSim. While training their model, they tried three different Convolutional Neural Network models, namely BojarskiCNN, ZhiluChenCNN and AdsharCNN. They concluded that Bojarski CNN has the best performance in the field compared to other models.

Aki and Dirik [9] conducted autonomous driving tests in a simulation environment. In their study, the self-driving vehicle in the simulation was achieved by a deep learning (DL) model and PID control. For the autonomous driving of the DL-based and PID-based self-driving vehicle, the calculation of the deviation values in one full lap was examined. As a result, it was observed that the driving of the PID-based self-driving vehicle oscillated too much to be suitable for real life, but the DL-based autonomous vehicle exhibited a smoother driving.

Okuyama et al. [10] observed the lane following of an autonomous car learning with Deep Q Network and its driving on static obstacles in a simulation environment. The action with the highest reward became mandatory. Unity was used for the simulation environment. The vehicle in the system was trained by driving at constant speed for 10 m/s, 15 m/s and 20 m/s and avoiding obstacles. As a result, the learning ability of the automobile decreased as the driving speed increased.

Ramarao et al [11] investigated different algorithms for detecting traffic lanes. Some methods required expensive sensors, while others relied on specialized sensors such as LiDAR. Methods such as Feature Selection Algorithm, Canny edge detection and Hough transform were compared. As a result of their research, they concluded that the OpenCV-based Lane Detection system is feasible and fast. As a result, they concluded that the real-time performance of the based system is fast and reliable.

Barrozo and Lazcano [12], designed autonomous vehicle for agriculture and created a vision-based control system for it. The data set they used was synthetic images and the results show that their proposed model has better performance than the others.

Swaminathan et al [13] presented an autonomous vehicle prototype and used the Belgian traffic sign dataset to evaluate its performance. Traffic detection approaches achieved 83.7% success.

Dangskul et al [14] investigated an off-the-shelf deep learning model. This model was implemented with CNN using Nvidia Jetson Nano which is implemented in an end-to-end system. Specifically, the research is based on the use of the Softmax activation function for steering angle estimation and classification instead of the traditional regression model.

In our study, Webots simulation environment which is an open learning platform was used. Visual data were obtained by driving in the simulation environment. The deep learning model was trained with the images obtained from the on board-camera of the vehicle. The steering angle was estimated in the range -1 to 1, where negative angle means left turn, 0 means straight going and positive angle means right turn. The vehicle was driven manually for one full lap on different tracks and data was collected from the on-board camera and steering angles. The autonomous feature of the vehicle is based on deep learning modeling. While training the model, three different optimizers were tried and different filters were applied. The MSE and accuracy values were used to evaluate the results. As a result of deep learning training, vehicle driving was monitored in a simulation environment and successful results were obtained.

II. MATERIALS AND METHODS

A. Webots Simulation Environment

Webots is an open source simulation environment used for the development and testing of robotics and artificial intelligence applications. Webots simulates different types of robots and sensors in real world conditions. Webots uses different programming languages (C, C++, Python, etc.). In this way, by coding the autonomous program and processing the sensor systems, it is possible to define how the autonomous vehicle should behave.

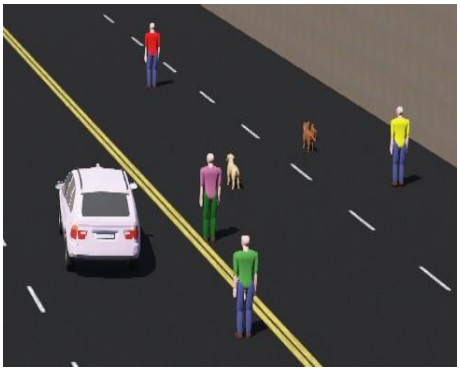

Figure 1: Autonomous vehicle that changes its path when it sees a human community.

Figure 2: Autonomous vehicle that sees motorizedvehicles and cats and changes course.

Figure 1 and Figure 2 show two sample images of the driving scenarios designed in the Webots environment for our study.

B. Data Collection

Behavioral cloning was used to capture human car driving and the situation leading to the action. These recordings were used as input to the deep learning model. The vehicle was driven manually in the designed environment. The camera in the vehicle captured images throughout the drive. Four different driving scenarios consists of a track. This is due to the fact that the vehicle encounters more objects and is that we prefer a driving simulation that is closer to life. The first track contains animals encountered in everyday life, such as dogs and cats. The second track is has a lot of people. The third track is an obstacle course with road construction work. The last track is a track with other vehicles. The vehicle was driven on these four tracks continuously for a full lap. The drive took approximately 2 minutes. As a result of the driving, 11,931 images and steering angle values were recorded.

C. Model Architecture

A Convolutional Neural Network (CNN) model was created using the Tensorflow and Keras libraries. The designed CNN architecture consists of 5 convolutional layers and 3 Max pooling2D layers. In order to improve the classification ability of the model, for the input layer, a larger filter (7x7) was designed as it can help to detect features at a higher level. For the next successive layers, a smaller filter (3x3) was designed as it can help to extract finer features. Number of neurons in convolution layers was 64,128,128, 256 and 256, respectively. Filter of (2x2) was chosen for the max pooling2D layers. Figure 3 shows the CNN model architecture.As shown in Figure 3, a flatten layer was added to smooth the outputs from the convolutional layers. Then two hidden fully connected dense layers are formed with 128 and 64 neurons respectively. Each of them comes with a ReLU activation function and a dropout layer. Dropout has been implemented with a ratio of 0.2 to help reduce overfitting. The last layer is a fully connected layer with a softmax activation function for 3 classes. This allows the model to classify between the various classes. These three classes refer to going right, going left and going straight. We minimize the model losses related to classification.

Three different optimizers have been tried for comparison purposes. These were Sgdm optimizer, Adam optimizer, Rmsprop optimizer, respectively.

III. EXPERIMENTAL RESULTS AND DISCUSSIONS

The designed CNN architecture is coded with Tensorflow and Keras libraries using Python programming language. CNN architecture batch size is set to 32 and Epoch amount to 100. The designed codes were written and trained in Visual Studio Code environment. For a 2-minute full track drive, training times (7-8 hours) were approximately the same for Adam optimizer and sgdm optimizer. The training took 15 hours for the rmsprop optimizer. The results were observed in three dimensions in the Webots simulation environment.

The accuracy values of the designed CNN architecture were obtained numerically. Filters values were changed and different optimizers were used to obtain the best results. In the convolution layers other than the first one, the filters 3x3, 4x4 and 5x5 were applied. The best result was obtained with the 3x3 filter.

In the simulation, a smooth lane tracking was observed to be able to do so. The vehicle's object detection was good, avoiding collisions for many objects. As a result, our vehicle realized an autonomous driving with 95,31% accuracy.

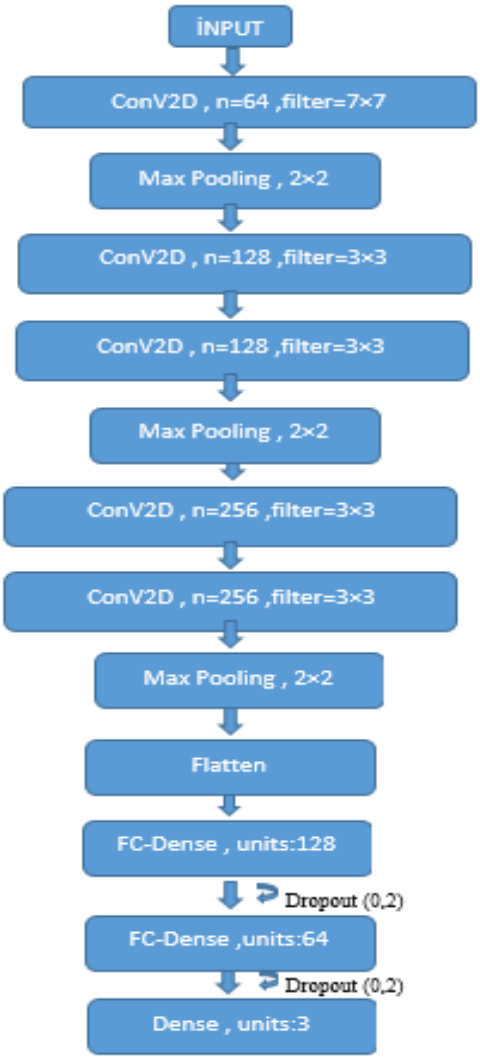

Figure 3: CNN Model Architecture

The Mean Squared Error (MSE) and accuracy values were used to evaluate the results. Table 1 shows the experimental results with respect to the accuracy and MSE values.

Table 1: Experimental results for the optimizers in CNN.

Optimizer	Accuracy values	MSE values
Sgdm	0,9531	0,3673
Adam	0,9501	0,3976
Rmsprop	0,9526	0,3885

According to the results given in Table 1, the best accuracy was obtained as 95.31% with Sgdm optimizer. On the other hand, the accuracy values were 95.01% and 95.26% for the Adam optimizer and the Rmsprop optimizer, respectively. The MSE values were recorded as 36.73%, 39.76% and 38.85% for Sgdm, Adam and Rmsprop, respectively. The test values were very close to each other and the best results were obtained with the sgdm optimizer.

The second best accuracy and MSE values belong to Rsmprop optimizer. However, the training duration took approximately 15 hours for Rmsprop optimizer while it was approximately 8 hours for Adam and Sgdm optimizers.

After training the CNN with Sgdm optimizer, autonomous driving was realized with 95,31% accuracy. The vehicle achieved a smooth lane tracking and avoided many different type of obstacles as shown in Figure 4.

Figure 4. Collision avoidance of an autonomous vehicle on a roadworks route.

Figure 4 shows a view of autonomous driving in Webots environment. In this image, it can be seen that the autonomous vehicle avoids obstacles on a route with different obstacles. In Table 2, we made a comparison between our study and other studies in the literature according to the MSE values.

Table 2: Comparison of our study with the literature.

Author(s)	Simulation Environment	Techniques	MSE
Lade et al. [3]	Udacity	CNNA	0.61
Bhalla et al. [4]	Udacity	Resnet50 DenseNet201 VGG16 VGG19 Proposed Model	0.3109 0.2590 0.5303 0.3153 0.2914
Rosyid et al [8]	AirSim	BojarskiCNN ZhiluChenCNN AdsharCNN	0.22 0.125 0.19
Our Study	Webots	CNN(Sgdm) CNN(Adam) CNN(Rmsprop)	0.3673 0.3976 0.3885

Table 2 compares the results of this study with other studies using deep learning algorithms in different simulation environments used in the literature. Our study had achieved comparable results with the studies given in the table. Two of the studies given in Table 2 used Udacity simulation environment and AirSim was used in another one. The studies which used Udacity applied many different deep learning models along with their proposed CNNs. They observed higher MSE values than our study with some of the CNN models. The study which used AirSim environment applied three different CNN models having smaller MSE values. However, the simulation environment, the driving scenario and the collected data are different in each of these studies. Therefore, the MSE values could only be fairly evaluated if the same simulation environment, driving scenario and the collected data were used.

With our study, it has been observed that autonomous driving is possible by avoiding obstacles of very different nature. As a future work, more complex road scenarios with different CNN architectures will be tested, including elements such as traffic lights and traffic signs.

REFERENCES

[1] Rathod, S. D. (2013). An autonomous driverless car: an idea to overcome the urban road challenges. Journal of Information Engineering and Applications, 3(13), 34- 38.

[2] Hofmann, M., Neukart, F., & Bäck, T. (2017). Artificial Intelligence and Data Science in the automotive industry. arXiv preprint arXiv:1709.01989.

[3] S. Lade, P. Shrivastav, S. Waghmare, S. Hon, S. Waghmode and S Teli,"Simulation of Self Driving Car Using Deep Learning," 2021International Conference on Emerging SmartComputing and Informatics (ESCI),Pune,India,2021,pp.175-180, doi:10.1109/ESCI50559.2021.9396941.

[4] A. Bhalla, M. S. Nikhila and P. Singh,"Simulation of Self-driving Car using Deep Learning," 2020 3rd International Conference on Intelligent Sustainable Systems (ICISS), Thoothukudi, India, 2020, pp. 519-525, doi: 10.1109/ICISS49785.2020.9315968.

[5] K. Bhujbal and D. M. Pawar, "Deep Learning Model for Simulating Self Driving Car," 2023 International Conference on Communication System, Computing and IT Applications (CSCITA), Mumbai, India, 2023, pp. 26-31, doi: 10.1109/CSCITA55725.2023.10104750.

[6] K. Burnett et al., "Building a Winning Self- Driving Car in Six Months,", 2019 International Conference on Robotics and Automation (ICRA), Montreal,QC,Canada,2019,pp.9583-9589,doi: 10.1109/ICRA.2019.8794029.

[7] U. Lee et al., "EureCar turbo: A self-driving car that can handle adverse weather conditions," 2016 IEEE/RSJ International Conference on Intelligent Robots and Syst(IROS), Daejeon, Korea (South), 2016, pp. 2301-2306, doi: 10.1109/IROS.2016.7759359.

[8] H. A. Rosyid, O. S. Burhan, I. A. E. Zaeni andA. N. C. Pee, "Comparison of Deep Learning Models in Pothole Avoidance for Self-Driving Car," 2021 7th International Conference on Electrical, Electronics and Information Engineering (ICEEIE), Malang, Indonesia, 2021, pp. 466-471, doi: 10.1109/ICEEIE52663.2021.9616639.

[9] Aki, K. & Dirik, A. E. (2020). Derin Öğrenme Tabanlı Ve PID Kontrol Tabanlı Sürücüsüz Araç Sistemleri . Mühendislik Bilimleri ve Tasarım Dergisi , Özel Sayı: International Conference on Artificial Intelligence and Applied Mathematics in Engineering (ICAIAME 2020) , 306-316 . DOI: 10.21923/jesd.829598

[10] T. Okuyama, T. Gonsalves and J. Upadhay, "Autonomous Driving System based on Deep Q Learnig,"2018 International Conference on Intelligent Autonomous Systems (ICoIAS),Singapore,2018,pp.201-205, doi:10.1109/ICoIAS.2018.8494053.

[11] Dr Narapareddy Ramarao, B Vivek Bhat, Kartik Kulkarni and Raban Akbary Ashley, "Lane Detection for Autonomous Vehicle", International Journal of Engineering Research and Applications (IJERA), vol. 9, no. 3, March 2019, [online] Available: www.ijera.com.

[12] J. Barrozo and V. Lazcano, "Simulation of an Autonomous Vehicle Control System Based on Image Processing", 2019 5th International Conference on Frontiers of Signal Processing (ICFSP), pp. 88-94, 2019.

[13] V. Swaminathan, S. Arora, R. Bansal and R. Rajalakshmi, "Autonomous Driving System with Road Sign Recognition using Convolutional Neural Networks", 2019 International Conference on Computational Intelligence in Data Science (ICCIDS), pp. 1-4, 2019.

[14] W. Dangskul, K. Phattaravatin, K. Rattanaporn and Y. Kidjaidure, "Real-Time Control Using Convolution Neural Network for Self-Driving Cars", 2021 7th International Conference on Engineering Applied Sciences and Technology (ICEAST), pp. 125-128, 2021.

Turkish and English Datasets in Paraphrase Generation Task with BART Model

H.TEKGOZ[1] and S.İLHAN OMURCA[2]

[1] Loodos Technology A.Ş. R&D Center, Kocaeli/Turkey, hilal.tekgoz@loodos.com
[2]Kocaeli University, Kocaeli/Turkey, silhan@kocaeli.edu.tr

***Abstract* - Paraphrase generation is a way of expressing the same meaning of a text or sentence using different syntax or words. It is one of the most challenging tasks of natural language processing due to the complexity and diversity of the language. However, with the recent progress in deep learning models, more promising results have been acquired for paraphrasing tasks. In this study, a pre-trained BART language model was trained both with English and Turkish paraphrasing datasets. Quora Question Pairs (QQR), Microsoft Common Object in Context (MSCOCO), and General Language Understanding Evaluation (GLUE) datasets were used for English paraphrasing, and for Turkish, these datasets were translated from English to Turkish using the Google Translate API. Cosine similarity, Bleu score, Rouge score, and novelty score metrics were considered for a comprehensive evaluation of the obtained results. Consequently, the experimental results show that BART is a successful model for Turkish paraphrasing as well as English paraphrasing.**

***Keywords* - Paraphrase Generation, Natural Language Processing, BART, Transformer, BLEU**

I. INTRODUCTION

In recent decades, Natural Language Processing (NLP) has become a more prominent topic in artificial intelligence, especially based on the success of deep learning techniques. Among many tasks of NLP, such as summarizing text, answering questions, and generating dialogs, the paraphrase generation task is considered one of the most important and challenging tasks. Paraphrase generation is the task of reconstructing an output sentence while preserving the meaning of the original input sentence. In other words, if the two sentences are equivalent in meaning but different in words and syntax, then they are paraphrases. Paraphrasing can play an important role in many language understanding and generation tasks, such as text summarization, machine translation, article writing, or question answering.

The underlying architectures chosen for paraphrase generation have shown a shift from classical learning approaches to transformer approaches in recent years, with the rapid and successful development of the transformers. In paraphrase generation studies, BART (Bidirectional and Auto-Regressive Transformers) [1] stands out among transformer models with its better performance. BART is a seq2seq model with a bidirectional (BERT-like) encoder and an autoregressive (GPT-like) decoder. A fine-tuned pretrained BART model can take a text sequence as input and produce a different text sequence at the output, as it is capable of learning underlying relationships in the output text with the various patterns in the input text.

In this study, a transformer-based paraphrasing application was developed for both Turkish and English. And datasets that can be used in Turkish paraphrasing studies have been published. Thus, our study contributed to the limited Turkish studies in this field [https://drive.google.com/drive/folders/10ULZFcGW2WF4Yb8S0J7IacFGjRMBssH7?usp=sharing].

The organization of this article is as follows: Section 2 reviews previous studies in related literature. Section 3 describes the techniques used. Section 4 covers datasets and the applied model. Finally, Section 5 discusses the conclusion and the future work.

II. RELATED STUDIES

The concept of paraphrase generation is a new and very common research topic in the field of natural language processing (NLP). With the successful applications of deep learning models in the field of text generation, it is observed that the use of paraphrasing has increased, especially in fields such as writing scientific articles. It can also play an important role in language comprehension tasks such as answering questions, machine translation, and semantic parsing, and is a good way to augment data [2].

With the advances in transformer based language models, the number of text generation studies have been increased [3]. Z. Li et al. [3] proposed an approach for paraphrase generation using reinforcement learning. They combined the Seq2Seq model with the reinforcement learning component for paraphrase generation and generated a fluent and semantically similar text to the original sentence. One of the main challenges in text generation studies is the validity of evaluation methods. When the relevant literature is examined, it has been observed that cross-entropy is used to measure semantic similarity in paraphrase generation. However,

Ranzato et al. have suggested using word-based measures such as BLEU [4] and ROUGE [5].

Ganitkevitch et al. [6] created a database called PPDB for synthetic data generation. More than 220 million description text pairs have been created for the English language. It has also been proposed for producing poetry in the style of Shakespeare, Whitman, or Cummings using existing language models. Badura et al. [7] have developed a system they call Bhairon that produces poems in the style of William Shakespeare, Walt Whitman, or Edward Estlin Cummings with a user-supplied first line. They fine-tuned the GPT-2 model, using each poet's work as training data. The system provides the ability to "translate" the user's input to Shakespearean style using the style transfer approach. For this task, they used the T5 model. They evaluated the experimental results with a collective BLEU score for 1-grams, 2-grams, 3-grams and 4-grams. In another study, a model called Latent Bag of Words was presented to re-express the texts with the same meaning. In that model, a Bag of Words vector is created for the input text. Then, the resulting vector was combined with the latent component to create a better text generation function [8]. Yufei Wang et al. [9], compared the success rates of the pre-trained BART language models in the Paraphrase generation task when the models are fine-tuned with different datasets. They concluded that the BART language model is better than other language models when evaluated under different datasets and test methods. In an approach called controlled paraphrase generation, a specific meaning is targeted for a sentence. For this purpose, a syntactic example is used to rewrite the sentence. A text with a similar structure is taken and rewritten in a way that does not distort the meaning of the text [10]. In the study by P. Xu and V. C. Ng [16], a method for paraphrase generation, which focuses on rewriting a text with a different expression while preserving its meaning, is proposed using a machine translation model that translates the original sentence into the target language. They aimed to use a different expression while preserving the meaning in the source sentence. The performance of their method was evaluated by testing it on different language pairs and different datasets, and it was concluded that it can be used in paraphrase generation and the large datasets provided by language translation models can be used for this purpose. The studies on paraphrase generation have shown that fine-tuned BART models with different datasets outperform other language models in the paraphrase generation approach. Bağcı and Amasyalı [16] compared mT5, mBart, and BERT2BERT models for Turkish paraphrasing, and they found that MBart is the most successful model according to BLEU and Rouge metris. Alkurdi et all. [17] presented a method to create paraphrase datasets and fine tuned the pre-trained encoder-decoders such as mT5 and trBART on their datasets.

III. Materials and Methods

A. Datasets

We conducted experiments on Quora Question Pairs (QQR) [19], Microsoft Common Object in Context (MSCOCO) [20] and General Language Understanding Evaluation (GLUE) [20] datasets, which are frequently used in paraphrase generation. The QQR dataset, that matches users' questions and similar questions, consists of more than 400,000 question-answer pairs. MSCOCO, which is frequently used in the Paraphrase Generation literature, is an image dataset with multiple annotations. By including tasks with limited training data, the GLUE dataset is designed to encourage models that share general grammar across tasks. GLUE also includes a handcrafted diagnostic test suite that provides detailed linguistic analysis of models [10]. As it is known, these 3 datasets have been prepared for the English language. In order to be able to work for the Turkish language, these datasets were translated from English to Turkish using google translate api. In this way, three labeled Turkish datasets that can be used in text generation studies such as paraphrase generation were obtained and presented to the use of researchers. In our study, QQR, MSCOCO, and GLUE datasets were used to fine-tune the BART model.

B. Transformers

In recent studies, transformers based on self attention blocks [21] have started to dominate the research field as state of the art networks, especially for Seq2Seq models. The main reason for this can be summarized as follows, whereas recurrent models such as LSTM [22] have the ability to use sequential text processing over time, transformers have the ability to parallelize text processing. Through the attention mechanism [23], transformers suffer less from the long-term dependency problem than LSTM networks, as the information at the beginning of the sentence is equally well represented in the context vector, especially for long sentences. Another obvious contribution of transformers is that the effectiveness of pre-trained language models such as BART [24] comes to the fore with transformer structures. As demonstrated in the related literature, we use the BART model in our experiments due to its superiority in paraphrase generation.

C. BART

BART is a noise canceling autoencoder for pretraining sequence-to-sequence models. It gives satisfying results when fine-tuned for particular text generation tasks. The working structure is to reconstruct the original sentence by disrupting the sentence given with the noise function. It uses a standard transformer-based neural architecture such as BERT (bidirectional encoder) and GPT in the background. It distorts the actual sentence, i.e. randomly shuffles it among itself, and evaluates a series of noisy approximations by filling sentence openings with a single mask symbol. The architecture of it is built with a bidirectional encoder and a Auto-Regressive decoder. Six layers are used in the encoder and decoder in the model. In the Large-BART model, 12 layers were used. BART contains 10% more parameters in total than the BERT model of similar size [11]. To improve the performance of a pre-trained BART model, it can be fine-tuned by feeding it with different datasets. In order to fine-tune the dataset, it is necessary to create a dataset and perform data preprocessing

steps on the dataset. Then the model and training parameters are adjusted and fine-tuning is continued.

D. Evaluation Metrics

We made a comprehensive assessment by using different evaluation metrics such as Cosine similarity, BLEU and Rouge scores. Cosine similarity is one of the popular evaşuation metrics in various natural language processing tasks such as text generation. The cosine similarity focuses on the similarity between two points based on the angle between the two vectors. It is also used to determine word overlap in different text segments. The BLEU score is used as an evaluation measure usually in machine translation and text generation tasks. It has been observed in the literature that the BLEU score correlates quite well with human judgments [12]. The BLUE score takes into account the match between the target annotations and the generated texts, taking into account n-gram combinations [13]. The Rouge score is a widely used metric to measure the similarities between texts. ROUGE(Recall-Oriented Understudy for Gisting Evaluation) is based on the number of words and n-gram associations between output texts and reference texts. It also has sub-dimensions such as ROUGE-L, ROUGE-N and ROUGE-S. ROUGE-N evaluates by looking at the commonality of n-grams between texts in natural language processing tasks. ROUGE-S performs similarity assessment at sentence level. ROUGE-L, on the other hand, makes calculations using the longest common sub-sentence/index [14]. Novelty Score is a rating metric used to measure the proportion of new and original words in the generated text relative to the reference text. This metric is commonly used in artificial intelligence technologies such as NLP and computerized language modeling (CLM). A higher novelty score means that the generated text contains different word and sentence structures from the input text content.

IV. Experiments

In this study, different methods have been tried for paraphrase generation in Turkish language. First of all, Quora, MSCOCO, GLue datasets were translated from English to Turkish with google translate api in order to fine-tune Turkish datasets. Then, it was fine-tuned with BART, the transformers model published by Facebook on hugging face. The fine-tuned BART model was trained according to the parameters shown in Table 1.

Table 1: Training configuration of BART models

Epoch	5
Batch Size	64
Learning Rate	5e-5
Max Lenght	128
Max Seq Lenght	128
Early Stopping	True

The datasets were fine-tuned in two different ways, in English and Turkish, and the evaluation of the English and Turkish paraphrasing results according to the Cosine, BLEU, ROUGE, and Novelty scores are given in Table 2 and Table 3 respectively.

Table 2: English paraphrasing results

Model	Cosine	BLEU	ROUGE-L	Novelty
Quora	0.95	0.72	0.87	0.17
MSCOCO	0.46	0.29	0.47	0.61
GLUE	0.93	0.80	0.90	0.22

Table 2 shows the fine-tuned BART model results on 3 different English datasets. Considering the results, it is realized that with the Glue dataset, more successful results were obtained due to the other two datasets. And also approximate performance values were obtained with the quora dataset. Although it is observed that lower Cosine, BLEU, and ROUGE scores were obtained with the COCO dataset, the highest novelty rate was obtained with this dataset. The lower novelty score acquired for the Quora dataset shows that the BART model for this dataset was not successful in generating novel words, although it produced sentences similar to the reference sentences in that dataset.

Table 3: Turkish paraphrasing results

Model	Cosine	BLEU	ROUGE-L	Novelty
Quora	0.92	0.79	0.85	0.24
MSCOCO	0.46	0.66	0.80	0.33
GLUE	0.89	0.69	0.81	0.33

When the results in Table 3 are examined, it is observed that the performance rate of the BART model, which was fine-tuned with the Quora dataset, is higher than the other datasets. For this dataset, the performance of Turkish paraphrasing is close to the performance of English paraphrasing. Besides, while the novelty score is 0.17 for English paraphrasing, it is 0.24 for Turkish. This shows that the BART model can generate sentences with more novel words in Turkish than in English. While a similar situation was seen in the Glue dataset, the novelty score for the COCO dataset decreased from 0.66 to 0.33. However, for the COCO dataset, Cosine, BLEU and ROUGE values for English paraphrasing were observed to be lower, while all of these performance values were higher for Turkish. Considering all these determinations and evaluations, it is concluded that the BART model is effective in paraphrasing tasks for Turkish as well as English.

For the qualitative analysis, example Turkish paraphrasing sentences are given in Table 4. The words in generated sentences which are different from the reference sentence words are highlighted.

Table 4: Example Turkish paraphrasing sentences

Reference Sentence-1	Jalari, Hindistandaki Hamirpur köylerinden biridir.
Generated Sentence-1	Jalari, Hindistandaki Hamirpur köylerindeki **Hindistanın kaptan bölgesinden** biridir.

Reference Sentence-2	1988-89 NBA sezonu, Ulusal Basketbol Birliğinin 43. sezonuydu.
Generated Sentence-2	**1988'dan 89'a** NBA sezonu, Ulusal Basketbol Birliğinin 43. sezonuydu.
Reference Sentence-3	Suçlamalar, Franklin İlçe Belediye Mahkemesinde reddedildi.
Generated Sentence-3	Franklin İlçe Belediye **Mahkemesini sorumlu suçlamalarını** reddetti.
Reference Sentence-4	ABD Sayım Bürosuna göre ilçe, kara ve (% 0.2) su bulunan toplam alandır.
Generated Sentence-4	ABD Sayım Bürosuna göre **ilçenin toplam yüzölçümü** kara ve (% 0.2) sudur.
Reference Sentence-5	Konseyin aktif bir üyesi olarak kabul edildi ve sık sık resmi Albany işi için Kanada'ya gönderildi.
Generated Sentence-5	Konseyin aktif bir üyesi olarak kabul edildi ve resmi Albany **işlerine** gönderildi.

In all examples reflected in Table 4, it has been determined that the generated sentence has the same meaning as the reference sentence, but has a different sentence structure.

V. Result and Future Studies

In this study, a pre-trained BART model was used for paraphrase generation both in Turkish and English languages. In order to fine-tune the BART model for Turkish, three paraphrasing datasets Quora, COCO and Glue which are also used in text generation studies were translated into Turkish. The effectiveness of BART based paraphrasing for both English and Turkish languages are examined using the translated and revised Turkish paraphrasing datasets and public English datasets. The experimental results were evaluated both qualitatively and quantitatively. We have presented the pairs of reference sentence and generated sentence for qualitative analysis. For the quantitative analysis, we used Cosine, BLEU, ROUGE and Novelty scores to make a comprehensive analysis. The experimental results show that the BART transformer is as an effective model in paraphrasing tasks for both Turkish and English languages. In future studies, it is planned to make a comparison between language models by using different pre-trained language models.

References

[1] A. Krizhevsky, I. Sutskever, and G. E. Hinton, "Imagenet classification with deep convolutional neural networks," Communications of the ACM, vol. 60, no. 6, pp. 84–90, 2017.

[2] J. Zhou and S. Bhat, "Paraphrase generation: A survey of the state of the art," in Proceedings of the 2021 Conference on Empirical Methods in Natural Language Processing. Online and Punta Cana, Dominican Republic: Association for Computational Linguistics, Nov. 2021, pp. 5075–5086.

[3] Z. Li, X. Jiang, L. Shang, and H. Li, "Paraphrase generation with deep reinforcement learning," arXiv preprint arXiv:1711.00279, 2017.

[4] K. Papineni, S. Roukos, T. Ward, and W.-J. Zhu, "Bleu: a method for automatic evaluation of machine translation," in Proceedings of the 40th annual meeting of the Association for Computational Linguistics, 2002, pp. 311–318.

[5] M. Denkowski and A. Lavie, "Meteor universal: Language specific translation evaluation for any target language," in Proceedings of the Ninth Workshop on Statistical Machine Translation. Baltimore, Maryland, USA: Association for Computational Linguistics, Jun. 2014, pp. 376–380. [Online]. Available: https://aclanthology.org/W14-3348

[6] J. Ganitkevitch, B. Van Durme, and C. Callison-Burch, "PPDB: The paraphrase database," in Proceedings of the 2013 Conference of the North American Chapter of the Association for Computational Linguistics: Human Language Technologies. Atlanta, Georgia: Association for Computational Linguistics, Jun. 2013, pp. 758– 764. [Online]. Available: https://aclanthology.org/N13-1092

[7] M. Badura, M. Lampert, and R. Dre˙zewski, "System supporting poetry generation using text generation and style transfer methods," Procedia Computer Science, vol. 207, pp. 3310–3319, 2022.

[8] Y. Fu, Y. Feng, and J. P. Cunningham, "Paraphrase generation with latent bag of words," Advances in Neural Information Processing Systems, vol. 32, 2019.

[9] Z. Li, Y. Wang, R. Fan, Y. Wang, J. Li, and S. Wang, "Learning to adapt to low-resource paraphrase generation," in Proceedings of the 2022 Conference on Empirical Methods in Natural Language Processing, 2022, pp. 1014–1022.

[10] M. Chen, Q. Tang, S. Wiseman, and K. Gimpel, "Controllable paraphrase generation with a syntactic exemplar," arXiv preprint arXiv:1906.00565, 2019.

[11] A. Wang, A. Singh, J. Michael, F. Hill, O. Levy, and S. R. Bowman, "Glue: A multi-task benchmark and analysis platform for natural language understanding," arXiv preprint arXiv:1804.07461, 2018.

[12] M. Lewis, Y. Liu, N. Goyal, M. Ghazvininejad, A. Mohamed, O. Levy, V. Stoyanov, and L. Zettlemoyer, "Bart: Denoising sequence-to-sequence pre-training for natural language generation, translation, and comprehension," arXiv preprint arXiv:1910.13461, 2019.

[13] R. O. Tan, "Towards more natural explanations of user preferences," Master's thesis, University of Stavanger, Norway, 2020.

[14] V. Zhukov, E. Golikov, and M. Kretov, "Differentiable lower bound for expected bleu score," arXiv preprint arXiv:1712.04708, 2017.

[15] C. Lin, "Recall-oriented understudy for gisting evaluation (rouge)," Retrieved August, vol. 20, p. 2005, 2005.

[16] A. Bağcı and M. F. Amasyali, "Comparison of turkish paraphrase generation models," in 2021 International Conference on INnovations in Intelligent SysTems and Applications (INISTA). IEEE, 2021, pp. 1–6.

[17] B. Alkurdi, H. Y. Sarioglu, and M. F. Amasyali, "Semantic similarity based filtering for turkish paraphrase dataset creation," in Proceedings of the 5th International Conference on Natural Language and Speech Processing (ICNLSP 2022), 2022, pp. 119–127.

[18] L. Sharma, L. Graesser, N. Nangia, and U. Evci, "Natural language understanding with the quora question pairs dataset," arXiv preprint arXiv:1907.01041, 2019.

[19] T.-Y. Lin, M. Maire, S. Belongie, J. Hays, P. Perona, D. Ramanan, P. Doll´ar, and C. L. Zitnick, "Microsoft coco: Common objects in context," in Computer Vision–ECCV 2014: 13th European Conference, Zurich, Switzerland, September 6-12, 2014, Proceedings, Part V 13. Springer, 2014, pp. 740–755.

[20] A. Wang, A. Singh, J. Michael, F. Hill, O. Levy, and S. R. Bowman, "Glue: A multi-task benchmark and analysis platform for natural language understanding," arXiv preprint arXiv:1804.07461, 2018.

[21] A. Vaswani, N. Shazeer, N. Parmar, J. Uszkoreit, L. Jones, A. N. Gomez, Ł. Kaiser, and I. Polosukhin, "Attention is all you need," Advances in neural information processing systems, vol. 30, 2017.

[22] S. Hochreiter and J. Schmidhuber, "Long short-term memory," Neural computation, vol. 9, no. 8, pp. 1735–1780, 1997.

[23] D. Bahdanau, K. Cho, and Y. Bengio, "Neural machine translation by jointly learning to align and translate," arXiv preprint arXiv:1409.0473, 2014.

[24] M. Lewis, Y. Liu, N. Goyal, M. Ghazvininejad, A. Mohamed, O. Levy, V. Stoyanov, and L. Zettlemoyer, "Bart: Denoising sequence-to-sequence pre-training for natural language generation, translation, and comprehension," arXiv preprint arXiv:1910.13461, 2019.UBMK 2023 8th international conference on computer science and engineering (UBMK).

Detection of DDOS Attacks with Deep Learning Methods

S.S.GUCLU[1] and A.OZTURK[1,2]

[1]KTO Karatay University, Konya/Turkey, smyyegclu@gmail.com
[1]KTO Karatay University, Konya/Turkey, ali.ozturk@karatay.edu.tr
[2]Havelsan A.S, Konya/Turkey, aliozturk@havelsan.com.tr

***Abstract* - Distributed Denial of Service Attacks (DDoS), which is the most common type of attack, is used to take targeted devices or servers offline, interrupt network services, and limit or prevent the target resource from providing service by maximizing resource consumption. Detecting this type of attack in advance allows us to prevent data loss, cost loss or resource consumption by ensuring early use of solution methods. For this reason, DDOS attack detection is of great importance in the field of cyber security. In this study, the use of deep learning methods to detect DDoS attacks is discussed. First of all, the data set containing DDOS attack types and normal traffic was edited and optimized. Then, the edited data set was applied to CNN and LSTM deep learning models. While the accuracy of detecting DDOS attacks of the CNN model was 76%, this rate was found to be 72% in the LSTM model.**

***Keywords* – DDOS Attacks, LSTM, CNN, Deep Learning**

I. INTRODUCTION

The increasing integration of the digital world into our daily lives has elevated the significance of the concept of security. With the growing prevalence of cyberattacks, efforts are being made to mitigate the potential costs and losses of information and data. Distributed Denial of Service (DDOS) attacks stand out as one of the most common threats in terms of cybersecurity. DDOS attacks often involve coordinated attacks originating from various points simultaneously or at different intervals. These attacks result in the disruption of services by causing excessive resource consumption on servers or networks [1]. DDOS attacks are typically carried out by overwhelming the targeted systems with a high volume of data requests or data transmissions, often utilizing compromised computers known as botnets. In the detection and prevention of DDOS attacks, machine learning methods are commonly employed, alongside deep learning techniques. This study focuses on the application of deep learning approaches to detect DDOS attacks within large datasets using artificial intelligence and learning models. Furthermore, it compares the outcomes of different models utilized in this context.

In their study, Shi et.al. employ a two-stage approach for detecting DDOS attacks. In the first stage, they determine the severity of the attack, while in the second stage, they use the K-Nearest Neighbors (KNN) algorithm, one of the machine learning methods, for attack detection. Additionally, the DDADA (Distributed Denial of Service Detection Algorithm) and DDAML (Distributed Denial of Service Mitigation Algorithm) are utilized, and these algorithms are compared with each other. The results of the comparison emphasize the superior performance of the DDADA and DDAML algorithms, suggesting the need for further refinement of these algorithms [2].

ZengGuang et.al. aim to develop hybrid defense methods by using the DCNN (Deep Convolutional Neural Network) algorithm to detect new unauthorized entries in LRDDOS (Low-Rate Distributed Denial of Service) attacks. The developed algorithm has demonstrated high performance in attack detection and prevention. However, the study indicates that when the existing data is highly sparse, there is room for improvement in detection performance [3].

In their work, Umang et.al focus on DDOS attack detection using machine learning methods. The study concentrates on semi-supervised machine learning approaches based on the Random Forest algorithm for DDoS detection. The research results show that this approach to DDoS detection reduces irrelevant normal traffic data in the unsupervised part, simultaneously decreasing the false positive rates and enhancing accuracy [4].

Douglas et.al.'s thesis discusses Software-Defined Networks (SDN), a network model designed to replace traditional networks. SDN centralizes network control through an operating system known as a controller, increasing flexibility and supporting various operations, including network security, quality of service, and load balancing. However, the dependence of SDN networks on controllers makes them vulnerable to attacks. Hence, this research employs a hybrid approach for detecting and preventing attacks in SDN-based networks. By integrating machine learning-based flow IDS (Intrusion Detection System) and an Entropy counter, this method enhances network security while considering the limited resources of SDN networks [5].

In their study, Chin-Shiuh et.al. examine the detection of a new type of DDOS attack known as "adversarial DDOS attacks." DDOS attacks, involving coordinated threats from numerous malicious computer systems simultaneously targeting a victim, pose a significant threat to network integrity. The study highlights the potential of adversarial DDOS attacks to evade traditional detection systems, emphasizing the need for improved countermeasures. To address this, the researchers propose the SDGAN (Symmetric Defense Generative Adversarial Network) architecture as a novel detection framework. Experimental results demonstrate the effectiveness of SDGAN in countering adversarial DDOS attacks, surpassing other machine learning models with a high True Positive Rate (TPR) [6].

Sarika et.al. propose using Deep Neural Networks (DNN) to detect attacks in the Internet of Things (IoT). The performance of DNN in attack detection is evaluated on widely used datasets, including KDD-Cup'99, NSL-KDD, and UNSW-NB15, with accuracy rates presented as outcomes [7].

Ibrahim et.al. investigate the suitability of the Knowledge Discovery and Data Mining (or Knowledge Discovery in Databases) KDD dataset for testing and evaluating various Machine Learning Techniques. The study underscores the significance of preparing a fair and valid experimental dataset by focusing on KDD data preprocessing. The research explores J48, Random Forest, Random Tree, MLP, Naïve Bayes, and Bayes Network classifiers, with results demonstrating that the Random Forest classifier achieves the highest accuracy rate in detecting attacks of various types (DOS, R2L, U2R, and PROBE) [8].

In this study, the most suitable dataset containing various types of attacks for DDoS attack detection was chosen. The most fundamental features were extracted from the selected dataset for use in attack detection, and these features were organized. Subsequently, the data was prepared for model training. CNN and LSTM models were chosen as the models, and appropriate layers were added to create the models. The dataset was then separately trained with the models to determine which model was more suitable for this dataset. Subsequently, the obtained rates were compared with those from previous studies.

II. Types of DDOS Attacks

Generally, there are three types of DDOS attack categories: volumetric attacks, protocol attacks, and application attacks.

The first of these is Volumetric DDOS Attacks. It is the most commonly used type of attack, which consumes the target server's network connection, processing capacity, or memory. As a result, the server or the relevant resource becomes unable to respond to incoming and outgoing requests. These attacks utilize bot networks or enslaved devices with the capacity to generate a large amount of traffic on the network. These bot networks are used to coordinate the attack and send heavy traffic to the target.

These types of attacks can pose a significant threat, especially to large websites, online service providers, and infrastructure providers. They can also lead to reputational damage for such large organizations. Examples of such attacks include UDP amplification attacks, ICMP (Internet Control Message Protocol) Flood attacks, SYN/ACK attacks, HTTP Flooding attacks, NTP, DNS, and Memcached attacks.

Another type of attack is Protocol DDOS Attacks. These attacks aim to disrupt or render a specific protocol within the network nonfunctional or inaccessible. Systems like Firewalls, Load Balancers, Routers, and others are targeted. This type of attack is executed by generating a high volume of connection requests, creating new requests before current sessions are completed. Examples of this attack type include SYN/SYN-ACK/ACK Flood, Ping of Death, and similar attacks.

Another type of attack is Application DDOS Attacks. This attack type specifically targets particular applications, often including Web servers, DNS servers, game servers, API services, email servers, among others. These attacks aim to overload network traffic and server resources, disrupting the normal operation of the target services. Examples of such attacks include Flood attacks on HTTP, HTTPS, DNS, and SMTP services [9].

III. Deep Learning Algorithms

CNN stands for Convolutional Neural Network. It is a type of artificial neural network primarily used in visual data analysis fields such as image recognition and processing. It consists of four fundamental layers. One of the major advantages of CNN algorithms is their hierarchical feature learning structure. Features are detected progressively, ranging from simpler features to more complex ones. Convolutional layers apply convolution operations on input data, scanning the data for the detection of different features. These layers are used to learn patterns and features in the data. Rectification layers, often referred to as ReLU (Rectified Linear Unit), compress the output from the convolutional layers and set negative values to zero. This enhances the network's learning capabilities. Pooling layers are used to subsample the data, reducing its dimension and computational load. Additionally, they reduce sensitivity to translations, ensuring that the features are position-independent. Fully connected layers are employed for the network to produce final outputs, such as classification or regression results [10].

LSTM, which stands for Long Short-Term Memory, is a type of artificial neural network used in deep learning and the field of artificial neural networks. LSTM algorithms are one of the artificial neural network types that can retain past information and model long-term dependencies. They offer several advantages over traditional Recurrent Neural Networks (RNNs) concerning their abilities to process sequential data and model long-term dependencies. These distinctive features are attributed to four fundamental components they employ. Cell State is the network's memory that carries the information required for predictions across cells. This allows past data to be propagated throughout the network chain. Which data to carry is determined through gates. The gates use a sigmoid activation that compresses the acquired data into a range between 0 and 1. Data with a value of 0 is forgotten, while data with a value of 1 is propagated throughout the network. Forget Gate, decides which information should be preserved and what information should be disregarded. It combines the previous cell state with the current information and subjects it to a sigmoid activation. As a result, data with a value of 0 is discarded, and data with a value of 1 continues to be carried forward in the cell state. Update Gate is responsible for updating the cell state information. It determines whether the cell state should be updated based on the sigmoid activation of the previous and current states. To regulate the network, it also employs the tanh activation function, which compresses the data into a range

between -1 and 1. The update is determined by multiplying the outputs of the sigmoid and tanh functions. The Output Gate determines the input for the next cell and is also used for prediction purposes. It passes the information on the cell state through the tanh function, and the two results are multiplied to determine the data that will be the input for the cell. Upon the completion of these gate operations, decisions are made regarding the Cell State and the Hidden State (denoted as ht), which represents the network's learned information and assists the model in predicting future states based on historical data [11].

IV. Dataset Selection

Before proceeding to model creation, the dataset must be determined. In this dataset, it is necessary to distinguish the features that will be included in the dataset and whether the data flowing in network traffic is normal or attack traffic. In this study, the KDD Cup dataset was used [12]. The reason for choosing the KDD Cup dataset is that it is a dataset created for the purposes of network traffic analysis and identifying cybersecurity threats. The dataset includes information such as duration, protocol type, service, flag, source bytes, destination bytes, country, wrong fragment, urgency level, access request, etc. Some of these features can be explained as follows;

Duration is a feature that determines how long each connection takes, generally given in seconds. Connection duration can be used to grant or deny access to specific resources or services in a network. Connection attempts with low connection duration can be detected and denied as DDoS attacks.

Protocol Type indicates the protocol type used in data communication, such as TCP, UDP, ICMP, etc. Since DDoS attacks often target network protocols, protocol type is effective in terms of determining the type of attack and its potential impacts. Attackers may focus on vulnerable protocols to create an attack.

Service defines the service established during the connection. For example, services like FTP, HTTP, SMTP, etc. can be provided. Since attacks aim to overload a specific service or resource during the connection and disrupt the normal operation of this service, the importance of this feature in attack detection is significant.

Flag specifies the connection state and flags specific to connection states. Examples include REJ, SF, S0, etc. In a normal network state, the flags are in a state like SYN/ACK or RST, but in attack situations, flags may concentrate abnormally. Especially, attack types like Syn Flood target the SYN flag state by sending a large number of SYN to the network, aiming to consume resources. The confirmation (ACK) and closing (RST) states of the connection also facilitate attack detection.

Source and Destination Bytes represent the number of bytes sent by the source during data transfer in a connection, and the destination bytes represent the number of bytes received by the destination. These byte values represent the size and content of network traffic. Network defense systems generally attempt to detect abnormal traffic patterns by monitoring these bytes.

V. Model Selection and Attack Detection

To avoid including every data point in the dataset, a specific protocol type was chosen. In this study, UDP protocol attacks were investigated. Therefore, data with a protocol type other than UDP were excluded. Unique values corresponding to different service types in the service column were extracted, and the midpoint of these values was calculated. Essential features and target classes were selected for data framing. The chosen features included service, source and destination bytes, wrong fragment count, connection count, service feature, destination host service count, and destination host different service ratio. To distinguish between attack and normal traffic, attack scenarios were labeled as 1, while normal scenarios were labeled as 0. Up to these stages, the data was prepared for training.

For model selection and training, an initial CNN model was created. The model used sigmoid and ReLU activations.

Sigmoid activation typically scales input values between 0 and 1. If the output value is above 0.5, it usually predicts that the event will occur, but if it is below 0.5, it predicts that the event will not occur.

The mathematical formula for the sigmoid activation is as follows:

$$S(x) = \frac{1}{1+e^{-\alpha x}} \quad (1)$$

Additionally, in the middle layer, ReLU activation is used. ReLU activation is a good predictive activation. This activation function sets the negative part of the input to zero while leaving the positive part unchanged. Therefore, the output is zero for all inputs below zero and maintains the input value for positive inputs. The mathematical formula for ReLU activation is as follows:

$$\sigma(x) = \begin{cases} max(0,x), & x >= 0 \\ 0, & x < 0 \end{cases} \quad (2)$$

The initial model used is a CNN model. The model consists of 13 layers, with 8 of them being dropout layers and 5 being dense layers. Among these layers, sigmoid activation has been employed in 8 dropout layers, while relu activation is used in one layer. To optimize the model, the Adam function has been utilized. A 10% portion of the dataset was reserved for testing. The binary cross-entropy was used as the loss function, and the Adam optimization algorithm was employed. Consequently, the model was trained, and accuracy rates were obtained. With this model, an accuracy rate of 76% was achieved.

The second model chosen is LSTM. In this model, nine layers have been employed, one of which is a bidirectional layer. This layer processes the input bidirectionally, computing both forward and backward passes at each time step, making it an artificial neural network layer. Particularly advantageous when working with sequential data, this layer leverages both past and future information in the data for improved predictions. Three LSTM layers and four dropout layers have been incorporated. Additionally, the Adam optimizer function

has been utilized to yield better results. For the second model selected for model selection and training, the LSTM model was used. Sigmoid was utilized as the activation layer in this model. 10% of the training data was reserved for testing. The Adam optimization algorithm was also applied to this model, resulting in an accuracy rate of 72%.

The graph in Figure 1 illustrates the change in accuracy rate resulting from the training of the CNN model. In this context, an epoch value of 1000 has been considered. Since an epoch signifies a period in which the entire dataset is processed and the network learns as part of a training process, increasing this number effectively enhances the data training accuracy. However, setting this number excessively high may exert a considerable burden on the training device. Hence, it is essential to maintain the number at an optimal level. In this graph, as the number of epoch increases, the accuracy rate also increases.

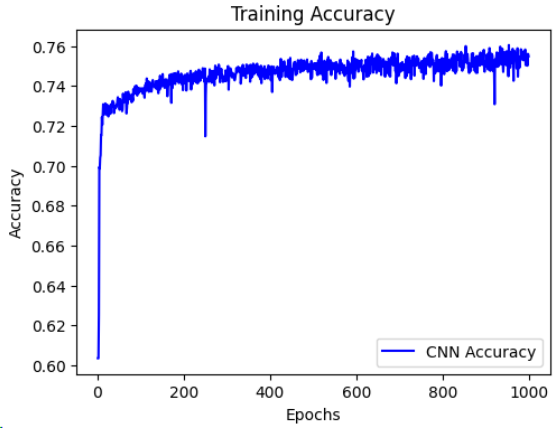

Figure 1: CNN Accuracy

The graph in Figure 1 illustrates the change in accuracy rate resulting from the training of the LSTM model. Here, the accuracy of the trained data is observed to increase in direct proportion to the number of epochs. In this context, an epoch value of 100 has been employed. Setting a higher number of epochs for this model tends to excessively prolong the training duration and exert a significant burden on the training device; therefore, 100 epochs have been chosen as the optimal value for this model.

Figure 2: LSTM Accuracy

VI. CONCLUSION

In this study, suitable DDOS attack data were selected, and the necessary features for DDOS attack detection were extracted. Some of these features include duration, protocol type, service, flag, source and destination bytes. Duration determines the time taken for each connection. The protocol type provides an advantage in determining the type of attack. Service defines the service that is established during the connection. Flag indicates the connection status. Source and destination bytes measure the size of the data transferred during the connection. These specified features were separated as the most essential data for detection, and the data were prepared for training by making adjustments.

CNN and LSTM models were created, and the prepared data were separately trained with these models. According to the training results, the data trained via the CNN model achieved an accuracy rate of 76%, while the data trained using the LSTM model reached an accuracy rate of 72%. Comparing the two models, the CNN model has a higher accuracy rate compared to the LSTM model. Therefore, the use of CNN models in DDOS attack detection leads to higher accuracy rates. To increase the accuracy rate, the dataset can be modified, the number of selected features can be adjusted, or the model can be improved. It should be noted that the accuracy rates were compared with other studies and algorithms used. Based on this data, it can be concluded that the CNN algorithm is a viable choice for attack detection.

Table 1: Comparison of our study with the literature.

Paper	Methods	Accuracy
Makori [13]	RF	89%
Dong and Sarem [14]	KNN	85%
Shieh et.al. [15]	SDGAN	70%
Choudhary and Kesswani [16]	DNN	90%
Obeidat et.al. [17]	BN,NB,MLP,RF	90%-93%
This Study	**LSTM,CNN**	**72%-76%**

Table 1 above provides information on other studies related to DDOS attack detection and the training rates obtained as a result of these studies. Discrepancies in the selected features in the data sets used in these studies are apparent. Furthermore, the training models employed vary. Among the models used, the highest rate is achieved by a type of machine learning, namely RF and DNN models. The lowest rate is observed in the SDGAN model. The CNN model used falls within an average range.

To improve the model's performance, the features of the selected data set can be enriched. Increasing these features may lead to a higher accuracy estimate since the model will be presented with an increased set of attributes to compare. In addition, one can modify the layers of the chosen model, alter the training path by increasing the number of epochs, and utilize a different optimizer function. Activation functions in the layers can be adjusted, and a function more suitable for the data set

can be chosen. Hybrid models composed of a combination of different models can also be employed.

REFERENCES

[1] A. Efe, E. Aksöz, N. Hanecioğlu, Ş.N. Yalman, "Smart security of iot against DDOS attacks1"International Journal of Innovative Engineering Applications 2, 2(2018), 35-43

[2] S. Dong, and M. Sarem , "DDOS attack detection method based on improved knn with the degree of ddos attack in software-defined networks," *IEEE Access*, vol. 8, pp. 5039 - 5048, December 2019.

[3] Z. Liu, Y. Hu, X. Yin, "CPSS LR-DDoS detection and defense in edge computing utilizing DCNN Q-Learning," *IEEE Access*, vol. 8, pp. (99):1-1, February 2020.

[4] U. Garg, M. Kaur, M. Kaushik, N. Gupta, "Detection of DDoS attacks using semi-supervised based machine learning approaches," *IEEE Access*, June 2022.

[5] D.O. Makori, "machine learning based ddos attack detection for software-defined networks (Thesis)," Ph.D. dissertation, Dept. Comp. and Inf. Eng., Sakarya Univ., Turkey, MA, 2018

[6] Shieh C-S, Nguyen T-T, Lin W-W, Lai WK, Horng M-F, Miu D. Detection of Adversarial DDoS Attacks Using Symmetric Defense Generative Adversarial Networks. Electronics. 2022; 11(13):1977. https://doi.org/10.3390/electronics11131977

[7] S. Choudhary and n. Kesswani " Analysis of KDD-Cup'99, NSL-KDD and UNSW-NB15 Datasets using Deep Learning in IoT," 2020 International Conference on Computational Intelligence and Data Science (ICCIDS), Ajmer, Rajasthan, India, pp. 1561–1573.

[8] Obeidat, I., Hamadneh, N., Alkasassbeh, M., Almseidin, M., & AlZubi, M. I. (2019). Intensive Pre-Processing of KDD Cup 99 for Network Intrusion Classification Using Machine Learning Techniques. International Journal of Interactive Mobile Technologies (iJIM), 13(01), pp. 70–84.

[9] Prasad, A., Chandra, S. VMFCVD: An Optimized Framework to Combat Volumetric DDoS Attacks using Machine Learning. Arab J Sci Eng 47, 9965–9983 (2022). https://doi.org/10.1007/s13369-021-06484-9

[10] Ö.Inik and E. Ulker, "Derin öğrenme ve görüntü analizinde kullanılan derin öğrenme modelleri," *Dergi Park*, vol. 6,no.3 pp. 85-104, 2017.

[11] A. Pulver and S. Lyu, "LSTM with working memory," 2017 International Joint Conference on Neural Networks (IJCNN), Anchorage, AK, USA, 2017, pp. 845-851, doi: 10.1109/IJCNN.2017.7965940.

[12] DataHub.io. (2018). 1999 Kddcup99 [Dataset]. Retrieved from https://datahub.io/machine-learning/kddcup99

[13] D.O. Makori, "machine learning based ddos attack detection for software-defined networks (Thesis)," Ph.D. dissertation, Dept. Comp. and Inf. Eng., Sakarya Univ., Turkey, MA, 2018

[14] S. Dong, and M. Sarem , "DDOS attack detection method based on improved knn with the degree of ddos attack in software-defined networks," *IEEE Access*, vol. 8, pp. 5039 - 5048, December 2019.

[15] Shieh C-S, Nguyen T-T, Lin W-W, Lai WK, Horng M-F, Miu D. Detection of Adversarial DDoS Attacks Using Symmetric Defense Generative Adversarial Networks. Electronics. 2022; 11(13):1977.

[16] S. Choudhary and n. Kesswani " Analysis of KDD-Cup'99, NSL-KDD and UNSW-NB15 Datasets using Deep Learning in IoT," 2020 International Conference on Computational Intelligence and Data Science (ICCIDS), Ajmer, Rajasthan, India, pp. 1561–1573.

[17] Obeidat, I., Hamadneh, N., Alkasassbeh, M., Almseidin, M., & AlZubi, M. I. (2019). Intensive Pre-Processing of KDD Cup 99 for Network Intrusion Classification Using Machine Learning Techniques. International Journal of Interactive Mobile Technologies (iJIM), 13(01), pp. 70–84.

A Non-Geometrical Feature Impact Comparison for Remote Sensing Image Classification

A. SAGLAM

Konya Technical University, Konya/Turkey, asaglam@ktun.edu.tr

***Abstract* -This work measures the impacts of the non-geometrical average feature values of the pixels in the segments gained from the remote sensing images which have the values of color, IR (Infrared) and nDSM (Normalized Digital Surface Model). In this work, image pixels are firstly segmented before the classification process because the images in the dataset are high resolutions (6000x6000 pixels), and so much data takes very long time to train. As classification methods, three methods (RF – Random Forest, SVM – Support Vector Machines and k-NN – k-Nearest Neighbors), which are used in the literature commonly, are tested. The pixels in the dataset (Potsdam) have RGB (Red, Green and Blue as color values), IR and nDSM values. The color value transformations between different color spaces also affect the segmentation and classification results. Therefore, the color values in the HSV, L*a*b* and YCbCr transferred from the RGB color space are also tested in both processes which are segmentation and classification. The results show that classification give better success if all the attributes (color, IR and nDSM) are used. In all the train and test processes, the SVM method gives better results. On the other hand, HSV and L*a*b* color spaces are the most suitable for the classification of remote sensing images.**

***Keywords* – Remote sensing, image classification, color spaces, RF, SVM, k-NN.**

I. INTRODUCTION

IMAGE classification is a high-level process applied to data obtained from the pre- and intermediate-process of the pixels [1,2]. In this process, some features extracted from the pixel eigen features such as radiometric features and their patterns are appointed to some groups according to a classification model trained by a classification algorithm and pre-defined information. Although nowadays, the classification process is generally advanced by convolutional neurol networks using the pattern, the pattern is yet determined by the eigen pixel features in images. In this reason, the image pre-processing such as the color transformation is important in the field of image classification. On the other hand, classical machine learning algorithm such as RF, SVM and k-NN is also used widely in the literature. The training process of classical machine learning algorithm is faster than the convolutional model. Besides the eigen pixel features, the geometrical shape features of the segments are also used by these algorithms.

Remote sensing images obtained by satellite devices are generally hyper spectral and have nDSM (normalized digital surface model) values. The remote sensing images int the dataset used in this study, named Postdam, have RGB (red, green and blue) colors, IR (infrared) and nDSM values. The color transformation from RGB to another color spaces such as HSV, L*a*b* and YCbCr is also widely used method as pre-processing. In this study, these color values (additional gray conversion) in some machine learning algorithms (RF, SVM and k-NN) are tested for image classification. In this way, the success of the algorithms are also tested for satellite image classification.

Like most satellite images, the images in the dataset used are high resolution. In such a dataset, using each pixel one by one in the training stage takes a large amount of processing time [3]. In the training stage, the semantic segments in the dataset would not be enough to train and the semantic segments consist of lots of pixels that may have different attributes. For this reason, the images are segmented to group pixels, at first. When segmenting the whole image into pixels, the pixels belong to different classes can be appointed into the same segment, because the success of any segmentation method is never be 100% according to human perception. In this case, the reference semantic segments included in the dataset (both train and test parts) have been segmented separately in this study instead of segmenting whole image.

To score the classification results, the pixels in each segment are labeled with the appointed class label of the segment it belongs to and accuracy values of the classification based on number of pixels have been measured. These results give information about which method, eigen feature and color space how effective will be to classification success.

II. MATERIAL AND METHODS

A. Dataset

This study were performed on the Postdam dataset available ISPRS (WGII/4) benchmark datasets provided by Commission III of the ISPRS [4]. The dataset have 24 images, such that 17 for training (Areas 2_10, 3_10, 3_11, 3_12, 4_11, 4_10, 5_10, 5_12, 6_8, 6_9, 6_10, 6_11, 6_12, 7_7, 7_9, 7_11 and 7_12) and 7 for testing (Areas 2_11, 2_12, 4_10, 5_11, 6_7, 7_8 and 7_10) [5,6]. The images in the dataset have the attributes that consist of R, G, B, IR, and DSM. The contest also provides the normalized DSM (nDSM) values of the pixels.

B. Color spaces

In the scope of this study, the RGB values have been converted to some other color spaces, which are HSV, L*a*b* and YCbCr, to determine which color attributes are appropriate for satellite image classification. The color values in different color spaces can indicate exclusive features about the objects to be classified [7,8]. Therefore, the color transformation may have high importance for some classification processes.

C. Segmentation

The segmentation process has been used to segment the semantic segments provided in the dataset to expose more homogenous sub-segments in this work. As segmentation method, a graph-based and fast method proposed in the study [9] named "Efficient Graph-Based Segmentation (EGS)" are applied to semantic segments after the color space transformation process. EGS method runs greedy and uses Kruskal's minimum spanning tree (MST) algorithm. According to the Kruskal's algorithm, the weighted connections between adjacent pixels are sorted in descended order. After that, the connections are added to MST being created according to the criteria in Eq. (1). In the equation, h_i and h_j are weight values which the highest weighted connections of the segment have. $|S_i|$ and $|S_j|$ are the numbers of the pixels in the segments which have the end of the connection to be added.

$$w(v_i, v_j) < \tau_{ij} = \min\left(h_i + \frac{k}{|S_i|}, h_j + \frac{k}{|S_j|}\right) \quad (1)$$

A part of an images and its colored semantic labels, colored ground-truth segmented semantic segments and lined semantic and sub-segments are shown in Fig. 1.

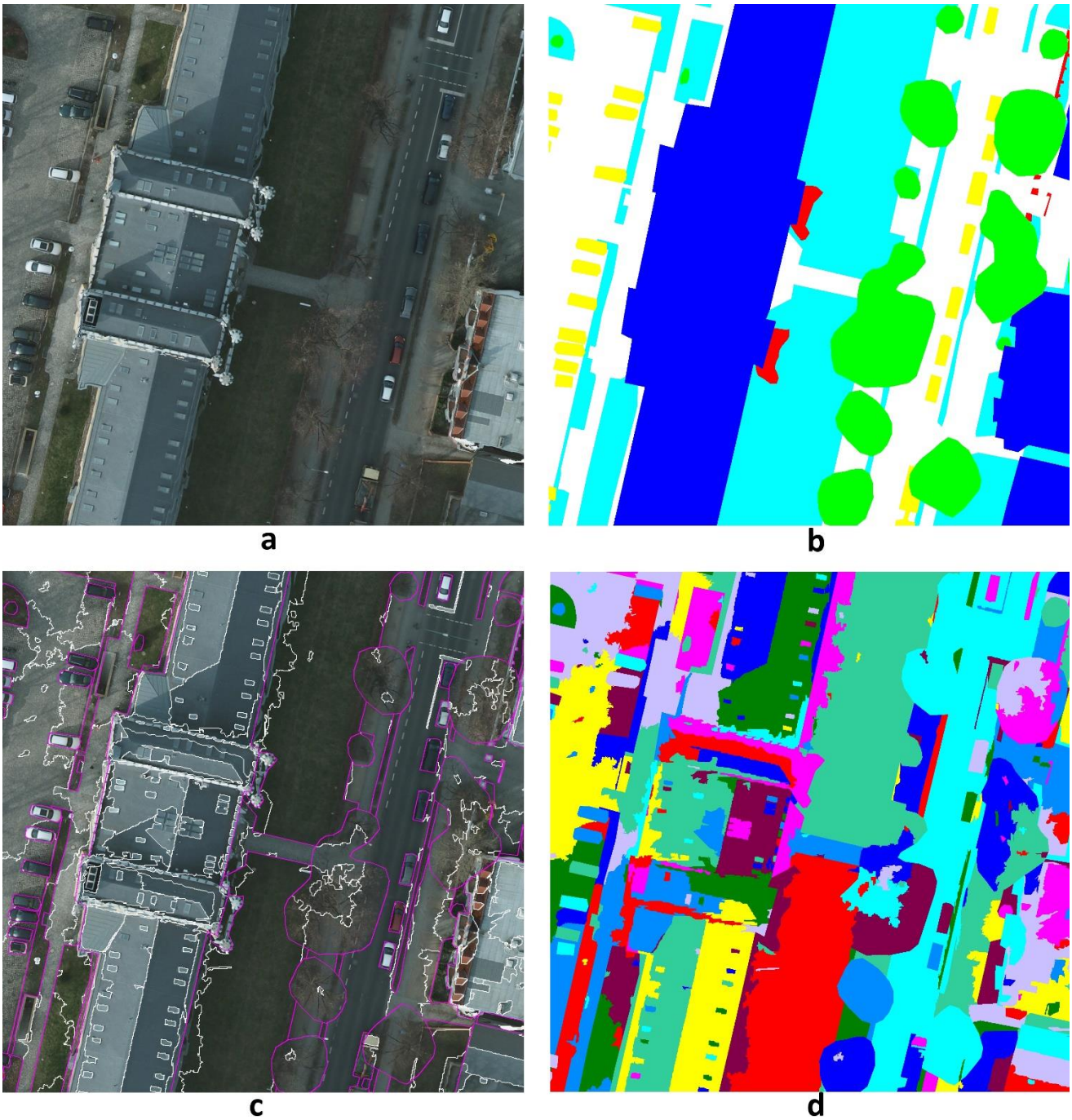

Figure 1: A part of an image (Area 3_12) in the Postdam dataset (a), colored ground-truth semantic segments (b), lined ground-truth semantic segments (purple lines) and sub-segments (white lines) (c) and colored sub-segments (d)

D. Feature extraction

As segment features, only the native pixel attributes and the color space attributes converted from the RGB values are used to get idea about which eigen pixel feature how effects the classification. In the classification process, the native attributes which are RGB, IR, and nDSM, and the derived attributes which are HSV, L*a*b*, HSV, and gray values are used as feature in the study.

E. Classification methods

In this study, the supervised classification methods RF, SVM and k-NN classifiers have been tested in the classification stage.

RF creates several randomly formed decision trees to create a random forest. The decision trees are separately trained with the subsets selected from data in a different way. In the test phase, RF classifies the new upcoming sequence data according to the majority vote of all decision trees [10,11]. As the training data or iteration increases, the dimension of the RF training model in the memory is increases.

SVM determines a hyperplane in a high-dimensional feature space, regression, or other tasks like outliers' detection. The final separation is reached by maximizing the distance from the hyperplane to the nearest data of a class and minimizing the generalization error of the classifier [12,13]. The kernel function Gaussian radial basis function (RBF) has been selected for SVM, by the way, the original input space can be transformed into a higher dimensional feature space non-linearly, because its effectiveness has been proved for many classification problems in previous studies.

K-NN is a simple machine learning algorithm. It takes into consideration the nearest neighbors of the similar features come from the train data [14]. K-NN is a instance based learning method, which are called lazy learners since they only store the training samples without building a classifier struct until if they do not need an unknown samples [15]. Lazy-learning algorithms need less computation time during the training phase than other classifiers [16].

III. Experimental Results

The experiments are conducted with the programming languages C++ for segmentation and Python with the scikit-learn library [17] for color space transformation and classification. The parameter k constant in the segmentation algorithm used determines the segmentation degree as under-segmentation or over-segmentation. In this study the values of the parameter k is used as 3000. The minimum segment size has been used as 100 in the study. The SVM classifier was used with C = 7 and the RBF kernel. The number of trees in RF classifier was determined as 200. The other parameters were released as default or automatic in the library used. The number of neighbors to be consideration in k-NN is applied as 15.

To measure the classification success, the mean accuracy values of images, such that the accuracy is the rate of the true appointed pixels to all pixels in an image [18]. The results are given in two tables in the study. The cross-validation train scores with 5 folds in Table 1 and the test scores in Table 2 are given. The best scores are high-lighted with the bold text.

Table 1: Train cross-validation Accuracy scores

	RF	SVM	k-NN	Average for the features
IRRG	0.5041	0.5340	0.5120	0.5167
RGB	0.5246	0.5460	0.5360	0.5355
HSV	0.5381	**0.5690**	0.5442	**0.5504**
L*a*b*	0.5109	0.5403	0.5196	0.5236
YCrCb	0.5041	0.5275	0.5121	0.5146
RGB + IR	0.5771	0.5870	0.5790	0.5810
HSV + IR	0.5912	**0.6109**	0.5918	**0.5980**
L*a*b*+ IR	0.5723	0.5935	0.5763	0.5807
YCrCb + IR	0.5704	0.5890	0.5755	0.5783
IRRG + nDSM	0.6900	**0.6980**	0.6839	**0.6906**
RGB + nDSM	0.6718	0.6825	0.6693	0.6745
HSV + nDSM	0.6844	0.6931	0.6800	0.6859
L*a*b*+ nDSM	0.6673	0.6744	0.6673	0.6697
YCrCb + nDSM	0.6584	0.6655	0.6547	0.6595
RGB + IR + nDSM	0.7164	0.7161	0.7079	0.7134
HSV + IR + nDSM	0.7271	**0.7320**	0.7173	**0.7254**
L*a*b*+ IR + nDSM	0.7133	0.7154	0.7074	0.7120
YCrCb + IR + nDSM	0.7114	0.7132	0.7052	0.7099
Average for the classifier	0.6185	**0.6326**	0.6189	

Table 2: Test Accuracy scores

	RF	SVM	k-NN	Average for the features
IRRG	0.5174	0.5461	0.5332	0.5323
RGB	0.5322	0.5677	0.5468	0.5489
HSV	0.5574	**0.5713**	0.5651	**0.5646**
L*a*b*	0.5405	0.5708	0.5405	0.5506
YCrCb	0.5197	0.5608	0.5159	0.5321
RGB + IR	0.5749	0.5745	0.5779	0.5758
HSV + IR	0.5777	**0.5913**	0.5804	0.5832
L*a*b*+ IR	0.5906	0.5856	0.5828	**0.5864**
YCrCb + IR	0.5838	0.5786	0.5810	0.5811
IRRG + nDSM	0.6625	**0.6787**	0.6638	0.6683
RGB + nDSM	0.6568	0.6640	0.6610	0.6606
HSV + nDSM	0.6330	0.6457	0.6438	0.6408
L*a*b*+ nDSM	0.6664	0.6691	0.6749	**0.6701**
YCrCb + nDSM	0.6529	0.6667	0.6545	0.6580
RGB + IR + nDSM	0.6727	0.6925	0.6784	0.6812
HSV + IR + nDSM	0.6605	0.6785	0.6673	0.6688
L*a*b*+ IR + nDSM	0.6843	**0.6973**	0.6878	**0.6898**
YCrCb + IR + nDSM	0.6800	0.6963	0.6838	0.6867
Average for the classifier	0.6091	**0.6242**	0.6133	

Looking at the results, the SVM classifier have a superiority for classifying the satellite image attributes. On the other hand, nDSM and IR values have an noticeable effect on the classifications. HSV color space is a superiority among the color spaces in most cases.

REFERENCES

[1] A. Vailaya, A. Jain, H.J. Zhang, On image classification: City images vs. landscapes, Pattern Recognit. 31 (1998) 1921–1935. https://doi.org/10.1016/S0031-3203(98)00079-X.

[2] D. Lu, Q. Weng, A survey of image classification methods and techniques for improving classification performance, Int J Remote Sens. 28 (2007) 823–870. https://doi.org/10.1080/01431160600746456.

[3] G. Vosselman, M. Coenen, F. Rottensteiner, Contextual segment-based classification of airborne laser scanner data, ISPRS Journal of Photogrammetry and Remote Sensing. (2017). https://doi.org/10.1016/j.isprsjprs.2017.03.010.

[4] 2D Semantic Labeling Contest, (n.d.). http://www2.isprs.org/commissions/comm3/wg4/semantic-labeling.html.

[5] M. Papadomanolaki, M. Vakalopoulou, K. Karantzalos, A novel object-based deep learning framework for semantic segmentation of very high-resolution remote sensing data: Comparison with convolutional and fully convolutional networks, Remote Sens (Basel). 11 (2019). https://doi.org/10.3390/RS11060684.

[6] H. Luo, C. Chen, L. Fang, X. Zhu, L. Lu, High-Resolution Aerial Images Semantic Segmentation Using Deep Fully Convolutional Network with Channel Attention Mechanism, IEEE J Sel Top Appl Earth Obs Remote Sens. 12 (2019). https://doi.org/10.1109/JSTARS.2019.2930724.

[7] H.D. Cheng, X.H. Jiang, Y. Sun, J. Wang, Color image segmentation: Advances and prospects, Pattern Recognit. 34 (2001) 2259–2281.

[8] A. Koschan, M. Abidi, DIGITAL COLOR IMAGE Processing, Image Processing. (2008) 375 pages.

[9] P.F. Felzenszwalb, D.P. Huttenlocher, Efficient graph-based image segmentation, Int J Comput Vis. 59 (2004) 167–181. https://doi.org/10.1023/B:VISI.0000022288.19776.77.

[10] M. Weinmann, S. Urban, S. Hinz, B. Jutzi, C. Mallet, Distinctive 2D and 3D features for automated large-scale scene analysis in urban areas, Computers and Graphics (Pergamon). (2015). https://doi.org/10.1016/j.cag.2015.01.006.

[11] R. Blomley, M. Weinmann, USING MULTI-SCALE FEATURES for the 3D SEMANTIC LABELING of AIRBORNE LASER SCANNING DATA, in: ISPRS Annals of the Photogrammetry, Remote Sensing and Spatial Information Sciences, 2017. https://doi.org/10.5194/isprs-annals-IV-2-W4-43-2017.

[12] T. Hastie, R. Tibshirani, J. Friedman, Elements of Statistical Learning 2nd ed., 2009. https://doi.org/10.1007/978-0-387-84858-7.

[13] J. Zhang, X. Lin, X. Ning, SVM-Based classification of segmented airborne LiDAR point clouds in urban areas, Remote Sens (Basel). (2013). https://doi.org/10.3390/rs5083749.

[14] T.M. Cover, P.E. Hart, Nearest Neighbor Pattern Classification, IEEE Trans Inf Theory. 13 (1967). https://doi.org/10.1109/TIT.1967.1053964.

[15] J. Han, M. Kamber, J. Pei, Data Mining: Concepts and Techniques, 3rd Editio, Elsevier, USA, 2012. https://doi.org/10.1016/C2009-0-61819-5.

[16] Comparative Study of K-NN, Naive Bayes and Decision Tree Classification Techniques, International Journal of Science and Research (IJSR). 5 (2016). https://doi.org/10.21275/v5i1.nov153131.

[17] F. Pedregosa, G. Varoquaux, A. Gramfort, V. Michel, B. Thirion, O. Grisel, M. Blondel, P. Prettenhofer, R. Weiss, V. Dubourg, J. Vanderplas, A. Passos, D. Cournapeau, M. Brucher, M. Perrot, É. Duchesnay, Scikit-learn: Machine learning in Python, Journal of Machine Learning Research. (2011).

[18] M. Sokolova, G. Lapalme, A systematic analysis of performance measures for classification tasks, Inf Process Manag. 45 (2009) 427–437. https://doi.org/10.1016/j.ipm.2009.03.002.

A Comparison of Three Fast Graph-Based Segmentation Algorithms on 3D Point Clouds

A. SAGLAM[1] and N.A. BAYKAN[2]

[1] Konya Technical University, Konya/Turkey, asaglam@ktun.edu.tr
[2]Konya Technical University, Konya/Turkey, nbaykan@ktun.edu.tr

***Abstract* - In this paper, the success of two graph-based methods which have significantly accelerated the literature in terms of success and speed in 2D image processing for 3D point cloud segmentation is measured. In our previous study, we propose a cut criterion for edges between boundary voxels and apply this criterion in our boundary constrained method (BCS – Boundary Constrained Segmentation). In this study, we use the same criterion on two older 2D image segmentation algorithms that inherently use Euclidean distance of color attributes for edges between pixels. 3D point clouds have color features rarely because 3D geometric features give more meaningful information about the objects. Many point cloud segmentation methods usually utilize normal and tangent vectors of point groups in voxels, which are rasterized cubic volumes that include local point groups. While both two methods use the MST (Minimum Spanning Tree) data structure, one (SGS – Sequential Graph-Based Segmentation) separates segments only respecting to gradients between the objects and the other one (EGS – Efficient Graph-Based Segmentation) also considers the object sizes. The methods have been tested on two datasets, and the results have been compared using the overall *F*-score values of the segments. According to our measurement results, the EGS method shows considerable high performance with 0.7019 and 0.6584 *F*-score values, relatively to the other two methods. The methods have been tested with different parameter values and the graphical results of the test scores are also given in this work.**

***Keywords* – Point cloud segmentation, graph-based segmentation, cut criterion, MST.**

I. INTRODUCTION

SEGMENTATION is an intermediate process that significantly accelerates many machine learning and computer vision processes and contributes greatly to the extraction of meaningful information. In this work, we compare some fast graph-based segmentation algorithms on two 3D point cloud segmentation datasets. 3D point clouds consist of unorganized sparse points which have spatial values in a three-dimensional space [1,2]. In order to segment 3D point clouds, spatially close points are commonly grouped according to geometrical features [3]. This stage is very important as it significantly reduces the amount of data as well as providing more distinctive features for subsequent processes [4]. But at this stage, processing large amounts of point data makes the segmentation process challenging [5].

Graph-based segmentation methods solve the spatial proximity problem within integrated structures for both 2D image segmentation and 3D point cloud segmentation by using weighted connections between data elements [6]. In graph-based point cloud processing methods, points are represented by vertices and the spatial relationship between them is represented by connections. The weight values of the connections are determined according to the differences between the points with connections between them. In addition to the difficulty of processing due to the un-rasterized structure of the point cloud, the advantage it offers is the 3D geometric features that have high discrimination value between point groups, such as normal and tangent vectors of the local point groups. Some algorithms provide these geometrical features by grouping nearest neighboring point groups [7], while some algorithms group local points into rasterized voxels structures [8–11].The algorithms that use voxel structure run very faster than the other ones [11].

Two graph-based image segmentation method which are "Efficient Graph-based Segmentation" (EGS) [12] and "Sequential Graph-based Segmentation" (SGS) [13] show a success on 2D rasterized images in respect to efficiency of correctness, execution time and easy implementation. These image segmentation algorithms use the Euclidean difference of color values between the connected vertices (adjacent pixels) as edge weights. On the other hand, the graph- and voxel-based 3D point cloud segmentation algorithm "Boundary Constrained Segmentation" (BCS) [11] achieves a superiority in terms of speed and success on some 3D point cloud datasets. This algorithm uses the normal and tangent features between the voxels (local point groups) and introduces a new edge cut criterion.

In this paper, we re-implement the EGS and SGS image segmentation algorithms for 3D point cloud segmentation using the cut criterion introduces by the BCS algorithm and compare them on two point cloud segmentation datasets. Because the three algorithm is graph-based and similarly fast, we compare their successes in respect to only segmentation success as *F*1-score.

II. METHODS

A. Efficient graph-based segmentation (EGS)

The EGS algorithm [12] is a mostly used graph-based segmentation algorithm. The algorithm uses a predicate to merge two regions. Firstly, the undirected adjacency graph G that includes the data elements and the connections between the

adjacent elements is considered as the input graph. According to the valuation of the connections in the graph G, the elements are merged or not. The evaluating criterion, seen in Eq. (1), takes into account both the local (connection weights) and non-local (the sizes of the regions and the highest weights in the regions) properties. According to the voxel-based implementation of this algorithm, if the weight value $w(v_i, v_j)$ of the connection between the voxels v_i and v_j is lower than the threshold τ_{ij} that consist of the predefined parameter k, the highest weight values h_i and h_j of the two segments S_i and S_j, and the sizes $|S_i|$ and $|S_j|$ of the segments, the segments are merged as one segment by labeling the elements of the two segments with the same label. The parameter k determines the degree of the segmentation as over-segmentation or under-segmentation.

$$w(v_i, v_j) < \tau_{ij} = \min\left(h_i + \frac{k}{|S_i|}, h_j + \frac{k}{|S_j|}\right) \quad (1)$$

According to the EGS algorithm, each element (every voxel) is regarded as a segment at first. In the first stage, the connections of the adjacency graph G are sorted by their weights in ascending order. Next, all the sorted connections are evaluated respectively for the merging process regarding to the merging criterion, starting from the edge that has the lowest weight value. When the two segments, which have the different labels, at the end of the connections are merged, the weight of the connection becomes the highest weight value of the new consisted segment.

B. Sequential graph-based segmentation (SGS)

The other graph-based segmentation method used in this study to evaluate the weight measures is the SGS algorithm [13]. This algorithm uses the undirected adjacency graph as the input graph like the EGS algorithm. According to the SGS algorithm, Prime's minimum spanning tree (MST) sequence [14,15] is extracted. The MST is an undirected and acyclic sub-graph of the input graph $G = (V, E)$ such that it connects all the vertices in the vertex set V with the minimum total weight. It starts from an element (selected arbitrarily) as the first vertex of the MST to be formed. At every step, the closest vertex (a vertex that has the least weight connection to the MST among all the other vertices which are not in the MST) and its connection to the MST are added to the MST. While the MST is formed, the connections and their corresponding weight values are inserted to at the end of a queue in the order of insertion. The queue is named as the Prime's sequential representation of MST (PSR-MST). For finding the closest vertices, the use of the Fibonacci heap data structure significantly reduces the computation time compared to the linear searching [16,17]. In the segmentation step, the PSR-MST queue is scanned and, in this process, the inconsistent connections whose weights are extreme compared to their surrounding connections in the PSR-MST queue are cut. The inconsistency measure is stated in Eq. (2).

$$w(v_i, v_j) > \min\big(\max(E_1), \max(E_2)\big) + c \quad (2)$$

The sub-strings E_1 and E_2, whose lengths are equal and specified by the input parameter l, include the connections on the left side and the right side, respectively, of the connection (v_i, v_j) in the PSR-MST queue [13,15,18]. The parameter c is a value to control the segmentation degree like the parameter l. In the study [13], an adaptive technique is proposed as shown in Eq. (3).

$$c = \frac{\sum_{i=1}^{z-1} |w_{i+1}^{Q} - w_i^{Q}|}{z - 1} \quad (3)$$

In Eq. (3), z is the length of the queue PSR-MST and, w_i^Q is the weight value of the connection at the ith index of the queue.

In the adaptation of the SGS method for 3D point cloud segmentation, some modifications have been implemented in this study. The adjacency graph usually does not connect all of the voxels of point clouds. Therefore, firstly, a connected component labeling (CCL) process has been realized using the basic implementation of the algorithm in the study [19]. As a result, more than one connected component comes out and, an individual PSR-MST queue is formed for each one. The segmentation process is conducted separately for each PSR-MST queue. In the original version of the SGS algorithm, another cut criterion is also considered. According to the criterion, the trees in both sides of an inconsistent connection found by the criterion in Eq. (2) are also evaluated with respect to the size of the trees. If the size of a tree at any side of the connection is smaller than l, the connection is not cut to avoid creating noise segments. This criterion is important for 2D image segmentation, because a 2D image is a complete grid and, a label must be appointed for each pixel. However, in 3D point cloud segmentation, some points can be ignored and excluded from the segmentation result. For this reason, this criterion is not conducted in our implementation. The points in the resulting segments that are smaller than the specified number of voxels, applied as 100 in this work, are excluded from the segmentation results in this study for all of the used methods.

C. Boundary Constrained Segmentation (BCS)

In the BCS algorithm, firstly the connections between the adjacent voxels are listed according to their weight values in ascending order. Each voxel is initially assumed to be a segment. Starting the least weighted connection, the two segments at the ends of the connection are taken into consideration to merge them. In consideration, the boundary voxels between the two segments are determined at first. After that, the boundary voxels in the two segments are on-to-one paired mutually by the smallest weighted connection priority. If all weight values of the connections between the voxel pairs are less than or equal the threshold angle parameter *t*, the segments are merged. If one of the two segments is a non-surface voxel, they are merged regardless of the merging criterion. A non-surface voxel can be merged once and is ignored in the future pairing processes.

III. EXPERIMENTS

A. Weighting connections

After the octree voxelization stage [9,20,21], to weight the connection between two adjacent voxels, the normals (n_i and n_j) of the voxels and the barycenters (X_i and X_j) of the points in the voxels are used [11]. One of the values, which is used in the weight measure, is the angle θ_{ij} between the normals n_i and n_j. The angle can be computed by Eq. (4).

$$\theta = \cos^{-1}(n_i \cdot n_j) \tag{4}$$

The other value used in the weight measure is the average of the angles α_i and α_j between the tangent vectors and the vector d_{ij} between X_i and X_j respectively. To obtain the two angles, firstly the angles between the normal vectors and d_{ij} is computed (if any of these angles is largest than 90°, the angle is replaced with its supplementary to 180° shown in Figure 4 (b)) and then, the complementary angles of them to 90° give the angles α_i and α_j. After the angles θ_{ij}, α_i and α_j are computed, the weight value w_{ij} is computed according to Eq. (5).

$$w_{ij} = \min\left(\theta_{ij}, \frac{\alpha_i + \alpha_j}{2}\right) \tag{5}$$

Since the normal values of the non-surface voxels cannot be computed, the weight value of the connections to these voxels can be computed using the angles α_i and α_j. Although they have not a normal vector, they have barycenter. In the weighting the connection between the voxels V_i and V_j, if the V_i is non-surface, w_{ij} is α_j, or vice versa. If both are non-surface, the connection between them is removed.

B. Refitting of non-planar patches

The sampling process may include a non-planar point group (patch), which is mostly on the edges and corners, in a voxel. These voxels can cause misleading the segmentation process. For this reason, the non-planar patches are divided into small planar patches with the k-means clustering algorithm as explained in the study [22]. The normal and barycenter features of the voxel are replaced with the features of the largest small planar patch that obtained after the clustering process. This process ensures the non-planar patch to belong a surface more precisely.

C. Parameter values of the segmentation methods

In the experiments, the voxel size is applied as 0.1 m. The *k* parameter for the EGS algorithm is tested in the range from 10 to 600 by 10 increments. The weight sequence length parameter *l* for the SGS algorithm is tested in the range from 5 to 300 by 5 increments. The threshold angle value parameter *t* for the BCS algorithm is tested in the range from 1 to 60 by 1 increment.

D. Datasets

Two outdoor datasets, which are named Dataset 1 and Dataset 2 in Fig. 1) have been used to test algorithms. These datasets were obtained with the permission of the authors of the study [23]. The numbers of segments of Dataset 1 and Dataset 2 are 66 and 101, respectively.

IV. RESULTS

As the success measurement, *F*1-score is measured in our experiments [11]. Because the number of result segments and the number of reference segments are most probably not equal, the results and reference segments are matched one-to-one [24]. A reference segment and its mostly overlapped result segment are matched with each other, or vice versa. After a segment is matched with its correspondence, it cannot be matched to another segment anymore. Therefore, the matching process should be started from larger segments. After the matching process is completed, the number of correctly assigned points of the results segments is counted up by comparing the segments with their corresponding segments. The overlapped points between two corresponding segments are assumed as correctly retrieved points, while not overlapped ones are assumed as incorrectly assigned points for result points, and incorrectly retrieved points for reference points. *F*1- score balances precision and recall by computing the harmonic mean of them.

Figure 1: The experimental datasets Dataset 1 (a) and Dataset 2 (b)

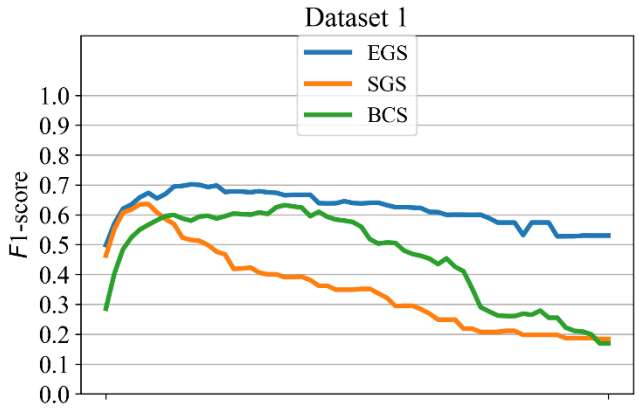

Figure 2: The *F*1-score lines of the methods with different parameter values on Dataset 1

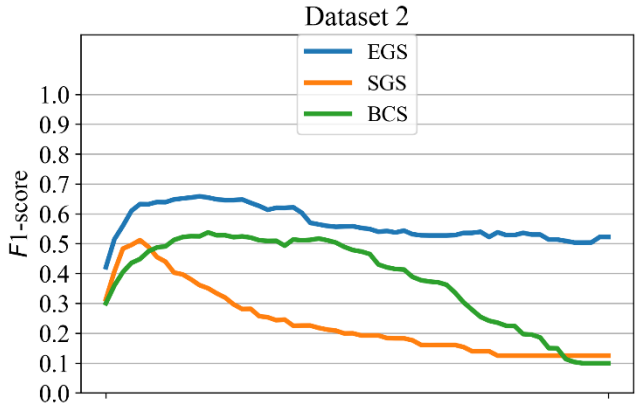

Figure 3: The *F*1-score lines of the methods with different parameter values on Dataset 2

The graphical result of the three algorithms on the two datasets with the parameter values described in Experiments section is seen in Fig. 2 and Fig. 3. According to the results, the EGS algorithm gives the best score when the parameter k is 110 for Dataset 1 and 120 for Dataset 2. The SGS algorithm gives the best score when the parameter l is 30 for Dataset 1 and 25 for Dataset 2. The BCS algorithm gives the best score when the parameter t is 22° for Dataset 1 and 13° for Dataset 2. A comparison of The F1-scores of the algorithms at these parameter values is seen in Table 1. According to Table 1, the EGS algorithm gives the best scores with 0.7019 and 0.6584 F1-scores on Dataset 1 and Dataset 2 consequently. The visual segmentation results of the algorithms can be seen in Fig. 4.

Table 1: F1-scores of the algorithms at their best parameter values

	Dataset 1	Dataset 2
EGS	**0.7019**	**0.6584**
SGS	0.6355	0.5117
BCS	0.6322	0.5376

REFERENCES

[1] H. Mahmoudabadi, M.J. Olsen, S. Todorovic, Efficient terrestrial laser scan segmentation exploiting data structure, ISPRS Journal of Photogrammetry and Remote Sensing. 119 (2016) 135–150. https://doi.org/10.1016/j.isprsjprs.2016.05.015.

[2] G. Vosselman, S. Dijkman, 3D building model reconstruction from point clouds and ground plans, International Archives of Photogrammetry and Remote Sensing. 34 (2001) 37–43. http://www.isprs.org/proceedings/XXXIV/3-W4/pdf/Vosselman.pdf.

[3] S. Barnea, S. Filin, Segmentation of terrestrial laser scanning data using geometry and image information, ISPRS Journal of Photogrammetry and Remote Sensing. 76 (2013) 33–48. https://doi.org/10.1016/j.isprsjprs.2012.05.001.

[4] Xiaolong Zhu, Huijing Zhao, Yiming Liu, Yipu Zhao, Hongbin Zha, Segmentation and classification of range image from an intelligent vehicle in urban environment, in: 2010 IEEE/RSJ International Conference on Intelligent Robots and Systems, 2010: pp. 1457–1462. https://doi.org/10.1109/IROS.2010.5652703.

[5] M. Weinmann, B. Jutzi, S. Hinz, C. Mallet, Semantic point cloud interpretation based on optimal neighborhoods, relevant features and efficient classifiers, ISPRS Journal of Photogrammetry and Remote Sensing. 105 (2015) 286–304. https://doi.org/10.1016/j.isprsjprs.2015.01.016.

[6] B. Peng, L. Zhang, D. Zhang, A survey of graph theoretical approaches to image segmentation, Pattern Recognit. 46 (2013) 1020–1038.

[7] T. Rabbani, F. a van den Heuvel, G. Vosselman, Segmentation of point clouds using smoothness constraint, International Archives of Photogrammetry, Remote Sensing and Spatial Information Sciences - Commission V Symposium "Image Engineering and Vision Metrology." 36 (2006) 248–253. https://doi.org/10.1111/1750-3841.12802.

[8] J. Papon, A. Abramov, M. Schoeler, F. Worgotter, Voxel cloud connectivity segmentation - Supervoxels for point clouds, in: Proceedings of the IEEE Computer Society Conference on Computer Vision and Pattern Recognition, 2013: pp. 2027–2034. https://doi.org/10.1109/CVPR.2013.264.

[9] A.V. Vo, L. Truong-Hong, D.F. Laefer, M. Bertolotto, Octree-based region growing for point cloud segmentation, ISPRS Journal of Photogrammetry and Remote Sensing. 104 (2015) 88–100. https://doi.org/10.1016/j.isprsjprs.2015.01.011.

[10] Y. Xu, L. Hoegner, S. Tuttas, U. Stilla, Voxel- and graph-based point cloud segmentation of 3D scenes using perceptual grouping laws, ISPRS Annals of Photogrammetry, Remote Sensing and Spatial Information Sciences. IV-1/W1 (2017) 43–50. https://doi.org/10.5194/isprs-annals-IV-1-W1-43-2017.

[11] A. Saglam, H.B. Makineci, N.A. Baykan, Ö.K. Baykan, Boundary constrained voxel segmentation for 3D point clouds using local geometric differences, Expert Syst Appl. 157 (2020) 113439. https://doi.org/10.1016/j.eswa.2020.113439.

[12] P.F. Felzenszwalb, D.P. Huttenlocher, Efficient graph-based image segmentation, Int J Comput Vis. 59 (2004) 167–181. https://doi.org/10.1023/B:VISI.0000022288.19776.77.

[13] A. Saglam, N.A. Baykan, Sequential image segmentation based on minimum spanning tree representation, Pattern Recognit Lett. 87 (2017) 155–162. https://doi.org/10.1016/j.patrec.2016.06.001.

[14] R.C. Prim, Shortest Connection Networks And Some Generalizations, Bell System Technical Journal. 36 (1957) 1389–1401. https://doi.org/10.1002/j.1538-7305.1957.tb01515.x.

[15] G.-W. Wang, C.-X. Zhang, J. Zhuang, Clustering with Prim's sequential representation of minimum spanning tree, Appl Math Comput. 247 (2014) 521–534. https://doi.org/https://doi.org/10.1016/j.amc.2014.09.026.

[16] T.H. Cormen, C.E. Leiserson, R.L. Rivest, C. Stein, Introduction to algorithms, Second edition, The MIT Press, 2001.

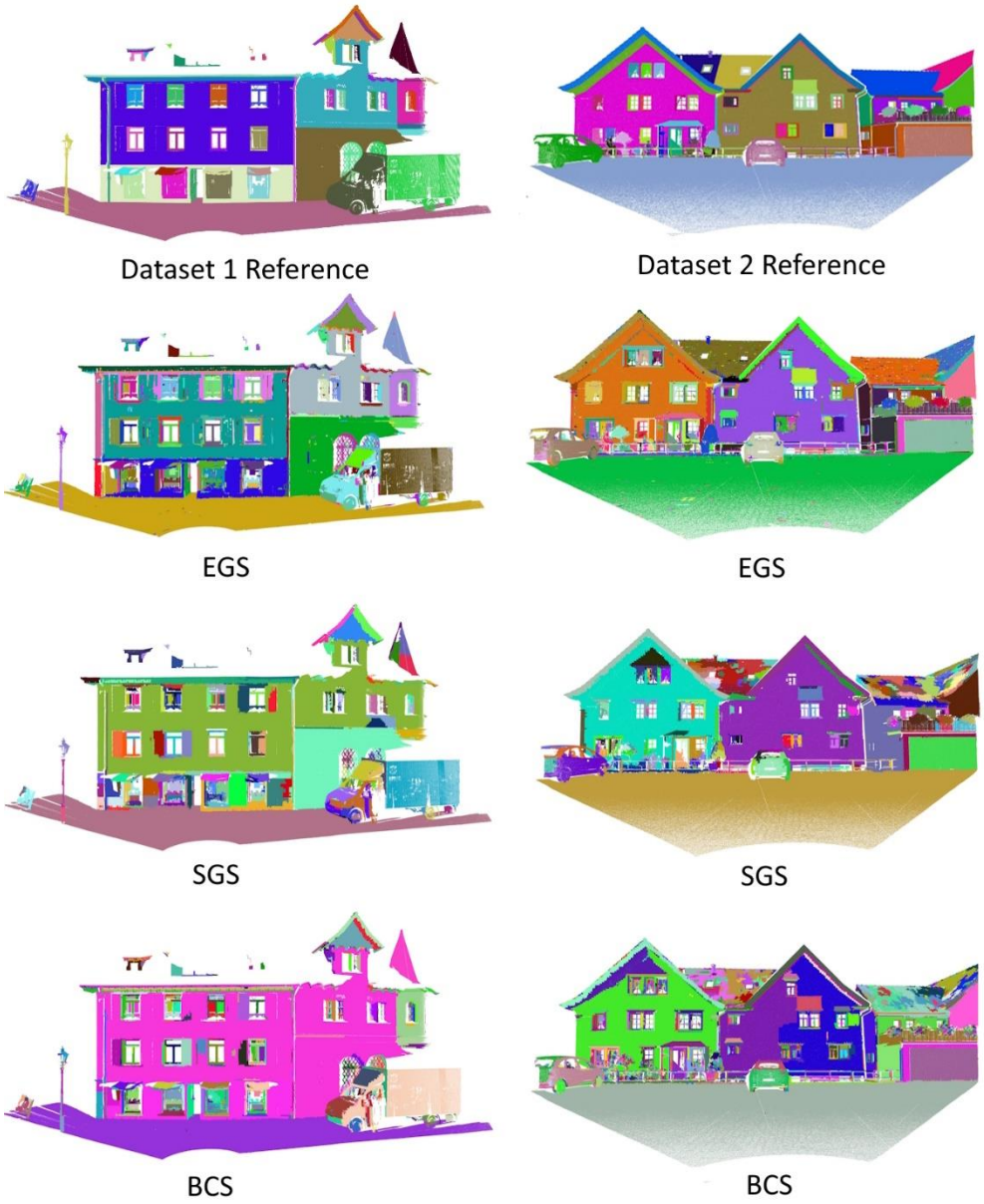

Figure 4: The segmentation results of the algorithms

[17] M.L. Fredman, R.E. Tarjan, Fibonacci Heaps and Their Uses in Improved Network Optimization Algorithms, J. ACM. 34 (1987) 596–615. https://doi.org/10.1145/28869.28874.

[18] A. Saglam, N.A. Baykan, Effects of color spaces and distance norms on graph-based image segmentation, 2017 3rd International Conference on Frontiers of Signal Processing (ICFSP). (2017) 130–135. https://doi.org/10.1109/ICFSP.2017.8097156.

[19] Q. Hu, G. Qian, W.L. Nowinski, Fast connected-component labelling in three-dimensional binary images based on iterative recursion, Computer Vision and Image Understanding. 99 (2005). https://doi.org/10.1016/j.cviu.2005.04.001.

[20] Y.T. Su, J. Bethel, S. Hu, Octree-based segmentation for terrestrial LiDAR point cloud data in industrial applications, ISPRS Journal of Photogrammetry and Remote Sensing. 113 (2016) 59–74. https://doi.org/10.1016/j.isprsjprs.2016.01.001.

[21] F. Poux, R. Billen, Voxel-based 3D Point Cloud Semantic Segmentation: Unsupervised geometric and relationship featuring vs deep learning methods, ISPRS Int J Geoinf. (2019). https://doi.org/10.3390/ijgi8050213.

[22] A. Saglam, H.B. Makineci, Ö.K. Baykan, N.A. Baykan, Clustering-based plane refitting of non-planar patches for voxel-based 3d point cloud segmentation using k-means clustering, Traitement Du Signal. 37 (2020). https://doi.org/10.18280/TS.370614.

[23] Y. Xu, W. Yao, S. Tuttas, L. Hoegner, U. Stilla, Unsupervised Segmentation of Point Clouds From Buildings Using Hierarchical Clustering Based on Gestalt Principles, IEEE J Sel Top Appl Earth Obs Remote Sens. 11 (2018) 4270–4286. https://doi.org/10.1109/JSTARS.2018.2817227.

[24] M. Awrangjeb, C.S. Fraser, An automatic and threshold-free performance evaluation system for building extraction techniques from airborne LIDAR data, IEEE J Sel Top Appl Earth Obs Remote Sens. (2014). https://doi.org/10.1109/JSTARS.2014.2318694.

Determination of Diabetic Retinopathy Grades using a Deep Learning-Based Classification

N.S.OZTEKIN[1] and A.SAGLAM[2]

[1] Konya Technical University, Konya/Turkey, nsoztekin@ktun.edu.tr
[2]Konya Technical University, Konya/Turkey, asaglam@ktun.edu.tr

Abstract **- Diabetic Retinopathy (DR), one of the most common causes of blindness in our age, is the damage caused by diabetes in the blood vessels in the retinal mesh layer of the eye. Early diagnosis and treatment of DR is of great importance so that patients do not lose their sight. In this study, a deep learning-based classification process has been applied using fundus images to determine the degrees of DR. In our study, some pre-processing methods (Gaussian blurring, thresholding to convert binary image, and Contrast Limited Adaptive Histogram Equalization - CLAHE) has been applied to the fundus images and a classification model has been trained using transfer learning methods. Three different datasets, named Asia Pacific Tele-Ophthalmology Society (APTOS), Retinal Fundus Multi-Disease Image Dataset (RFMID) and Indian Diabetic Retinopathy Image Dataset (IDRID), have been used in the training and testing phases. As a result, 95.82% accuracy value is achieved for APTOS, while the precision value is 95.66% and the recall value is 94.49%. The results for RFMID show that the accuracy value is 91.24%, the precision value is 91.24% and the recall value is 90.64%. On the other hand, the accuracy value for IDRiD is 94.40%, the precision value is 88.42% and the recall value is 95.79%.**

Keywords **- Diabetic Rethinopathy, Deep Learning, Classification, EfficientNetB5, Transfer Learning.**

I. INTRODUCTION

Diabetes is a lifelong metabolic disease that occurs when blood sugar rises in the body due to the pancreas' inability to produce enough insulin hormone or to use insulin hormone effectively. The number of people with diabetes in the world in 2019 is estimated to be 463 million and this number is expected to reach 578 million in 2030 [1].

Diabetic Retinopathy (DR), one of the most common causes of blindness, is damage to the blood vessels in the retinal mesh layer due to diabetes. In DR, the frequency of its occurrence in society increases in parallel with the duration of diabetes, and it is generally seen in 30% of diabetics [2].

DR disease is examined in two categories as Non-Proliferative DR (NPDR) and Proliferative DR (PDR). NPDR is defined as the early stage of the disease, while PDR is defined as the advanced stage. The NPDR stage of the disease is divided into three classes as mild, moderate and severe. In the mild NPDR stage of the disease, fundus images are observed microaneurysms and a small number of small hemorrhages. In the moderate NPDR stage of the disease, diffusely increased microaneurysms, hemorrhages, exudates, venous changes and IntRaretinal Microvascular Anomalies (IRMA) are observed in at least one retinal layer on fundus images. In the severe NPDR stage of the disease, fundus images are observed predominantly microaneurysms, hemorrhages, and exudates, as well as diffuse arteriolar occlusions, venous changes, and increases in IRMA density. In the PDR stage of the disease, in addition to the findings in the NPDR stage, retinal neovascularizations and minimal fibrous tissue proliferation findings are detected in fundus images [3].

Deep learning is a field of study powered by artificial neural networks containing one or more layers, defined as deep networks. Deep learning refers to learning patterns in data samples using neural networks containing multiple layers of interconnected artificial neurons [4]. Deep learning methods show superior performance in extracting automatic features from raw data. With the development of technology and the increase in the size of data sets, deep learning has become one of the popular fields of study. With the ImageNet dataset, which emerged in 2012 and is called the world's largest dataset, the subject of deep learning, which has been stagnant for a while, has come to life again. In recent years, studies on deep learning methods have turned to work on GPU in order to shorten the training time and obtain more reliable results.

In this study, experimental studies are carry out on APTOS, RFMID, IDRiD data sets with deep learning methods. EfficientNetB5 architecture is used with Transfer Learning in the studies.

II. MATERIALS AND METHODS

In this section, pathological findings, deep learning, artificial neural networks and APTOS, RFMID, IDRID datasets used in the methods used for the early diagnosis and classification of diabetic retinopathy are mentioned. Various preprocessing techniques have been applied on the datasets. The obtained data is first processed through gaussian blur and threshold, then CLAHE preprocessing. EfficientNetB5, one of the transfer learning methods, is used after data pre-processing.

A. Pathological Findings

a. Microaneurysm

They are small buds in the blood vessels that can cause a small amount of blood to leak. When the retina is examined, the

swelling is observed as red dots. Microaneurysms are the first clinical symptom of diabetic retinopathy.

b. Hemorrhage
When the wall of the small bubbles in the microaneurysm ruptures and bursts, the blood in it leaks into the retinal tissue and hemorrhage (bleeding) occurs.

c. Hard Exudate
When the permeability of the vessels is impaired, molecules such as proteins, lipids, and lipoproteins that should circulate in the vessels leak into the retinal tissue. The yellow, shiny, distinctly bordered structures is called hard exudates. Even if this leakage stops, the body's reabsorption of these substances can take months or even years. Along with these findings, the eye's blood vessels start to become blocked.

d. Soft Exudate (Cotton Wool Spots)
If the vessels feeding the nerve fibers in the retina are blocked, the axoplasmic flow is interrupted here, and a region similar to the same cotton is formed on the outer edges with no clear white-yellow borders. This area is called soft exudate or cotton wool spots.

e. Intraretinal Microvascular Anomalies (IRMA)
After the eye blood vessels start to become blocked, the cells inside cannot find the oxygen they need and an ischemic environment occurs. Since the eye cannot find enough oxygen, it begins to produce new blood vessels abnormally in order to replace the blocked vessels. If this new vessel formation is in the form of capillaries inside the eye, it is called IRMA.

f. Neovascularization
Since the eye cannot find enough oxygen, it begins to produce new blood vessels abnormally in order to replace the blocked vessels. If this new vessel formation is not capillary but consists of prominent vessels larger than the origin of the optic disc, it is called neovascularization.

g.Venous Lumen Irregularities
The veins in the eye are in the form of a wire, and the edge structures are straight. However, as the structure of the vessels due to diabetes begins to deteriorate, bead-shaped vascular structures appear in some regions. In some regions, it is in the form of nodes. This is called venous lumen irregularity.

B. Deep Learning
The concept of deep learning is a method of machine learning, and machine learning is a sub-branch of artificial intelligence. It allows us to train artificial intelligence to predict outputs with a given dataset. Deep learning is concerned with larger datasets and more complex tasks compared to conventional machine learning methods. Additionally, while in machine learning methods, feature selection can be taught to the system due to the advantage of having less data to improve performance, in deep learning, the system itself should perform feature extraction [5].

Deep learning is based on multi-layer artificial neural networks. Multiple neurons come together to form layers. The artificial neural network, which is formed by ordering the created layers one after another, is also called the Deep Neural Network (DNN). The deep expression here indicates the number of layers in the created network. As the number of layers increases, the network structure gets deeper.

C. Artificial Neural Networks (ANNs)
Artificial neural networks are one of the most important methods of learning in artificial intelligence. ANNs are information processing structures inspired by the human nervous system. This method has many capabilities such as learning from inputs, generalizing, working with an unlimited number of variables [6]. By using ANN, it is aimed that machines can learn like humans.
Each node in the layers of artificial neural networks passes the inputs they receive through a series of mathematical functions. These functions are mostly statistical analyses, such as linear regression. The outcome of each node is transmitted to the next node in artificial neural networks, and it continues until the error in the system is minimized.

D. Datasets
a.Asia Pasific Tele-Ophthalmology Society (APTOS)
The fundus image dataset consists of a total of 3662 retinal images collected from multiple clinics under various imaging conditions using fundus photography by technicians at Aravind Eye Hospital in India.

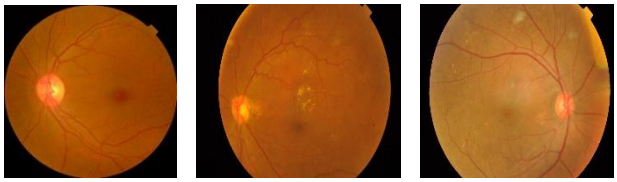
Figure 1: APTOS Dataset Examples [8]

b.Retinal Fundus Multi-Disease Image Dataset (RFMID)
The dataset is the only publicly available dataset that accounts for a wide variety of diseases that occur in routine clinical settings. It consists of 3200 fundus images taken using three different fundus cameras, with 46 conditions explained with the approval of two senior retinal specialists.


Figure 2: RFMID Dataset Examples [9]

c.Indian Diabetic Retinopathy Image Dataset (IDRiD)
The dataset is the first to represent an Indian population. It provides information about the disease severity of diabetic retinopathy and diabetic macular edema and consists of 516 images.

Figure 3: IDRID Dataset Examples [10]

E. Pre-Processes

a. Gaussian Blur

Gaussian blur is an image processing technique, a popular method used to reduce noise and soften details in an image. It got its name from the Gaussian function, which is basically known as a normal distribution. With this method, each pixel in an image is recalculated by taking the weighted average of the surrounding pixels.

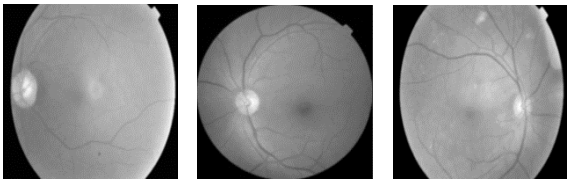

Figure 4: Fundus images of the APTOS dataset after applying Gaussian Blur pre-processing

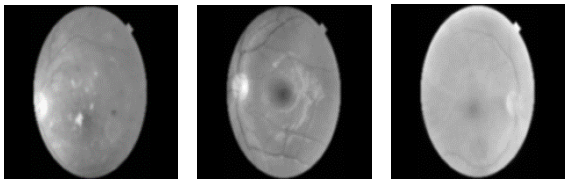

Figure 5: Fundus images of the RFMID dataset after applying Gaussian Blur pre-processing

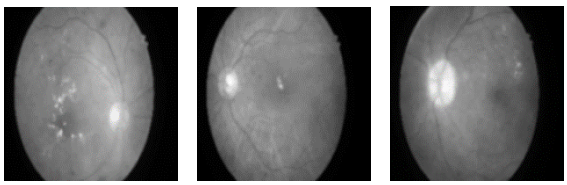

Figure 6: Fundus images of the IDRID dataset after applying Gaussian Blur pre-processing

b. Threshold

The threshold method is a technique used to convert the given input image into a binary image. Binary image is a description of the image as black and white. It is used for various purposes, such as reducing noise on the image or object detection, similar to morphological operators. Depending on the type of thresholding applied to the input image, pixels are updated as either black or white based on the given threshold.

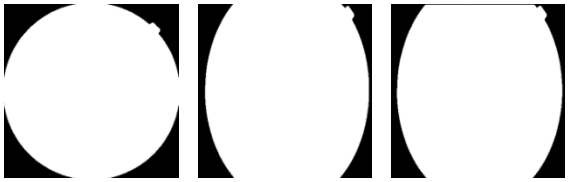

Figure 7: Fundus images of the APTOS dataset after applying Threshold pre-processing

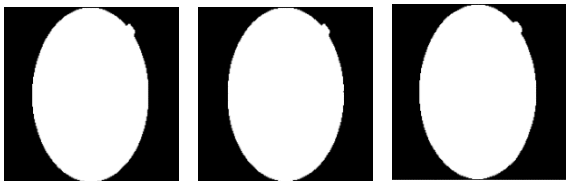

Figure 8: Fundus images of the RFMID dataset after applying Threshold pre-processing

Figure 9: Fundus images of the IDRID dataset after applying Threshold pre-processing

c. Contrast Limited Adaptive Histogram Equalization (CLAHE)

Histogram Equalization is an image processing technique used to adjust the intensity of an image. It is employed to enhance contrast. It works by spreading out the values in the image's intensity range, redistributing the most densely populated area to its neighbors. However, in traditional histogram equalization, if the image pixels are not uniformly distributed (if there are peaks within a specific value range), the image can become distorted. To overcome this issue, Adaptive Histogram Equalization is used, where the image is divided into small regions and equalization is performed. If this process is conducted without a contrast limit, excessive contrast can occur in some parts of the image, leading to an effect known as noise. Noise can significantly reduce the success of the model. Therefore, Contrast Limited Adaptive Histogram Equalization (CLAHE) is used.

The difference of the CLAHE method compared to the traditional histogram equalization is that it divides the image into parts and makes histogram equalization within each frame and also allows to set a contrast limit. Therefore, we can obtain the information that simplifies to separate images.

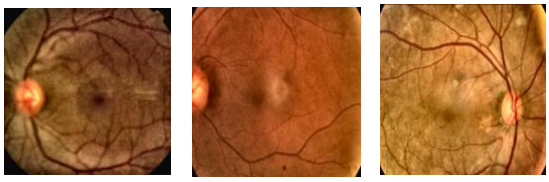

Figure 10: Fundus images of the APTOS dataset after applying CLAHE pre-processing

Figure 11: Fundus images of the RFMID dataset after applying CLAHE pre-processing

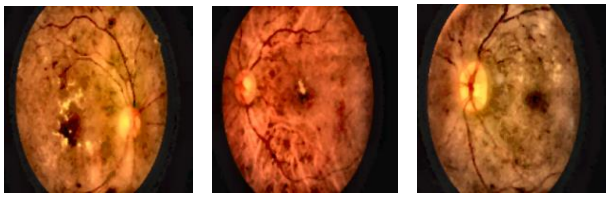

Figure 12: Fundus images of the IDRID dataset after applying CLAHE pre-processing

F. Transfer Learning

Transfer learning is the process where machine learning methods store the knowledge gained while solving one problem, and then use that knowledge when encountering another problem. With transfer learning, models can achieve higher success and faster learning using previous knowledge, requiring less training data [7].

I would like to explain Transfer Learning with an example. Let's say we are trying to create a deep learning model, but we don't have enough data. At this point, someone else has trained a classification model with a dataset containing a hundred thousand cat-dog photos and achieved a high accuracy score. Thanks to the features learned during this process, the model trained for cat-dog classification can even diagnose a rare skin disease. To perform this process, we need to remove the probability-calculating final layer of the cat-dog model and replace it with a suitable classification layer for our own data.

III. EXPERIMENTAL RESULTS

In this study, deep learning methods are employed to determine the grades of diabetic retinopathy using three different datasets named APTOS, RFMID, and IDRID, and the results are shown in Table 1. As seen in Table 1, the APTOS data set gave better results than other data sets in terms of both accuracy and F1-score.

Table 1: Results Table

	accuracy	precision	recall	F1-score	loss
APTOS	0.9582	0.9566	0.9449	0.9506	0.1027
RFMID	0.9124	0.9124	0.9064	0.9092	0.2437
IDRID	0.9440	0.8842	0.9579	0.9194	0.3044

IV. CONCLUSION

In our study, some pre-processing methods were applied to the fundus images and a classification model has been trained using transfer learning methods. Performance metrics accuracy, precision, recall and F1-score were used with 3 different data sets called APTOS, RFMID and IDRID. With an F1-score value of 95%, the APTOS dataset gave better results than other datasets. While the IDRID set came next with an F1-score value of 91%, the RFMID dataset gave the lowest result with an F1-score value of 90%.

REFERENCES

[1] Saeedi, P., et al., *Global and regional diabetes prevalence estimates for 2019 and projections for 2030 and 2045: Results from the International Diabetes Federation Diabetes Atlas, 9(th) edition*. Diabetes Res Clin Pract, 2019. **157**: p. 107843.

[2] Klein, B.E., *Overview of epidemiologic studies of diabetic retinopathy*. Ophthalmic Epidemiol, 2007. **14**(4): p. 179-83.

[3] Aiello, L.M., *Perspectives on diabetic retinopathy*. Am J Ophthalmol, 2003. **136**(1): p. 122-35.

[4] Singh, S.P., et al., *3D Deep Learning on Medical Images: A Review*. Sensors (Basel), 2020. **20**(18).

[5] LeCun, Y., Y. Bengio, and G. Hinton, *Deep learning*. Nature, 2015. **521**(7553): p. 436-444.

[6] Jain, A.K., M. Jianchang, and K.M. Mohiuddin, *Artificial neural networks: a tutorial*. Computer, 1996. **29**(3): p. 31-44.

[7] https://medium.com/novaresearchlab/%C3%B6%C4%9Frenme-aktar%C4%B1m%C4%B1-transfer-learning-c0b8126965c4.

[8] https://www.kaggle.com/competitions/aptos2019-blindness-detection/data

[9] https://ieee-dataport.org/open-access/retinal-fundus-multi-disease-image-dataset-rfmid

[10] https://ieee-dataport.org/open-access/indian-diabetic-retinopathy-image-dataset-idrid

A Distributed Algorithm for Backbone Construction in Three-Dimensional WNSNs

O. GULEC[1]

[1] Department of Management Information Systems, Pamukkale University, Denizli/Turkey, omer@pau.edu.tr

***Abstract* - In light of recent developments in nanotechnology, the Internet of Nano-Things (IoNT) concept has become a crucial field in today's world which realizes the communication of nano-machines that enable measurements at the molecular domain. The communication between these nano-machines, such as nano-sensors and nano-routers, is provided through a network which is called Wireless Nano-Sensor Networks (WNSNs). However, the energy should be used efficiently while establishing communication on the network due to the limited resources of nano-machines. One of the solutions to this problem is constructing energy-efficient network backbones and providing packet routing over these backbones. Therefore, in this paper, a distributed network backbone construction algorithm is proposed for three-dimensional WNSNs. The proposed algorithm successfully clusters the nodes, selects cluster heads and constructs the efficient network backbone around these nodes in a 3D medium.**

***Keywords* – Wireless Nano-Sensor Networks, Internet of Nano-Things, Network Backbone Construction, Three-Dimensional Networks, Distributed Algorithm**

I. INTRODUCTION

Internet of Nano-Things (IoNT) paradigm is an emerging field for exploring the nano-domain through recent developments in nanotechnology [1]. The wireless communication between these nano-machines such as nano-sensor nodes and nano-routers occurs on a special kind of Wireless Sensor Networks (WSNs) which is called Wireless Nano-Sensor Networks (WNSNs) [2, 3].

As in traditional WSNs, one of the challenging issues is how to achieve efficient data transmission. This is directly related to routing and a crucial issue that needs to be considered. Therefore, many studies have been proposed to ensure effective data transmission over efficient routing paths in the literature [4]. Unfortunately, traditional routing protocols are not suitable for WNSNs due to nano-domain characteristics. Hence, routing protocols need to be proposed to support communication in the nano-domain [5, 6].

In order to provide efficient communication on a network, it should occur through the network backbone instead of broadcasting the messages as flooding [3]. To this end, there exist several approaches for constructing the network backbone in the literature [7]. The main objective of the network backbone is to provide data flow from the nodes to the base station over this structure. Thus, the nodes save their energy or consume it in an efficient way by sending the data from themselves to the backbone nodes. These chosen backbone member nodes then send the data to the base station over the backbone structure. In the literature, there exist several solutions for network backbone construction for sensor networks. Traditional backbone construction is related to selecting backbone members and binding them to each other. In this approach, tree or graph-based solutions can be used such as connected dominating sets (CDS) [8]. To this end, Chowdhury et al. (2022) [9] proposed a new scheme for solar energy harvesting-enabled IoT networks that maintain a sustainable and adaptive CDS. Tang et al. (2019) [10] used minimal CDS (MCDS) in order to form the virtual backbone of medical WSNs with energy consideration for extreme healthcare environments.

Another approach for network backbone construction is related to clustering the nodes and then binding them with each other [11]. In this approach, cluster heads (CH) are determined on the network and the paths between these CHs are formed as a network backbone. In a WNSN, the communication backbone is the nano-links between selected nano-sensor nodes. These selected nano-nodes are responsible for gathering data from their neighbors and sending them to the nano-router over the network backbone. Therefore, with this scheme, efficient routing over the backbone of a WNSN is provided. Hence, Gulec and Sahin (2023) [12] proposed Red Deer Algorithm (RDA)-based clustering algorithm to achieve efficient routing in WNSNs. Similarly, Gulec (2022) [3] proposed a clustering-based routing algorithm for IoNT applications that extends WNSN lifetime. Bouchedjera et al. (2020) [13] proposed a clustering algorithm namely DCCORONA for WNSNs. Xu et al. (2022) [14] proposed an energy-efficient routing scheme for nano-networks.

In this paper, a distributed algorithm is provided in order to construct the backbone of three-dimensional WNSNs by clustering the nodes and choosing the proper cluster heads (CHs) as backbone members.

The rest of the paper is organized as follows. The system model including the proposed algorithm is given in Section II. Simulation setup and experimental results are discussed in Section III. Finally, Section IV concludes the study.

II. SYSTEM MODEL

Initially, all nano-sensor nodes are distributed to a three-dimensional medium randomly. Then a nano-sensor node broadcasts *HELLO_MESSAGE* in order to know its neighbor nodes. When a nano-node receives this message, it adds the sender node to its neighbor list.

After this process ends, it means all nano-sensor nodes know their neighbors, they all send *IMPACT_MESSAGE* to their neighbors. When a nano-sensor node receives this message, it calculates its own impact factor. In order to construct the network backbone of WNSNs, the proposed algorithm firstly clusters the nodes and finds suitable cluster heads (CHs). To this end, the proposed algorithm selects CHs according to the nodes' impact factor given in Equation 1 where $|\Gamma_m|$ is node degree and d_{origin} is the node distance to the origin point of the medium.

$$impact\_factor = \frac{|\Gamma_m|}{d_{origin}} \quad (1)$$

According to the equation, when a nano-sensor node has the highest backbone impact compared to its neighbor nodes, it becomes one of the backbone members and it changes its state to *backbone_member*. When a nano-sensor node has a higher degree and less distance to the origin, it has more chance to be selected as a CH compared to the other nano-sensor nodes.

In the second phase, if a node is selected as CH, then it should find the other CH nodes in order to connect with each other to form the network backbone. To this end, a CH nano-sensor node broadcasts *CONNECT_MESSAGE* to its neighbors. When a nano-node is a CH node and receives this message, it adds the sender CH node to its CH member list.

If a CH nano-sensor node has no CH neighbor then it selects one of its cluster members as CH in order to form the network backbone. For this process, it sends *SELECT_MESSAGE* to the selected cluster member node whose backbone impact is the maximum then it changes its state to *backbone_member*. This process is repeated until all CH nano-sensor nodes construct a network backbone in a three-dimensional medium. Nevertheless, there exist several nano-sensor nodes that are neither *backbone_member* nor *cluster_member* namely uncovered nodes. This situation is related to the node coverage problem on the network that needs to be considered. The flowchart of the proposed system is given in Figure 1.

In order to clarify the proposed system, a WNSN consists of 300 nano-sensor nodes that is distributedly deployed on a three-dimensional medium is shown in Figure 2. According to the figure, the blue nodes are CHs and the red nodes are cluster members.

The network area is $0.001 \times 0.001 \times 0.001\ m^2$ and the transmission range of a nano-sensor node is $0.0015\ m$. In the second phase of the proposed algorithm, it builds a network backbone binding the CH nodes to each other. The network backbone construction on a WNSN is given in Figure 3.

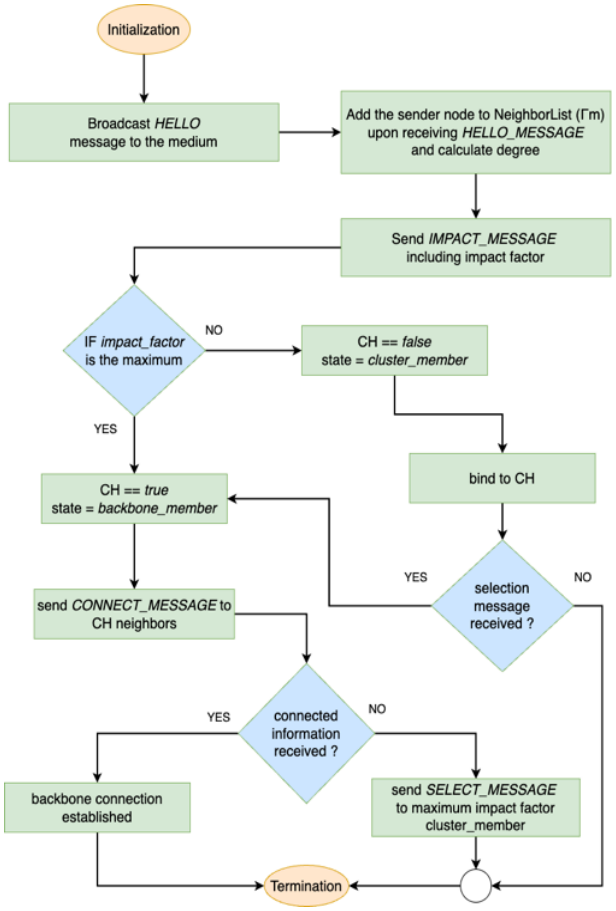

Figure 1: Flowchart of the proposed system

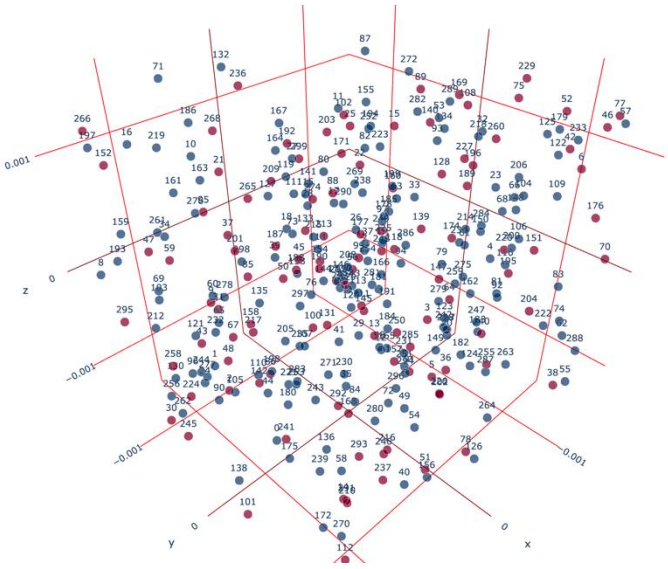

Figure 2: Clustering and CH selection on a three-dimensional WNSN

III. SIMULATION AND RESULTS

The proposed algorithm is developed under NS-3 [15] and Nano-Sim [16, 17] framework. In order to simulate the proposed algorithm, 50 different topologies were generated for each set with 300, 400 and 500 nano-nodes in a three-dimensional network. Python packages such as Pygal [18] and Plotly [19] are used for illustrating the network.

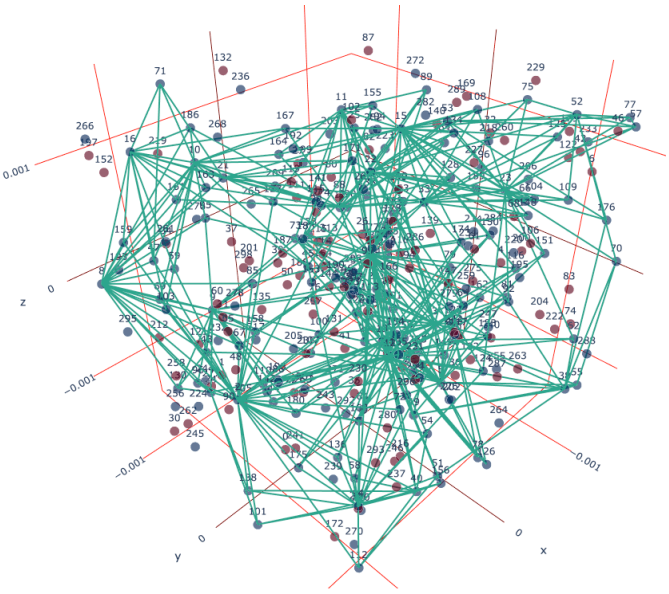

Figure 3: The backbone construction on a WNSN

According to the simulation results, when a WNSN has 300 nano-sensor nodes, the proposed algorithm selects 95 nodes as backbone members, 128 nodes as cluster members and 77 nodes remain uncovered in 9.578 s where the coverage percentage is 74.33% on average.

When a WNSN consists of 400 nano-sensor nodes, the proposed algorithm selects 167 nodes as backbone members, 139 as cluster members and 94 nodes remain uncovered in 26.044 s where the coverage percentage is 76.5% on average.

Finally, if there are 500 nano-sensor nodes on the network, the proposed algorithm selects 178 nodes as backbone members, 185 nodes as cluster members and 137 nodes remain uncovered in 60.199 s where the coverage percentage is 72.6% on average in order to construct network backbone. All experimental results are given in Table 1.

Table 1: Experimental Results

Node Count	**300**	**400**	**500**
Backbone Member Count	95	167	178
Cluster Member Count	128	139	185
Uncovered Node Count	77	94	137
Coverage Percentage	74.33	76.5	72.6
Total Time (s)	9.578	26.044	60.199

For comparison, the count of nano-sensor nodes that form the backbone of the network, the count of nodes that take place in the clusters and the count of uncovered nodes are given in Figure 4. Additionally, the coverage of the nodes that the proposed algorithm provides and the total simulation time are given in Figure 5. According to the figures, the proposed algorithm successfully clusters the nodes, finds optimal cluster heads as backbone member nodes and binds these cluster heads in order to construct the network backbone in three-dimensional WNSNs with a coverage percentage of 76.5% on average.

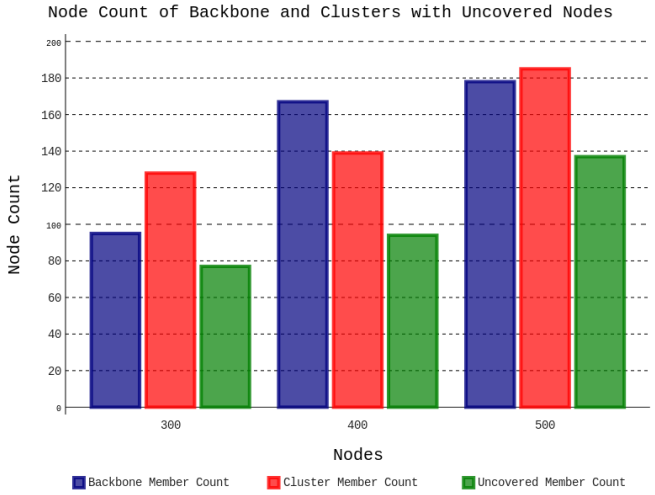

Figure 4: Node count values for backbone, clusters and uncovered nodes

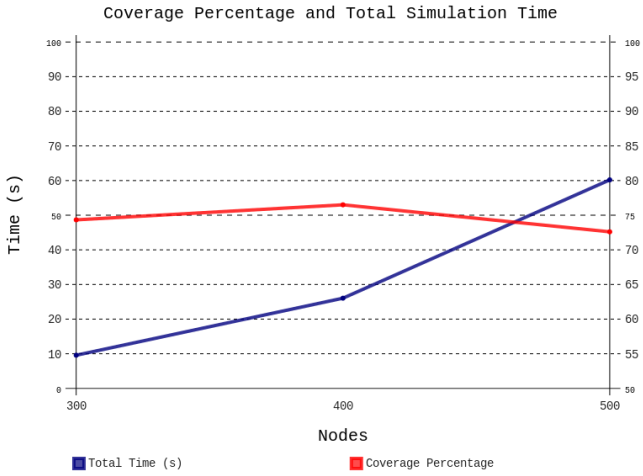

Figure 5: Coverage percentage and simulation time (s) results

IV. CONCLUSION

Communication is one of the basic processes in sensor networks. When resources such as energy are limited, this paradigm becomes more important due to its consumption while establishing communication between the nodes. Moreover, due to the characteristics of nano-sensor nodes, energy is more important for these devices to communicate in the nano-domain. Therefore, energy-efficient communication solutions should be provided for WNSNs. To this end, a distributed algorithm is proposed in this paper to construct energy-efficient network backbones in three-dimensional WNSNs.

According to the simulation results, the proposed algorithm

successfully clusters the nodes while selecting cluster heads according to the nodes' metrics then, it constructs a communication backbone around these selected nano-sensor nodes. This backbone construction process leads to cluster member nodes transmitting the data to the cluster heads instead of transmitting it to each other. Therefore, at the end, the data will transmitted to the base station over this newly constructed network backbone in a three-dimensional medium.

Although the proposed algorithm is designed to construct efficient backbones in three-dimensional WNSNs, it selects redundant nodes as cluster heads. Therefore, these redundant nodes should be pruned or the algorithm should be optimized to select fewer nodes. Besides, the proposed algorithm should be tested on dense WNSNs having more nano-sensor nodes. Additionally, while selecting the cluster heads as backbone members, cluster head selection methods that exist in the literature should be considered in future studies.

[1] Gulec, O., "Hybrid FFBAT optimized multi-hop routing in Internet of Nano-Things", Internet of Things, 24, 100938, 2023.
[2] I. F. Akyildiz and J. M. Jornet, "The Internet of nano-things", IEEE Wireless Communications, 17 (6), 58–63, 2010.
[3] O. Gulec, "Extending lifetime of Wireless Nano-Sensor Networks: An energy efficient distributed routing algorithm for Internet of Nano Things," Future Generation Computer Systems, 2022.
[4] Galal, A., and Hesselbach, X., "Probability-based path discovery protocol for electromagnetic nano-networks", Computer Networks, 174, 107246, 2020
[5] A. O. Balghusoon and S. Mahfoudh, "Routing protocols for wireless nanosensor networks and internet of nano things: A comprehensive survey", IEEE Access, 8, 200724–200748, 2020.
[6] GÜLEÇ, Ö., "Machine Learning Supported Nano-Router Localization in WNSNs", Sakarya University Journal of Science, 27(3), 590-602, 2023.
[7] E. Sahin and O. Gulec, "Obstacle Aware Density Based Nano-Router Localization in IoNT," 2023 8th International Conference on Computer Science and Engineering (UBMK), pp. 318-323, 2023.
[8] Varsa, G. S., and Sridharan, D., "A balanced energy efficient virtual backbone construction algorithm in wireless sensor networks", AEU-International Journal of Electronics and Communications, 107, 110-124, 2019.
[9] Chowdhury, C. R., Mandal, C., and Misra, S., "Sustainable maintenance of connected dominating set by solar energy harvesting for IoT networks", IEEE Transactions on Green Communications and Networking, 6 (4), 2115-2127, 2022.
[10] Tang, Q., Yang, K., Wang, J., Luo, Y., Li, K., and Yu, F., "Wireless sensor network MCDS construction algorithms with energy consideration for extreme environments healthcare", IEEE Access, 7, 33130-33144, 2019.
[11] Wohwe Sambo, D., Yenke, B. O., Förster, A., and Dayang, P., "Optimized clustering algorithms for large wireless sensor networks: A review", Sensors, 19(2), 322, 2019.
[12] O. Gulec and E. Sahin, "Red Deer Algorithm based nano-sensor node clustering for IoNT," Journal of Network and Computer Applications, p. 103591, 2023.
[13] I. A. Bouchedjera, L. Louail, Z. Aliouat, and S. Harous, "Dccorona: Distributed cluster-based coordinate and routing system for nanonetworks," in 2020 11th IEEE Annual Ubiquitous Computing, Electronics & Mobile Communication Conference (UEMCON). IEEE, pp. 0939–0945, 2020.
[14] J. Xu, H. Huang, J. Kan, and R. Wang, "Energy-balanced routing protocol based on data priority for lung terahertz nanosensor networks," in 2022 IEEE 95th Vehicular Technology Conference:(VTC2022-Spring). IEEE, pp. 1–5, 2022.
[15] NS-3, https://www.nsnam.org, accessed 30 October 2023.
[16] Nano-Sim, https://telematics.poliba.it, accessed 30 October 2023.
[17] E. Sahin, O. Dagdeviren, and M. A. Akkas, "An evaluation of internet of nano-things simulators," in 2021 6th International Conference on Computer Science and Engineering (UBMK). IEEE, pp. 670– 675, 2021.
[18] Pygal, https://www.pygal.org, accessed 30 October 2023.
[19] Plotly, https://plotly.com, accessed 30 October 2023.

Developing a Desktop Application for Real-Time Detection of Acromegaly from Facial Images with Artificial Intelligence

M.ÖZEL[1], N.DOĞAN[2], R.KARAKIŞ[3], M.KIZILGÜL[4], M.M.YAPICI[5], E.DUMAN[6],

[1] Selcuk University, Konya/Turkey, 208264002003@lisansustu.selcuk.edu.tr
[2]Selcuk University, Konya/Turkey, nurettin.dogan@selcuk.edu.tr
[3]Sivas Cumhuriyet University, Sivas/Turkey, rkarakis@cumhuriyet.edu.tr
[4]Sağlık Bilimleri University, Ankara/Turkey, muhammed.kizilgul@saglik.gov.tr
[5]Ankara University, Ankara/Turkey, mutluyapici@ankara.edu.tr
[6]Mehmet Akif Ersoy University, Burdur/Turkey, eduman(at)mehmetakif.edu.tr

Abstract **- In this study, a desktop application was implemented that automatically recognizes acromegaly from real-time facial images by using deep learning algorithms in the early diagnosis of acromegaly and facilitates the diagnosis of the disease. The application was prepared using the data and methods in the study previously developed by Kızılgül et al. It is possible to evaluate instant facial images, previously captured images and video images in the desktop application. The application developed in the study produces results such as "Healthy" or "You May Have Acromegaly" for the relevant facial image. The developed desktop application has been tested on 54 patients so far. As a result of this trial, it gave healthy results to all 54 people. The desktop application developed with this study aims to contribute to the early diagnosis of Acromegaly disease by placing it on Kiosk devices in places such as hospitals and shopping malls.**

Keywords - Acromegaly, Desktop, Deep Learning, Artificial Intelligence.

I. INTRODUCTION

Acromegaly is a disease that occurs when your body produces too much growth hormone (GH). GH, produced mainly in the pituitary gland, controls the physical growth of the body. In adults, too much of this hormone causes bones, cartilage, body organs, and other tissues to increase in size. Common changes in appearance include enlarged or swollen nose, ears, hands, and feet. Symptoms of acromegaly usually appear very slowly over years. This makes diagnosis difficult. Doctors make a diagnosis based on your medical history, a comprehensive clinical evaluation, and special tests such as blood tests and imaging tests.

Deep learning is an artificial intelligence method that uses multi-layered artificial neural networks in areas such as object recognition, speech recognition, natural language processing, and is one of the types of machine learning. Deep learning, unlike traditional machine learning methods, instead of learning with coded rules; It can automatically learn from the symbols of images, videos, audio and text data. A deep learning model can only make sense of what it has seen before. It is extremely sensitive to changes in the input. Therefore, models need to be retrained and redeployed as new data becomes available.

Many studies have been conducted in the field of health using deep learning models. Early diagnosis of acromegaly is important for the treatment of the disease. No software or application that can make instant decisions is used for the early diagnosis of acromegaly.

Studies on the detection of acromegaly disease with deep learning methods were examined.

Schneider, H. J. and their colleagues conducted a study to evaluate the illumination of acromegaly with software on their faces. The study was conducted on 57 acromegaly patients (29 women, 28 men). Front and side photographs of the faces were taken and divided into groups. It was classified as mild, moderate or severe acromegaly facial feature examples by 2 doctors who are experts in the field. Face classification was then carried out with the software tool FIDA (facial image diagnostic aid), developed for facial identity recognition and subsequently developed by MG and RPW at the Ruhr University Bochum (copyright reserved). The software correctly classified 71.9% of patients and 91.5% of controls. The classification accuracy of experts is 80.8% and 87.0%. Classification accuracy according to the software was higher than that of medical experts, especially in patients with mild acromegaly symptoms.

In their study, Kong, X and her colleagues tried to prove theoretically the automatic early detection of Acromegaly from facial photographs. In this study, they used several popular machine learning algorithms to train a dataset consisting of 527 acromegaly patients and 596 normal subjects. First, they used OpenCV for face detection and cropped all images to have the same pixel size. Generalized Linear Models (LM), K-nearest neighbors (KNN), Support Vector Machines (SVM), randomized tree forests (RT), Convolutional Neural Network (CNN) Ensemble Method (to automatically identify acromegaly with only frontal images) They used many popular machine learning methods, including EM). To evaluate the results, they compared the results of the photo-only machine learning method in terms of sensitivity and specificity, PPV and NPV, with the evaluations of 9 specialized board-certified endocrinologists and neurosurgeons. The best result of their proposed methods showed 96% PPV, 95% NPV, 96% sensitivity and 96% specific effect rate. They concluded that artificial intelligence can automatically detect acromegaly early with its high sensitivity and specific effect rate.

Guo, X. et al. The aim was to measure facial features in acromegaly patients using 3D stereophotography for the first time, analyze gender-specific features and discover clinical influencing factors. 39 acromegaly patients and 39 age- and

gender-matched healthy individuals were prospectively included in the study. Facial features and angles were measured for each subject using 3D stereophotography. They used hormone levels (IGF-1) and disease duration as factors in the evaluation because they are related to facial changes. They compared nose width, length, height and depth, upper and lower lips, face length, face width and gonion-gnathion distances, and nasofrontal and columella-labial angles. Analyzes between facial changes, hormone levels and disease duration of acromegaly patients were used to reach the results. It has been proven that patients with acromegaly exhibit a unique trend in facial changes and that features are not the same between genders. They concluded that 3D stereophotography is an accurate and reliable tool for investigating facial features, recognition of facial features can help early diagnosis and timely treatment of acromegaly.

Meng, T. and colleagues aimed to achieve results by combining the use of 3D imaging and machine learning techniques. They used face upright, side and 45 degree shots. They studied 124 participants, including 62 acromegaly patients and 62 control individuals. They determined 58 facial parameter points for each face and examined the changes of these points according to disease status and gender. Using two-way analysis of variance (ANOVA) and post-hoc t-tests and linear discriminant analysis (LDA) to examine the changes of these parameters by disease status and gender, they characterized which combinations of parameters could best predict disease status and their relative contributions. They found the prediction accuracy to be 92.86% in women, $p < 0.0001$, and 75% in men, $p < 0.001$.

Kızılgül et al. Data obtained from 77 acromegaly patients and 71 healthy individuals were used, taking into account gender and age matching. They used three architectures named ResNet50, DenseNet121 and InceptionV3 for the transfer learning-based convolutional neural network (CNN) model developed to classify facial images as "Healthy" or "Acromegaly". They also trained these CNN machine learning methods to create an Ensemble Method (EM) for face detection of acromegaly. The positive predictive values obtained by ResNet50, DenseNet121, InceptionV3 and EM for acromegaly were calculated as 0.958, 0.965, 0.962 and 0.997, respectively. They found the average sensitivity, specificity, precision and correlation coefficient values calculated for each of the ResNet50, DenseNet121 and InceptionV3 models to be very close to each other. They found that EM outperformed these three CNN architectures, providing the best overall performance in terms of sensitivity, specificity, accuracy, and precision, with 0.997, 0.997, 0.997, and 0.998, respectively. This study emphasizes that artificial intelligence programs are promising methods for detecting acromegaly in the future.

II. MATERIAL AND METHOD

In this study, the method and data set developed by Kızılgül et al. were used. Python Graphical User Interface (GUI) was used to convert the software prepared in Python program into desktop software. Python is an interpreted, object-oriented, high-level programming language with dynamic semantics developed by Guido van Rossum. Python is a modern programming language that supports object-oriented, functional and imperative programming styles. Python is used for server-side web development, software development, mathematics and system scripting, and is popular as a scripting or paste language for connecting existing components due to its high-level built-in data structures for Rapid Application development. Additionally, Python is widely used for efficiency in back-end web development, data analysis, artificial intelligence and scientific computing projects.

GUI is a desktop interface that allows communication with computers. It makes it easy to use the results of text-based codes on desktop computers, laptops and other mobile devices. There are various libraries for GUI in Python programming language. The most used of these is, Tkinter, Kivy, Python QT ve wxPython dır. Tkinter is the most preferred GUI application because it is fast and easy to use. Tkinter is a Python library that can be used to create basic graphical user interface (GUI) applications. It is the most widely used module for GUI applications in Python. It can be used directly without the need for external installation.

III. CONCLUSION

The software that can instantly and accurately diagnose acromegaly disease was prepared using the deep learning model and data created by Kızılgül et al. In the pictures, snapshots and videos to be tested in the software, care was taken to include only one person in the picture and to have a white background.

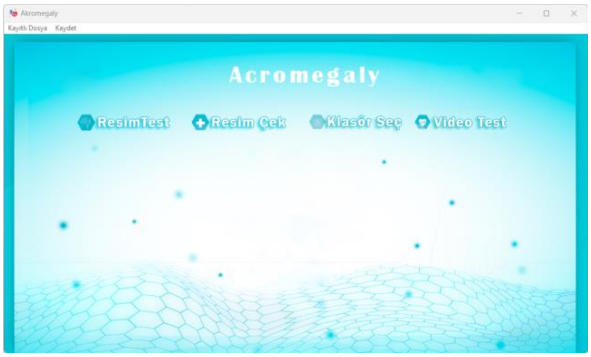

Figure-1 Program Login Screen

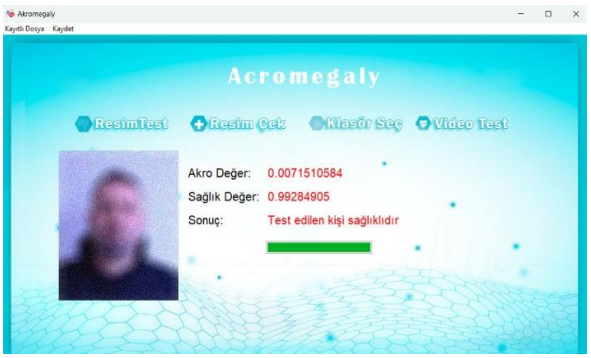

Figure-2 Acromegaly Program Screenshot

The login screen of the software is prepared as shown in figure-1. As seen in Figure-2, when the image to be tested is selected with the Test image option, the result appears on the screen as "Healthy" or "Acromegaly patient". In the testing feature by taking a picture from the instant camera, the test process is applied to the picture saved in the memory by taking a picture with the device's camera. The feature of testing all pictures in the folder tests all pictures in the folder and shows the results. With the video test feature, the test process is performed by recording the face as an image as

soon as the face is found in the video with the face detection algorithm.

The prepared software was tested with 54 people (33 men, 21 women). The age range and health results of the people and the results of having Acromegaly are shown in Table-1.

Table-1 Software Test Results

	Male	Female
Healthy	33	21
Acromegaly Patient	0	0
Healthy Highest Value	0,99284905	0,99315487
Healthy Minimum Value	0.71056440	0.72545580
Acromegaly Highest Result	0.28943560	0.27454420
Acromegaly Lowest Result	0.00715095	0.00684513

According to the test results of 33 male and 21 female individuals tested, all 54 individuals were found to be healthy. The deep learning model used in healthy individuals gave the highest value of 0.99315487 in a female individual. The lowest healthy value was 0.710556440 in a male individual. Snapshots of all of these people were taken with the camera fixed and the background white.

The software is prepared to be installed on all computers. It can be used with Kiosk machines to be placed in places such as hospitals, public living areas and shopping malls, contributing to the early diagnosis of Acromegaly disease.

REFERENCES

[1] Muhammed Kizilgul, Rukiye Karakis, Nurettin Dogan, Hayri Bostan, Muhammed Mutlu Yapıci, Umran Gul, Bekir Ucan, Elvan Duman, Hakan Duger, Erman Cakal, Omer Akin, Real-time detection of acromegaly from facial images with artificial intelligence, European Journal of Endocrinology, Volume 188, Issue 1, January 2023, lvad005, https://doi.org/10.1093/ejendo/lvad005

[2] Kong X, Gong S, Su L, Howard N & Kong Y.

[3] Automatic detection of acromegaly from facial photographs using camera setup methods. eBioMedicine 2018 27 94–102. https://doi.org/10.1016/j.ebiom.2017.12.015,

[4] Guo X, Meng T, Huang J, Wang X, Lian W, Deng K, Gao L, Wang Z, Xing B & Long X.

[5] 3D facial analysis in acromegaly: Gender-specific features and clinical correlations. Frontiers in Endocrinology 2018 9 722. doi: 10.3389/fendo.2018.00722

[6] He K, Zhang X, Ren S & Sun J.

[7] Deep persistent learning for image recognition. In IEEE Computer Vision and Pattern Recognition Conference 2016, p. 770–778. https://doi.org/10.1109/CVPR.2016.90

[8] Huang G, Liu Z, Van Der Maaten L and Weinberger KQ. Densely connected convolutional networks. Computer Vision and Pattern Recognition at the IEEE Conference 2017 p. 2261–2269. https://doi.org/0.1109/CVPR.2017.243

[9] Szegedy C, Vanhoucke V, Ioffe S, Shlens J & Wojna Z. Rethinking the startup architecture for computer vision. In IEEE Conference on Computer Vision and Pattern Recognition 2016, pages 2818–2826. https://doi.org/0.1109/CVPR.2016.308

[10] Miller RE, Learned-Miller EG, Trainer P, Paisley A & Blanz V. Early diagnosis of acromegaly: failure versus computers. Clinical Endocrinology (Oxford) 2011 75 226–231. https://doi.org/10.1111/j.1365-2265.2011.04020.

[11] Kızılgül M, Duger H, Nasiroglu NI, Sencar E, Hepsen S, Akhanlı P, Berker D, Çakal E, Bostan H & Uçan B. Efficacy of cabergoline add-on therapy in patients with acromegaly resistance to somatostatin analogues treatment and review of the literature. Archives of Endocrinology and Metabolism 2022 66 278-285. https://doi.org/10.20945/2359-3997000000481

[12] Colao A, Grasso LFS, Giustina A, Melmed S, Chanson P, Pereira AM & Pivonello R. Acromegaly. Nature Reviews Disease Primers 2019 5 20. https://doi.org/10.1038/s41572-019-0071-6

[13] Kelly, S. (2016). What Is Python?. In: Python, PyGame and Raspberry Pi Game Development. Apress, Berkeley, CA. https://doi.org/10.1007/978-1-4842-2517-2_2

[14] Agbolade, O., Nazri, A., Yaakob, R., Ghani, A. A., & Cheah, Y. K. (2020). Down syndrome face recognition: a review. Symmetry, 12(7), 1182.

[15] Yılmaz, Ö. Ü. A., & Yayın, k. (2021). Deep learning. Kodlab Publishing Distribution Software Ltd. Ltd.

[16] Schneider, H. J., Kosilek, R. P., Günther, M., Roemmler, J., Stalla, G. K., Sievers, C., ... & Würtz, R. P. (2011). A novel approach to the detection of acromegaly: accuracy of diagnosis by automatic face classification. The Journal of Clinical Endocrinology & Metabolism, 96(7), 2074-2080.

[17] Kong, X., Gong, S., Su, L., Howard, N., & Kong, Y. (2018). Automatic detection of acromegaly from facial photographs using machine learning methods. EBioMedicine, 27, 94-102.

[18] Guo, X., Meng, T., Huang, J., Wang, X., Lian, W., Deng, K., ... & Long, X. (2018). 3D facial analysis in acromegaly: gender-specific features and clinical correlations. Frontiers in endocrinology, 9, 722.

[19] Meng, T., Guo, X., Lian, W., Deng, K., Gao, L., Wang, Z., ... & Xing, B. (2020). Identifying facial features and predicting patients of acromegaly using three-dimensional imaging techniques and machine learning. Frontiers in endocrinology, 11, 492.

[20] Colao A, Grasso LFS, Giustina A, Melmed S, Chanson P, Pereira AM & Pivonello R. Acromegaly. Nature Reviews Disease Primers 2019 5 20. https://doi.org/10.1038/s41572-019-0071-6

[21] Petrossians P, Daly AF, Natchev E, Maione L, Blijdorp K, Sahnoun-Fathallah M, Auriemma R, Diallo AM, Hulting AL, Ferone D, Hana V Jr, Filipponi S, Sievers C, Nogueira C, Fajardo- Montañana C, Carvalho D, Hana V, Stalla GK, Jaffrain-Rea ML, Delemer B, Colao A, Brue T, Neggers SJCMM, Zacharieva S, Chanson P & Beckers A. Acromegaly at diagnosis in 3173 patients from the Liège Acromegaly Study (LAS)) database. Endocrine Related Cancer 2017 24 505–518. https://doi.org/10.1530/ERC-17-0253

[22] Reid TJ, Post KD, Bruce JN, Nabi Kanibir M, Reyes-Vidal CM and Freda PU. The characteristics of the 324 patients with acromegaly at diagnosis did not change from 1981 to 2006: acromegaly was underrecognized and underdiagnosed. Clinical Endocrinology (Oxford) 2010 72 203–208. https://doi.org/10.1111/j.1365-2265.2009.03626.x

[23] Siegel S, Streetz-van der Werf C, Schott JS, Nolte K, Karges W & Kreitschmann-Andermahr I. Diagnostic delay is associated with psychosocial impairment in acromegaly. Pituitary 2013 16 507–514. https://doi.org/10.1007/s11102-012-0447-z

[24] Vilar L, Vilar CF, Lyra R, Lyra R & Naves LA. Acromegaly: clinical features at diagnosis. Pituitary 2017 20 22–32. https://doi.org/10.1007/s11102-016-0772-8 Schneider HJ, Kosilek RP, Günthe

[25] Schneider HJ, Kosilek RP, Günther M, Roemmler J, Stalla GK, Sievers C, Reincke M, Schopohl J & Würtz RP. A new approach for acromegaly detection: diagnostic accuracy with automatic face classification. Journal of Clinical Endocrinology and Metabolism 2011 96 2074–2080 doi: 10.1210/jc.2011-0237.

Enhancing On-Time Performance through Flight Time Prediction: A Machine Learning Approach

S. SOYKAN[1] and S. BADAY[2]

[1] Istanbul Technical University, Informatics Institute, 34469 İstanbul/Turkey, soykans@itu.edu.tr
[2] Istanbul Technical University, Informatics Institute, 34469 İstanbul /Turkey, badays@itu.edu.tr

***Abstract* - Aviation industry efficiency and on-time performance are vital to passenger satisfaction and operational excellence. This study focuses on improving on-time performance by accurately predicting flight duration. We combined on-time performance data from the Bureau of Transportation Statistics (BTS) with Microsoft Azure-sourced weather data to create a diverse dataset. A comprehensive analysis of machine learning algorithms, including linear regression, random forest, and XG Boost, was conducted to predict flight duration. Notably, the XG Boost algorithm outperformed its counterparts, demonstrating its potential for optimizing aviation operational efficiency. Our models underwent rigorous evaluation of standard metrics such as Mean Absolute Error (MAE), Root Mean Squared Error (RMSE), R-squared and Mean Absolute Percentage Error (MAPE). The XG Boost model consistently exhibited the lowest MAE and RMSE, confirming its reliability in forecasting flight duration. The mean absolute error consistently remained below the aviation industry's accepted delay threshold of 15 minutes. The chosen model achieved a proportion of variance explained value of 0.97 in predicting flight duration. Furthermore, the integration of weather data sheds light on the influence of meteorological conditions on flight schedules, thereby augmenting the model's predictive capabilities. This holistic approach to flight duration forecasting enhances our understanding of this domain.**

In conclusion, our research underscores the pivotal role of accurate flight duration prediction in bolstering on-time performance. The XG Boost algorithm, in conjunction with weather data, is a potent tool for this purpose. These findings furnish invaluable insights for aviation stakeholders seeking to optimize their operations, elevate passenger satisfaction, and mitigate unforeseen disruptions. Future research endeavors will refine the model, encompass relevant factors such as taxi durations, and broaden its applicability within the aviation sector.

***Keywords* - Aviation industry, On-time performance (OTP), Flight time, Machine Learning, Prediction**

I. INTRODUCTION

THE elevated on-time performance metrics within the context of airlines hold significance across numerous dimensions. Delays can lead to a cascade of problems, affecting customer satisfaction, operational costs, and planning. Specifically, regarding customer satisfaction, the repercussions of missed connecting flights in the case of transfer passengers can result in both dissatisfaction and potential compensation for passengers affected by airline-related delays. Furthermore, deviations in arrival times may incur additional expenses, such as airport penalties. Beyond financial implications, performance discrepancies can also necessitate extra "operational efforts, like reassigning crews and flight planning adjustments. Moreover, these disruptions can significantly harm the airline's brand image. Traffic delays result in significant financial losses for airlines, including expenses from increased fuel consumption, compensation for disgruntled passengers due to delayed flights, and the impact on the costs of subsequent flights. To address this issue, researchers globally have conducted numerous studies to explore potential solutions for mitigating traffic delays [3].

For all these reasons, our study aims to enhance on-time performance by predicting flight durations, thereby contributing to on-time performance during the planning phase. In this context, we have utilized OTP data provided by the Bureau of Transportation Statistics (BTS). Additionally, we have explored the influence of weather conditions, using weather data obtained through Azure DevOps.

Within the scope of this study, we have focused on employing various regression techniques to identify the best predictors and parameters for accurate predictions. The outcome of this study is expected to be instrumental for airline companies, particularly during the schedule planning phase, allowing them to anticipate potential disruptions to on-time performance and plan actions to mitigate these disruptions in advance.

II. RELATED WORKS

Numerous studies have been conducted in the field of aviation to contribute to on-time performance metrics. Table 1 shows a summary of related work. Flight duration predictions have been examined in multiple prior studies, as exemplified in [1], [2], [3], and [4], where a combination of deep learning and machine learning algorithms were utilized. Ke Liu et al. [5] crafted a comparative framework between America and China, utilizing data from the Federal Aviation Administration. Some studies have focused on block time predictions, which incorporate taxi times into flight duration calculations.

Table 1. Related works

No	Author	Purpose	Datasets	Research method	Year
1	Xinting Zhu, Lishuai Li	Utilizing DL for Flight Time Prediction to Inform Fuel Loading Decisions	Airline records, ADS-B data, and METAR data.	LSTM, SWRNN	2021
2	Zhang, J. et al.	Predicting Arrival Aircraft Flight Times in Terminal Areas Using Data-Driven Approaches	Guangzhou Baiyun International Airport	LR, LASSO, RF, LGB	2021
3	Stefanovič, P et al.	Utilizing Supervised Machine Learning Models for Predicting Flight Time Deviations	lithuanian-airports-flight-dataset.	MLP, KNN, DT, RF	2020
4	Noboru Takeichi	Adaptive Forecasting for Ground-Based 4D Trajectory Management Flight Time Uncertainty	Secondary surveillance radar Mode S	SSR Mode S, Global Spectral Model (GSM)	2018
5	Ke Liu et al.	Comparative Analysis of Airborne Flight Time Between the United States and China.	CAAC, ASPM and FAA	OLS	2022
6	Ahmed Abdelghany et al.	Limitations of ML-Based Models in Predicting Block Time for Airline Flights	FAA, OAG	RT, RFR, and XG Boost Regression	2022
7	Lu Hao, Mark Hansen	Ensuring Block Time Reliability and Establishing Scheduled Block Times	BTS, OAG, FAA	OLS	2014
8	Chunzheng Wang et al.	Enhancing the Spatial-Temporal Generalization of Flight Block Time Prediction through Stacked Models Development	BTS	ET, GBM and Stacking	2022
9	Nabin Kafle, Bo Zou	Analytical-econometric approach for studying the spread of flight delays	BTS	OLS, Percentile	2016
10	Paolo Malighetti et al.	Analyzing the turnaround strategies on airlines' efficiency	European airports	Baseline Model	2023
11	Shervin AhmadBeygi, Amy Cohn et al.	Investigating the likelihood of delay spread within passenger airline networks	US passenger airlines	Propagation Model	2008
12	Hajar Alla et al.	Evaluating the influence of aircraft performance and prediction of flight arrival delays	US domestic flight	RF, DT, KNN, Naive Bayes	2022
13	Navoneel Chakrabarty	Utilizing a data mining approach to predict flight arrival delays for American Airlines	US domestic flight	GBM	2019
14	Mehmet Cemal Atlıoğlu et al.	Supervised Learning Approaches to Flight Delay Prediction	Federal	CART, KNN, XGB	2020
15	Hasan Khaksar, et al.	Predicting airline delays using ML	US Flight	CART, Hybrid Model	2017
16	Maryam Farshchian Yazdi et al.	Predicting flight delays using a combination of DL and the Levenberg-Marquardt algorithm	US Flight Dataset	Levenberg-Marquart algorithm	2020

In this context, [6], [7], [8], and [9] have worked with various machine learning algorithms, such as XG Boost, Gradient Boosting, and random forest, using BTS and FAA datasets. Malighetti et al. [10] presented an analysis of airlines' efficiency and on-time performance (OTP). Shervin AhmadBeygi, Amy Cohn et al. [11] emphasized passenger-based delay analysis. Alla et al. [12] and Chakrabarty [13] utilized US domestic flight data, focusing on arrival delays. [14-15] outlined a framework for flight delay predictions in these studies. Yazdi et al. [16] conducted research on deep learning and the Levenberg-Marquardt algorithm methodology for predicting delays.

In our study, different methods were tried in the feature extraction and feature selection steps, and features created based on origin and destination contributed to the increase of model success.

III. MATERIAL AND METHODS

A. Dataset

The data for this study was sourced from the Bureau of Transportation Statistics (BTS) database, maintained by the Department of Transportation in the United States. The analysis focused on on-time performance data spanning from January 1, 2021, to June 30, 2023. In total, the study was conducted on a dataset comprising 82,064 rows. Only records of flights that successfully arrived at their destinations were considered, while flights with divert, cancel, or duplicate statuses were excluded from the dataset. Additionally, the study honed in on airlines that exhibited suboptimal performance in terms of departing on time and arriving punctually. Specifically, carriers with subpar performance in terms of flight duration were selected.

For the purpose of this study, two distinct datasets were used: one for training before January 1, 2023, and another for training from January 1, 2023, to June 6, 2023.

Furthermore, to assess the impact of weather conditions on flight duration, weather data was collected through Azure DevOps. The date range mentioned above was cross-referenced with port information. This allowed for the acquisition of variables such as temperature, precipitation, and snowfall status through the weather dataset.

Figure 1 shows some fields of flight terms in the dataset.

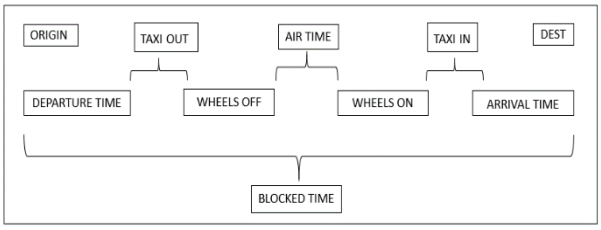

Figure 1. Flight duration terms

B. Data Preprocessing

The initial dataset was comprised of 2,858,039 million records. To ensure data quality, we conducted a thorough data cleaning process. This included checking for missing values, outliers, and inconsistencies in the data. Duplicate records, of which there were approximately 295,251, were identified and removed to avoid redundancy.

To make the dataset suitable for modeling, we performed several data transformations, including:

• Categorical Variables: Categorical variables were converted into binary variables using the one-hot encoding technique. This approach expanded the dataset by generating binary columns for each category, effectively converting them into a format that can be utilized in machine learning models.

• Numerical Variables: Numeric variables were standardized or normalized as needed to ensure that they contribute consistently to the modeling process. This step is crucial for models that are sensitive to the scale of input features.

• Date Variables: Date variables were transformed into features such as quarters and months. Historical averages of flight and weather data were computed on a quarterly and monthly basis, enriching the dataset with temporal information.

Exploratory Data Analysis (EDA) is a fundamental step in the data analysis process. In this study, we employ the Pandas Profiling Report and Sweet viz libraries to conduct an initial analysis, with the primary objective of gaining an overview of the dataset. Specifically, we perform separate visualizations for categorical and numerical variables, investigating distribution, skewness, kurtosis, bias, and identifying outlier values.

Figure 2 visually represents the distribution of months, which are categorized into discrete units such as January, February, March, and so on. Each month is a distinct category, and there is no inherent order or numerical value associated with them. This type of data is commonly used for tracking patterns and variations across different categories, allowing for insights into seasonality or other categorical trends.

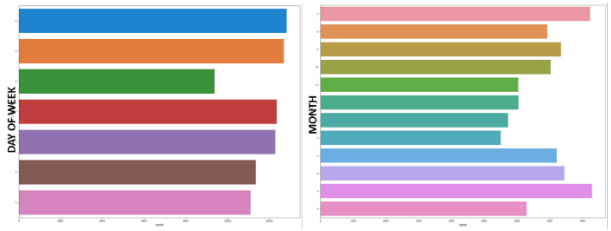

Figure 2. Bar of the Month and Day of Week

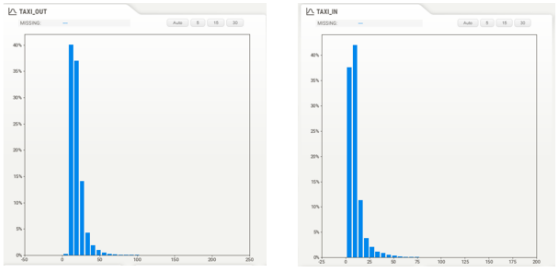

Figure 3. Distribution chart of Taxi Out and Taxi In

Figure 3 shows both the taxi-out and taxi-in times. Taxi-out time represents the duration between an aircraft's departure from the gate and its takeoff from the runway, while taxi-in time refers to the period from the aircraft's landing on the runway to its arrival at the designated gate. Both taxi-out and taxi-in times are numerical variables, measurable in minutes, and provide crucial insights into the efficiency of airport operations and air traffic management.

C. Feature Engineering

Feature extraction is a critical component of predictive

modeling, as it involves generating new features from the existing dataset. In our study, we applied feature engineering techniques to improve the model's predictive power. Specifically, we:

- Calculated quarterly and monthly averages for flight-related variables, enabling the model to capture the historical performance of flights over time.
- Computed quarterly and monthly averages for weather data, providing insights into historical weather patterns that may influence flight outcomes.

To enhance the predictive success of the model, various feature selection methods were employed. In the feature selection step, pre-models such as OLS and decision tree were built to assess the explanatory power of independent variables. Additionally, methods like Pearson correlation and heatmap matrix were employed to consider relationships between dependent and independent variables, and features above a certain threshold value were selected.

An initial pre-model was established using the Ordinary Least Squares method. The model results were scrutinized to examine the p-values and significance of the independent variables. Furthermore, the coefficients of each variable derived from the model and multicollinearity situations were also analyzed.

In decision tree algorithms, data pattern and the significance of features are captured. The significance of each feature in the model is established by calculating feature importance. High-importance features derived from these tree models significantly contribute to the feature selection process. In this study, the explanatory power of inputs in the model was examined by calculating feature importance using a decision tree model.

Additionally, the feature importance was computed using the Decision Tree method to compare the interpretability of inputs in the model. The relationships between variables were further explored using heatmap plots.

The use of a heatmap graph and a Pearson correlation matrix has contributed to the feature selection process, aiding in decision-making steps.

D. Model

With the help of the methods mentioned in the feature selection step, the independent variables that were most descriptive on the dependent variable were selected and added as input. Since the dependent variable of flight time is a continuous variable, regression models were used for prediction. In this context, Linear Regression, Lasso, Ridge, Elastic, Bagging Regression and XG Boost Regression models were studied.

In the conducted study within the scope of Python, the XG Boost library was used for the XG Boost model, while the scikit learn library was utilized for other regression models. Additionally, the seaborn and matplotlib libraries were employed for visualization purposes.

Default parameters were assigned to the models. For example, the lasso model was instantiated with an alpha value of 0.1, while the random forest model was initialized with random state=0 and n estimators=300 values. In the Bagging Regressor model, K Neighbors Classifier function was used, along with max samples=0.5 and max features=0.5. To better evaluate the performance of the models, mitigate bias and variance issues, and assess their generalizability, cross validation was applied. In this context, a 5-fold cross validation approach was employed.

IV. RESULTS AND DISCUSSIONS

The results of the model evaluation were assessed using Mean Absolute Error (MAE), Mean Squared Error (MSE), Root Mean Squared Error (RMSE), R-Squared, Mean Absolute Percentage Error (MAPE) metrics. Table 2 displays the outcomes of these methods. As can be observed, XG Boost has demonstrated higher performance in all evaluation metrics.

Table 2. Model Results

Model	MAE	MSE	RMSE	R^2 Score	MAPE
LR	13.99	340.65	18.46	0.96	5.32
Lasso	15.67	406.18	20.15	0.95	6.52
Elastic Net	21.68	726.03	26.94	0.91	10.09
Ridge	14.01	341.26	18.47	0.96	5.32
Bagging	13.19	315.49	17.76	0.96	4.77
RF	13.16	314.83	17.74	0.96	4.76
XGB	12.95	304.96	17.46	0.96	4.69

A hyperparameter optimization has been performed on the XG Boost Regressor, which has the highest success rate compared to other models. The Grid Search CV algorithm was used to determine the most suitable parameters. The parameters used are as follows:

- N estimators: It controls the number of trees to be created.
- Learning rate: It controls the contribution of each tree to the final result.
- Max depth: It determines the maximum depth of each tree.
- Min child weight: It controls the minimum number of samples required to prevent overfitting.
- Gamma: It controls the growth of trees.
- Col sample by tree: It determines the percentage of necessary features for each tree.

The model was re-tuned using these parameters. As shown in Table 3, after hyperparameter optimization, an improvement in performance metrics has been observed in all evaluation metrics.

Table 3. Hyperparameter Optimization Results

Model	MAE	MSE	RMSE	R^2 score	MAPE
XGB Regressor	12.95	304.96	17.46	0.96	4.69
XGB Regressor Tuned	12.50	300.96	15.46	0.97	4.65

V. CONCLUSION AND FUTURE WORKS

In the scope of this study, the aim was to contribute to the on-time performance (OTP) goals of airlines by predicting flight times. The BTS dataset was analyzed, and a relatively less successful carrier was selected as the OTP performance criterion. As the problem involves a continuous target, various regression models were experimented with. Upon comparing all models, the XG Boost model yielded the best results with a proportion of explained variance value of 0.97 and a mean absolute error of 12.50. To improve the model's accuracy, cross-validation and hyperparameter optimization were implemented. This model holds the potential to be employed in decision support systems within the airline industry to contribute to OTP goals. In future research, exploration of different carrier types, datasets from more international regions, and feature sets with potentially diverse impacts on weather conditions should be considered. Such further investigations can provide a deeper understanding of OTP performance in the aviation sector and offer insights into enhancements for future endeavors. In conclusion, this study showcases the potential of a robust model for predicting OTP performance in the airline industry, representing a significant step that can guide future research efforts.

REFERENCES

[1] Abdelghany, A., Guzhva, V., & Abdelghany, K. (2023). the limitation of machine-learning based models in predicting airline flight block time. journal of air transport management, 107, 102339. https://doi.org/10.1016/j.jairtraman.2022.102339

[2] S. AhmadBeygi, A. Cohn, Y. Guan, & P. Belobaba, "analysis of the potential for delay propagation in passenger airline networks", journal of air transport management, vol. 14, no. 5, p. 221-236, 2008. https://doi.org/10.1016/j.jairtraman.2008.04.010

[3] H. Alla, L. Moumoun, & Y. Balouki, "impact of aircraft performance and time of the day on flight arrival delays prediction in the united states: a machine learning classification", itm web of conferences, vol. 48, p. 03005, 2022. https://doi.org/10.1051/itmconf/20224803005

[4] M. C. Atlıoğlu , M. Bolat , M. Şahin , V. Tunalı ve D. Kılınç , "Supervised Learning Approaches to Flight Delay Prediction", Sakarya University Journal of Science, c. 24, sayı. 6, ss. 1223-1231, Ara. 2020, doi:10.16984/saufenbilder.710107

[5] N. Chakrabarty, "a data mining approach to flight arrival delay prediction for american airlines",, 2019. https://doi.org/10.1109/iemeconx.2019.8876970

[6] N. Kafle and B. Zou, "modeling flight delay propagation: a new analytical-econometric approach", transportation research part b methodological, vol. 93, p. 520-542, 2016. https://doi.org/10.1016/j.trb.2016.08.012

[7] H. Khaksar and A. Sheikholeslami, "airline delay prediction by machine learning algorithms", scientia iranica, vol. 0, no. 0, p. 0-0, 2017. https://doi.org/10.24200/sci.2017.20020

[8] K. Liu, Z. Zhe, B. Zou, & M. Hansen, "airborne flight time: a comparative analysis between the u.s. and china", journal of air transport management, vol. 107, p. 102341, 2023. https://doi.org/10.1016/j.jairtraman.2022.102341

[9] H. Lu and M. Hansen, "block time reliability and scheduled block time setting", transportation research part b methodological, vol. 69, p. 98-111, 2014. https://doi.org/10.1016/j.trb.2014.08.008

[10] P. Malighetti, C. Morlotti, R. Redondi, & S. Paleari, "the turnaround tactic and on-time performance: implications for airlines' efficiency", research in transportation business & management, vol. 46, p. 100874, 2023. https://doi.org/10.1016/j.rtbm.2022.100874

[11] Á. Rodríguez-Sanz, F. Comendador, R. Valdés, J. Pérez-Castán, P. García, & M. Godoy, "4d-trajectory time windows: definition and uncertainty management", aircraft engineering and aerospace technology, vol. 91, no. 5, p. 761-782, 2019. https://doi.org/10.1108/aeat-01-2018-0031

[12] P. Stefanovič, R. Štrimaitis, & O. Kurasova, "prediction of flight time deviation for lithuanian airports using supervised machine learning model", computational intelligence and neuroscience, vol. 2020, p. 1-10, 2020. https://doi.org/10.1155/2020/8878681

[13] C. Wang, M. Hu, L. Yang, & Z. Zhao, "improving the spatial-temporal generalization of flight block time prediction: a development of stacking models", journal of air transport management, vol. 103, p. 102244, 2022. https://doi.org/10.1016/j.jairtraman.2022.102244

[14] M. Yazdi, S. Tabbakh, S. Chabok, & M. Kheirabadi, "flight delay prediction based on deep learning and levenberg-marquart algorithm", Journal of Big Data, vol. 7, no. 1, 2020. https://doi.org/10.1186/s40537-020-00380-z

[15] J. Zhang, Z. Peng, C. Yang, & B. Wang, "data-driven flight time prediction for arrival aircraft within the terminal area", iet intelligent transport systems, vol. 16, no. 2, p. 263-275, 2021. https://doi.org/10.1049/itr2.12142

[16] X. Zhu and L. Li, "flight time prediction for fuel loading decisions with a deep learning approach", transportation research part c emerging technologies, vol. 128, p. 103179, 2021. https://doi.org/10.1016/j.trc.2021.103179

Performance Evaluation of Classification Algorithms For Defect Detection in Patterned Fabric Images

Y.E.MERAL[1] and O. GOKALP[2]

[1] Izmir Katip Celebi University, Izmir/Turkiye, yunusemremeral.cs@gmail.com
[2] Izmir Katip Celebi University, Izmir/Turkiye, osman.gokalp@ikcu.edu.tr

Abstract **- Defect identification holds substantial relevance across diverse industries, encompassing the textile sector, as well as materials like marble and metal. Automatic defect detection technology, by minimizing human factors influenced by employee distraction and limited concentration time, offers consistent and accurate identification of defects. This study aims to evaluate the performance of various classification algorithms on automatic defect detection in patterned fabric images. The feature extraction stage incorporates Grey-Level Co-occurrence Matrix utilizing seven distinct statistics, as well as Local Binary Pattern techniques. The obtained results on 4 public datasets indicate that Random Forest and XGBoost consistently outperform other classifiers in terms of accuracy, precision, recall, and F1 score across all datasets. This suggests that ensemble methods are well-suited for fabric image classification tasks.**

Keywords **– automatic defect detection, feature extraction, GLCM, fabric images, classification.**

I. Introduction

Defect detection is a field with significant applications in various industries including the textile sector, as well as materials such as marble and metal. Its primary objective is to detect and identify defects on material surfaces. This has the potential to improve product quality, enhance manufacturing processes, and reduce costs. Fabric defect identification is a quality control procedure designed to detect and find defects on fabrics [1]. Fabric defects can lead to losses of approximately 45-65% in selling prices. Furthermore, around 85% of rejected products in the ready-to-wear sector are attributed to fabric defects [2].

Manual defect detection can lead to missing or incorrect results due to factors such as employee distraction and limited concentration time. Automatic defect detection technology offers the ability to consistently identify defects by minimizing human factors. Furthermore, artificial intelligence and image processing techniques allow automatic systems to rapidly analyze large datasets, enabling continuous quality control on the production line. The limited concentration time of quality control personnel and the difficulty of recognizing only clearly visible defects demonstrate the limitations of the manual approach. According to research, even under test conditions, approximately 30% of defects may go undetected, and in some well-performing companies considered as good, the repeatability of defect assessments by quality control personnel has not exceeded 50%. Therefore, the automation of the fabric inspection process is a heavily researched topic [2, 3].

Feature extraction is a process utilized to reduce the dimensionality of input data and to transform it into meaningful information that represents its main characteristics. It renders the data more comprehensible and manageable while emphasizing the fundamental attributes of the data to enhance the effectiveness of classification or analysis procedures. In tasks such as fabric defect detection, where the aim is to reduce the dimensionality of input data, the relevant information, referred to as features, is chosen or transformed for accurate classification. This process simplifies the data and enhances the efficiency of data processing algorithms by focusing on the most distinguishing aspects of the data. In the context of fabric defect detection, feature extraction may encompass the identification and quantification of specific visual attributes or patterns within fabric images that signify defects, thereby facilitating a machine learning algorithm's ability to discern differences between normal and defective samples.

GLCM (Grey-Level Co-occurrence Matrix) is a highly effective technique for extracting features from textured images. This matrix systematically evaluates the relationships between pixel values within an image. Specifically, this method holds substantial potential for examining the textural characteristics of images in detail. One of the most noteworthy attributes of GLCM is its position-invariant property, which ensures consistent and reliable results when extracting features from images of an object in different positions.

In this study, feature extraction from images was carried out using GLCM. In particular, the features computed by GLCM were employed for the purpose of analyzing and classifying images to better understand and identify patterns, textures, and objects within them. This demonstrates how GLCM serves as an effective tool in applications such as object recognition and image analysis.

The remainder of the paper is organized as follows. Section 2 gives the literature review and gap. Section 3 explains materials and methods used in this study. Section 4 shares the results obtained after experimental work. Finally, section 5 discusses the findings and concludes the paper.

II. Literature Review

Ngan et al. [4] utilized the direct thresholding approach, based on the wavelet transform of detailed sub-images, as an automated visual inspection technique for discovering defects in patterned fabric. The authors reported a success rate of 96.7% in detecting defects on a common class of patterned jacquard fabric using the wavelet pre-processed golden image

subtraction method. The authors used 30 defect-free images and 30 defective patterned images in their study. This method segments out defective regions effectively by employing wavelet-based techniques to extract detailed and approximation sub-images from a histogram equalized defective image. These sub-images were subsequently processed for defect detection.

Kang et al. [5] used a genetic algorithm (GA) to optimize Gabor filters for defect detection in patterned fabrics. Their method, implemented in MATLAB, aimed to reduce noise in printed patterned fabrics and achieve efficient defect detection. The research employed distance matching and the Regular Band to determine fabric units. It enabled fast and effective detection of both random and regular patterned fabrics. The Gabor filter enhanced defect regions by removing background interference, but it faced challenges in cases where defects were not clearly distinguishable from the fabric background. The study also highlighted the importance of color differences between fabric defects and backgrounds for Gabor filtering. Training with non-defective fabrics facilitated real-time defect detection with minimal computational complexity. The proposed methods offered swift and real-time defect detection, especially for regular patterns.

Reddy et al. [6] developed a texture classification system that is robust to changes in illumination. They used a combination of the Gray Level Co-occurrence Matrix (GLCM) and different binary patterns. Their model included adaptive histogram equalization normalization to enhance local contrast. The binary patterns were used to extract texture features, and a rotation-invariant, scale-invariant steerable decomposition filter was applied at different angles. Statistical measures such as mean, standard deviation, contrast, correlation, angular second moment, entropy, and difference entropy were used to capture image content. They employed three classifiers (k-NN, PNN, and SVM) for texture similarity and defect classification. The proposed method, combining binary patterns and GLCM, achieved a 100% defect classification accuracy for both SVM and K-NN classifiers. Additionally, it outperformed individual binary pattern methods in similarity classification, achieving a high rate of 93.75% with SVM and K-NN and 31.25% with PNN.

Despite numerous studies focusing on automatic defect detection in patterned fabric images, there is a lack of comprehensive performance evaluations that simultaneously consider a wide range of classification algorithms. Previous research has not addressed this gap, and there is a need to conduct a comparative evaluation of multiple algorithms to gain insights into their effectiveness. By considering the "no free lunch" theorem in machine learning [7], which suggests the absence of a universally superior algorithm, this study aims to provide a thorough performance evaluation of diverse classification algorithms for defect detection in patterned fabric images. The findings will assist in guiding the selection of appropriate algorithms for real-world applications in the textile industry.

III. Materials and Methods

A. Feature Extraction for Patterned Images Using GLCM

In our study, we employed a feature extraction technique for the analysis of patterned images. This technique primarily revolves around the utilization of the Gray-Level Co-occurrence Matrix (GLCM). We calculated GLCM matrices from the input images to capture their inherent textural characteristics. The matrices were further subjected to various statistical calculations to obtain specific textural properties, which include contrast, dissimilarity, homogeneity, energy, correlation, angular second moment, and mean. These properties collectively constitute an essential feature set that enables a comprehensive characterization of the image textures.

B. Classification Algorithms

To classify the image data and evaluate its patterns, we employed a range of distinct classification algorithms. These algorithms were specifically chosen to cater to the complexities of the problem at hand. The set of algorithms used in our analysis comprises the Random Forest, Bagging, Logistic Regression, Support Vector Classifier, K-Nearest Neighbors, Naive Bayes, Decision Tree, Gradient Boosting, and XGBoost. In our study, each of these algorithms underwent a training process on the feature vectors derived from our training dataset. Subsequently, they were assessed and validated using a separate test dataset.

C. Data Acquisition and Processing

The data utilized in this study was obtained from the TILDA dataset, specifically focusing on the c3-r1, c3-r3, c4-r1, and c4-r3 datasets, which contain patterned image samples. Each dataset classifies images into 7 classes; 6 different kinds of defects labels and 1 defect-free label. To prepare the data, the Grey-Level Co-occurrence Matrix was computed for each image, capturing the relationships among pixel values in various orientations and distances. The GLCM matrices were normalized and contained 256 levels to ensure consistency in feature extraction across all images.

In the context of data preparation and preprocessing, these GLCM matrices served as a fundamental step. They were employed for subsequent feature extraction, specifically to calculate contrast, dissimilarity, homogeneity, energy, correlation, angular second moment, and mean values. Additionally, local binary pattern features were computed from the images, further enriching the feature set. The combination of these features laid the foundation for the classification tasks.

D. Evaluation of Classification Results

Our study meticulously evaluated the classification results using various well-defined metrics, including accuracy, precision, recall, and F1 score. These metrics allowed us to thoroughly assess the performance of the classification algorithms in classifying patterned images.

Accuracy scores were computed for each classification algorithm, providing a quantitative measure of how effectively the algorithms classified the images. The accuracy was calculated using the formula (1):

$$\text{Accuracy} = \frac{TP+TN}{TP+TN+FP+FN} \quad (1)$$

However, accuracy alone does not provide a complete picture of performance.

In addition to accuracy metric, precision, recall, and F1 score metrics were also analyzed.

Precision measures the proportion of true positive predictions out of all positive predictions, indicating the algorithm's ability to avoid false positives. It is calculated using the formula (2):

$$\text{Precision} = \frac{TP}{TP+FP} \quad (2)$$

Recall, on the other hand, assesses the proportion of true positive predictions out of all actual positive instances, demonstrating the algorithm's capability to detect all relevant patterns. The formula for recall is (3):

$$\text{Recall} = \frac{TP}{TP+FN} \quad (3)$$

Furthermore, we calculated the F1 score, which is a harmonic mean of precision and recall. It offers a balanced evaluation of a classification algorithm's performance by considering both false positives and false negatives. The F1 score is computed as in (4):

$$\text{F1Score} = \frac{2(precision-recall)}{precision+recall} \quad (4)$$

IV. Experimental Work

In this section, we detail the experimental setup used for our analysis. The experiments were conducted using Python version 3.10.12 and the scikit-learn library version 1.2.2. The analysis aims to evaluate the performance of classification algorithms in the context of fabric defect detection. Default hyper-parameters were used for the classification algorithms except the following settings:

- Random Forest: A Random Forest classifier with 100 estimators was used, and the random state was set to 42 for reproducibility.
- Bagging: A Bagging classifier, primarily utilizing Decision Tree classifiers, was employed with 100 estimators. The random state was set to 42.
- Logistic Regression: Logistic Regression was performed with a maximum of 1000 iterations.
- Gradient Boosting: A Gradient Boosting classifier with 100 estimators was employed, and the random state was set to 42 for reproducibility.

The dataset used in the experiments contains patterned images obtained from the TILDA database, specifically including four different datasets: c3-r1, c3-r3, c4-r1, and c4-r3. When splitting the dataset into training and test data, a test data split ratio of 20% was applied. The results of the experiments are presented in the next section.

The performance metrics used in the paper include Accuracy, precision, recall and F1 Score evaluations.

The results for four different data sets are shown in the tables below (Tables 1-4).

Table 1: The Results obtained with the C3-R1 dataset.

Classifier	**Accuracy**	**Precision**	**Recall**	**F1 Score**
Random Forest	0.864	0.878	0.864	0.859
Bagging	0.778	0.804	0.778	0.782
Logistic Regression	0.457	0.454	0.457	0.416
Support Vector Classifier	0.346	0.304	0.346	0.248
K-Nearest Neighbors	0.531	0.557	0.531	0.531
Naïve Bayes	0.519	0.611	0.519	0.505
Decision Tree	0.630	0.688	0.630	0.645
Gradient Boosting	0.790	0.808	0.790	0.789
XGBoost	0.864	0.878	0.864	0.859

Table 2: The Results obtained with the C3-R3 dataset.

Classifier	**Accuracy**	**Precision**	**Recall**	**F1 Score**
Random Forest	0.667	0.731	0.667	0.663
Bagging	0.691	0.736	0.691	0.694
Logistic Regression	0.370	0.393	0.370	0.374
Support Vector Classifier	0.333	0.350	0.333	0.328
K-Nearest Neighbors	0.420	0.460	0.420	0.426
Naïve Bayes	0.457	0.457	0.457	0.449
Decision Tree	0.580	0.587	0.580	0.572
Gradient Boosting	0.667	0.703	0.667	0.670
XGBoost	0.704	0.722	0.704	0.699

Table 3: The results obtained with the C4-R1 dataset.

Classifier	Accuracy	Precision	Recall	F1 Score
Random Forest	0.642	0.691	0.642	0.647
Bagging	0.704	0.716	0.704	0.706
Logistic Regression	0.407	0.497	0.407	0.411
Support Vector Classifier	0.173	0.174	0.173	0.142
K-Nearest Neighbors	0.345	0.392	0.345	0.354
Naïve Bayes	0.481	0.543	0.481	0.470
Decision Tree	0.556	0.589	0.556	0.556
Gradient Boosting	0.654	0.684	0.654	0.656
XGBoost	0.704	0.725	0.704	0.706

Table 4: The results obtained with the C4-R3 dataset.

Classifier	Accuracy	Precision	Recall	F1 Score
Random Forest	0.675	0.699	0.675	0.647
Bagging	0.700	0.720	0.700	0.689
Logistic Regression	0.375	0.418	0.375	0.373
Support Vector Classifier	0.312	0.323	0.312	0.274
K-Nearest Neighbors	0.375	0.455	0.375	0.397
Naïve Bayes	0.450	0.417	0.450	0.412
Decision Tree	0.475	0.525	0.475	0.489
Gradient Boosting	0.688	0.731	0.688	0.699
XGBoost	0.675	0.688	0.675	0.675

V. Discussion and Conclusion

A. Performance Comparison Across Datasets

Experiments on various datasets consistently demonstrate the superior performance of Random Forest and XGBoost. Particularly, in the C3-R1 and C3-R3 datasets, these two algorithms exhibit a significant advantage over other classifiers (See Table 1 and Table 2). In the case of the C4-R1 and C4-R3 datasets, Random Forest and XGBoost also stand out with high accuracy, precision, recall, and F1 scores (See Table 3 and Table 4).

B. Ensemble Methods' Superiority

The obtained results indicate that Random Forest and XGBoost consistently outperform other classifiers in terms of accuracy, precision, recall, and F1 score across all datasets. This suggests that ensemble methods are well-suited for fabric image classification tasks. Conversely, Logistic Regression, Support Vector Classifier, and Naive Bayes yield lower performance scores, underscoring their limitations in handling complex fabric patterns.

C. Impact of Dataset Selection

The results underscore the substantial influence of dataset selection on classifier performance. Depending on the diversity of fabric textures, classification methods yield better or worse predictions. This highlights the critical importance of selecting the most appropriate dataset for specific applications.

D. Future Directions and Significance

In conclusion, our study offers valuable insights into fabric image classification. We emphasize the pivotal role of classifier selection in achieving accurate results. Random Forest and XGBoost have proven to be the top choices for this task, emphasizing the importance of considering dataset characteristics when choosing the most suitable model. Our research contributes to the fields of computer vision and textile industry applications. These findings underscore the potential of machine learning in enhancing automated quality control and product identification processes in textile manufacturing. Future studies may encompass improving the dataset collection process and exploring advanced deep learning models for enhanced accuracy.

References

[1] M. S. Priyanka, P. D. Manish, & R. S. Shekhar, (2012),"Overview: Methods of Automatic Fabric Defect Detection", Global Journal of Engineering, Design and Engineering., Education, published by Global Institute for Research and Vol. 1(2), pp 42-46, ISSN 2319 – 7293, 2019.

[2] Arıkan C.O., "Developing an Intelligent Automation and Reporting System for Fabric Inspection Machines" Tekstil ve Konfeksiyon, 29 (1), pp:86-93.

[3] Büyükkabasakal, K, "Kumaş dokuma hatalarının tespiti ve sınıflandırılması", İzmir, Ege Üniversitesi, 2010.

[4] H. Y. T. Ngan, G. K. H. Pang, S. P Yung, and M. K Ng,. "Wavelet-based Methods on Patterned Fabric Defect Detection", Pattern Recognition, Vol. 38, No.4, pp. 559–576, 2005.

[5] X. Kang, P. Yang, and J. Jing , "Defect Detection on Printed Fabrics Via Gabor Filter and Regular Band", Journal of Fiber Bioengineering and Informatics, Volume 8, Issue 1 pp 195–206, 2015.

[6] R. O. K Reddy, B. E. Reddy, and E. K Reddy, "Classifying Similarity and Defect Fabric Textures based on GLCM and Binary Pattern Schemes", International Journal of Information Engineering and Electronic Business, 5, pp 25-33, 2013.

[7] Adam, S. P., Alexandropoulos, S. A. N., Pardalos, P. M., & Vrahatis, M. N. No free lunch theorem: A review. Approximation and optimization: Algorithms, complexity and applications, 57-82, 2019.

On Trends of Investment Portfolio Management: A Bibliometric Analysis

D.Sabaliauskas[1] and J. Miliauskaitė[2]

[1] Department of Information Systems, Faculty of Fundamental Sciences, Vilnius Gediminas Technical University, Vilnius/Lithuania, dariussabaliauskas@stud.vilniustech.lt

[2] Department of Information Systems, Faculty of Fundamental Sciences, Vilnius Gediminas Technical University, Vilnius/Lithuania, jolanta.miliauskaite@vilniustech.lt, ORCID: 0000-0003-1237-3499

***Abstract* — this paper conducts a thorough bibliometric analysis of Investment Portfolio Management research, unveiling its intellectual landscape, emerging trends, and key contributors. By employing advanced bibliometric techniques on a vast collection of articles from Web of Science databases, we map the evolution of IPM research, identify influential works and authors, and reveal thematic clusters. Our analysis spans traditional portfolio optimization to modern themes like artificial intelligence and machine learning integration. We also illuminate global research networks. This study offers a holistic view of IPM, aiding scholars, practitioners, and policymakers in understanding its trajectory and fostering interdisciplinary collaborations. Therefore, our survey advances comprehension of the field, encourages research innovation, and informs strategies for navigating complex financial markets. The study's findings help academics and practitioners to navigate the literature on socially responsible investing, provide a systematic basis for developing the field, and suggest promising avenues for further research.**

***Keywords* — investment portfolio management, portfolio optimization, financial predictions, investment, portfolio allocation, algorithms, bibliometric analysis**

I. INTRODUCTION

The field of investment portfolio management (IPM) stands at the crossroads of finance, economics, and technology, navigating the intricate landscapes of risk [1] and return [2], asset allocation [3, 4], and market dynamics [5]. Nowadays, there are a lot of attempts to find solutions for managing portfolios [6, 7, 8]. The profound impact of investment strategies [9, 10, 11] on wealth generation and financial stability has fueled an ever-expanding body of research aimed at deciphering the complexities inherent in this domain [12]. In the era of information explosion and data-driven decision-making, understanding investment portfolio management research trajectory has gained paramount importance [12, 13, 14].

Researchers widely use quantitative, qualitative, or mixed methods to understand IPM topics better [15, 16, 17, 18]According to [15] authors have performed quantitative analysis [16].

According to [19], the authors comprehensively analyze the fuzzy portfolio domain using bibliometric analysis.

This study aims to conduct a bibliometric analysis, examine the trends in investment portfolio management between 1991 and 2023 August, and reveal and highlight the development of the respective year. According to [20], bibliometric analysis is employed in this paper as a literature review device to investigate the scientific research on investment portfolio management.

To discern potential research topics to address these gaps, this review seeks to understand the knowledge that has accumulated in this field of exchange rate forecasting by addressing four specific research questions:

The main research question follows: What are the predominant methodologies and models employed in investment portfolio management research? According to the main research question, the following research questions are defined: 1) how have topics of IPM and its related models, changed over different time periods? 2) Are certain methodologies and models more prevalent in specific geographic regions within the field of IPM research? 3) What are the most frequently used methodologies and models of IPM research?

This paper embarks on a bibliometric analysis (BA) to unravel the underlying trends, scientific contributors, and emerging themes within investment portfolio management research, drawing insights from the rich repository of the Web of Science (WoS) database.

The structure of the paper is as follows. After this introduction, Section 2 describes the methodology of a bibliometric analysis of the Investment portfolio allocation and portfolio optimization approaches for IPM. Section 3 presents the results of the BA. Section 4 discusses the results and methodological limitations, finally, Section 5 concludes the paper with possible directions for future works.

II. SURVEY METHODOLOGY

This review of investment portfolio management used a bibliometric approach, which is suitable for examining a large body of selected literature without limitation [21]. The flow diagram with the main analysis steps for this research is performed (see Figure. 1). The management flow consists of the following five steps: research design, compilation of bibliometric data, analysis, data visualization, and interpretation of results.

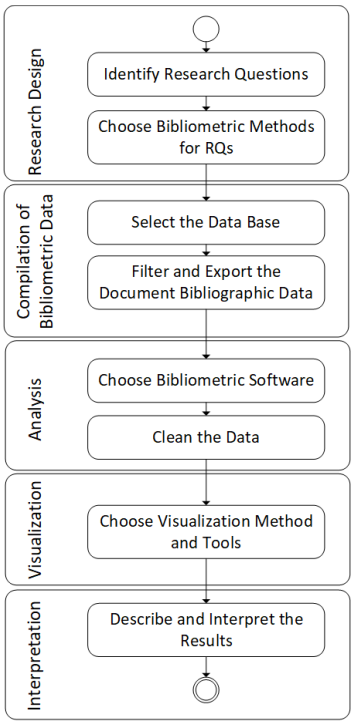

Figure 1: The flow diagram for our BA.

A. Research design

In this step, the following activities are performed.

a) Research Questions

The main research question (MRQ) follows: *What are the predominant methodologies and models employed in investment portfolio management research?* According to MRQ, the following research questions (RQ) are defined:

- RQ-1: How have **topics** of IPM and its related models, changed over different time periods?
- RQ-2: Are certain methodologies and models more prevalent in specific **geographic regions** within the field of IPM research?
- RQ-3: What are the most frequently used **methodologies and models** of IPM research?

b) Choosing Bibliometric analysis methods

The bibliometric analysis has five main methods: co-citation analysis, bibliographic coupling, citation, co-author, and co-word.

For this research, we chose appropriate methods of bibliometric analysis for all three Research Questions as follows:

- Chronological visualization and analysis (RQ-1) for this RQ has used the co-word method and method using author's keywords, and time slicing done two points;
- Countries visualization and analysis (RQ-2) for this RQ has used the co-author (co-authoring) method because bibliographical data contain information about authors` institutional affiliations and their geographical location and this method can analyze the issues on the level of countries and threshold of documents was chosen minimum 5 documents for one country and minimum 1 citation for one country;
- Keyword occurrence visualization based on APY and analysis (RQ-3) for this RQ has used the co-word method because this method uses the words in the document to create relationships and build a conceptual structure of the domain. The idea is that when words frequently co-occur, i.e., they are closely related. The result of the analysis shows a relationship between themes and those that represent the space of a domain. The threshold of the document to find co-occurrence of authors' keywords has used nine co-occurrences.

B. Compilation of bibliometric data

1) Select the database

WoS database was used based on the experience reported in [22]. Gusenbauer and Haddaway [23] have found that 14 of 28 academic search systems (ASS) are well-suited to SLR. Emphasizing the Computer Science research area, the main ASS are the following: ACM Digital Library, Bielefeld Academic Search Engine (BASE), ScienceDirect, Scopus, WoS, and Wiley Online Library. Moreover, another important attribute is the quality of the presented research. Consequently, we have found that WoS meets all those requirements. WoS allows tracking ideas across disciplines and a time of nearly 1.9 billion references cited in more than 171 million records [24].

2) Filter and Export the Document Bibliographic Data

First, we find two main concepts for the search as follows:

- Concepts related to investment portfolio;
- Concepts related to relevant methods and models in investment portfolio management.

The concepts used to develop WoS search requirements are as follows:

("investment portfolio*" OR "asset allocation*" OR "diversification*" OR "portfolio optimization*" OR "portfolio allocation*" OR " financial instrument*" OR "portfolio management*" OR "portfolio rebalancing*" OR "securities*" OR "financial prediction*") AND ("artifici* intelligence*" OR "machi* learn*" OR "quantitative method*" OR "statistical*" OR "algorithms*" OR "mathematical*" OR "heuristic*" OR "simulation*")

In this step, we have used the defined search query for the bibliometric analysis. An initial set of document entries and thesaurus are presented on GitHub (https://github.com/DarrellSab/On-Trends-of-Investment-Portfolio-Management-A-Bibliometric-Analysis (accessed on 18 August 2023). Moreover, as presented in Table 1, we have limited the search by database (DB), document type, language, and categories. We have not limited research areas, since it is related to RQ-2. As search results (SR), we have received 3009 document entries.

Table 1: Results of Identification and Data Cleansing Steps.

DB	Document Type	Language	Categories	SR
WoS	*article* **OR** *proceedings papers* **OR** *review*	English	*Computer sciences Artificial Intelligence* **OR** *Computer science Information Systems* **OR** *Computer science Interdisciplinary Applications*	3009

C. Analysis

1) Choose bibliometric software

In this step, we have chosen the VOSviewer (https://www.vosviewer.com/) software tool for conducting and visualizing bibliometric networks [23] and we used a library Biblioshiny of RStudio [25] too. Relevant papers obtained were transferred to VOSviewer or Biblioshiny.

A set of developing a keywords map on IPM, we have used keywords from the relevant papers. VOSviewer uses an automatic keyword identification technique [23]. It creates the keywords map according to the closeness and strength of existing links between found keywords calculating the number of papers, in which both keywords have occurred together. The size of the frames presents the occurrence of keywords.

Moreover, in this BA we concentrate on the keywords map coloring according to Average Publication Year (APY) which indicates the average publication year of the papers in which a keyword occurs [26]. Note that APY is a positive rational number.

2) Clean the data

The cleaning was done with a thesaurus list and a list of removed words with synonyms, plurals, and insignificant words. All identified papers' titles, abstracts, and keywords were checked for completeness and consistency.

D. Visualization

VOSviewer and Biblioshiny are used for visualization. We have chosen the keymap (see Figure. 3) from VOSviewer and the theme evolution graph from Biblioshiny (see Figure. 4) and used Excel for visualization RQ2 (see Figure. 2).

E. Interpretation

In BA the content is analyzed as:

- Chronological visualization and analysis RQ1;
- Research countries visualization and analysis RQ2;
- Keywords occurrence visualization based on APY and analysis RQ3.

The found keywords were analyzed quantitatively according to APY (RQ-3) and for searching, we used threshold 9 minimum of occurrence of keywords and results with 90 keywords as follows:

- Newest keywords – those keywords' occurrence is between 9 and 118, but the high is just two keywords deep learning (78) and machine learning (118) others are in intervals (9-38) (i.e., in the context of this BA), but their APY is new [2019-2021] (see Figure. 3);
- Older keywords – those keywords' occurrence can be similar to the newest between 9 and 129; genetic programming has 129 occurrences and their APY is old [2011-2015] (see Figure. 3).

III. MAIN RESULTS OF BA

The topics changed over a time period and the main keywords of the found publications on IPM (RQ-1) are presented in the Sankey diagram Figure. 4. The found publications were published in the period of 1991 – 2023 (August). The graphs show an increase in new keywords related to new models and methods for portfolio optimization in the publications on the analyzed topic: diversification, machine learning, risk management, neural network, portfolio allocation, etc., and it was started in 2015.

The distribution of the analyzed topic according to **countries** (RQ-2) is presented in Figure. 2. As can be seen, the ten most active countries are as follows: China, the United States, India, Australia, Japan, the United Kingdom France, Spain, Canada, and South Korea. Other countries are those which have less than 140 publications in WoS.

The developed keyword map, which presents the main **methodologies and models** being investigated in IPM (RQ-3) according to (APY), is presented in Figure. 3. Keywords colored in yellow are found in articles published in recent years (APY ~ 2020); green – APY ~ 2018; blue – APY ~ 2014 (see Figure. 3).

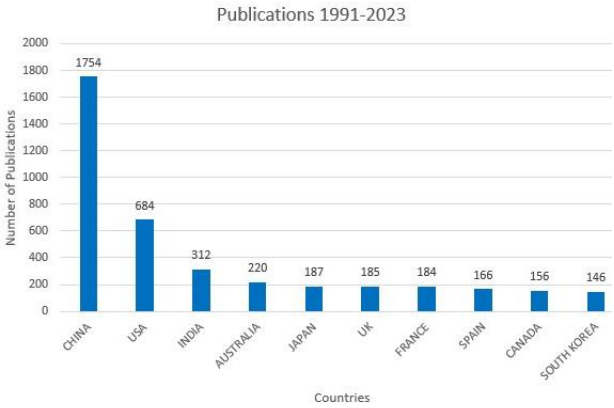

Figure 2: Countries analyzing IPM (RQ-2).

Moreover, the bigger frames present the more occurring keywords, and the smaller frames – less occurring keywords, which can be trends or unexpanded and forgotten topics depending on their color.

Yellow frames represent new keywords, i.e., their APY is equal to current years, which means novelty and new trends. Green and large frames present keywords that occur continuously in all the analyzed periods. Green and small frames present keywords in [2018; 2020]. Blue frames present older keywords.

So, we can see from Figure. 3, the newest keywords (APY (2019; 2021]; color – yellow), like deep learning, deep reinforcement learning, portfolio allocation, machine learning, reinforcement learning, search problems, mathematical model, uncertainty, LSTM, convolutional neural network, sentiment analysis, etc.; continuous occurrence of keywords (APY (2017; 2018] color – green), like artificial intelligence, optimization, feature selection, firefly algorithm, swarm intelligence, cardinality constraints, artificial bee colony, swarm intelligence, forecasting, etc.; and older keywords (APY (2014; 2016] color – blue), like, fuzzy logic, data mining, portfolio management, metaheuristic, tabu search, combinatorial optimization, clustering, diversification, ant colony optimization, risk management, support vector machine, financial time series, multi-agent systems, etc.

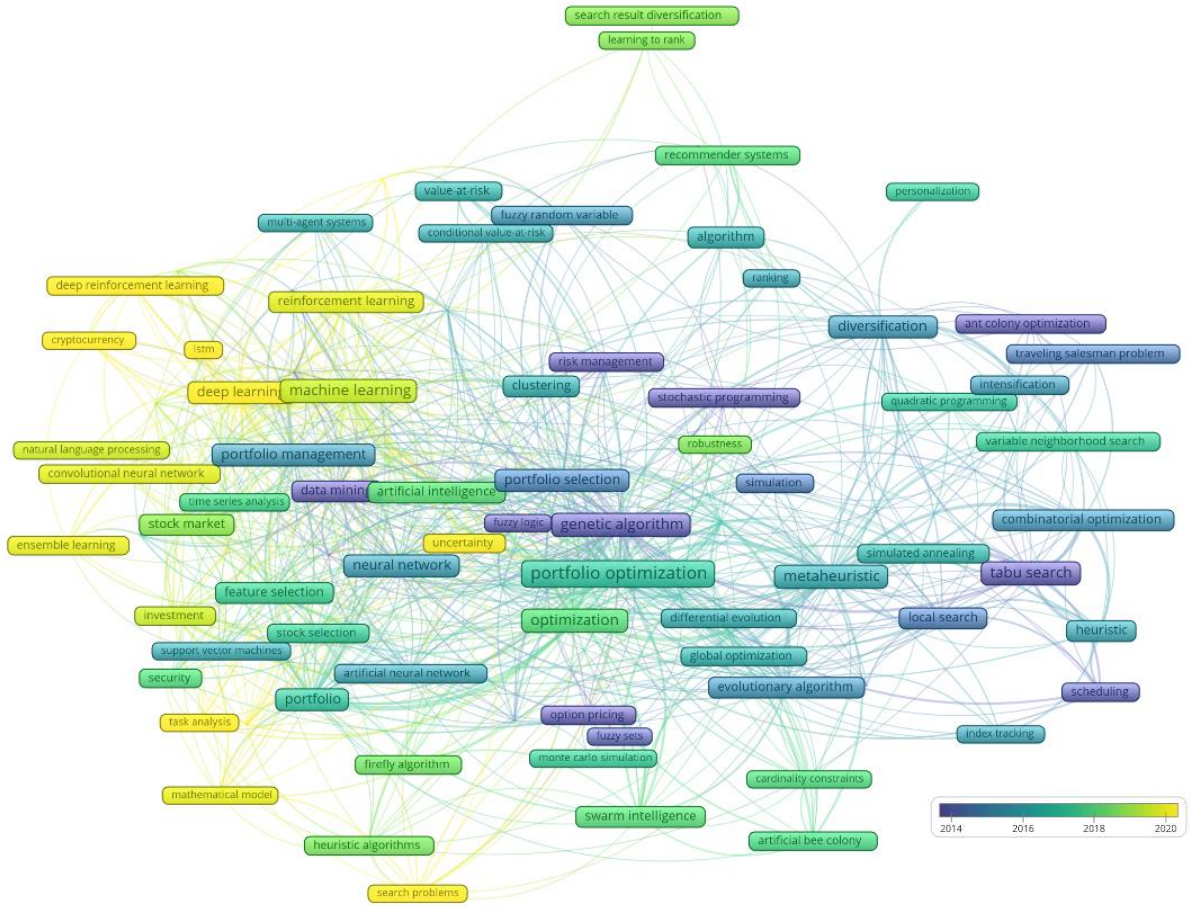

Figure 3: The keyword map (RQ3).

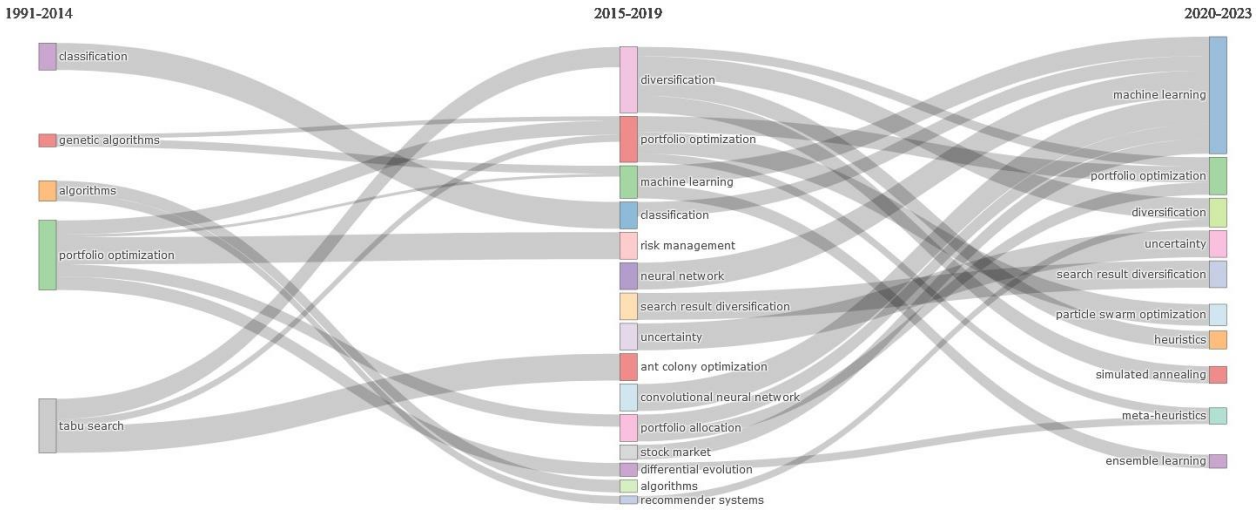

Figure 4: The changed topics over time of the found publications on IPM (RQ-1).

Table 2: Results of classification of concepts to investment portfolio and models, methods for portfolio management.

APY	Investment portfolio	Methods and Models for Portfolio Management
2021	task analysis	--
2020	cryptocurrency	deep learning, deep reinforcement learning, search problems, LSTM
2019	investment, natural language processing, extraction, portfolio allocation, uncertainty	sentiment analysis, machine learning, convolutional neural network, reinforcement learning, ensemble learning, mathematical model, unsupervised learning, feature
2018	diversification, stock market, algorithmic trading	firefly algorithm, heuristic algorithms, robustness, learning to rank, search result
2017	stock selection, forecasting, security, recommender systems, optimization,	quadratic programming, personalization, Monte Carlo simulation, variable neighborhood search, feature selection, time series analysis, artificial bee colony, cardinality constraints, swarm intelligence, artificial intelligence
2016	classification, multi-objective optimization, portfolio, portfolio optimization	support vector machines, metaheuristic, financial time series, differential evolution, conditional value-at-risk, clustering, iterated local search, multi-agent systems, algorithm, global optimization, value-at-risk, simulated annealing, particle swarm optimization
2015	Sharpe ratio, finance, diversification, intensification, asset allocation, artificial neural network, index tracking, ranking	evolutionary algorithm, combinatorial optimization, fuzzy random variable, portfolio management, neural network, evolutionary computation, heuristic
2014	Scheduling, portfolio selection	fuzzy sets, memetic algorithms, simulation, traveling salesman problem, local search, collaborative filtering
2013	data mining	genetic programming, ant colony optimization, genetic algorithm, stochastic programming
2012	Risk management	--
2011	financial prediction	tabu search
2010	--	Fuzzy logic

According to the classification of concepts to Investment portfolio (Column 2), Methods and Models for Portfolio Management (Column 3), the newest found terms are presented in Table 2. Note that years are APY (Column 1), but not the real year of the paper publication.

Based on Table 2, we can see that the analyzed scope that was found in the Investment portfolio scope is as follows: task analysis, investment, natural language processing, extraction, portfolio allocation, uncertainty diversification, stock market, algorithmic trading stock selection, security, recommender systems, classification, multi-objective optimization, portfolio, Sharpe ratio, finance, asset allocation, artificial neural network, index tracking.

The Investment portfolio *processes* are as follows: forecasting, portfolio selection, simulation, multi-criteria decision-making; data mining, identification, diversification, intensification, risk management, optimization, portfolio optimization, ranking, scheduling, and financial prediction.

The found methods and models for Portfolio Management terms are as follows: deep learning, deep reinforcement learning, search problems, LSTM, sentiment analysis, machine learning, convolutional neural network, reinforcement learning, ensemble learning, mathematical model, unsupervised learning, feature, firefly algorithm, heuristic algorithms, robustness, learning to rank, search result, quadratic programming, personalization, Monte Carlo simulation, variable neighborhood search, feature selection, time series analysis, artificial bee colony, cardinality constraints, swarm intelligence, artificial intelligence, support vector machines, metaheuristic, financial time series, differential evolution, conditional value-at-risk, clustering, iterated local search, multi-agent systems, algorithm, global optimization, value-at-risk, simulated annealing, particle swarm optimization, evolutionary algorithm, combinatorial optimization, fuzzy random variable, portfolio management, neural network, evolutionary computation, heuristic, fuzzy sets, memetic algorithms, simulation, traveling salesman problem, local search, collaborative filtering, genetic programming, ant colony optimization, genetic algorithm, stochastic programming, tabu search, Fuzzy logic.

IV. DISCUSSION

This bibliometric analysis was started to answer the main research question: *What are the predominant methodologies and models employed in investment portfolio management research?* It was decomposed into the following sub-questions: (RQ-1) How have **topics** of IPM and its related models, changed over different time periods? (RQ-2) Are certain methodologies and models more prevalent in specific **geographic regions** within the field of IPM research? (RQ-3) What are the most frequently used **methodologies and models** of IPM research? The BA on the IPM topic shows a significant increase in papers since 2015 from 1991-2023 (till August) (RQ-1). It can be explained by the development of better computer hardware, which helps to use AI and machine learning techniques and the appearance of their application in the analyzed topic.

The analysis of countries investigating IPM (RQ-2) shows that the most active and influencing ten countries are as follows: China, the United States, India, Australia, Japan, the United Kingdom France, Spain, Canada, and South Korea.

In order to answer RQ-3, the mapping with VOSviewer has been performed and the keywords map based on keyword occurrence and APY have been developed. It shows that the newly occurring keywords in the scope of IPM are as follows: cryptocurrency, deep learning, LSTM, mathematical model, convolutional neural network, and ensemble learning.

The most visible and applicable ten methods in IPM are heuristic algorithms, artificial neural networks, collaborative filtering, multi-objective optimization,

diversification, tabu search, firefly algorithm, evolutionary algorithm, personalization, and classification.

Summing up, there are a lot of methods and models for Portfolio Management Therefore, there is a need for more investigation, into which one or several are the best for Portfolio management.

V. CONCLUSIONS

The presented BA briefly reviews the current state of the methodologies and models for investment portfolio management. The methods and models for Portfolio Management are found and summarized.

From the current BA, it is obvious that effective methods and models are an important topic, which should be analyzed further in more detail. Though there are approaches to IPM, there is a need for deeper analysis in future research and better usage of methods and models for managing Investment portfolios.

VI. BIBLIOGRAPHY

[1] H. Geboers and B. Depaire, "A Rational Risk Policy? Why Path Dependence Matters.," *Entropy,* vol. 25, no. 2, 2023.

[2] C. Boido and A. Fasano, "Mean-variance investing with factor tilting," *Risk Management,* vol. 25, no. 2, 2023.

[3] H. Rezaei, H. Faaljou and G. Mansourfar, "Intelligent Asset Allocation using Predictions of Deep Frequency Decomposition," *Expert Systems with Applications,* vol. 186, 2021.

[4] F. Kyriazi, S. Tarani and D. D. Thomakos, "Median-adaptive portfolios: a minimum criteria approach to asset allocation," *Annals of Operations Research,* pp. 1-24, 2023.

[5] B. Shaju and N. Valliammal, "An Advanced Deep Learning Approach for Nickel Price Prediction Model Evading Outliers Using Enhanced Multikernel LSTM," in *International Conference on Hybrid Intelligent Systems*, Cham , 2021.

[6] N. Nazareth and Y. V. R. Reddy, "Financial applications of machine learning: A literature review," *Expert Systems with Applications,* vol. 216, 2023.

[7] Y. Ma, R. Han and W. Wang, "Portfolio optimization with return prediction using deep learning and machine learning," *Expert Systems with Applications,* vol. 165, 2021.

[8] W. Chen, H. Zhang, M. K. Mehlawat and L. Jia, "Mean-variance portfolio optimization using machine learning-based stock price prediction," *Applied Soft Computing,* vol. 100, 2021.

[9] Z. Tao and G. Gupta, "Stock Investment Strategies and Portfolio Analysis," in *Proceedings of Academia-Industry Consortium for Data Science: AICDS*, Singapore, 2022.

[10] N. Maknickienė and D. Sabaliauskas, "Investment portfolio analysis by using neural networks," in *International Scientific Conference „Contemporary Issues in Business, Management and Economics Engineering*, Vilnius, 2019.

[11] J. Y. Shyng, H. M. Shieh and G. H. Tzeng, "An integration method combining Rough Set Theory with formal concept analysis for personal investment portfolios," *Knowledge-Based Systems,* vol. 23, no. 6, 2010.

[12] T. K. Lee, J. H. Cho, J. H. Kwon and S. Y. Sohn, "Global stock market investment strategies based on financial network indicators using machine learning techniques," *Expert Systems with Applications,* vol. 117, pp. 228-242, 2019.

[13] V. V. Dombrovsky and E. A. Lashenko, "Robust control of linear systems with random parameters and multiplicative disturbances with application to the investment portfolio management," in *SICE 2003 Annual Conference*, Fukui, 2003.

[14] A. Gunjan and S. Bhattacharyya, "A brief review of portfolio optimization techniques," *Artificial Intelligence Review,* vol. 56, no. 5, 2023.

[15] I. Ruiz Roque da Silva, E. H. Junior and P. P. Balbi, "Cryptocurrencies trading algorithms: A review," *journal of Forecasting,* vol. 41, no. 8, 2022.

[16] W. A. Edmonds and T. D. Kennedy, An Applied Guide to Research Designs: Quantitative, Qualitative, and Mixed Methods, Los Angeles: Sage Publications, 2016.

[17] H. Ghanbari, M. Safari, R. Ghousi, E. Mohammadi and N. Nakharuta, "Bibliometric analysis of risk measures for portfolio optimization," *Accounting,* vol. 9, no. 2, pp. 95-108, 2023.

[18] E. N. Hasanah, S. K. Wiryono and D. P. Koesrindartoto, "Financial Robo-Advisor: Learning from Academic Literature," *urnal Minds: Manajemen Ide dan Inspirasi,* vol. 10, no. 1, pp. 17-40, 2023.

[19] T. Horvatinovic, M. Mikic and M. Dabić, "Dissecting entrepreneurial team research: a bibliometric analysis," *Review of Managerial Science,* pp. 1-39, 2023.

[20] I. Zupic and T. Čater, "Bibliometric Methods in Management and Organization," *Organizational research methods,* vol. 18, no. 3, 2015.

[21] D. Kalibatienė and J. Miliauskaitė, "A Hybrid Systematic Review Approach on Complexity Issues in Data-Driven Fuzzy Inference Systems Development," *Informatica,* vol. 32, no. 1, 2021.

[22] N. Van Eck, L. Waltman, E. Noyons and R. Buter, "Automatic term identification for bibliometric mapping," *Scientometrics,* vol. 82, no. 3, 2010.

[23] A. R. B. D. Carvalho, A. R. D. Sousa Neto, M. D. F. D. Silva, D. R. J. D. Freitas and M. E. B. Moura, "Global research trends related to coronavirus disease 2019 and the aged: a bibliometric analysis," *Sao Paulo Medical Journal,* vol. 142, no. 2, 2024.

[24] M. Aria and C. Cuccurullo, "bibliometrix: An R-tool for comprehensive science mapping analysis," *Journal of informetrics,* vol. 11, no. 4, pp. 959-975, 2017.

[25] N. Jan van Eck and L. Waltman, "https://www.vosviewer.com," 1 September 2012. [Online]. Available: https://www.vosviewer.com/documentation/Manual_VOSviewer_1.5.2.pdf.

USING BIG DATA FOR OPTIMIZING ADVERTISING CAMPAIGNS IN SOCIAL NETWORKS

A.KRASNIQI[1], B.MAKSUTAJ1 & E.JANUZAJ[1]

[1]University ''Haxhi Zeka'', Peje/Kosovo, arjan1.krasniqi@student.unhz.eu
[1]University ''Haxhi Zeka'', Peje/Kosovo, maksutajberat@gmail.com
[1]University ''Haxhi Zeka'', Peje/Kosovo, januzajerblin@gmail.com

Abstract - ***In the digital era, advertising on social networks has become a crucial element of marketing strategies. With the increasing number of users on platforms such as Facebook, Twitter, Instagram, and others, companies have unprecedented opportunities to target and engage consumers.***

This paper aims to examine the role and importance of Big Data usage in optimizing marketing campaigns on social networks. In an era where data is limitless, Big Data has become a valuable resource for businesses looking to understand consumer behavior and improve the efficiency of advertising campaigns.

In this paper, we will shed light on the history and development of Big Data, including their volumes and sources. We will explore the potential of Big Data and categorize their sources to better understand how they can be leveraged for social media marketing.

Furthermore, we will analyze the benefits and challenges of using Big Data in marketing. Additionally, we will examine cases where the use of Big Data has failed to optimize advertising campaigns on social networks and focus on the influence of Big Data in digital marketing, including personalization and sales promotion. We will also explore the technologies and methodologies used for making marketing decisions using Big Data.

This study concludes that Big Data offers exceptional potential for innovation in the field of advertising on social networks, helping companies cope with rapid changes in consumer preferences and market dynamics. The results indicate that the strategic use of Big Data can lead to a deeper understanding of consumer behavior and offer a competitive advantage in a crowded and fast-paced market.

Keywords: Big Data, advertising optimization, social networks, digital marketing.

I. INTRODUCTION

a. Context and Importance of the Study

In the era of information, Big Data has become the cornerstone of digital transformation and has fundamentally changed how businesses reach and communicate with their consumers. With the ever-increasing volume of data flowing from interactions on social networks, businesses have extraordinary opportunities to optimize their advertising strategies to reach their audience most efficiently and effectively.

The importance of studying the use of Big Data in advertising campaigns lies in the ability to understand consumer behavior, improve audience targeting and message personalization, as well as predict and measure the performance of advertising campaigns. This means that businesses can make more informed decisions, reduce unnecessary costs, and increase ROI (return on investment).

This study aims to explore in-depth the role and impact of Big Data in the field of digital advertising, especially in the context of dynamic and ever-changing social networks. It will analyze how big data can be used to create campaigns that not only attract consumers' attention but also build a stronger connection between brands and their users.

Through this analysis, the paper will help uncover best practices, challenges, and opportunities presented by the use of Big Data in the social media advertising sector, offering a clear and detailed perspective on how Big Data can be leveraged to drive innovation and efficiency in digital marketing.

b. Objectives and Objectives of the Work

This study aims to investigate and analyze the critical role that Big Data plays in optimizing advertising campaigns on

social networks. The specific goals and objectives of this work are as follows:

Main Objective:

- To deeply understand how Big Data can be used to increase the efficiency and effectiveness of advertising campaigns on social networks.

Specific Objectives:

1. **Analyze the History and Development of Big Data:**
   - Conduct a literature review to understand the historical trajectory and evolution of Big Data as a vital source of information in digital marketing.
2. **Identify the Role of Big Data in Digital Marketing:**
   - Study the impact of Big Data on understanding and modeling consumer behavior in the digital environment.
3. **Evaluate the Use of Big Data in Social Networks:**
   - Analyze specific ways in which Big Data influences the creation and optimization of advertising campaigns on various social platforms.
4. **Exploit the Five Vs of Big Data:**
   - Apply the concepts of Volume, Velocity, Variety, Veracity, and Value to illustrate how each contributes to the analysis and use of data for more effective advertising campaigns.
5. **Explain the Advantages and Challenges:**
   - Determine the competitive advantages that the use of Big Data brings, as well as identify the challenges that companies face when integrating this data into their advertising strategies.
6. **Define Methods and Technologies:**
   - Explore current technologies and methodologies used to process and analyze Big Data, to improve marketing decisions and personalize the consumer experience.

Expected Outcome:

- Provide a practical guide for marketers and business professionals on how to integrate Big Data into their advertising strategies to achieve higher customer engagement and greater ROI.

This study will contribute to existing literature by offering a detailed and updated perspective on the use of Big Data in the context of digital marketing, as well as proposing recommendations for best practices in the social media advertising industry.

II. LITERATURE REVIEW

Big data is the term that describes a collection of data so large and complex that it cannot be processed with existing database management tools or traditional data processing applications. Procedures and processes for capturing, curating, storing, searching, sharing, transferring, analyzing and visualizing are different for big data [1].

Big data represents one of the most profound and widespread developments in the digital world. Examples of Big Data come from Internet of Things (IoT) devices, as well as smart cars, but also the use of social networks, industries, and so on. Data sources are numerous and constantly growing, and, therefore, what characterizes big data is not only the volume, but also the complexity caused by the heterogeneity of the information that can be obtained [2].

The term "big data" defines large sets of data that are characterized by a wide, complex, and heterogeneous structure, causing challenges in their storage, analysis and, visualization for further use in processes or to derive concrete results [3].

Big Data refers to the massive volume of structured and unstructured data (images, social media posts, videos,) that are distributed daily in businesses. To illustrate their scale, consider this: every day, people search Google 8.5 billion times [4], send 500 million tweets (Twitter Usage Statistics, n.d.), and watch up to 1 billion hours of YouTube videos [5].

Big data is a term that describes large volumes of hard-to-manage data—both structured and unstructured—flowing into businesses every day. But it's not just the type or amount of data that's important, it's what organizations do with the data that matters. Big data can be analyzed to draw insights that improve decisions and provide certainty to make strategic business moves [6].

It can be said that big data is another technological revolution after the development of the Internet, cloud

computing, and the Internet of Things, which are attractive for social media marketing [7].

The term "Big data" is broad and includes large amounts of data, social media analytics, next-generation data management capabilities, real-time data, and much more. It also stands for advanced trends in technology that open doors to a new approach to understanding the latest trends and making intelligent decisions [8].

The term "Big Data" was coined to describe the rapid and massive growth of data, which reaches the size of zettabytes. This data can be processed through computers to discover patterns, trends, and connections, especially those related to human behavior and interactions [9].

a. History and Development of Big Data

In 2003, humanity had created 5 exabytes (10^18 bytes) of data. Today, a similar amount of information is produced in just two days. By 2012, the digital universe of data expanded to 2.72 zettabytes (10^21 bytes). It is predicted that this amount of data will double every two years, reaching a total of about 8 zettabytes by 2015 [10]. According to IBM, every day we create 2.5 exabytes of data, and interestingly, 90% of this data was generated in the last two years [11]. A personal computer typically has a capacity of about 500 gigabytes (10^9 bytes). It would take about 20 billion personal computers to store the current amount of data in the world. The process of deciphering the human genome, which once took about 10 years, can now be completed in less than a week.

Multimedia data continues to occupy a significant portion of Internet traffic, and this traffic is expected to increase by 70% by 2013. Google itself reports that it has more than one million servers in use around the world. There are approximately 6 billion mobile subscriptions globally, and 10 billion text messages are sent every day. By 2020, it is expected that 50 billion devices will be connected to the network and the Internet [12]. Introduction The Internet has experienced continuous growth and development, past and present, creating digital footprints that can be collected and processed to determine various individual schemas, useful for distinguishing the behaviors of different individuals and those of the group. This is indeed a time when a large amount of information has an extraordinary speed for distribution in networks: data equipped with these characteristics have been called "big data" [13].

History of Big Data Big data is taken to describe data that is so large, fast, or complex that it is difficult or impossible to process through traditional methods. The act of accessing and storing large amounts of information for analysis has been around for a long time. However, the concept of Big Data gained momentum in the early 2000s, when industry analyst Doug Laney summarized today's definition of Big Data as the three Vs we'll cover in the following chapters.

III. THEORY AND CONCEPTUAL BASES

a. The Importance of Big Data

Why is Big Data important? The importance of big data is not just about how much data you have. The value is in how you use it. By taking data from any source and analyzing it, you can find answers that:

1. **Rationalize resource management,**
2. **Improve operational efficiency,**
3. **Optimize product development,**
4. **Increase opportunities for income and business growth,**
5. **Allow smart decisions to be made.**

When you combine big data with high-performance analytics, you can perform business-related tasks such as:

- Determining the root causes of failures, problems, and defects in near-real time.
- Detection of anomalies faster and more accurately than the human eye.
- Improve patient outcomes by quickly converting medical image data into information.
- Recalculation of the entire risk portfolio in minutes.
- Improving the ability of deep learning models to accurately classify and react to changing variables.
- Detecting fraudulent behavior before it affects your organization (Sas, n.d.).

b. The Potential of Big Data

The McKinsey Global Institute has identified the potential of Big Data in five key areas [14]:

1. **Healthcare**: In this sector, Big Data can contribute to the advancement of clinical decision-making systems and provide personalized analyses for each patient based on their health profile. This leads to more personalized medicine, performance-based pricing of healthcare personnel, advanced analysis of disease patterns, and overall, improved public health.
2. **Public sector:** The use of Big Data can help create more transparency through linked data. This can be used to discover the needs of citizens, improve the performance of public services, provide personalized actions for different services and

products, help decision-making through automatic systems that reduce risks, and bring innovation to the creation of products and services.

3. **Retail**: Analyzing consumer behavior in stores can help optimize distribution and logistics and develop online marketplaces.
4. **Manufacturing**: Big data can impact improved demand forecasting, effective supply chain planning, supporting sales processes, and advancing manufacturing operations, including applications that are based on online research.
5. **Personal location data**: This data can be used to create more intelligent journeys, for advertising that targets consumers based on their geographic location, for more efficient responses to emergencies, for urban planning, and to develop models of business cloud.

Through these applications, big data can bring fundamental transformations and help develop new strategies in a wide range of sectors.

c. Volumes of Big Data

The history of Big Data is taken to describe data that is so large, fast, or so complex that it is difficult or impossible to process through traditional methods. The act of accessing and storing large amounts of information for analysis has been around for a long time. But the concept of Big Data gained momentum in the early 2000s when industry analyst Doug Laney summarized today's definition of Big Data as the three Vs (Sas, n.d.):

Using the 3Vs model is a common way to describe the main characteristics of "big data". "Big data" refers to the large amount of information that is influenced by three main factors: High Volume, Velocity, and Variety (De Mauro, 2015). These 3Vs can be further explained as follows:

Volume - refers to the tremendous amount of data, but also to the fact that more than 90% of the world's data has been created in recent years. Issues related to this feature concern the efficient acquisition, storage, and control of information of all kinds that, in contrast, must be organized, verified, and analyzed (Laney, 2001).

Organizations collect data from a variety of sources, including transactions, smart devices (IoT), industrial devices, video, images, audio, social media, and more. In the past, storing all this data would have been very expensive, but cheaper storage through data lakes, Hadoop, and the cloud has eased the burden (Sas, n.d.). Data is widely available, typically in quantities ranging from terabytes to petabytes [14].

Velocity - understood as the uninterrupted speed with which data is propagated in networks, and the speed required for real-time data analysis. This is a key feature of Big Data and marks a difference between them and a simple set of Big Data [8].

As Internet coverage increases, data flows into businesses at an unprecedented speed and must be handled promptly. RFID tags, sensors, and smart meters push the need to cope with these data flows in the short term (Sas, n.d.). Big data is characterized by real-time availability and a very fast growth rate [9].

(Sas, n.d.)

Variety - Data comes in all kinds of formats - from structured, numeric data in traditional databases to unstructured text documents, email, video, audio, data stock market, and financial transactions. Big data collects and processes text, images, audio, and video. Furthermore, it overcomes data gaps by combining them through data fusion techniques [12].

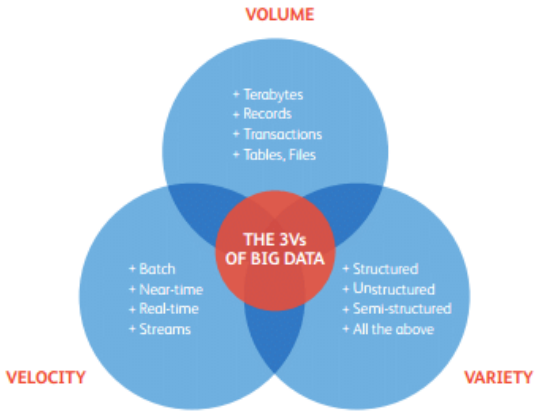

Figure 1: The "3Vs" of Big Data

SAS[1] considers two additional dimensions when it comes to big data:

Variability - In addition to increasing the speed and variety of data, data flows are unpredictable - they change often

[1] SAS is an information technology company originating in the United States of America. SAS is an abbreviation that comes from "Statistical Analysis System", and the company specializes in developing and providing software products and services for data analysis, business intelligence, big data analysis (big data), and risk analysis, among others.

and change a lot. It's challenging, but businesses need to know when something is trending on social media, and how to manage daily, seasonal, and event-driven data loads.

Veracity - Veracity is related to the quality of the data. Because data comes from many different sources, it is difficult to connect, adapt, clean, and transform data across systems. Businesses need to connect and correlate multiple relationships, hierarchies, and data connections. Otherwise, their data can quickly get out of hand [15]

d. Sources of Big Data

The volume of data today has significantly exceeded terabytes and petabytes. This large amount of information has made traditional methods of data storage and analysis inadequate, leaving these techniques behind in terms of efficient management of large amounts of information [16]. This data originates from various sources: sensors that capture information, posts, and comments on social networks, multimedia content, online transactions, and mobile network usage, just to name a few. Every mouse click, keyboard keystroke, or smartphone screen tap contributes to the collection of massive data - otherwise known as 'big data'. Therefore, in the digital world, consumers, service providers, and various organizations are producing and consuming large amounts of information [15].

Big Data sources can be broadly classified into three main categories:

1. **Data Streams**: This includes data activity that is generated or processed by devices such as computers and mobile phones, such as log files, data from sensors, location tracking systems, and data that is produced from processors, etc.

2. **Social Networks (Social Network):** This category contains information shared and used by people on different platforms, such as Google+, Facebook, YouTube, Twitter, LinkedIn, blogs, WhatsApp, Instagram, Pinterest, and others.

3. **Public Domains:** Includes data that is publicly available on the Internet, such as government portals, Wikipedia, World Bank, SEC/Edgar, Microsoft Azure MarketPlace/DataMarket, etc.

Among these, social networks have become one of the main means of addiction and communication in the daily lives of people around the world. They produce a large amount of unclassified data that reflects the everyday emotions of users, which are authentic and produced in real-time. Data flowing from social networks is a natural resource and comes in various forms and types, but unlike any other source, it is constantly growing. This continuous growth makes data extraction, processing, and analysis challenging, as it is variable and unclassified. Furthermore, data that is not cleaned cannot be used effectively [14].

Social Media as a Source of Big Data

Social media produces a significant amount of data, including likes, shares, comments, and more, which reflect consumer behavior and the effectiveness of marketing initiatives. However, the management of these Big Data presents challenges due to the size and rapid pace of their production, making it difficult to use traditional database management systems.

To cope with this data flow, advanced analysis is needed that is enabled by dedicated software and technologies such as Hadoop and NoSQL databases, which enable fast and efficient processing of large volumes of information [13].

e. Categorization of Big Data Sources

Big data originates from a wide range of sources and can typically be categorized into three types:

1. **Structured;**
2. **Semi-structured and**
3. **Unstructured.**

Structured data is organized into specific databases, making it easy to catalog and analyze. On the other hand, unstructured data is less organized and, as a result, more difficult to analyze. Meanwhile, semi-structured data does not fit completely within the boundaries of fixed fields but contains labels that help identify different segments of information [15].

IV. THE ROLE OF BIG DATA IN THE UNDERSTANDING OF CONSUMER BEHAVIOR AND THE OPTIMIZATION OF ADVERTISING CAMPAIGNS

a. The benefits of Big Data in marketing

The benefits of embracing Big Data in marketing are many, giving companies a competitive edge in the changing market landscape. Here are some key advantages:

1. **A single view of the customer:** Big data empowers marketers to consolidate customer data from disparate sources such as CRM and customer databases, logs of online interactions, data sets of their purchases, etc. This means you create a 360-degree overview of individual preferences [8] purchase history, and engagement patterns. And when you know the customer that well, you can tailor your marketing efforts to hit the right notes.
2. **Better Targeted Marketing:** Big data analysis helps organizations better understand consumer behaviors and preferences. By analyzing purchasing trends, reactions to previous marketing campaigns, and social media usage, companies can create personalized campaigns that better resonate with their audience. This means that marketing messages are more attractive and targeted to individuals who are more likely to respond, making marketing more efficient and costs lower.

3. **Identifying New Sales and Market Opportunities:** Using massive data analysis, companies can discover new opportunities in markets that may not be evident at a cursory glance. This may include discovering new consumer trends, developing new products, entering new geographic markets, or building new strategic partnerships. By being able to identify and exploit these opportunities, companies can expand their portfolio and grow efficiently.

4. **Development of new products:** Big data provides a wealth of information about the needs and pain points of customers, and helps in the development of innovative products and services that satisfy exactly the demands of the market [13].

The production, processing, and application of Big Data offer media marketing new opportunities, including precision marketing models and others. And in the future, it is necessary to build advanced and accurate social media marketing platforms with big data. So in the future, social media marketing in the context of Big Data should further develop the ability to collect and complete data, improve the applicability of data, and ensure the prerequisites of media marketing [16].

b. Big Data challenges in marketing

Although a considerable number of people consider massive data as an opportunity, both now and for the future, some others see it as a challenge due to the difficulties in managing it [17]. Using Big Data analytics to achieve marketing success also presents several challenges:

1. **Data integration:**
Consolidating data from different sources into a consistent and usable format can be complex and time-consuming. Each data source resides in a different location and needs extensive cleaning before it can be used.

2. **Data governance:**
Ensuring data security, privacy, and regulatory compliance is very important in the era of Big Data. However, this also places a heavy burden on marketing teams.

3. **Data quality and accuracy:** The reliability of the records depends heavily on the quality and accuracy of the data collected. Without testing the data pipelines that generate marketing messages, there is a risk of spending the marketing budget on insufficient communication strategies.

4. **Lack of qualified personnel:** Demand for data-savvy marketers often outstrips supply, making it difficult to find qualified personnel to handle big data. Alternatively, marketing teams rely on the IT or data department for their work. This often creates friction and delays in marketing activities.

5. **Real-time analysis and action:** Timely data analysis is important to take advantage of emerging opportunities, which requires strong capacities for real-time data collection and analysis [15].

6. **Migration from traditional data to Big Data:**
When legacy analytics systems are replaced, organizations may face problems such as the inability to manage large volumes of data, insufficient support for the analytical models that are needed, slow data loading, as well as requirements for a state-of-the-art analytics platform that the IT department may not be able to complement.

When implementing big data analytics, some of the potential challenges include incompetent or irresponsible personnel, high costs, lack of ongoing support from the business, difficulties in designing and implementing analytical systems, and the lack of software -updated for databases [5].

Based on the survey conducted by the Intel IT Center for Big Data Analytics, the challenges facing Big Data management are numerous. They include the exponential growth of data volume, the need for appropriate data infrastructures, governance and regulatory policies affecting data management, their integration, the need to process data at high speed, managing the diversity of data, the

implementation of various legislations related to data, as well as the challenge of their effective visualization.

In addition, the Intel IT Center identifies various barriers related to big data, including security concerns, high capital, and operational costs, network bottlenecks due to increased data traffic, shortage of data professionals specialized in data science, difficulties in managing data velocity, challenges in making copies of data, inefficiencies in data compression, high latency in networks and limited power of computer processors [6].

c. Cases where the use of Big Data has failed to optimize social media advertising campaigns?

There are several cases where the use of Big Data has failed to optimize social media advertising campaigns. Some of these cases are:

1. **Lack of accurate data:** If the data used for the analysis of advertising campaigns is not accurate, then there may be a failure in the optimization of the campaigns.

2. **Lack of technical knowledge:** To use Big Data most effectively, employees must have technical knowledge and the ability to adapt to new technologies.

3. **Lack of proper strategy:** To use Big Data most effectively, it is necessary to have a clear and defined strategy for your campaign.

4. **Lack of reliable sources:** Another reason why Big Data can fail to optimize campaigns is the lack of reliable and valid sources.

5. **Lack of ability to adapt to changes:** To use Big Data most effectively, employees must have the ability to adapt to changes and adapt to new technologies.

d. The Influence of Big Data on Digital Marketing

With Big Data, businesses can get the information they need to understand their target audience, big data has become an indisputable part of any digital marketing strategy.

Big data can help organize data, market segmentation, and create customer personas based on characteristics such as behavior, purchasing patterns, hobbies, geographic location, etc. Also, they help improve the user experience.

As a result, they eliminate all doubts and are thus an effective marketing method.

Big Data helps digital marketing in the following ways:

1. Information on Customers

2. Data translation has become a critical component of implementing marketing strategies in today's digital age.

3. Big data helps extract real-time consumer insights. Therefore, marketers can understand the tastes and preferences of their target audience.

When businesses communicate with consumers through social media, they can understand what consumers expect from them. Therefore, you can structure your digital marketing campaign to stand out from your competitors.

Personalization

In today's competitive business landscape, businesses cannot avoid personalization. Big data can help businesses personalize their digital marketing campaigns. With insights into consumer behaviors, businesses can understand tastes and preferences, so they can structure their digital marketing campaigns in a targeted and personalized way.

Digital marketing is all about delivering the right message at the right time. Targeted emails and ads can help personalize digital marketing campaigns.

With targeted emails, businesses can create a stronger connection with their customers. Email marketing can help marketers create more personalized and efficient campaigns by delivering the right message. business

Businesses can target these emails through browsing history, behaviors, purchase history, etc.

Big data can help businesses create more efficient targeted advertising. Marketers may use third-party sources to display advertisements to users. As a result, businesses can increase brand awareness, revenue, and brand loyalty.

Boost Sales

With big data, businesses can predict the demand for a product or service. Information about user behavior can help businesses answer many types of questions, such as what types of products consumers buy, how often they buy

or request a product or service, and what payment methods they prefer to use.

Not every visitor to your website will make a purchase. Therefore, if businesses have answers to these questions, they can create a seamless user experience and identify and target user pain points [7].

e. Companies that trust Big Data for the Optimization of Advertising Campaigns in Social Networks

The use of big data by companies to optimize advertising campaigns in social networks is a common and efficient strategy. Here are some examples of different companies using big data in this way:

1. **Amazon**: Amazon uses big data to improve the customer experience in two main ways: with dynamic pricing and product recommendations. Their prices change up to 2.5 million times a day based on various patterns such as buying behavior, competitor prices, and whether the product is mainstream or not. This strategy contributes to 35% of Amazon's annual sales [8].
2. **Netflix:** As the largest online platform for streaming movies and series, Netflix uses big data to create personalized experiences for its users. They collect data such as how long subscribers watch a program, whether they watch it continuously or not, and whether they pause and resume later. This data is used to create personalized accounts for each customer and to create original movies and series that respond to their preferences [9].
3. **Apple**: Uses big data to learn how people use apps in real life and change future designs in line with customer preferences. Apple also uses big data to track the health and improve the lifestyle of its users [10].
4. **Google**: Uses big data to understand what its users want based on various parameters such as search history, locations, trends, and many more. Google uses this data to optimize search results and provide more personalized experiences [11].
5. **eBay:** eBay uses technologies such as Apache Spark, Storm, and Kafka to analyze and act on incoming data in real-time (streamed data). This allows the company's data analysts to search for information tags that are associated with the data (metadata) and make the data consumable for as many people as possible with the right level of security and permissions [12].
6. **Facebook:** uses big data to create short videos containing memories from users' old photos and uses image recognition technology to assess details in photos or videos [13].

f. Technologies and Methodologies for Using Big Social Data for Marketing Decisions

In the intersection of Big Data and social media, we see the use of Big Data technologies by social networks in the design and development of their information technology infrastructure. The classical paradigms of programming and storage cannot be used to handle the large amount of data coming from social media and social networks.

For this reason, Google has defined and patented the **MapReduce** distributed programming model [14].

- **MapReduce** is based on three elements: the mapper function, the combiner function and, the reducer function. To finish efficiently, the input data is converted into key values, which are grouped and joined together based on their similarities. In the end, they reduce to a small set of output values [16]. The MapReduce paradigm can be implemented in several different programming languages, and Apache Hadoop [11] can be considered one of the most important projects in this field.

- **Hadoop** provides storage capabilities, such as the Hadoop Distributed File System (HDFS), which shares copies of data across many different computers and provides parallel processing capabilities, based on the MapReduce paradigm.

- **Apache Spark1 -** To overcome some of Hadoop's shortcomings, one possible solution is to use the Apache Spark1 framework, especially when you are involved in iterative work.
- **Spark** is a framework for parallel computing and allows the use of data across multiple parallel operations. Compared to Hadoop, it offers many times faster performance for some specific applications, thus allowing efficient data processing [10]. However, Spark cannot be used as a standalone system but requires a distribution manager of its class and a third-party distributed storage system, such as HDFS. Distributed data can be easily handled by other systems such as

MongoDB 2, HyperDex3, DocumentDB4, etc., which are document-based systems and store data in a similar way to the JSON format.

- **NoSQL** - Similarly, NoSQL databases, which use the key-value model to perform fast queries in a distributed environment, can be successfully used for managing social Big Data. In this context, graph-based databases, which are capable of describing social relationships between users, can play an important role. This category includes Neo4J, Virtuoso, Stardog, and others.
- **NoSQL** databases - NoSQL includes a wide range of different database technologies that have been developed to design modern applications. It describes a database called non-SQL or non-relational that provides a method to accumulate and retrieve data. They are used in real-time web applications and Big Data analytics.
  It stores unstructured data provides faster performance, and offers flexibility when dealing with different types of data on a large scale. Examples included are MongoDB, Redis, and Cassandra [6].

If the extraction needs to take at least a few hours, then technologies like Hadoop, Spark, and NoSQL databases are certainly suitable for extracting useful information from big social data. But if you are working with data streams that are produced quickly, change quickly, and require real-time analysis, other technologies such as Apache Storm and Apache Samza may be more suitable.

- **Apache Storm** is a distributed real-time computing system that is very useful for the rapid analysis of large data streams. This system is based on a master-slave structure and includes a complex event processor and a distributed computing framework.

- **Apache Samza** is another framework that handles leak messages as they come in, one at a time. Streams are divided different chunks, which are a regular series of read-only messages.

However, the above technologies should be used together to combine automatic machine learning, natural language processing, network analysis, and statistics to extract interesting insights from big social data, known as social media analysis.

V. CONCLUSIONS AND RECOMMENDATIONS

This study has deeply explored the role and impact of Big Data in optimizing social media advertising campaigns. From our research, it is clear that Big Data offers tremendous opportunities for innovation in the field of digital marketing, allowing companies to adapt their advertising campaigns to the changing needs and preferences of consumers.

We have identified several key advantages of Big Data in marketing, including the creation of a comprehensive view of the customer, focused and personalized marketing, and the discovery of new market and sales opportunities. These advantages provide a solid foundation for companies to increase the efficiency and effectiveness of their advertising campaigns.

However, the study also pointed out the challenges associated with the use of Big Data, which include data integration, security and privacy, data quality and accuracy, and the need for qualified personnel. These challenges should be carefully considered by companies that intend to use Big Data in their marketing strategies.

In conclusion, Big Data has the potential to fundamentally change the way companies run and optimize social media advertising campaigns. Based on the findings of this study, we recommend that companies continue to invest in big data technologies and develop clear strategies to manage and use this data most effectively. To be competitive in a rapidly changing digital marketplace, marketplace, companies must adopt a data-driven approach and focus on building a culture that values data analysis and adapting to constant change.

Bibliography

[1] A. Vailaya. (2012, December). What's All the Buzz Around "Big Data?". *IEEE Women in Engineering Magazine, 6*(2), 24-31. doi:10.1109/MWIE.2012.2215256

[2] B. Gerhardt, K. G. (2012, June). Unlocking Value in the Fragmented World of. *Cisco Internet Business Solutions Group*.

[3] Bello-Orgaz & G., J. J. (2016). Social big data: Recent achievements and new challenges. *Information Fusion*. doi:https://doi.org/10.1016/j.inffus.2015.08.005

[4] Bello-Orgaz, G. J. (2016). Social big data: Recent achievements and new challenges. *Information Fusion*, 45-59. doi:https://doi.org/10.1016/j.inffus.2015.08.005

[5] C. Eaton, D. D. (2012). *Understanding Big Data: Analytics for Enterprise Class Hadoop and Streaming Data.* Gjetur në https://dl.acm.org/citation.cfm?id=2132803

[6] Center, I. I. (2012). *Peer Research: Big Data Analytics.* IT. Intel IT Center. Gjetur në

https://www.intel.com/content/dam/www/public/us/en/documents/reports/data-insights-peer-research-report.pdf

[7] COOK, S. (2023, 06 2023). *30+ YouTube Statistics and Facts [Currentyear]*. Gjetur në comparitech: https://www.comparitech.com/tv-streaming/youtube-statistics/#:~:text=YouTube%20users%20view%20a%20whopping,and%2013%20minutes%20in%202019).

[8] Da Fonseca, N. L. (2015). *Cloud services, networking, and management.* Wiley-IEEE Press eBooks.

[9] DataFlair. (2023, 05 15). *5 Big Data Case Studies – How big companies use Big Data*. Gjetur në DataFlair: https://data-flair.training/blogs/big-data-case-studies/

[10] De Mauro, A. G. (2015). What is big data? A consensual definition and a review of key research topics. *Nucleation and Atmospheric Aerosols.* doi:https://doi.org/10.1063/1.4907823

[11] Dean, J. M. (2018). MapReduce: Simplified data processing on large cluster. *International Journal of Research and Engineering, 5*. doi:https://doi.org/10.21276/ijre.2018.5.5.4

[12] Ducange, P. P. (2017). A glimpse on big data analytics in the framework of marketing strategies. *Soft Computing*, 325-342. doi:https://doi.org/10.1007/s00500-017-2536-4

[13] Erevelles, S. F. (2016). ig Data consumer analytics and the transformation of marketing. *Journal of Business Research*, 897-904. doi:https://doi.org/10.1016/j.jbusres.2015.07.001

[14] Fabio Arena, G. P. (2020). An overview of big data analysis. *Bulletin of Electrical Engineering and Informatics, 4*. doi:https://doi.org/10.11591/eei.v9i4.2359

[15] Hilbert, M. (2015). Big Data for Development: A review of promises and challenges. *evelopment Policy Review, 1*. doi:https://doi.org/10.1111/dpr.12142

[16] Kebola. (2023, 08 22). *Big Data In Marketing: 9 Examples & Use Cases*. Gjetur në Keboola: https://www.keboola.com/blog/big-data-in-marketing-examples

[17] Keboola. (2022, 04 28). *The Secrets Behind Personalization: The Customer 360 view*. Gjetur në Kebola: https://www.keboola.com/blog/the-secrets-behind-personalization-the-customer-360-view

[18] Kumari, R. (2021, March 10). *AnalyticStep*. Gjetur në 10 Companies that Uses Big Data: https://www.analyticssteps.com/blogs/companies-uses-big-data

Range-Angle Beam Pattern Synthesis with Logarithmically Increasing Concentric Circular Frequency Diverse Array

Uğur YEŞİLYURT[1]

[1] Electrical Electronics Engineering, Faculty of Engineering, Erzurum Technical University, Erzurum/Turkey, ugur.yesilyurt@erzurum.edu.tr

Abstract **- A phased array antenna with the same carrier frequency for all elements provides only an angle-dependent beam pattern. Unlike a phased array antenna, which employs phase shifters, a frequency diversity array (FDA) is capable of creating a unique beam pattern that depends on both angle and range by adjusting a small frequency shift between array elements. Conventional linear FDA produces an S-shaped beam pattern that depends on range and angle. In order to decouple the beam pattern depending on the range and angle, which is the disadvantage of the FDA, many studies have been carried out in the literature on how the frequency increase of the FDA affects the beam pattern. In this study, the logarithmically increasing concentric circular frequency diverse array (CCFDA) is proposed to obtain a well-focused dot-shaped beam pattern. A non-linear logarithmic frequency increase is applied to eliminate the range periodicity in the FDA beam pattern. In addition, thanks to the circular symmetry feature of the proposed CCFDA structure, a smooth dot-shaped beam pattern is created. Since the proposed logarithmically increasing CCFDA structure also scans in the azimuthal plane, it provides a more accurate dot-shaped beam pattern compared to the linear FDA structure limited to two-dimensional space. By examining both the array geometry and the frequency increase, it has been confirmed with numerical results that a range-independent dot-shaped radiation pattern can be obtained with the proposed logarithmically increasing CCFDA structure.**

Keywords **- Phased array antenna, Frequency diverse array, Concentric circular array.**

I. INTRODUCTION

THE array antennas are quite popular due to their flexibility to direct beams in different directions [1]. Traditional phased array antennas, in which only the directions of the beam pattern can be adjusted, are inadequate in terms of the range properties of the beam pattern. Frequency Diverse Array (FDA) as a promising new array structure was first introduced in 2006 by Antonik et al [2]. FDAs have attracted increasing attention in recent years due to the synthesis of range-dependent beam patterns. Compared to a phased array, the FDA uses different carrier frequencies between array elements that have a small frequency offset relative to the operating frequency. Also, unlike phased arrays, the FDA creates the transmission beam pattern as a function of angle, range, and time [3-6]. Standard FDA generally results in an S-shaped beam pattern depending on range and angle. The range- and angle-dependent beam pattern precludes the FDA's employees in more advanced engineering applications. For this reason, the periodicity of the FDA's beam pattern in terms of angle, range, and time has been examined, and investigations have also been carried out on different frequency offsets [7-10] and array configurations [11-14].

An FDA with logarithmic frequency offsets (Log-FDA) between elements is also proposed to separate the range and angle in the FDA. With the non-linear frequency increase, the dependence of the beam pattern on range and angle decreases slightly and the maximum point is reached [15]. To further improve the focusing performance, the FDA structure using non-uniform logarithmic frequency increments is proposed in [16]. It provides a more advanced range-angle localization thanks to the reduced side lobe values obtained in the beam pattern with nonuniform log-FDA. Symmetric logarithmically increasing frequency offsets (SLFOs) are proposed in [17] to obtain a symmetrical beam pattern with only a single maximum value in the range-angle domain. In another study [18], a random logarithmic frequency increase is applied to the FDA elements in order to create a dot-shaped beam with more intense energy and lower sidelobe energy. In the studies carried out so far, an attempt has been made to obtain a beam pattern with a maximum at a single point with various frequency offsets on the linear FDA array. Unlike the above studies where frequency offsets are evaluated, in [19], the array geometry is changed to provide a smooth dot-shaped beam pattern. Since the beam pattern obtained in linear array geometry depends on only one angle, true 3D dot-shaped beam formation does not occur. It provides a distinctive scanning pattern in azimuth angle with frequency diversity increasing outwards in its concentric circular structure [20-22]. However, the linear frequency increase applied between the rings causes a maximum to occur at multiple points instead of a single point in the beam pattern.

This study proposes a logarithmically increasing concentric circular frequency diverse array (CCFDA) structure, where both the frequency shift and the array geometry are nonlinear. In the proposed logarithmically increasing CCFDA structure, a more uniform dot-shaped beam pattern is obtained depending on the azimuth angle with the help of concentric circular arrays. The dot-shaped beam pattern formed at more than one point can be realized at a single point with the non-linear frequency

offsets increasing outward between the rings. Moreover, by increasing the logarithmic frequency both between the elements within the ring and between the rings, a uniform dot-shaped beam pattern is obtained at only a single point.

II. Theoretical Analysis and Formulation

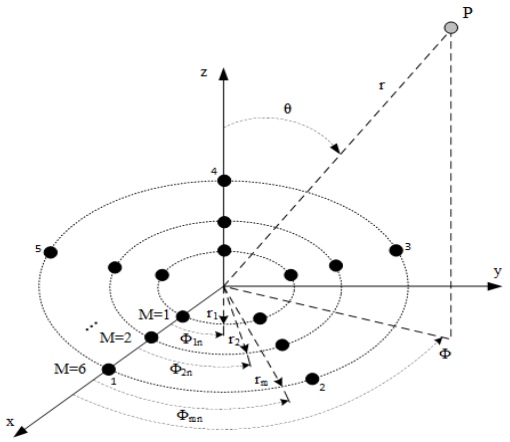

Figure 1: The geometric structure of a concentric circular array in the free space. There are an equal number of antennas per ring. (N=5, M=6)

The general geometric structure of a concentric circular array (CCA) with M rings, which has an equal number of elements in each ring, is shown in Figure 1. N identical elements are evenly spaced in each ring of this CCA structure. Unlike conventional phased array antenna, a different frequency increment is applied to the array elements in each ring of a concentric circular frequency diverse array (CCFDA). Therefore, the carrier frequency of the array elements in the *mth* ring of the CCFDA denotes:

$$f_m = f_0 + \Delta f_m \tag{1}$$

where f_0 represents the carrier frequency of the reference ring (i.e. the first ring) of the CCFDA. Δf_m represents the frequency increase or decrease across array elements with different rings according to the carrying frequency. The frequency offset Δf_m satisfies $f_0 \gg \max\{\Delta f_m\}$. Thus, while array elements of the same ring radiate the same frequency, frequency diversity is applied to array elements in different rings. In addition, the range of the *nth* element in the *mth* ring of the CCFDA to the far-field point target is denoted by R_{mn} and can be approximately expressed as:

$$R_{mn} \cong r - \hat{a}_r.\left(r_m \cos\varphi_{mn}\,\hat{a}_x + r_m \sin\varphi_{mn}\,\hat{a}_y\right) \cong r - r_m \sin\theta\cos(\varphi - \varphi_{mn}) \tag{2}$$

for phase term, and $R_{mn} \cong r$ for amplitude term. r_m indicates the radius of the *mth* ring. θ is the elevation angle of the observation point, φ is the azimuth angle of the observation point, and φ_{mn} is the azimuth angle of the *nth* element of the *mth* ring in the CCFDA system referenced to the x-axis. Since the number of elements in each ring is equal, it can be simplified as $\varphi_{mn} = \varphi_n = \frac{2\pi n}{N}, n = 1,2,3,\dots,N$ The measured electric field expression of CCFDA at the far-field observation point can be expressed as follows:

$$E_{CCFDA}(r,\theta,\varphi,t) = \sum_{m=1}^{M}\sum_{n=1}^{N}\frac{e^{j2\pi f_m\left(t-\frac{R_{mn}}{c}\right)}}{R_{mn}}. \tag{3}$$

By substituting (1) and (2) in (3), the electric field expression can be rewritten as:

$$E_{CCFDA}(r,\theta,\varphi,t) \cong \sum_{m=1}^{M}\sum_{n=1}^{N}\frac{1}{r}\,e^{j2\pi(f_0+\Delta f_m)\left(t-\frac{r-r_m\sin\theta\cos(\varphi-\varphi_{mn})}{c}\right)}. \tag{4}$$

Due to the $f_0 \gg \max\{\Delta f_m\}$ inequality in the FDA the term $2\pi\ \Delta f_m r_m \sin\theta\cos(\varphi-\varphi_{mn})$ can be neglected in the electric field expression, and the new electric field expression can be expressed as:

$$E_{CCFDA}(r,\theta,\varphi,t) \cong \frac{1}{r}\,e^{j2\pi f_0\left(t-\frac{r}{c}\right)} \sum_{m=1}^{M} e^{j2\pi\ \Delta f_m\left(t-\frac{r}{c}\right)}\sum_{n=1}^{N} e^{j\frac{2\pi f_0}{c}r_m\sin\theta\cos(\varphi-\varphi_{mn})} \tag{5}$$

As can be seen from equation (5), the beam pattern obtained with CHCFDA depends on the observation time (t), elevation angle (θ), as well as azimuth angle (φ), which is the distinguishing feature of CCA from the linear array. The beam pattern also depends on the frequency offset (Δf_m) and the target range (r_0). For the CCFDA structure with linear frequency increase between rings, the radiation frequency of the array elements in the *mth* ring can be expressed as follows:

$$f_m = (m-1)\Delta f, \quad m = 1,2,\dots,M. \tag{6}$$

where Δf is a fixed frequency configuration parameter. In order to obtain a more uniform point-shaped beam pattern with the proposed CCFDA structure, a logarithmic frequency increase is applied between the rings and the radiation frequency of the array element in the *mth* ring can be expressed as follows:

$$f_m = log(m+1)\Delta f, \quad m = 1,2,\dots,M. \tag{7}$$

Although a uniform dot-shaped beam pattern is obtained with the CCFDA structure, which has a logarithmic frequency increase between rings, there are maximum points that cannot be neglected when viewed over a wide range. In order to obtain a radiation pattern in which these maximum points are more suppressed, a logarithmic frequency increase is proposed both between the rings and between the array elements in the ring. Therefore, the carrier frequency of the *nth* element of the *mth* ring of the CCA, where a logarithmic frequency increase is applied both between the rings and between the array elements in the ring, can be expressed as follows:

$$f_{mn} = f_0 + \Delta f_{mn}, \quad m = 1,2,\dots,M, \quad n = 1,2,\dots,N. \tag{8}$$

where Δf_{mn} represents the frequency increase or decrease across the *nth* array element of the *mth* ring according to the carrying frequency. When the frequency offset in equation (8) is replaced in the electric field expression, the new electric field expression of CCFDA, where all elements have different frequencies, can be written as follows:

$$E_{CCFDA(r,\theta,\varphi,t)} \cong \frac{1}{r}\, e^{j2\pi f_0\left(t-\frac{r}{c}\right)} \sum_{m=1}^{M}\sum_{n=1}^{N} e^{j2\pi\ \Delta f_{mn}\left(t-\frac{r}{c}\right)} e^{j\frac{2\pi f_0}{c} r_m \sin\theta\cos(\varphi-\varphi_{mn})} \quad (9)$$

III. Simulation Results and Discussion

In this section, the beam pattern obtained with the proposed CCFDA is simulated and the results are presented comparatively. The proposed CCA structure consists of 30 antennas in total, with 6 concentric arrays and 5 elements in each array (M=6 and N=5). The rings of CCA have a distance of $\lambda/2$ and since the radius of the first ring is λ, the radius of the last ring is $7\lambda/2$. Among the array parameters, the carrier frequency f_0 is set to 10 GHz, and the frequency offset Δf is set to 100 kHz. Firstly, the normalized beam pattern of CCFDA is obtained by applying linear frequency increase in equation (6) between the rings. Keeping the independent variables $\varphi = 90^{\circ}$ constant, the beam pattern at the desired time $t = t_0$ and the target location $r_0 = 4km$ is shown in Figure 2.

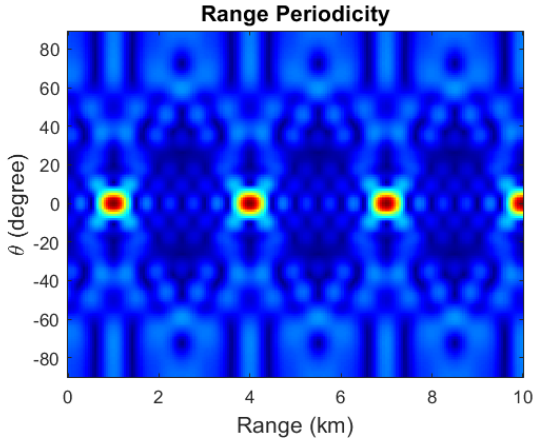

Figure 2: The beam pattern of CCFDA with linear frequency increase between rings, the total observation region is $0km \le R \le 10km$, and $-90^{\circ} \le \theta \le 90^{\circ}$.

Due to the distinctive feature of the FDA, the beam pattern of the proposed CCFDA is periodic in the range $r = \frac{c}{\Delta f} = 3km$. For this reason, maximum points occur outside the target point. As seen in Figure 2, apart from the target location of 4km, maximum points occur at 1km, 7km, and 10km, and increasing distances with range periodicity.

In order to suppress these maximum points occurring outside the target point, logarithmic frequency offsets in equation (7) are applied between the rings in CCA. In the logarithmically increasing CCFDA, the antenna elements in the first ring have the frequency offset $\Delta f_1 = \log(2)\Delta f$ and the antenna elements in the last ring have the frequency offset $\Delta f_6 = \log(7)\Delta f$. Therefore, since the frequency difference between the rings of CCFDA is not linear, the resulting beam pattern will not be periodic. The radiation pattern of CCFDA with logarithmic inter-ring increase can be observed in Figure 3 for the same $0km \le R \le 10km$ observation region. As seen in Figure 3, a radiation pattern with only one maximum point and a wider single beam is obtained in the same range.

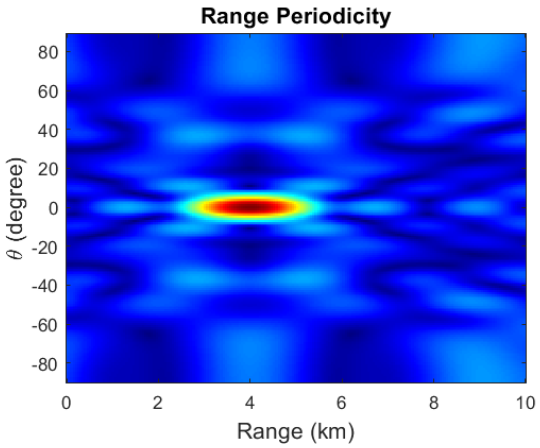

Figure 3: The beam pattern of CCFDA with logarithmic frequency increase between rings, the total observation region is $0km \le R \le 10km$, and $-90^{\circ} \le \theta \le 90^{\circ}$.

When we look from a wider range, the radiation pattern in Figure 4 is observed. Figure 4 shows that there are maximum points (interferers) at longer distances that cannot be neglected.

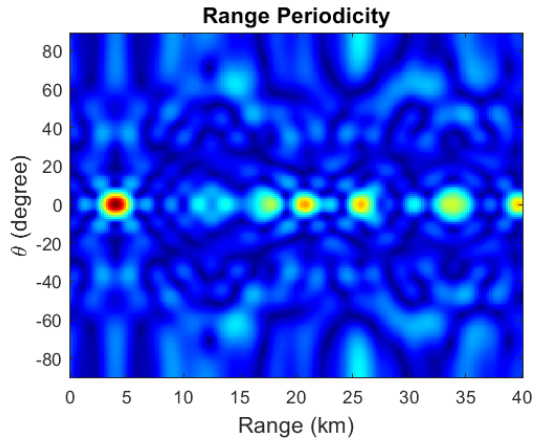

Figure 4: The beam pattern of CCFDA with logarithmic frequency increase between rings, the total observation region is $0km \le R \le 40km$, and $-90^{\circ} \le \theta \le 90^{\circ}$.

The radiation pattern obtained with the CCFDA structure, which has a logarithmic frequency increase both between the rings and between the elements of the same ring, is given in Figure 5. Compared to the radiation pattern of CCFDA, which only has a logarithmic frequency increase between rings (see Figure 3), a more uniform dot-shaped beam pattern concentrated at the target location can be seen in Figure 5.

When viewed in the $0km \le R \le 40km$ range as in Figure 6, it is observed that the undesirable interferes (maximum points) are more suppressed when compared to the radiation pattern in

Figure 4.

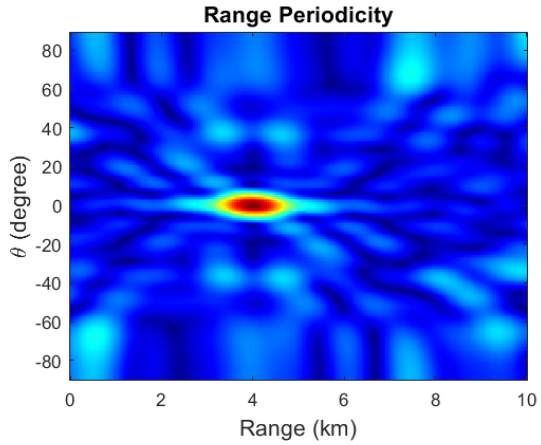

Figure 5: The beam pattern of CCFDA which has a logarithmic frequency increase both between the rings and between the elements of the same ring, the total observation region is $0km \leq R \leq 10km$, and $-90^{\circ} \leq \theta \leq 90^{\circ}$.

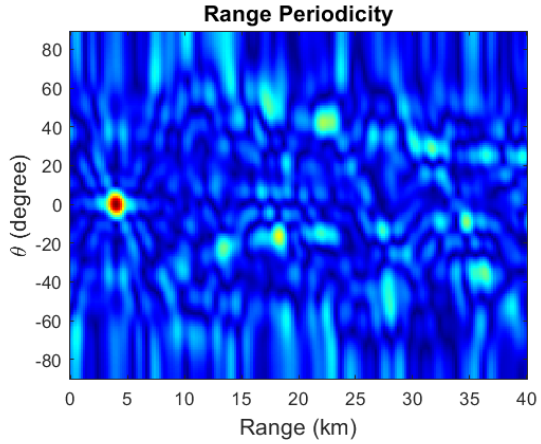

Figure 6: The beam pattern of CCFDA which has a logarithmic frequency increase both between the rings and between the elements of the same ring, The total observation region is $0km \leq R \leq 40km$, and $-90^{\circ} \leq \theta \leq 90^{\circ}$.

IV. Conclusion

In this study, a CCFDA structure with a logarithmic frequency increase is proposed to create a range-angle-dependent beam pattern. First, it is shown that a dot-shaped periodic beam pattern is formed by applying a linear frequency increase outward between the rings of the CCFDA. Then, similarly, by applying logarithmic frequency offsets between the rings of the CCFDA, the periodicity in the resulting beam pattern is eliminated and a single maximum beam pattern is obtained. However, it involves interferers of a magnitude that cannot be neglected. By applying a logarithmic frequency increase both between the rings and between the elements in the ring, in addition to a more uniform dot-shaped beam pattern, undesirable beam interferers are further suppressed. In addition, thanks to the geometric structure, the beam pattern depending on the azimuth angle is another advantage of obtaining more uniform beam patterns.

References

[1] H. L. Van Trees, "Detection, Estimation, and Modulation Theory, Optimum Array Processing," Hoboken, NJ, USA: Wiley, 2004.
[2] P. Antonik, M. C. Wicks, H. D. Griffiths, and C. J. Baker, "Frequency diverse array radars," 2006 IEEE Conference on Radar, pp. 3, Verona, NY, USA, 2006.
[3] M. Secmen, S. Demir, A. Hizal and T. Eker, "Frequency Diverse Array Antenna with Periodic Time Modulated Pattern in Range and Angle," 2007 IEEE Radar Conference, pp. 427-430, Waltham, MA, USA, 2007.
[4] W. -Q. Wang, "Frequency Diverse Array Antenna: New Opportunities," IEEE Antennas and Propagation Magazine, vol. 57, no. 2, pp. 145-152, 2015.
[5] W. -Q. Wang, "Range-Angle Dependent Transmit Beampattern Synthesis for Linear Frequency Diverse Arrays," IEEE Transactions on Antennas and Propagation, vol. 61, no. 8, pp. 4073-4081, 2013.
[6] Z. Wang, Y. Song, T. Mu, and Z. Ahmad, "A Short-Range Range-Angle Dependent Beampattern Synthesis by Frequency Diverse Array," IEEE Access, vol. 6, pp. 22664-22669, 2018.
[7] Wang, W.-Q, "Overview of frequency diverse array in radar and navigation applications," IIET Radar Sonar Navig., vol. 10, pp. 1001-1012, 2015.
[8] H. Shao, J. Dai, J. Xiong, H. Chen and W. -Q. Wang, "Dot-Shaped Range-Angle Beampattern Synthesis for Frequency Diverse Array," IEEE Antennas and Wireless Propagation Letters, vol. 15, pp. 1703-1706, 2016.
[9] Y. Liao, H. Tang, X. Chen and W. -Q. Wang, "Frequency Diverse Array Beampattern Synthesis with Taylor Windowed Frequency Offsets," Antennas and Wireless Propagation Letters, vol. 19, no. 11, pp. 1901-1905, 2020.
[10] W. -Q. Wang, H. C. So, and H. Shao, "Nonuniform Frequency Diverse Array for Range-Angle Imaging of Targets," IEEE Sensors Journal, vol. 14, no. 8, pp. 2469-2476, 2014.
[11] Y. Zhou et al., "High-Resolution and Wide-Swath SAR Imaging Mode Using Frequency Diverse Planar Array," IEEE Geoscience and Remote Sensing Letters, vol. 18, no. 2, pp. 321-325, 2021.
[12] W. T. Li, C. Cui, X. T. Ye, X. W. Shi and H. C. So, "Quasi-Time-Invariant 3-D Focusing Beampattern Synthesis for Conformal Frequency Diverse Array," IEEE Transactions on Antennas and Propagation, vol. 68, no. 4, pp. 2684-2697, 2020.
[13] W. Khan, I. M. Qureshi, A. Basit, and W. Khan, "Range-Bins-Based MIMO Frequency Diverse Array Radar with Logarithmic Frequency Offset," IEEE Antennas and Wireless Propagation Letters, vol. 15, pp. 885-888, 2016.
[14] D. M. Azzam, S. H. Zainud-Deen, H. A. Malhat and M. M. Badawy, "New Configurations of Frequency Diverse Antenna Arrays Based on Dot-Shaped Beampatterns," 2022 39th National Radio Science Conference (NRSC), Cairo, Egypt, pp. 83-91, 2022.
[15] W. Khan, I. M. Qureshi and S. Saeed, "Frequency Diverse Array Radar with Logarithmically Increasing Frequency Offset," IEEE Antennas and Wireless Propagation Letters, vol. 14, pp. 499-502, 2015.
[16] M. Mahmood and H. Mir, "Frequency Diverse Array Beamforming Using Nonuniform Logarithmic Frequency Increments," Antennas and Wireless Propagation Letters, vol. 17, no. 10, pp. 1817-1821, 2018.
[17] Y. Xu and K. -M. Luk, "Enhanced Transmit–Receive Beamforming for Frequency Diverse Array," IEEE Transactions on Antennas and Propagation, vol. 68, no. 7, pp. 5344-5352, 2020.
[18] J. Gao and X. Zhang, "Frequency Diverse Array Antennas with Random Logarithmically Increasing Frequency Offset," 2023 5th International Conference on Intelligent Control, Measurement and Signal Processing (ICMSP), Chengdu, China, pp. 143-146, 2023.
[19] A. Akkoc, E. Afacan and E. Yazgan, "Dot-Shaped 3D Range-Angle Dependent Beamforming with Discular Frequency Diverse Array," IEEE Transactions on Antennas and Propagation, vol. 69, no. 10, pp. 6500-6508, 2021.
[20] C. Wang and X. Zhu, "Three-Dimensional Parameter Estimation of Uniform Circular Frequency Diverse Array Radar with Two-Stage Estimator," IEEE Sensors Journal, vol. 21, no. 16, pp. 17775-17784, 2021.
[21] S. Rastgar Kisomi, S. H. Mohseni Armaki, A. J. Rashidi and M. Fallah, "A circular planar frequency diverse array for monostatic radar applications," Remote Sensing Letters, vol. 10, no. 9, pp. 835-843, 2019.
[22] M.A. Panduro, A. Reyna, D.H. Covarrubias, "Non-Uniform Concentric Rings Design for Ultra-Wideband Arrays," Sensors, vol. 19, no. 10, 2019.

Rule-Based Diagnostic Algorithm Based on Pathological Findings of Breast Cancer

Hilal Hazel YÖRDAN[1] and Muhammed Kürşad UÇAR[1,2]
[1]MKU Technology, Sakarya University Technopolis, Serdivan, Sakarya, Turkey, hhazelyrdn@gmail.com
[2]Electrical-Electronics Engineering,Faculty of Engineering, Sakarya University, Serdivan, Sakarya, Turkey, mucar@sakarya.edu.tr

***Abstract*—Breast cancer is the second most common type of cancer among women worldwide and is a disease that causes a high rate of death. Early diagnosis is a critical factor in reducing the mortality rate of breast cancer. Developing machine learning techniques are achieving very successful results in this field, where experts must interpret and diagnose tests. Machine learning is a branch of artificial intelligence that can quickly detect problems in complex and large data stores by learning from existing data. Therefore, machine learning is widely used, especially in breast cancer diagnosis. In this study, rule-based diagnostic algorithms were developed with the help of decision trees that can classify between benign and malignant types of breast cancer. These models can play an essential role in the early diagnosis and treatment process, with the ability to select benign and malignant cancer types. According to the results, the type of breast cancer can be detected with high accuracy, with a 91% accuracy rate and a specificity and sensitivity rate of 0.91. These results, model creation, and optimization process, together with the effective use of machine learning techniques, show the possibility of a new approach to breast cancer diagnosis.**

***Keywords*—Breast cancer, Machine Learning, Rule Based Diagnostics, Feature Selection.**

I. Introduction

Breast cancer is a type of cancer that is most common among women worldwide. It usually occurs in the lobule, duct, and connective tissue regions of the breast and is caused by the abnormal proliferation and movement of cells in these regions. It accounts for approximately 30% of all other cancers. According to the World Health Organization's 2020 data, 2 million 260 thousand people in the world were diagnosed with breast cancer, and approximately 685 thousand women died due to breast cancer that year. Early diagnosis of a fatal disease such as breast cancer is of great importance in order to increase the survival rate of patients. When the disease is detected early, cancerous cells may spread to other organs through blood and lymph vessels (metastasis) [1].

Although there is no single cause for the development of breast cancer, factors such as advances in health sciences, development of early detection methods, and social awareness play an important role. Many factors, such as reproductive age, nutritional habits, socioeconomic status, lifestyle, and environmental factors, may be influential in the development of breast cancer. Therefore, understanding and combating breast cancer requires a multidisciplinary approach [2].

The rapid development of artificial intelligence technologies brings about a significant transformation in the diagnosis of diseases. Today's computers can process beyond human speed but have yet to reach the decision-making ability that humans have. For this reason, various machine learning techniques have been developed and are still being developed so that computers can make more comprehensive analyses and decisions [3]. Machine learning is a field that includes statistical, probabilistic, and optimization techniques that make computers well-suited to learning by quickly identifying patterns in complex and large data sets and to medical applications that rely on complex proteomic and genomic measurements. Thanks to these features, machine learning is frequently used in cancer diagnosis and diagnosis [4].

II. Material and Method

The work will be modeled in Figure 1. First, the data will be obtained, then the Fisher Feature Selection algorithm will be used to increase the success rate of artificial intelligence in diagnosing the disease, and the best features will be selected. Finally, decision trees, one of the machine learning methods, will be used for Breast Cancer and the behavior of cancer cells.

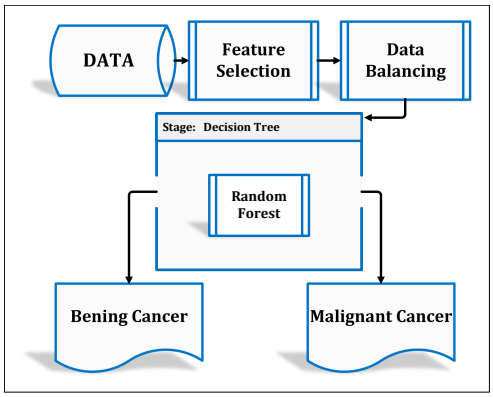

Fig. 1: Working flow diagram

A. Collection of Data

In this study, an open source dataset from UCI (University of California, Irvine) Machine Learning Repository was used [5]. At the University of Wisconsin Hospital, Dr. The dataset

collected by William H. Wolberg and shared for research consists of 569 samples containing breast cancer findings. Each sample was classified based on 30 different intrinsic features measured by the Xcyt treatment imaging technique. The number of qualifications in this study is 32. However, since the ID and tag group were not taken, 30 real-value entries were specifically processed. These features reflect the biological characteristics, morphological structures and sizes of cancer formation [5]. General data are shown in table I.

TABLE I: WDBC dataset summary

Özellik No	Feature Name	Mean	Standard deviation	Minimum	Maximum
1	*radius_mean*	1890.25	2156.96	9	9904
2	*texture_mean*	1773.85	653.16	17	3928
3	*perimeter_mean*	5531.85	3406.44	63	9958
4	*area_mean*	4241.03	2414.49	181	9989
5	*smoothness_mean*	5377.94	3913.07	1	9997
6	*compactness_mean*	3980.75	2988.91	6	9965
7	*concavity_mean*	3182.63	2539.02	0	9966
8	*concavepoints_mean*	3688.31	2807.70	0	9961
9	*symmetry_mean*	1647.01	551.01	18	2906
10	*fractal_dimension_mean*	5670.02	1881.67	6	9744
11	*radius_se*	3283.00	2123.08	1	9948
12	*texture_se*	3550.06	3190.46	12	9988
13	*perimeter_se*	2708.42	1863.86	2	9975
14	*area_se*	2960.03	2324.35	14	9904
15	*smoothness_se*	5126.59	2601.64	1	9976
16	*compactness_se*	3103.84	2378.75	12	9947
17	*concavity_se*	3184.66	2243.86	0	9959
18	*concavepoints_se*	3392.43	3065.13	0	9997
19	*symmetry_se*	1913.36	1119.54	15	9947
20	*fractal_dimension_se*	3190.11	1905.40	6	9875
21	*radius_worst*	1756.62	1528.98	14	9981
22	*texture_worst*	2330.07	951.51	18	4954
23	*perimeter_worst*	4585.73	3666.06	78	9971
24	*area_worst*	4415.37	2635.46	248	9936
25	*smoothness_worst*	1805.44	2096.25	13	9994
26	*compactness_worst*	3057.96	2246.82	1	9995
27	*concavity_worst*	3342.87	2387.59	0	9996
28	*concavepoints_worst*	3522.81	2925.74	0	9993
29	*symmetry_worst*	2580.33	1042.83	3	6638
30	*fractal_dimension_worst*	6252.12	2974.59	12	9981
31	*diagnosis*	-	-	-	-
32	*ID*	-	-	-	-

Xcyt [6] is a software initiative that bears the signature of a software project at the University of Madison in Wisconsin, USA, in the 1990s. This software project was implemented to achieve two essential stages such as breast cancer diagnosis (diagnosis) and prediction (prognosis). Within the scope of this project, the images obtained as a result of magnifying the tissue samples collected in the chest area 63 times under the microscope were used, and the specially developed edge extraction and center separation Xcyt program aimed to cut the general features of the tissue samples by analyzing them with their detailed features. After this software automatically identified a large compatible section, general data for this area was collected.

Ten of the data examined included measurements obtained directly from the nuclei of cancer cells. In these measurements, essential features of the cell, such as radius, tissue density, diameter, area, surface roughness, density, concavity, number of concave points, symmetries, and fractal dimension, are reflected. The other 20 features are numerical values that include mean, standard error, and lowest and highest values derived based on these essential features.

Data samples are associated with a class label by which cancer cells are classified as benign (B - benign) or malignant (M - malignant). This class label represents an essential resource in critical application areas such as assessing the severity of a cancer diagnosis, broad probability predictions, and providing medical decision support.

B. Fisher Feature Selection Algorithm

Fisher score is a statistical measure and plays a vital role in measuring the distinction between classes and the difference in features. Moreover, it is frequently used in data mining, feature selection, and classification problems. Fisher score considers the significant mean difference and low deviation value of features between two different classes. Therefore, features with a high score are considered to be the features that best distinguish the classes [7]. This method helps us determine how well classification predictions fit the dataset by measuring the agreement between actual and predicted values. The calculation formula of Fisher Score is as in Formula 1 [8].

$$F(x_i) = \frac{|\mu_i^+ - \mu_i^-|}{\sigma_i^+ - \sigma_i^-} \tag{1}$$

This score is calculated separately for each feature and allows the difference between classes to be compared with the deviation. A high Fisher score means a feature reflects significant differences and low variance between two classes. Therefore, features with high Fisher scores are the features that best distinguish the classes. The + and - signs in the formula represent two different classes. While μ_i^+ and μ_i^- values show the arithmetic means of the classes, σ_i^+ and σ_i^- values show the standard deviations of the classes [8]. This information provides measures of distinction between classes and differences in features. After the scores are calculated, the features are sorted from largest to smallest, and the desired number of features is selected. A high Fisher score reflects a significant mean difference and a low deviation value of the feature of interest between two classes. Therefore, to select the features that best separate the two classes features with high Fisher scores are preferred [9]. In Table II below, the Fisher Scores of the features are listed from high to low.

TABLE II: Fisher score coefficients of features

FN	R	FN	R	FN	R
23	0.68	5	0.09	25	0.02
3	0.59	2	0.07	21	0.01
13	0.27	18	0.07	1	0.01
11	0.22	27	0.07	20	0.01
28	0.22	9	0.05	19	0.00
8	0.19	29	0.04	15	0.00
6	0.18	30	0.03	4	0.00
14	0.12	17	0.03	16	0.00
24	0.11	7	0.03	10	0.00
22	0.10	26	0.03	12	0.00

FN: Feature Number

C. Decision Trees

Decision Trees (DT) is a data mining technique frequently used in the literature to solve many classification and regression problems. Since it contains classification and feature selection algorithms in its decision trees structure, it can perform classification and feature selection operations simultaneously [10]. Decision trees have three essential parts: root, node, and leaf. Each attribute in the tree structure is represented by a node [11]. At the root node, which is the first node of the tree, questions begin to be asked to classify the data and create the tree structure, and this process continues until nodes or leaves without branches are found [12]. A test data set is used to evaluate the generalization ability of a new data set. A new test data arriving at the tree structure created with the training data set is processed starting from the tree's root. This new data is directed to an appropriate child node according to the test result at the root. This process continues until it reaches a specific tree leaf [13]. Each data is divided into categories using nodes, that is, classified. Various approaches are used to interpret the accuracy rate and performance of the model while performing classification. As for the success rate of this model, six different performance evaluation criteria were used: accuracy rate, sensitivity, specificity, precision, F-measure, Kappa, and AUC.

D. Random Forest Algorithm

Random Forest (RF) is the primary analytical tool and one of the supervised classification algorithms of this research. RF is an ensemble learning method created by combining many independent decision trees. This algorithm is trained by random sampling and random feature selection and selects the highest-scoring value by combining many decision trees that work independently. Figure 2 shows this phenomenon more clearly. The main difference between Random Forest (RF) and Decision trees is that in the RF algorithm, finding the root node and dividing the nodes is random [14]. In addition, due to its random selection, it provides a natural resistance to overfitting and essentially prevents this phenomenon, thus increasing the performance of the model.

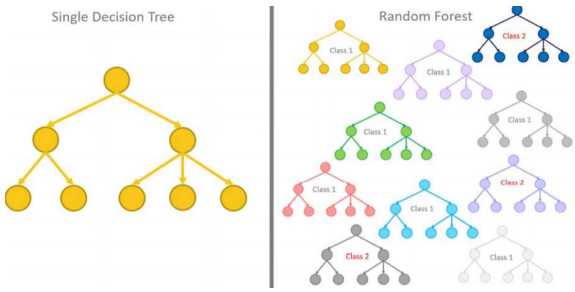

Fig. 2: General structure of the random forest algorithm

The associated coefficients of the features were calculated with the Fisher correlation used in the study, and the pathological and statistical features selected according to these calculated scores, and those with high scores in the RF decision tree classification model were randomly grouped among themselves and trained to create ten different new models. According to the performance evaluation criteria of these models, Model 2, which gave the highest accuracy (91.51%), was selected, and a new rule-based diagnostic algorithm was developed accordingly. The performance evaluation criteria of the models are shown in Table III.

TABLE III: Performance evaluation criteria of RF-trained models

Model	AR	Sen	Spe	F-M	Kappa	AUC
1	91.04	0.92	0.91	0,91	0,82	0,91
2	91.51	0.91	0.92	0,91	0,83	0,92
3	89.15	0.87	0.92	0.89	0.78	0.89
4	89.15	0.87	0.92	0.89	0.78	0.89
5	89.15	0.88	0.91	0.89	0.78	0.89
6	86.79	0.89	0,85	0.87	0.74	0.87
7	89.62	0.90	0.90	0.90	0.79	0.90
8	89.62	0.90	0.90	0.90	0.79	0.90
9	89.62	0.90	0.90	0.90	0.79	0.90
10	90.09	0.90	0.91	0.90	0.80	0.90

AR Accuracy Rate, Sen Sensitivity, Spe Specificity, F-M F-Measurement, AUC Area under the ROC Curve

III. Results

When these developed models were evaluated, breast cancer type was detected with 91.51% accuracy, 0.91 sensitivity, and 0.92 specificity with the data set created by using at least three features.

It has been determined that a healthier and safer diagnostic system can be created by detecting only those with high interaction without the need to use all the features offered for disease diagnosis. The Decision Tree Algorithm (Model 2) of this system developed in MATLAB is shown in Figure 3.

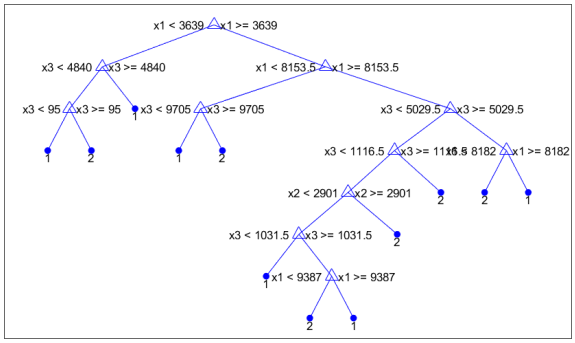

Fig. 3: Decision tree structure of model 2

Compared to other studies, this model has been shown to make the diagnostic process more effective by making it possible to use only highly interactive features. Additionally, thanks to the Decision Tree Algorithm implemented in the

MATLAB environment, the application and adaptation of the model are relatively straightforward.

The developed rule-based diagnostic algorithm may be necessary in early breast cancer diagnosis. Early diagnosis can increase patients' chances of receiving more effective treatment and improve their quality of life. The algorithm can positively affect the treatment process by enabling patients to be diagnosed earlier.

IV. Discusion

When we look at other studies in this field in the literature, one of the critical studies conducted for the early detection of breast cancer is a study conducted by Oklahoma State University. Accuracy rates of 91.2% with artificial neural networks and 89.2% with logistic regression were determined [15].

P. Sathiyanarayanan et al. In his study, identifying breast cancer was initially carried out using different algorithms, including the Support Vector Machine (SVM) algorithm, k-Nearest Neighbor (kNN) algorithm, Multi Layer Perceptron (MLP) algorithm, etc. There are. Despite the use of these algorithms, the detection accuracy of cancer has not reached the expected level. Later, by adding the Decision Trees algorithm to one of the supervised machine learning techniques, they could determine with 99% accuracy whether the predicted cancer was Malignant or Benign.

Tsehay Admassu Assegie et al. In his study, a machine learning model is proposed using learning algorithms such as SVM and decision tree. Analysis results show that the SVM algorithm has higher accuracy, less misclassification rate, and better precision. The average accuracy of the SVM model is 91.92%, while the accuracy of the Decision Tree classification model is 87.12% [16].

Reza Rabiei et al. RF, MLP, gradient boosting trees (GBT), and genetic algorithms (GA) were used in their study. The models were initially trained with demographic and laboratory features. Then, the models were trained with all demographic, laboratory, and mammography features to measure the effectiveness of mammography features in predicting breast cancer. It was observed that RF methods exhibited a higher performance accuracy of 80% compared to other techniques.

V. Conclusion

This study aimed to develop an effective rule-based algorithm that can be used in breast cancer diagnosis. As a result of the evaluations, 91.51% accuracy, 0.91 sensitivity, and 0.92 specificity rates were obtained with a data set containing at least three features. These high rates indicate that the proposed model can be valuable for clinical applications.

In this context, the results obtained in our current study are at a level that can compete with other essential studies in the literature. In particular, using only highly interactive features has made the diagnostic process more effective and safe.

References

[1] Togacar Mesut Calıskan Abidin Ates Feyzi Ferat. An artificial intelligence based hybrid model proposal for the detection of breast cancer, 2022.

[2] Fatma Eti Aslan and Aysel Gürkan. The risk of breast cancer at the women. *Journa of Breast Health*, 3, 2007.

[3] B Sayar Acta Medica Ruha. Use of artificial intelligence in medicine. *International Journal of Medicine and Health Sciences*, 1, 2023.

[4] Şerife Güzel, Hilal Akman Dömbekci, and Fettah Eren. The use of artificial intelligence in the health institutions: A qualitative research. *Celal Bayar University Health Sciences Institute Journal*, 9:509–519, 12 2022.

[5] Street W, Wolberg W, and Mangasarian O. Breast cancer wisconsin (diagnostic), 1995.

[6] M Danacı, M Çelik, and AE Akkaya ve. Breast cancer data prediction and diagnosis using data mining methods. *Innovations and Applications in Intelligent Systems Symposium*, 2010.

[7] PE Hart, DG Stork, and RO Duda. Pattern classification. *ResearchGate*, 2000.

[8] Hüseyin Budak. Feature selection methods and a new approach. *Süleyman Demirel University Journal of Natural and Applied Sciences*, 22:21–31, 10 2018.

[9] V. Bolón-Canedo, N. Sánchez-Maroño, A. Alonso-Betanzos, J. M. Benítez, and F. Herrera. A review of microarray datasets and applied feature selection methods. *Information Sciences*, 282:111–135, 10 2014.

[10] I Guyon and Elisseeff A. An introduction to variable and feature selection. *Journal of machine learning research*, 3:1157–1182, 2003.

[11] Kavzoğlu T and İ Çölkesen. Classification of satellite images using decision trees: Kocaeli case. *Electronic Magazine of Mapping Technologies*, 2, 2010.

[12] M Pal and PM Mather. An assessment of the effectiveness of decision tree methods for land cover classification. *Remote Sensing of Environment*, 86, 2003.

[13] Nilay Taçyildiz, Buse Nur Karaman, Zeynep Bağdatlı, Sude Çiğnitaş, and Muhammed Kürşad Uçar. Development of rule-based diagnostic algorithms with artificial intelligence methods for the determination of cardiovascular diseases. *El-Cezeri Journal of Sciences and Engineering*, 9:1265–1273, 12 2022.

[14] Ece Akdaglı. Random forest algorithm in machine learning, 2021.

[15] SY Chou, OA Bamodu, WT Chiu, CT Hong, and Reports L Chan Scientific2022. Artificial neural network-boosted cardiac arrest survival post-resuscitation in-hospital (caspri) score accurately predicts outcome in cardiac arrest patients. *Scientific Report*, 12, 2022.

[16] Tsehay Admassu Assegie. A support vector machine and decision tree based breast cancer prediction 2973. *Semantic Scholar*, 2020.

Polarization and Oblique Incidence Insensitive Dual-Band Metamaterial Absorber for Wi-Fi Applications

B. ILA[1] and E. YALDIZ[1]

[1] Konya Technical University, Konya/Turkey, bila@ktun.edu.tr
[1] Konya Technical University, Konya/Turkey, eyaldiz@ktun.edu.tr

***Abstract* - In this work, polarization and oblique incidence insensitive dual-band metamaterial-based absorber is designed for Wi-Fi bands. The proposed metamaterial absorber (MMA) structure consists of a resonator layer, dielectric layer, and ground plane. The resonator layer occurs from two closed square rings. While the first ring ensures absorbance at 2.45 GHz, second one provides absorbance at 5 GHz. MMA structure has been designed and analyzed with Ansys HFSS full-wave electromagnetic (EM) simulation software. According to the results under normal incidence MMA provides in 2.45 GHz and 5 GHz 98.8% and 99.66% absorption rate, respectively. In addition, the EM wave to the MMA structure has been examined under TE and TM polarizations, polarization angle, and oblique incidence angle. It has been observed that the peak absorptions remain constant in TE and TM polarization. On the other hand, the proposed MMA is ensured over 92% absorbance in oblique incidence in 2.45 GHz and 5 GHz at $\theta = 50^{\circ}$. According to the results, MMA is quite insensitive for both polarization and oblique incidence. These results obtained show that the structure for the Wi-Fi bands can be efficient for communication systems applications.**

***Keywords* – Metamaterial, absorber, resonator, Wi-Fi band.**

I. INTRODUCTION

THERE is an increasing demand for the development of suitable materials and procedures to mitigate the effects of EM waves. This demand has been met by introducing absorbers into the communications world [1]. Metamaterials are widely used as absorber materials due to their unusual EM properties. In 2008, Landy et al. designed the first reported MMA using a split ring resonator (SRR) and cut-wire and achieved narrow band absorption by magnetic coupling between the SRR plane and the cut-wire plane [2]. MMAs are used in different civil and military applications such as sensor applications [3-5], radar cross-section reduction [6], antenna applications [7-8], and energy harvesting [9-10] with their features such as absorption rate, absorption bandwidth, adjustable absorption frequency and thinner thicknesses [11]. MMAs generally consist of a metamaterial resonator layer, a dielectric layer, and a ground plane, as shown in Figure 1. Resonators, which can be designed in various shapes, are widely used as metamaterial elements of microwave absorbers. The main advantages of such absorbers are compactness, ease of fabrication, and polarization independence in the wide frequency band. High absorption coefficient can be obtained for wide incidence angles and dynamic adjustment possibilities [12].

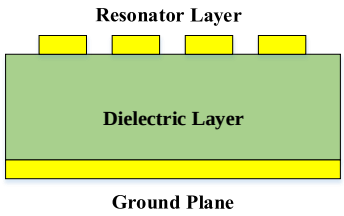

Figure 1: MMA block diagram.

MMA's absorption rate is related to reflection coefficient $|S_{11}(\omega)|$ and transmission coefficient $|S_{21}(\omega)|$, and can be calculated as [2]:

$$A(\omega) = 1 - |S_{11}(\omega)|^2 - |S_{21}(\omega)|^2 \quad (1)$$

where ω is angular frequency of EM wave. As shown in Figure 1, if an MMA structure has a conductive ground plane, the transmission coefficient is near zero. Therefore, absorption can be related only reflection coefficient and can be calculated as:

$$A(\omega) = 1 - |S_{11}(\omega)|^2. \quad (2)$$

This paper presents polarization and oblique incidence insensitive dual-band MMA for Wi-Fi bands. MMA structure has been designed and analyzed with Ansys HFSS full-wave EM simulation software. The resonator layer of the MMA structure designed using FR-4 material occurs from two closed rings and while the first ring ensures absorbance in 2.45 GHz, second one provides absorbance in 5 GHz. MMA structure has been examined from 0° to 60° the polarization incidences. According to obtained results, the MMA structure has been assessed.

II. DESIGN AND SIMULATION

Figure 2 shows the top and perspective views of the proposed MMA designed and simulated using the Ansys HFSS full-wave EM simulation software. The proposed MMA, which is made of a two 45° rotated square ring resonator layer, the dielectric layer, and the ground plane. The dielectric layer is 1.5 mm thickness, double side copper covered FR4 with a dielectric constant 4.3, and a loss tangent of 0.025 at 10 GHz. The copper

thickness is 0.035 mm. The design parameters seen in Figure 2 have been chosen for maximum absorption in 2.45 GHz and 5 GHz and their values have been given in Table 1.

Table 1: Design parameters and values.

Parameters	L_x	L_y	L_{r1}	L_{r2}	w_1	w_2
Value (mm)	30	30	20	12.3	7.9	5.9

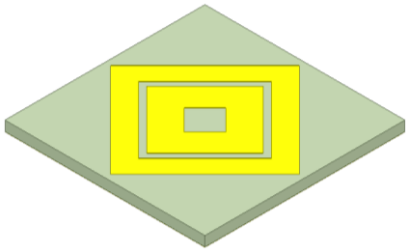

(a)

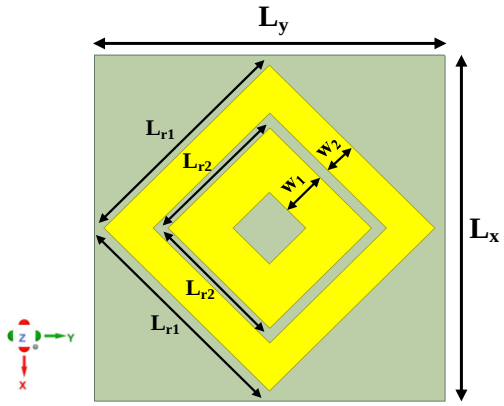

(b)

Figure 2: Proposed MMA structure (a) perspective view and (b) top view with design parameters.

MMA structure excitation has been made with floquet port in HFSS and simulation results have been examined. Subsequently, reflection coefficient, transmission coefficient, and equation (2) based absorption have been obtained.

III. Results And Discussions

Reflection and transmission coefficient plots obtained from the simulation are given in Figure 3. This figure shows a dual band is attained at 2.45 GHz and 5 GHz. In addition, to analyze the dual-band resonance behavior of the MMA structure, surface current and electric field distributions have been computed and shown in Figure 4 and Figure 5, respectively.

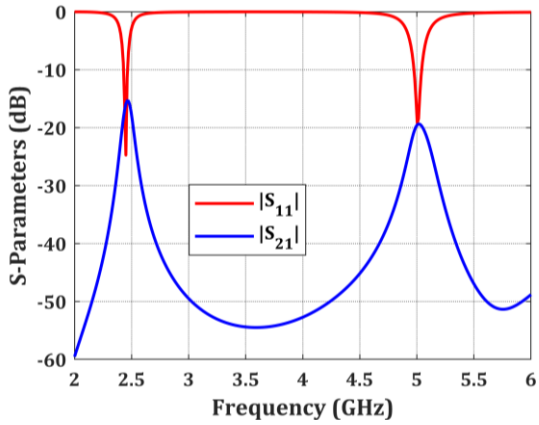

Figure 3: S-Parameters of MMA structure.

As shown in Figure 4 (a) and Figure 5 (a) outer ring exhibited higher surface current and electric field distribution values and supported the 2.45 GHz resonance. Moreover, as shown in Figure 4 (b) and Figure 5 (b) inner ring exhibited higher surface current and electric field values and supported the 5 GHz resonance.

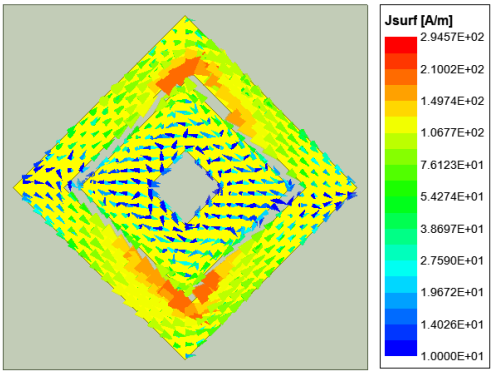

(a)

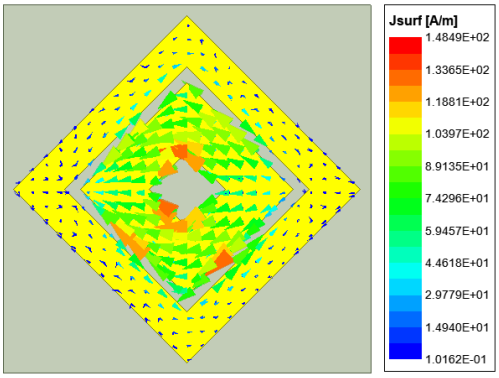

(b)

Figure 4: MMA's surface current distributions, (a) at 2.45 GHz, (b) at 5 GHz.

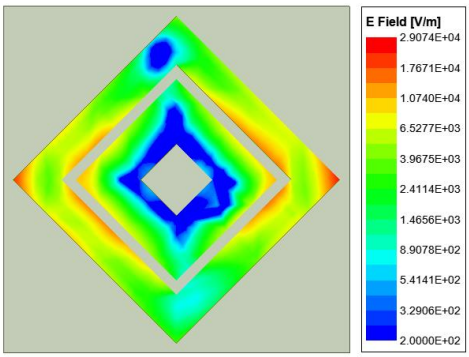

(a)

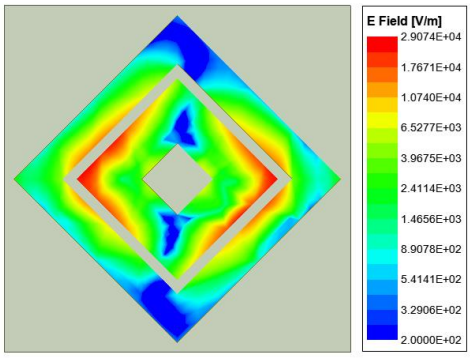

(b)

Figure 5: MMA's electric field distributions, (a) at 2.45 GHz, (b) at 5 GHz.

After the investigation of surface current and electric field distributions, reflection and absorption rates have been obtained using simulation results and equation (2) as shown in Figure 6. The bottom side of the MMA structure has a copper ground plane. Therefore, there is no transmission of the EM wave from the bottom of the MMA structure to the outside and the transmission coefficient is close to zero. According to Figure 6, MMA has been exhibited high absorption values of 98.8% and 99.66% at 2.45 GHz and 5 GHz, respectively, at normal incidence.

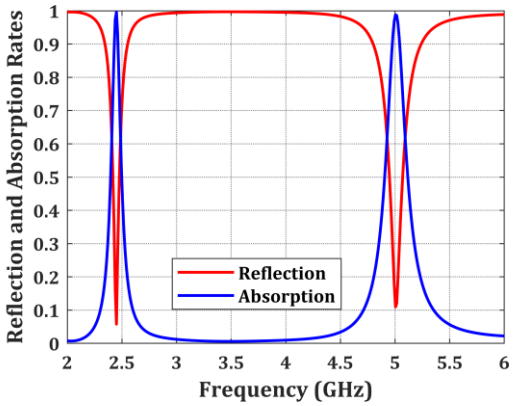

Figure 6: Reflection and absorption rates of MMA structure.

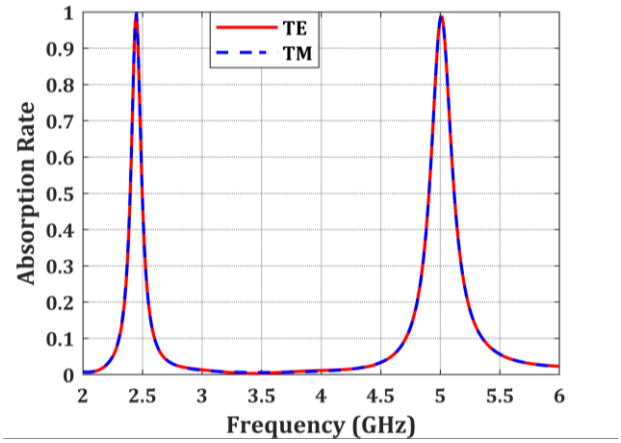

Figure 7: Absorption rate of TE and TM polarization.

High angular stability in the absorption profile is essential a MMA to be as a perfect absorber [13]. Therefore, initially EM wave is kept constant in the z-direction normal incidence to the MMA. MMA for both transverse electric (TE) and transverse magnetic (TM) polarization have been investigated, and the simulation results are shown in Figure 7. It is observed from Figure 7 that the peak absorption and bandwidth remain constant for both polarizations.

In addition, the impact of polarization angle change (ϕ) on absorption response under normal incidence has been investigated. The simulation results of change ϕ have been given in Figure 8. Absorption is nearly constant with the change in ϕ from 0° to 60°. Thus, the proposed MMA structure has been shown quite stable for change polarization angle change.

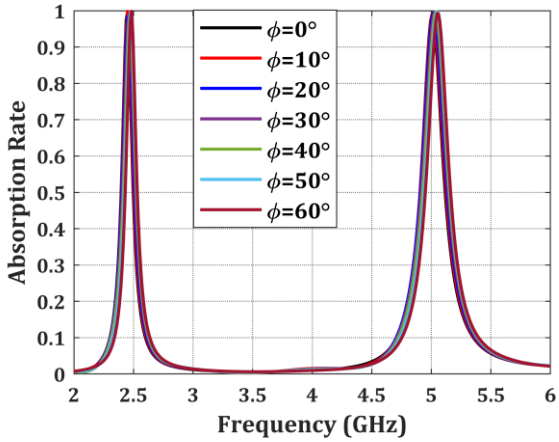

Figure 8: Absorption rates for various ϕ polarization angles.

On the other hand, MMA has been investigated under oblique incidence. EM wave oblique incidence has been varied by an angle of θ from 0° to 60° and absorption simulation results have been obtained versus the change of θ is shown in Figure 9. Up to $\theta = 50°$, two peaks with over 92% absorbance have been obtained, while at $\theta = 60°$, a decrease in absorbance down to 83% has been observed. Thus, the proposed MMA structure has been shown quite stable for change oblique incidence.

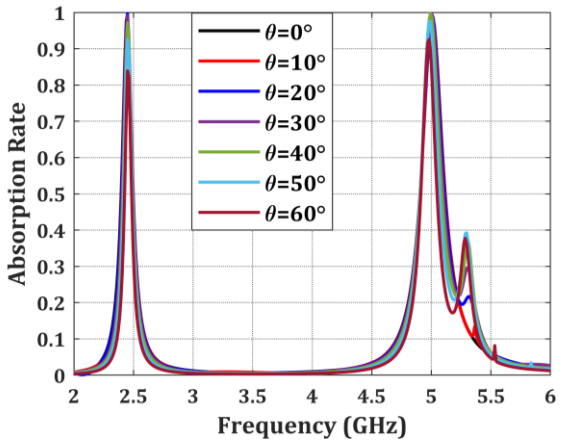

Figure 9: Absorption rates for various θ oblique incidence angles.

IV. CONCLUSION

In this paper, it has been proposed polarization and oblique incidence insensitive dual-band MMA for Wi-Fi bands. MMA is made of two 45° rotated closed square rings. The first ring ensures absorbance at 2.45 GHz, second one provides absorbance at 5 GHz. MMA structure has been designed by Ansys HFSS full-wave EM simulation software and analyzed with floquet port. According to the simulation results under normal incidence MMA provides in 2.45 GHz and 5 GHz 98.8% and 99.66% absorption, respectively. The EM wave incidence to the MMA structure was examined under TE and TM polarizations, both polarization angle and oblique incidence angle from 0° to 60°. It has been observed that the peak absorptions remain constant in both TE and TM polarizations. On the other hand, the proposed MMA ensures over 92% absorption rate in oblique incidence in 2.45 GHz and 5 GHz at $\theta = 50^{\circ}$. According to the results, MMA is polarization and oblique incidence quite insensitive. These results show that the proposed structure for the Wi-Fi bands can be efficient for communication systems applications.

REFERENCES

[1] M. Amiri, F. Tofigh, N. Shariati, J. Lipman, and M. Abolhasan, "Review on Metamaterial Perfect Absorbers and Their Applications to IoT," *IEEE Internet Things J.*, vol. 8, no. 6, pp. 4105–4131, 2021.

[2] N. I. Landy, S. Sajuyigbe, J. J. Mock, D. R. Smith, and W. J. Padilla, "Perfect metamaterial absorber," *Phys. Rev. Lett.*, vol. 100, no. 20, pp. 1–4, 2008.

[3] M. Amiri, M. Abolhasan, N. Shariati, and J. Lipman, "Remote Water Salinity Sensor Using Metamaterial Perfect Absorber," *IEEE Trans. Antennas Propag.*, vol. 70, no. 8, pp. 6785–6794, 2022.

[4] H. Singh, A. Gupta, R. S. Kaler, S. Singh, and A. S. Gill, "Designing and Analysis of Ultrathin Metamaterial Absorber for W Band Biomedical Sensing Application," *IEEE Sens. J.*, vol. 22, no. 11, pp. 10524–10531, 2022.

[5] H. Zhu *et al.*, "A High Q-factor Metamaterial Absorber and Its Refractive Index Sensing Characteristics," *IEEE Trans. Microw. Theory Tech.*, vol. 70, no. 12, pp. 5383–5391, 2022.

[6] A. Sharma *et al.*, "In-band RCS Reduction and Isolation Enhancement of a 24 GHz Radar Antenna Using Metamaterial Absorber for Sensing and Automotive Radar Applications," *IEEE Sens. J.*, vol. 20, no. 21, pp. 13086–13093, 2020.

[7] P. Garg and P. Jain, "Isolation Improvement of MIMO Antenna Using a Novel Flower Shaped Metamaterial Absorber at 5.5 GHz WiMAX Band," *IEEE Trans. Circuits Syst. II Express Briefs*, vol. 67, no. 4, pp. 675–679, 2020.

[8] J. Zhang, J. Li, and J. Chen, "Mutual Coupling Reduction of a Circularly Polarized Four-Element Antenna Array Using Metamaterial Absorber for Unmanned Vehicles," *IEEE Access*, vol. 7, pp. 57469–57475, 2019.

[9] X. Duan, X. Chen, Y. Zhou, L. Zhou, and S. Hao, "Wideband Metamaterial Electromagnetic Energy Harvester with High Capture Efficiency and Wide Incident Angle," *IEEE Antennas Wirel. Propag. Lett.*, vol. 17, no. 9, pp. 1617–1621, 2018.

[10] R. Agrahari *et al.*, "Triple-band Metasurface Absorber for RF Energy Harvesting Applications," *Microw. Opt. Technol. Lett.*, vol. 65, no. 8, pp. 2252–2261, 2023.

[11] C. M. Watts, X. Liu, and W. J. Padilla, "Metamaterial Electromagnetic Wave Absorbers," *Adv. Mater.*, vol. 24, no. 23, 2012.

[12] I. A. Buriak, V. O. Zhurba, G. S. Vorobjov, V. R. Kulizhko, O. K. Kononov, and O. Rybalko, "Metamaterials: Theory, Classification and Application Strategies (Review)," *J. Nano- Electron. Phys.*, vol. 8, no. 4(2), pp. 04088-1-04088–11, 2016.

[13] M. Moniruzzaman, M. Tariqul Islam, F. M. Mohd, M. S. Soliman, N. Misran, and M. Samsuzzaman, "Tuning Metallic Stub Loaded Symmetrical Resonator Based Dual Band Metamaterial Absorber for Wave Shielding from Wi-Fi Frequencies," *Alexandria Eng. J.*, vol. 63, pp. 399–414, 2023.

Design and Implementation of BLDC Motor Thrust Measurement and Test System

A.DURMUŞ[1], E.DUYMAZ[2], A. M. KADIOĞLU[3], F. BAYKAL[4], C. ÖLMEZ[5] and H. ATASOY[6]

[1] Ostim Technical University, Ankara/Turkey, alpaslan.durmus@ostimteknik.edu.tr
[2] Ostim Technical University, Ankara/Turkey, erol.duymaz@ostimteknik.edu.tr
[3] Ostim Technical University, Ankara/Turkey, murat.kadioglu@ostimteknik.edu.tr
[4] Ostim Technical University, Ankara/Turkey, fatih.baykal@ostimteknik.edu.tr
[5] Ostim Technical University, Ankara/Turkey, cebrail.olmez@ostimteknik.edu.tr
[6] Ostim Technical University, Ankara/Turkey, hudaver.atasoy@ostimteknik.edu.tr

***Abstract* - Some problems may arise during the determination of the propulsion system combination, especially in the selection of the right engine and propeller. In general, motor manufacturers specify the recommended propeller combination for BLDC motors. However, the fact that engine and propeller performance data are generally not available can cause problems in selecting the right propeller for the desired flight performance. In addition, if a different propeller engine combination is required, problems may be encountered in determining the thrust power to be obtained. In addition, determining the rpm value to be obtained from the designed engine and propeller combination and the amount of current to be drawn from the circuit is important in order to obtain accurate flight parameters. At the same time, the current drawn from the battery depending on the desired thrust power is important in determining the flight duration. Empirical approaches to determine the characteristics of propellers and engines are more preferred because they are practical. The development of Thrust Benchmarking Systems (TBS: Trust Benchmarking Systems) for electric UAV propulsion systems provides convenience in comparing UAV systems with different battery, engine and propeller systems. The TBS system, realized with the BAP support provided by OSTİM TECHNICAL UNIVERSITY, was developed from low-cost materials. It also has a graphical interface so that users can easily perform analyzes and monitor all performance data. The TBS is equipped with various sensors that will perform the data collection necessary to determine the optimal combination of the electric UAV propulsion system. The developed thrust meter system has a wide capacity and development potential as a static propulsion test device. It is designed to measure key parameters such as static thrust, battery voltage, battery current output, engine temperature, engine speed controller temperature and propeller rotation speed (RPM). At this point, it has a wide potential for use in Türkiye and around the world. It can be easily used by teams in Teknofest and other competitions to measure thrust power and other parameters accordingly, as well as to measure thrust system parameters of industrial electric UAV systems with small adjustments that can be made on the system.**

***Keywords* – Thrust, BLDC, Propulsion system, BLDC Test Bech**

I. INTRODUCTION

The use of electric unmanned aerial vehicles (UAVs) is increasing in a variety of defense and civilian applications. Small unmanned aerial vehicles (UAVs) are finding increasing use, from agriculture to commercial mapping, from defense to reconnaissance and surveillance. In parallel with these increasing uses, improved performance and range requirements are emerging to maximize effectiveness and utility during a particular UAV mission. In parallel with the rapid development of UAV systems in recent years, designing an efficient propulsion system has become more important for the design of an effective UAV system. UAV propulsion systems generally powered by electric batteries; It consists of battery, motor driver, motor and propeller. Electric propulsion systems also enable the use of energy systems such as hybrid and fullcell. UAV systems with electric propulsion systems enable the use of low-cost and silent components. Professional UAV systems use brushless DC (BLDC) motor and electronic speed controller (ESC). ESC generally produces a square wave or trapezoidal PWM signal for the motor. BLDC motors and ESCs by different manufacturers vary significantly in efficiency and performance. Additionally, there is limited data on the performance of motors and ESCs. This makes it difficult to predict the overall performance of the propulsion system from the battery, motor and ESC combination for a particular application. At the same time, one of the important components that affects the performance of the propulsion system is the ESC (Electronic Speed Controller) [1]. ESC is an electronic component that produces square wave or trapezoidal PWM signals for BLDC motors. The generated signal is used for ESC to control the motor speed. How much voltage should be applied to the engine by the ESC is determined by the signal sent by the flight controller or controller. The rotation speed of the engine, that is, RPM (Repeat Per Minute - number of revolutions per minute), is calculated with the formula RPM = Kv x V. Kv value is among the data provided by engine manufacturers[2]. Kv value is simply the number of revolutions the vehicle makes per volt applied to the engine. KV value directly affects thrust power.

Some problems may arise during the determination of the propulsion system combination, especially in the selection of the right engine and propeller [3]. In general, motor manufacturers specify the recommended propeller combination for BLDC motors. However, the fact that engine and propeller performance data are generally not available can cause

problems in selecting the right propeller for the desired flight performance. In addition, if a different propeller engine combination is required, problems may be encountered in determining the thrust power to be obtained. In addition, determining the rpm value to be obtained from the designed engine and propeller combination and the amount of current to be drawn from the circuit is important in order to obtain accurate flight parameters. At the same time, the current drawn from the battery depending on the desired thrust power is important in determining the flight duration [4].

The basic method of determining the thrust characteristic produced by a propeller is to model and perform aerodynamic analysis using simulation software [5]. However, to obtain appropriate and satisfactory results, airfoil geometry and other parametric data of the propeller are needed. Considering the difficulty of obtaining such data from the manufacturer itself, empirical methods become more important [6]. Empirical approaches to determine the characteristics of propellers and engines are more preferred because they are practical. The development of Thrust Benchmarking Systems (TBS: Trust Benchmarking Systems) for electric UAV propulsion systems provides convenience in comparing UAV systems with different battery, engine and propeller systems. The developed thrust meter system has a wide capacity and development potential as a static propulsion test device [7]. It is designed to measure key parameters such as static thrust, battery voltage, battery current output, engine temperature, engine speed controller temperature and propeller rotation speed (RPM). At this point, it has a wide potential for use in Türkiye and around the world [7,8,9,10]. It can be easily used by teams in Teknofest and other competitions to measure thrust power and other parameters accordingly, as well as to measure thrust system parameters of industrial electric UAV systems with small adjustments that can be made on the system.

Approximately 75% - 90% of the total power consumption of rotary wing Unmanned Aerial Vehicle (UAV) systems is generated by the propulsion system. For this reason, it is important to design the propulsion system, which is directly related to flight performance parameters such as aircraft flight time, maneuverability, level of resistance to operational conditions, and payload capacity, to be suitable for the weight of the aircraft and to be highly efficient. It is the realization of the desired capabilities and flight performance features with an aircraft of minimum weight and dimensions, or the ability of the aircraft to cruise in the air for longer periods of time without compromising other flight performance features compared to similar products with similar weight, size and capabilities. Rotary wing UAV propulsion system consists of engine, propeller, ESC (Electronic Speed Controller) and battery components. The propulsion system architecture is schematically shown in Figure 1.

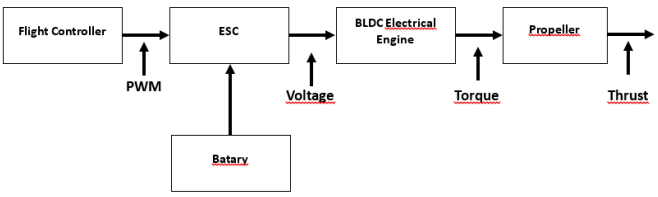

Figure 1: Block Diagram of Electrical Propulsion System

II. DESIGN OF TRUST BENCHMARKING SYSTEM

The working of the whole system is shown in the block diagram given in Figure 1. The load cell to which the motor is connected will transmit the necessary data to the Arduino system using an HX711 24bit ADC. A high-power large relay and optical encoder will be used to connect the LI-PO battery to the system. For BLDC motors, the ESC will be easily controlled using the PWM signal. BLDC speed will be controlled by PWM signal. The data received by Arduino will be transferred to the computer and processed. The result and necessary parameters can be viewed in the graphical interface.

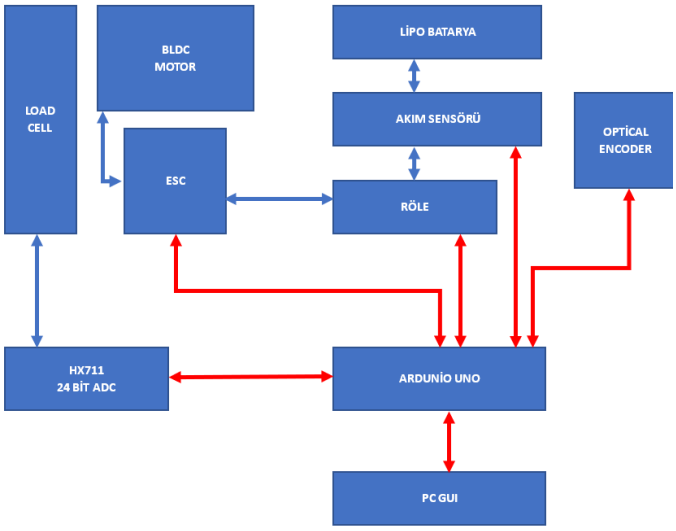

Figure 2: Block Diagram of BLDC Engine Thrust Measurement and Test System

Thrust measurement system to be coded with embedded software with a graphical interface;

a. Thrust measurement
b. Current measurement
c. Voltage measurement
d. RPM measurement
f. Automatic chart drawing
g. Creating instant graphics of data,
h. Automatic creation of motor test sequences

III. ELECTRONIC DESIGN

Below is the schematic drawing of the thrust meter system. An Arduino Nano will be used as the main part. The Arduino is connected to a current sensor that can measure up to 30A. There is a single analog pin used to read this value. ESC will be used

to control the BLDC motor. For main power control, switch and relay are used. To monitor whether the relay is open or not, an optocoupler is used.

The most commonly used ADC for load cells is the HX711. The HX711 is a 24-bit sigma delta ADC capable of doing 10 samples per second or 80 samples per second.

IV. SOFTWARE DESIGN

The software part consists of 2 parts, one will be the Arduino side that will communicate with all sensors and send this data, and the other will be the interface that will be used for interaction, that is, the GUI side.

V. EMBEDDED SOFTWARE DESIGN

It reads the data from the load cell and currently from the current meter and sends this data serially to the interface in the specified ms. It sends a string packet that can be easily parsed into data in Python.

VI. GRAPHICAL INTERFACE DESIGN

It is included in the GUI that will be connected to Arduino Nano. The settings section allows us to change the number of blades on the propeller and choose whether we want it to operate in automatic or manual mode. The relay section is a safety indicator that aims to show us whether the relay is open or closed. Dials, as the name suggests, are dials that can display thrust, throttle, RPM and current. Manual controls allow us to manually shift the throttle and start/stop data recording using a slider. Automatic controls allow us to select the test/procedures we want to run automatically, program throttle curves and things like that. There will also be a live chart section, which is a chart that will display our data and update it live as our testing continues.

The first thread reads the data from Arduino and the second thread displays the data in the GUI. The function called convertString will be used to read the data from the Arduino interface.

VII. CONCLUSION

The TBS system, realized with the BAP support provided by OSTİM TECHNICAL UNIVERSITY, was developed from low-cost materials. It also has a graphical interface so that users can easily perform analyzes and monitor all performance data. The TBS is equipped with various sensors that will perform the data collection necessary to determine the optimal combination of the electric UAV propulsion system. The developed thrust meter system has a wide capacity and development potential as a static propulsion test device. It is designed to measure key parameters such as static thrust, battery voltage, battery current output, engine temperature, engine speed controller temperature and propeller rotation speed (RPM). At this point, it has a wide potential for use in Türkiye and around the world. It can be easily used by teams in Teknofest and other competitions to measure thrust power and other parameters accordingly, as well as to measure thrust system parameters of industrial electric UAV systems with small adjustments that can be made on the system.

ACKNOWLEDGMENT

This study was supported by the OSTİM Technical University BAP Commission within the scope of the project numbered BAP202233 (Development of a thrust metering system with a graphical interface for BLDC and propeller systems used in Unmanned Aerial Vehicle Systems). We would like to thank OSTİM Technical University and BAP Commission for their support to the study.

REFERENCES

[1] Zabunov, S. & Mardirossian, G. (2018). Scales for measuring UAV micro-motor static thrust. Aerospace Research in Bulgaria, 30, 96-102. https://doi.org/10.3897/arb.v30.e08

[2] Theys, B., Dimitriadis, G., Hendrick, P., & Schutter, J. D. (2016). Influence of propeller configuration on propulsion system efficiency of multi-rotor Unmanned Aerial Vehicles. 2016 International Conference on Unmanned Aircraft Systems (ICUAS). https://doi.org/10.1109/icuas.2016.7502520

[3] Hossain, M. R. & Krouglicof, N. (2010). Propeller dynamometer for small Unmanned Aerial Vehicle. Ccece 2010. https://doi.org/10.1109/ccece.2010.5575152

[4] Virginio, R., Fuad, F. A., Jihadil, M., Ramadhani, M. J., Rafie, M., Stevenson, R., & Adiprawita, W. (2018). Design and implementation of low cost thrust benchmarking system (TBS) in application for small scale electric UAV propeller characterization. Journal of Physics: Conference Series, 1130. https://doi.org/10.1088/1742-6596/1130/1/012022

[5] Gundlach, J. (2012). Designing Unmanned Aircraft Systems: A Comprehensive Approach (AIAA Education Series). American Institute for Aeronautics and Astronautics.

[6] Muzar, D. & Lanteigne, E. (2016). Experimental characterization of brushless dc motors and propellers for flight application. Proceedings of the Canadian Society for Mechanical Engineering International Congress 2016.

[7] Gong, A., Palmer, J. L., Brian, G., Harvey, J. R., & Verstraete, D. (2016). Performance of a hybrid, fuel-cell-based power system during simulated small unmanned aircraft missions. International Journal of Hydrogen Energy, 41(26), 11418-11426.

[9] Kotarski, D., Krznar, M., Piljek, P., & Simunic, N. (2017). Experimental Identification and Characterization of Multirotor UAV Propulsion. Journal of Physics: Conference Series, 870, 012003. https://doi.org/10.1088/1742-6596/870/1/012003

[10] Szafranski, G., Czyba, R., & Blachuta, M. (2014). Modeling and identification of electric propulsion system for multirotor unmanned aerial vehicle design. 2014 International Conference on Unmanned Aircraft Systems (ICUAS). https://doi.org/10.1109/icuas.2014.6842287

Impact of Feature and Sensor Selection on EMG Signal Processing

E. MOLLAHASANOĞLU[1] and Y. SEVİM[2]

[1] Karadeniz Technical University, Trabzon/Turkey, emin.mollahasanoglu@ktu.edu.tr
[2]Karadeniz Technical University, Trabzon/Turkey, ysevim@ktu.edu.tr

***Abstract* - Electromyography (EMG) signals, widely used medical method for measuring the electrical activity of muscles, represent the electrical activity of muscles during contraction and relaxation. The main objective of this study is to investigate the importance of the influence of feature and sensor selection to improve the success rate of EMG signal classification. To enhance the classification success, the study assesses the influence of each of the 13 different feature extraction techniques on classification performance. This is achieved by evaluating their individual and combined effects in dual, triple, and quadruple combinations. Various mathematical and statistical methods such as Zero Crossing Point, Wilson Amplitude, AR Coefficients were used as feature extraction methods. K-Nearest Neighborhood (K-NN) was used as the classification algorithm. In addition, variance calculation was performed among 128 sensors and the sensor array was reorganized according to the highest variance ranking and it was shown that this sensor selection improved the classification performance. With the K-NN classification algorithm, a high success rate of 99.75% was achieved with 120 sensors and a dual combination of Zero Crossing Point and Slope Signal Variation features.**

Keywords **Electromyography, Feature Selection, Sensor Selection, Classification, KNN**

I. INTRODUCTION

ELECTROMYOGRAPHY signals are now a widely used technique for measuring and analyzing muscle activity and are used in many fields such as rehabilitation and human-machine interaction. Recently, it has been used especially in hand gesture classification, facial gesture recognition, myoelectric prostheses, muscle fatigue, etc. [1]. The EMG signal is transferred to the computer environment and recorded by electrodes. Various types of electrodes such as needle electrodes, microelectrodes, surface electrodes are used in biomedical signal acquisition applications [2]. Needle electrodes are implanted under the skin and allow biomedical signals to be received from the body. Microelectrodes are placed inside the cell to measure the potential differences between the cell membrane and the extracellular space. Surface electrodes are the most widely used electrode type today due to their ease of use, EMG signals are obtained by placing them on the skin and the number of surface electrodes varies depending on the application [3]. Surface electrodes transfer electrical activity information over the muscle to the computer environment according to the number of channels.

Considering that using the raw EMG signal directly in EMG signal classification studies would lead to poor performance, researchers have extracted features from the EMG signal and used these features as input in classification algorithms [4], [5]. The most used features in the literature are the mean value, absolute value, slope, change in slope sign of the signal [5]–[7].

Improving the performance of classification algorithms that process EMG signals will increase the areas where EMG signals are used [8]–[10]. The most important factor in improving the performance of classification algorithms is the extraction of useful features from EMG signals [11]. In addition, using the appropriate combination of these features will also increase the classification performance.

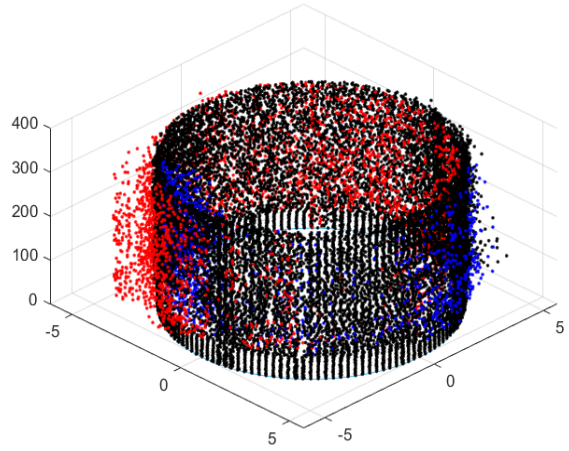

Figure 1. Circular Diagram of the Sensor Assembly

This study addresses two key factors to improve the classification performance of EMG signals: sensor selection and combination of different features. For the combination of different features, the features are combined in twos, threes, and fours and how they contribute to the classification performance is analyzed. The basis for sensor selection is the knowledge that electrical activity in muscles does not occur with the same intensity on all sensors, which is clearly visible in the circular plot of sensors in Figure-1. As can be seen in the figure, some sensors contain high information (red and blue colors), while others contain low or no information (black color). It was thought that identifying and using sensors with high electrical activity information would improve the classification performance. For this purpose, variance calculation was performed for 128 sensors in this study. Sensor signals were then ranked from the highest variance to the lowest variance. The first 80, 120 and 128 sensor signals with the highest variance were selected, respectively, and features were extracted, and classification was performed. With these improvement studies, it is thought that it can contribute to the development of EMG-based systems with a wide range of application potential from medical diagnostics to robotic applications.

In the remaining sections of this study, the methods used, the experimental results and the findings obtained will be described in detail.

II. MATERIAL AND METHODS

A. Dataset

The datasets contain EMG signals from surface EMG electrodes and these signals were used for recognition and analysis of hand movements. In this study, CapgMyo, specifically created for surface

EMG gesture recognition research, was used as the dataset [12], [13]. It offers great potential for researchers who want to make progress in the fields of motion recognition and EMG signal analysis. The CapgMyo dataset was obtained from 23 healthy participants aged 23 to 26. The dataset consists of 3 separate sub-databases as DB-a, Db-b, Db-c. DB-a contains EMG signals from 18 of the 23 participants and is the dataset that forms the basis of the study [14].

B. Feature Extraction

In this study, a total of 13 different features are used for detailed analysis and classification of EMG signals. These features were chosen to capture important information in EMG signals and improve classification accuracy. The features used in the study:

Zero Crossing Point: This method calculates the number of times the signal crosses the x-axis. A threshold value can be used to reduce the noise effect [15]. The equation for calculating the zero-crossing point is given in equation (1).

$$sgn(-x_k * x_{k+1})\ ve\ (|x_k - x_{k+1}| \geq threshold) \quad (1)$$

Willison Amplitude: In the analysis of consecutive samples of the signal, the Willison Amplitude value is increased by one when the voltage difference between two samples exceeds a certain threshold value and is expressed as in equations (2) and (3).

$$WG = \sum_{i=1}^{L-1} f(|x_i - x_{i+1}| - t) \quad (2)$$

$$f(x) = \begin{cases} 1 & if\ x \geq threshold \\ 0 & in\ other\ cases \end{cases} \quad (3)$$

Wavelength: It is calculated by summing the changes between successive samples of the signal. The equation that calculates the wavelength is given in equation (4).

$$WL = \sum_{i=1}^{L} |(x_i - x_{i-1})| \quad (4)$$

where L is the number of samples of the signal.

Slope Sign Change: In this method, the number of points where the signal slope changes are calculated, and a threshold value is used to filter out noise. If the conditions in Equations (5), (6) and (7) are satisfied, the slope sign is increased by one [14]. The slope sign change is calculated with the following formula.

$$x_k > x_{k-1}\ and\ x_k > x_{k+1}\ or\ x_k < x_{k-1}\ or\ x_k < x_{k+1} \quad (5)$$

$$and\ |x_k - x_{k-1}| > treshold \quad (6)$$

$$or\ |x_k - x_{k+1}| > treshold \quad (7)$$

Mean Absolute Value: In this method, the feature is obtained by averaging the absolute values of each sample [16]. It is obtained with the formula given in Equation (8).

$$\overline{X_k} = \frac{1}{L}\sum_{i=1}^{L} |x_i| \quad (8)$$

Root Mean Square: The expression in equation (9) is used to extract this feature.

$$RMS = \sqrt{\frac{1}{L}\sum_{i=1}^{L} (x_i)^2} \quad (9)$$

In this study, in addition to these features, features commonly used in fields such as time series analysis and signal processing were also used [17]. Wavelet Transform, which facilitates feature extraction by separating different frequency components of muscle activity in EMG signals, was also used [18]. All features used and their abbreviations are listed below.

Abbreviations of Features:

- Zero Crossing (ZC)
- Slope Sign Change (SSC)
- Root Mean Square (RMS)
- Wavelength (WL)
- Mean Absolute Value (MAV)
- Auto Regressive (AR)
- S Transform (ST)
- Wavelet Transform (WT)
- Zero Crossing Area (ZCA)
- Zero Crossing Different (ZCD)
- Zero Crossing Different Location (ZCDL)
- Zero Crossings Reproduced Different Locations (ZCRDL)
- Willison Amplitude (WAMP)

The zero-crossing points feature plays an important role in capturing the changes of electrical activity in the signal, and studies have shown that this feature yields very high classification performance. Therefore, different types of zero crossing point features, namely Zero Crossing Area (ZCA), Zero Crossing Differential (ZCD), Zero Crossing Differential Locations (ZCDL) and Zero Crossings Reproduced Differential Locations (ZCRDL), have been derived [17]. These features helped to improve the classification accuracy by representing different aspects and features of the signal.

C. Windowing

Windowing is an important data processing technique used when processing EMG signals. This method divides the data into more meaningful and useful chunks. In this study, a frame size of 256 samples was used and 64 samples were selected as the repetition step. This means that the windowing method divides the data into smaller and more manageable chunks. Furthermore, the windowing method provides the flexibility that the signal required for testing in the trained classifier can be taken from any part of the EMG signal. In addition, windowing is a way to increase the number of samples.

D. Sensor Selection

This study was carried out in a framework where the EMG signal was collected from the arm region with 128 different sensors. However, not all sensors have the same ability to detect electrical activity and therefore the importance of sensor selection is emphasized to improve classification accuracy and better discriminate classes. In particular, the sensor selection process aimed to identify sensors with high information content to better analyze the class information. For

this purpose, variance calculation was used to evaluate the electrical distributions of each of the 128 sensors. Variance values reflect the extent to which sensors capture electrical activity. When the variance values of the sensors were ranked from highest to lowest, the highest 80 sensors were selected first, followed by 120 sensors. It was also evaluated in a case where all 128 sensors were used. Classification performance was compared using these different sensor combinations. Sensor selection allowed for more efficient processing and classification of EMG data and improved the classification accuracy. This method is not based on feature selection, but on extracting the useful features to better represent the EMG signal using sensors that are considered to contain important information.

E. Classification / Cross-Validation

In this study, K-NN classification algorithm, which gives very high performance in EMG signals, is preferred to classify EMG signals. K-NN is a simple and effective algorithm that is frequently used in classification processes. This algorithm makes decisions to classify a dataset based on the classes of nearest neighbors. The KNN classification algorithm is highly sensitive to data variations. This highlights the algorithm's ability to adapt to different data variations in a scenario where EMG signals may be inherently variable. This feature contributes to more consistent and reliable results in the study.

In addition, cross-validation method was applied in this study. Cross-validation is an important technique used to assess the reliability and generalizability of our model. When splitting the dataset into training and testing subsets, cross-validation allows us to evaluate how the model performs on different data.

III. FINDINGS

In this study, the variance values of 128 sensor signals were determined and sensors were selected according to the highest variance value. The 80 and 120 sensors with the highest variance values were selected and classification studies were carried out, but due to the large number of results, the results of the 120 sensors with the highest classification success are given in the tables.

Table 3 shows the performance rates of the 13 features obtained from 120 selected sensors classified with single and binary feature combinations. In the table, the values on the diagonal show the classification performance of each feature on its own, while the off-diagonal features show the performance of the binary combination. As can be seen from Table 3, while the **ZC** feature shows a very high performance on its own, **ZC+SSC** features give the highest performance in binary combinations.

Table 2 shows the results of quadruple combinations of features. When the results are analyzed, the combination of **ZCD + ZCDL + ZCRDL +WAMP** features have the highest accuracy rate, while the combination of **ZC+WT+ZCA+ ZCD** has the lowest accuracy rate. Looking at the data in Tables 1, 2 and 3, it is found that **WT** and **ZCA** features decrease the accuracy rate both alone and in binary, triple, and quad combinations. The highest success rate was obtained from the binary combination of **ZC** and **SSC** features. This success rate is **99.75%.** Other combinations of **ZC** and **SSC** features also increase the performance.

Table 1. Success rates of triple feature combinations

Features	Accuracy	Features	Accuracy
SSC+ ZCDL + ZCRDL	99.65	RMS+WT +ZCA	81.94
RMS+ ZCD + ZCDL	99.59	ZC+WT +ZCA	82.00
ST+ ZCD + ZCDL	99.58	MAV+WT +ZCA	82.42
ZC+ ZCD + ZCRDL	99.53	WT+ZCA + ZCD	83.49
MAV+ ZCD +ZCDL	99.52	ZCA+ ZCRDL +WAMP	83.60

Table 1 shows the results of the 3-way combination of the features. As can be seen from the results, **SSC + ZCDL + ZCRDL** feature combination gives the highest performance.

Table 2. Success rates of quadruple feature combinations

Features	Accuracy	Features	Accuracy
ZCD+ZCDL + ZCRDL +WAMP	99.61	ZC+WT +ZCA + ZCD	84.13
ZC+SSC +RMS +WL	99.53	WT+ZCA + ZCD + ZCDL	84.95
RMS+ ZCD + ZCDL + ZCRDL	99.47	ZCA+ ZCD + ZCDL + ZCRDL	85.38
ZC+WT +ZCA + ZCD	99.41	RMS+ST +WT +ZCA	85.40
WL+ ZCDL + ZCRDL +WAMP	99.33	WL+WT +ZCA + ZCD	85.59

IV. CONCLUSION

This study investigates feature extraction methods in EMG signal processing and the impact of sensor selection in detail. In total, 13 different features were used. First, these features were used alone and the performance rates of each of them were obtained. Then, binary, triple and quadruple combinations of the features were created, and their classification performance was evaluated. The results showed that the highest performance was obtained with the features obtained from 120 sensors. This result shows that variance information can be used in sensor selection. When the combinations of the features are analyzed, a high success rate of 99.75% was obtained in the binary combination of **ZC** and **SSC** features.

When the features are used alone, the **WT** feature has a performance rate of 14%. When **WT** was used in combination with other features, it was found to decrease the performance rate. These findings may contribute to the development of more effective and accurate methods in the field of EMG signal analysis and classification.

Table 3. Classification performance rates of single and binary combinations of features in 120 selected sensors

Features	ZC	SSC	RMS	WL	MAV	AR	ST	WT	ZCA	ZCD	ZCDL	ZCRDL	WAMP
ZC	**99,60**	99,75	99,40	99,29	99,51	92,54	99,43	99,43	81,32	99,52	99,61	99,33	99,49
SSC	0,00	**99,52**	99,40	99,24	99,12	93,68	99,18	99,52	83,24	99,67	99,74	99,26	99,29
RMS	0,00	0,00	**98,65**	98,68	98,59	92,19	98,38	97,66	82,44	99,51	99,48	97,28	98,29
WL	0,00	0,00	0,00	**98,10**	98,57	92,43	98,10	96,90	82,80	99,48	99,64	94,93	98,04
MAV	0,00	0,00	0,00	0,00	**98,78**	92,59	98,56	98,26	82,68	99,55	99,46	97,23	98,44
AR	0,00	0,00	0,00	0,00	0,00	**91,07**	93,36	91,10	87,04	94,46	94,39	91,03	92,74
ST	0,00	0,00	0,00	0,00	0,00	0,00	**98,26**	97,60	84,15	99,55	99,40	97,31	98,17
WT	0,00	0,00	0,00	0,00	0,00	0,00	0,00	**14,20**	79,76	99,61	99,52	57,32	87,14
ZCA	0,00	0,00	0,00	0,00	0,00	0,00	0,00	0,00	**79,58**	83,69	83,14	80,06	83,39
ZCD	0,00	0,00	0,00	0,00	0,00	0,00	0,00	0,00	0,00	**99,57**	99,49	99,55	99,51
ZCDL	0,00	0,00	0,00	0,00	0,00	0,00	0,00	0,00	0,00	0,00	**99,54**	99,35	99,38
ZCRDL	0,00	0,00	0,00	0,00	0,00	0,00	0,00	0,00	0,00	0,00	0,00	**51,43**	88,18
WAMP	0,00	0,00	0,00	0,00	0,00	0,00	0,00	0,00	0,00	0,00	0,00	0,00	**86,85**

REFERENCES

[1] A. Chowdhury *et al.*, "Muscle Computer Interface: A Review," pp. 411–421, 2013, doi: 10.1007/978-81-322-1050-4_33.

[2] K. F. Wu and Y. T. Zhang, "Contactless and continuous monitoring of heart electric activities through clothes on a sleeping bed," *5th Int. Conference on Information Technologyon Biomedical and Health Engineering, IS3BHE 2008 and Applications in Biomedicine, ITAB 2008 in conjunction with 2nd Int. Symposium and Summer School* , pp. 282–285, 2008, doi: 10.1109/ITAB.2008.4570586.

[3] O. P. Singh, A. Bocchino, T. Guillerm, and C. O'mahony, "Design, Fabrication and Performance Assessment of Flexible, Microneedle-Based Electrodes For ECG Signal Monitoring," *Proceedings of the Annual International Conference of the IEEE Engineering in Medicine and Biology Society, EMBS*, vol. 2022-July, pp. 846–849, 2022, doi: 10.1109/EMBC48229.2022.9871073.

[4] M. Zardoshti-Kermani, B. C. Wheeler, K. Badie, and R. M. Hashemi, "EMG Feature Evaluation for Movement Control of Upper Extremity Prostheses," *IEEE Transactions on Rehabilitation Engineering*, vol. 3, no. 4, pp. 324–333, 1995, doi: 10.1109/86.481972.

[5] B. Hudgins, P. Parker, and R. N. Scott, "A new strategy for multifunction myoelectric control," *IEEE Trans Biomed Eng*, vol. 40, no. 1, pp. 82–94, 1993, doi: 10.1109/10.204774.

[6] S. Mishra and M. Bhattacharya, "A combined Feature extraction technique for cancer classification based on deep learning approach," *Proceedings - 2021 IEEE International Conference on Bioinformatics and Biomedicine, BIBM 2021*, pp. 2287–2293, 2021, doi: 10.1109/BIBM52615.2021.9669466.

[7] J. K. Hundal and S. T. Hamde, "Some feature extraction techniques for voice based authentication system," *IEEE International Conference on Power, Control, Signals and Instrumentation Engineering, ICPCSI 2017*, pp. 419–421, Jun. 2018, doi: 10.1109/ICPCSI.2017.8392328.

[8] R. Jain and V. K. Garg, "EMG Classification Using Nature-Inspired Computing and Neural Architecture," *2021 9th International Conference on Reliability, Infocom Technologies and Optimization (Trends and Future Directions), ICRITO 2021*, 2021, doi: 10.1109/ICRITO51393.2021.9596077.

[9] J. Feng, X. Wang, and X. Zhang, "Smart car control system based on EMG signal," *Proceedings of the World Congress on Intelligent Control and Automation (WCICA)*, pp. 1891–1894, 2008, doi: 10.1109/WCICA.2008.4593212.

[10] Y. J. Kim, H. S. Lee, and S. Jung, "Line tracking control of a mobile robot using EMG signals from human hand gestures," *2015 12th International Conference on Ubiquitous Robots and Ambient Intelligence, URAI 2015*, p. 354, Dec. 2015, doi: 10.1109/URAI.2015.7358976.

[11] D. C. S. Manikanta, G. Gowtham, and K. Gantasala, "Implementation of Feature Extraction of Neuro Muscular EMG Signal," *2nd IEEE International Conference on Advanced Technologies in Intelligent Control, Environment, Computing and Communication Engineering, ICATIECE 2022*, 2022, doi: 10.1109/ICATIECE56365.2022.10047002.

[12] Y. Du, W. Jin, W. Wei, Y. Hu, and W. Geng, "Surface EMG-Based Inter-Session Gesture Recognition Enhanced by Deep Domain Adaptation," *Sensors (Basel)*, vol. 17, no. 3, Mar. 2017, doi: 10.3390/S17030458.

[13] W. Geng, Y. Du, W. Jin, W. Wei, Y. Hu, and J. Li, "Gesture recognition by instantaneous surface EMG images," *Scientific Reports 2016 6:1*, vol. 6, no. 1, pp. 1–8, Nov. 2016, doi: 10.1038/srep36571.

[14] E. A. Clancy, E. L. Morin, and R. Merletti, "Sampling, noise-reduction and amplitude estimation issues in surface electromyography," *Journal of Electromyography and Kinesiology*, vol. 12, no. 1, pp.

1–16, Feb. 2002, doi: 10.1016/S1050-6411(01)00033-5.

[15] M. Zecca, S. Micera, M. C. Carrozza, and P. Dario, "Control of multifunctional prosthetic hands by processing the electromyographic signal," *Crit Rev Biomed Eng*, vol. 30, no. 4–6, pp. 459–485, 2002, doi: 10.1615/CRITREVBIOMEDENG.V30.I456.80.

[16] A. Phinyomark, C. Limsakul, and P. Phukpattaranont, "A Novel Feature Extraction for Robust EMG Pattern Recognition," *J Med Eng Technol*, vol. 40, no. 4, pp. 149–154, Dec. 2009, doi: 10.3109/03091902.2016.1153739.

[17] Y. Sevim, "A New Feature Extraction Method for EMG Signals," *Traitement du Signal*, vol. 39, no. 5, pp. 1615–1620, Oct. 2022, doi: 10.18280/TS.390518.

[18] A. Belkhou, A. Achmamad, and A. Jbari, "Classification and diagnosis of myopathy EMG signals using the continuous wavelet transform," *2019 Scientific Meeting on Electrical-Electronics and Biomedical Engineering and Computer Science, EBBT 2019*, Apr. 2019, doi: 10.1109/EBBT.2019.8742051.

Machine Learning-Based Classification of Neonatal Hyperspectral Signatures

M. M. ERGİN[1], M. CİHAN[2] and M. CEYLAN[3]

[1]Konya Technical University, Konya/Turkey, f221222075@ktun.edu.tr
[2]Konya Technical University, Konya/Turkey, mcihan@ktun.edu.tr
[3]Konya Technical University, Konya/Turkey, mceylan@ktun.edu.tr

Abstract **- Hyperspectral Imaging (HSI) is a method that allows for the acquisition of diverse two-dimensional data across a wide spectral range. HSI holds significant importance in the biomedical field due to its non-contact nature and its ability to provide diagnostic information about tissues. In this study, a total of 220 data were collected from neonates using the HSI method. Subsequently, spectral signatures for these data were extracted within a computerized environment. These spectral signatures were then classified using five different machine learning methods: Linear Discriminant Analysis (LDA), Naive Bayes (NB), Support Vector Machine (SVM), K-Nearest Neighbors (KNN), and Tree methods. Following the classification processes, the best results were achieved with LDA, which exhibited accuracy, sensitivity, and specificity rates of 81.81% each.**

Keywords **- Machine Learning, Classification, Neonatal, Hyperspectral Imaging, Signatures.**

I. INTRODUCTION

Remote sensing technologies in the health field make Hyperspectral Imaging (HSI) important because it enables the acquisition of high-dimensional and interrelated data. HSI, also called imaging spectrometry, means measuring the energy reflected from surface materials at many narrow and contiguous wavelengths [1]. The imaging system uses a separate sensor in each spectral band. This allows each pixel to measure the reflected or emitted energy of the object or area at that wavelength. HSI is used in various applications such as biomedical [1-2], biomedicine [3], forensic medicine [4], and crime scene detection [5]. HSI is an imaging method that first emerged for medical applications and has significant potential for medical purposes [6].

HSI is particularly suitable for neonatal studies since neonates have weak immune systems, and minimizing physical contact is essential. According to World Health Organization (WHO) data, 15 million babies worldwide are born yearly before the 37th week of pregnancy [7]. Preterm birth, defined as birth before the 37th week of gestation, is an essential cause of neonatal deaths [8]. Rapid monitoring of the health status of neonates within minutes is critical to prevent high mortality rates in preterm neonates with deficient birth weight and receive care and treatment in Neonatal Intensive Care Unit (NICU) incubators [9].

Machine Learning is a subfield of artificial intelligence focused on learning from data [10]. Data diversity plays a vital role in machine learning as algorithms are trained to identify and predict features in diverse datasets. Furthermore, the choice of algorithm is critical; a better algorithm leads to more accurate predictions [10]. In this study, HSI and machine learning algorithms are used to detect the health status of neonates. Five different machine learning algorithms were employed: Linear Discriminant Analysis (LDA), Naive Bayes (NB), Support Vector Machine (SVM), K-Nearest Neighbors (KNN), and Tree methods.

In this study, hyperspectral data were collected from unhealthy and healthy neonates in a non-contact manner and were classified using machine learning methods. Hyperspectral data of 220 neonates (110 unhealthy and 110 healthy) are available. At first, spectral signatures were extracted from these data, and then spectral signature averages were created. These values classified unhealthy and healthy neonates with different machine learning methods.

II. MATERIAL AND METHOD

This section mentions the definition of HSI, obtaining HSI data from neonates, extracting spectral signatures, and methods used for classification.

A. *Hyperspectral Imaging (HSI)*

HSI sensors capture information from a wide range of electromagnetic spectrum. Some specific things leave a unique "fingerprint" across the electromagnetic spectrum. These fingerprints are known as spectral signatures. A three-dimensional data called a hypercube is obtained with HSI, containing two spatial dimensions and one spectral dimension. When examining the point data (pixels) of the hypercube, spectral signatures on the wavelength intensity scale are obtained [10]. These spectral signatures classify data based on specific spectral characteristics, as done in this study.

B. HSI Data Acquisition and Dataset

Data can be obtained in many areas with a hyperspectral camera. In this study, the imaging system designed by *MS Spektral* was used to obtain HSI data from neonates. It is a system that can acquire HSI data between 480nm and 1100nm wavelengths. The spectral resolution is approximately 0.3nm, resulting in a total of 2018 HSI bands. This system, which receives HSI data with the point scanning technique, is a point spectrometer that can collect light at a distance of 0.5m and at a diameter of 50mm.

This system includes the AFBR-S20M2VN Qmini VIS/NIR-Miniature USB spectrometer developed by BROADCOM. A BaSO4-based white reference panel and a 21V 150W halogen light source were used for measurement calibration.

HSI data from neonates were obtained from unhealthy and healthy babies in the Neonatal Intensive Care Unit (NICU) of Selçuk University, Faculty of Medicine. HSI data were collected under the same conditions using a halogen light source. A total of 220 data were obtained from the body regions of neonates, including respiratory distress syndrome (RDS), coarctation of aorta, pneumothorax, and healthy neonates.

C. Extracting Spectral Signatures from Hyperspectral Data

After data at different wavelengths were taken, they were transferred to the computer environment, and 1538 noise-free bands between 500nm and 1000nm were extracted using MATLAB2022b. First, the data taken in $10\times10\times1538$ volumetric size was taken, then the averages were reduced to $1\times1\times1538$ size and the average signatures were given as input to machine learning. All spectral signatures and their averages for an unhealthy and a healthy neonate are shown in Figure 1.

Spectral signatures of the data were extracted using the spectral values of a pixel under different wavelengths. In Figure 1(a) and Figure 1(c), the spectral signatures for all pixels are visible in the graph on the wavelength intensity scale. In Figure 1(b) and Figure 1(d), the average spectral signature obtained by averaging the spectral signatures of all pixels is given. In this way, hyperspectral data is expressed with a single spectral signature.

D. Machine Learning Algorithms

Average spectra obtained from neonates were classified with five different machine learning methods: Linear Discriminant Analysis (LDA), Naive Bayes (NB), Support Vector Machine (SVM), K-Nearest Neighbors (KNN), and Tree methods. These methods are detailed below.

LDA is a machine learning method that distinguishes different classes in a dataset by reducing the data size and maximizing the differences between types. LDA creates a new plane by decreasing the two-dimensional plane to a single dimension, and this plane can be used for classification, dimensionality reduction, and data feature interpretation [10].

For problems with two classes, LDA's linear discriminant function y(x) is as follows: *A* and *B* are the classes, *x* is the input vector, *w* is the weight of the feature vector, w_0 is the bias value (threshold value), and *C* represents the classification process (1) (2) [11].

$$y(x) = (w^t)x + w0 \tag{1}$$

$$C = \begin{cases} \text{İf } y(x) > 0, x \in A \\ \text{İf } y(x) < 0, \ x \in B \end{cases} \tag{2}$$

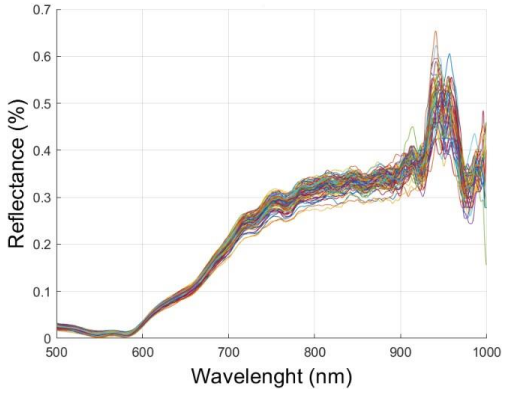

(a)

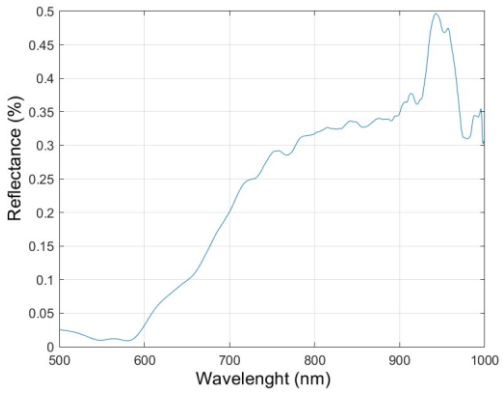

(b)

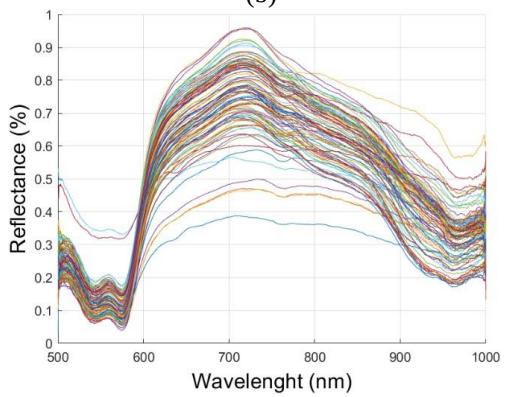

(c)

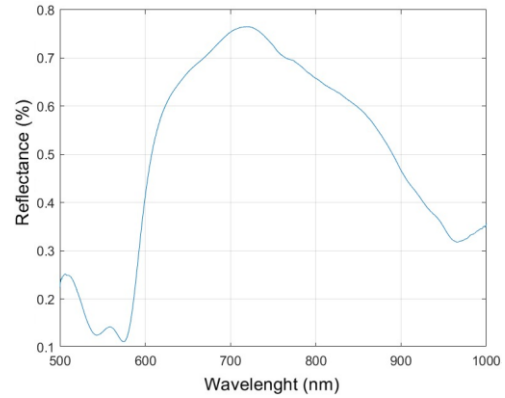

(d)

Figure 1: Spectral signatures. (a) Unhealthy all spectra, (b) Unhealthy average signature of spectra, (c) Healthy all spectra, (d) Healthy average signature of spectra.

NB is a powerful and simple machine learning method that works based on Bayes theorem. NB can be known as the Bayes network since each attribute is conditionally independent of the other, and the concept of discovery is conditionally dependent on the features. It is used to assign a data point to a particular class. NB is a probabilistic approach with a premise that requires each input variable, attribute, or parameter to be statistically independent. It can be used in various classification applications [12].

SVM is a machine learning technique used to distinguish different classes within a dataset. SVM could separate data into two or more classes through linear separation mechanisms in a two-dimensional space, planar separation in a three-dimensional space, and hyperplane separation in a high-dimensional space [13]. It operates by mapping data into a high-dimensional feature space, enabling the categorization of data even when it may not be separable otherwise. A differentiator between categories is found, and subsequently, the data is transformed as the differentiator can be drawn as a hyperplane. The features of new data are utilized for prediction in the classification of incoming data.

KNN is a machine learning method based on the similarities of data. Similarities are calculated using a distance measure such as Euclidean or Manhattan distance. To predict the class of new data, KNN looks at the classes of training data closest to this data point and observes which class is the most common among these training data. KNN, which does not have a complex structure, provides competitive results, and can perform better than more complex learning techniques in some cases [14].

Decision trees have already been successfully used for medical predictions and they seem to be a reliable decision-making technique [15]. The Tree Method is a machine learning method that divides large quantities of data sets into smaller sets by applying simple decision-making steps. This method makes the best decision by listing all options and calculating all possible risks. The Tree Method creates a tree model by dividing the data into branches and leaves from the root node. The branches represent the operations on the features, while the leaves represent the class labels.

III. EXPERIMENTAL RESULTS

In this study, a total of 220 HSI data were used, and the health status of neonates was aimed to be determined by HSI and machine learning methods. The dataset was divided into two classes: 110 unhealthy neonates and 110 healthy neonates.

The data obtained under the same conditions were transferred to the computer environment and hypercubes were created using MATLAB R2022b. Average spectral signatures were extracted by selecting volumetric regions of interest with dimensions of 1x1x1538. Instead of using all the spectral signatures of a neonate, this study uses the average spectral signatures obtained from the body of this neonate. Average spectral signatures were classified using LDA, SVM, NB, KNN, and Tree methods. 70% of the data was used for training and 30% for testing. The 10-fold cross-validation method is used to ensure that all data was used in both training and testing. As a result of the classification, a confusion matrix was created, and values such as accuracy, sensitivity, and specificity were obtained from this matrix. *Sensitivity* is the rate of correctly predicting unhealthy neonates, *Specificity* is the rate of correctly predicting healthy neonates, and *Accuracy* is an indicator of the extent to which unhealthy and healthy data are correctly predicted. The results are shown in Table 1.

Table 1: Classification results.

Method	**Performance Evaluation Criteria (%)**		
	Accuracy	**Sensitivity**	**Specificity**
LDA	**81.81**	**81.81**	81.81
SVM	78.20	70.90	85.50
NB	69.10	47.30	**90.90**
KNN	80.00	72.70	87.30
TREE	67.75	47.25	88.25

Table 1 shows that the best results were obtained using LDA, with an accuracy of 81.81%. The KNN model came in second with an accuracy of 80.00%. The worst results were obtained using the Tree model, with an accuracy of 67.75%. This is because the tree model fails to predict unhealthy data. Besides LDA, SVM and KNN models outperformed other methods in detecting unhealthy neonates, while models like NB and TREE excelled in detecting healthy neonates. LDA provided the most balanced results by effectively detecting both unhealthy and healthy neonates.

IV. CONCLUSION

The obtained results demonstrate that HSI and machine learning methods yield favorable outcomes in neonatal health detection. HSI is particularly suitable for neonatal studies due to its non-contact nature and its ability to provide diagnostic information about tissues.

In this study, five different machine learning algorithms were employed for data classification, with the best results achieved using LDA. It correctly predicted 90 out of 110 unhealthy neonates and 90 out of 110 healthy neonates, resulting in *accuracy*, *sensitivity*, and *specificity* of 81.81%.

Spectral information from neonates at different wavelengths provides important information about the health status of neonates, and using this information, health status can be successfully detected by machine learning algorithms.

ACKNOWLEDGMENT

This study was supported by the Scientific and Technological Research Council of Türkiye (TUBITAK, project number: 122E021).

REFERENCES

[1] G. Lu, and B. Fei, "Medical hyperspectral imaging: a review," *IEEE Journal of Selected Topics in Applied Earth Observations and Remote Sensing*, 19(1), pp. 1-23, 2019.

[2] R. K. Kumrular, and A. Polat, "Advanced Biomedical Imaging Technologies in Clinical Applications," *European Journal of Science and Technology*, (23), pp. 207-221, 2021.
[3] O. Carrasco, R. B. Gomez, A. Chainani, and W. E. Roper, "Hyperspectral imaging applied to medical diagnoses and food safety," proc. SPIE 5097, pp. 215-221, 2023.
[4] R. S. Hatipoglu, S. Canan, and M. Ceylan, "Depending on The Time Of Body Fluids For Criminal Examination Determination of Its Change by Hyperspectral Imaging," *European Journal of Science and Technology*, (Special Issue), pp. 148-153, 2020.
[5] S. Swain, et al. "Hyperspectral Imaging Techniques for Forensic Analysis: A Comprehensive Review," *IEEE Access*, vol. 8, pp. 161358-161376, 2020.
[6] M. Cihan, "Hiperspektral görüntüleme yöntemi kullanılarak yenidoğan sağlık durumlarının derin öğrenme metotları ile sınıflandırılması [Classification of Neonatal Health Conditions using Hyperspectral Imaging Method with Deep Learning Methods] (Master's Thesis)," Department of Electrical and Electronics Engineering, Konya Technical University, Konya, 2020.
[7] S. R. Walani, "Global burden of preterm birth," *International Journal of Gynecology & Obstetrics*, 150(1), pp. 31-33, 2020.
[8] J. E. Lawn, et al. "Every Newborn: progress, priorities, and potential beyond survival," *The Lancet*, 384(9938), pp. 189-205, 2014.
[9] M. Cihan, M. Ceylan, H. Soylu, and M. Konak, "Fast Evaluation of Unhealthy and Healthy Neonates Using Hyperspectral Features on 700-850 Nm Wavelengths, ROI Extraction, and 3D-CNN," *IRBM*, 43(5), pp. 362-371, 2021.
[10] M. Cihan, and M. Ceylan, "Comprasion of Linear Discriminant Analysis, Support Vector Machines and Naive Bayes Methods in the Classification of Neonatal Hyperspectral Signatures," *In 2021 29th Signal Processing and Communications Applications Conference (SIU)*, pp. 1-4, 2021.
[11] B. Çağlıyan, and U. Köse, "Classification of Epilepsy EEG Data by Machine Learning Techniques," *European Journal of Science and Technology*, (23), pp. 163-172, 2021.
[12] K. P. Murphy, "Naive bayes classifiers," *University of British Columbia*, 18(60), pp. 1-8, 2006.
[13] G. Aysun, M. Uysal, and Ö. Doğrusöz, "The effect of parameter optimization of support vector machines on emotion analysis," *Journal of Engineering Sciences of DEU Faculty of Engineering*, 16(48), pp. 86-93, 2014.
[14] D. Kaya, "Classification of Erythmato-Squamous Disease Types by Subspace k-NN," *Fırat University Journal of Engineering Sciences*, 31(2), pp. 583-587, 2019.
[15] A. Albu, "From logical inference to decision trees in medical diagnosis," *In 2017 E-Health and Bioengineering Conference (EHB)*, pp. 65-68, 2017.

Comparison of Different Segmentations in Automated Detection of Hypertension Using Electrocardiography with Empirical Mode Decomposition

Y.E. ERDOĞAN [1, 2], A. NARİN [2] and W. HARIRI [3]

[1] Eregli Iron and Steel Co., Zonguldak, Turkey, yeerdogan@erdemir.com.tr

[2] Electrical and Electronics Engineering Department, Zonguldak Bülent Ecevit University, 67100, Zonguldak, Turkey, alinarin45@gmail.com

[3] Labged Laboratory, Computer Science department, Badji Mokhtar Annaba University, Annaba, Algeria, hariri.walid@hotmail.com

Abstract **Hypertension (HPT) refers to a condition where the pressure exerted on the walls of arteries by blood pumped from the heart to the body reaches levels that can lead to various ailments. Annually, a significant number of lives are lost globally due to diseases linked to HPT. Therefore, the early and accurate diagnosis of HPT is of utmost importance. This study aimed to automatically and with minimal error detect patients suffering from HPT by utilizing electrocardiogram (ECG) signals. The research involved the collection of ECG signals from two distinct groups. These groups consisted of ECG data of both five thousand and ten thousand data points in length, respectively. The performance in HPT detection was evaluated using entropy measurements derived from the 5-layer Intrinsic Mode Function (IMF) signals through the application of the Empirical Mode Decomposition method. The resulting performances were compared based on the nine features extracted from each IMF. To summarize, employing the 5-fold cross-validation technique, the most exceptional accuracy rates achieved were 99.9991% and 99.9989% for ECG data of lengths five thousand and ten thousand, respectively, using decision tree algorithms. These remarkable performance results indicate the potential usefulness of this method in assisting medical professionals to identify individuals with HPT.**

Keywords **- HPT, ECG, Segmentation, Empirical Mode Decomposition, Decision Trees.**

I. INTRODUCTION

Hypertension (high blood pressure) is a health concern characterized by excessive pressure within the arteries [1]. In our country, hypertension affects one in every three adults [2]. If left untreated, hypertension can lead to various health problems and organ damage. Among the root causes of hypertension, hereditary factors and high salt consumption take the lead in research. However, the precise cause of hypertension in most patients remains unknown [3]. Hypertension is a condition that requires careful management; sudden spikes in blood pressure can result in conditions like stroke and even cerebral hemorrhage [4]. Common symptoms of hypertension include headaches, dizziness, shortness of breath, palpitations, chest pain, and vision issues [5]. One prominent diagnostic method for hypertension is monitoring ambulatory blood pressure over a 24-hour period [6]. However, this method may not effectively detect certain forms of hypertension. Therefore, additional measurements such as electrocardiography (ECG) and echocardiography are necessary for hypertension diagnosis. Because hypertension can significantly affect a person's daily life and quality of life, early and accurate diagnosis is critically important. In the scientific literature, there are studies focused on the automatic detection of hypertension using biomedical signal processing and machine learning methods. Khan and colleagues conducted a study to identify individuals with hypertension using pulse plethysmography signals. They performed feature extraction using Empirical Mode Decomposition (EMD) and demonstrated their detection performance using the k-Nearest Neighbors (k-NN) classifier. Engaging the k-NN algorithm, they achieved a remarkable 99.4% accuracy rate [7]. Rajput and colleagues used ECG signals to identify individuals with hypertension. They extracted features using non-linear methods like wavelet entropy and sample entropy, along with the 5-level wavelet transform. They reported performance results using k-NN, Support Vector Machines (SVM), Ensemble Bagged Tree (EBT), and decision tree algorithms. The highest accuracy, 99.95%, was achieved using the EBT algorithm [8]. In another study, Soh and colleagues focused on the automatic detection of hypertension patients using ECG signals. They used Convolutional Neural Network (CNN) models and achieved a remarkable 99.99% accuracy [9]. Poddar and colleagues used heart rate variability (HRV) signals to identify individuals with hypertension. They worked with time domain, frequency domain, and non-linear entropy measurements. Utilizing the DVM algorithm, they achieved a remarkable 100% accuracy rate [10].

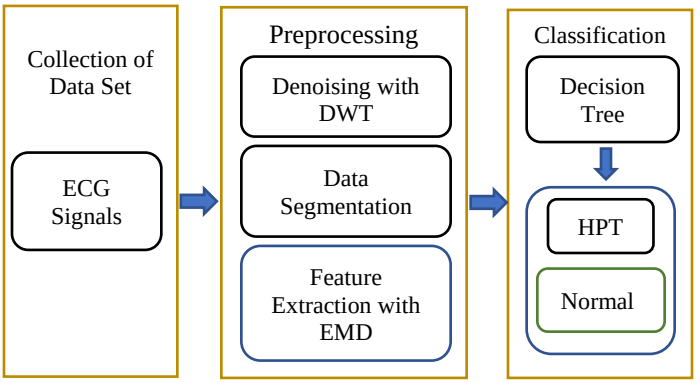

Figure 1: Flow Diagram of the Method Proposed in the Study

In this study, publicly available data obtained free of charge from the Physionet.org website was used to make a healthy comparison with studies in the literature. The data set includes ECG data from two classes: healthy and HPT patients. Unlike other studies, ECG signals were examined with two different approaches. These approaches are respectively; They are 5000 and 10000 length ECG signals. 5-layer Internal Mode Functions (IMF) were obtained using the EMD method for each signal type. Time domain characteristics from each IMF signal included the utilization of standard deviation, mean, and root mean square. Non-linear chaotic assessments encompassed the application of measurements such as Shannon entropy, log energy, threshold, time, norm, and approximate entropy. The flow diagram is given in detail in Figure 1. In the following sections of the study, the adjustment of the data used, the pre-processes applied on the data, the measurements used for feature extraction, classifier illumination, performance demonstrations are mentioned, and the final data, the results obtained and the discussion are included.

II. MATERIAL AND METHODS

A. Dataset

The data on HPT patients and normal individuals given in Table 1 are available on publicly accessible Phsionet.org. The ECG data of HPT patients is taken from the "Smart Health for Assessing the Risk of Events via ECG (SHAREE) database" [11]. HPT treatment consists of 139 ECG data from people aged 55 and over, 49 of whom are women and 90 are men. Running the ECG belonging to the class that can be kept in a normal environment, the "Massachusetts Institute of Technology-Beth Israel Hospital (MIT-BIH) normal sinus rhythm database" data can be run. It consists of 18 ECG signals in total [12]. A recording consists of approximately 24-hour periods. These recordings were sampled with 128 samples with 8-bit images.

Table 1. Data Used in the Study and Their Characteristics

Class	Number of Data	Female	Male	Age Range	Data Length
HPT	139	49	90	46-92	1.000.000
Normal	18	13	5	20-50	1.000.000

The first parts of each HPT signal between 0 and 20000 were excluded from the study because they contained a distorted ECG signal.

B. Noise Elimination with Discrete Wavelet Transform (DWT)

In order to purify the ECG signal from noise, the process of decomposing the noisy signal is started by applying wavelet transform. Thanks to the wavelet transform, it is possible to separate the signal into coefficient groups at different frequency levels. Understanding how the signal behaves in different frequency segments will allow choosing the most appropriate threshold in the next stage. The next step is to determine the best threshold values and eliminate unwanted data by applying threshold values to these coefficients. The last step of the algorithm is to reconstruct the ECG signal using filtered coefficient sets**.**

C. Data Segmentation

In this study, each signal consisting of one 980 thousand long data was divided into ten thousand and five thousand length parts and used, respectively. At the end of this process, data for 1800 healthy and 13622 HPT patients were created for ten thousand length data. Also, data for 3600 healthy and 27244 HPT patients were created for five thousand length data.

D. Empirical Mode Decomposition

EMD stands as a suitable method for examining both stationary and non-linear data sequences, primarily focusing on local-level oscillatory signals [13,14]. Within this algorithm, the Intrinsic Mode Functions (IMFs) serve as the cornerstone. The EMD process commences with the identification of local signal peaks. Once located, these peaks become the foundation for constructing overlapping curves, achieved through 3rd-degree polynomials. Simultaneously, a sub-winding curve is formed based on local signal minima. Subsequently, the mean values of the upper and lower winding curves are computed and subtracted from the original signal, effectively filtering out the low-frequency component. If the resulting signal qualifies as an IMF, the process concludes. However, if it doesn't meet IMF criteria, the algorithm restarts for the new signal. The determination of IMF eligibility hinges on specific conditions. First, the count of zero crossings in the signal should either match or exceed the number of peaks. Secondly, symmetry between the winding curves, established through local minima and maxima, must be satisfied. Time-related attributes extracted from each IMF signal involved the use of standard deviation, mean, and root mean square. The assessment of non-linear, chaotic features involved employing measurements such as Shannon entropy, log energy, threshold, time, norm, and approximate entropy.

E. Decision Trees

A decision tree is composed of nodes and connections. The tree initiates from a node known as the root node, which serves as the starting point and does not have any incoming connections. Nodes leading to other nodes are referred to as internal nodes or decision nodes, while all other nodes are termed as terminal or leaf nodes. Internal nodes segment input data into two or more subsets based on specific discrete functions of the input features. Furthermore, each leaf node can contain a probability vector that represents the likelihood of the target feature having a particular value. Following the determinations made by the internal nodes, data samples are guided through the tree from the root to a leaf node for classification.

F. Performance Metrics

In this study, the outcomes were evaluated utilizing five distinct performance measures [15-18]. These:

$$Accuracy(Acc) = \frac{TP + TN}{TP + FN + FP + TN} \quad (1)$$

$$Recall(Rec) = \frac{TP}{TP + FN} \quad (2)$$

$$Specifity(Spe) = \frac{TN}{TN + FP} \quad (3)$$

$$Precision(Pre) = \frac{TP}{TP + FP} \quad (4)$$

$$F1 - score(F1) = \frac{2 * PRE * REC}{PRE + REC} \quad (5)$$

In the context of classification, TP (True Positives) represents the count of individuals correctly identified as having HPT by the classifier. FN (False Negatives) denotes the count of individuals inaccurately classified as normal when they actually have HPT. TN (True Negatives) represents the count of individuals correctly identified as normal by the classifier when they are indeed normal. Lastly, FP (False Positives) signifies the count of individuals mistakenly labeled as having HPT when, in fact, they do not have the condition [19].

III. EXPERIMENTAL RESULTS

This research study involved the execution of all procedures through MATLAB 2021a software. Subsequently, 45 measures based on Intrinsic Mode Functions (IMF) were derived. The comparison of various segmentations is presented in Table 1. As illustrated in Table 1, the most notable accuracy rate, reaching 99.9991%, was achieved when employing Decision Tree on ECG data with a length of five thousand.

IV.DISCUSSION

The results were compared with 9 time domain and nonlinear measurements obtained from 5 different IMF signals. Results were obtained using two different segmentations. In order to achieve more reliable and stable results, all data were trained and tested with the 5-fold cross-validation method. The performance values found by using the features taken from all IMF measurements for denoised signals are shown in Table 2. In these studies, traditional machine learning approaches are mostly used. From Table 3. Considering the results obtained, Khan et al. applied the Empirical Mode Decomposition (EMD) technique in conjunction with the k-Nearest Neighbors (k-NN) classifier. Their results demonstrated an accuracy of 99.4% as reported in [7]. Rajput et al. used wavelet transform and they achieved 99.95% accuracy by using the method and k-NN, SVM, EBT classifiers. [8]. Soh et al. achieved 99.99% accuracy using CNN and fully connected layer (FCL) [9]. Poddar et al. used time domain measurements and FFT measurements over HRV signals and 100% accuracy value was achieved using the SVM classifier [10]. In this study, each data was increased by dividing it into ten thousand and five thousand length segments. Data obtained without noise used. Observing Figure 2, it becomes evident that 14 individuals in the HPT category were identified erroneously, whereas 27230 were accurately recognized. In contrast, 13 individuals in the normal category were misclassified, while 3587 were correctly identified. With the features obtained from the 5-level IMFs obtained by the EMD method, an accuracy value of 99.9991% was achieved using decision trees algorithms via five thousand (5000) length signals. Additionally, as depicted in Figure 3, it's evident that 7 individuals belonging to the HPT category were mistakenly identified, while 13615 were accurately recognized. Conversely, 9 individuals from the normal category were misclassified, whereas 1791 were correctly identified. With the features obtained from the 5-level IMFs obtained by the EMD method, an accuracy value of 99.9989% was achieved using decision trees algorithms via ten thousand (10000) length signals. From this point of view, it can be understood that if data segmented smaller parts, it will increase the accuracy. Additionally, working with short data eases the computational burden. It is also thought that it will reduce the stress of patients during data collection. It has been shown that it provides more successful results than many similar studies in detecting HPT patients. The most critical parameter limiting this study the data is not distributed evenly. In future studies, without manual feature extraction deep learning methods that take an end-to-end approach in detecting HPT patients is planned to investigate their performance.

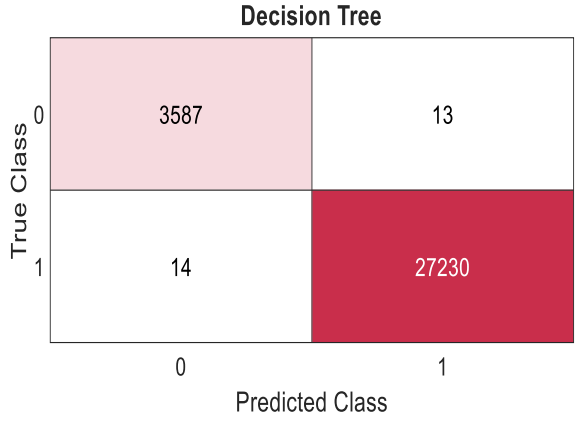

Figure 2. Confusion matrice of the highest performance achieved with DT for 5000 length signal

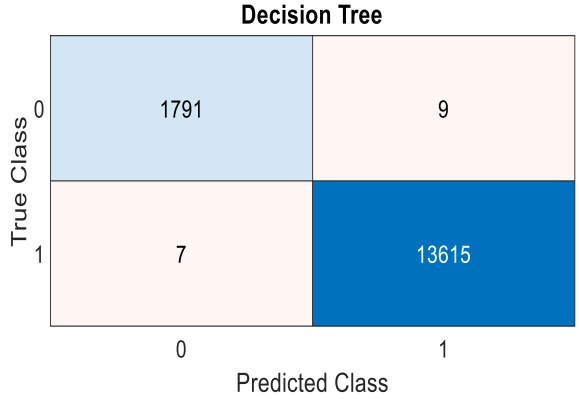

Figure 3. Confusion matrice of the highest performance achieved with DT for 10000 length signal

Table 2: Performance comparison of segmentations for all EMD based features.

Decision Tree	Performances (%)				
	Acc	**Rec**	**Spe**	**Pre**	**F1**
Five thousand Length	99.9991	99.9994	99.6	99.9995	99.9995
Ten thousand Length	99.9989	99.9994	99.5	99.9993	99.9994

Table 3: HPT detection engaging ECG signals in the literature. (Acc, accuracy).

Authors	**Methods and Classifiers**	**Classification**	**Performance (%)**
Khan ve arkadaşları [7]	EMD	k-NN	Acc = 99.4
Rajput ve Ark. [8]	DWT	k-NN, SVM, EBT	Acc=99.95
Soh ve ark. [9]	CNN	FCL	Acc=99.99
Poddar ve ark.[10]	TD and FFT measurements	SVM	Acc=100
This study(5000 length ECG)	**EMD basis features**	**DT**	**Acc=99,9991**
This study(10000 length ECG)	**EMD basis features**	**DT**	**Acc=99,9989**

REFERENCES

[1] Tabassum N., Ahmad F., Role of natural herbs in the treatment of hypertension, Pharm. Rev. 5 (9) (2011) 30–40.

[2] Sarıışık A.,Oğuz A.,Uzunlulu M., Control of hypertension in Turkey is it improving The Kocaeli 2 study Türkiye'de hipertansiyon kontrolü: Düzelme var mı? Kocaeli 2 çalışması M.D. Department of Internal Medicine, Göztepe Training and Research Hospital, İstanbul

[3] Chalmers J. Implementation of guidelines for management of hypertension. Clinical and Experimental Hypertension, 1992, 21:647–657.

[4] Drozdz D.,Kawecka-Jaszcz K., Cardiovascular changes during chronic hypertensive states, Pediatr. Nephrol. 29 (9) (2014) 1507–1516.

[5] Ni H.,Wang Y.,Xu G.,Shao Z.,Zhang W., and Zhou X., "Multiscale Fine-Grained Heart Rate Variability Analysis for Recognizing the Severity of Hypertension," Comput. Math. Methods Med., vol. 2019, 2019, doi: 10.1155/2019/4936179.

[6] Hermida R.C., Smolensky M.H., Ayala D.E., Portaluppi F., Ambulatory Blood Pressure Monitoring (ABPM) as the reference standard for diagnosis of hypertension and assessment of vascular risk in adults, Chronobiol. Int. 32 (10) (2015) 1329–1342.

[7] Khan M.U.,Aziz S.,Akram T.,Amjad F.,Iqtidar K.,Nam Y.,Khan M.A., Expert Hypertension Detection System Featuring Pulse Plethysmograph Signals and Hybrid Feature Selection and ReductionScheme,Sensors,21,2021,1,247,doi:10.3390/s21010247,htGPs ://www.mdpi.com/14248220/21/1/247

[8] Rajput J.S.,Sharma M.,Tan R.S., Acharya UR. Automated detection of severity of hypertension ECG signals using an optimal bi-orthogonal wavelet filter bank. Comput Biol Med. 2020 Aug;123:103924. doi: 10.1016/j.compbiomed.2020.103924. Epub 2020 Jul 23. PMID: 32768053.

[9] Soh D.C.K.,Ng E.Y.K.,Jahmunah V.,Oh S.L.,Tan R.S.,Acharya U.R., Automated diagnostic tool for hypertension using convolutional neural network, Computers in Biology and Medicine,Volume 126,2020,103999,ISSN 0010-4825, htGPs://doi.org/10.1016/j.compbiomed.2020.103999.

[10] Poddar M.G.,Kumar V.,Sharma Y.P.,Linear-nonlinear heart rate variability analysis and SVM based classification of normal and hypertensive subjects, Journal of Electrocardiology,Volume 46, Issue 4,2013,Page e25,ISSN 0022-0736.

[11] Moody G.B., Mark R.G., Goldberger A.L., PhysioNet: physiologic signals, time series and related open source software for basic, clinical, and applied research, Conf. Proc. IEEE Eng. Med. Biol. Soc. 2011 (2011) 8327–8330. Cambridge, MA 20139, USA.

[12] Melillo P., Izzo R., Orrico A., Scala P., Attanasio M., Mirra M., Luca N.D.,Pecchia L., Automatic prediction of cardiovascular and cerebrovascular events using Heart Rate Variability analysis, PloS One (2015). March 20.

[13] Erdogan YE, Narin A. "COVID19 detection with traditional and deep features on cough acoustic signals," Computers in Biology and Medicine, Volume 136, 2021,104765, ISSN 0010-4825, https://doi.org/10.1016/j.compbiomed.2021.104765.

[14] Erdogan YE, Narin A. "Performance of Emprical Mode Decomposition in Automated Detection of Hypertension Using Electrocardiography," 2021 29th Signal Processing and Communications Applications Conference (SIU), 2021, pp. 1-4, doi: 10.1109/SIU53274.2021.9477887.

[15] Narin A., Özer M. and İşler Y., "Effect of linear and non-linear measurements of heart rate variability in prediction of PAF attack," 2017 25th Signal Processing and Communications Applications Conference (SIU), 2017, pp. 1-4, doi: 10.1109/SIU.2017.7960358.

[16] Narin A., "Accurate detection of COVID19 using deep features based on X-Ray images and feature selection methods," Computers in Biology and Medicine,Volume 137,2021,104771,ISSN 0010-4825, https://doi.org/10.1016/j.compbiomed.2021.104771.

[17] Erdoğan, Y. E., & Narin, A. (2022). Comparison of classification algorithms for COVID19 detection using cough acoustic signals. arXiv preprint arXiv:2201.04872.

[18] Erdoğan Y. E., Narin A., "Elektrokardiyografi Yardımıyla Hipertansiyonun Otomatik Belirlenmesinde Ampirik Kip Ayrışımının Gürültülü ve Gürültüsüz Sinyaller Üzerindeki Performansının Karşılaştırılması", El-Cezeri, vol. 9, no. 2, pp. 788-800, May. 2022, doi:10.31202/ecjse.1009456

[19] Erdogan, Y. E., Narin, A. Comparison of COVID-19 Prediction Performances of Normalization Methods on Cough Acoustics Sounds. arXiv preprint arXiv:2201.06078, 2022.

Permanent Magnet Synchronous Motor Design for Rope-Driven Gearless Elevator Machine

A. FENERCIOĞLU[1], D. ATAKAY[2], E. PINARBAŞI[3]

[1]Bursa Technical University, Bursa / Turkiye, ahmet.fenercioglu@btu.edu.tr

[2,3] Emlak Konut Asansör Sistemleri (EKA) A.Ş., İstanbul /Turkiye, dagkan.atakay@emlakkonutasansor.com.tr, emre.pinarbasi@emlakkonutasansor.com.tr

***Abstract* - The new generation gearless machines used in elevators operate with permanent magnet synchronous motors (PMSMs) that provide direct drive without the use of a reducer. These motors can provide high torque at low speeds with their multi-pole structure. Their efficiency is high and torque ripple are low. Since they are driven by an inverter, they provide soft start. Therefore, they offer a comfortable travel. Gearless systems can be connected to the elevator shaft without the need for a machine room. Thus, by providing a more efficient and economical solution, elevator systems allow high speeds for modern buildings and high-rise buildings. This study includes the design verification of a permanent magnet synchronous motor with a power of 6.1 kW for 1000 kg carload and 1 m/s speed by finite element analysis (FEA). Torque ripple, which affects efficiency and passenger comfort, has been optimized. The electrical and mechanical power, efficiency, speed, current, torque and torque ripple, magnetic flux density and current density parameters that determine the output performance of the motor are analysed.**

Key words - Gearless elevator machine, Permanent magnet synchronous motor

I. INTRODUCTION

Electrically driven geared and gearless elevator systems are the most widely used elevator types today. Geared traction elevator machines use asynchronous motors coupled to a reducer. The gears transmit power to the pulley that controls the ropes that provide movement. Their energy efficiency is low due to reducer losses. Machine room is needed in geared elevator systems. In elevators with gearless traction system, permanent magnet synchronous motors transfer power to the pulley and rope. PMSM can provide high torque at low speeds with its multi-pole structure. Gearless systems can be coupled to the elevator shaft without the need for a machine room. This approach provides a more efficient and economical solution, allowing elevator systems to achieve high speeds (>10 m/s) for modern buildings and high-rise buildings [1]. Figure 1 shows an overview of geared and gearless elevator motors and elevator systems with and without machine room. Figure 2 shows pictures of geared and gearless elevator drive machines.

a) b)

Figure 1: a) Geared elevator with machine room and b) Gearless elevator without machine room

a)

b)

Figure 2: Elevator drive machines a) Flow ZF102 geared elevator machine b) Flow SMT-200AC-15 gearless machine

II. PERMANENT MAGNET SYNCHRONOUS MOTOR

Synchronous motors are electric motors in which a magnetic synchronization is achieved between the stator and rotor. PMSMs have permanent magnets instead of the rotor windings found in field wound synchronous motors. Due to the magnetized structure, it is possible to obtain a high pole number in a small volume. Since the stator and rotor work synchronously in, PMSMs, there is no loss in the rotor and it offers higher efficiency. The motor is compact as the magnetized structure increases the power density (W/kg) of the machine. PMSMs for elevator drive systems are widely preferred in industry due to their advantages such as quiet operation, high efficiency, long lifespan, high torque per volume and stable torque-speed characteristics [2-3]

III. ANALYTICAL DESIGN OF THE MOTOR AND FEM ANALYSIS

In order to calculate the mechanical power of the motor, an approximate power calculation was made by considering the requirements and mechanical parameters of the elevator system given below, assuming that half of the car weight is balanced with a counterweight. The mechanical efficiency of the system is taken as 85% and the rope weight is not taken into account [1].

Carrying Capacity (Q) : 1000 kg
Cabin Rated Speed (V_c) : 1.0 m/s
Load Balance : 50%
Hanger Type (A_r) : 2:1
System efficiency (η_s) : %85
Torque (T) : (Nm)
Motor Speed (n_r) : (rpm)
Motor power (P) : (W)
Gravitational acceleration (g): 9.81 m/s^2

According to the given data, the rated speed of the motor is calculated by Eq.1, torque by Eq.2 and motor power by Eq.3 [1].

$$n_r = \frac{60\, V_c A_r}{\pi D_p} \quad (1)$$

$$T = \frac{\frac{Q}{2} g \frac{D}{2}}{A_r \eta_s} \quad (2)$$

$$P = T\omega_r = T\,\frac{2\pi n_r}{60} \quad (3)$$

With these formulas, motor speed was calculated as 159.2 rpm, torque as 346.24 Nm and motor power as 5769.4 W. Taking into account other losses that may occur in the system, the motor power was determined as 6.1 KW. Accordingly, the rated speed of the motor is 160 rpm and the rated torque is 364.2 Nm. The analytical calculation of the PMSM was performed with MATLAB software using equations [3] and output equations obtained from the literature. Preliminary analytical designs were analysed by finite element method and optimizations were performed with genetic algorithm in order to provide high efficiency and comfort parameters.

IV. FEM ANALYSIS (FEA) RESULTS

The 2D magnetic model and network structure used in the finite element analysis are given in Figure 3. Since the designed motor will be used as an elevator carrier motor, especially high comfort is expected. For this reason, a total of 5 degrees of skew is applied to the stator to minimize torque ripple.

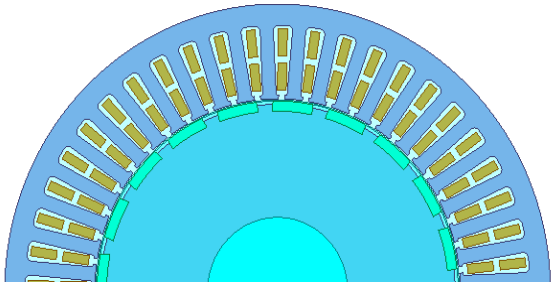

a)

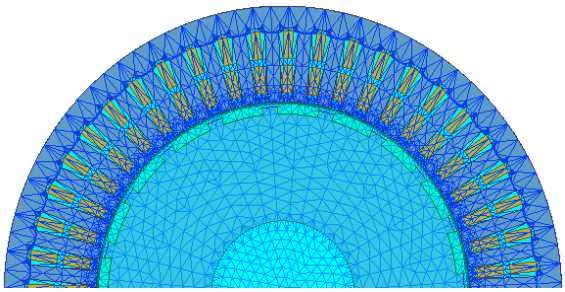

b)

Figure 3: ANSYS Maxwell design model a) 2D representation b) Mesh structure

Figure 4 shows the motor torque graph. The electromagnetic torque produced by the motor is 373 Nm. The load torque taken from the shaft is 364 Nm. The ratio of the peak-to-peak torque value to the average torque in the Electromagnetic

Torque curve is expressed as torque ripple and is calculated as 0.62% according to the analysis results.

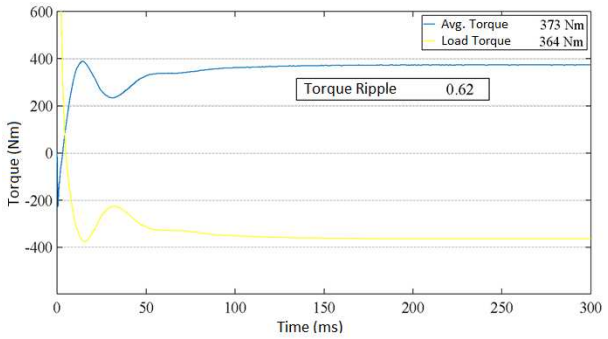

Figure 4: Time-Torque graph

Figure 5 shows the motor phase current graph. The phase current rms value is calculated as 14.88 A.

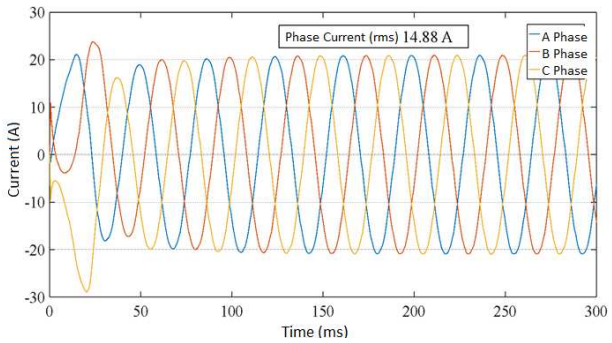

Figure 5: Time-phase current graph

Figure 6 shows the electrical and mechanical power graphs of the motor. The mechanical output power of the motor is 6100 W and the electrical input power is 7400 W. The efficiency of the motor is calculated as 82.4% from the power values.

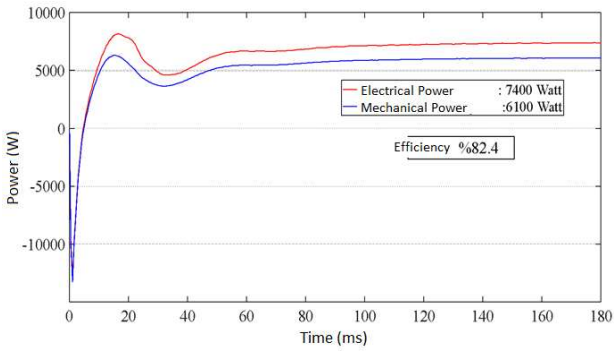

Figure 6: Time-Power current graph

The speed graph of the motor is given in Figure 7. The rated speed of the motor is 160 rpm.

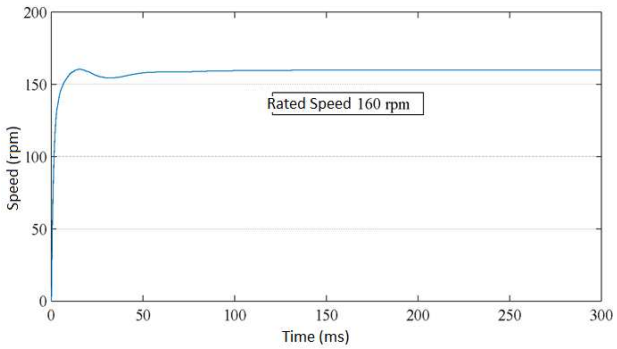

Figure 7: Time-Speed graph

According to the results of the 2D FEA, at 5 degrees of skew, the motor provides a comfortable ride with a peak-to-peak torque ripple of 2.34 Nm (0.62%) at full load. The rated current is calculated as 14.88 A. Motor efficiency is determined as 82.4%. It is determined that the motor settles to synchronous speed in 50 ms time interval. Figure 8 shows the results and values of the electric current density and magnetic flux density of the motor.

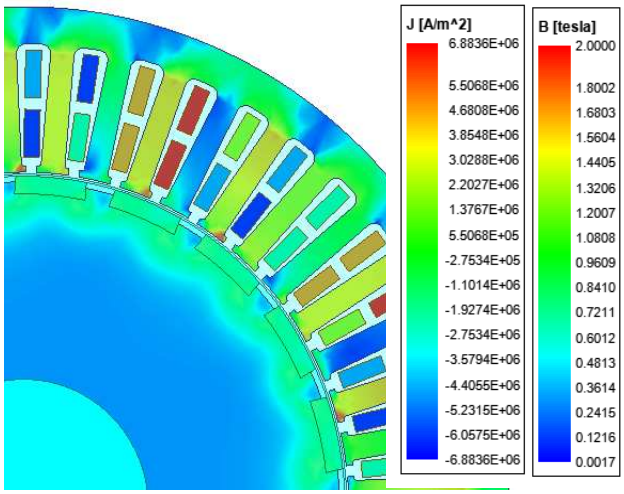

Figure 8: Electric current density (A/m^2) and magnetic flux density (T)

In recent years, gearless elevator machines that produce mechanical power with PMSM are preferred in elevator systems. Since these machines are compact compared to geared machines, they can be installed in the elevator shaft. For this reason, it reduces construction costs as it does not require a machine room. In addition, gear transmission motors reduce gearbox motor efficiency. Since the motor efficiency is high in gearless machines, it reduces energy costs. Gearless machines do not require maintenance because they do not contain gearboxes.

The motor parameters obtained as a result of the analysis are given in Table 1.

Table 1: Motor parameters

Parameter	**Value**	**Unit**
Rotor type	In runner	-
Number of Poles, N_p	20	-
Mechanical Power P_{out}	6100	W
Frequency F	26.66	Hz
Voltage, V	360	V
Rated Angular Speed, ω_m	160	d/d
Rated Phase Current I_{rms}	14.88	A (rms)
Rated Torque, T_R	364	Nm
Slot number, N_{slot}	48	-
Motor Efficiency	82,4	%
Magnet Grade	N35SH	
Connection	Star	-
Winding	Distributed	-
Lamination Steel	M470-50A	-
Stator Outer Diameter, D	315	mm
Stack Length, L	180	mm

V. CONCLUSION

In this study, the electrical and magnetic design of an PMSM with a mechanical power of 6.1 kW for elevator systems with a payload of 1000 kg and a cabin declaration speed of 1 m/s was performed and the design was verified with FEA. In the proposed design, the motor speed is 160 rpm, rated torque is 364 Nm, phase current is 14.88 A and electrical efficiency is 82.4%. The torque ripple of the motor is solved as 0.62%. Thanks to the 5-degree skew applied to the stator, it provides passenger comfort. The current density of the motor was analysed as 6.88 A/mm^2 instantaneously. This value is close to the thermal stress limit of the motor in continuous operation. In general, forced cooling is required above a current density of 6.5 A/mm^2 in the literature. Since the elevator machines operate intermittently in S3 operating mode with 40% duty cycle, there will be no heat problem in the motor. Since the magnetic flux density values are in the range of 1.7-1.8 T, it is seen that the material operates in the efficient region at the near magnetic saturation limit. The motor operates with a 360 V sinusoidal output inverter.

ACKNOWLEDGEMENT

This paper is derived from R&D project is Gearless Elevator Machine Design and Application for Rope Elevator Systems which has carried out at EKA Corporation.

REFERENCES

[1] M., Mıhçılar, "Asansör Makina Hesaplamalarının Önemi ve Zarureti", *Asansör Sempozyumu* 25-27 Eylül 2014 İzmir

[2] H.,Yetis, T.Göktaş, "Comparative Design of Permanent Magnet Synchronous Motors for Low-Power Industrial Applications" *Balkan Journal of Electrial and Computer Engineering,* 2020 Vol.8(3) pp. 218-224

[3] Y. Avşar, "Design and application of permanent magnet synchronous motor with integrated mechanism for belt lift systems" Tokat Gaziosmanpaşa Üniversitesi, Doktora Tezi 2023,

Brain Tumor Segmentation and Classification from MRI Images

A. ÖZÇELİK[1], H. ERKEN[1] , M. BÜYÜKBAŞ[1] , H. AKSEBZECİ[2]

[1] Abdullah Gül University, Electrical - Electronics Engineering, Kayseri/Turkey, alperen.ozcelik@agu.edu.tr
[1]Abdullah Gül University, Electrical - Electronics Engineering, Kayseri/Turkey, hasanhuseyin.erken@agu.edu.tr
[1] Abdullah Gül University, Electrical - Electronics Engineering, Kayseri/Turkey, mahmut.buyukbas@agu.edu.tr
[2]Abdullah Gül University, Biomedical Engineering, Kayseri/Turkey, hakan.aksebzeci@agu.edu.tr

***Abstract* - Brain tumors are crucial to human health as they can lead to severe disabilities or even life-threatening consequences. Brain tumors consist of two types benign and malignant. Glioma is a benign tumor whereas, meningioma and pituitary are malignant tumors. Magnetic Resonance Imaging (MRI) is a valuable tool for detecting brain tumors due to its ability to provide detailed images of the brain's structures and abnormalities. This study aims to improve and facilitate the brain tumor detection process from MRI images. To improve the precision and efficiency of brain tumor diagnosis, this study focuses on the use of image processing techniques and machine learning algorithms. Different classification methods were applied to classify brain MRI images into 4 classes (glioma, meningioma, pituitary and no tumor). The Random Forest method provided the best classification accuracy of 96.32%.**

***Keywords* - Brain tumor, MRI, image segmentation, image classification, machine learning.**

I. INTRODUCTION

Magnetic resonance imaging (MRI) is a non-invasive imaging technique that provides images of the inside organs and tissues of the body by using strong magnetic fields and radio waves [1,2]. Due to its outstanding capacity to record high-resolution images of soft tissues, MRI is often used in the medical profession, especially for brain imaging. In the context of brain tumor, MRI is extremely important to effectively detecting and classifying tumors. [3]. The size, extent, and connection of the tumor to adjacent brain structures may all be discovered with an MRI, which also reveals the tumor's location and size. That is why the usage of MRI plays a crucial role in the early diagnosis of brain tumor disease.

An abnormal development of cells within the brain or the central nervous system is referred to as a brain tumor [4]. It happens when there is uncontrolled cell division and multiplication, which causes a mass or tumor to develop [5]. Brain tumors come in both benign and malignant varieties, and they can develop inside the brain or spread from other regions of the body. More than 120 different tumor forms have been classified as benign or malignant categories [6]. One of the examples of malignant brain tumors is Glioma. A glioma is a tumor that develops as a result of uncontrolled glial cell growth. Normally, these cells assist the central nervous system in functioning by supporting nerves. Although they can develop in the spinal cord, gliomas often develop in the brain. Despite gliomas are cancerous, some of them might develop extremely slowly. Glioma tumors are primary brain tumors, which means that the brain is where they develop. Although gliomas typically only affect the brain or spine, they can expand into other parts of the brain. This situation makes it difficult to access them surgically and creates a life-threatening hazard. Moreover, in adults Glioma is the most frequent seen primary intracerebral tumors [7]. Some of the examples of benign brain tumors are meningioma and pituitary. Meningioma tumors are developed in the meninges that protect the brain and spinal cord. These tumors usually grow slowly. Pituitary tumors are developed in pituitary gland cells and do not spread to other organs of the body. These tumors can be categorized according to the type of hormone-producing cells.

Brain tumor detection from MRI images is still performed manually by physicians. Due to the problems arising from the complex structure of the human brain, it takes a long time to detect the tumor. In this study, brain tumor types are detected from MRI images using image processing techniques and classification algorithms. In the image processing part, image filtering, segmentation and feature extraction methods were applied to obtain quantitative data from the region of interest (ROI). In the classification part, a feature selection method was applied to the extracted features and then various machine learning algorithms were used to determine the tumor type.

II. DATASET

In this study "Brain Tumor MRI Dataset" was used [8]. There are four classes within this dataset: Glioma, Meningioma, Pituitary, and No Tumor. The dataset contains a total of 3264 images, and Table 1 displays the distribution of images according to the classes. Figure 1 shows sample brain MRI images from the dataset.

Table 1: Image distribution by tumor class.

Tumor Type	Number of Images
Glioma	926
Meningioma	937
Pituitary	901
No Tumor	500
Total	**3264**

III. METHODOLOGY

The first step is application of image pre-processing. For this purpose, some image pre-processing methods are executed such as image resizing, grayscale imaging, Gaussian Filtering, Morphological operations, and Contrast Limited Adaptive Histogram Equalization (CLAHE). After that, image segmentation process is applied to determine tumor region which is the ROI. Following the image segmentation step, 71 essential image features are extracted to run the classification algorithms. Histogram-based features, Shape features, Local Binary Pattern (LBP) features, Scale-Invariant Feature Transform (SIFT) features

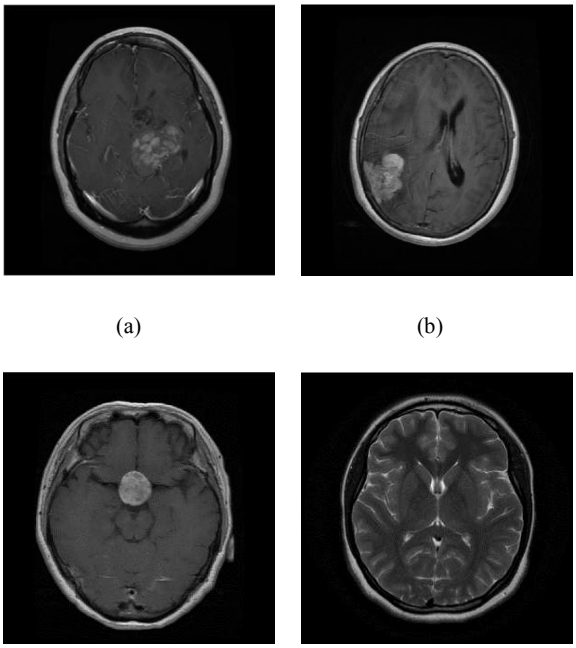

(a) (b)

(c) (d)

Figure 1: Brain MRI examples: (a) Glioma tumor, (b) Meningioma tumor, (c) Pituitary tumor, and (d) no tumor.

are some of these extracted image features. In the next step, correlation-based feature selection is applied. The final step of the project procedures is classification and performance evaluation. The applied classification algorithms are Random Forest, Decision Tree, Logistic Regression, K-Nearest Neighbor (KNN), Naïve Bayes and Support Vector Machine (SVM). The results of these algorithms have been evaluated through various classifier performance metrics. The methodology followed in this study is shown as a flowchart in Figure 2.

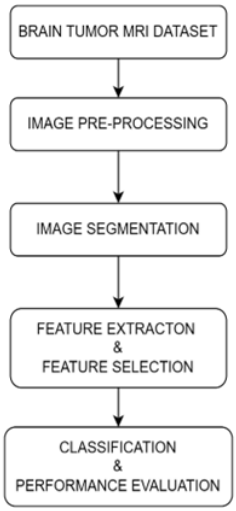

Figure 2: Flowchart of the methodology.

A. *Image Pre-processing*

The fundamental objective of image pre-processing is to improve the overall image quality, eliminate undesired artifacts or noise, and make the images more appropriate for further analysis. The utilized image pre-processing methods are explained below.

1)Gaussian Filtering

The use of a Gaussian filter on MR images helps to highlight important features, enhance the image quality, and minimize noise. It also makes it easier to do further analysis activities, including segmentation or feature extraction. In addition, it is essential for preparing MR images so that they are more suited for precise interpretation, diagnosis, and quantitative analysis. Thus, 5x5 Gaussian Filter is applied to all images in dataset. Figure 3b shows the Glioma tumor with Gaussian filter applied.

2)Morphological Operations

MR images are sensitive to noise for a variety of reasons, including equipment constraints or patient movement. by removing imperfections and enhancing the edges of objects of interest, morphological processes like erosion and opening can assist to minimize noise. In addition, Mohsin et al. proposed that morphological operations has an important positive effect on removal of skull [9]. In this project, Morphological Operations are exerted on the dataset images. Firstly, small noisy spots are removed via erosion procedure. Then images are returned to their original shape by applying the dilation procedure. These applied procedures are similar to the proposed procedures by Roslan et al. [10]. Figure 3c shows a glioma tumor after morphologic operations applied.

3)Contrast Limited Adaptive Histogram Equalization (CLAHE) Filter

Maragatham et. al. asserts that an image enhancement method called CLAHE is used to increase the contrast and visibility of digital images [11]. CLAHE is used to create a more even and improved image, it divides the image into smaller sections, computes the histogram of each zone, and redistributes the pixel intensities within each subpart. The

goal of CLAHE is to increase the visual quality and details of images, especially when there are notable contrast differences between various sections of the image. Figure 3d shows a glioma tumor after applying the CLAHE filter.

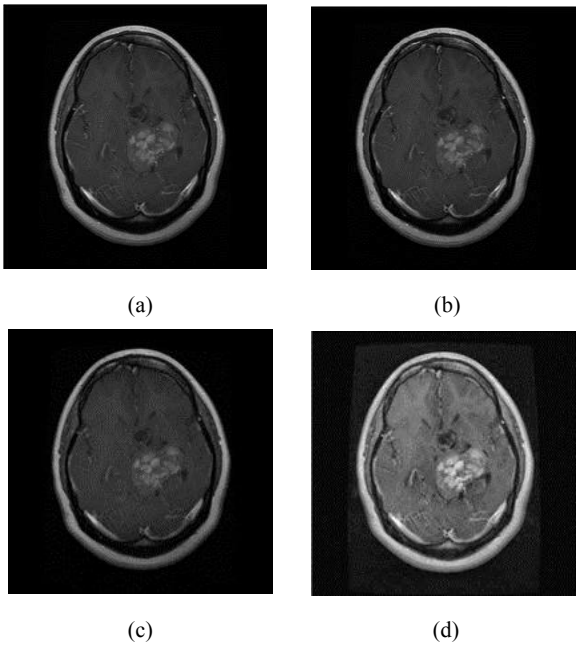

(a) (b)

(c) (d)

Figure 3: Glioma tumor MRI images: (a) original image, (b) Gaussian filtered, (c) after morphological operations, (d) CLAHE filtered.

B. Image Segmentation

For the segmentation part, the Otsu thresholding method was used. This method is widely preferred in the literature [12,13]. Main goal was to extract tumor regions, which are ROIs, from pre-processed brain tumor MRI images. In order to execute this segmentation process, firstly, Otsu's thresholding method is applied to all pre-processed images for image binarization. After that the opening operation is applied on acquired binary images to eliminate noise, soften curves, and distinguish connected objects. Then, connected component analysis is exerted and each connected component is labeled to determine the maximum component area which helps to segment brain. Image segmentation of a pituitary tumor is shown in Figure 4. The tumor region is obtained by using thresholding method.

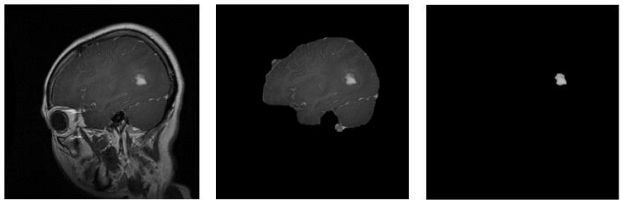

(a) (b) (c)

Figure 4: Pituitary tumor MRI images: (a) original image, (b) skull removed image, (c) tumor segmented image.

C. Feature Extraction and Feature Selection

Feature extraction mainly a process which converts large image input data into low dimensional feature vector [14-16]. For classification and diagnostic applications, extracted features can be used to train machine learning or pattern recognition algorithms. The algorithms can more reliably differentiate between various tumor kinds, forecast tumor aggressiveness, or assist in treatment planning by choosing the most informative aspects. The derived features aid more accurate and objective decision-making in the context of brain tumor diagnosis and prognosis by providing useful quantitative evaluations. For this purpose, 71 features are extracted for each image. These extracted features can be classified under 6 methods which are Intensity Statistics, Intensity-related features, Histogram-based features, Shape features, Local Binary Pattern (LBP) features, Scale-Invariant Feature Transform (SIFT) features. Extracted feature list is given in Table 2.

Table 2: Extracted features.

Features	Number of Features
Intensity Statistics	15
Intensity-related	8
Histogram-based	5
Shape	11
LBP	18
SIFT	14
Total	**71**

For feature selection, the main goal is to determine which features are strongly correlated with the 4 different types of tumor classes which are glioma, meningioma, pituitary, no-tumor. In order to select optimum features, correlation-based feature selection method is utilized. A method for selecting features from a dataset that have a significant correlation or relationship with the target variable is called correlation-based feature selection. In this method, each feature's correlation with the target variable is measured, and the features with the greatest correlation values are chosen. This method aids in lowering the dimensionality of the dataset by eliminating duplicate or unnecessary features and concentrating on those that are most useful or predictive for the target variable. This approach tries to increase the effectiveness and precision of subsequent data analysis or machine learning activities by choosing characteristics based on their correlation. As a result of this method, correlation matrix and correlation heatmap is obtained. Then, correlation coefficients of features are sorted in descending order. Finally, the features which have 0.1 and more correlation coefficient are selected, and other features are removed.

D. Classification and Performance Evaluation

In classification and performance evaluation part of this study, two steps are carried out. First step is classification methods. In this part, different types of classification methods are applied to determine which is suitable for the Brain Tumor MRI Dataset. Second step is performance evaluation, all the applied classification models are

compared according to their accuracy, precision, recall, and F1 score metrics.

The goal of classification is to accurately predict the label for a collection of input data using supervised machine learning. In this research, in order to classify four classes of the dataset, Random Forest, Decision Tree, Logistic Regression, K-Nearest Neighbor (KNN), Naive Bayes and Support Vector Machine (SVM) methods are utilized.

Random Forest is an effective machine learning algorithm which provides accurate predictions or classifications with the help of a collection of decision trees. When it is compared to the individual decision trees, this method's accuracy and resilience are improved since it synthesizes the results of several different trees to provide a final prediction.

Decision Tree algorithm is a machine learning technique that bases choices or predictions on input information on a tree-like structure. To come up with a decision, the algorithm divides the data into branches and makes decisions at each node.

Logistic Regression is a statistical machine learning algorithm. By computing the weighted sum of input characteristics and using a sigmoid function to convert the result into a probability value, it determines the probability that an input will belong to one class. For tasks like spam identification, disease diagnosis, and credit scoring, it adjusts its settings to minimize a loss function.

KNN uses the similarity of a new data point's k nearest neighbors in the training dataset to predict the class or value of that new data point. It does not make any assumptions about the distribution of the underlying data and it is utilized for both classification and regression tasks.

Naïve Bayes is a quick and straightforward machine learning approach for classification tasks. The algorithm determines the likelihood of each class based on the feature values and predicts that the features are independent of one another. The class with the highest likelihood is then chosen as the predicted class.

Support Vector Machine (SVM) is a supervised machine learning algorithm used for classification and regression tasks. Primary goal of SVM is to find the optimal hyperplane that best separates data points into different classes.

For classifier performance evaluation, the main goal is to obtain several metrics to evaluate model performances. These metrics are accuracy, precision, recall and F1 score.

IV. RESULTS

Before classification algorithms are applied, the dataset has been randomly divided into a training (80%) and a testing (20%) set. Classification algorithms were compared using performance evaluation metrics. The results based on the these metrics are shown in Table 3. The confusion matrix of Random Forest classifier is shown in Figure 5.

In addition to the comparison table of machine learning algorithms Receiver Operating Characteristic (ROC) curves and Area Under Curve (AUC) of each classification algorithm is obtained. ROC is a plot which illustrates the link between a binary classification model's true positive rate and false positive rate. The area under the ROC curve is frequently used as a statistic to assess the general quality of the model. In addition, The ROC curves of Random Forrest classifier are given in Figure 6. Since the dataset has multiple classes, one-vs-all method is utilized to acquire ROC curve and AUC for each class. According to the ROC curve it can be said that for class 1, which is Meningioma tumor, the algorithm classified it successfully. Moreover, for class 0, which is Glioma tumor, the algorithm showed the least performance in classification it with 0.95 AUC score. In addition, class 2 is pituitary tumor and class 3 is no tumor.

Table 3: Performance comparison of machine learning algorithms.

Algorithm	Accuracy	Precision	Recall	F1 Score
Random Forest	0.9632	0.9543	0.9638	0.9583
Decision Tree	0.9326	0.9232	0.9253	0.9240
Logistic Regression	0.8024	0.7933	0.7849	0.7885
KNN*	0.7917	0.7915	0.7800	0.7845
Naïve Bayes	0.7764	0.7649	0.7675	0.7657
SVM **	0.6814	0.6989	0.6690	0.6668

* $k = 5$
** Kernel function: Radial basis function

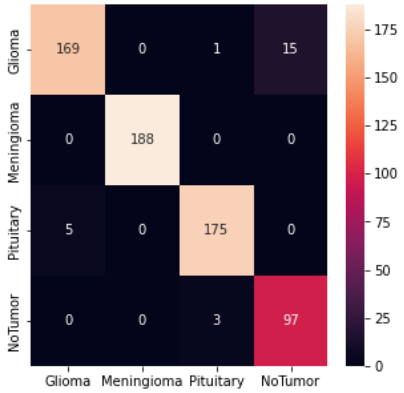

Figure 5: Confusion matrix of Random Forest classifier.

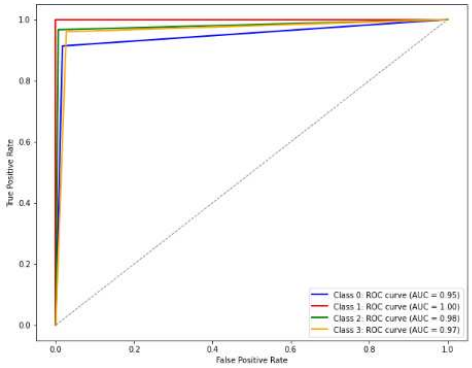

Figure 6: ROC curves of Random Forest classifier.

V. CONCLUSION

In this study, image processing techniques and machine learning algorithms are utilized to detect and classify brain tumor types in the dataset. The results reveal that for this dataset and extracted features, Random Forest and Decision Tree algorithms have the best performances with an accuracy of higher than 90%. Also, it is observed that as the number of extracted features is increased, the obtained performance results of all classifiers improved. This proves that image processing techniques have a crucial impact on the success of this research. Additionally, ROC curves and AUC scores indicate the effectiveness of classification algorithms on the dataset. For example, Random Forest classification algorithm has the highest AUC scores for classes. Therefore, Random Forest is the most effective machine learning algorithm for this dataset.

This research enhances the current understanding of brain tumor classification and detection through the use of MRI images. These developments might have a significant impact on medicine, especially it can help to more accurate diagnosis and treatment for brain tumors. Additionally, to ensure the model's robustness across various datasets, further analysis and validation are necessary.

REFERENCES

[1] Kasban, H. (2015). A comparative study of medical imaging techniques. *ResearchGate*. https://www.researchgate.net/publication/274641835_A_Comparative_Study_of_Medical_Imaging_Techniques

[2] Ṣiddiqi, M. Z., Alsayat, A., Alhwaiti, Y., Azad, M., Alruwaili, M., Alanazi, S., Kamruzzaman, M. M., & Khan, A. (2022). A precise medical imaging approach for brain MRI image classification. *Computational Intelligence and Neuroscience*, *2022*, 1–15. https://doi.org/10.1155/2022/6447769

[3] Tomasila, G., & Emanuel, A. W. R. (2020). MRI image processing method on brain tumors: A review. *Nucleation and Atmospheric Aerosols*. https://doi.org/10.1063/5.0030978

[4] Seetha, J., & Raja, S. S. (2018). Brain tumor classification using convolutional neural networks. Biomedical and Pharmacology Journal, 11(3), 1457–1461. https://doi.org/10.13005/bpj/1511

[5] Pichaivel, M., Anbumani, G., Panneerselvam, T., & Gopal, M. (2022). An overview of brain tumor. In *IntechOpen eBooks*. https://doi.org/10.5772/intechopen.100806

[6] Nasor, M., & Obaid, W. (2020). Detection and Localization of Early-Stage Multiple Brain Tumors Using a Hybrid Technique of Patch-Based Processing, k-means Clustering and Object Counting. International Journal of Biomedical Imaging, 2020, 1–9. https://doi.org/10.1155/2020/9035096

[7] Rasmussen, B. K., Hansen, S., Laursen, R. J., Kosteljanetz, M., Schultz, H., Nørgård, B. M., Guldberg, R., & Gradel, K. O. (2017). Epidemiology of glioma: clinical characteristics, symptoms, and predictors of glioma patients grade I–IV in the the Danish Neuro-Oncology Registry. *Journal of Neuro-oncology*, *135*(3), 571–579. https://doi.org/10.1007/s11060-017-2607-5

[8] Sartaj Bhuvaji, Ankita Kadam, Prajakta Bhumkar, Sameer Dedge, & Swati Kanchan. (2020). Brain Tumor Classification (MRI) [Data set]. Kaggle. https://doi.org/10.34740/KAGGLE/DSV/1183165

[9] Mohsin, S., Sajjad, S., Malik, Z. K., & Abdullah, A. H. (2012). Efficient Way of Skull Stripping in MRI to Detect Brain Tumor by Applying Morphological Operations, after Detection of False Background. *International Journal of Information and Education Technology*, 335–337. https://doi.org/10.7763/ijiet.2012.v2.145

[10] R. Roslan, N. Jamil, and R. Mahmud, ―Skull stripping of MRI brain images using mathematical morphology,‖ Proc. 2010 IEEE EMBS Conf. Biomed. Eng. Sci. IECBES 2010, no. December, pp. 26–31, 2010.

[11] Maragatham, G., & Roomi, S. M. M. (2015). A review of image contrast enhancement methods and techniques. *Research Journal of Applied Sciences, Engineering and Technology*, *9*(5), 309–326. https://doi.org/10.19026/rjaset.9.1409

[12] Bindu, H. (2009). An improved medical image segmentation algorithm using OTSU Method. *ResearchGate*. https://www.researchgate.net/publication/229048987_An_improved_medical_image_segmentation_algorithm_using_OTSU_Method

[13] Jardim, S., António, J., & De Mora, C. (2023). Image thresholding approaches for medical image segmentation - short literature review. *Procedia Computer Science*, *219*, 1485–1492. https://doi.org/10.1016/j.procs.2023.01.439

[14] Kumari, S., & Rani, K. U. (2020). Analysis on various feature extraction methods for medical image classification. In *Learning and analytics in intelligent systems* (pp. 19–31). https://doi.org/10.1007/978-3-030-46943-6_3

[15] Sharma, R., & Abrol, P. (2020). Image feature extraction techniques. *ResearchGate*. https://www.researchgate.net/publication/350975404_Image_feature_extraction_techniques

[16] M.Vasantha, Bharathi, Dr.V.Subbiah, & S.Dhamodharan. (2010). Medical Image Feature, Extraction, Selection And Classification. *ResearchGate*. https://www.researchgate.net/publication/50281851_Medical_Image_Feature_Extraction_Selection_And_Classification

Agrivoltaic Systems: Combining Food and Energy Production

M. S. ENDİZ[1]

[1] Necmettin Erbakan University, Konya/Turkey, msendiz@erbakan.edu.tr

Abstract **- The worldwide use of photovoltaic (PV) energy, a prominent renewable energy source, has significantly increased in recent years due to its numerous benefits. PV energy generation requires a significant land area. Agrivoltaic (AV) systems, which integrate agricultural and electricity production by placing solar modules several meters above the ground, are gaining popularity in renewable energy and farming sectors. The purpose of this study is to investigate AV systems for widespread adoption. The concept, opportunities, challenges, and real applications of AV systems around the world are explained. The optimal integration of AV systems will both meet the growing energy demands and enhance agricultural productivity.**

Keywords **- Agrivoltaic, solar power generation, agriculture, electricity production.**

I. INTRODUCTION

Renewable energy sources, primarily derived from the sun and readily available, are consistently replenished by natural processes. These sources do not emit greenhouse gases or contribute to air pollution [1]. As the global population continues to rise, efforts are made to meet the fast-expanding demand for energy by developing various forms of renewable energy. Solar photovoltaic (PV) energy is a prominent renewable energy source that significantly contributes to global electricity generation. Recent advances in PV technology have made it possible to harness a massive, clean, and sustainable energy source to provide the electrical needs of modern society. However, the installation of PV systems requires a substantial land area [2, 3].

Although PV modules can convert sunshine into electricity, the land on which they are installed is useless for farming. The continued construction of large-scale PV systems has raised worries about the diversion of farmland in different countries toward economical PV energy generation [4].

The rapid growth of the global population has led to an increase in energy demand, while climate change has had a detrimental impact on agricultural production. Increasing temperatures have a significant negative impact on agricultural yields, leading to the proliferation of weeds and pests in farmland. Therefore, the optimal utilization of agricultural lands is becoming increasingly significant. PV technology has been employed in agriculture for an extended period to provide sustainable electricity for agricultural production[5].

Agrivoltaic (AV) systems were first proposed more than three decades ago and they combine agricultural and photovoltaic activities on the same land [6]. Multiple studies have highlighted the fundamental principles that form the basis of these systems [7]. A recent study has shown that AV systems have the potential to enhance land productivity by allowing the simultaneous use of land for both agricultural purposes and energy generation. Increased productivity can greatly affect the financial status of rural communities [8].

A research indicates that solar power installations could potentially occupy 5-10% of the total land area. Besides, this study examines the ideal conditions and site factors for the installation of solar modules on agricultural land [9]. Another study examines the climate resilience of AV systems. These systems can mitigate water loss through transpiration and improve crop resilience to climate variability by offering shade during hot periods [10]. The suitability of various crops for cultivation in areas with partial shade resulting from the presence of solar modules is conducted. The study emphasizes the need to ensure crop-module compatibility while designing AV systems [11]. A research investigation has revealed that these systems have a significant role in facilitating the development of sustainable energy, hence assisting in the mitigation of greenhouse gas emissions [12]. The water efficiency of AV systems and how it relates to the cooling of solar modules are examined. This efficiency enhances overall sustainability [13].

Another study focuses on the benefits to biodiversity and soil health provided by AV systems. These systems can improve soil quality and encourage biodiversity by shading the ground and lowering temperatures [14]. According to a study, energy generation and agriculture systems have the potential to offer additional income opportunities for farmers, thereby making them a viable option for rural development [15]. The primary challenge lies in concurrently generating energy and cultivating crops while mitigating potential conflicts. There are numerous commercial AV plants and small-scale research facilities already operational in different parts of the world. Vegetables with lush greens like lettuce, cabbage, and spinach, and vegetables with tubers like potatoes, carrots, radishes, and beets, benefit greatly from this kind of cultivation. According to a study, this method can increase product efficiency by as much as 70% [16].

II. AGRIVOLTAIC SYSTEMS AND OPPORTUNITIES

Population growth from the turn of the twentieth century

has increased agricultural consumption per person. To meet increasing consumption demands, it is necessary to enhance agricultural production and technologies. In 1982, German researchers Goetzberger and Zastrow proposed the concept of an AV system to realize the simultaneous use of farmlands for PV energy generation and plant growth as shown in Figure 1. AV systems, which integrate agriculture and solar power generation, have gained considerable interest in recent times.

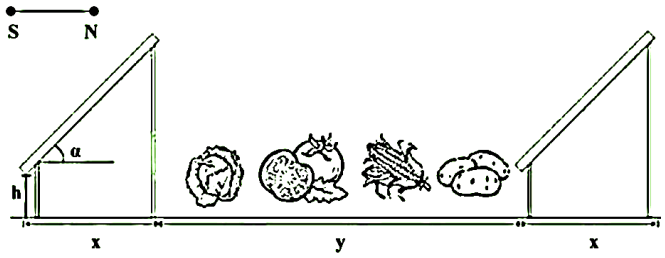

Figure 1: Concept design of an AV system.

In Figure 1, x denotes the horizontal projection of PV (in meters), y represents the distance between rows of PV arrays (in meters), α represents the tilt angle (in degrees), and h represents the height (in meters) of steel structures. The idea of AV system, which at first gained little attention, eventually became quite popular. Especially in desert places where water, energy, and food supplies are scarce, the major goal of the AV system is to generate electricity while producing plants in the same area.

Despite being proposed over 30 years ago, it took some time for the term "agrivoltaics" to be developed and for the full benefits of this technology to be recognized. Growing crops and solar modules on the same area of land is an example of AV, which is the practice of combining agriculture with renewable energy production.

To allow farm machinery to reach the crops below, the solar modules are mounted a few meters from the ground on solid support systems. Farming machinery requires suitable height and spacing of steel structures to navigate between PV rows. In AV systems, the standard spacing between PV array rows is typically 5-10 meters. The purpose of creating a gap between rows is to prevent PV shadows from affecting the adjacent row. This gap should be designed to optimize crop harvesting.

The opportunities of AV systems are outlined as follows: It increases land productivity based on mutual common use, it has a positive effect on the module efficiency and some kind of crops due to the shade effect, and maximizes the use of solar energy. By employing the same area for both energy generation and cultivation, AV systems maximize land usage resulting in increased productivity per unit of land.

The presence of solar modules, which offer partial shadowing, may lead to positive results for crops. The use of this measure serves to decrease the rate of evaporation, regulate temperature levels, and mitigate the impact of severe weather phenomena. These factors have the potential to result in enhanced agricultural productivity and superior crop characteristics. The use of solar modules to provide shade can effectively mitigate water evaporation in arid or hot climates. This can provide significant benefits for crops that require high water consumption and help decrease the overall dependence on irrigation. AV systems can help keep the power grid stable by making solar energy on or near the place where it is used. This is especially important in rural or remote places where the power grid is not stable. AV systems have the potential to incorporate indigenous flora and vegetation that can attract pollinators, including bees and butterflies. This contributes to the preservation of local biodiversity and can have positive effects on neighboring crops by enhancing the process of pollination. Crops can help keep solar modules clean by preventing dust and other debris from building up on them. This could lower the costs of cleaning and keeping the solar system. AV systems help reduce greenhouse gas emissions by producing sustainable electricity and keeping carbon on farmland. AV systems can assist farmers in diversifying their income by providing them with a constant source of energy profits. AV projects can be more appealing to farmers and investors if governments and regulatory authorities offer incentives and support for them. Feed-in tariffs, grants, and tax breaks are all examples of possible incentives for renewable energy production. AV systems are an emerging area of study that holds potential for advancements in solar technology and agricultural practices. Ongoing research and experimentation in this field can contribute to innovation and improvements. The long-term benefits of this can be advantageous for both industries.

Figure 2 shows the scheme of an AV system where the microclimate effect arises in the immediate area of the PV modules integrated with agricultural land.

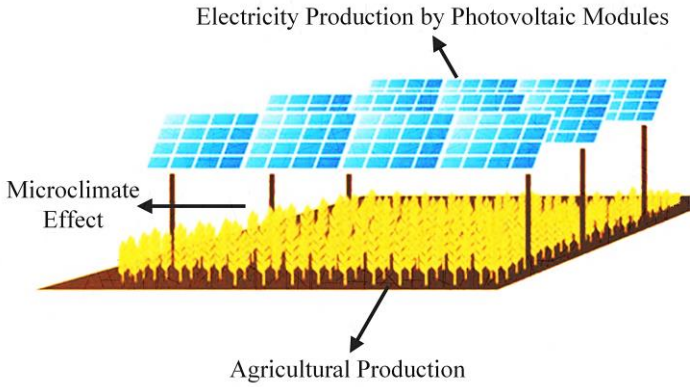

Figure 2: Scheme of an AV system.

III. CHALLENGES OF AGRIVOLTAIC SYSTEMS

AV systems have several advantages, but they also have certain drawbacks. Some farmers may be hesitant to take advantage of AV technology due to the high cost of setting up the system. Besides, the integration of these systems requires diligent management to optimize crop health and solar module efficiency.

Regular maintenance and monitoring are essential. Certain crops may not be well-suited for integration into AV systems due to their inability to grow successfully in the partial shade cast by the solar modules. The selection of crops and the

subsequent planning are very important. For farmers to properly deploy and maintain these systems, they need to have a fundamental understanding of both agricultural and solar technology.

IV. Real applications of Agrivoltaic systems

AV systems are becoming increasingly accepted globally as a sustainable and unique method for simultaneously harvesting solar energy and enhancing agricultural output. Swiss farmers have integrated AV systems, which involve a combination of solar modules and dairy farming. The installation of modules offers shade to the cows, enhancing their comfort and milk production, while simultaneously generating renewable energy for the farm.

AV systems are increasingly popular in Germany. Solar modules are installed above crops such as barley and wheat, creating a land-use approach that optimizes agricultural and energy output.

Large-scale AV fish farming initiatives have been designed and implemented in China. The modules' shading effect reduces the temperature of the water in fishponds, making the area more suitable for fish farming. With this method, farmers can collect solar energy during food production.

AV systems have been installed in Australia's arid regions to lessen the country's reliance on imported water for agriculture. These devices protect vital water supplies and sustain agriculture in harsh environments by shading crops and lowering the amount of water evaporating.

AV systems have been implemented in multiple states across the United States. The University of Massachusetts Amherst initiated a research project that integrates solar modules with crops such as berries and vegetables. The Solar Power and Agricultural Resilience (SPAR) project in Colorado aims to optimize land use efficiency by combining agriculture and solar energy generation.

Japan has implemented AV projects due to its limited land availability. The Solar Sharing project in Kyoto is a notable example of raising solar panels above crops, such as soybeans and vegetables, to enhance sunlight exposure and increase crop yields.

France has played a leading role in the development and implementation of AV systems, with a particular focus on wine-growing regions. Solar panels have been installed on frames in vineyards to provide shade for grapevines, thereby regulating sunlight exposure and improving the quality of grapes. These systems have the dual benefit of decreasing energy expenses and enhancing the aroma and flavor of the wine.

V. Conclusion

Integrating solar modules into farming has many benefits, including minimizing the effects of global warming and increasing both food and energy production. AV systems are a potentially useful solution to the problems of inefficient land use, clean energy generation production, and sustainable agriculture. Although there are obstacles, AV systems are appealing because of their potential benefits, such as higher agricultural yields, lower emissions, and more revenue diversification. AV systems could contribute significantly to a future that is more robust and sustainable as awareness and technology become more advanced.

Policymakers could lower the initial investment barrier for AV systems by offering financial incentives and subsidies. Farmers should receive training and technical assistance from government authorities. In this context, there should be support for promoting research on appropriate crop combinations and system designs. It is necessary to raise awareness of the environmental and economic benefits of AV systems. Therefore, AV systems are of utmost significance and have the potential to contribute to a more sustainable world by addressing economic, agricultural, and environmental challenges.

References

[1] A. Olabi and M. A. Abdelkareem, "Renewable energy and climate change," *Renewable and Sustainable Energy Reviews*, vol. 158, p. 112111, 2022.

[2] M. S. Guney, "Solar power and application methods," *Renewable and Sustainable Energy Reviews*, vol. 57, pp. 776-785, 2016.

[3] E. Kabir, P. Kumar, S. Kumar, A. A. Adelodun, and K.-H. Kim, "Solar energy: Potential and future prospects," *Renewable and Sustainable Energy Reviews*, vol. 82, pp. 894-900, 2018.

[4] F. Mancini and B. Nastasi, "Solar energy data analytics: PV deployment and land use," *Energies*, vol. 13, no. 2, p. 417, 2020.

[5] A. Yano and M. Cossu, "Energy sustainable greenhouse crop cultivation using photovoltaic technologies," *Renewable and Sustainable Energy Reviews*, vol. 109, pp. 116-137, 2019.

[6] A. Goetzberger and A. Zastrow, "On the coexistence of solar-energy conversion and plant cultivation," *International Journal of Solar Energy*, vol. 1, no. 1, pp. 55-69, 1982.

[7] A. E. Coşgun, "The potential of Agrivoltaic systems in TURKEY," *Energy Reports*, vol. 7, pp. 105-111, 2021.

[8] M. A. Al Mamun, P. Dargusch, D. Wadley, N. A. Zulkarnain, and A. A. Aziz, "A review of research on agrivoltaic systems," *Renewable and Sustainable Energy Reviews*, vol. 161, p. 112351, 2022.

[9] S. Amaducci, X. Yin, and M. Colauzzi, "Agrivoltaic systems to optimise land use for electric energy production," *Applied energy*, vol. 220, pp. 545-561, 2018.

[10] G. A. Barron-Gafford *et al.*, "Agrivoltaics provide mutual benefits across the food–energy–water nexus in drylands," *Nature Sustainability*, vol. 2, no. 9, pp. 848-855, 2019.

[11] H. Marrou, L. Guilioni, L. Dufour, C. Dupraz, and J. Wery, "Microclimate under agrivoltaic systems: Is crop growth rate affected in the partial shade of solar panels?," *Agricultural and Forest Meteorology*, vol. 177, pp. 117-132, 2013.

[12] H. Dinesh and J. M. Pearce, "The potential of agrivoltaic systems," *Renewable and Sustainable Energy Reviews*, vol. 54, pp. 299-308, 2016.

[13] E. Hassanpour Adeh, J. S. Selker, and C. W. Higgins, "Remarkable agrivoltaic influence on soil moisture, micrometeorology and water-use efficiency," *PloS one*, vol. 13, no. 11, p. e0203256, 2018.

[14] E. J. Nordberg, M. J. Caley, and L. Schwarzkopf, "Designing solar farms for synergistic commercial and conservation outcomes," *Solar Energy*, vol. 228, pp. 586-593, 2021.

[15] R. Mahto, D. Sharma, R. John, and C. Putcha, "Agrivoltaics: A climate-smart agriculture approach for Indian farmers," *Land*, vol. 10, no. 11, p. 1277, 2021.

[16] C. Dupraz, H. Marrou, G. Talbot, L. Dufour, A. Nogier, and Y. Ferard, "Combining solar photovoltaic panels and food crops for optimising land use: Towards new agrivoltaic schemes," *Renewable energy*, vol. 36, no. 10, pp. 2725-2732, 2011.

Characteristics of Foam Concrete with Capric Acid/Diatomite Composite

S. ASLANTAŞ[1*] and A. YARAŞ[1]

[1*] Bartin University, Bartın/Turkey, sultanaslantas@gmail.com
[1]Bartin University, Bartın/Turkey, aliyaras@bartin.edu.tr

***Abstract* – In this investigation, porous diatomite (DA) utilized as a support material was directly impregnated with capric acid (CA), a phase change material. Leakage experiments showed that DA could adsorb up to 50% of CA by mass. The prepared CA/DA composites were incorporated into foam concrete at three different rates (15, 20 and 25% by weight). Foam concrete specimens with CA/DA were examined for physical characteristics (porosity and water absorption) and compressive strength. Porosity and water absorption rose in comparison to reference sample, but mechanical performance dropped. For foam concrete with 25% CA/DA, the values for porosity, water absorption and compressive strength were 31.5%, 22.6%, and 8.93 MPa, respectively.**

***Keywords* – Phase change material, diatomite, foam concrete, porosity, compressive strength.**

I. INTRODUCTION

The concern about global warming is intensifying across globe, reaching a level where it is becoming a threat to human existence. Primary contributors to this adverse climate change are harmful emissions, predominantly CO_2 [1]. The building sector particularly has played a substantial role in the increase of global energy usage and the release of greenhouse gases. Consequently, technologies for thermal energy storage (TES) are gaining traction due to their potential in enhancing energy efficiency in buildings. Given their ability to store a significant amount of energy in slight temperature variations, phase change materials (PCMs) focused on latent heat storage are widely endorsed among various thermal storage solutions. PCM stands out as an optimal choice for boosting energy efficiency in structures and tailoring indoor climates [2].

PCMs are substances that possess significant latent heat of fusion and distinct melting points. They are categorized into three main types: organic, inorganic, and eutectic mixtures[3]. When environmental temperature exceeds the melting point, triggering a solid-to-liquid phase shift, PCM consumes heat and transitions to its liquid form. Conversely, when temperature descends below solidification threshold, PCM releases the stored energy and solidifies. Organic PCMs exhibit various advantageous properties, such as suitable phase transition temperatures, commendable latent heat, non-toxic nature, excellent thermal resilience, and chemical consistency. Nevertheless, during solid-liquid phase shift, they encounter leakage problems which impede their thermal energy storage potential. To counter this, composite PCMs that prevent leakage can be crafted by embedding PCM within a harmonious support matrix[4].

Foam concrete (FC) is a type of cellular concrete classified as lightweight concrete, with densities ranging from 400–1850 kg/m^3, featuring randomly distributed air pockets created by blending a foaming agent into mortar mixture. Broadly, foam concrete belongs to a category of lightweight concrete characterized by a markedly decreased density and a pronounced level of porosity, primarily utilized as insulating composite substances. However, it is understood that such foams cannot hold a significant quantum of thermal energy, serving predominantly for insulation[5].

To bolster the thermal capabilities of FCs, PCMs are employed. However, integrating PCM into FC presents challenges, notably the issue of leakage. Existing studies have addressed this leakage concern by leveraging porous waste substances rich in silica and having a distinct surface area[6]. Diatomite (DA), which predominantly consists of silica, is characterized by its porosity, light volumetric weight, flexible structure, insulating properties, and robust porosity[7].These traits make it valuable for applications in soil stabilization, civil engineering, and sustainable energy. Additionally, it acts as an effective medium to combat leakage challenges associated with PCM and offers cost-effective alternatives in building materials industry[2].

In this study, DA served as support material and CA as PCM. DA/CA composites were formed by direct impregnation method. Aggregate was replaced with three different ratios of DA/CA composites mixed into foam concrete. Porosity, water absorption and compressive strength tests of the produced foam concretes with DA/CA were carried out.

II. MATERIALS METHODS

A. Raw Materials

CA was of analytical grade and was obtained from Sigma. DA was purchased from a commercial company. Sand and cement were supplied from cement factory in Bartın. The foaming agent was purchased from a commercial company.

B. Preparation of foam concrete composites with CA/DA

After solid CA was melted at the appropriate temperature, DA was impregnated. Direct impregnation technique was used to prepare CA/DA composites. As a result of leakage tests, it was

determined that DA could absorb a maximum of 50% of CA without leakage. Then, CA/DA composites with 50% CA content were prepared. CA/DA composites were used as a substitute for aggregate in foam concrete at three different ratios (15, 20 and 25% by weight). Also, a reference foam concrete sample without CA/DA composite was produced for comparison.

III. RESULTS AND DISCUSSIONS

A. *Porosity and water absorption*

The findings presented in Figure 1 indicate a tendency for both water absorption and porosity to increase in comparison to the reference. Values for porosity and water absorption range from 20.8-31.5% to 12.5-22.6%, respectively. For the foamed concrete sample containing 15% CA/DA, porosity and water absorption increased by 51.4% and 80.8%, respectively, in comparison to the reference. Here, the high water absorption capacity of DA increases the absorption of water in the medium. The absorbed water is released during the hydration of the concrete sample, increasing the apparent porosity value[8].

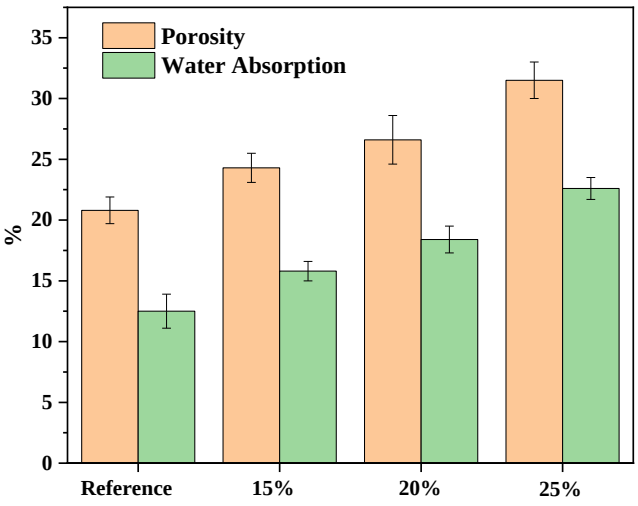

Figure 1: Porosity and water absorption results

B. *Compressive Strength*

Figure 2 displays the compressive strength findings following a 28-day curing period. As a result, when quartz was substituted with CA/DA composite, the compressive strength reduced. The maximum 55.43% reduction (8.93 MPa) in compressive strength was seen at 25% CA/DA content when compared to reference (16.11 MPa). The fact that diatomite has a lower specific gravity than quartz could be the cause of this reduction. Furthermore, porosity and water absorption results coincides with compressive strength measurements. Numerous researchers have previously published similar findings in the literature [9,10].

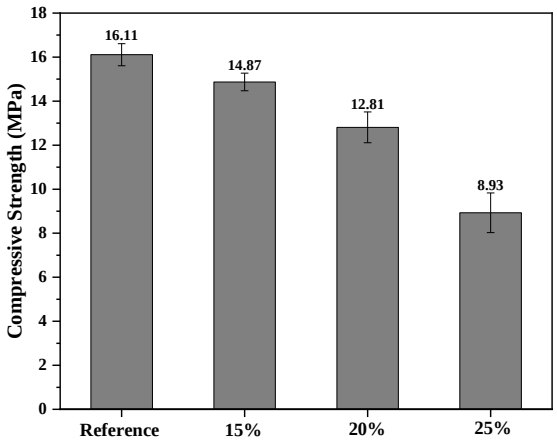

Figure 2: Results of compressive strength of specimens

IV. CONCLUSION

The applicability of DA as a PCM support material in foam concrete was investigated in this work. According to experimental results, the prepared CA/DA composites are compatible with foam concrete, and following can be stated;

- Using the direct impregnation method, CA was incorporated into the DA body. It was determined that the rate of CA without leakage was 50% by mass.
- Both apparent porosity and water absorption have a tendency to rise in comparison to the reference. This may be attributed to the porous structure of diatomite.
- As the percentage of CA/DA composite increased, compressive strength reduced.

For further studies, it is planned to produce building materials by incorporating DA into different structures such as gypsum using different PCMs and to analyze their thermoregulation performances.

ACKNOWLEDGMENT

This study was produced from Sultan ASLANTAS's master's thesis.

REFERENCES

[1] Cunha S, Silva M, Aguiar J. "Behavior of cementitious mortars with direct incorporation of non-encapsulated phase change material after severe temperature exposure", *Constr Build Mater*, vol. 230, 2020.

[2] Gencel O, Sarı A, Kaplan G, Ustaoglu A, Hekimoğlu G, Bayraktar OY, et al. "Properties of eco-friendly foam concrete containing PCM impregnated rice husk ash for thermal management of buildings", *Journal of Building Engineering*, vol. 58, 2022.

[3] Baetens R, Jelle BP, Gustavsen A. "Phase change materials for building applications", *Energy Build*, vol.42, 2010.

[4] Kong X, Lu S, Li Y, Huang J, Liu S. "Numerical study on the thermal performance of building wall and roof incorporating phase change material panel for passive cooling application", *Energy Build*, vol. 81, pp. 404-15, 2014.

[5] Gencel O, Nodehi M, Hekimoğlu G, Ustaoğlu A, Sarı A, Kaplan G, et al. " Foam Concrete Produced with Recycled Concrete Powder and Phase Change Materials ", *Sustainability*, vol. 81, 2022.

[6] Chen J, Ling Z, Fang X, Zhang Z. "Experimental and numerical investigation of form-stable dodecane/hydrophobic fumed silica composite phase change materials for cold energy storage" , *Energy Convers Manag*, vol. 105, pp. 817-25, 2015.

[7] Pınarcı İ, "Pomza ve Diatomitin Yüzey Özelliklerinin Portland Çimentosunun Fiziksel ve Mekanik Özelliklerine Etkisi", vol. 8(3), pp. 1385-1394, 2021.

[8] Cunha S, Silva M, Aguiar J. "Behavior of cementitious mortars with direct incorporation of non-encapsulated phase change material after severe temperature exposure", *Constr Build Mater*, vol. 230, 2020.

[9] Kizhakkumodom Venkatanarayanan H, Rangaraju PR. "Effect of grinding of low-carbon rice husk ash on the microstructure and performance properties of blended cement concret", *Cem Concr Compos*, vol. 55, pp. 348-63, 2015.

[10] Wi S, Yang S, Park JH, Chang SJ, Kim S. "Climatic cycling assessment of red clay/perlite and vermiculite composite PCM for improving thermal inertia in buildings", *Build Environ*, vol.167, 2020.

Foam Concretes Containing Capric Acid/Expanded Perlite Composite: Physico-Mechanical Properties

Z. YUKSEL[1*] and A. YARAŞ[1]

[1*] Bartin University, Bartın/Turkey, yukselzeliha1901@gmail.com
[1]Bartin University, Bartın/Turkey, aliyaras@bartin.edu.tr

***Abstract* – The aim of this study is to investigate the usability of capric acid (CA)/expanded perlite (EP) composites replace aggregate in foam concrete production. For this purpose, firstly, CA/EP composites that absorb the highest amount of CA (58%) without leakage were prepared. In foam concrete mixture, the produced CA/EP composites were added at ratios of 15, 20, and 25% by weight. Using Archimedes method, water absorption and porosity characteristics of foam concrete specimens were determined. Porosity and water absorption values rose together with CA/EP content. In the presence of 25% CA/EP, porosity and water absorption values rose by 69.7% and 98.4%, respectively, in comparison to reference sample. A decrease in compressive strength was also observed and the lowest compressive strength was measured as 5.39 MPa for 25% CA/EP content.**

***Keywords* – Expanded perlite, capric acid, foam concrete, physico-mechanical properties.**

I. INTRODUCTION

Buildings are now considered to have a significant impact on greenhouse gas emissions and energy usage [1,2]. Because heating, cooling and air conditioning systems are used effectively to improve the thermal comfort of people living in buildings. Furthermore, it is inevitable that the need for energy would rise in the upcoming years due to the growing population and the corresponding requirement for shelter [3,4]. For all these reasons, researchers have focused on studies on efficient use of energy and reducing greenhouse gas emissions. Thermal energy storage systems (TES) are one of the many methods for using energy in buildings efficiently [5].

Since phase change materials (PCM) absorb and release heat during the phase change, they are useful for controlling ambient temperature. PCMs nowadays using several processes like vacuuming, impregnation, and microcapsule, it is frequently utilized to improve the thermal performance of building materials. There are many studies in the literature on the use of PCMs in building materials [6–8]. One of these building materials is foam concrete. It is a lightweight, air-gap-containing material with thermal insulation qualities [9]. A foaming agent is needed for the production of foam concrete [10]. The issue of leaking is the main drawback of utilizing PCM in foamed concrete [11]. In this context, porous materials are preferred both for high absorption of PCM and for solving the leakage problem [12]. For this purpose, the use of expanded perlite (EP), which is naturally porous, can be successful. A porous, low-density substance known as EP is produced by rapidly heating raw perlite to a temperature of between 750 and 1100 ˚C. When raw perlite grain is expanded, it increases approximately 10-30 times in volume [13]. Since the density of perlite is quite low compared to other building materials (cement, aggregate, etc.), it plays an important role in both reducing the load in buildings and improving the thermal properties of the produced material. It can be used with binding-property aggregates or pozzolanic materials, particularly in the construction sector to create high-performance lightweight concretes [14].

In this study, CA/EP composites were prepared using the direct impregnation method. Then, the prepared CA/EP composites were incorporated into foam concrete at different rates (15, 20 and 25%), mechanical and physical properties of the samples were examined.

II. MATERIALS METHODS

A. Raw Materials

In this study, expanded perlite (EP) used as support material was purchased from a commercial company. Capric acid (CA) was of analytical purity and was obtained from Sigma. Sand and cement were supplied from cement factory in Bartın. The foaming agent was purchased from a commercial company.

B. Preparation of EP/CA composites

Initially, solid CA was melted at roughly 50˚C, which is its melting temperature. Subsequently, EP body was directly impregnated with various ratios (50, 55, 58, 60, and 65% by weight). Following leakage test, EP was found to be able to absorb up to 58% of CA without leaking.

C. Production of foam concrete with CA/EP composite

For foam concrete production, the water/foam mixture was first prepared and foamed with a mechanical mixer. CA/EP composites at three different rates (15, 20 and 25%) were incorporated to the resulting foam, replacing sand. After addition of cement, mixture was stirred with a mechanical mixer for 5 minutes to ensure a homogeneous mixture. The prepared mixtures were poured into molds and dried for 1 day, then left to cure in a water bath at room temperature for 28 days.

III. RESULTS AND DISCUSSIONS

A. Porosity and water absorption

Porosity is one of the key factors that influences the technical qualities of construction materials. In this investigation, porosity ranged from 21.5 to 36.5% (Figure 1). Compared to the control sample, porosity increased by approximately 70% in the presence of 25% CA/EP composite. This illustrates how EP functions as a porous agent inside the foam concrete. Similar outcomes were previously attained with PCM-impregnated porous materials [15].

It is well known that porosity and water absorption are directly correlated. This is in fact confirmed by the findings in Figure 1. Water absorption value of the control sample was 13.1%, however with 25% CA/EP content, it increased by almost 100%. Because pores in EP have a detrimental effect on the closed packing of concrete, this rise can be explained.

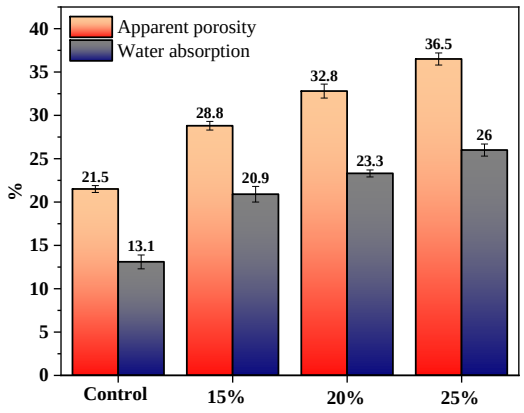

Figure 1: Results of apparent porosity and water absorption

B. Compressive Strength

Figure 2 illustrates how the compressive strength decreases with the addition of CA/EP composite. Compressive strength of foam concrete with 15, 20, and 25% CA/EP was found to be 42.9, 56.3, and 67.2% lower than that of the control, respectively. Undoubtedly, this is closely related to porosity. The greater the porosity, the lower the compressive strength. As a result, because the CA/EP composites inside the foam concrete are unable to offer enough resistance against crack propagation, the load-carrying capacity (compressive strength) drops. Similar results in terms of mechanical performance have been observed in previous studies [15].

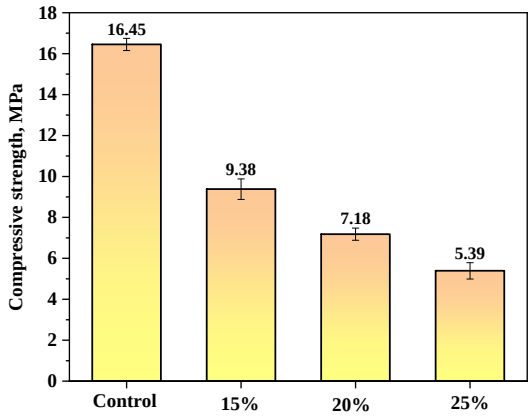

Figure 2: Compressive strength values of specimens

IV. CONCLUSION

Within the scope of this study, a new CA/EP composite was synthesized, incorporated into foam concrete at different rates, and its mechanical and physical properties were characterized. Experimental findings can be summarized as follows;

- The highest CA impregnation rate in CA/EP composite was found to be 58% by mass.
- Porosity of foam concrete exhibited an increasing trend with the incorporation of CA/EP composite.
- Compressive strength was found to have significantly decreased as a result of the increased porosity, however water absorption rose.

ACKNOWLEDGMENT

This study was produced from Zeliha YUKSEL's master's thesis.

REFERENCES

[1] Yang L, Jin X, Zhang Y, Du K. "Recent development on heat transfer and various applications of phase-change materials", *J Clean Prod*, vol. 287, pp. 124432, 2021.

[2] Konuklu Y, Ostry M, Paksoy HO, Charvat P. "Review on using microencapsulated phase change materials (PCM) in building applications", *Energy Build*, vol. 106, pp. 134–55, 2015.

[3] Ürge-Vorsatz D, Cabeza LF, Serrano S, Barreneche C, Petrichenko K. "Heating and cooling energy trends and drivers in buildings", *Renew Sustain Energy Rev*, vol. 41, pp. 85–98, 2015.

[4] Zingre KT, Yang E-H, Wan MP. "Dynamic thermal performance of inclined double-skin roof: Modeling and experimental investigation", *Energy*, vol. 133, pp. 900–12, 2017.

[5] Li Q, Ju Z, Wang Z, Ma L, Jiang W, Li D, et al.

"Thermal performance and economy of PCM foamed cement walls for buildings in different climate zones", *Energy Build*, vol. 277, pp. 112470, 2022.

[6] Castell A, Farid MM. "Experimental validation of a methodology to assess PCM effectiveness in cooling building envelopes passively", *Energy Build*, vol. 81, pp. 59–71, 2014.

[7] Eddhahak-Ouni A, Drissi S, Colin J, Neji J, Care S. "Experimental and multi-scale analysis of the thermal properties of Portland cement concretes embedded with microencapsulated Phase Change Materials (PCMs)", *Appl Therm Eng*, vol. 64, pp. 32–9, 2014.

[8] Yaras A, Ustaoglu A, Gencel O, Sarı A, Hekimoğlu G, Sutcu M, et al. "Characteristics, energy saving and carbon emission reduction potential of gypsum wallboard containing phase change material", J *Energy Storage*, vol. 55, pp. 105685, 2022.

[9] Thongtha A, Khongthon A, Boonsri T, Hoy-Yen C. "Thermal effectiveness enhancement of autoclaved aerated concrete wall with PCM-contained conical holes to reduce the cooling load", *Materials (Basel)*, vol. 12, pp. 2170, 2019.

[10] Gencel O, Oguz M, Gholampour A, Ozbakkaloglu T. "Recycling waste concretes as fine aggregate and fly ash as binder in production of thermal insulating foam concretes", *J Build Eng*, vol. 38, pp. 102232, 2021.

[11] Cui H, Tang W, Qin Q, Xing F, Liao W, Wen H. "Development of structural-functional integrated energy storage concrete with innovative macro-encapsulated PCM by hollow steel ball", *Appl Energy*, vol. 185, pp. 107–18, 2017.

[12] Chen J, Ling Z, Fang X, Zhang Z. "Experimental and numerical investigation of form-stable dodecane/hydrophobic fumed silica composite phase change materials for cold energy storage", *Energy Convers Manag*, vol. 105, pp. 817–25, 2015.

[13] Uluer O, Karaağaç İ, Aktaş M, Durmuş G, Ağbulut Ü, Khanlari A, et al. "Genleştirilmiş perlitin ısı yalıtım teknolojilerinde kullanılabilirliğinin incelenmesi", *Pamukkale Üniversitesi Mühendislik Bilim Derg*, vol. 24, pp. 36–42, 2018.

[14] Türkmen İ, Kantarcı A. "Effects of expanded perlite aggregate and different curing conditions on the physical and mechanical properties of self-compacting concrete", *Build Environ*, vol. 42, pp. 2378–83, 2007.

[15] Al-Absi ZA, Hafizal MIM, Ismail M, Awang H, Al-Shwaiter A. "Properties of PCM-based composites developed for the exterior finishes of building walls", *Case Stud Constr Mater*, vol. 16, pp. e00960, 2022.

Statistical Analysis of Hardness of High Density Polyethylene Composites

E. AYDIN[1*], A. YARAŞ[1], B. DEMİREL[2] , B.KURSUNCU[1]

[1*] Bartin University, Bartın/Turkey, ecmaydn27584 @gmail.com
[1]Bartin University, Bartın/Turkey, aliyaras@bartin.edu.tr
[2]Erciyes University, Kayseri/Turkey, bilaldemirel@erciyes.edu.tr
[1]Bartin University, Bartın/Turkey, bkursuncu@bartin.edu.tr

***Abstract* – Within the scope of this study, high density polyethylene (HDPE) composites were prepared by using various additives (ethylene vinyl acetate (EVA), graphite and calcite) and cross-linker (maleic anhydride) at different rates through the extrusion process. Afterwards, samples for hardness testing were prepared by the injection process. The effects of composite components on linear model were analyzed by analysis of variance (ANOVA). According to analysis findings, incorporating EVA to composites has the greatest impact on their hardness, while binder has the least impact.**

***Keywords* – HDPE composite, hardness, ANOVA**

I. INTRODUCTION

Low-cost, and light weight, polymer-based composites are widely preferred in the industry due to their simple production [1]. Thanks to their high strength/weight ratio, they have replaced traditional metals in many sectors such as aviation and automotive [2]. Today, different organic/inorganic fillers are used to lower the price of polymer composites or to enhance their mechanical and thermal qualities [3–5].

Polyethylene (PE) is a thermoplastic obtained as a result of the polymerization of ethylene. PE is a solid at ambient temperature, however, it has low viscosity when heated. It may also be heated and cooled repeatedly without decomposing since they possess thermoplastic characteristics. It is divided into three groups according to density and chain structure: high density, low density and linear low density [6]. HDPE is a semi-transparent material with a partially straight chain structure and a density of 0.94-096 g/ml. HDPE, which is generally used in pipe production, is also used in production of bottles, barrels, toys, electrical and electronic goods.

Analysis of Variance (ANOVA), which combines a number of mathematical and statistical methodologies, is preferred to conventional methods for multivariate process optimization. It is often used to observe the simultaneous effects of different independent variables. Through planned experimental designs, this offers a set of empirical equations comprising the experimental parameters. In this way, it is possible to improve efficiency and reduce costs by optimizing processes in a short time [7,8].

In this study, HDPE was chosen as the primary polymer matrix, and mixtures with varying amounts of EVA, graphite and calcite were prepared. MA was employed as a binder. Samples were produced using extrusion and injection techniques. The experimental findings were analyzed by ANOVA once the hardness tests were completed. The relationship between hardness and additive quantity/type was presented with graphs and equations.

II. MATERIALS METHODS

A. Raw materials

HDPE used in experiments was obtained from Petkim (Izmir) and its melt flow rate and density are 5.5 g/min and 0.961 g/cm3, respectively. The following additives were used in experiments; thermoplastic elastomer (BASEL), graphite (Aklar Chemistry, Ankara), calcite (Nanokar, Istanbul), Ethylene-vinyl acetate (EVA) (Plastdepo, Bursa), and maleic anhydride (MA) (Aker Chemistry, Istanbul).

B. Production of samples

HDPE composites were produced by melt blending technique using a twin screw extruder. Screw diameter (D) of extruder is 40 mm and length/diameter (L/D) is 16 mm. To remove moisture, HDPE and additives were dried at 80 ˚C for 24 h prior to extrusion. From feeding zone to molding outlet, temperature of extruder was adjusted to six different temperatures for melt blending process. Then, molten sample was cooled in a water bath at ambient temperature and granulated. All granules were cooled to 80˚C for 12 h before molding and then mixed to ensure homogeneity. Using a microinjection equipment (Xplore IM 12, Netherlands), the produced granule composites were shaped to sample geometry appropriate for specific analyses. Mixing ratios of the prepared specimens are given in Table 1.

C. Hardness test

A shore instrument was used to test hardness. On the sample surfaces, measurements were made at intervals of around 3 mm and each measurement was repeated three times.

Table 1: Prepared experimental design.

Step	EVA	MA	Graphite	Calcite	Elastomer
1	0	0	0.0	0	0.0

2	20	0	0.0	40	0.0
3	0	5	0.0	0	5.0
4	0	0	25.0	0	5.0
5	20	5	0.0	40	5.0
6	20	0	25.0	40	5.0
7	20	5	0.0	0	0.0
8	20	0	25.0	0	0.0
9	20	5	25.0	0	5.0
10	0	2.5	0.0	40	25.0
11	0	5	0.0	20	0.0
12	0	2.5	25.0	20	5.0
13	0	0	25.0	40	0.0
14	0	5	12.5	40	5.0
15	20	0	0.0	0	5.0
16	0	0	0.0	40	5.0
17	0	5	25.0	0	0.0
18	10	5	25.0	40	2.5
19	20	5	12.5	40	0.0
20	10	2.5	0.0	40	0.0
21	10	5	12.5	20	2.5
22	0	0	25.0	20	0.0
23	0	5	12.5	0	0.0
24	10	5	25.0	20	5.0
25	20	2.5	25.0	40	0.0
26	0	0	25.0	40	2.5

III. RESULTS AND DISCUSSIONS

ANOVA results are given in Table 2. Accordingly, p value for hardness property is <0.05 and is significant. The relavent model's standard deviation and R^2 value were determined to be 2.18 and 0.8730, respectively. These findings demonstrate a high degree of agreement between the experimental design parameters and hardness of composites. Mathematical model equation for hardness property of composites is as follows;

Table 2. ANOVA results

Source	Sum of squares	DF	Mean square	F value	p-value
Model	554.68	8	69.34	14.61	<0.0001
A- EVA	183.98	1	183.98	38.76	<0.0001
B- MA	12.72	1	12.72	2.68	0.1200
C- Graphite	85.55	1	85.55	18.02	0.0005
D- Calcite	145.73	1	145.73	30.70	<0.0001
E- Elastomer	33.41	1	33.41	7.04	0.0167
AD	20.42	1	20.42	4.30	0.0536
BC	29.61	1	29.61	6.24	0.0231
DE	53.02	1	53.02	11.17	0.0039
Residual	80.69	17	4.75		
Cor.Total	635.37	25			
Std. Dev.	2.18				
R^2	0.8730				

$$y = +47.30 - 3xA - 0.7906xB + 2xC + 2.70xD - 1.26xE - 1.07xAxD + 1.31xBxC + 1.76xDxE$$

A, B, C, D, and E in the equation above stand in for EVA, MA, graphite, calcite, and elastomer, respectively. Accordingly, the effectiveness ranking of the components on hardness; A (EVA) > D (Calcite) > C (Graphite) > E (Elastomer) > B (Maleic anhydride). Here, the presence of EVA, MA and elastomer had a decreasing effect on hardness, while the addition of graphite and calcite increased it. Since they are based on EVA, MA and elastomer polymers, they are not hard by nature. Similar to this, graphite has a hardness of 1 and is soft by nature. Calcite, on the other hand, has a hardness level of 3. They have both been employed as fillers. As a result, it is likely that the pertinent additives will affect hardness in this way. Three-dimensional graphics in Figure 1 show the effects of composite components and amounts on hardness.

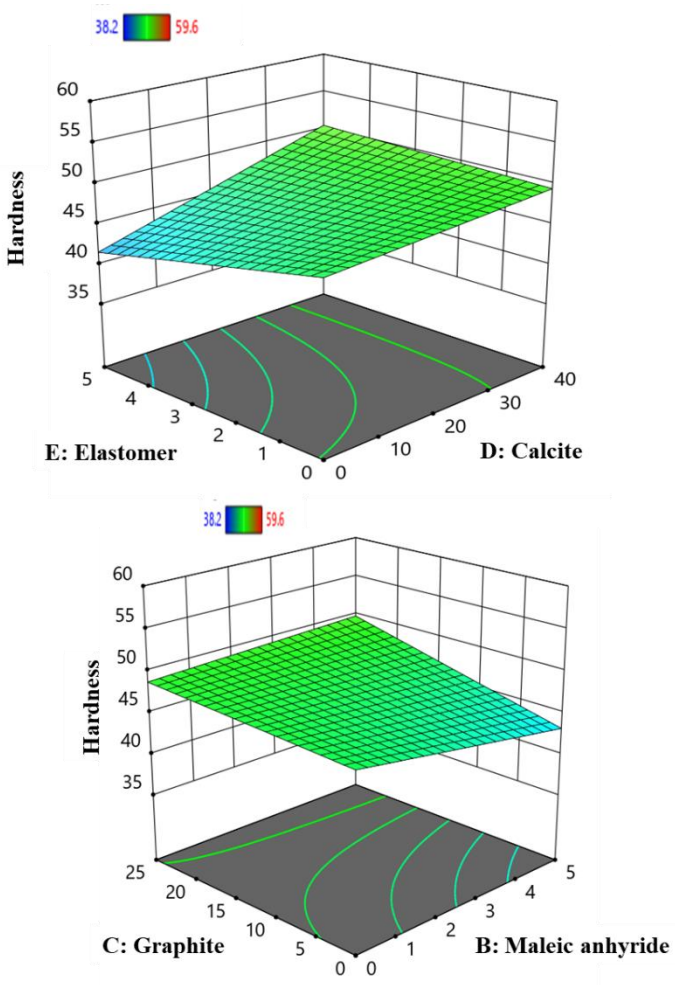

Figure 1: 3D graphics of relationship between additive type/amount and hardness.

IV. CONCLUSION

The experimental findings of this study, which looked at how various additive types and quantities affected the hardness of HDPE composites, are as follows;

EVA is the material that has the greatest impact on hardness, followed by calcite, graphite, elastomer, and MA. ANOVA

findings further demonstrate that the suggested model and the experimental outcomes are consistent.

Mechanical, thermal, and electrical properties of samples can be statistically assessed for later studies.

ACKNOWLEDGMENT

This study was produced from Ecem AYDIN's master's thesis.

REFERENCES

[1] Kismet Y, Doğan A. "Saman Takviyeli Yüksek Yoğunluklu Polietilen Kompozitlerin Mekanik Özellikleri ve Su Emme Kapasitelerindeki Değişimlerin İncelenmesi", *Dokuz Eylül Üniversitesi Mühendislik Fakültesi Fen ve Mühendislik Dergisi* vol. 25, pp. 193–204, 2023.

[2] Doğan A, Kismet Y. "Gama Işımasının Kolza Takviyeli Polipropilen Kompozit Malzemenin Mekanik Özellikleri Üzerindeki Etkisi", *Int J Pure Appl Sci* vol. 7, pp. 490–9, 2021.

[3] Çeven Ek, Necati Er, Günaydin Gk. "Nanopartikül Katkili Polimer Yüzeylerin İletkenlik Özelliklerinin Optimizasyonu", *Uludağ Üniversitesi Mühendislik Fakültesi Dergisi*, vol. 26, pp. 345–64, 2021.

[4] Mirik M. "Karbon nanotüp takviyeli yüksek yoğunluklu polietilen (YYPE) nanokompozit malzemelerin mekanik özelliklerinin araştırılması", Selçuk Üniversitesi, 2010.

[5] Fouad H, Elleithy R. "High density polyethylene/graphite nano-composites for total hip joint replacements: Processing and in vitro characterization", *J Mech Behav Biomed Mater*, *vol*. 4, pp. 1376–83, 2011.

[6] Osman MA, Atallah A, Suter UW. "Influence of excessive filler coating on the tensile properties of LDPE–calcium carbonate composites", *Polymer (Guildf)*, vol. 45, pp. 1177–83, 2004.

[7] Dixit S, Yadav VL. "Optimization of polyethylene/polypropylene/alkali modified wheat straw composites for packaging application using RSM", *J Clean Prod*, vol. 240, pp. 118228, 2019.

[8] Abdulrahman Oyekanmi A, Abd Latiff AA, Daud Z, Saphira Radin Mohamed RM, Ismail N, Ab Aziz A, et al. "Adsorption of cadmium and lead from palm oil mill effluent using bone-composite: Optimisation and isotherm studies", *Int J Environ Anal Chem*, vol. 99, pp. 707–25, 2019.

Use of Drinking Water Treatment Sludge and Egg Shell for Clay-Free Brick Production

G. BAKIROGLU[1*] and A. YARAŞ[1]

[1] Bartin University, Bartın/Turkey, gizem.7799@hotmail.com
[1]Bartin University, Bartın/Turkey, aliyaras@bartin.edu.tr

Abstract **- Consumption of limited clay reserves in brick production is a serious problem in terms of fertile soils in nature. Egg shell (ES) were employed in the brick-making process as a pore-forming agent and drinking water treatment sludge (DWTS) was substituted for clay to address this issue. To achieve this, specimens containing three different ES components (5, 10 and 15% by weight) were fired at 900°C. Water absorption, porosity, and density values were calculated according to Archimedes method. There was a drop in density and compressive strength and an increase in porosity and water absorption with a rise in ES content. Porosity, water absorption, density and compressive strength values were 43.73%, 30.49%, 1.44 g/cm^3 and 15.7 MPa in the presence of 15% ES, respectively.**

Keywords **- Drinking water treatment sludge, egg shell, brick, porosity, mechanical strength.**

I. INTRODUCTION

The building material industry is one of the sectors that acts as a driving force for the economies of most countries. Clay and cement based bricks are known as indispensable building materials in construction applications. Clay-based bricks are more preferred by both manufactures and consumers since they are less expensive than cement-based bricks [1,2]. Brick properties frequently develop and renew since building materials are expected to meet changing and increasing demands. In addition to low cost, clay-based bricks are also known to have some important properties such as resistance to chemicals and frost, corrosion resistance, lightness and easy production. Also, a building built using clay-based bricks can also last a very long time because of their extended service life [3].

Annual requirement for clay to produce clay bricks around world is about 340 billion tons [4]. As a result, clean and useful clay reserves are being used up more quickly. Because of this, certain nations, most notably China, restrict the use of clay through their environmental laws and regulations [5]. Due to this circumstance, brick producers substitute other materials for clay. An essential strategy for eco-friendly and sustainable manufacturing is to use diverse industrial process wastes as a secondary source of raw materials in production of bricks [6].

Utilization of various agricultural and industrial wastes in manufacture of clay-based bricks has been extensively studied in literature [7–13]. Another waste is chicken ESs, which have a high $CaCO_3$ content. ES is rich in calcium and has a similar structure to limestone. Most of it, 93-97%, consists of calcium carbonate ($CaCO_3$) [14]. Reusing ESs from places such as restaurants, homes, and egg breaking facilities can help recycle waste [15,16]. There are more and more studies on usage of eggshell waste in various production processes. For instance; calcium carbonate was produced from waste egg shells and this substance was used as a filler in production of office paper [17]. Another study assessed mechanical performance and use of eggshell-mixed mortars as building materials. In this context, eggshells were added in certain proportions instead of sand, and mortars were produced using cement and water. It was discovered that mortar samples with waste eggshell additives had decreased ultra sound transmission rate, bending, and compressive strength [18].

Nowadays, water in nature needs to undergo some processes to become drinkable. For example, many chemicals are employed in water treatment facilities to remove contaminants from drinking water, including ferric sulfate, aluminum sulfate, and lime [19,20]. DWTS is the by-product discharged during the purification process and may contain a variety of organic/inorganic chemicals, bacteria, and oxides [21,22]. Given that significant quantities of DWTS are discharged every day all over the world, it is inevitable that it will result in a number of environmental and waste management issues [23]. Currently, this issue is resolved by routinely storing DWTS or releasing it into rivers.

Several research demonstrate that clay brick manufacture can use DWTS [23,24]. For example; DWTS was added up to 30% by mass into clay and bricks were fired at 800, 900 and 1000˚C. The compressive strength of bricks with DWTS is higher than that of bricks that do not contain it, and the highest compressive strength was achieved with 30% DWTS content [25]. For firing temperatures of 1000˚C and higher, it has been determined that 10% and 20% of DWTS, respectively, can be incorporated to clay body [24]. In this study, DWTS was used as an alternative to clay for brick production and ES was employed as a pore-forming agent. The produced bricks were examined for their mechanical strength in addition to their physical characteristics, such as bulk density, water absorption, and porosity.

II. MATERIALS METHODS

ESs were supplied from a local Bartın company. DWTS was taken from Bartın Municipality Drinking Water Treatment Facility. After drying, grinding and sieving processes, particle sizes of the raw materials (<200 μm) were made usable for brick production.

Mixture proportions for brick production are given in Table 1. To ensure homogeneity, raw materials were stirred with a mechanical mixer for 5 minutes. To facilitate molding, 10% of its weight of water was sprayed into dry powder mixture. The prepared semi-dry powders were compressed in a pellet mold

with a hydraulic press under 50 MPa pressure. In a laboratory electric oven, firing was done at 900˚C and a heating rate of 5°C/min. Archimedes method was used to test porosity, water absorption, and bulk density of the produced brick samples [26]. Compressive strength tests were carried out according to ASTM standard [27].

Table 1: Mixture rates of prepared bricks.

Sample code	Egg shell (%, wt.)	Drinking water treatment sludge (%, wt.)
0%	0	100
5%	5	95
10%	10	90
15%	15	85

III. RESULTS AND DISCUSSIONS

A. *Bulk density*

According to findings in Figure 1, bulk density ranges from 2 to 1.44 g/cm^3. This means that amount of ESs in mixture had an impact on the bricks' bulk density. The bulk density of brick decreased as ES content increased. This decrease may be attributed to decomposition of carbonate compounds in ES at firing temperature.

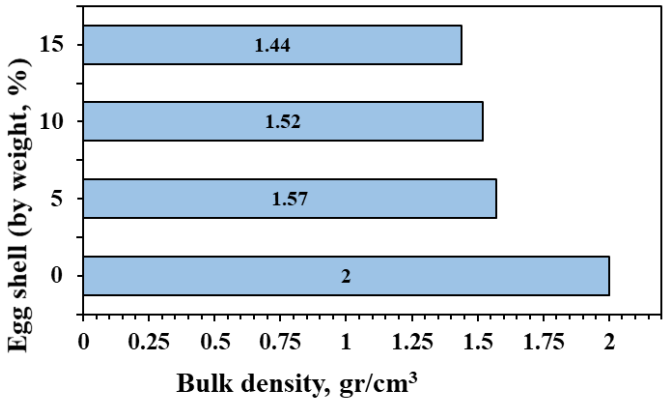

Figure 1: Bulk density results.

B. *Porosity and Water Absorption*

For thermal characteristics and mechanical performance of bricks, porosity is a crucial factor. Figure 2 displays porosity values. Porosity increased from 25.4% to 43.73% as ES content rose from 0% to 15%. Findings show that quantity of ES significantly influences pore development. That is, calcium carbonate compound in ES decomposes at firing temperature and turns into calcium oxide and carbon dioxide. During CO_2 release, pores form in brick. On the other hand, calcium oxide, which is highly reactive, can form new phases such as calcium alumina-silicates at firing temperature [28]. Similarly, previous studies have reported that adding marble waste and carbonation sludge with calcium carbonate to clay body increases porosity [28,29]. In addition, according to information in Figure 3a, density and porosity of fired bricks are inversely related.

Water absorption is an indicator of moisture resistance for ceramic materials, especially bricks [30]. High resistance and high durability of brick to environmental stress are anticipated if water absorption is less [25]. Experimental results show that water absorption properties of bricks increase with amount of DWTS (Figure 2). Water absorption of brick without ES was 12.5% and it increased to 30.49% in the presence of 15% ES. Also, it is well known that porosity and water absorption are closely related (Figure 3b).

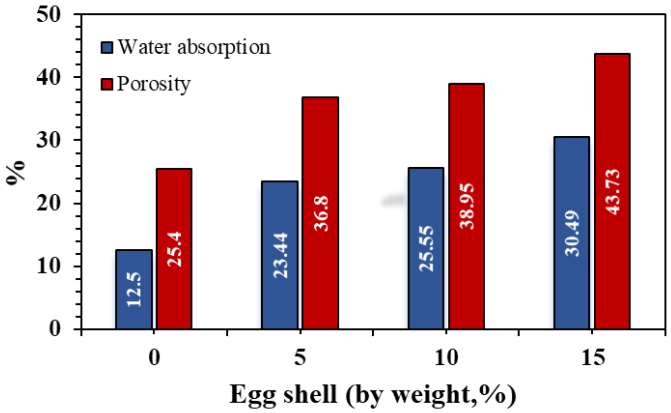

Figure 2: Porosity and water absorption results.

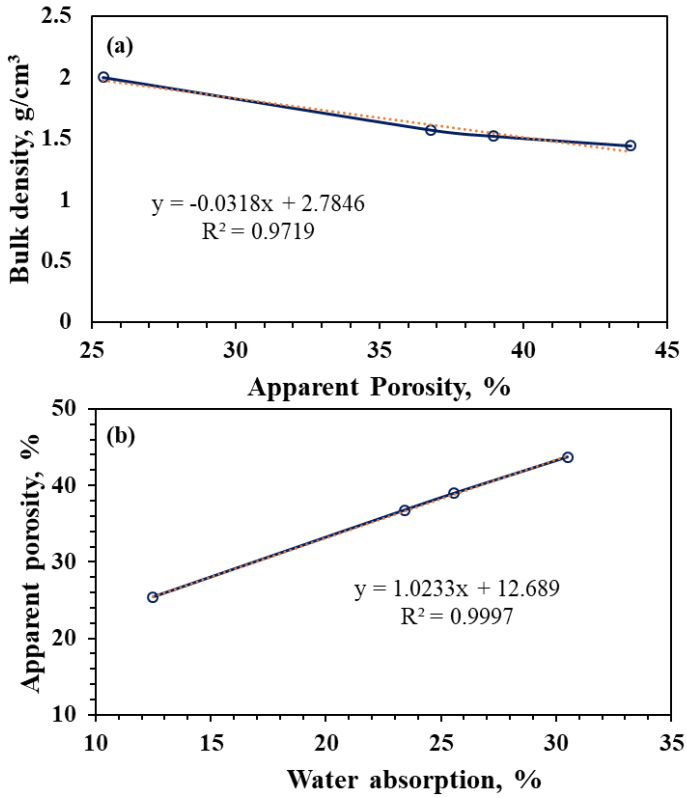

Figure 3: Relationships between bulk density and apparent porosity (a), apparent porosity and water absorption (b).

C. Compressive Strength

Another of the most crucial engineering characteristics of bricks is its compressive strength. Compressive strength of brick should be at least 7 MPa in order to meet standards. As shown Figure 4, compressive strength varies between 26.4 MPa and 15.7 MPa. Compressive strength tended to decline as ES content rose. It is obvious that there is a linear relationship between ES content and compressive strength. The existence of pores in brick is without a doubt cause of reduction in strength. The relationship between compressive strength and porosity is depicted in Figure 5.

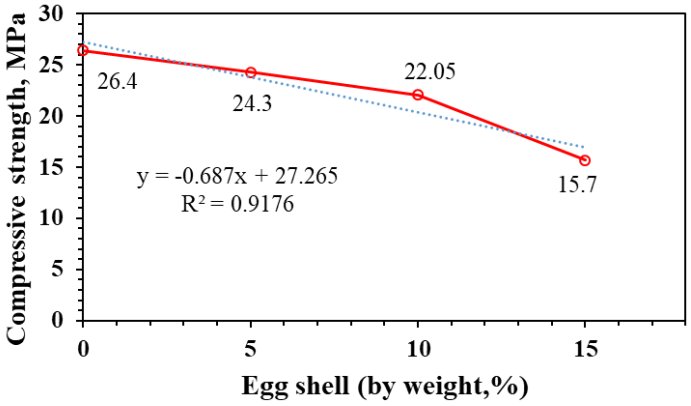

Figure 4: Compressive strength results.

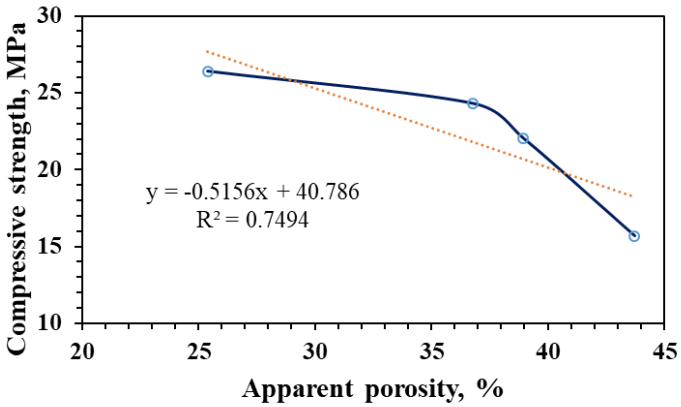

Figure 5: Relationship between compressive strength and apparent porosity.

IV. Conclusion

Findings of this investigation, in which DWTS was instead of clay and ES was utilized as a pore-forming agent, might be summed up as follows;

- Fired bricks containing 15% ES can be considered as thermal insulation materials thanks to their high porosity (43.73%).

- Regarding compressive strength performance, all bricks made complies with international standards.

- For all specimens, it was discovered that there was a linear relationship between density, porosity, water absorption, and compressive strength. These empirical equations allow for the prediction of the performance of clay-free bricks with known physical characteristics.

In future studies, higher eggshell contents can be tested at different cooking temperatures.

Acknowledgment

This study was produced from Gizem BAKIROĞLU's master's thesis.

References

[1] Muñoz P, Morales MP, Mendívil MA, Juárez MC, Muñoz L. "Using of waste pomace from winery industry to improve thermal insulation of fired clay bricks. Eco-friendly way of building construction", *Constr Build Mater*, vol. 71, pp. 181–7, 2014.

[2] Madurwar M V, Mandavgane SA, Ralegaonkar R V. "Development and feasibility analysis of bagasse ash bricks", *J Energy Eng*, vol. 141, pp. 4014022, 2014.

[3] Ozturk S, Sutcu M, Erdogmus E, Gencel O. "Influence of tea waste concentration in the physical, mechanical and thermal properties of brick clay mixtures", *Constr Build Mater*, vol. 217, pp. 592–9, 2019.

[4] Riaz MH, Khitab A, Ahmed S. "Evaluation of sustainable clay bricks incorporating Brick Kiln Dust", *J Build Eng*, vol. 24, pp. 100725, 2019.

[5] Chen Y, Zhang Y, Chen T, Zhao Y, Bao S. "Preparation of eco-friendly construction bricks from hematite tailings", *Constr Build Mater* vol. 25, pp. 2107–11, 2011.

[6] Munir MJ, Kazmi SMS, Wu Y-F, Hanif A, Khan MUA. "Thermally efficient fired clay bricks incorporating waste marble sludge: an industrial-scale study", *J Clean Prod*, vol. 174, pp. 1122–35, 2018.

[7] Muñoz P, Morales MP, Letelier V, Mendívil MA. "Fired clay bricks made by adding wastes: Assessment of the impact on physical, mechanical and thermal properties", *Constr Build Mater*, vol. 125, pp. 241-252, 2016.

[8] Velasco PM, Ortíz MPM, Giró MAM, Velasco LM. "Fired clay bricks manufactured by adding wastes as sustainable construction material–A review", *Constr Build Mater*, vol. 63, pp. 97–107, 2014.

[9] Zhang L. "Production of bricks from waste materials–A review", *Constr Build Mater*, vol. 47, pp. 643–55, 2013.

[10] Gencel O, Sutcu M, Erdogmus E, Koc V, Cay VV, Gok MS. "Properties of bricks with waste ferrochromium slag and zeolite", *J Clean Prod*, vol. 59, pp. 111–9, 2013.

[11] Görhan G, Şimşek O. "Porous clay bricks manufactured with rice husks", *Constr Build Mater*, vol. 40, pp. 390–6, 2013.

[12] Sutcu M, del Coz Díaz JJ, Rabanal FPÁ, Gencel O, Akkurt S. "Thermal performance optimization of hollow clay bricks made up of paper waste", *Energy Build* vol. 75, pp. 96–108, 2014.

[13] Sutcu M, Ozturk S, Yalamac E, Gencel O. "Effect of olive mill waste addition on the properties of porous fired clay bricks using Taguchi method", *J Environ Manage*, vol. 81, pp. 185–92, 2016.

[14] Erol A. "Yumurta tavuklarında rasyona farklı kalsiyum kaynakları ilavesinin performans ve yumurta kabuk kalitesine etkisi", MS thesis, Selçuk University Fen Bilimleri Enstitüsü, 2011.

[15] Pliya P, Cree D. "Limestone derived eggshell powder as a replacement in Portland cement mortar", *Constr Build Mater*, vol. 95, pp. 1–9, 2014.

[16] Gowsika D. "Experimental investigation of egg shell powder as partial replacement with cement in concrete", *Int J Eng Trends Technol* vol. 14, pp. 65–8, 2014.

[17] Tutus A, Killi U, Cicekler M. "Evaluation of eggshell wastes in office paper production", *Biomass Convers Biorefinery*, vol. 12, pp. 1115–24, 2022.

[18] Akyıldız A. "Yumurta Kabuğu Katkılı Harçların Mekanik Özellikleri", *Karaelmas Fen ve Mühendislik Derg* vol. 8, pp. 570–4, 2018.

[19] Kashyap S, Datta D. "Reusing industrial lime sludge waste as a filler in polymeric composites", *Mater Today Proc*, vol. 4, pp. 2946–55, 2017.

[20] Sales A, De Souza FR, Almeida F do CR. "Mechanical properties of

concrete produced with a composite of water treatment sludge and sawdust". *Constr Build Mater*, vol. 25, pp. 2793–8, 2011.

[21] Ahmad T, Ahmad K, Alam M. "Sustainable management of water treatment sludge through 3 'R'concept", *J Clean Prod* vol. 124, pp. 1–13, 2016.

[22] Babatunde AO, Zhao YQ. "Constructive approaches toward water treatment works sludge management: an international review of beneficial reuses", *Crit Rev Environ Sci Technol*, vol. 37, pp. 129–64, 2007.

[23] Gomes SDC, Zhou JL, Li W, Long G. "Progress in manufacture and properties of construction materials incorporating water treatment sludge: A review", *Resour Conserv Recycl*, vol. 145, pp. 148–59, 2019.

[24] Teixeira SR, Santos GTA, Souza AE, Alessio P, Souza SA, Souza NR. "The effect of incorporation of a Brazilian water treatment plant sludge on the properties of ceramic materials", *Appl Clay Sci*, vol. 53, pp. 561–5, 2011.

[25] Benlalla A, Elmoussaouiti M, Dahhou M, Assafi M. "Utilization of water treatment plant sludge in structural ceramics bricks", , vol. 118, pp. 171–7, 2015.

[26] ASTM C20-00, Standard Test Methods for Apparent Porosity, Water Absorption, Apparent Specific Gravity, and Bulk Density of Burned Refractory Brick and Shapes by Boiling Water. West Conshohocken, *Am Soc Test Mater* 2005.

[27] ASTM C67-03, Standard test methods for sampling and testing brick and structural clay tile. Philadelphia, *PA Am Soc Test Mater* 2003.

[28] Yaras A, Sutcu M, Gencel O, Erdogmus E. "Use of carbonation sludge in clay based building materials processing for eco-friendly, lightweight and thermal insulation", *Constr Build Mater* vol. 224, pp. 57–65, 2019.

[29] Sutcu M, Alptekin H, Erdogmus E, Er Y, Gencel O. "Characteristics of fired clay bricks with waste marble powder addition as building materials", *Constr Build Mater* vol. 82, pp. 1–8, 2015.

[30] Krishnan P, Jewaratnam J. "Recovery of water treatment residue into clay bricks", *Chem Eng Trans*, vol. 56, pp. 1837–42, 2017.

Design and Implementation of Inclusive/Modular USB Charging Supported Embedded Stop Button for Buses

Cem Eker[1], Alev Yüksel Peçeli[2,a], Ferhat Cömert[3], Yunus Emre Tarhan[1,b], Damla Ceren Tektaş[1,c], Eda Nur Üyük Maden[1,d], Yavuz Çatmaz[4,a], Abdullah Vidinlioğlu[5,a], Duygu Çelik[6,a]

[1]Mecahnical Desing Department, Design Center, KNS Automotive, 54580, Arifiye, Türkiye
[a]0009-0004-8317-3085, cemeker@knsotomotiv.com
[b]0009-0003-0722-1746, yunusemretarhan@knsotomotiv.com
[c]0009-0008-8609-5595, damlatektas@knsotomotiv.com
[d]0009-0001-6619-0308, edamaden@knsotomotiv.com
[e]0009-0009-2437-4895, enesgenc@@knsotomotiv.com
[2]Intellectual Industrial and Commercial Property Rights Department, Design Center, KNS Automotive, 54580, Arifiye, Türkiye
[a]0009-0000-3590-5756, alevpeceli@knsotomotiv.com
[3]Electronic Design Department, Design Center, KNS Automotive, 54580, Arifiye, Türkiye
[a]0000-0003-1320-4419, ferhatcomert@knsotomotiv.com
[4]Cost Department, Design Center, KNS Automotive, 54580, Arifiye, Türkiye
[a]0009-0007-2870-4332, yavuzcatmaz@knsotomotiv.com
[5]Industrial Design Department, Design Center, KNS Automotive, 54580, Arifiye, Türkiye
[a]0009-0002-8601-9759, abdullahvidinlioglu@knsotomotiv.com
[6]Project Management Department, Design Center, KNS Automotive, 54580, Arifiye, Türkiye
[a]0009-0005-7999-7986, duygucelik@knsotomotiv.com

***Abstract*- The bus accessibility button is an accessibility tool that enables passengers with disabilities or mobility limitations to request assistance without the need for the driver or bus attendant when boarding or alighting the bus. These buttons can be located inside or outside the buses and are generally quite simple to use. The fundamental functions of bus accessibility buttons include boarding requests, where a disabled passenger indicates their intention to board or disembark by pressing the button. This informs the driver or bus attendant of the passenger's desire to alight. Assistance for alighting is provided when the button is pressed, and the bus driver or attendant assists the passenger by halting the bus to ensure a safe exit. Some bus accessibility buttons offer auditory or visual alerts when pressed, notifying the driver or bus attendant. Exterior accessible buttons can also be present at bus stops or ramps, indicating the approach of the bus or the need for disembarkation.These types of buttons assist in providing better service to disabled users on buses, making public transportation systems more accessible. Generally, disability buttons are used within the scope of accessibility measures carried out by local public transportation authorities. Disability buttons on buses, inside and outside, are an important element in facilitating accessible travel. Stop buttons should be placed on handrails and flat surfaces for easy access by all passengers. To be easily usable by both disabled and non-disabled individuals, the stop button should feature 'Stop' in both the Latin alphabet and Braille. It should have a suitable design to prevent accidental presses. Modern buses have significantly more easily accessible and numerous stop buttons compared to older models. However, the protruding structure of these buttons causes accidental and inadvertent presses. The purpose of this study is to design a stop button that can be mounted on both flat surfaces and handrails to be easily accessible to all passengers. The aim is to embed these buttons slightly into the body to prevent accidental presses. The design of the button housing aims to provide functionality by enabling the assembly of an electronic card and a front frame within the same body, allowing the product to function as a USB charging device**

***Key Words- Stop* Button, Public Transportation, USB Charging, Modular Design, Embedded Stop Button Stop Buton**

I. INTRODUCTION

The United Nations Convention on the Rights of Persons with Disabilities [1], based on the Universal Declaration of Human Rights and the International Declaration of Human Rights, calls for the implementation of both national and international measures to protect the rights of disabled individuals. Bearing in mind the necessity of preventing physical and mental disability, helping disabled individuals develop their capacities in various activity areas, and enhancing their inclusion in daily life, it is their right to have access to the basic conditions of a decent life to the fullest extent possible, regardless of the cause of their disability or impairment. There is an ongoing need for specialized designs

and engineering efforts aimed at enabling disabled individuals to navigate public spaces independently, safely, and actively, without the need for assistance from others.

"Universal design" is the creation of products that offer equal usability for all individuals, disabled or not. It's an approach to design that aims to create environments or design products that allow as many users (individuals) as possible to use them, regardless of age, ability, or status. Universal design is also known by terms like design for all or inclusive design [2].

It should not be forgotten that arrangements that prevent the participation of disabled individuals in the mainstream of social life also mean their exclusion from social life. It is necessary for public facilities to be designed for people with disabilities to facilitate their inclusion in societal life by eliminating physical barriers that obstruct movement, such as wheelchairs and walking aids in the streets, roads, rain gutters, and sidewalks, as well as in public transportation vehicles that assume a common level of mobility for passengers, and public information formats like directional signs that assume a common level of visual and auditory ability [3].

Accessibility refers to the ability to access and benefit from the rights and services in all areas of life [4]. Accessibility refers to enabling disabled individuals to live independently like other individuals in society and to have full and active participation in all aspects of life; it means having equal access to the physical environment, transportation, information and communication technologies, and systems. Preventing their access to social life leads to a social life where they are absent [12]. Hence, all areas of social life must be designed for everyone. The approach of design for all aims to create spaces that meet the spatial, social, and individual needs of all user groups, including disabled and mobility-impaired individuals [5].

Any building and its immediate surroundings that allow people with any form of disability (especially wheelchair users or those with sensory impairments) and all users under normal conditions to enter and exit, move around, and benefit from all services offered without assistance are considered to have accessible features [6].

With advancing technology, engineers are working on developing the use, functionality, and new technical features of the disabled button to increase ease of use. Accordingly, different features of disabled buttons are designed for different public transport vehicles according to needs and goals. Various disabled buttons are available on the market, featuring electronics, Braille alphabets, audible warnings, and light signaling systems. Although all disabled buttons may have different designs, they must be designed and produced in compliance with Law No. 5378 on Disabled People [7], the Accessibility Monitoring and Supervision Regulation [8], TS 9111 [9], and 2001/85/EC [10] standards. These laws and standards specify the technical requirements that the disabled button must meet. These requirements provide the fundamental technical requirements from a safety and ergonomic perspective. These requirements may vary at the national level. The design of disabled buttons must be meticulously carried out to maximize the accessibility and ease of use for users. These features help make public transportation more accessible and user-friendly for disabled users. Generally, the desired features for disabled buttons include: High contrast and visibility - disabled buttons should be clearly distinguishable, using high-contrast colors and a distinct appearance from other buttons or surfaces. This enables individuals with low vision to see the buttons more easily [11]. Tactile feedback - When pressed, the disabled buttons should provide tactile feedback to users. This allows users to feel that the button has been effectively pressed. This feedback can be in the form of touch or click sounds, vibrations, or different tactile sensations [11]. Large and easy-to-press size - disabled buttons should be large and easy to press. The use of large buttons makes it easier, especially for individuals with limited motor skills. Tactile sensitivity - disabled buttons should be sensitive to light pressure or touch. This allows users to respond to the button easily. Use of color and light - the color and lighting of the disabled buttons should provide users with information about the operation status [11].

For example, a green light can indicate that the button is active, while a red light indicates that the button is disabled. Braille codes and secondary signs - disabled buttons may have signs or secondary signs with Braille letters written on them. This explains the function of the button for visually impaired users. Marking and instructions - next to the disabled buttons, there should be explanations or markings on how to use them. This helps new users understand how to use the button [11]. Sensitivity adjustment - some public transport disabled buttons may have mechanisms that allow for sensitivity adjustments. This allows for the adjustment of the button's response sensitivity according to different user needs. Ease of cleaning and maintenance - the design of disabled buttons should allow for ease of cleaning and maintenance. Since buttons need regular cleaning, the design should consider this need.

II. MATERIAL AND METHOD

In this study, the design and production of a stop button for use by disabled individuals on buses were carried out. An electronic card supporting Universal Serial Bus (USB) 5V 2A was included to allow passengers to charge their phones during travel. After completing all the designs, a visual and physical assembly integrity of the product was examined. For testing purposes, a prototype was prepared using Stereolithography (SLA) printing.

Figüre 1: The existing designs of disabled-friendly bus buttons in the market

Figüre 2: Disabled-friendly bus buttons are designed as universal design by KNS Automotive.

For the prototype production, ABS-like resin was preferred due to its suitability for mold-based mass production and strength. Subsequent to the prototype, mold designs were created, and molds were produced using Computer Numeric Control (CNC) vertical machining centers. Injection machines were then used for mass production following mold production. Automotive regulation tests were repeated as the final test after mass production. ABS material was used considering visual integrity, strength, and flame resistance for mass production. Additionally, a LED was added to the button, and due to its light transmittance, polycarbonate (PC) was chosen as the button material.

For passengers to charge their phones during travel, a Universal Serial Bus (USB) 5V 2A supported electronic card design was added to this product. This design aims to facilitate passengers in maintaining their communication and charging their devices while traveling.

Following the completion of all designs, a prototype was prepared using Stereolithography (SLA) printing for the examination of the product's visual and physical assembly integrity and testing. This prototyping stage is crucial to confirm the practical applicability and usability of the design. For the prototype production, a mold-based approach suitable for mass production was adopted, and an ABS-like resin was chosen for its strength, ensuring better alignment with the production processes and durability.

Figüre 3: Include the disabled button designed according to universal standards.

After the completion of prototype production, mold designs were prepared and molds were produced using Computer Numeric Control (CNC) vertical machining centers. The purpose of mold production was to prepare for the mass production of the product. Following mold production, mass production was initiated using injection machines, enabling the rapid and efficient large-scale production of the products.

Post mass production, automotive regulation tests were repeated as the final test. These tests are conducted to confirm that the product meets the requirements of the automotive industry. ABS-like material was used for mass production, considering visual integrity, strength, and flame resistance. ABS material provides positive results in terms of durability and fire resistance.

Furthermore, a LED was added to the product, and polycarbonate (PC) was chosen as the button material due to its light transmittance. This LED is used to indicate to the user that the operation has been completed, and polycarbonate is a material that ensures proper transmission of light.

III. RESULTS AND DISCUSSION

When designing the disabled button, embedded design principles were utilized to prevent inadvertent activation due to impact, thereby creating modular structures. These modular structures eased the circular and flat surface mounting of the design, enhancing the product's integrity. Furthermore, the engineering work for the 5V - 2A supported USB charging device card was designed to function in all vehicles operating with 12V and 24V.

Figüre 4: The disabled buttons designed by KNS Automotive are suitable for both day and night usage.

To ensure similarity to the final product, the prototype was produced using Acrylonitrile Butadiene Styrene (ABS)-like resin for Stereolithography (SLA) printing. The use of ABS-like resin is primarily due to its elongation at break between 20-30%, while pure ABS material offers a 25% elongation at break.

Practical tests were applied for the successful assembly of the prototype on various surfaces, confirming the product's assembly requirements.

As an alternative approach to traditional products, reducing the number of molds from four to two decreased mold costs, mold change times, and mold stocks by 50%.

Functional tests revealed that the product maintained a stable voltage range of 4.9V-5.1V within the supply voltage range of 9-32 volts. Additionally, the product's current capacity was tested up to 2.1 A.

Radiated emission tests were performed under the most adverse scenario at a 12V operating voltage, compliant with CISPR 25 standards. Furthermore, the product demonstrated successful immunity to transient currents and emission tests at a 24V operating voltage, compliant with the 2nd edition of ISO 7637-2.

All tests were successfully completed, and the product obtained an E2410R06/024814*00 approval certificate from an external laboratory.

The climate test inspected the visual and design wear of the ABS material during a 24-hour period, including 4 hours of cooling at -40°C and 4 hours of heating at 120°C, without any deformations.

During the button's life test stage, the product successfully completed the required 75,000 activation tests in compliance

with automotive regulations and was effectively tested up to 100,000 activations.

IV. Conclusion

Based on the obtained design and production results, our product has been determined to possess various added values. These added values are as follows:

Ergonomic and embedded modular design: The product adopts an ergonomic embedded design to minimize collision risks. The modular structure allows easy mounting on pipes and flat surfaces. Aimed at an inclusive button, a raised structure was incorporated into the product's design to create an accessible button.

Equipped with a 5V-2A USB charging module, the product offers the functionality of charging electronic devices for passengers, thus adding practicality to the disabled button.

Enhanced technical durability: The product successfully completed 100,000 activation tests, demonstrating its durability. The electronic card design adheres to ECE-R10 EMC tests, providing high electromagnetic compatibility standards.

Manufactured with only two molds, setting it apart from competitor products, this reduction in mold number minimizes mold costs and storage requirements, enabling cost-effective and faster production through the possibility of mass production.

Compliance with automotive regulations suitable for bus use, a common application in the automotive industry, enhances the product's value.

These added values indicate that our product surpasses industry standards in terms of quality and functionality. Its suitability for widespread use in buses establishes it as a solution catering to passengers' needs within bus interiors.

Acknowledgment

This scientific publication is the product of KNS Automotive's R&D studies within the scope of the "Scientific Publication Preparation Training for R&D Centers" given to the Design Center by Assoc. Prof. Dr. Muhammed Kürşad UÇAR. All rights of the products belong to KNS Automotive.

References

[1]United Nations Convention on the Rights of Persons with Disabilities, https://treaties.un.org/Pages/Home.aspx, (Access Date: 11.10.2017)

[2] Uslu, Aysel; Shakouri, Nasim (2014), "Independent Movement Opportunities for Disabled/Elderly Individuals in Urban Landscapes and the Concept of Universal Design", Kastamonu University Journal of Forestry, Volume: 14, Issue: 1, pp. 7-14.

[3] Gleeson, Brendan (2011), "Can Technology Overcome the Disabling City?", (Ed. Bezmez, Dikmen; Yardımcı, Sibel; Şentürk, Yıldırım), Disability Studies, Koç University Publications, Istanbul, 363-384.

[4] Yılmaz M. (2012), Inclusive Design and Space, Mimarist, Issue 43, pp. 107-111.

[5] Mishchenko E.D. (2014), Design For Everyone: An Experience of Participatory Approach to Universal Design, Mimarist, Issue 50, pp. 105-111.

[6] TS 9111/ November 2011: Accessibility Requirements for Buildings for People with Disabilities and Mobility Limitations (This standard has been enacted in place of the canceled TS 9111-April 1991 standard.)

[7] Law on Disabilities, (1/7/2005), Official Gazette of the Republic of Turkey, 25868, July 1, 2005.

[8] Accessibility Monitoring and Inspection Regulation, (July 20, 2013), Official Gazette of the Republic of Turkey, 28713, July 20, 2013.

[9] TS-9111. (2011). Accessibility requirements for people with disabilities and mobility limitations in buildings.

[10] Directive 2001/85/EC of the European Parliament and of the council ,2001, OJ L 42, 13.2.2002.

[11] UNE EN 1756-2:2005+A1:2010 Tail lifts - Platform lifts for mounting on wheeled vehicles - Safety requirements - Part 2: Tail lifts for passengers.

[12] Öz, Şaban (2013). "From Disabled Religious Education to 'Unfettered' Religious Education Model: Issues Encountered in the Religious Education of 'Othered' Disabled Individuals and Solution Proposals", Hikmet Yurdu Journal of Thought-Comment Social Sciences Research, 6 (11), pp. 75-89.

Design and Implementation of an Ergonomic Disabled Ramp for Use in Public Transportation Vehicles

Cem Eker[1,a], Ömer Doğan Doğancık[1,b], Metehan Onat[1,c], Semih İçyüz[2,a], Yavuz Çatmaz[3,a], Elif Çak[4,a,] Duygu Çelik[5,a], Alev Yüksel Peçeli[6,a]

[1]Mechanical Design Unit, Design Center, KNS Otomotiv, 54580, Arifiye, Turkey
[a]0009-0004-8317-3085, cemeker@knsotomotiv.com
[b]0009-0007-1630-4083 omerdogancik@knsotomotiv.com
[c]0009-0004-8537-3689, metehanonat@knsotomotiv.com
[2]Electronic Design Unit, Design Center, KNS Otomotiv, 54580, Arifiye, Turkey
[a]0009-0009-7700-3991, semihicyuz@knsotomotiv.com
[3]Costing Unit, Design Center, KNS Otomotiv, 54580, Arifiye, Turkey
[a]0009-0007-2870-4332, yavuzcatmaz@knsotomotiv.com
[4]Industrial Design Unit, Design Center, KNS Otomotiv, 54580, Arifiye, Turkey
[a]0009-0004-1640-4023, elifcak@knsotomotiv.com
[5]Project Unit, Design Center, KNS Otomotiv, 54580, Arifiye, Turkey
[a]0009-0005-7999-7986, duygucelik@knsotomotiv.com
[6]Intellectual Industrial and Commercial Property Rights Department Design Center, KNS Automotive, 54580, Arifiye, Türkiye
[a]0009-0000-3590-5756, alevpeceli@knsotomotiv.com

***Abstract*- Electronic and mechanical systems, such as disabled ramps, are essential for individuals with disabilities to travel on public transportation and independently board vehicles. Various types of disabled ramps are being designed and developed with the aim of enhancing the quality of life for disabled individuals and promoting their independence in daily life. The design of the ramp targets dimensions compliant with Law No. 5378 on Disabled Persons, the Accessibility Monitoring and Inspection Regulation related to the law, TS 9111, and the 2001/85/EC standards, specifically focusing on a ramp that operates only when the vehicle is stationary. The minimum ramp width should be over 80cm and have a load-bearing capacity of 350kg. The weight of a disabled ramp with a 350kg load capacity can vary between an average of 30 kg and 35 kg. This design aims to reduce the weight of a disabled ramp with the same load-bearing capacity by 50%. By reducing the weight of the ramp used in the project by 50%, the aim is to provide short-term cost and weight advantages, while in the long term, mitigating carbon emissions resulting from weight reduction.Through the conducted design studies and analyses, the weight of the designed and produced ramp, meeting the desired technical criteria, was reduced from 35kg to 16.0003kg by reducing the material's thickness by 55% and the section thickness by 33%. The disabled ramp has thus been lightened by 55%, making it more ergonomically useful**

***Keywords*- Disabled Ramp, Transportation Technologies, Wheelchair, Passenger Vehicles, Disabled Individual, Portable Ramp.**

I. INTRODUCTION

The United Nations Convention on the Rights of Persons with Disabilities, based on the Universal Declaration of Human Rights and the International Declaration of Human Rights [1], calls for both national and international measures to protect the rights of disabled individuals. Always mindful of the need to prevent physical and mental disabilities, assist disabled individuals in developing their abilities across various domains, and enhance their integration into normal life, it is a right for individuals, irrespective of the cause of their disabilities, to have access to decent living conditions as much as possible. There is an ongoing need for special designs and engineering efforts aimed at designing public spaces and city planning in a way that enables disabled individuals to use them independently, safely, and actively, without the need for assistance, to continue their daily lives.

The concept of 'Universal Design' involves the creation and design of products that offer equal usability for individuals, whether disabled or not. It is an approach to design that ensures the maximum possible usability for all users (individuals) despite differences in age, ability, or circumstances, in the environment or in all designed products. Universal design is also referred to by terms such as design for all or inclusive design [2].

It should not be forgotten that regulations hindering the participation of individuals with disabilities in the mainstream of societal life simultaneously indicate their exclusion from social life. It is essential to design public information formats for disabled individuals to enable their participation in societal life, such as eliminating or reducing physical barriers that hinder their mobility, like obstacles in streets, roads, rain gutters, and sidewalks that limit the effectiveness of mobility aids such as wheelchairs and walkers, and public transportation vehicles assuming a common level of mobility for passengers, as well as directional signs assuming a common level of visual and auditory ability [3].

Accessibility refers to the ability to access and benefit from rights and services in all areas of life [4]. Accessibility ensures that individuals with disabilities can live independently like other members of society and have complete and effective participation in all areas of life, providing them equal access to the physical environment, transportation, information and communication technologies, and systems. Hindering their access to social life results in a societal life that excludes them [11]. Therefore, all areas of societal life need to be designed for everyone. The design approach for everyone aims to create spaces that respond to the spatial, social, and individual needs of all user groups, including individuals with disabilities and mobility constraints [5].

Any facility enabling people with disabilities (especially wheelchair users or those with sensory impairments), as well as all users of a building and its immediate surroundings, to independently and comfortably enter, exit, move around inside, and benefit from all services under normal conditions, is considered accessible [6].

Ramps for disabled individuals present in public transportation vehicles play a crucial role, particularly for individuals using wheelchairs due to physical disabilities, in providing freedom for independent travel. Ramps developed to address the difference in level between the vehicle and the curb must comply with the dimensions stipulated within standards and laws [7].

With advancing technology, engineers are developing disabled ramps not only for safety and ergonomics but also to enhance ease of use, reduce weight, or add new technical features. Accordingly, disabled ramps with different features are designed for various public transportation vehicles based on needs and objectives. Besides technically diverse ramps like portable, foldable, mobile, and electric, there are ramps made from different materials available in the market. Although all disabled ramps have different features, they should fundamentally comply with Law No. 5378 on Disabled Persons [7], the Accessibility Monitoring and Inspection Regulation related to the law [8], TS 9111 [9], and 2001/85/EC [10] standards.

The technical specifications required for disabled ramps are detailed in the relevant laws and standards. These specifications provide basic technical requirements for safety and ergonomics. Even with different features and technological advancements, all disabled ramps must meet the fundamental criteria listed below.

According to the standards, the technical specifications for a disabled ramp are as follows:

In public areas, if there is a level difference of more than 1.3 cm, it is mandatory to implement a suitable sloped disabled ramp.

Load-bearing capacity: 350 kg/m2

Ramp Width: Min. 80 cm

As for the slope:

h: 15 cm or less, the slope should be at most 1:10 (10%)

h: Between 16 cm and 50 cm, the slope should be at most 1:11 (9%)

h: Between 51 cm and 100 cm, the slope should be at most 1:12 (8%)

h: Above 100 cm, the slope should be at most 1:16 (6%).

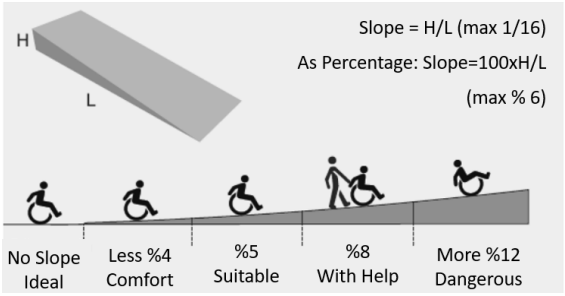

Figure 1: Gradient Ratios of Disabled Ramps According to Standards.

The disabled ramp should provide a minimum area of 150 cm x 150 cm for wheelchair maneuvering at the beginning and end. If the height traversed by the disabled ramp is over 15 cm, the sides of the ramp's gap must have two handrails, one at 70 cm and the other at 90 cm. If the ramp changes direction with a platform, the maneuvering area for the wheelchair should be at least 150 cm x 150 cm. The edges of the ramp and platforms must have a minimum 5 cm protection. The ramp surface must be flat, made of stable, durable material, and designed not to be slippery in wet or dry conditions.

As per disability regulations and standards, the weight of disabled ramps designed for vehicles with a 350 kg weight-bearing capacity is between 30-35 kg. To enable usage by disabled individuals, the ramp located at the base of the vehicle can be lifted and opened, preventing obstruction caused by ground cover. With the objective of addressing the challenge of lifting an average 15-20 kg part and reducing the load on the vehicle, there is an aim to reduce the weight of the ramp with a 350 kg weight-bearing capacity by 50%, a development pursued by KNS Otomotiv. The goal is to reduce one part of the two-piece ramp from 15-20 kg to as low as 9 kg.

II. MATERIAL AND METHOD

The mechanical design of the disabled ramp developed by KNS Automotive was initially conducted through CAD application in line with disabled ramp standards and automotive regulations to adapt to the existing production line. Static analysis was performed using Ansys. Revisions were made as necessary for production, followed by repeated Ansys static analyses. External extrusion molds were designed and produced for manufacturing aluminum profiles. Extrusion printing was obtained for the prototype. Aluminum profiles were processed using CNC for prototype production. Steel was processed using sheet metal laser cutting and underwent a textured paint process for a stable base. The prototype assembly was conducted, and strength tests of 350 kg were performed. Mechanical strength tests were applied to examine deformation. Subsequently, the transition to mass production was achieved.

A load of 350kg was applied to each mobile aluminum block over time, and the results were observed. The total deformation was calculated as 0.079mm, with a maximum stress calculated at 179.46MPa. As the material used was Aluminum 6063-T6, the found values were within safe limits. In another analysis scenario, an analysis was conducted for each of the 6 aluminum blocks with a load of 58.3kg. The total deformation was calculated as 0.015mm, with a total stress of 24.011MPa. When

evaluating individual parts, it was determined that Aluminum 6063-T6, the material chosen for this product, was suitable.

Additionally, fall-preventive measures were incorporated into the product design. A non-slip band was used to minimize the risk of slippage on the ramp. This was intended to enhance the safety of disabled individuals while using the ramp.

Aligned with the objectives, benchmarking and reverse engineering were conducted to analyze other disabled ramps, particularly those used in commercial vehicles in the market. Studies were carried out to design the ramp for the reduction in weight and cost. The aim was to minimize the thickness of Aluminum 6063-T6 extruded profiles and the section thickness of the ramp, ensuring it maintains the desired load resistance through Ansys static analyses. As a result of the design studies and analyses, it was anticipated that reducing the thickness of the disabled ramp by 55% and the section thickness by 33% would ensure compliance with the desired technical criteria. Consequently, the ramp's weight, designed and manufactured in this manner, was reduced from 35 kg to 16.0003 kg. Although the length and width dimensions of the disabled ramp remained the same as the rival product subjected to reverse engineering, the decrease in product weight not only provided comfort and ergonomic advantages to the end user but also facilitated a reduction in the overall weight of the vehicle. Additionally, the reduction in material usage decreased the cost of the ramp by 40%

III. Results and Discussion

To enhance the quality of life for individuals with disabilities and to facilitate their daily lives, disabled ramps hold significant importance. In this context, this article entails a cost analysis of the initially developed product and addresses its compliance with the currently used disabled ramps.

Initially, the product design was fashioned to be in line with existing disabled ramps. The product was designed using the fixed ground profile through the extrusion method, ensuring a durable and reliable structure. This design aimed to establish a platform that individuals with disabilities could confidently use.

Additionally, measures to prevent falls were integrated into the product design. The use of a non-slip band reduced the risk of slippage on the ramp to a minimum. Thus, the objective was to increase the safety of individuals with disabilities while using the ramp.

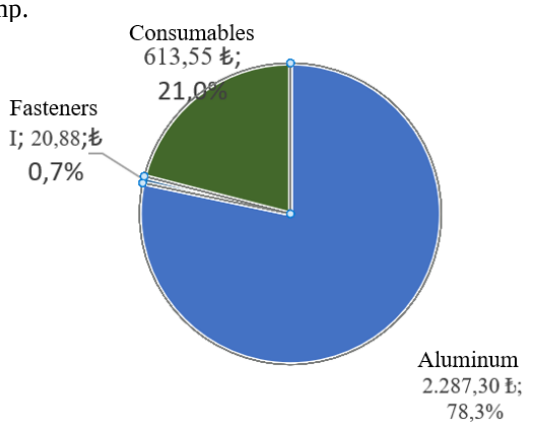

Figure 2: The Raw Material Cost of Existing Handicap Ramps in the Market

However, upon consideration of the advantages provided by the design and safety measures, it was determined that high costs were incurred when cost analyses were conducted. The use of quality materials and the need for specialized design have led to increased expenses. Nevertheless, the product's significant advantages in terms of quality and safety cannot be overlooked.

As a result, upon reviewing the design and cost analysis of the initially developed product suitable for disabled ramps, it is evident that it complies with the existing disabled ramps. However, exploring more cost-effective alternatives and optimizing the design could enhance the product's broader usability. Developing more suitable solutions for the needs of individuals with disabilities will contribute to promoting an inclusive life within society.

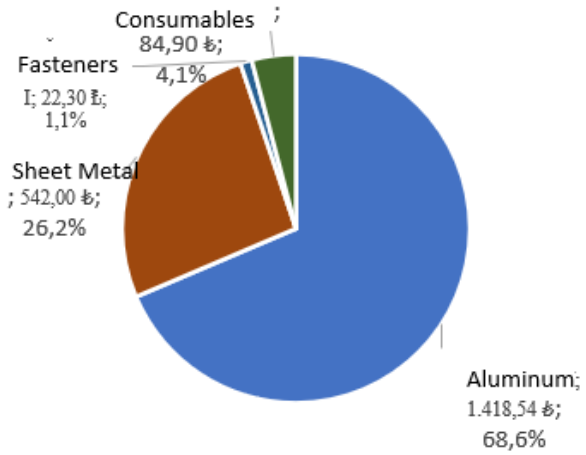

Figure 3: The Raw Material Cost of the Handicap Ramp Developed at KNS Automotive.

Each mobile aluminum block was loaded with a weight of 350 kg over time, and the results were observed. Total deformation was calculated as 0.079 mm, and the maximum stress was calculated as 179.46 MPa as shown below. Given the use of Aluminum 6063-T6 material, the obtained value is within safe limits.

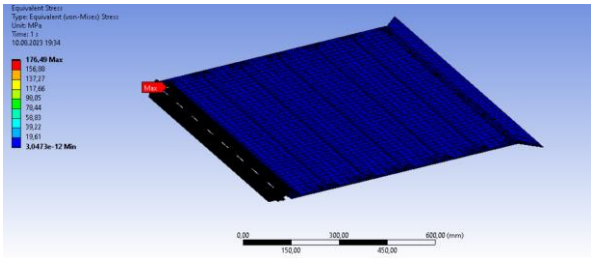

Figure 4: The maximum stress value (Von-Mises Stress) under a 350kg load over time.

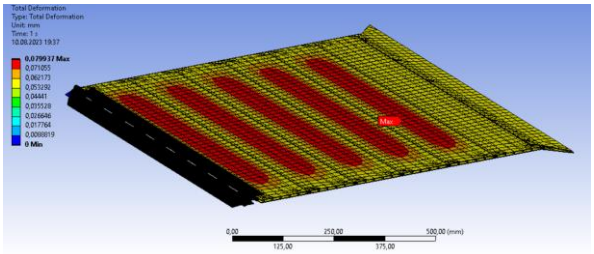

Figure 5: The total deformation amount under a 350kg load over time.

In another analysis option, the analysis was conducted with each of the 6 aluminum blocks subjected to a load of 58.3 kg. The total deformation was calculated as 0.015 mm, and the total stress was calculated as 24.011 MPa. Upon evaluating the individual parts, it was determined that the chosen Aluminum 6063-T6 material is suitable for this product.

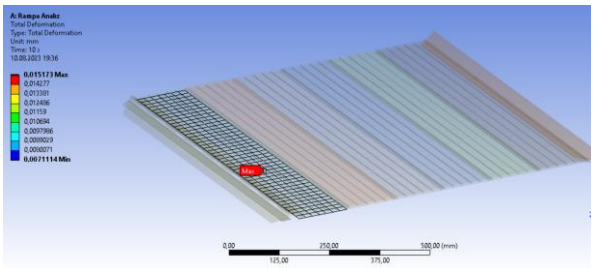

Figure 6: The total deformation amount under a load of 58.3 kg per aluminum block.

IV. Conclusion

In the conducted study, the aim was to improve the design of the wheelchair ramp to obtain a lighter and more ergonomic product. Analysis revealed that the foldable wheelchair ramps found in commercial vehicles on the market were excessively heavy. For the desired wheelchair ramp with a 360 kg weight capacity, it was observed that the weight could be reduced from 35 kg to 16.0003 kg by using Aluminum 6063-T6 material, while maintaining the same load capacity. With the reduction in weight, the cost of labor decreased due to the reduced material used and production time, resulting in a 40% decrease in ramp cost.

Acknowledgment

This scientific publication is the product of KNS Automotive's R&D studies within the scope of the "Scientific Publication Preparation Training for R&D Centers" given to the Design Center by Assoc. Prof. Dr. Muhammed Kürşad UÇAR. All rights of the products belong to KNS Automotive.

References

[1] "United Nations Convention on the Rights of Persons with Disabilities, https://treaties.un.org/Pages/Home.aspx, (Access Date: 11.10.2017)"

[2] Uslu, Aysel; Shakouri, Nasim (2014), "Independent Mobility and the Concept of Universal Design for People with Disabilities/Elderly in Urban Landscapes," Kastamonu University Journal of Forestry Faculty, Year: 14, Issue: 1, pp. 7-14.

[3] Gleeson, Brendan (2011), "Can Technology Overcome the Disabling City?", (Eds. Bezmez, Dikmen; Yardımcı, Sibel; Şentürk, Yıldırım), Disability Studies, Koç University Publications, Istanbul, 363-384.

[4] Yılmaz M. (2012), Inclusive Design and Space, Mimarist, Issue 43, pp. 107-111.

[5] Mishchenko E.D. (2014), With / For Everyone Design: Experience of an Inclusive Approach to Universal Design, Mimarist, Issue 50, pp. 105-111.

[6] TS 9111/ November 2011: Accessibility Requirements in Buildings for People with Disabilities and Mobility Impairments (This standard is enacted in place of the TS 9111-April 1991 standard that was cancelled.)

[7] Law on Disabilities, (1/7/2005), Official Gazette of the Republic of Turkey, 25868, 1 July 2005.

[8] Regulation on Accessibility Monitoring and Control, (20 July 2013), Official Gazette of the Republic of Turkey, 28713, 20 July 2013.

[9] TS-9111. (2011). Accessibility requirements in buildings for the disabled and mobility-impaired individuals.

[10] Directive 2001/85/EC of the European Parliament and of the council, 2001, OJ L 42, 13.2.2002.

[11] Öz, Şaban (2013). "From Disabled Religious Education to 'Disability-free' Religious Education Modeling: Problems Encountered by 'Othered' Disabled Individuals in Religious Education and Solution Proposals", Hikmet Yurdu Journal of Social Sciences Research, 6 (11), pp. 75-89.

Artificial Intelligence Supported Unmanned Aerial Vehicle with Semi-autonomous Flight Control for Forest Fire Detection

E. KOYUN[1] and A. GENC[2]

[1]Isparta University of Applied Sciences, Isparta/Turkey, emrekoyun4819@gmail.com
[2]Isparta University of Applied Sciences, Isparta/Turkey, abdullahgenc@isparta.edu.tr

***Abstract* - In this project, it is aimed to make early detection of forest fires using UAV (Unmanned Aerial Vehicle) and image processing technology. The UAV is designed and manufactured, and in the image processing process, a data set is created and trained, and fire and smoke detection are provided with the created data set. Image processing is performed with Raspberry pi 4, UAV parts are manufactured by 3D printing and APM 2.8 is used as the control card. The reason for the preference of the control card is that it supports autonomous flight. With the trained data set, image processing results were achieved with 94% accuracy**

***Keywords* - Image processing; UAV design and production; Forest fire detection; Autonomous flight; Artificial intelligence;**

I. INTRODUCTION

FOREST fires are destructive events that damage the ecosystem and the environment worldwide, and such disasters also jeopardize life. Fires can be caused by humans as well as natural pathways. The frequency and severity of fires are increasing day by day with the effect of climate change and drought. Therefore, early detection and intervention of fires is of vital importance.

Traditional fire detection methods are based on manpower and fixed observation towers. Scanning large forest areas with these methods is time consuming and very limited. For these reasons, more effective and faster solutions are needed.

In [1], a work on fire and smoke detection using RGB (Red Green Blue) colors on image processing was carried out. In another work in the literature, it is aimed to detect fluctuation data by converting RGB color data into HSV color feature data and performing Fourier transform [2]. In addition, in [3], the change of Landsat-8 satellite temperature data in burning regions was analyzed. A training model on fire detection with image processing was created [4]. An algorithm for fire detection and tracking was created and studies on color model analysis were conducted [5]. In another work, a work aiming for the fastest result and the highest accuracy rate was carried out using image processing techniques [6]. Finally, a drone was designed for the detection of forest fires [7].

In line with the information obtained from the literature, there are some advantages and disadvantages of using UAVs in forest fires. The advantages of these methods are early detection of fire, minimization of human errors and remote fire detection with image processing. The disadvantages are high cost, false alarm risks and data processing difficulties.

In this work, it is aimed to make early detection of forest fires by using UAV (Unmanned Aerial Vehicle) and image processing technology. Firstly, the UAV is mechanically designed and manufactured with 3D printing technology. Fire and smoke detection is performed using the OpenCV library image processing method. The area to be scanned by the UAV was pre-programmed with a computer and transferred to the flight card. Autonomous and manual control of the control card during flight was provided by providing Raspberry Pi 4 and APM 2.8 communication. In this work, UAV design and production is carried out for the detection of forest fires. Image processing algorithms (ResNet 18) are used for the detection of forest fires. A dataset was created using a total of three thousand photographs, 33% of these photographs contain forest fire, 33% smoke and 34% non-fire forest images. This training set was tested with a total of three thousand photographs consisting of different images. UAV design is created and manufactured in computer environment. Appropriate control card and machine elements were selected and manufactured to support autonomous flight. UAV designs are analyzed to be used in the detection of forest fires. The appropriate design is realized in line with the designs in the work and the equipment to be used. In addition, although there are similar studies in the literature, this work contributed to the literature by increasing the accuracy of the image processing process with the use of artificial intelligence and image processing technology.

II. MATERIAL AND METHOD

The mechanical and electronic materials to be used in the design of the UAV are selected. The design was made according to these products. While selecting each part, the desired features and the compatibility of the parts with each other were examined. In this direction, the necessary materials were procured and the UAV was designed to be compatible with these parts.

A. MECHANICAL DESIGN OF THE UAV

During the UAV design process, 3D drawings are made for the weight, size, compatibility of mechanical and electronic parts, and the smooth operation of the production and assembly stages. Possible problems that may occur before production were observed with the assembly feature in the Solidworks programme shown in Figure 1. The static analyses of the parts are made by means of the design programme. The lower body of the UAV is designed by considering the mechanical elements to be used in the design process. The battery compartment was designed in the lower body to ensure weight balance. The Raspberry Pi 4 device is mounted on the lower body because it is safe and protective from external factors (Figure 1a).

The upper body was designed due to the need for GPS, control card placement and protection for the lower body. While designing, effects such as ease of assembly were taken into consideration. At the same time, it provides body integrity with its connection to the UAV arms (Figure 1b).

The UAV arm made with the design programme clamps the upper and lower body together. At the same time, the engine and ESC connection is also made to the UAV arm. Considering these requirements, the UAV arm must be robust. Two different designs were made during the work phase, and the design used is shown in Figure 1(c).

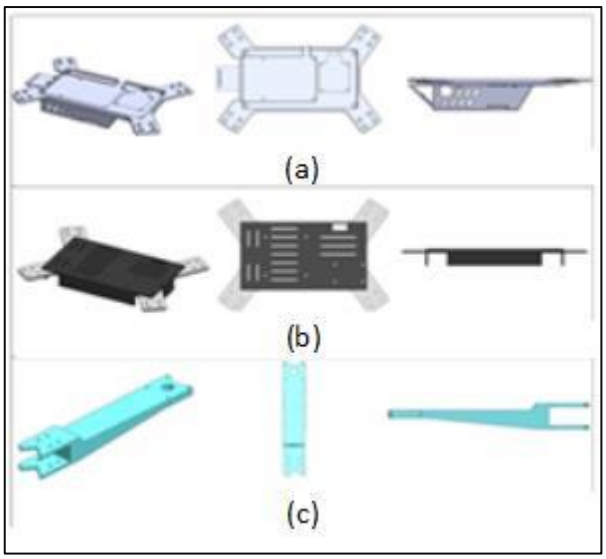

Figure 1. UAV design (a) lower fuselage view (b) upper body view (c) UAV arm view

B. MECHANICAL DESIGN OF THE UAV

Figure 2 shows the electronic components used. The control card provides the controls required for flight; GPS, compass, barometer and acceleration sensors are used to realize autonomous flight. It also transmits the PWM (Pulse Width Modulation) signals required for flight to the ESC (Electronic Speed Controller) (Figure 2a). The task of the Raspberry Pi 4 device is to provide communication with the ground and to perform fire detection using image processing algorithms. The power supply is provided from the legs on the power distribution board giving 5V 2A output (Figure 2b).

In the selection of the brushless motor, the thrust force applied by the motor, the operating current and the appropriate power value were determined and the appropriate brushless motor was selected (Figure 2c). ESC provides a stable flight by controlling the rotation speed of the motors. It adjusts the rotation of the motor according to the signals sent by the control card. While selecting the ESC, the maximum current value that the motor draws at instantaneous load was taken into consideration (Figure 2d). GPS support is required for autonomous flight. NEO-6m module was used for high accuracy, low power consumption and easy operation (Figure 2e). In addition, the power distribution element distributes power for the ESC. Since the Raspberry Pi 4 device will be used in the system, a power distribution board with 5V 2A output support was selected (Figure 2f)

The camera module required for the Raspberry Pi 4 device to detect fire and smoke using the image processing algorithm. It is mounted on the lower body (Figure 2g). On the other hand, a Li-Po battery capable of discharging current at high amperage values was selected to provide the energy required for flight. Since its weight is higher than its capacity, it is taken into account when calculating the flight time. 3s 4200 mAh battery was preferred (Figure 2h).

The propellers are connected to the motors. During the installation, the propeller suitable for the engine direction was mounted to that engine. There are 2 types of propellers, clockwise and anti-clockwise. In this work, a propeller with a diameter of 9 inches and a pitch of 15 degrees was selected (Figure 2i). Also, the data processed by the Raspberry Pi 4 processor needs to be sent to the ground station, for which a long-range wireless module is used (Figure 2j).

Lastly, the energy from the battery needs to be connected to the power module before being connected to the power distribution board. With this module, we can measure current and voltage values and transfer this information to the flight card. The current drawn by the system was calculated and the power module was selected to handle the current drawn (Figure 2k). The technical specifications of the finally designed UAV are given in Table 1.

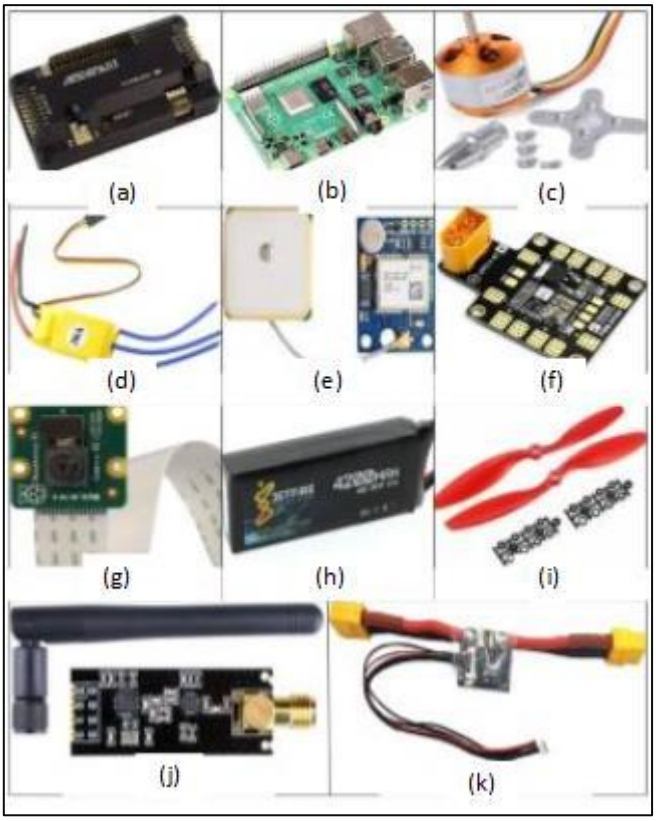

Figure 2. Mechanical and electronic parts. (a) controller board (b) Raspberry Pi 4 (c) brushless motor (d) ESC (e) GP S module (f) power distribution board (g) camera sensor (h) Li-Po Battery (i) propeller (j) wireless module (k) power module

Table 1. UAV technical specifications.

Parameters	Specifications
UAV dimensions	560×550×210 mm
Wing lengthzunluğu	228.6 mm
UAV weight	1100 grams
Battery capacity	11.1 V 4200 mAh
Remote control distance	2000 metres
Communication distance	1000 metres
Flight time	6 minutes
Battery charging time	180 minutes
Processing power	1.5 GHz

Figure 3 shows the assembly image of the UAV and the image of the fire detection application with image processing on the computer screen. The screen shows the prediction value, probability value of the prediction and FPS (Frame Per Second) values.

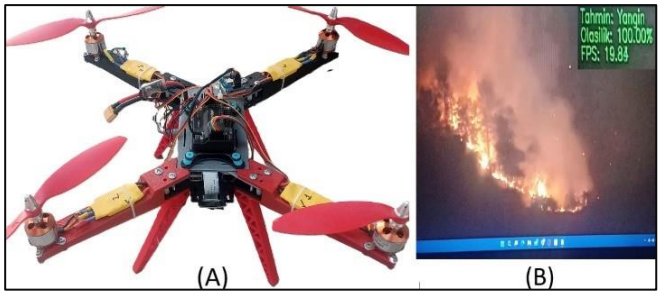

Figure 3. (a) Unmanned aerial vehicle assembly (b) image processing screen

Then, the mechanical assembly of the UAV, which was designed and manufactured, was completed. One brushless motor was connected to each arm. Each brushless motor was controlled by separate ESCs to provide power to the motors. ESCs were controlled by the signal received from the control card. The Raspberry Pi 4 device was mounted in the place set in the body of the UAV and the camera connection was completed. The transceiver circuit was fixed and the prototype was made operational by connecting the battery. The system was powered and the control connection was made. ESCs were calibrated and it was observed whether they were working correctly. It was checked whether the motors were working in harmony with each other. In addition, with the connection with the ground station, altitude, compass, battery value and acceleration sensor control of the data from the control card were provided.

III. REALISATION OF AUTONOMOUS FLIGHT USING IMAGE PROCESSING

The training module required for processing the images to be processed on the Raspberry Pi 4 device was trained with the data set containing forest fire, smoke and non-fire images. As a result of the training, the trained model was found to work with 94% accuracy and is given in Table 2. The flow chart showing the working stages of the system is shown in Figure 4.

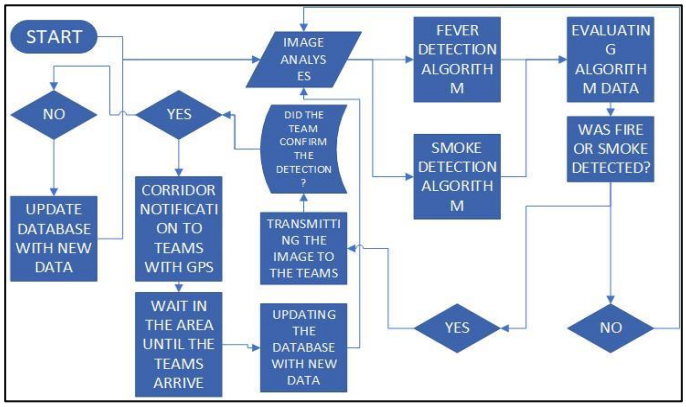

Figure 4. Process flow chart

While creating the training module, data sets consisting of forest fire, smoke and non-fire images taken from the Kaggle field were analyzed. Using these data sets, a data set was created by selecting one thousand photographs for each group suitable for the work. The created dataset was trained using ResNet18 network. In the trained model, the model with the highest accuracy rate (94%) was selected among different training cycles (Figure 5).

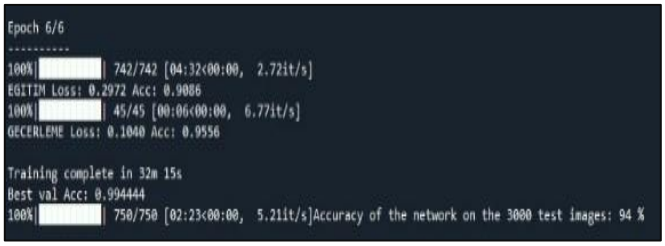

Figure 5. Accuracy result of the trained model

All codes are written using Python software language. The codes that will run on the Raspberry Pi 4 operating system enable the flight to be controlled by instantly processing the images from the camera and sending the processed results to the control card as a PWM signal. At the same time, information is transmitted to the center based on the image processing results. The route required for autonomous flight was created by controlling the APM 2.8 card with autonomous flight support with the mission planner application and the autonomous flight control screen is given in Figure 6. The GPS module required for autonomous flight is activated and the drone performs autonomous flight over its instantaneous position. As a result of the PWM signals sent to the APM 2.8 controller card as a result of image processing, the drone was able to fly autonomously by receiving the signals to remain stationary in its position during autonomous flight, to return to the ground station and to continue autonomous flight.

Figure 6. Autonomous flight control screen

With the 4200 mAh battery used in the UAV, flight time was calculated for windy and windless environment. A flight time of 6 minutes was calculated in a windless environment and a flight time of 5.5 minutes in a windy (3m/s) environment. In addition, the same calculation was made with a battery of 8400 mAh, and since the capacity increased, the flight time of 10 minutes was calculated for the windless environment and 9 minutes for the windy environment, taking into account the increase in the total weight of the UAV.

With these values, the area scanned with the camera view angle was calculated depending on the flight height of the UAV. If the UAV flies at a height of 100 meters, it can scan 120 acres, while it can scan 70 acres when it flies at a height of 50 meters.

Table 2. Accuracy rates of the system

Detections	Number of tests	Successful result	Accuracy rate
Fire detection	3000	2983	99%
Smoke detection	3000	2657	89%

IV. CONCLUSION

This work is developed with the aim of reducing the destructive effects of forest fires and minimizing forest fires. In line with this purpose, the following objectives have been determined:

- ✓ Increasing the use of UAVs in forest fire detection
- ✓ To create an autonomous system infrastructure that provides the ability to control the area without interruption.
- ✓ To achieve high accuracy rates by using artificial intelligence and image processing technology in fire detection.
- ✓ To ensure that the UAV can operate uninterruptedly.
- ✓ To design and produce a UAV that updates its database with the images it obtains, thus continuously improving itself.

In addition, a fast and effective early detection system was created by using UAV and image processing technology in a synchronized manner. In the implementation phase of the work, pilot regions should be selected and tests should be carried out, problems should be identified and deficiencies should be eliminated. Thanks to the newly collected data, image processing should be improved to reach higher accuracy values.

ACKNOWLEDGMENT

All authors would like to thank TUBITAK for its support within the scope of 2209-A University Students Research Projects Support Program (Project No: 1919B012220549).

REFERENCES

[1] Thou-Ho Chen, Ping-Hsueh Wu, and Yung-Chuen Chiou, "*An early fire-detection method based on image processing*", In 2004 International Conference on Image Processing, 2004. ICIP '04., Singapore: IEEE, 2004, pp. 1707-1710. doi: 10.1109/ICIP.2004.1421401.

[2] H. Yamagishi ve J. Yamaguchi, "*Fire flame detection algorithm using a color camera*", içinde MHS'99. Proceedings of 1999 International Symposium on Micromechatronics and Human Science (Cat. No.99TH8478), Nagoya, Japan: IEEE, 1999, pp. 255-260. doi: 10.1109/MHS.1999.820014.

[3] A. CiHan, K. CeriT, ve A. Erener, "*Yangın Alanında Uydu Görüntüleri ile Yer Yüzey Sıcaklık Değişimi Gözlemi ve Mekânsal Alan Tespiti*", Doğal Afetler ve Çevre Dergisi, vol. 8, pp 1, pp. 142-155, Oca. 2022, doi: 10.21324/dacd.942724.

[4] B. Aksoy, K. Korucu, Ö. Çalişkan, Ş. Osmanbey, ve H. D. HaliS, "*İnsansız Hava Aracı ile Görüntü İşleme ve Yapay Zekâ Teknikleri*

Kullanılarak Yangın Tespiti: Örnek Bir Uygulama", Düzce Üniversitesi Bilim ve Teknoloji Dergisi, vol. 9, pp. 112-122, Dec. 2021, doi: 10.29130/dubited.1016195.

[5] C. Yuan, Z. Liu, ve Y. Zhang, "*UAV-based forest fire detection and tracking using image processing techniques*", In 2015 International Conference on Unmanned Aircraft Systems (ICUAS), Denver, CO, USA: IEEE, June. 2015, pp. 639-643. doi: 10.1109/ICUAS.2015.7152345.

[6] T. Celik, "*Fast and Efficient Method for Fire Detection Using Image Processing*", ETRI J, vol. 32, pp. 881-890, Dec. 2010, doi: 10.4218/etrij.10.0109.0695.

[7] A. Demirtaş, "*Döner kanatlı insansız hava araçları ile görsel verilere dayalı erken yangın algılama sistemi*", masterThesis, Ankara: Ankara Üniversitesi: Fen Bilimleri Enstitüsü: Bilgisayar Mühendisliği Anabilim Dalı: Bilgisayar Mühendisliği Bilim Dalı, 2019. https://dspace.ankara.edu.tr/xmlui/handle/20.500.12575/69061

[8] M. İ. Ekmen ve Ö. Aydoğdu, "*İnsansız Hava Araçları İçin Görüntü İşleme Tabanlı Otonom İniş*", European Journal of Science and Technology, 2020, doi: 10.31590/ejosat.804502.

[9] T. Bieler, M. Perrottet, V. Nguyen, and Y. Perriard, "*Contactless power and information transmission*", IEEE Trans. on Ind. Applicat., vol. 38, pp. 1266-1272, Sep. 2002, doi: 10.1109/TIA.2002.803017.

[10] V. M. Becerra, "*Autonomous Control of Unmanned Aerial Vehicles*", Electronics, vol. 8, pp. 452, Apr. 2019, doi: 10.3390/electronics8040452.

Tubular Permanent Magnet Linear Motor Design For Aircraft Actuator Instead Of Hydraulic Actuators

H.UZUNER[1] and K. ERKAN[2]

[1] Yildiz Technical University, Istanbul/Turkey, halit_uzuner41@hotmail.com
[2]Yildiz Technical University, Istanbul/Turkey, kerkan@yildiz.edu.tr

Abstract **- The aviation industry has long struggled with the hydraulic leakage and wear problems in traditional hydraulic actuators, and the maintenance costs that come with these issues, necessitating the search for more efficient and eco-friendly alternatives. This paper presents design of a Tubular Permanent Magnet Linear Motor (TPMLM) as a prospective solution to these problems, aiming to replace hydraulic actuators in aircraft control systems.**

Hydraulic actuators have been plagued by issues such as fluid leakage and component wear, leading to costly maintenance and potential safety concerns. The TPMLM, known for its simplicity, compactness and low mechanical friction offers a promising remedy for these challenges. In this study, we conducted magnetostatic and transient simulations using the Finite Element Method (FEM) implemented in ANSYS Maxwell to comprehensively evaluate the performance of TPMLM and the simulation results were compared with the hydraulic actuators used in aircraft.

Keywords **- Tubular permanent magnet linear motor, TPMLM, Tubular linear motor**

I. INTRODUCTION

In the aviation industry, hydraulic actuators are generally used to provide flap, slat and landing gear movements in aircraft. These actuators provide the necessary force and torque for the landing gear, slat, flap, cargo door, MLG door etc. movements of aircraft. However, one of the biggest disadvantages of these actuators is hydraulic leakage problems, and another is wear problems caused by mechanical friction [1].

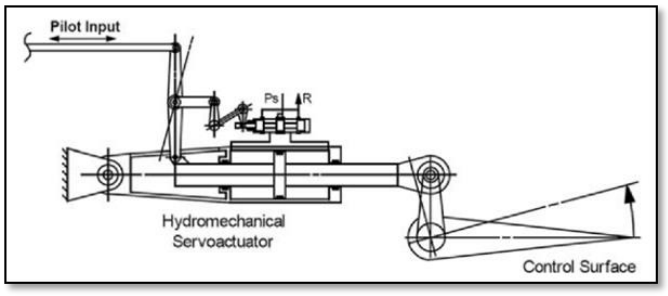

Figure 1: Aircraft Spoiler Actuator [3]

An example of spoiler actuator that enable the opening and closing the spoilers in aircraft. This actuator has approximately 45 cm stroke. The hydraulic full weight of the actuator is 12 kg. Its output force is 7 kN [2].

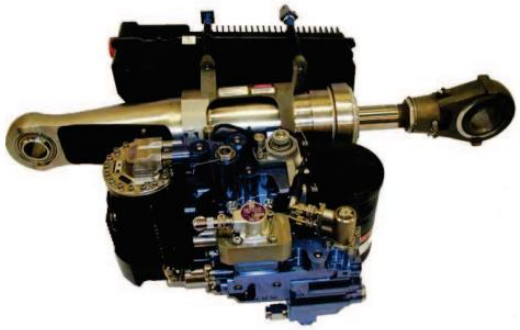

Figure 2: Electrical Backup Hydraulic Actuator from A380 Rudder [4]

Another example of hydraulic actuators used in aircraft is the Electrical Backup Hydraulic Actuator from A380 rudder. This actuator allows the rudder to move left and right. The actuator is approximately 60 cm long. Its full hydraulic weight is 60kg and its stroke length is 50cm. It operates at a load capacity of approximately 2500 daN [4].

It is thought that by using TPMLM instead of these hydraulic actuators, the necessary slat, flap, cargo door and MLG door movements can be made for the aircraft and hydraulic leakage problems can be eliminated and wear problems can be minimised.

TPMLM has a number of advantages that will allow them to be used in place of hydraulic actuators. They are direct drive systems, meaning they do not require a gear mechanism and have high linear force densities. They operate with almost zero friction. Therefore, wear problems almost never occur [5].

A permanent-magnet tubular linear motor (TPMLM) is a collection of coils wrapped around a cylinder which encloses a movable rod with permanent magnets aligned in alternating and opposing directions. It operates using identical physics principles as conventional electric motors i.e. Ampere's Law. The current passing through the coils creates a magnetic field,

and this magnetic field interacts with the magnetic field on the rotor to create the force. In the case of conventional electric motors, the arrangement of electromagnets creates a moving magnetic field along the perimeter of a circle. In the case TPMLMs, the arrangement of electromagnets creates a moving magnetic field along the inner axis of a cylinder [5], [6].

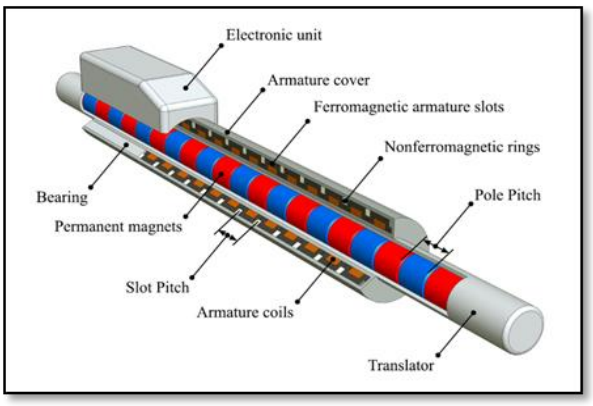

Figure 3: Structure of TPMLM [6]

There are various designs that adopt different magnetization directions and flux paths. Magnetization of permanent magnets affects the magnetic field strength, magnetic losses and output power of TPMLM. Magnetization topologies are examined under three main headings: radial, axial and Halbach. Schematic views of the three topologies are shown in Figure 4 below [7].

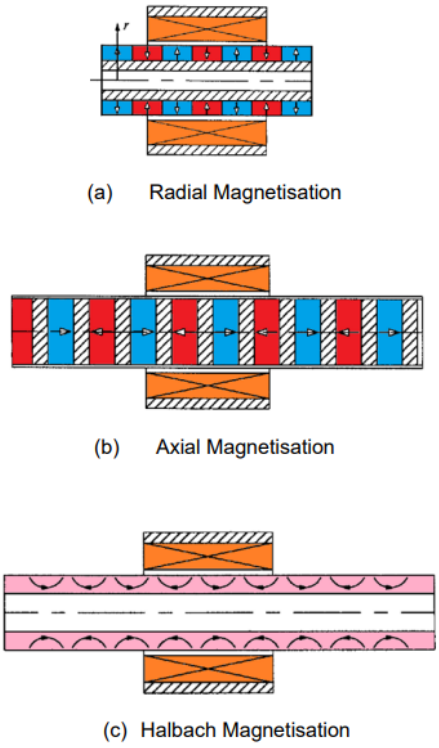

Figure 4: Tubular Permanent Magnet Linear Motor Topologies [7]

II. Material and Methods

The working principle of Tubular Permanent Magnet Linear Motors is based on Ampere's Law, Lorentz Force. Lorentz force occurs as a result of the interaction of the magnetic field created by Permanent Magnets and the magnetic field created by the current flowing through the coils. It can be written as [7]:

$$F_L = \int_v JxB_d \, dv \tag{1}$$

Here B_d is the flux density and J is the current density. If the current is in the Z-direction and the motion is in the X-direction, for single - turn coils, the forces can be written as [7]:

$$F_L = -NI_cL_eB_{avg} \tag{2}$$

where L_e is the length of the coil, I_c is the current and B_{avg} is [7]:

$$B_{avg} = \frac{1}{A_c}\left(\int_{a^+} B_y \, da - \int_{a^-} B_y \, da\right) \tag{3}$$

and we can present magnetic flux density in the air gap as [7]:

$$B = \frac{\Psi_m}{A_r} \tag{3}$$

Based on the flux density and force equations, rotor design for TPMLM has started. First of all, since the implementation of the Halbach array is costly and difficult to produce, it was decided that the magnets would be axial magnetized and the motor topology was chosen as axial magnetisation topology. Neodymium (NdFeB)Nd35 standard magnets were preferred due to their magnetic properties and high magnetic flux density. Due to the size of the magnets used in this study, the magnets were placed in pairs.

In order to get maximum torque from the motor, maximum magnetic flux must be provided from the rotor. For this reason, 2D FEM analyzes were performed to decide on the placement of spacers between magnet pairs. In the first analysis, magnets were placed without a spacer between the magnets. As a result of the analysis, the magnetic flux density created by the magnets is seen in Figure 5.

FEM analysis was performed by placing non-ferromagnetic spacers between the magnet pairs. In the analysis, spacer lengths between 0.5mm and 4mm were examined. Analysis results are shown in Figure 6. FEM analysis was repeated by placing a ferromagnetic spacer between the magnet pairs. In the analysis, spacer lengths between 0.5mm and 4mm were examined. Analysis results are shown in Figure 7. All 3 analysis results were examined and the spacer material was

determined as ferromagnetic material due to the rotor providing a higher magnetic flux density.

Another factor that affects the magnetic flux density of the rotor is the material of the shaft. Two different FEM analyzes were performed to determine the material of the shaft. In the first analysis, the shaft material was selected as non-ferromagnetic material and the analysis results are shown in Figure 8. In the second analysis, the shaft material was chosen as ferromagnetic material and the analysis results are shown in Figure 9. The results were examined and it was seen that the magnetic flux density was higher when a non-ferromagnetic material shaft was used. Thus, the shaft material was chosen as non-ferromagnetic material.

Since higher power is obtained, the stator design consists of 3 phase windings with +U, -W, +V, -U, +W, -V winding shape. The air gap is determined as 1mm. As a result of the engine stroke length and operating requirements, it was decided to create the stator from 36 coils.

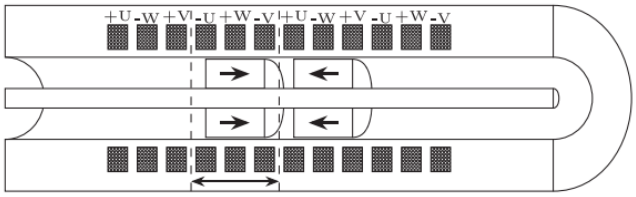

Figure 10: +U, -W, +V, -U, +W, -V Winding Shape [8]

As a result of the results obtained in the analysis and the operating requirements, the parameters of the engine were determined as in Table 1.

Motor Design Parameters	Values
Outer Radius of Magnet	18 mm
Inner Radius of Magnet	5 mm
Length of Magnet	9 mm
Outer Radius of Spacer	18 mm
Inner Radius of Spacer	5 mm
Length of Spacer	4 mm
Radius of Shaft	5 mm
Length of Shaft	350 mm
Air Gap	1 mm
Outer Radius of Coil	28 mm
Inner Radius of Coil	20 mm
Length of Coil	7 mm
Number of Coils	50 turns
Length of Between Coils	1 mm
Number of Magnets	16
Number of Turns	36

Table 1. Motor Design Parameters

As a result of the determined parameters, the concept design of the study is shown in Figure 11.

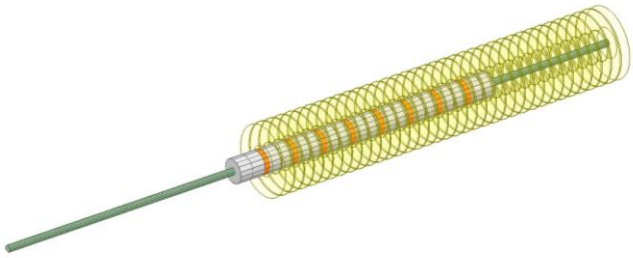

Figure 11: TPMLM Consept Design

III. Results and Discussion

Transient analyzes of the tubular linear actuator, whose parameters and concept design were determined, were carried out using the ANSYS Maxwell. 3 phase current is given as 5A and frequency is selected as 1 Hz. The analysis result is shown in Figure 12.

IV. Conclusion

Within the scope of this study, a tubular type linear actuator design is presented instead of the hydraulic actuator systems used in aircraft. Considering future experimental studies, the proposed linear actuator was scaled and designed in smaller dimensions to obtain 80 N force. Spacer dimensions were determined by iterative FEM analysis to maximize the magnetic flux density. Afterwards, different materials for the spacer and shaft were analyzed and the most suitable material for the proposed actuator was determined. According to the analysis results, a targeted force of over 80 Newtons was achieved with a 35cm motor and the final design was presented. The results obtained with experimental studies will be confirmed in future studies.

References

[1] P. Jänker, F. Claeyssen, B. Grohmann, M. Christmann, T. Lorkowski, R. LeLetty, O. Sosniki, A. Pages, "New Actuators for Aircraft and Space Applications, Journal of Nuclear Materials", 11th International Conference on New Actuators, Bremen, Germany, 2008

[2] LI, Jianming, et al. A review of electromechanical actuation system for more electric aircraft. In: 2016 IEEE International Conference on Aircraft Utility Systems (AUS). IEEE, 2016. p. 490-497.

[3] S. Wang, M. Tomovic, H. Liu, "Commercial Aircraft Hydraulic Systems, 2016

[4] J. W. Bennett, "Fault tolerant electromechanical actuators for aircraft", PhD Thesis, Newcastle University, 2010

[5] J. A. Woodroffe, "Design and Construction of a Liquid-Cooled, Flexible,Permanent-Magnet Tubular Linear Motor Artificial Muscle", Northeastern University, 2020

[6] N. Quang, H. Quang, N. P. Quang, V. L. Nguyen, "A sensorless approach for tracking control problem of tubular linear synchronous motor", International Journal of Electrical and Computer Engineering, 2022.

[7] N. Gargov, "Permanent Magnet Linear Generators for Marine Wave Energy Converters", University of Exeter, 2013

[8] F. Dreishing, C. Kreischer, "Experimental and Analytical Analysis of a Compact Ironless Permanent-Magnet Tubular Linear Motor (PM-TLSM)", In: Electromechanical Drive Systems 2021, ETG Symposium. VDE, 2021, p. 1-6

I. GRAPHIC FIGURES

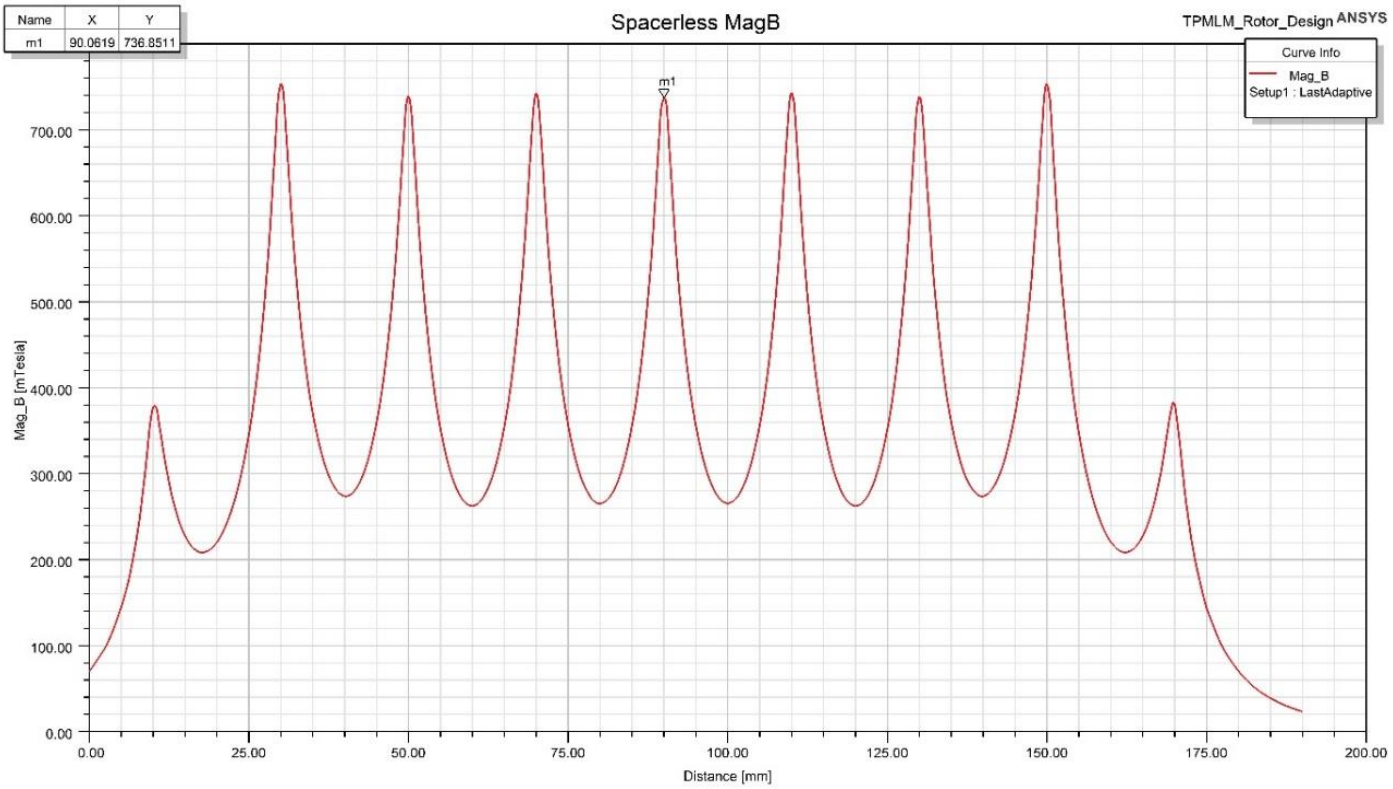

Figure 5: Spacerless Rotor MagB

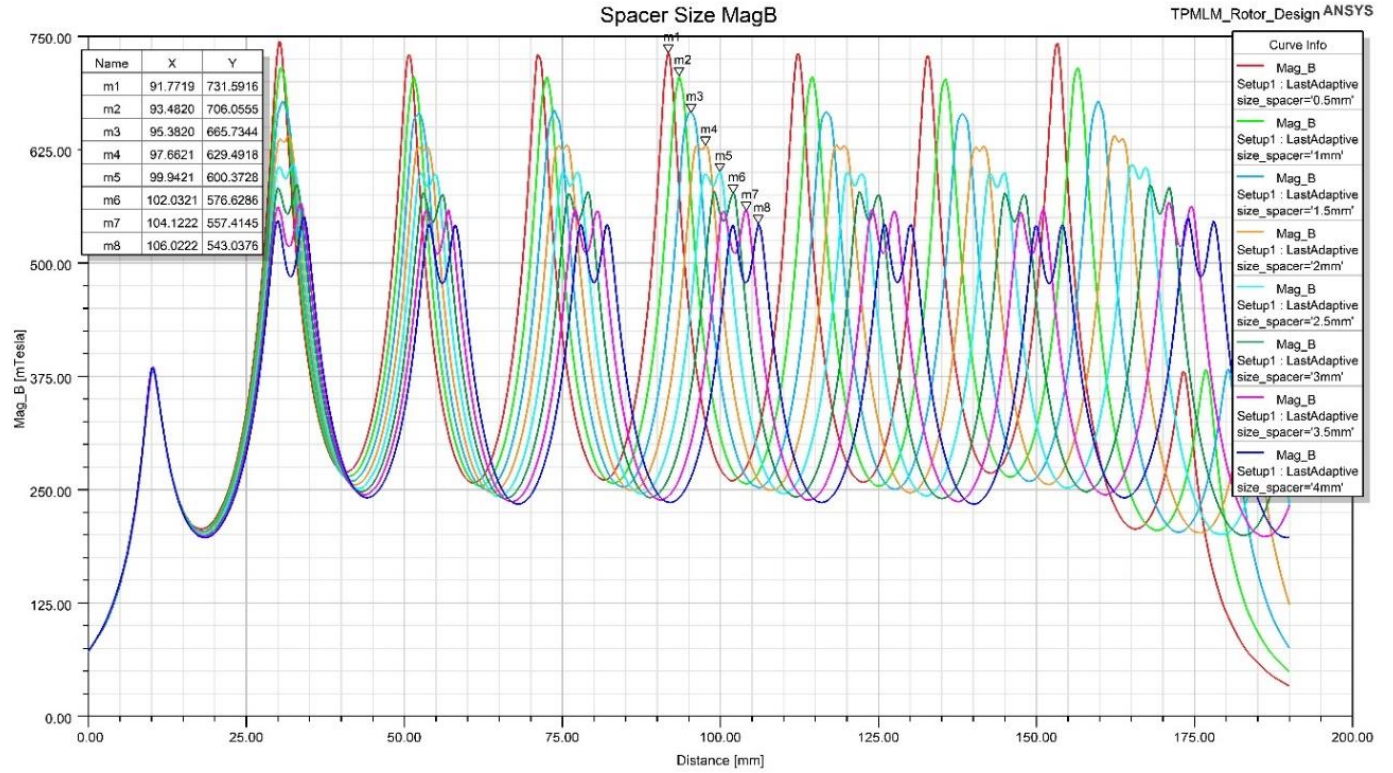

Figure 6: Non-ferromagnetic Spacer MagB

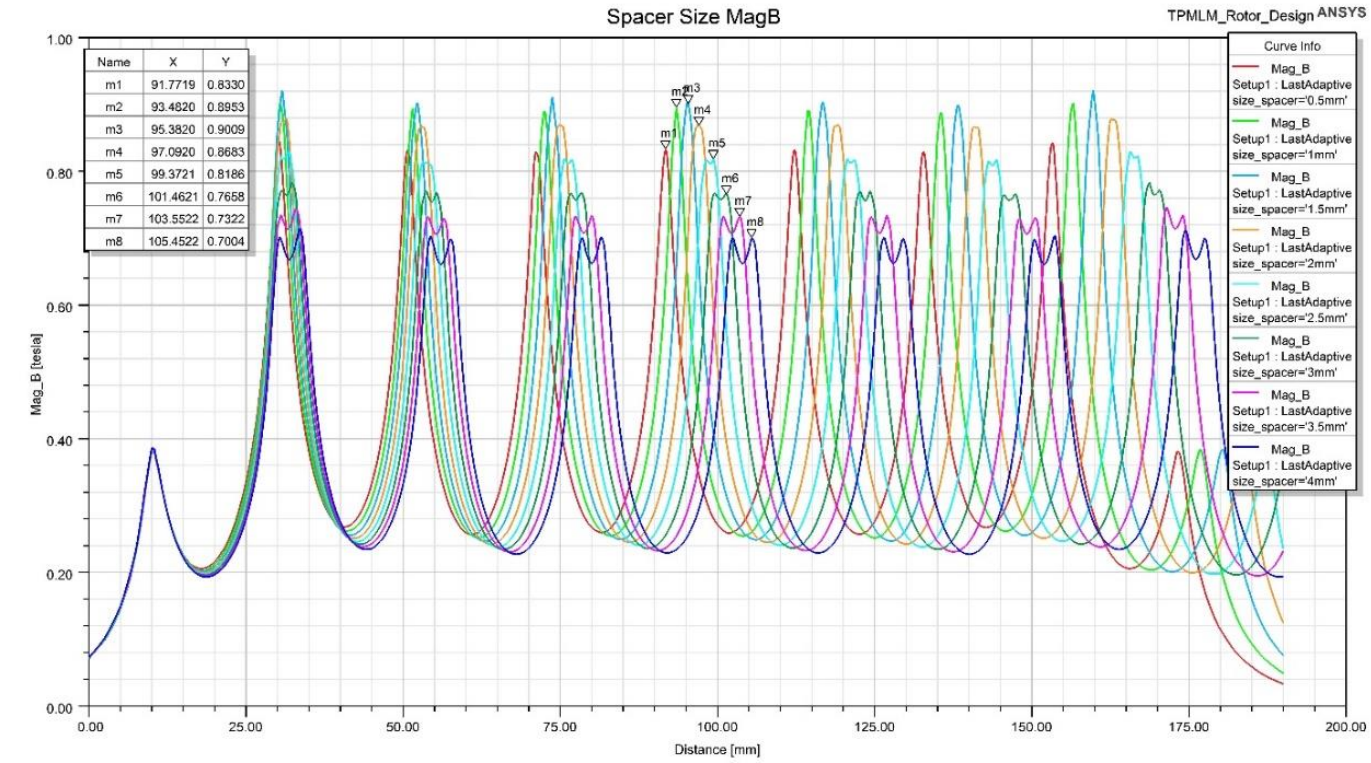

Figure 7: Ferromagnetic Spacer MagB

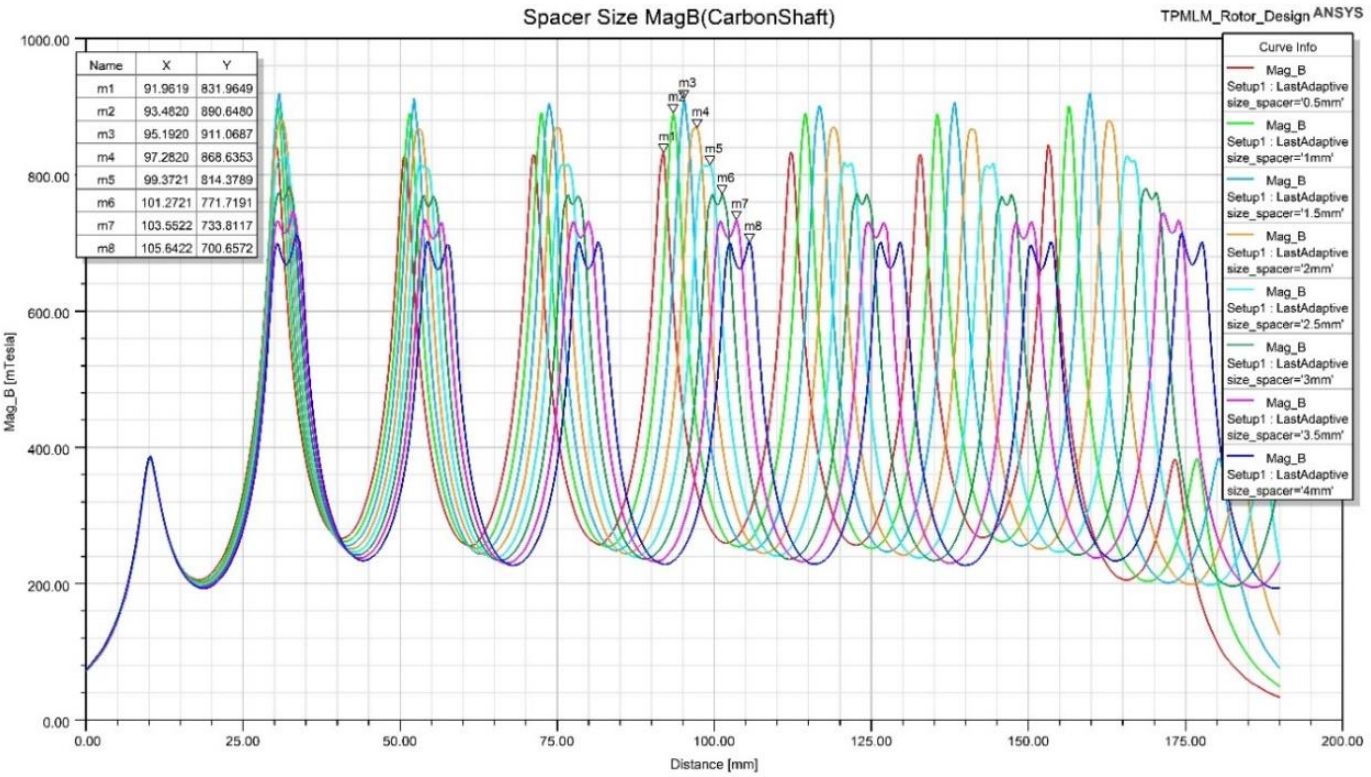

Figure 8: Carbonfiber Shaft Spacer Size MagB

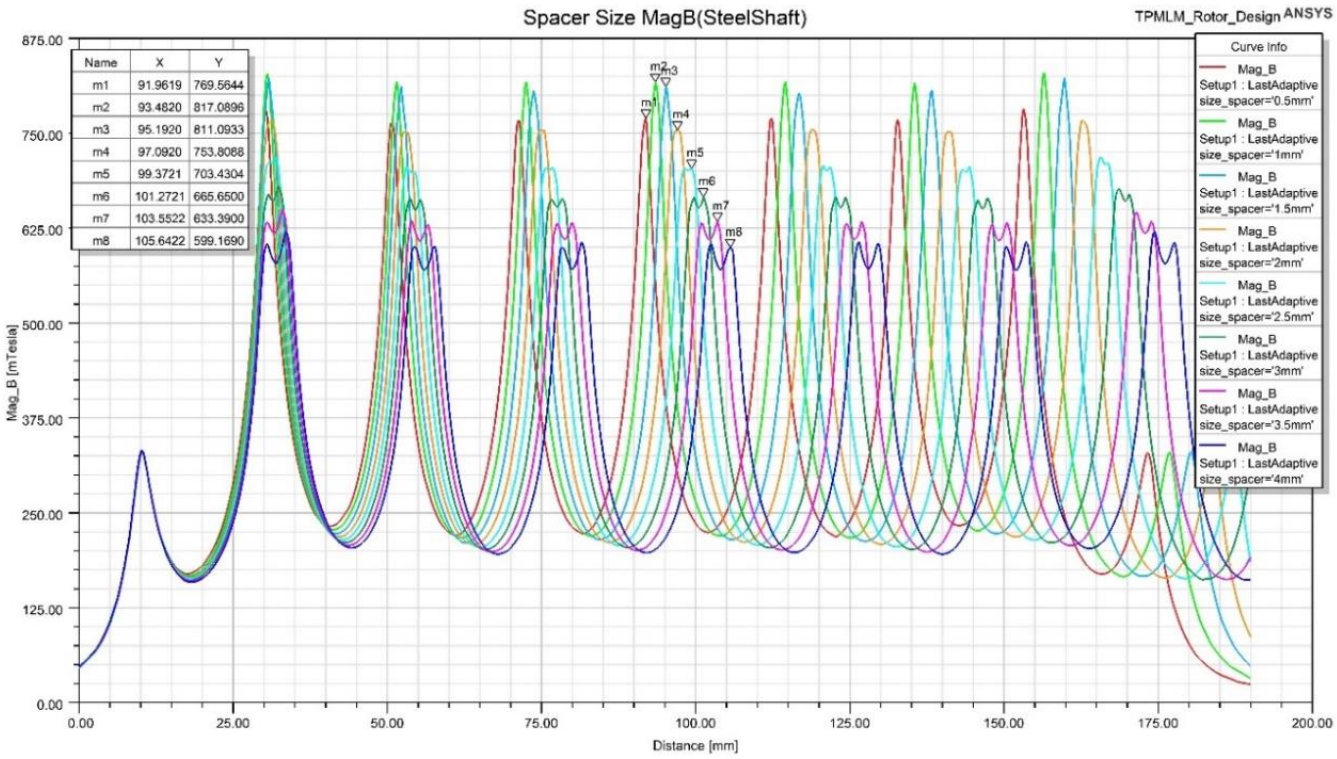

Figure 9 Steel Shaft Spacer Size MagB

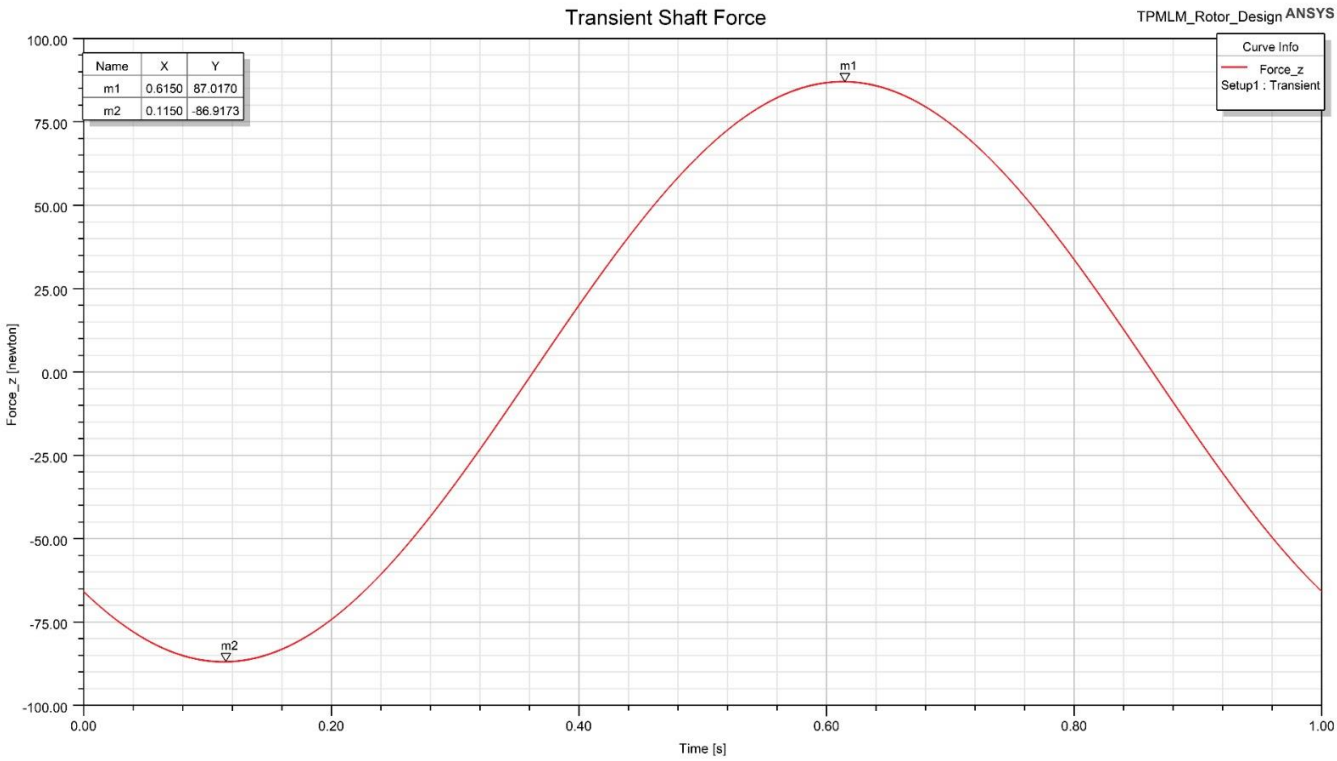

Figure 12 Consept Design Torque Output

Optimal Spherical Mechanism Design For Sun Tracking On Two Axis

Ziya ÖZÇELİK[1], Osman ACAR[2] and Azim HANSU[3].

[1]Selcuk University, Konya/Turkey, zozcelik@selcuk.edu.tr
[2]Selçuk University, Konya/Turkey, osmanacar@selcuk.edu.tr
[3]Selcuk University, Konya/Turkey, azimhansu@gmail.com

Abstract - This paper presents a research for minimum torques on the fixed joints rotation axis of optimum spherical mechanism design with five bar and two degree of freedom which can provide a solar panel to get sun rays perpendicular. In this context, the objective function and constraints of the optimization problem were created. The solution was obtained using the Artificial Harmonic Bee Colony (AHBC) algorithm. The schematic design of mechanism was given as result with the best design variables.

Keywords - Spherical mechanism, Solar Energy, Sun tracking system, Heuristic optimization, Artificial Harmonic Bee Colony algorithm

I. INTRODUCTION

The usage of fossil fuels will decline as solar energy-related technology advances and becomes more widely used, which will reduce air pollution. Solar tracking systems make sure the solar panel, which uses the sun's rays to generate power, is in the best possible position every day, hour, and minute of the year to generate more energy. In recent years, the solar panel sector has grown quickly. The annual production of solar panels climbed by an average of 56% per year between 2005 and 2012, a sixteen-fold increase in production. Between 2005 and 2012, using solar energy to produce electricity was more expensive than using coal or natural gas, which are more commonplace energy sources. In spite of this cost disadvantage, the sector has grown quickly because to large subsidies in many nations. These government subsidies have frequently been defended on the grounds that supporting the solar business will result in an increase in the amount of solar energy produced. This assumption is primarily supported by the fact that there are learning externalities and static economies of scale in the sector. Reduction in production costs and price of solar panels. Based on this information, additional design studies were necessary to enable the production of solar tracking systems at cheaper costs, allowing for their widespread application [1].

A two-axis solar tracking system was created by Nijmeh et al. using a gear mechanism and a programmable logic controller to allow the solar panel to be moved to five different positions throughout the day. This system offers 43.87% more efficiency for two axes, east-west tracking, than a fixed solar panel inclined at 32° south. was able to generate electricity [2].

By moving two rod mechanisms on two linear slides perpendicular to one another and coupled to a wind-resistant parabolic solar panel that casts the smallest possible shadow, Barker and Neber were able to monitor the sun. They discovered that this system had an efficiency of 30% [3].

Yao and Hu developed a biaxial two-degree-of-freedom planar mechanism for usage on building rooftops that has a 30% efficiency and good wind resistance [4].

By analyzing the kinematic characteristics of a motion platform made up of three universal joints, two prismatic joints, and two spherical joints for solar tracking, Cammarata contributed the ideal working space to the literature [5].

In their study, Sungur et al. determined the azimuth and elevation angles of the sun for a year at a latitude of 37.6° in the Northern Hemisphere, which is Turkey, and created an electromechanical system that follows the sun in accordance with these angles. An analog module and programmable logic control (PLC) have been used to create and construct a module with two axes. The performance measurements of the solar panel were first taken while the solar panel was in a fixed position, then the solar panel was checked by following the sun in azimuth and sun elevation angles, and the necessary measurements were taken. This was done after the mechanical control unit of the designed system was put into operation The control system has been seen to operate without any problems. Additionally, it was discovered that the two-axis solar tracking system produced 42.6% more energy than the fixed system when the data from the measurements were compared [6].

Eke et al. examined the performance of two dual-axis solar tracking photovoltaic (PV) systems after one year of operation in their study. They erected two identical 7.9 kWp PV systems with the same modules and inverters on the Muğla University campus in October 2009. PV system measured data was compared to simulated data. PV system performance measurements were taken first in a fixed position, then the PV systems were controlled by tracking the sun in two axes (azimuth and sun elevation angles) and the necessary measurements were taken. Annual PV electricity efficiency was computed as 11.53 MWh with an energy value of 1459 kWh/kWp for each system with 28 preset tilt angles. It has been calculated that the dual-axis solar tracking system produces 30.79% more PV electricity than the latitude-inclined fixed system. The annual PV electricity fed to the grid for the dual-axis solar tracking PV system was determined to be 15.07 MWh with 1908 kWh/kWp between April 2010 and March 2011. The difference in energy values between simulation and measurement was determined to be less than 5% [7] .

Seme et al. investigated a dual-axis solar tracking system for a photovoltaic system in this research. They used an optimization approach to find the trajectories. The purpose of optimization is to increase electrical energy production in a photovoltaic system while accounting for monitoring system consumption. A nonlinear and constrained optimization problem is employed to determine the inclination angle and azimuthal angle trajectories. Due to the lack of an explicit form of the objective function, a stochastic search process known as Differential Evolution is used as an optimization tool. The

models are used to evaluate the objective function, calculate current solar radiation, and monitor system consumption using the efficiencies of solar cells, a DC/DC converter, and an inverter. A new technique for time-dependent assessment of current solar radiation is presented. It is calculated using the length of a solar ray's journey through the atmosphere as well as statistical data from a pyrometer, which measures total and scattered solar energy at a specific location on Earth. Bounds for optimization are given in the form of angular velocity, lower and upper bounds for both angles, and angle quantization. The results reported in this research show that watching the sun with appropriate orbits can help boost electrical energy production in solar systems [8] .

According to Lazaroiu et al.'s study, photovoltaic technology allows the direct conversion of solar energy into electrical energy with clear advantages such as no environmental impact during operation, system reliability and durability, low operating costs and maintenance, and the ability to supply remote customers while also easily connecting to the electrical grid. This paper compares the performance of two photovoltaic systems: one fixed and one with a solar tracker. The goal of this study is to examine the daily growth in energy produced by the solar tracking system. The analysis also considers the solar tracker's energy consumption. A system analytical technique is proposed. To validate the results with experimental tests, a low-power PV system with two options was built. A PV source, an MPPT (Maximum Power Point Tracker) power converter, and a 12 V-40 A h electrochemical battery serve as the electrical load in each system. The solar tracking device has demonstrated a considerable boost in morning and evening energy generation [9].

Yilmaz et al. observed that photovoltaic systems are gaining popularity around the world, and research into them is becoming increasingly vital. Solar radiation values, light incidence angle, temperature, and other parameters required to be examined in order to create new PV systems that could be deployed in a more efficient and suitable manner. As a result, theoretical investigations were conducted in the study for the solar radiation and incidence angle values of any place, and an experimental study was conducted on a system that tracks the sun in two axes and in a fixed system. The completed prototype was also converted into a 4.6 kW PV system. The theoretical data is consistent with the data acquired from the 4.6 kW PV installation. They came to the conclusion that this study will be a valuable resource for future PV power plants [10].

Eldin and others. Depending on the time and place, they claimed solar tracking technologies will probably boost a PV module's efficiency. The performance of PV panels, especially crystalline silicon panels, is influenced by a variety of factors. Overheating happens in hot climates like those in the Sun Belt nations because of too much sun exposure. As a result, a Sun Belt nation might not require a tracking system. The purpose of this research is to mathematically ascertain how well a PV panel performs in relation to tracking the sun and operational circumstances. The employed mathematical model is empirically verified before being used in a variety of situations, such as hot and cold locations. It has been calculated that the gain in electrical energy obtained by following the sun is roughly 39% in the case of a cold city like Berlin, Germany. Due to solar panels overheating in a hot city like Aswan, Egypt, the energy gain was only 8% or less. Tracking the sun will not be effective in hot countries, they concluded, and when the 39% efficiency obtained is evaluated, they come to the conclusion that tracking the sun will be successful in cold cities. The energy needed to operate the monitoring system, which varies between 5% and 10% of the energy produced, is included in this analysis [11] .

In their study, Kivrak et al. discovered that the duration and intensity of sunlight are the two factors that have the biggest impact on the amount of electrical energy that can be generated by photovoltaic panels. Use of sunshine at its optimal intensity is crucial because sunlight duration cannot be depended upon continually. Experimental research and tests have shown that photovoltaic panels' and sun tracking systems' production capacities for electrical energy can both be boosted by 25%–50%. After conducting extensive research on photovoltaic panels, they came to the conclusion that the drop in photovoltaic panel sales prices to $0.5 per watt decreased the demand for expensive solar tracking systems. This is because manufacturers of photovoltaic panels focused their investments primarily on solar panel systems rather than tracking. In this study, the tracking system was upgraded and made easier to install in an effort to lower the costs of solar tracking systems to some extent. Just two tiny photovoltaic panels positioned back to back were used to produce the movement required for the tracking system. For system movement and control, an electronic circuit board was also created. The system's average price is predicted to be around $48. They came to the conclusion that such a solar tracking system offers a significant cost benefit over the systems now in use, as well as a higher profit [12] .

Including Kelly Nelson A. In order to increase the quantity of solar energy gathered during overcast periods, this paper outlines solar radiation measurements taken during certain times. They made use of data showing that 2-axis tracking, in which solar panels are oriented at the sun, increases the amount of solar energy that can be captured by a given module area by 30 to 50% compared to fixed tilt modules. Up to 90% of the solar energy on bright days comes from direct sunshine, with the remaining 10% coming from dispersed (scattered) sunlight. But when there is cloud cover, practically all of the sun radiation is diffuse and isotropically dispersed throughout the whole sky. The study's data analysis revealed that tilting a solar module or sensor away from the zenith during cloudy conditions reduces the irradiance in comparison to a horizontal configuration where the sensor or module is pointed at the zenith and thus receives a solar module or sensor. The maximum amount of isotropically dispersed sky radiation can be found here. A sophisticated tracking algorithm was developed in response to this finding, which allows solar arrays to monitor the sun utilizing 2-axis tracking while the solar disk is visible during cloudless periods and switching to a horizontal configuration when the sky is clouded. When compared to 2-axis solar tracking over the same foggy time, a horizontal module orientation has been proven to boost solar energy acquisition by about 50%. Since rotation enhances energy capture on days of lowest hydrogen generation, it is vital to boost solar energy harvesting on cloudy days when using solar energy on a regular basis to recharge long-range electric vehicles or refuel fuel cell electric vehicles [13].

Sunanda Sinha et al. Using a 6 kWp roof-mounted power plant with fixed and tracking photovoltaic systems to increase the potential for electricity generation in a low wind environment, we investigated fixed slope and solar tracking photovoltaic based micro wind hybrid power systems in Indian mountainous terrain with good solar resource. finds the best configurations for the hybrid system powered by microwind. By concentrating on the photovoltaic element of the hybrid system, the study's major goal is to produce more power. The Hybrid Optimization Model for Electric Renewable Resources was used to compare the power output of several hybrid system configurations with fixed slope, monthly optimum slope, annual optimum slope, and six distinct sun tracking photovoltaic systems The annual optimal slope angle is 29.25°, with monthly and seasonal optimum slope angles for the location ranging from 0° to 60°. It was discovered that a 7 kWp photovoltaic system, a 5 kWp wind turbine, 10 batteries, and a 2 kWp inverter were the ideal configurations for all solar tracking systems, with the exception of the two-axis solar

tracking system. An 8 kWp photovoltaic system, one 5 kWp wind turbine, ten batteries, and a 2 kWp inverter were found to be the ideal configuration for the two-axis tracking system and two different types of fixed tilt systems. The findings indicate that compared to the existing fixed tilt photovoltaic system, the monthly adjusted horizontal axis, daily adjusted horizontal axis, constantly adjusted horizontal axis, and two-axis tracking system yield 4.88-26.29% more energy annually. Two-axis tracking was shown to have a greater energy cost than all other tracking systems combined with fixed tilt photovoltaic systems. Two-axis tracking has been found to be superior to other systems, despite the greater expenses for increasing the power output of hybrid systems. It has been determined that the technology used can be used to increase the energy production capability of photovoltaic-micro wind based hybrid systems for any region in the world [14] .

No work has been identified in the literature where the minimum constant joint torque was taken into consideration when designing a sun-tracking spherical mechanism.

II. SUN MOVEMENT IN SKY

The position of the Sun in the sky is a function of time and geographic coordinates of an observer on Earth. As the Earth revolves around the Sun throughout the year, the Sun appears to move along an elliptical spectrum relative to the Earth. The rotation of the Earth on its axis causes the fixed stars to move across the sky as seen in Figure 1. In the GMT (Greenwich Mean Time) time measurement method in astrology, the time when the Sun is at right angles to the Greenwich observation meridian is accepted as noon. However, this calculation was made with an error of 16 minutes due to the irregular speed and tilt of the Earth's rotation axis. UTC (Coordinated Universal Time) universal coordinated time calculation was used to get more precise results. In order to calculate the position of the Sun in the local time and position of the observer, the position calculation in the horizontal plane of the elliptical orbit in Figure 1, conversion to the equatorial coordinate system, conversion to the horizontal plane coordinate system can be performed.

Since the day and night are caused by the rotation of the Earth around its axis, calculations are made by making the Sun rotate as shown in Figure 1, assuming the Earth is fixed in the celestial sphere. The position of the Sun relative to the Earth is determined using spherical geometry in the equatorial and horizontal coordinate system.The azimuth angle (γ) is the angle that the projection vector of a vector directed from the observer to the relevant point on the horizontal plane makes with the north-south axis of the horizontal plane as Figure 1.

Elevation angle (α) expresses the angle between the horizontal plane and the vector directed from the observer to the Sun. The hour angle (ω) indicates the angle between a plane containing the Earth's rotation axis and zenith and the plane containing the zenith and the point where the clock is to be found, as shown in Figure 1. The declination angle (δ) is defined as the angular distance of a star relative to the equatorial plane in the celestial sphere. Zenith angle (z) is the complementary angle of the elevation angle. Angle of latitude (φ), 0° to 90° from the equator to the poles. are scaled latitude values. The tilt angle (n) is the angle between the Earth's orbit and its axis of rotation.

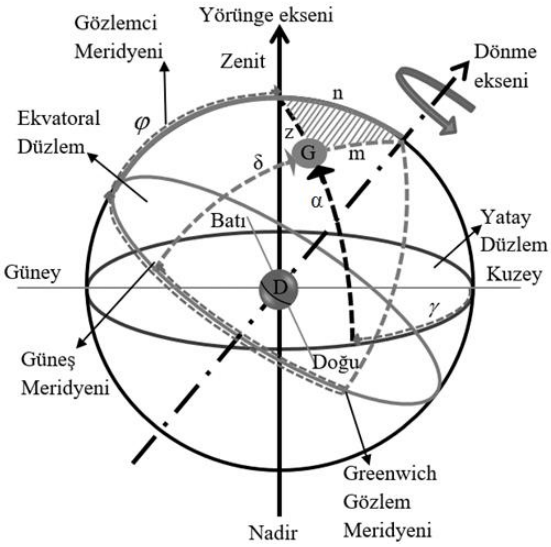

Figure 1: Movement of the Sun in the celestial sphere.

Hour, azimuth and elevation angles depend on the declination angle. The declination angle, on the other hand, varies between -23.5° < δ < 23.5° depending on the day number in equation (1) (d), as in Figure 2. The declination angle is at the limit values of 23.44° at the summer solstice of June 21st and -23.48° at the winter solstice of December 21st, and zero at the equinoxes of March 21st and September 23rd, due to the angular distance of the Sun's rays from the equatorial plane and the celestial sphere. Equation (1) is the angular expression of the Earth's position in the celestial sphere, centered on the Sun, based on the day number. Equation (2) is an empirical equation used for precise calculation of the declination angle depending on the angle of the Earth's position in the celestial sphere [15].

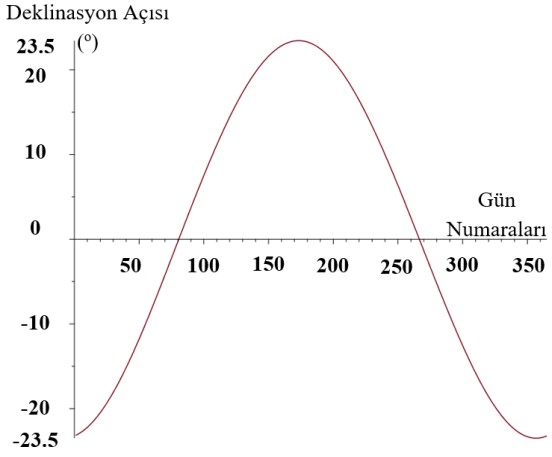

Figure 2: Declination angle change throughout the year.

$$t = 2\pi(d-1)/365 \quad (1)$$

$$\delta = 0{,}322 - 22{,}971\cos(t) - 0{,}358\cos(2t) - 0{,}144\cos(3t) + 3{,}95\sin(t) + 0{,}019\sin(2t) + 0{,}06\sin(3t) \quad (2)$$

Since the sun position calculations are made on the celestial

sphere, spherical geometry relations are used. Sun elevation and azimuth angles were calculated using Napier formulas from spherical geometry in the spherical triangle in Figure 3, which is a section from Figure 1 [16].

Cosine theorem in spherical geometry;

$$cos\mathrm{a} = cosbcosc + sinbsinccosA \quad (3)$$

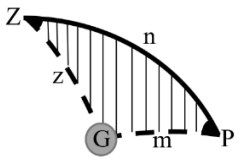

Figure 3: The spherical triangle formed by the Sun and the Earth's axis of rotation and orbit in the sky.

If the cosine theorem is arranged for Figure 3;

$$cosz = cosncosm + \mathrm{sin}n\mathrm{sin}mcosP \quad (4)$$

If this equation is rearranged according to the complementary angles from Figure 1;

$$cos\alpha = \mathrm{sin}\varphi\mathrm{sin}\delta + cos\varphi cos\delta cos\omega \quad (5)$$

By arranging this equation, equations for solar elevation and hour angles are obtained. The sundial angle indicates the angle in the equatorial plane between the meridian where the observer is located and the meridian where the Sun is located in the celestial sphere. While the sun hour angle is negative in the morning, it takes the value of zero at noon and takes a positive value in the afternoon. The local hour angle is equal in all positions on the same meridian because it expresses the angle between the meridian where the Sun is located in the celestial sphere and the meridian where the observer is located. Since the Earth completes one rotation around itself in 24 hours, it completes 360° by making 15° rotations per hour. The sundial angle ω is derived from Equation (6) and calculated as in Equation (7). Since the elevation angle α is zero at sunrise, Equation (8) is used for the calculation of the solar hour angle. By dividing the hour angle found for sunrise by 15°, it is calculated how many hours after noon will occur on the determined date in the meridian where the observer is located. The same calculation is made for the sunset.

$$\omega = \arccos\left(\frac{cos\alpha - cos\varphi cos\delta}{sin\varphi sin\delta}\right) \quad (6)$$

$$\omega_s = \arccos\left(-tan\varphi tan\delta\right) \quad (7)$$

The solar elevation angle is the angle the Sun makes with the horizontal plane of the celestial sphere, as shown in Figure 1. The solar elevation angle, which increases from sunrise to noon and reaches its maximum value, is the complement of the Sun's angle with the zenith in the celestial sphere and is the Sun coordinate value depending on the sundial, latitude and declination angles as in Equation (8).

$$\alpha = \arcsin\left(sin\varphi sin\delta + cos\varphi cos\delta cos\omega\right) \quad (8)$$

The solar azimuth angle is the angle that the Sun makes with the northern axis in the horizontal plane of the meridian in the celestial sphere. In Figure 3, if the cosine theorem is written for the side m and arranged according to its complement angles, the Sun azimuth angle is;

$$sin\delta = sin\alpha\mathrm{sin}\varphi + cos\alpha\mathrm{cos}\varphi cos\gamma \quad (9)$$

$$\gamma = \arccos\left(\frac{sin\delta - sin\alpha sin\varphi}{cos\varphi cos\alpha}\right) \quad (10)$$

Using the obtained Equations (8) and (10), the Sun's orbits are determined by calculating the Sun's azimuth and elevation angles for each day of a year. In Figure 4, the changes in the azimuth and elevation angles of the Sun during the equinox and solstices in the 15° hour angle time periods determined during the day are shown. As can be seen in these figures, the azimuth angle of the Sun reached the highest value in half of the total daily time periods expressing the noon hour and continued to decrease. This is because the azimuth value measured from the positive direction of the northern axis of the horizontal plane in the morning is measured from the negative direction in the afternoon. In Konya, located at 37° 52' North latitude, there is a 228° change in the Sun azimuth angle on 21 June, while a 106° change takes place on 21 December. The solar elevation angle is calculated as 73° at midday, reaching the maximum value of the year on 21 June, and 27° at midday, reaching the minimum value of the year on 21 December. In Figure 5, the orbits followed by the Sun in the celestial sphere on the same dates are shown by calculating.

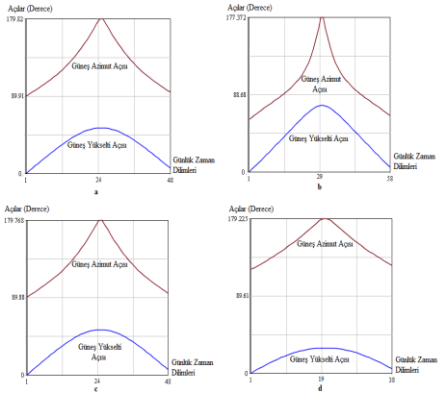

Figure 4: a) 21 March, b) 21 June, c) 23 September, d) The variation of the Sun azimuth and elevation angles in 15° hour angle time zones in the months of 21 December.

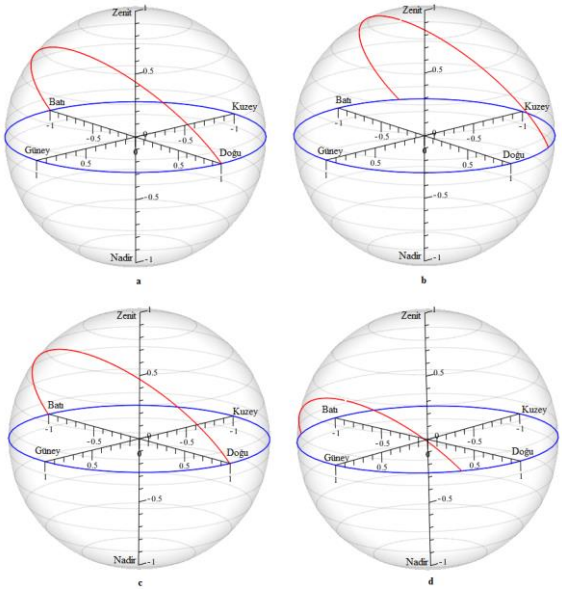

Figure 5. A) March 21, b) June 21, c) September 23, d) Representation of the orbits of the Sun in the celestial sphere during the months of December 21 on the unit sphere.

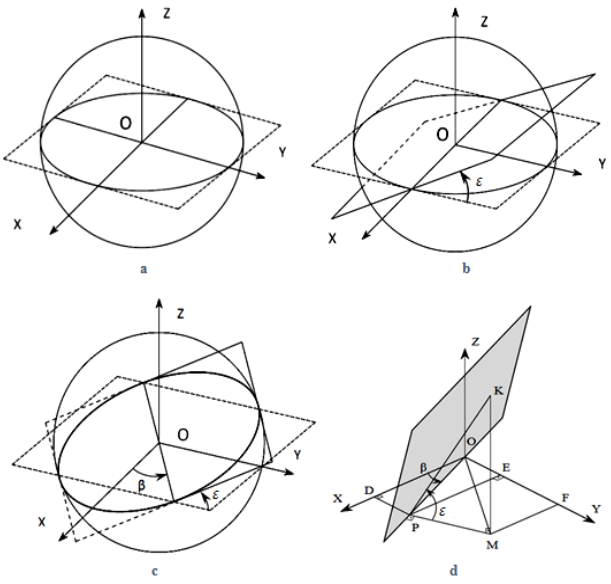

Figure 6. a) OXY plane b) rotated by ε, c) rotated by β d) Axis set and rotated plane [17].

III. OPTIMIZATION PROBLEM

As seen in Figure 6a for spherical motion, the OXY plane is also called the equatorial plane in the OXYZ Cartesian coordinate system whose origin is at the center of the sphere. Let this plane be rotated about the X axis by ε in the positive direction as in Figure 6b. Then rotate it about the Z axis by β in the positive direction as in Figure 6c. The large circles, which are the intersection of this plane sphere, are shown in Figures 6a, b, c. All great circles on the sphere surface can be obtained in this way. The plane in question always passes through the center of the sphere (O), as can be seen in Figures 6a, b, c. By varying the angles ε and β between -180° and +180°, all the great circles on the sphere surface are obtained as the intersection of the plane and the sphere. [17].

Let M point, which is the projection of any point K on this plane on the OXY plane, as in Figure 6d. Let the foot of the perpendicular drawn from M be the point P to the line that is the intersection of the plane with OXY, and the foot of the perpendicular drawn from this point to the X axis be the point D. It is clear that the length KM is the z-coordinate of the point K. Since the KPM angle is ε;

$$tan\varepsilon = \frac{KM}{MP} = \frac{z}{MP} \quad (11)$$

From here for z;

$$z = MPtan\varepsilon \quad (12)$$

obtained. The top view of the OXY plane is shown in Figure 7. Here the coordinates of point K in this plane are OG = x and OF = y. From Figure 7;

$FR = PN = ycos\beta$ and $OM = OG$ can be seen to be.

$MP = PN - MN$ by writing and $MN = FMsin\beta = xsin\beta$ taking into account that;

$$MP = ycos\beta - xsin\beta \quad (13)$$

If equation (12) is put into place in this expression and arranged;

$$z = tan\varepsilon(ycos\beta - xsin\beta) = 0 \quad (14)$$

This equation is the general equation of the plane passing through the origin and rotated about the X-axis by ε and about the Z-axis by β. This equation is also valid for the points on the great circle, which is the intersection of this plane and the sphere [17].

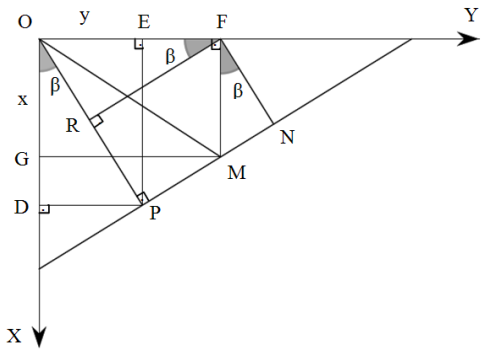

Figure 7. Projection on the OXY plane [17].

If this plane, which is expressed by rotating in the center of the unit sphere by equation (14), is considered as a solar panel, it can be ensured that the panel receives the Sun's rays at a right angle by following the orbits given in Figure 5 to the plane normal vector as shown in Figure 8. Figure 8 shows the afternoon part of the Sun's orbit, the elevation angle (α), the azimuth angle (γ) and the negative rotation angles of the panel expressed as plane by ε around the X axis and β around the Z axis. It is essential to establish a correlation between these aspects. Therefore, for the afternoon;

$\varepsilon = 90^o - \alpha$

$\beta = 90^o - \gamma$ equations are written.

In the afternoon;

$\varepsilon = \alpha - 90^o$

$\beta = \gamma - 90^o$ equations are written. As can be seen from here, the angle ε and β will take a negative sign in the afternoon.

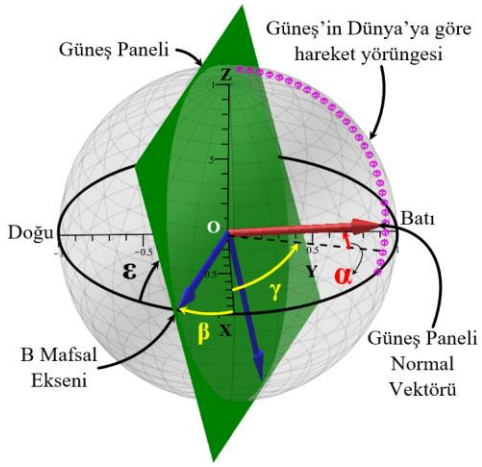

Şekil 8. Güneş panelinin hareketi.

The aim of this study is to design a mechanism that will apply the maximum wind load (P) of the panel rotating around the center of a spherical plane and the minimum torque (T) to carry the panel weight. Torque and wind load calculations are taken from studies[18].

$$\boldsymbol{min(T, 1/P) = f(x_1, x_2, x_3, x_4 \ldots)} \qquad (15)$$

IV. SPHERICAL MECHANISM

If a planar panel that will follow the Sun is driven by a spherical mechanism with 2 degrees of freedom, which is geometrically very suitable for tracking movement, by rotating its geometric center, which is the intersection point of its diagonals, around its two axes so that it remains constant at the center of a sphere, it is foreseen that the torque to be applied on the drive axes will be minimized. Because a fixed joint cannot rotate in a direction other than its own axis. The torque that the panel and wind load cannot create in the rotation axis of the fixed joint can be carried by the strength of the limbs and joints. In Figure 9, randomly arranged spherical mechanism members are shown to explain the movement mechanism. Here, points A_0, A and B denote fixed, movable and connecting rod point hinges, respectively. Since limb dimensions in spherical mechanisms are expressed by the angle between the intersecting axes of successive hinges at the center of the sphere, the limb dimensions between A_0 and A, A and B joints are α_2, α_3 angles, respectively, as shown in Figure 9. The angle θ_2 is the angle of rotation of the drive arm about the fixed joint axis OA_0 with respect to the horizontal plane.

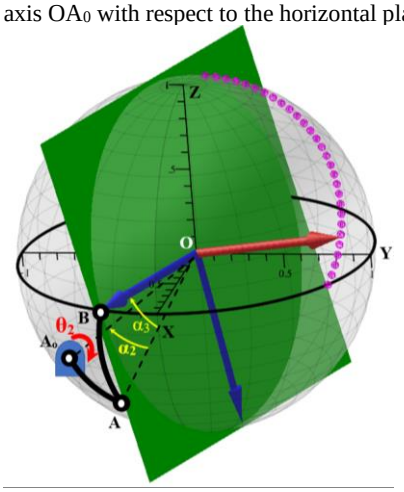

Figure 9. Spherical mechanism driving the solar panel.

In order for the solar panel to receive the Sun's rays at a right angle, it must perform a movement of two degrees of freedom. For such a movement, the appropriate spherical mechanism must have five limbs. Single-degree-of-freedom spherical mechanisms with four limbs are not suitable for tracking the Sun, as they can perform 3-degree-of-freedom motion in a fixed orbit. Because the movement of the Sun relative to the Earth has different orbits throughout the year. In Figure 9, the unit sphere fixed member represents the large circular arc actuating arm between A_0 and A joints, and the large circular arc connecting rod between A and B joints. In Figure 10, 2 parts of the 5-arm spherical mechanism, which are not shown in Figure 9, are shown. Here, the point B' is the point at which the B joint is symmetrical with respect to the O sphere center and where the panel and the solid arc of the B'D great circle are connected. In other words, the mechanism member number 4 consists of the combination of the B'D large circle spring and the panel. Points D and D_0 represent the movable joint and the fixed joint, respectively. The size of the large circle arc B'D is expressed by the angle α_4 and the size of the large circle arc DD_0 is expressed by the angle α_5. Angle θ_5 represents the angle made by the DD_0 great circle arc with the horizontal plane, which rotates around the fixed joint axis OD_0. The coordinates of the orthonormal vectors of the planar panel, whose motion is defined by the change of ε and β angles in equation (14), can be calculated by the Gram Schimidt method.

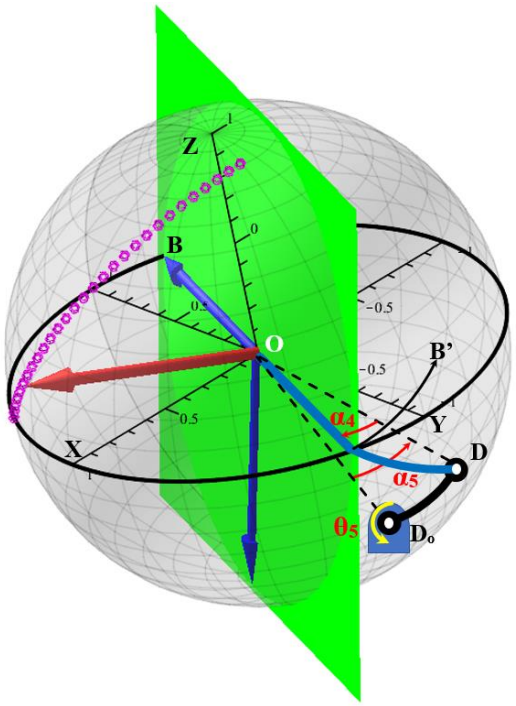

Figure 10. The limbs of the spherical mechanism.

A. Constraints

When the solar panel is viewed as a plane, the coordinates of its normal vector should be the same as the coordinates of the solar orbit. These coordinates can be determined with the help of the angles calculated by Equation (8, 10) and the B joint positions shown in Figures 8, 9, 10 can be calculated using the Gram-Schimidt method. The coordinates of the point B' are calculated symmetrically with respect to the center of the O unit sphere. For the coordinates of the A and D hinge points;

$g1$:

$$-1 < X_A, Y_A, Z_A, X_D, Y_D, Z_D < 1 \qquad (16)$$

range is searched. However, this constraint alone is not sufficient search criteria. The orbit of the sun is in the region of the unit sphere with the positive Z axis as shown in Figures 5, 8, 9, 10. In order for the solar panel to receive the sun's rays unhindered, the coordinates of the fixed joint points must be in the lower region of the equatorial plane of the unit sphere. Because;

$g2$:

$$-1 < X_{Ao}, Y_{Ao}, X_{Do}, Y_{Do} < 1 \qquad (17)$$

constraint is written. Here $-1 < Z_{Do}, Z_{Ao} < 0$ is in the range. $g1$ *and* $g2$ The dimensions of limbs 2 and 3 in the search intervals α_2, α_3, α_4, α_5 can be calculated by the scalar product of the vectors expressing the hinge points. The trajectories given in Figure 5 show the working space of the mechanism in a way. In order to avoid singularity problems during the motion in these orbits, the spherical angle μ in the spherical triangle ABA_0 shown in Figure 11 must be different from 0° and 180°.

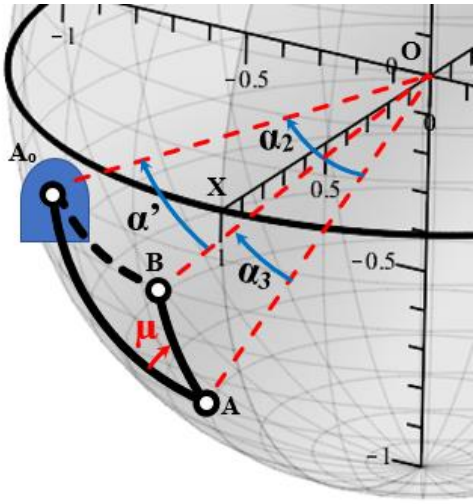

Figure 11. Spherical triangle.

The same should be considered for the spherical angle η in the spherical triangle $B'DA_0$ in limbs 4 and 5 of the restriction mechanism. Because;

$g3$:

$$0 < \mu, \eta < \pi \qquad (18)$$

constraint is written. Required account in this range;

$$\mu = \arccos\left(\frac{cos\alpha' - cos\alpha_2 cos\alpha_3}{sin\alpha_2 sin\alpha_3}\right) \qquad (19)$$

$$\eta = \arccos\left(\frac{cos\alpha'' - cos\alpha_4 cos\alpha_5}{sin\alpha_4 sin\alpha_5}\right) \qquad (20)$$

done with equations. Ratio between limb sizes for quality of mechanism motion transmission according to[19];

$g4$:

$$0.5 < \frac{\alpha_2}{\alpha_3}, \frac{\alpha_3}{\alpha_2}, \frac{\alpha_4}{\alpha_5}, \frac{\alpha_5}{\alpha_4} < 1.5 \qquad (21)$$

should be in the range. Finally, elevation angle and azimuth angle for the geological location of Konya to follow the trajectory every day of the year;

$g5$:

$$0^o < \alpha < 73^o \qquad (22)$$

$g6$:

$$0^o < \gamma < 114^o \qquad (23)$$

should be in the range. In these intervals, the normal vector of the plane obtained by Equation (14) and the coordinates of the Sun's orbit calculated with the angles α and γ must be equal.

$g7$:

$$\begin{bmatrix} X_G \\ Y_G \\ Z_G \end{bmatrix} = \begin{bmatrix} r\,cos\alpha\,cos\gamma \\ r\,cos\alpha\,sin\gamma \\ r\,sin\alpha \end{bmatrix} = \begin{bmatrix} X_N \\ Y_N \\ Z_N \end{bmatrix} \qquad (24)$$

In line with these constraints, r=1 will be taken since a mechanism that follows the Sun on the unit sphere will be designed. In summary, in the mechanism design optimization problem

$$f(x*) = min[T, 1/P] \qquad (25)$$

for minimum torque (T) at the fixed joints when the panel is under maximum wind load (P),

$g_k(x)$ $k = 1, \ldots, 7$

The design that satisfies the 7 constraints indicated by

$x* = (\alpha_2, \alpha_3, \alpha_4, \alpha_5, X_A, Y_A, Z_A, X_D, Y_D, Z_D,$

$X_{Ao}, Y_{Ao}, Z_{Ao}, X_{Do}, Y_{Do}, Z_{Do})$ limb dimensions and joint coordinates will be investigated.

B. Algorithm

The Artificial Harmonic Bee Colony (YHAK) Algorithm developed by the author was used to solve the optimization problem[20]. Since this algorithm is obtained by incorporating harmonic memory operation, it can search with high precision [21]. The process steps are shown in Figure 12.

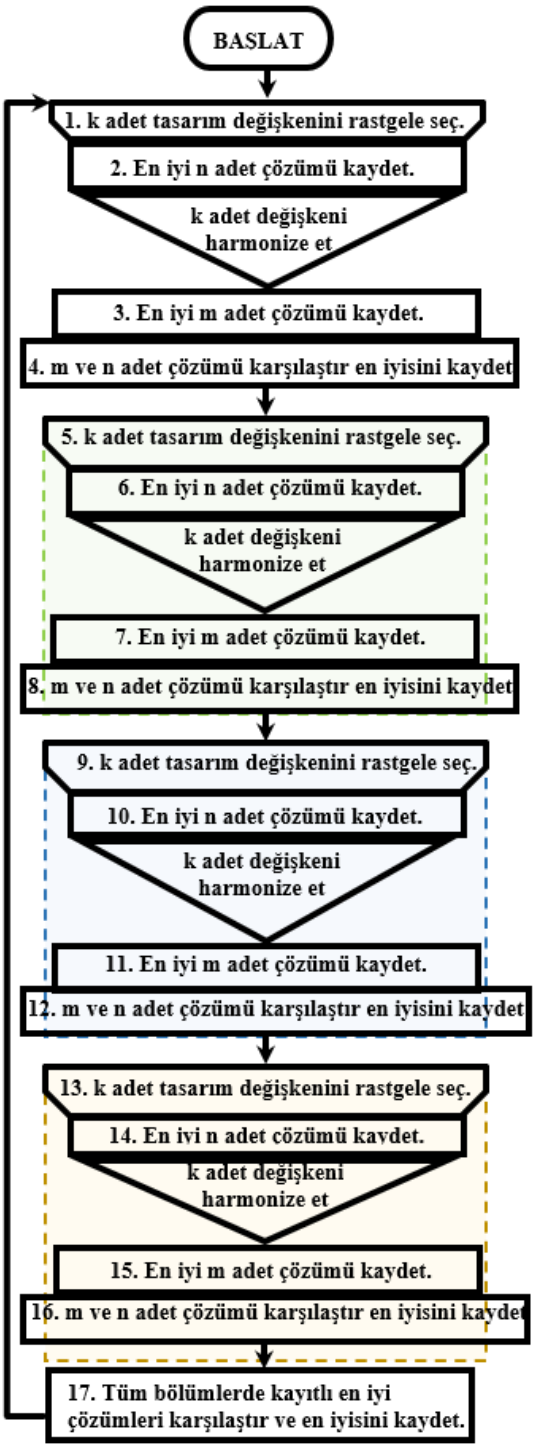

Figure 12. Artificial Harmonic Bee Colony Algorithm operation procedure.

The letter k in the processing procedure of the YHAK algorithm

$x* = (X_A, Y_A, Z_A, X_D, Y_D, Z_D, X_{Ao}, Y_{Ao}, Z_{Ao}, X_{Do}, Y_{Do}, Z_{Do})$ It expresses the number of values that should be randomly generated in the interval specified in Equation (16, 17) for each of the joint points coordinates. After these values are produced, pre-selection is made by subjecting the constraints. N values are selected and saved from each design variable with the smallest objective function value given in Equation (25), calculated with the design variables that passed the elimination. After that, it is repeated to generate the k random values originally generated. Design variables that pass the re-qualification. This time, m values are selected and saved from each design variable with the smallest objective function value given in Equation (25). Thus, a single best value is determined and recorded by comparing m and n selected best values again. This process is done 3 more times in the same way, and a total of 4 best values are recorded at each stage. A cycle of the algorithm is completed by comparing these 4 values for the last time and determining the best value. This cycle is continued until the objective function value closest to zero is obtained. This completes the optimization.

V. RESULTS

In the 470 iterations of the YHAK algorithm, the torque on the axis of rotation of the DO joint is minimized as shown in MDo Figure 13. During this process, the values given in Table 1 for the design variables were determined, taking into account the lowest value for the torque MA_0, which occurs in the axis of rotation of the joint A_0.

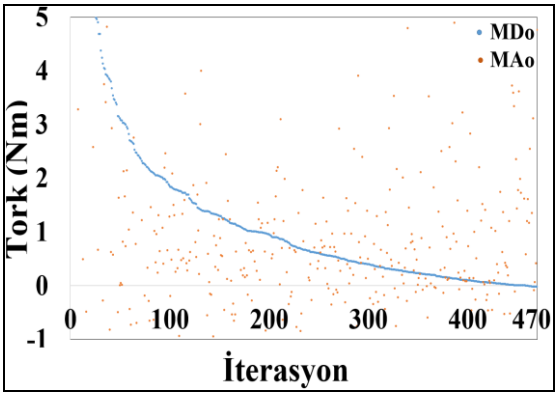

Figure 13. Optimization algorithm convergence result.

Table 1. Best design variables.

X_A	Y_A	Z_A
0.857	-0.516	0
X_{Ao}	Y_{Ao}	Z_{Ao}
0.72	0.694	0
X_D	Y_D	Z_D
0.98	0.196	-0.0332
X_{Do}	Y_{Do}	Z_{Do}
0.068	0.096	-0.993
M_{Ao}	M_{Do}	
0.938	0.080	(Nm)
α_2	α_3	α_4
66.35°	75°	116.4°
α_5	83.2°	

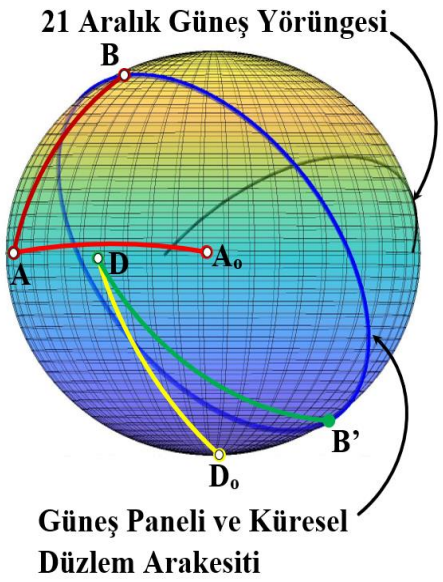

Figure 14. Schematic view of the optimum mechanism.

In this study, the movement of the Sun in the celestial sphere relative to the Earth was examined on the unit sphere. Since the prevailing wind with a speed of 10 km/h blowing in the North-South direction will create the highest load on the solar panel at noon on December 21st, the best values for the design variables where the panel will create minimum torque on the rotation axes of the fixed hinges of the solar tracking mechanism have been investigated. The resulting design was drawn schematically. It was found that the normal vector of the solar panel for all days of the year provides the Sun orbit.

REFERENCES

1. Pillai, U.J.E.e., *Drivers of cost reduction in solar photovoltaics.* 2015. **50**: p. 286-293.
2. Abdallah, S., S.J.E.c. Nijmeh, and management, *Two axes sun tracking system with PLC control*. 2004. **45**(11-12): p. 1931-1939.
3. Barker, L., M. Neber, and H.J.S.E. Lee, *Design of a low-profile two-axis solar tracker*. 2013. **97**: p. 569-576.
4. Yao, Y., et al., *A multipurpose dual-axis solar tracker with two tracking strategies.* 2014. **72**: p. 88-98.
5. Cammarata, *Mechanism and Machine Theory 83*. 2015: p. 175–186.
6. Sungur, C.J.R.e., *Multi-axes sun-tracking system with PLC control for photovoltaic panels in Turkey*. 2009. **34**(4): p. 1119-1125.
7. Eke, R. and A.J.S.E. Senturk, *Performance comparison of a double-axis sun tracking versus fixed PV system.* 2012. **86**(9): p. 2665-2672.
8. Seme, S. and G.J.S.e. Štumberger, *A novel prediction algorithm for solar angles using solar radiation and differential evolution for dual-axis sun tracking purposes.* 2011. **85**(11): p. 2757-2770.
9. Lazaroiu, G.C., et al., *Comparative analysis of fixed and sun tracking low power PV systems considering energy consumption.* 2015. **92**: p. 143-148.
10. Yilmaz, S., et al., *Design of two axes sun tracking controller with analytically solar radiation calculations.* 2015. **43**: p. 997-1005.
11. Eldin, S.S., M. Abd-Elhady, and H.J.R.E. Kandil, *Feasibility of solar tracking systems for PV panels in hot and cold regions.* 2016. **85**: p. 228-233.
12. Kivrak, S.J.J.o.R. and S. Energy, *Design of a low cost sun tracking controller system for photovoltaic panels.* 2013. **5**(3).
13. Kelly, N.A. and T.L.J.S.E. Gibson, *Improved photovoltaic energy output for cloudy conditions with a solar tracking system.* 2009. **83**(11): p. 2092-2102.
14. Sinha, S., S.J.E.c. Chandel, and management, *Analysis of fixed tilt and sun tracking photovoltaic–micro wind based hybrid power systems.* 2016. **115**: p. 265-275.
15. Hassan, I. and K. Islam, *Two Axis Sensorless Solar Tracking System.* 2010.
16. Chiang, C.-H., *Kinematics of spherical mechanisms*. 1988: Cambridge University Press.
17. Özçelik, Z., O. Acar, and K. Konya, *KÜRESEL MEKANİZMALARDA BİYEL EĞRİSİ ÇİZİMİ İÇİN BİR YÖNTEM.* 2015.
18. Acar, O.J.I.J.o.M. and M. Engineering, *Two Degree of Freedom Spherical Mechanism Design for Exact Sun Tracking.* 2016. **10**(1): p. 186-191.
19. Söylemez, E., F.J.M. Freudenstein, and M. Theory, *Transmission optimization of spatial 4-link mechanisms.* 1982. **17**(4): p. 263-283.
20. Kuntoğlu, M., et al., *Parametric optimization for cutting forces and material removal rate in the turning of AISI 5140.* 2021. **9**(5): p. 90.
21. Acar, O., M. Kalyoncu, and A. Hassan. *Proposal of a Harmonic Bees Algorithm for Design Optimization of a Gripper Mechanism*. in *IFToMM World Congress on Mechanism and Machine Science*. 2019. Springer.

Numerical investigation of flow and heat transfer in asymmetrical triangular corrugated channels with triangular obstacles

S. AKÇAY[1]

[1] Cankiri Karatekin University, Cankiri/Turkey, selma.352@hotmail.com

***Abstract* - In this study, flow and heat transfer in asymmetrical triangular corrugated channels with triangular obstacles were numerically investigated. Numerical study was carried out with the help of the ANSYS Fluent solver. In the study, triangular barriers were placed in the channel in two different configurations (Case 2 and Case 3), and the results were compared to the corrugated channel without obstacles (Case 1). The walls of the corrugated channel are kept at a constant temperature of 330 K. The working fluid is air. Reynolds number changed in the range of 2000 ≤ Re ≤ 8000. To observe the effects of the triangular obstacles on flow and thermal fields, the velocity and temperature contours were obtained. According to the findings, while less pressure drop occurred at Case 3, the highest Nusselt number was obtained at Case 2. For both the triangular obstacle cases, the heat transfer and the pressure drops increased with increasing Reynolds number. The numerical results indicated that the flow and heat transfer were substantially affected by Reynolds number, triangular obstacle configuration, and channel geometry.**

***Keywords* – Triangular corrugated channel, triangular obstacle, heat transfer, turbulent flow, friction factor.**

I. INTRODUCTION

IN recent years, heat transfer enhancement methods are of great interest as a current research topic. These methods play an important role in many engineering applications such as, solar air ducts, heat exchangers, and chemistry processes [1-4]. On the other hand, efficient operation of thermal devices is possible by providing the necessary thermal conditions. Therefore, it is necessary to increase the heat transfer rate on the surface with innovative techniques. One of the widely used heat transfer enhancement methods is the use of corrugated channels with different geometries [5]. Flow and heat transfer in corrugated channels with different geometries were numerically and experimentally investigated [6-12]. The results of these works indicated that corrugated surfaces provide higher thermal performance than smooth channels.

Zhang and Che [13] investigated the flow and heat transfer in different corrugated channels (trapezoidal, sinusoidal, triangular, rectangular, and elliptical) and declared that the heat transfer and friction factor were higher in trapezoidal corrugated channels. Ahmet et al. [14] numerically studied the flow and heat transfer in sinusoidal, trapezoidal, and triangular corrugated channels. The highest heat transfer and pressure drop were found the trapezoidal grooved channels. Salami et al. [15] found the highest heat transfer in the trapezoidal corrugated channel, while the best thermohydraulic performance was provided in the sinusoidal wavy channel. Ameur and Sahel [16] reported that heat transfer enhanced, and pressure drop decreased in rectangular, triangular, and semicircular wavy channels, respectively. Shahsavar et al. [17] studied the thermal performance of nanofluids in different corrugated channels (triangular, trapezoidal, and sinusoidal), and reported that higher heat transfer was provided in the sinusoidal profile. Kumar et al. [18] numerically investigated heat transfer, fluid flow and entropy behavior in 15000≤Re≤37500 in wavy channels consisting of hybrid configurations of arc, triangular and trapezoidal shapes. They reported that heat transfer increased in all channel profiles compared to smooth channels and. Also, they indicated that the highest heat transfer was obtained in the inward arc-outward triangular hybrid arrangement, and the highest friction factor was found in the inward trapezoidal-outward trapezoidal arrangement at all Re. Togun et al. [19] numerically examined the heat transfer performance of hybrid nanofluids in a semicircular grooved channel for different arrangement of ribs at 10000≤Re≤25000. They declared that the heat transfer increased as the Reynolds number increased, and the highest heat transfer was achieved at φ=0.02 particle volume fraction for Re=25000.

Another heat transfer enhancement method is the use of extended surfaces and obstacles such as baffles, and fins added to the channels. The main aim of these modifications is to change the flow direction of the fluid, and to increase the heat transfer surface area [20, 21]. The use of only corrugated surface geometries to improve the heat transfer performance is very limited. Higher thermal performance can be provided by using more than one heat transfer enhancement methods together. For this reason, obstacles and baffles in different configurations are added to corrugated channels. The geometry, number, and placement of obstacles are often determined by channel geometry and flow velocity. Although the use of obstacles increases heat transfer, it will increase friction factor and pumping power due to the blocking in the flow area. The effects of the obstacles and baffles added into the channel on the flow and heat transfer have been investigated by many researchers. The work results indicated that the obstacles and baffles provide important enhancement in heat transfer along with an increase in pressure drop [22, 24]. Alnak [25] numerically analyzed the impacts of the baffle angles on

the thermal and hydraulic performance at 1000≤*Re*≤6000 in a duct with V-shaped corrugated lower wall and a flat upper wall. It was determined that for *Re*=6000, the heat transfer at α=90° baffle angle was 52.8% higher than at α=60° baffle angle. Koca [26] numerically examined the heat transfer at different Reynolds numbers in a backward step combined with a triangular wavy surface. He reported that the highest Nusselt number was obtained on the 5 mm triangular surface at Re=20000, the highest performance evaluation criteria (PEC) was obtained on the 10 mm triangular bottom surface at Re=5000 and Re=10000, and at Re=15000 and Re=20000 on the 20 mm triangular bottom surface. Hassani et al. [27] studied the effect of inclined turbulators with different arrangements in a rectangular channel to enhance heat transfer. They examined circular, rectangular and diamond-shaped inclined turbulators for four different arrangements and reported that the best performance factor was provided in the circular-shaped turbulator in the forward-vertical arrangement. Feng et al. [28] investigated the heat transfer of triangular channel flow with trapezoidal baffles in different arrangements. They indicated that the Nu and friction factor increased by 1.7 times and 3.5 times, and the PEC value by 30% in the trapezoidal baffles, compared to the channel without baffles.

The researchers' goal is to design the channel geometry that provides the highest heat transfer while keeping pumping costs to a minimum. Therefore, this study focused on the flow and heat transfer of the asymmetrical triangular corrugated channels with triangular obstacles configurations.

II. Numerical Study

A. Numerical Model

Figure 1a shows 2d geometric schemes of asymmetrical triangular corrugated channels with/without triangular obstacles. Figure 1b gives the detail images. The minimum and maximum height of the channels are H_1=40mm and H_2=60mm, respectively. There is an adiabatic straight section of L_1=5H_1 length at the inlet and outlet of the channels. The total length of the corrugated section of the channel is L_2=10H_1. The lengths a and b of the triangular corrugated parts are 20 and 60 mm, respectively. The channel contains a total of 5 corrugated sections.

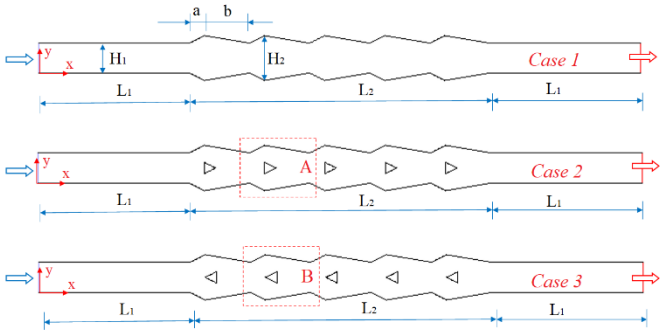

(a)

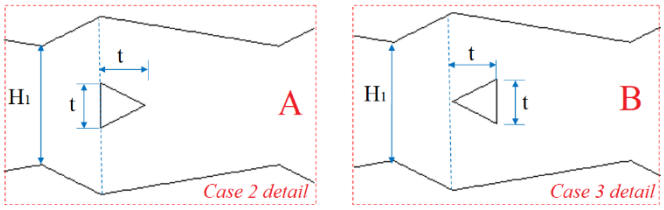

(b)

Figure 1: (a) Geometries of the numerical models, (b) Detail images for Case 2 and Case 3.

Triangular obstacles are placed in the channel in two different positions and these channels are named Case 2 and Case 3 (Fig. 1 b). The dimensions of the triangular obstacles are t=15 mm. The corrugated channel without obstacle was named Case 1.

B. Mathematical Model

In this study, the working fluid is air. The fluid is considered single-phase, incompressible, and Newtonian type. The fluid flows turbulence regime and steady conditions. The computational field is 2d. Fluid properties are constant. Body forces (gravity, etc.) and heat transfer with radiation are ignored. According to these assumptions, the governing equations for standard k-ε turbulence model are written by:

$$\frac{\partial}{\partial x_i}(\rho\bar{u}_i) = 0 \tag{1}$$

$$\frac{\partial}{\partial t}(\rho\bar{u}_i) + \frac{\partial}{\partial x_j}(\rho\bar{u}_i\bar{u}_j) = -\frac{\partial\bar{p}}{\partial x_i} + \frac{\partial}{\partial x_j}\left[(\mu+\mu_t)\left(\frac{\partial\bar{u}_i}{\partial x_j}+\frac{\partial\bar{u}_j}{\partial x_i}\right)\right] - \rho\overline{u_i'u_j'} \tag{2}$$

$$\frac{\partial}{\partial t}(\rho c\bar{T}) + \frac{\partial}{\partial x_j}(\rho\bar{u}_i\bar{T}) = \frac{\partial}{\partial x_j}\left[(\Gamma+\Gamma_t)\left(\frac{\partial\bar{T}}{\partial x_j}\right)\right] \tag{3}$$

$$-\rho\overline{u_i'u_j'} = (\mu_t)\left(\frac{\partial u_i}{\partial x_j}+\frac{\partial u_j}{\partial x_i}\right) \tag{4}$$

$$\frac{\partial}{\partial t}(\rho k) + \frac{\partial}{\partial x_i}(\rho k\bar{u}_i) = \frac{\partial}{\partial x_j}\left[\left(\mu+\frac{\mu_t}{\sigma_k}\right)\frac{\partial k}{\partial x_j}\right] + G_k - \rho\varepsilon \tag{5}$$

$$\frac{\partial}{\partial t}(\rho\varepsilon) + \frac{\partial}{\partial x_i}(\rho\varepsilon\bar{u}_i) = \frac{\partial}{\partial x_j}\left[\left(\mu+\frac{\mu_t}{\sigma_\varepsilon}\right)\frac{\partial\varepsilon}{\partial x_j}\right] + C_{1\varepsilon}\frac{\varepsilon}{k}G_k - C_{2\varepsilon}\rho\frac{\varepsilon^2}{k} \tag{6}$$

In this study, flow and heat transfer in different corrugated channel cases are investigated for Reynolds numbers between 2000≤Re≤8000. Hydraulic diameter (D_h) is calculated by Eq. (7), Reynolds number (Re) is calculated by Eq. (8):

$$D_h = H_{min} + H_{max} \tag{7}$$

$$Re = \frac{\rho u_o D_h}{\mu} \tag{8}$$

where, ρ is the fluid density, μ is the dynamic viscosity, and u_o is the mean velocity.

The overall Nusselt number (*Nu*) is given by:

$$Nu = \frac{h\,D_h}{k_f} \quad (9)$$

where, k_f is the thermal conductivity and h is the heat transfer coefficient.

The convection heat transfer coefficient (h) is calculated by:

$$h = \frac{q''}{\Delta T_{lm}} \quad (10)$$

here q" represents the heat flux and ΔT_{lm} indicates the logarithmic temperature difference.

The logarithmic temperature difference is calculated as:

$$\Delta T_{lm} = \frac{(T_i - T_o)}{\ln\left(\frac{T_w - T_i}{T_w - T_o}\right)} \quad (11)$$

where, T_i, T_o, and T_w are the inlet and outlet temperatures of the fluid and the wall temperature of the corrugated channel, respectively.

The relative Nusselt number (Nu_{rel}) is defined as the ratio of the heat transfer in the corrugated channel with triangular obstacles to the heat transfer in the corrugated channel without obstacles and is given as Equation (12):

$$Nu_{rel} = \frac{Nu_t}{Nu_s} \quad (12)$$

where, Nu_s and Nu_t are the Nusselt number for corrugated channel without obstacles and corrugated channel with obstacles, respectively.

The friction factor (f) is defined by:

$$f = \frac{2\Delta P D_h}{\rho L u_o^2} \quad (13)$$

where, ΔP is the pressure difference between the channel inlet and outlet.

The relative friction factor (f_{rel}) is calculated by:

$$f_{rel} = \frac{f_t}{f_s} \quad (14)$$

where, f_s and f_t are the friction factor for corrugated channel flow without obstacles and corrugated channel with obstacles, respectively.

The performance criteria (PC) can be calculated by:

$$PC = \frac{(Nu_{rel})}{(f_{rel})^{1/3}} \quad (15)$$

C. Boundary Conditions

The fluid enters the channel at a temperature of T_i=300K with an average velocity u_o and the inlet velocity is considered uniform. At the exit of the channel, the pressure outlet boundary condition is defined. The straight sections (L_1) are described as adiabatic. The corrugated surfaces of the channel (L_2) are kept constant at T_w=330 K. The triangular obstacles have adiabatic and non-slip boundary conditions. In addition, the non-slip boundary condition is defined for all wall surfaces of the channel.

D. Numerical Solution Procedure

The geometries and mesh structures of the 2d numerical models were created with the Gambit software. As a result of the element independence test, it was decided that the 80878-element number was sufficient for the calculations. The numerical simulations were carried out with Ansys Fluent solver [29]. The convection parameters were discretized using a second-order upwind scheme. The governing equations were solved by a segregated implicit iterative scheme. The iterations for the velocity-pressure coupling were solved with the SIMPLE (semi-implicit pressure-linked equation) algorithm. The convergence criterion for energy equations was 10^{-7}, for other residuals was 10^{-5}.

III. Results and Discussion

The simulation results of the present study, Ref. [30]'s experimental and numerical results were compared. The agreement between the results of this study and the result of the previous study was indicated in Figure 2.

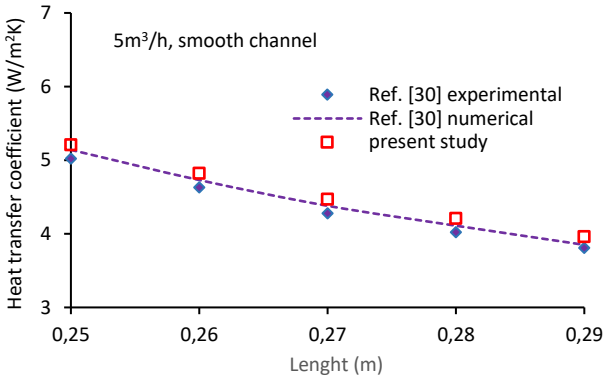

Figure 2: Validation of the numerical study.

In this study, the velocity and temperature contours were obtained at different Reynolds numbers to observe the effect of triangular obstacles on flow and heat transfer. Figures 3a and 3b showed velocity contours for all channel flows at Re=2000 and Re=8000, respectively. The channel geometry, the configuration of the triangular obstacles and the Reynolds number significantly affected the flow field. In Case 1, the flow structure changed due to the asymmetric corrugated channel geometry. At the end of each corrugated profile, the flow velocity increased due to the narrowing of the cross-sectional area. In Case 2 and Case 3, triangular obstacles divided the main flow into two branches and diverted the fluid to the corrugated surfaces. It was seen that the corrugated surfaces were better contact with the fluid in Case 2 than in Case 3.

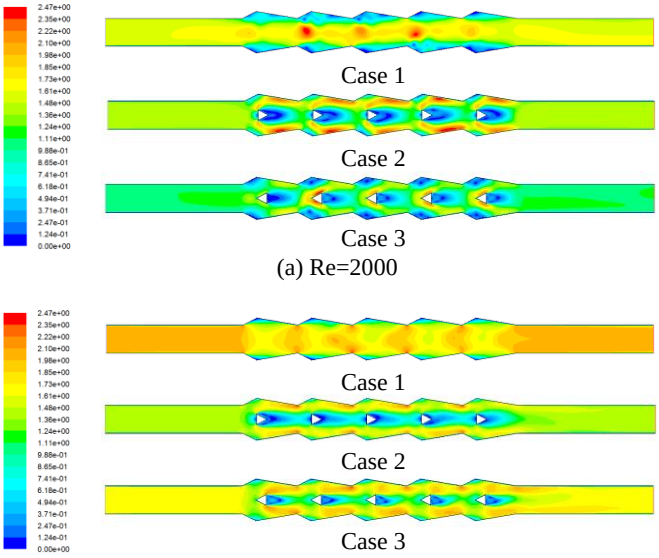

Figure 3: Velocity contours, (a) Re=2000, (b) Re=8000.

In all channel flows, it was observed that at Re=2000, less fluid contacted the corrugated channel surfaces, and at Re=8000, more fluid penetrated the corrugated channel surfaces due to the increase in inertia forces.

Figures 4a and 4b showed temperature contours for all channel flows at Re=2000 and Re=8000, respectively. The temperature contours changed by the channel geometry, the configuration of the triangular obstacles and the Re. At Re=2000, the temperature gradient is quite high in all channels. It was observed that the temperature gradient decreased considerably at Re= 8000. Increasing Re allowed more cold fluid to contact the corrugated channel surfaces. The temperature of the corrugated channel surfaces in contact with the cold fluid decreased. The triangular obstacles directing the fluid to the corrugated surfaces contributed to the reduction of the channel surface temperature.

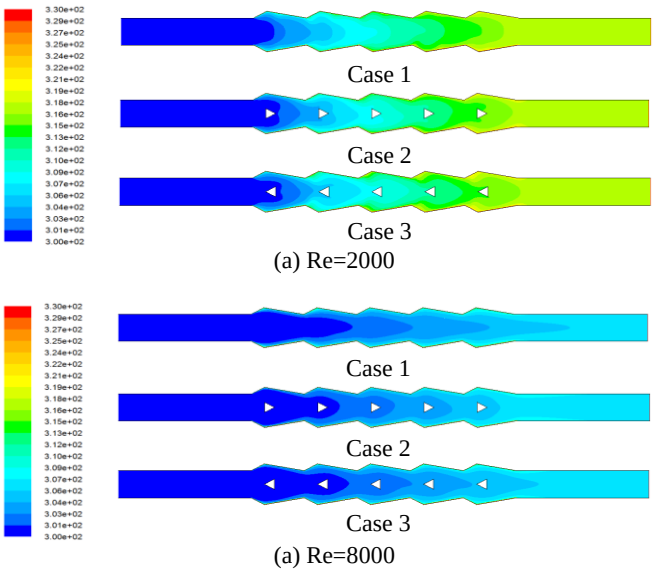

Figure 4: Temperature contours, (a) Re=2000, (b) Re=8000.

Figure 5 showed the variation of the Nu with the Re for all channel flows. As the Re increases, the Nu increases. For Re=8000, the highest Nu was obtained in Case 2 as Nu=13.05 and the lowest Nu in Case 1 as Nu=10.98.

Figure 6 indicated the variation of the relative Nu with the Re. The Nu obtained in the channel flow without triangular obstacles (Case 1) was accepted as a reference. Heat transfer improvement is obtained by the ratio of Nusselt numbers obtained from Case 2 and Case 3 to Case 1. Heat transfer improvement was defined by the relative Nusselt number. The heat transfer improvement in both triangular obstacle modifications was found to be higher than the Case 1. However, in the Case 2, this improvement appears to be greater. The highest heat transfer improvement was found to be 1.20 in Case 2 at Re=8000.

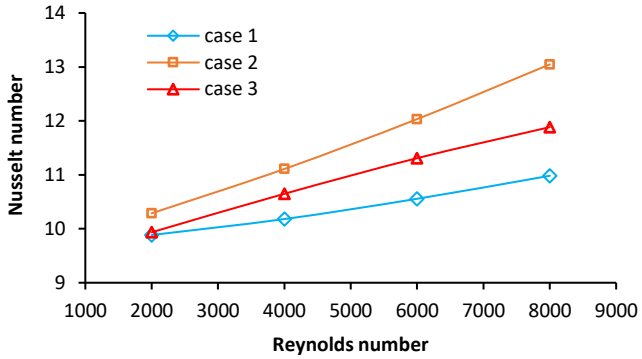

Figure 5: Nusselt number versus Reynolds number.

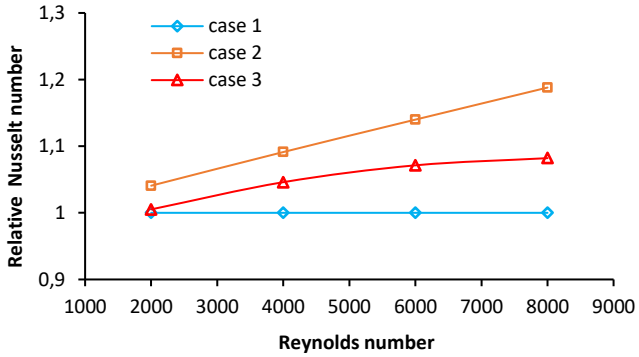

Figure 6: Relative Nusselt number versus Reynolds number.

Figure 7 showed the pressure drop with Re for all channel flows. It was seen that the pressure drop increases with the Reynolds number because the triangular obstacles in the channel prevent the flow. At Re=8000, the highest-pressure drop was 31.5 Pa in Case 2, and the lowest-pressure drop was 6.96 in Case 1.

The variation of the friction factor calculated according to the pressure drop with the Reynolds number in all channel cases is given in Figure 8. As the Re increases, the friction factor decreases. The highest friction factor was obtained in Case 2, and the lowest friction factor was obtained in Case 1.

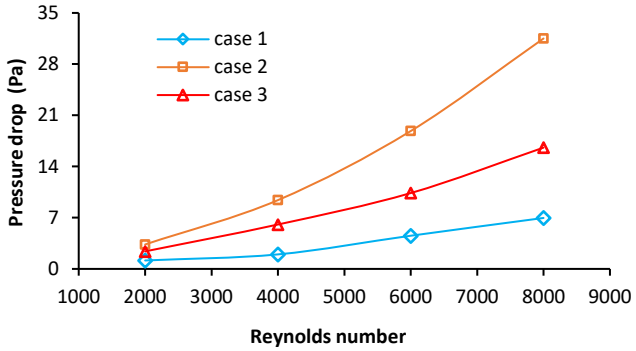

Figure 7: Pressure drop versus Reynolds number.

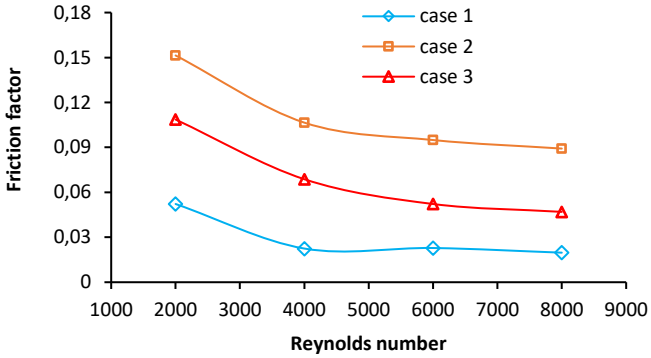

Figure 8: Friction factor versus Reynolds number.

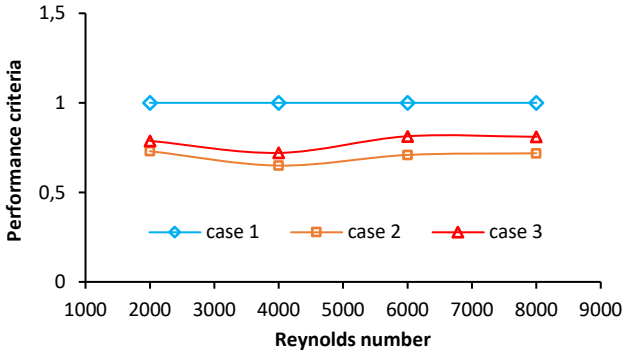

Figure 9: Performance criteria versus Reynolds number.

Figure 9 presented the variation of the performance factor versus the Reynolds number. Case 1 was taken as reference. The performance factor of both channels with triangular obstacles was found below the reference value. Although triangular obstacles increased the heat transfer, they also caused an increase in pressure drop in the duct. Since the pressure drop is higher than the heat transfer improvement, the performance factor was obtained below the reference value.

This study showed that triangular obstacles placed in a corrugated channel can increase heat transfer with an increase in pressure drop. In future studies, the flow and heat transfer behavior can be analyzed by changing the geometry of the obstacles and their placement in the channel by using different corrugated channel geometry and the optimum parameters that provide high performance value can be searched.

REFERENCES

[1] J.M. Wua, and J. Zhao, "A review of nanofluid heat transfer and critical heat flux enhancement—research gap to engineering application," *Progress in Nuclear Energy*, vol. 66, pp. 13-24, July 2013. https://doi.org/10.1016/j.pnucene.2013.03.009

[2] T. Alam, R.P. Saini, and J.S. Saini, "Use of turbulators for heat transfer augmentation in an air duct–A Review," *Renewable Energy*, vol. 62, pp. 689-715, February 2014. doi:10.1016/j.renene.2013.08.024.

[3] A. Kaood, and M.A. Hassan, "Thermo-hydraulic performance of nanofluids flow in various internally corrugated tubes," *Chemical Engineering & Processing: Process Intensification*, vol. 154, pp. 08043, 2020. https://doi.org/10.1016/j.cep.2020.108043

[4] H. Ameur, D. Sahel, and Y. Menni, "Numerical investigation of the performance of perforated baffles in a plate-fin heat exchanger," *Thermal Science*, vol. 25, no. 5B, pp. 3629–3641.2021. https://doi.org/10.2298/TSCI190316090A

[5] S.S.M. Ajarostaghi, M. Zaboli, H. Javadi, B. Badenes, and J.F. Urchueguia, "A review of recent passive heat transfer enhancement methods," *Energies*, vol. 15, pp. 986, 2022. https://doi.org/10.3390/en15030986

[6] N. Kurtulmus, and B. Sahin, "A review of hydrodynamics and heat transfer through corrugated channels," *International Communications in Heat and Mass Transfer*, vol. 108, pp. 104307, 2019. https://doi.org/10.1016/j.icheatmasstransfer.2019.104307

[7] S.R. Nfawa, A.R. Abu-Talib, S.U. Masuri, A.A. Basri, and H. Hasini, "Heat transfer enhancement in a corrugated-trapezoidal channel using winglet vortex generators," *CFD Letter*, vol. 11, pp. 69-80, 2021. https://akademiabaru.com/submit/index.php/cfdl/article/view/3190

[8] H. Zontul, H. Hamzah, N. Kurtulmuş, and B. Şahin, "Investigation of convective heat transfer and flow hydrodynamics in rectangular grooved channels," *International Communications in Heat and Mass Transfer*, vol. 126, pp. 105366, 2021. https://doi.org/10.1016/j.icheatmasstransfer.2021.105366

[9] E.N. Krishnan, H. Ramin, A. Guruabalan, and C.J. Simonson, "Experimental investigation on thermo-hydraulic performance of triangular cross-corrugated flow passages," *International Communications in Heat and Mass Transfer*, vol. 122, pp. 105160, 2021. https://doi.org/10.1016/j.icheatmasstransfer.2021.105160.

[10] M.A. Alfellag, H.E. Ahmed, M.G. Jehad, and A.A. Farhan, "The hydrothermal performance enhancement techniques of corrugated channels: A review," *Journal of Thermal Analysis and Calorimetry*, vol. 147, pp. 10177-10206, 2022. https://doi.org/10.1007/s10973-022-11247-1

[11] S. Akcay, "Numerical analysis of heat transfer improvement for pulsating flow in a periodic corrugated channel with discrete V-type winglets," *International Communications in Heat Mass Transfer*, vol. 134, pp. 105991, March 2022. DOI:10.1016/j.icheatmasstransfer.2022.105991.

[12] S. Akcay, "Numerical analysis of hydraulic and thermal performance of Al_2O_3-water nanofluid in a zigzag channel with central winglets," *Gazi University Journal of Science*, vol. 36, no. 1, pp. 383-397. 2023. DOI:10.35378/gujs.1012201

[13] L. Zhang, and D. Che, "Turbulence models for fluid flow and heat transfer between cross corrugated plates," *Numerical Heat Transfer, Part A: Applications*, vol. 60, pp. 410–440, 2011. https://doi.org/10.1080/10407782.2011.600583

[14] M. Ahmed, M. Yusoff, K. Ng, and N. Shuaib, "Effect of corrugation profile on the thermal–hydraulic performance of corrugated channels using CuO–water nanofluid," *Case Studies in Thermal Engineering*, vol. 4, pp. 65-75, 2014. https://doi.org/10.1016/j.csite.2014.07.001

[15] M. Salami, M. Khoshvaght-Aliabadi, and A. Feizabadi, "Investigation of corrugated channel performance with different wave shapes," *Journal of Thermal Analysis and Calorimetry*, vol. 138, pp. 3159-3174, 2019. DOI:10.1007/s10973-019-08361-y

[16] H. Ameur, and D. Sahel, "Effect of some parameters on the thermo-hydraulic characteristics of a channel heat exchanger with corrugated walls," *Journal of Mechanical and Energy Engineering*, vol. 3, pp. 53-60, 2019. DOI:10.30464/jmee.2019.3.1.53

[17] A. Shahsavar, S.S. Alimohammadi, I.B. Askari, and H.M. Ali, "Numerical investigation of the effect of corrugation profile on the hydrothermal characteristics and entropy generation behavior of laminar forced convection of non-Newtonian water/CMC-CuO nanofluid flow

inside a wavy channel," *International Communications in Heat and Mass Transfer*, vol. 121, pp. 105117, 2021. https://doi.org/10.1016/j.icheatmasstransfer.2021.105117

[18] K. Kumar, R. Kumar, and R.S. Bharl, "Thermohydraulic performance enhancement using novel hybrid corrugation configuration channels in thermal systems," *International Communications in Heat and Mass Transfer*, vol. 134, pp. 105999, May 2022. https://doi.org/10.1016/j.icheatmasstransfer.2022.105999

[19] H. Togun, R.Z. Homod, Z.M. Yaseen, A.M. Abed, J.M. Dhabab, R.K. Ibrahem, S. Dhahbi, M.M. Rashidi, G., W. Ahmadi Yaïci, and J.M. Mahdi, "Efficient heat transfer augmentation in channels with semicircle ribs and hybrid Al_2O_3-Cu/water nanofluids,**"** *Nanomaterials*, vol. 12, no. 15, pp. 2720, 2022. https://doi.org/10.3390/nano12152720

[20] Z-X. Li, S-Q. Sung, C. Wang, C-H. Liang, S. Zeng, T. Zhong, W-P. Hud, and C-N. Feng, "The effect of trapezoidal baffles on heat and flow characteristics of a cross-corrugated triangular duct," *Case Studies in Thermal Engineering*, vol. 33, pp. 101903, May 2022. https://doi.org/10.1016/j.csite.2022.101903

[21] Akcay S, U. Akdag, "Heat Transfer Enhancement in a Channel with Inclined Baffles under Pulsating Flow: A CFD Study," *Journal of Enhanced Heat Transfer*, vol. 30, no.5, pp. 61-79, 2023. DOI: 10.1615/JEnhHeatTransf.2023047227

[22] C.E. Bensaci, A. Moummi, F.J. Sanchez de la Flor, E.A. Rodriguez Jara, A. Rincon-Casado, and A. Ruiz-Pardo, "Numerical and experimental study of the heat transfer and hydraulic performance of solar air heaters with different baffle positions," *Renew Energy*, vol. 155, pp. 1231–1244, 2020. https://doi.org/10.1016/j.renene.2020.04.017

[23] A.T. Inan, H. Koten, and M.K. Kartal, "Experimental comparison and CFD analysis of conventional shell and tube heat exchanger with new design geometry at different baffle intervals," *Numerical Heat Transfer, Part A: Applications*, 28 Jul 2022. DOI:10.1080/10407782.2022.2101801.

[24] S. Akçay, "Investigation of thermo-hydraulic performance of nanofluids in a zigzag channel with baffles," *Adıyaman Üniversitesi Mühendislik Bilimleri Dergisi*, vol. 8, no. 15, pp. 525-534, Dec. 2021, doi:10.54365/adyumbd.1000525

[25] D.E. Alnak, "Thermo hydraulic performance study of different square baffle angles in cross-corrugated channel," *Journal of Energy Storage*, vol. 28, pp. 101295, April 2020. https://doi.org/10.1016/j.est.2020.101295

[26] F. Koca, "Numerical investigation of corrugated channel with backward-facing step in terms of fluid flow and heat transfer," *Journal of Engineering Thermophysics*, vol 31, no:1, pp. 187-199. 2022. https://doi.org/10.1134/S1810232822010143

[27] S.M., Hassani, M., Khoshvaght-Aliabadi, A., Feizabadi, S. Rehman, and A. Alimoradi, "Experimental and numerical analysis of curved turbulators in different arrangements through a rectangular channel," *Experimental Heat Transfer*, vol. 35, no. 1, pp. 22-44, 2022. https://doi.org/10.1080/08916152.2020.1817177

[28] C-N. Feng, C-H. Liang, and Z-X. Li, "Friction factor and heat transfer evaluation of cross-corrugated triangular flow channels with trapezoidal baffles," *Energy & Buildings*, vol, 257, pp. 111816, 2022. https://doi.org/10.1016/j.enbuild.2021.111816

[29] ANSYS Inc., ANSYS Fluent User Guide & Theory Guide- Release 15.0, USA, 2015.

[30] Z. Brodniansk´a, S. Kot˘smíd, "Heat transfer enhancement in the novel wavy shaped heat exchanger channel with cylindrical vortex generators," *Applied Thermal Engineering*, vol. 220, pp. 119720, 2023. https://doi.org/10.1016/j.applthermaleng.2022.119720

The Effect of Backward Triangular Type Vortex Generators on NACA 0012 Airfoil at Different Chordwise Directions

M. SEYHAN[1] and M. AKİF ÖZDEN[2]

[1] Karadeniz Technical University, Trabzon/Turkey, mehmetseyhan@ktu.edu.tr
[2] Necmettin Erbakan University, Konya/Turkey, muhakifozden@gmail.com

Abstract **- The effects of a backward triangular type vortex generators on the suction surface of NACA 0012 airfoil was performed to investigate at a suction type of wind tunnel. Vortex generators (VGs) that have a length of 15 mm, a height of 5 mm, a distance between VGs of 5 mm, a distance between VGs pairs (λ) of 20 mm and an angle of (β) VG of 15 ° attached to the surface of the airfoil at different chordwise locations changing between 0.1c and 0.4c with an increment of 0.1c. This airfoil dimensions are a chord (c) of 150 mm and spanwise length (s) of 300 mm. The Reynolds number based on the chord is $6x10^4$. Force measurements experiment is carried out with the help of six axis load cell at the angle of attack changing from 0º to 30º with an increment of one degree. This study aims to provide important insights about the backward triangular type vortex generators at low Reynolds number and reveal the aerodynamic performance of these airfoils. According to the force measurement experiments, the results reveals that backward triangular type vortex generators at low Reynolds number significantly enhanced stall characteristic and maximum lift coefficient as compared to baseline airfoil.**

Keywords **- Triangular vortex generator, NACA 0012, lift coefficient and drag coefficient.**

I. Introduction

AVIATION plays a pivotal role in the modern world, significantly impacting various aspects of human life. At the heart of aviation lies the fundamental aerodynamic concepts of lift, drag and stall. Lift is the force that enables aircraft to defy gravity, allowing them to soar through the skies, while drag acts as a resistive force opposing their forward motion. Stall is the decrease in the lift force obtained from the wings of an aircraft in flight to the point that it cannot resist gravity, that is, it cannot carry the aircraft.

The importance of lift and drag in aviation cannot be neglected. Achieving an optimal lift-to-drag (L/D) ratio is a critical goal in aviation, as it directly influences an aircraft's efficiency and performance. In accordance with this purpose, In the pursuit of improved flight performance and safety, flow control methods have been extensively researched [5,15]. NACA 0012 airfoil is a widely used airfoil design in the field of aviation and aerodynamics. Various experimental and numerical studies have been conducted in the literature on the airfoil characteristics of NACA 0012 at low Reynolds numbers [1-4].

Significant progress has been achieved in the realm of flow control in recent years, a research domain with substantial implications for both military and civilian applications. Recent advancements have expanded the feasibility of actively managing turbulent flows, holding promise for prospective practical implementations. Additionally, less intricate control strategies, encompassing both passive and active approaches, have reached a stage of greater market readiness, thereby experiencing renewed scholarly [5-6].

Flow control methods are divided into two groups: active and passive [5]. While in passive methods it is possible to add various mechanisms to the system without using additional power, in active methods an external energy input is required. Gursul et al. [7] vortex control strategies employed for both slender and nonslender delta wings, emphasizing the impact of wing sweep angle on flow control phenomena such as separation, vortex formation, reattachment, breakdown, and instabilities. Various methods for flow control are discussed, including multiple vortices, control surfaces, blowing and suction, excitation techniques, feedback control, passive control through wing flexibility, and plasma actuators. Notably, lift enhancement, particularly for nonslender wings, and re-formation of vortices can be induced with adequate forcing at optimal frequencies. Flow control encompasses a range of methods used to optimize the aerodynamic characteristics of aircraft, thus delaying the onset of stall conditions. Among these methods, passive flow control stands out as an effective strategy. Passive flow control employs fixed or mechanical components to optimize aerodynamic behavior. In this context, vortex generators have emerged as significant devices, contributing to the manipulation of airflow and enhancing aircraft performance.

Vortex generators were first introduced in 1947 and found their initial application in the domain of aircraft wing flow control [14]. The fundamental concept behind the effectiveness of vortex generators in managing flow separation lies in their capacity to generate concentrated vorticity as a fluid flow over them [8]. Due to their simple structure and convenient installation, VGs are widely used in the field of flow control [9-11]. Vortex generators (VGs) constitute a prevalent passive flow control approach employed for mitigating flow separation on airfoils. VGs typically consist of small plates characterized by various shapes and sizes, strategically positioned at an angle

relative to the incident airflow. These VGs are strategically oriented to induce the formation of longitudinal vortices, a mechanism that facilitates the entrainment of high-momentum fluid from the outer flow towards the boundary layer in close proximity to the surface (Wang et al.) [12]. VGs play a crucial role in enhancing L/D ratio by regulating the airflow over an aircraft's wing surfaces. By creating controlled vortices, VGs improve lift generation while mitigating the increase in drag. The significance of VGs lies in their remarkable influence on L/D ratio, a paramount factor in aviation performance. VGs excel in delaying stall, a critical aerodynamic phenomenon where the wing's angle of attack becomes excessive, causing a sudden drop in lift and a loss of control. By strategically deploying VGs on wing surfaces, aviation engineers can achieve a substantial increase in lift production while mitigating the simultaneous surge in drag, thereby significantly enhancing the L/D ratio. optimization of L/D is paramount in achieving superior flight performance and fuel efficiency. This optimization not only promotes superior flight performance and fuel efficiency but also contributes to safer flight conditions, especially during low-speed flight regimes. Consequently, VGs have evolved into indispensable tools for achieving the delicate balance between lift and drag in aviation. Tebbiche et al. [15] conducted an investigation into flow control mechanisms, specifically focusing on the implementation of novel vortex generator shapes characterized by counter-rotating vortices. These configurations were derived through modifications to previously studied designs. Employing an experimental design methodology, an optimized geometric form was identified within this research. The outcomes of the study revealed a notable enhancement in the relative lift force, estimated to be approximately 14%, along with a concurrent reduction in drag force by approximately 16.

This study aims to examine the effects of the backward triangular type vortex generators mounted onto the NACA 0012 airfoil suction surface at different chordwise directions for the low Reynolds numbers (Re = $6x10^4$). Since the number of studies on backward counter-rotating vortex generators type is limited in the literature, this study aims to add originality to the literature.

II. MATERIAL AND METHOD

The experiments were carried out in the Aerodynamics and Wind Energy Research Laboratory of the Mechanical Engineering Faculty at Karadeniz Technical University. Within this facility, a suction-type subsonic wind tunnel was utilized. The wind tunnel's test section had dimensions of 570x570x12 millimeters and exhibited a low turbulence intensity, measuring smaller than 1%. Figure (1 a and b) shows both the schematic and the assembled version of the wind tunnel, respectively. An experimental setup for force measurement was prepared to examine the effects of VGs on the NACA 0012 airfoil. The experimental setup and its schematic representation are shown in Figure 2 and 3. This setup comprised essential components, including a load cell, a rotary unit, a connecting rod support unit, a connecting rod, end plates, and an airfoil model equipped with vortex generators on its surface.

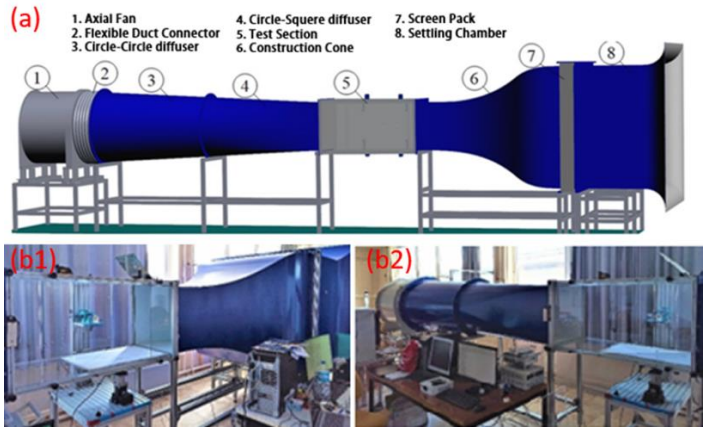

Figure 1: (a) Subsonic wind tunnel diagram, (b1) and (b2) View of the subsonic wind tunnel from different perspective.

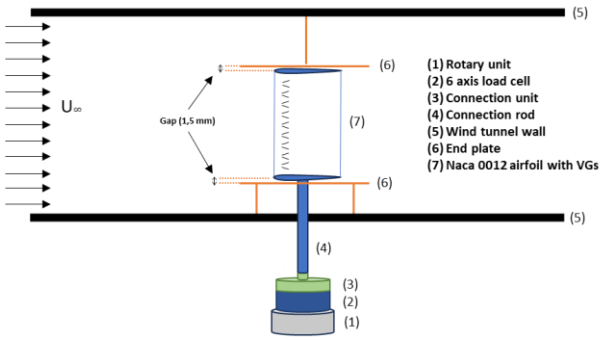

Figure 2: Force measurement setup diagram.

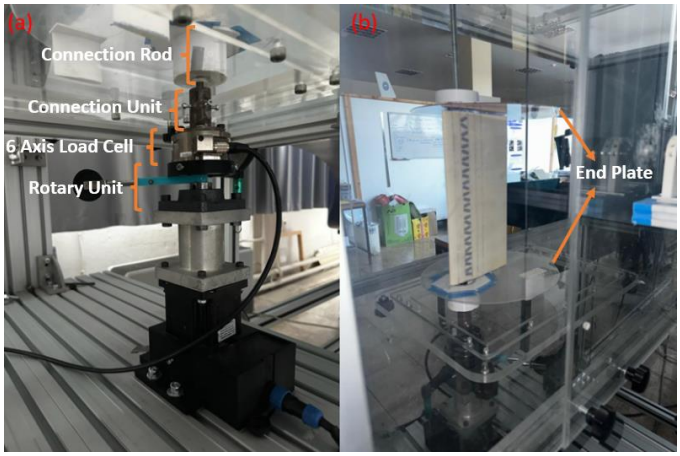

Figure 3: The experimental instruments outside (a) and inside (b) the wind tunnel.

The airfoil model used in the experiments closely resembled the NACA0012 airfoil, featuring a chord length of 150 mm and a wingspan of 300 mm. To ensure its precision, the airfoil model was produced using a Cura model 3D printer and meticulously sanded with various grit sandpapers, ranging from 80 to 1000. During the experiments, the airfoil model was positioned in the wind tunnel test area, centered between two endplates, with a minimal distance of no more than 1.5 mm between the wing and the endplates. Vortex generators were

strategically placed on the suction surface of the airfoil at intervals denoted as XVG/c=0,1, as illustrated in Figure 4 and 5. These VGs were affixed to the airfoil surface using double-sided tape and were characterized by aerodynamically optimized geometric dimensions, including l = 15 mm, h = 5 mm, d = 5 mm, λ = 20 mm, t=0.25 mm and β = 15º shown in figure 4. Notably, these VGs were fabricated using resin through a Stereolithography (SLA) 3D printer. The baseline models, which did not incorporate VGs, were identified as such, while models featuring VGs were designated as $VGsX_{10}$, $VGsX_{20}$, $VGsX_{30}$, and $VGsX_{40}$ from 0.1c to 0.4c respectively, as shown in figure 4, each indicating the number and positioning of VGs on the airfoil surface.

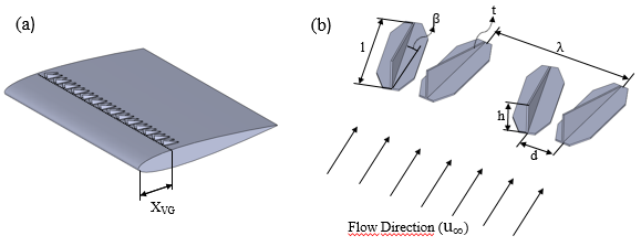

Figure 4: (a) Placement of VGs on airfoil, (b) geometric shape diagram of VGs

Figure 5: Location of XVGs on NACA 0012 airfoil

The experimental investigations were carried out at a Reynolds number (Re) of 6×10^4. The initial series of force experiments were conducted in the absence of vortex generators on the airfoil, followed by subsequent experiments with VGs positioned at locations X_{VGs}/c=0,1 to 0,4 along the airfoil surface. The investigation involved the precise measurement of lift and drag forces at various angles of attack (α), with the models incrementally rotated by 1 degree within the range of $0º \leq \alpha \leq 30º$. Force measurements were collected using a 6-axis ATI Gamma DAQ F/T type load cell sensor, recording a total of 20,000 data measurements for each degree of angle of attack, with a sampling frequency of 1000 for a duration of 20 seconds.

III. RESULT AND DISCUSSION

This research endeavors to explore the influence of backward triangular type vortex generators on the NACA 0012 airfoil. The investigation encompasses four distinct VGs positions, ranging from X_{VGs}/c = 0.1-0.4 conducted at a Reynolds number (Re) of 6×10^4.

Figure 6, which is presented in the study, illustrates the variation in coefficient of lift (C_L) as a function of angle of attack. It specifically examines two scenarios: one involving the baseline model without VGs and another incorporating VGs positioned at X_{VGs}/c = 0.1 to 0.4 locations, all at a Reynolds number of 6×10^4.

When examining Figure 6, it is observed that the baseline model experiences stall at an angle of attack (α) of 12 degrees. However, it can be stated that only the $VGsX_{10}$ configuration delays the stall point by 1 degree, while the $VGsX_{20}$ configuration advances it by 1 degree. There was no noticeable change in stall angle for the $VGsX_{30}$ and $VGsX_{40}$ configurations. It was observed that for the $VGsX_{20}$ configuration, the lift coefficient (C_L) is generally higher than the baseline from α = 0° to the stall angle, whereas the $VGsX_{30}$ configuration exhibits lower C_L values. The $VGsX_{10}$ and $VGsX_{40}$ configurations, on the other hand, closely follow the baseline up to 10 degrees of α, after which their C_L values become higher until stall angle.

For post-stall conditions, nearly all configurations exhibit an increase in C_L compared to the baseline. For C_{Lmax}, the $VGsX_{10}$ configuration shows a %7.84 increase, while the $VGsX_{40}$ configuration shows a %7.83 increase. After stall, the $VGsX_{40}$ and $VGsX_{30}$ configurations have higher C_L values, whereas the situation is different for the $VGsX_{10}$ and $VGsX_{20}$ configurations. For the $VGsX_{10}$ configuration, the lift remains high up to $\alpha = 18°$, and it is approximately the same after stall angle. In contrast, for the $VGsX_{20}$ configuration, C_L values are very similar after $\alpha = 16°$.

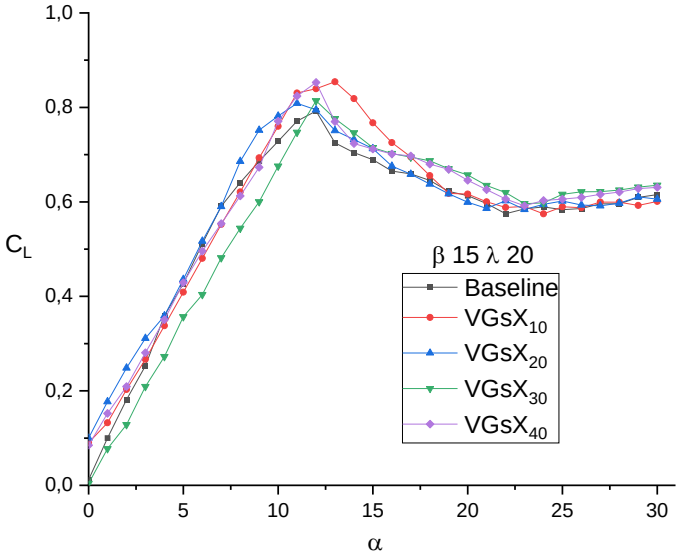

Figure 6: Variation of C_L as a function of angle of attacks.

The graph of the C_D values obtained in the experiments is shown in Figure 7. It is evident that for the $VGsX_{10}$ configuration, except at 13 degrees of angle of attack (α), the C_D value is higher in all angles. For the $VGsX_{20}$ configuration, the C_D value is high for $\alpha < 9°$ and $\alpha > 16°$.Moreover, it can be observed that, in this configuration, unlike the baseline and other configurations, the transition from angle $\alpha = 12°$ to $\alpha = 13°$ is characterized by a significant increase in C_D values. In contrast, in this configuration, a similar phenomenon occurs when transitioning from angle $\alpha = 11°$ to $\alpha = 12°$. When the graph for $VGsX_{30}$ is examined, it is observed that the Cd value is higher than the baseline in the $\alpha < 5°$ range, is lower than the baseline value in the $5° \leq \alpha \leq 21°$ range and approximately same for $\alpha > 21°$ range. The most striking situation for $VGsX_{40}$ was observed that the cd value was significantly lower than the baseline in the range of $5° \leq \alpha \leq 12°$. A decrease between 24% and 44% was observed in this range of values.

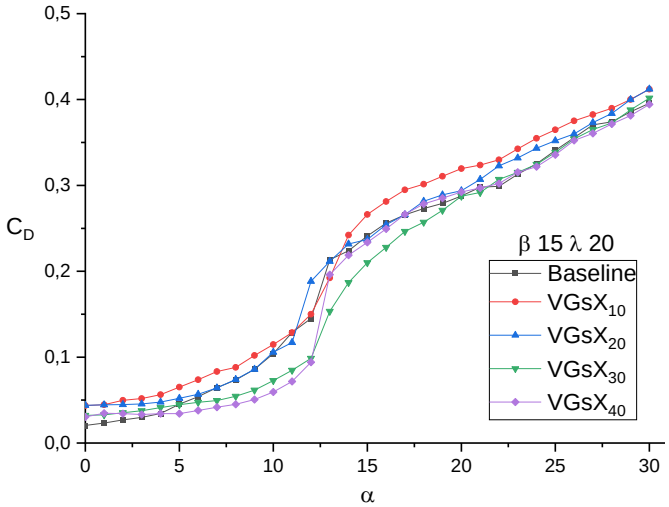

Figure 7: Variation of C_D as a function of angle of.

When Figure 8 is examined, it is observed that the best performance in terms of C_L/C_D values up to the stall point was achieved in the $VGsX_{40}$ configuration. In this configuration, there was an improvement of $VGsX_{30}$ percent in the C_L/C_{Dmax} ratio. Although the $VGsX_{10}$ configuration delayed stall, the C_L/C_D value was observed to be lower compared to the baseline value. The $VGsX_{20}$ and $VGsX_{30}$ configurations yielded lower results up to an α of 7 degrees, followed by higher results up to 16 degrees α. After $\alpha=16°$, they closely followed the baseline value. As a result, the $VGsX_{40}$ configuration demonstrated better performance compared to the baseline. Additionally, it is noteworthy that between $7° \leq \alpha \leq 13°$ degrees, the $VGsX_{20}$ and $VGsX_{30}$ configurations also exhibited better performance.

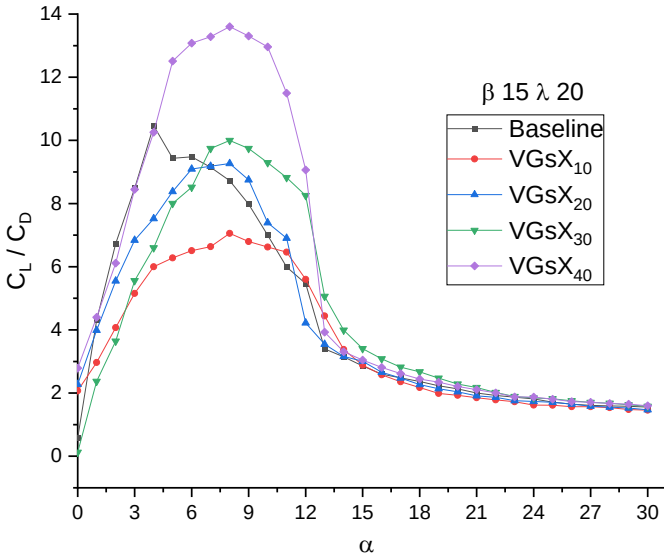

Figure 8: Variation of C_L / C_D as a function of angle of attacks.

IV. CONCLUSION

In this study, the influence of backward triangular vortex generators (VGs) on the aerodynamic performance of a NACA 0012 airfoil was thoroughly examined. A series of experiments were conducted in a wind tunnel at a low Reynolds number (Re) of 6×10^4, encompassing VGs positioned at different chordwise locations (X_{VGs}/c = 0.1-0.4). The results showed significant improvements in stall characteristics and the maximum lift coefficient (C_L) when VGs were employed. $VGsX_{10}$ configurations indicated stall delay by 1 degree. $VGsX_{10}$ and $VGsX_{40}$ configurations demonstrated stall delay by 1 degree and a notable increase in CL_{max}. The $VGsX_{40}$ configuration exhibited the best overall performance with a superior C_L/C_D ratio. It is evident that the implementation of these backward triangular VGs at low Reynolds numbers provides valuable insights into enhancing the aerodynamic characteristics of airfoils, presenting potential benefits in various practical applications.

REFERENCES

[1] D. H. Kim, J.W. Chang, & J. Chung, (2011). Low-Reynolds-number effect on aerodynamic characteristics of a NACA 0012 airfoil. *Journal of aircraft*, 48(4), 1212-1215.

[2] J. N. Counsil, & K. Goni Boulama (2013). Low-reynolds-number aerodynamic performances of the NACA 0012 and Selig–Donovan 7003 Airfoils. *Journal of aircraft*, 50(1), 204-216.

[3] S. S. Bhat, & R. N. Govardhan, (2013). Stall flutter of NACA 0012 airfoil at low Reynolds numbers. *Journal of Fluids and Structures*, 41, 166-174.

[4] C. Pranesh, M. Sivapragasam, M.D. Deshpande & H.K. Narahari, (2019). Negative lift characteristics of NACA 0012 aerofoil at low Reynolds numbers. *Sādhanā*, 44(1), 21.

[5] M. Gad-el-Hak, (1989). Flow control. Appl. Mech. Rev. Oct 1989, 42(10): 261-293

[6] M. Gad-el-Hak, (1996). Modern developments in flow control. Appl. Mech. Rev. Jul 1996, 49(7): 365-379 (15 pages)

[7] I. Gursul, Z. Wang, & E. Vardaki, (2007). Review of flow control mechanisms of leading-edge vortices. Progress in Aerospace Sciences, 43(7-8), 246-270.

[8] H. D. Taylor, The Elimination of Diffuser Separation by Vortex Generators; United Aircraft Corporation: Moscow, Russia, 1947.

[9] J. Hu, R. Wang & D. Huang (2018). Flow control mechanisms of a combined approach using blade slot and vortex generator in compressor cascade. *Aerospace Science and Technology*, 78, 320-331.

[10] A. Grébert, J. Bodart, S. Jamme & L. Joly (2018). Simulations of shock wave/turbulent boundary layer interaction with upstream micro vortex generators. *International Journal of Heat and Fluid Flow*, 72, 73-85.

[11] A. Urkiola, U. Fernandez-Gamiz, I. Errasti & E. Zulueta Computational characterization of the vortex generated by a Vortex Generator on a flat plate for different vane angles. *Aerosp. Sci. Technol*. 2017, 65, 18–25.

[12] H. Wang, B. Zhang, Q. Qiu & X. Xu, Flow control on the NREL S809 wind turbine airfoil using vortex generators. Energy 2017, 118, 1210–1221.

[13] H. Tebbiche (2016). Evolution et contrôle de la couche limite dans le cas de profil NACA, PHD thesis. Mouloud Mammeri University of Tizi Ouzou, Alegria.

[14] H. D. Taylor, H. D. (1947). The elimination of diffuser separation by vortex generators. *Research department report no. r-4012-3, United Aircraft Corporation, East Hartford, Connecticut*, *103*.

[15] J. Donovan, L. Kral, & A. Cary, (1998, January). Active flow control applied to an airfoil. In *36th AIAA Aerospace Sciences Meeting and Exhibit* (p. 210).

Recent Developments on Refrigeration Systems that Use Ejectors as Expanders for Performance Enhancement

O. ÇALIŞKAN[1] and H. K. ERSOY[2]

[1] Department of Mechanical Engineering, Konya Technical University, Konya/Türkiye, ocaliskan@ktun.edu.tr
[2] Department of Mechanical Engineering, Konya Technical University, Konya/Türkiye, hkersoy@ktun.edu.tr

***Abstract* – Global warming and the rise in energy costs force engineers to develop more efficient refrigeration systems and use environment-friendly refrigerants. The use of ejectors for expansion is becoming a widespread application in refrigeration. Ejector has no motor or moving parts, which reduces operation and maintenance costs. This study presents recent developments on refrigeration systems with ejector expansion. Transcritical CO_2 cycles as well as cycles with new-generation refrigerants were investigated. It is obvious that ejector expansion is a suitable solution to improve the performance of the refrigeration cycles for a sustainable future.**

***Keywords* – Ejector, energy efficiency, environmental impact, refrigeration.**

I. INTRODUCTION

GLOBAL warming and rise in energy costs force engineers to improve the performance of refrigeration systems and use environment-friendly refrigerants complying with current regulations. With Paris Climate Agreement coming into force, European Union countries plan to be climate-neutral by 2050 [1]. Turkish Government signed Paris Agreement in 2016 and put it into force in 2021 with the goal of having net zero emission by 2053 [2].

Isenthalpic expansion occurs in the expansion valves and therefore there is a significant amount of work loss. The use of ejectors to reduce throttle losses in the expansion valves is an increasingly common application. The ejector has no motor or moving parts hence operation and maintenance costs are low. It can be used in thermal-driven refrigeration systems as a compression unit [3] as well as an expander in vapor compression refrigeration systems. There are two flow models for ejectors in the literature: Constant area and constant pressure, as shown in Figure 1. In the constant-pressure flow model, two streams are mixed at constant pressure. In the constant area model, however, two streams are mixed in a mixing chamber having a constant cross-section area. According to Keenan et al. [4] the performance of the constant pressure ejectors is better than constant area ejectors but theoretical results obtained by using the constant area model agree with experimental results and it is difficult to obtain an agreement between theoretical and experimental results for the constant pressure model [5].

High-pressure refrigerant coming from the condenser/gas cooler (primary stream) is sent to the motive nozzle converting its pressure energy to kinetic energy. Low pressure at the motive nozzle outlet allows the low-pressure refrigerant coming from the evaporator (secondary stream) to be dragged into the suction nozzle. Two streams are mixed in the mixing chamber and kinetic energy is converted to pressure energy in the diffuser. Two-phase flow at the diffuser outlet is separated in a flash tank. Vapor is sent through the compressor, while liquid is sent to the expansion valve of the evaporator.

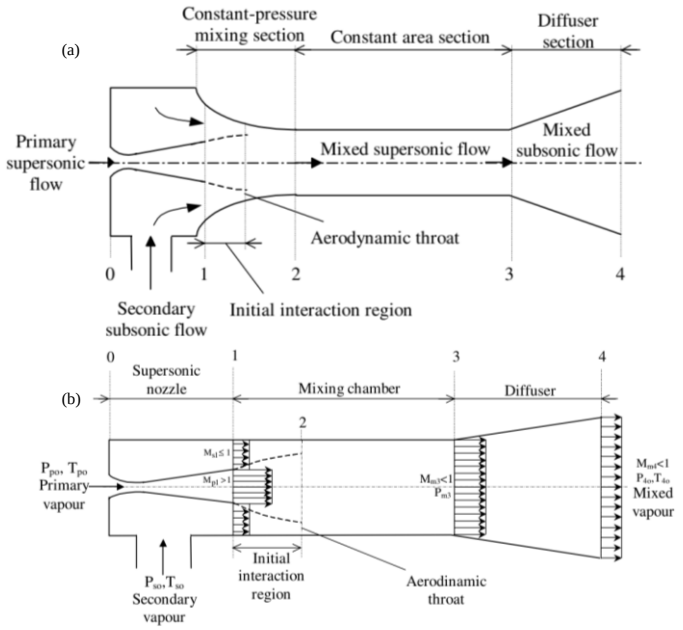

Figure 1: Cross-sectional view of (a) constant pressure ejector, (b) constant area ejector [5].

This paper presents a review of various applications of ejector expansion refrigeration cycles to show the performance enhancements.

II. APPLICATIONS OF EJECTOR EXPANSION IN REFRIGERATION CYCLES

Figure 2 presents the schematic views of one-stage conventional (a) and ejector expansion (b) refrigeration cycles while Figure 3 shows the cycles on the pressure-enthalpy

diagram. It can be seen that compressor suction pressure in ejector expansion cycle is higher and vapor quality at the evaporator inlet is lower than conventional cycle. Increase in the suction pressure reduces the power consumption of the compressor while decrease in the vapor quality at the evaporator inlet increases the enthalpy difference and thus reduction of the mass flow rate in the evaporator for the same capacity.

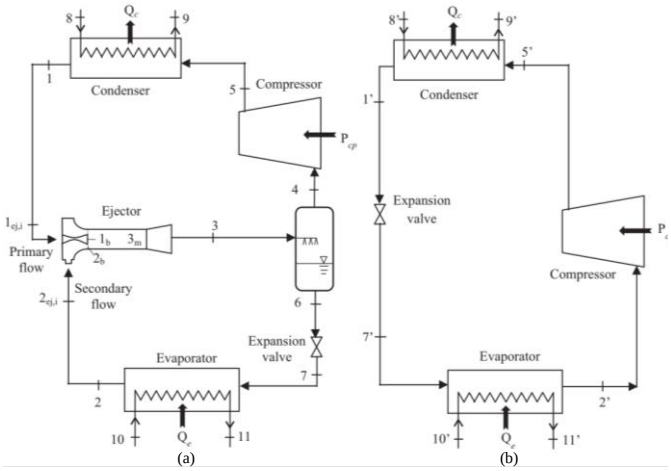

Figure 2. (a) Conventional, (b) ejector expansion refrigeration cycle [6].

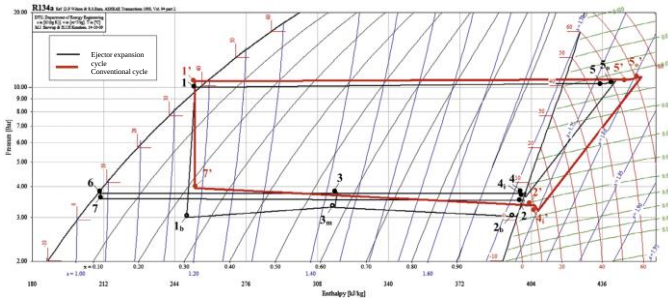

Figure 3. Pressure-enthalpy diagram of the conventional cycle and ejector expansion cycle [6].

Ersoy and Bilir Sag [6] experimentally investigated a one-stage ejector expansion refrigeration cycle using R134a and obtained 7.34-12.87% COP enhancement compared to conventional cycle under the same external conditions and cooling capacity. The authors also indicated that exergy efficiency of the ejector expansion cycle is 6.6-11.24% higher than conventional cycle.

There are plenty of studies with ejector expander refrigeration cycles using new-generation fluids due to legal restrictions on high-GWP refrigerants. Atmaca et al. [7] theoretically compared one-stage ejector expansion cycles using R1234yf, R1234ze(E) as well as R134a. The authors obtained that R1234yf has the highest improvement potential between the investigated refrigerants. İşkan and Direk [8] experimentally investigated several low-GWP refrigerants in a dual-evaporator ejector expansion refrigeration cycle. The authors considered that R516a (GWP=687) is the best alternative to R134a (GWP=1300).

There are also numerous studies with transcritical CO_2 refrigeration cycles with ejector expansion, especially two-stage and two-evaporator supermarket refrigeration cycles. Commercial refrigerators have the highest CO_2 equivalent emissions and account for 25-60% of the electricity used in supermarkets [9, 10]. CO_2 which has a GWP value of 1 is becoming popular in commercial refrigeration systems. Higher operation pressure and lower critical temperature of CO_2 lead to lower performance compared to HFC cycles and therefore performance enhancements are needed. Ejector expansion has significant potential due to the high pressure difference between the evaporator and gas cooler. Lawrence and Elbel [11] compared various ejector metrics in the literature and indicated that CO_2 ejectors can achieve better performance than R134a ejectors. The reasons considered are that R134a ejectors are more sensitive to optimal ejector design than CO_2 ejectors, CO_2 cycles have higher operation pressure and smaller difference between liquid and vapor densities than R134a cycles. Deng et al. [12] theoretically investigated a one-stage transcritical CO_2 refrigeration cycle with ejector expansion and found that the cycle performance is highly dependent on entrainment ratio (ratio of the secondary and primary mass flows). The authors obtained COP enhancements of up to 18.6% compared to internal heat exchanger cycle and 22% compared to conventional cycle. Elbel and Hrnjak [13] experimentally investigated a one-stage transcritical CO_2 refrigeration cycle with ejector expansion and obtained up to 7% COP enhancement compared to conventional cycle. Ersoy and Bilir [14] numerically modeled a transcritical CO_2 refrigeration cycle with ejector expansion. The authors indicated that the suction nozzle pressure drop has a significant effect on the cycle performance. They obtained the optimum pressure drop at the suction nozzle between 4.7-8.7 bar at 5 °C evaporator temperature and 40 °C gas cooler outlet temperature. They also found that ejector expansion cycle had 39.1% less irreversibility compared to conventional cycle under investigated conditions. Manjili and Cheraghi [15] proposed a novel two-stage transcritical CO_2 refrigeration cycle with single evaporator and serially connected two ejectors. The authors claimed COP enhancement between 20-80% compared to one-stage cycle with single ejector. Transcritical booster (BRC), parallel compression (PRC), and ejector expansion (ERC) supermarket refrigeration cycles were modeled and compared by Caliskan and Ersoy [16]. Plant layout and pressure-enthalpy diagram of ERC are presented in Figure 4. Freezer temperature and capacity were chosen as -35 °C and 25 kW, respectively while chiller temperature and capacity were chosen as -10 °C and 120 kW, respectively. COP of ERC is 13-28% higher than PRC and 23-47% higher than BRC. Power consumption of ERC is 11-22% less than PRC and 19-32% less than BRC as shown in Figure 5. The difference is more significant at higher gas cooler outlet temperatures due to high pressure difference between the gas cooler and chiller.

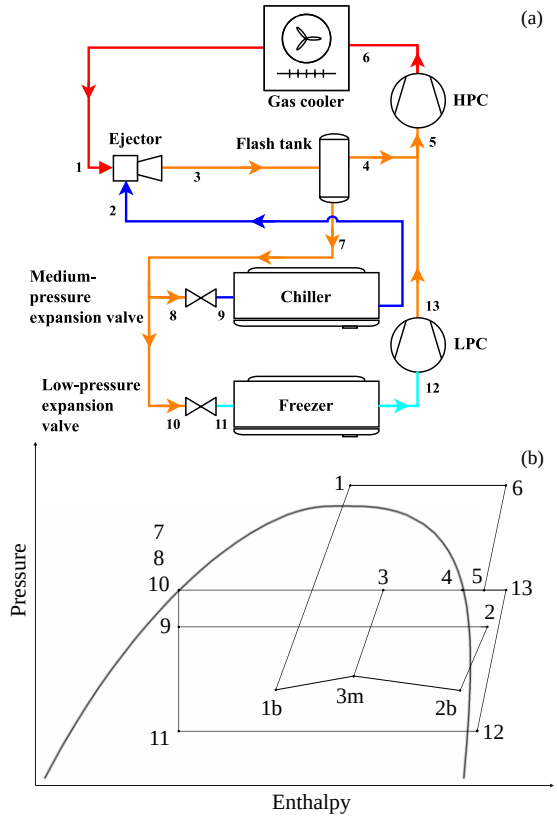

Figure 4. Transcritical CO_2 supermarket refrigeration cycle with ejector expansion (a) plant layout, (b) pressure-enthalpy diagram [16].

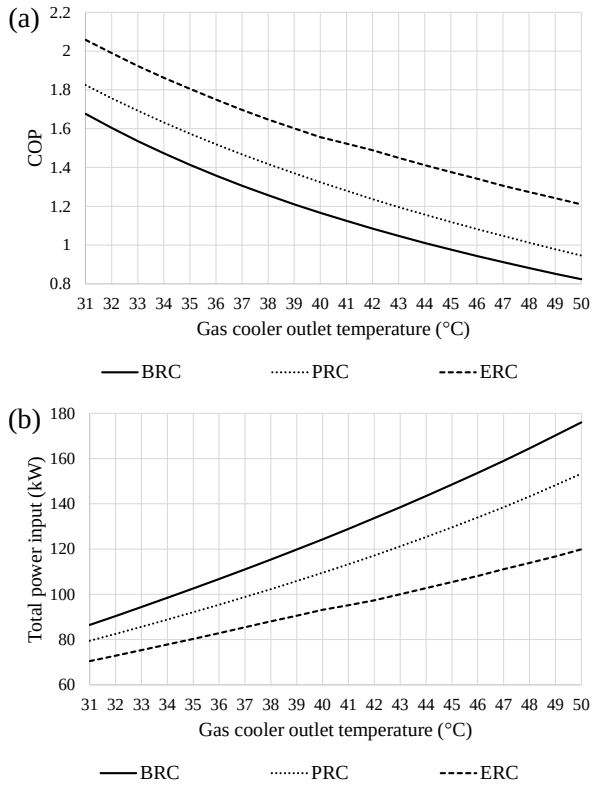

Figure 5. Performance comparison of the booster, parallel compression, and ejector expansion cycles in terms of (a) COP, (b) total power consumption [16].

Hafner et al. [17] developed a multi-ejector block for transcritical CO_2 refrigeration cycles consisting of separate ejectors with different geometries for different capacities. The capacity requirement is matched by using different combinations of the ejectors [18]. Figure 6 shows the cross-sectional view of a multi-ejector block commercially produced by Danfoss. Gullo et al. [19] theoretically compared annual energy consumption of a transcritical CO_2 supermarket refrigeration cycle consisting of multi-ejector expansion, parallel compressor, and flooded evaporator, as shown in Figure 7 with conventional R404A cycle finding out 15.6%-27.3% energy saving for Southern Europe. In a similar study, Tsimpoukis et al. [20] modeled an all-in-one transcritical CO_2 supermarket refrigeration cycle consisting of multi-ejectors, parallel compressor, air conditioning, space heating, adiabatic gas cooler, and subcooler with groundwater using field data of a real supermarket in Athens, Greece. The authors obtained 20.9% less annual energy consumption and 34.7% less TEWI compared to R448A refrigeration and R410A heat pump units. Elbarghthi et al. [21] experimentally investigated a transcritical CO_2 supermarket refrigeration cycle using multi-ejector cartridge commercially manufactured by Danfoss. The authors stated that the cycle had better performance at transcritical operation and obtained that the ejectors were able to recover up to 36.9% of the available work rate. Sengupta and Dasgupta [22] investigated a novel transcritical CO_2 supermarket refrigeration cycle with multi-ejectors, parallel compressor, flooded evaporators, and mechanical subcooler claiming performance enhancement between 18.7-46.8% compared to R404A cycle and between 41.4-82.5% compared to conventional booster cycle.

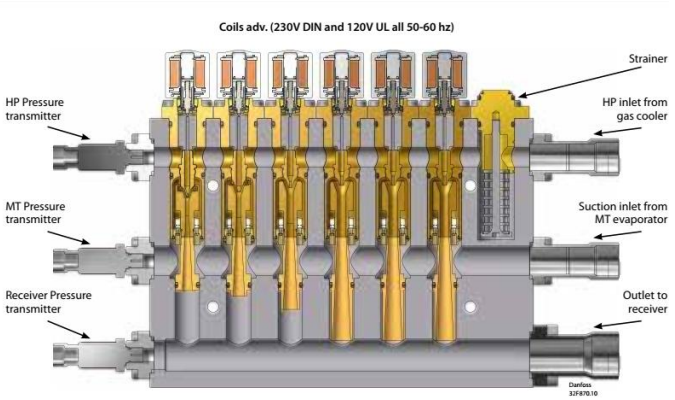

Figure 6. Cross-sectional view of multi-ejector block [18].

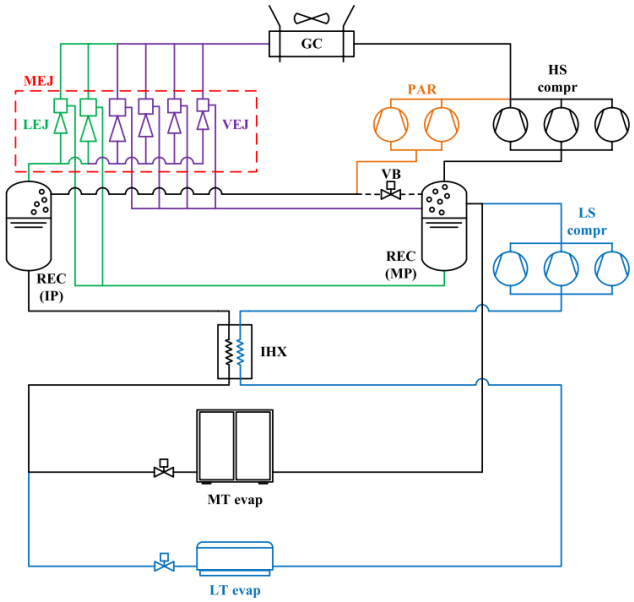

Figure 7. Plant layout of transcritical CO_2 supermarket refrigeration cycle with multi-ejectors, parallel compression, and flooded evaporators [19].

III. Conclusion

In this study, recent developments on ejector expansion refrigeration cycles were investigated in terms of performance. Due to increasing energy costs and regulations on high-GWP refrigerants, it is more important to improve the performance of the cycles using environment-friendly refrigerants such as CO_2. Ejector expansion has a significant potential on performance enhancement of transcritical CO_2 cycles due to their high operation pressures, especially in warm climates. Multi-ejector cartridges are commercially available in the market to satisfy different capacity demands and ensure optimum operation conditions. All-in-one systems including space heating and air conditioning along with refrigeration are being developed by researchers for a complete solution. The researchers have obtained remarkable performance enhancements with ejector technology. Developing energy-efficient systems using environment-friendly refrigerants may contribute to a sustainable future.

Nomenclature

Abbreviations

BRC	Booster refrigeration cycle
compr	Compressor
COP	Coefficient of performance
ERC	Ejector expansion refrigeration cycle
evap	Evaporator
GC	Gas cooler
GWP	Global warming potential
HFC	Hydrofluorocarbon
HP	High pressure
HPC	High-pressure compressor
HS	High stage
IHX	Internal heat exchanger
IP	Intermediate pressure
LEJ	Liquid ejectors
LP	Low-pressure
LPC	Low-pressure compressor
LS	Low stage
LT	Low temperature
MEJ	Multi ejector block
MP	Medium pressure
MT	Medium temperature
PAR	Parallel compressor
PRC	Parallel compression refrigeration cycle
REC	Receiver
TEWI	Total equivalent warming impact
VB	Vapor-bypass valve
VEJ	Vapor ejectors

Acknowledgment

This work was supported by Konya Technical University Academic Staff Training Program (Grant No. 2016-OYP-046). In addition, the present paper constitutes part of the Ph.D. thesis of Oguz Caliskan.

References

[1] European Council, "Paris Agreement on climate change," 2023. [Online]. Available: https://www.consilium.europa.eu/en/policies/climate-change/paris-agreement/. [Accessed: 15-Sep-2023].

[2] N. Erkul Kaya, and G. Çağatay, "Paris Anlaşması Türkiye'de yürürlüğe giriyor," *Anadolu Ajansı*, 2021.

[3] M. E. Tolu, D. N. Özen, and U. Köklü, "Thermodynamic analysis of an ejector cooling system using R123 as refrigerant under different working conditions," *Int. J. Energy Appl. Technol.*, vol. 5, no. 2, pp. 61–67, Oct. 2018.

[4] J. H. Keenan, E. P. Neumann, and F. Lustwerk, "An Investigation of Ejector Design by Analysis and Experiment," *J. Appl. Mech.*, vol. 17, no. 3, pp. 299–309, Sep. 1950.

[5] R. Yapici, and H. K. Ersoy, "Performance characteristics of the ejector refrigeration system based on the constant area ejector flow model," *Energy Convers. Manag.*, vol. 46, no. 18–19, pp. 3117–3135, 2005.

[6] N. Bilir Sag, H. K. Ersoy, A. Hepbasli, and H. S. Halkaci, "Energetic and exergetic comparison of basic and ejector expander refrigeration systems operating under the same external conditions and cooling capacities," *Energy Convers. Manag.*, vol. 90, pp. 184–194, 2015.

[7] A. U. Atmaca, A. Erek, and O. Ekren, "Investigation of new generation refrigerants under two different ejector mixing theories," *Energy Procedia*, vol. 136, pp. 394–401, Oct. 2017.

[8] Ü. İşkan, and M. Direk, "Experimental performance evaluation of the dual-evaporator ejector refrigeration system using environmentally friendly refrigerants of R1234ze(E), ND, R515a, R456a, and R516a as a replacement for R134a," *J. Clean. Prod.*, vol. 352, p. 131612, Jun. 2022.

[9] IPCC/TEAP, "Safeguarding the ozone layer and the global climate system: Issues related to hydrofluorocarbons and perfluorocarbons," Intergovernmental Panel on Climate Change Technology and Economic Assessment Panel, 2005.

[10] EPA, "Putting energy into profits : Energy Star guide for small business," U.S. Environmental Protection Agency, 2007.

[11] N. Lawrence, and S. Elbel, "Analysis of two-phase ejector performance metrics and comparison of R134a and CO2 ejector performance," *Sci. Technol. Built Environ.*, vol. 21, no. 5, pp. 515–525, 2015.

[12] J. Deng, P. Jiang, T. Lu, and W. Lu, "Particular characteristics of transcritical CO2 refrigeration cycle with an ejector," *Appl. Therm. Eng.*, vol. 27, no. 2–3, pp. 381–388, 2007.

[13] S. Elbel, and P. Hrnjak, "Experimental validation of a prototype ejector designed to reduce throttling losses encountered in transcritical R744 system operation," *Int. J. Refrig.*, vol. 31, no. 3, pp. 411–422, 2008.
[14] H. K. Ersoy, and N. Bilir, "Performance characteristics of ejector expander transcritical CO2 refrigeration cycle," *Proc. Inst. Mech. Eng. Part J. Power Energy*, vol. 226, no. 5, pp. 623–635, 2012.
[15] F. Eskandari Manjili, and M. Cheraghi, "Performance of a new two-stage transcritical CO2 refrigeration cycle with two ejectors," *Appl. Therm. Eng.*, vol. 156, pp. 402–409, Jun. 2019.
[16] O. Caliskan, and H. K. Ersoy, "Energy analysis and performance comparison of transcritical CO2 supermarket refrigeration cycles," *J. Supercrit. Fluids*, vol. 189, p. 105698, Oct. 2022.
[17] A. Hafner, S. Försterling, and K. Banasiak, "Multi-ejector concept for R-744 supermarket refrigeration," *Int. J. Refrig.*, vol. 43, pp. 1–13, 2014.
[18] P. Kalinski, "The Danfoss Multi Ejector range for CO2 refrigeration: design, applications and benefits," Danfoss A/S, DKRCE.PE.001.C1.02, Mar. 2019.
[19] P. Gullo, A. Hafner, and G. Cortella, "Multi-ejector R744 booster refrigerating plant and air conditioning system integration – A theoretical evaluation of energy benefits for supermarket applications," *Int. J. Refrig.*, vol. 75, pp. 164–176, 2017.
[20] D. Tsimpoukis, E. Syngounas, D. Petsanas, et al., "Energy and environmental investigation of R744 all-in-one configurations for refrigeration and heating/air conditioning needs of a supermarket," *J. Clean. Prod.*, vol. 279, Jan. 2021.
[21] A. F. A. Elbarghthi, A. Hafner, K. Banasiak, and V. Dvorak, "An experimental study of an ejector-boosted transcritical R744 refrigeration system including an exergy analysis," *Energy Convers. Manag.*, vol. 238, Jun. 2021.
[22] A. Sengupta, and M. S. Dasgupta, "A novel IMS-ejector based supermarket CO2 refrigeration system for the extended south of CO2 equator," presented at the 10th IIR Conference on Ammonia and CO2 Refrigeration Technologies, Ohrid, North Macedonia, 2023.

Thermal Analysis And Design Of Composite UAV 1 Wings Under Realistic Flow Conditions

D. PEHLİVAN[1] and Prof. Dr. H. AYDOGAN[2]

[1] PhD. Student, Selcuk University, Konya/Turkey, damlapehlvan@gmail.com
[2] Technology Faculty, Selcuk University Konya/Turkey, haydogan@selcuk.edu.tr

Abstract

Composites are the material of choice for the wing structures of unmanned aerial vehicles (UAV) due to their high specific strength. However, their strength properties deteriorate faster with the changes in the temperature, and they have low thermal conductivity. Due to these reasons, for anti icing and de-icing purposes, conventional technique of using heated air from the engine cannot be used. Without a proper de icing solution, overall aerodynamic performance of the wing will be hampered and the flight safety will be greatly reduced.

An alternative technique, known as electrothermal heating is used for the anti icing and de icing of UAV wings. In this technique, heat generating fabrics are utilized inside o rover the wing structure to avoid and/or remove the ice under cold weather conditions. Using, 2D and 3D composite thermal analysis, the composite structure can be optimized.

Keywords **–** Composite structures, thermal analysis, thermal anisotropy, electrothermal heating

I. INTRODUCTION

In the literature, various electrothermal heating solutions exist.

Roy et al. (2021) has carried out thermal modelling studies on carbon fiber reinforced plastics (CFRP) wing structures. In tis study, convection coefficients are taken from the correlation equations available in 1D equations. In the numerical analysis, two different heating configuration(15 heating strips, 5 heating strips) were utilized. No optimization studies were done on the size, position or the surface temperature of the heater.

Mohseni (2012) has studied the thermal behaviour of glass fiber reinforced epoxy (GFRP) structure experimentally .Metal heating strips have been added to the structure. The position of the heating strips have been changed to optimise the surface temperature on the wings. In this study, an infrared camera is used. Under -17 centigrade and 27 m/s flow conditions, icing can be observed especially close to the leading edge of the wing. To avoid icing, it is stated that it could be useful to apply different currents (hence different heat fluxes to the metal heating strips) No calculation has been performed for the optimum currents for different metal heating strips.

Kim et al(2016) has performed experimental heat transfer studies on chopped carbon fiber mats. Mats with different percent fiber weight have been manufactured, and these mats have been heated with a copper plate on the mat. The temperatures on the surface as a function of voltage applied has been studies. No study on the convection heat transfer is performed, and no numerical modelling and analysis has been realized as part of the study.

Laroche(2017) has studied the heat transfer behavior of composite plates with the finite element method. Different heating materials, and different heat fluxes were utilized. The target surface temperature was selected as 4 Celsius. The efficiency of heating elements in the form of pads and strips have been compared. The cost effectiveness of different materials are also discussed. Again, size, location and shape of the heating elements were only subjected to a few trials without a systematic search of the optimum design.

Falzon et al (2015) has studied the heat transfer behavior of carbon composite structures using mats with electrical conductivity. To overcome excessive heating an insulation layer between carbon fiber layer and heating layers is also inserted.

Barzi (2014) has performed optimization studies to improve wing heating systems. He made a study to optimize electricity consumption.

Habashi and Pourbagian (2015) have conducted a numerical study to optimize de-icing duration. Optimum heating loop (power and duration) was sought within the limit of a pre-specified energy consumption limit, taking 266 K temperature and 44 m/s velocity as the reference freestream conditions.

Mutnuri (2006) has conducted a study to understand the effect of various resins on the heat conduction behavior. It was shown that the heat conduction coefficient is not isotropic, and the heat conduction coefficient somewhat increases with the temperature. Besides, Mutnuri (2006) has studied the out of plane heat conduction coefficients comparatively. In this study, models used in the estimation of out of plane heat conduction coefficient of composites were examined. It was shown that the models are more successful with the glass reinforced fiber composites. This situation can be related to the carbon fiber's having a higher degree of anisotropy in terms of thermal conduction.

Szymiczek et al. (2022) have studied the thermal properties (k, Cp) of composites by manufacturing 4 different composite plates with different fiber/resin weight fraction. Composite plates were manufactured with the hand lay-up technique. In this study, vinyl ester was used as the resin. After the test

samples were produced, heat conduction coefficients were determined. It was observed that the sample with the carbon fibers have the highest heat conduction coefficient. In the measurement of temperatures, active thermography and a FLIR A615 infrared camera was utilized. Hear conduction coefficients in the out of plane axis was measured.

Ibrahim et al. (2019) manufactured a series of carbon composite plates with electrothermal heating system, and tested them in the Arctic environment. In this study, heating metal surfaces were created within the carbon fiber prepreg. For electrical insulation, capton film was utilized.

Composite materials with active electrothermal management can be done with materials such as; carbon tows (1), constantan wires (2), electrically conductive carbon mats (3), carbon nanotube paper (4), metal surfaces with electrical heating used for heat generation. Heating elements should;

-Not increase the temperatures where heat is applied excessively, although prevent icing by keeping the temperature over the wing above a certain temperature threshold

-Not cause delamination within the composite structure, not cause significant deterioration in elastic properties

-Not require high levels of energy consumption, and be efficient.

II. METHOD

In this study, the following analyses were performed;

1. 2D isotropic plate analysis with heat generation with CFD solver
2. 2D orthotropic plate analysis with heat generation with CFD solver
3. 3D isotropic plate analysis with heat generation with CFD solver
4. In-House Solver for plate Analyses
5. Optimization Studies

Saripally (2015) expresses the glass fiber reinforced plastics specific heat capacity values as given in Table 1.

Table 1. Specific heat capacities obtained experimentally, Saripally(2015)

Fiber volume ratio	Specific heat capacity [J/kgK]
0.4	1132.27
0.6	989.68

To calculate the heat conduction coefficient of composites, various models exist.

Longitudinal heat conduction coefficient can be calculated with the rule of mixtures.

$$k_x = v_f * k_f + (1 - v_f) * k_m \quad \text{(eqn. 1)}$$

Transverse heat conduction coefficient can be calculated with the Halpin and Kardos(1976) model;

$$k_y = k_m * \frac{k_m*(1-v_f)+k_f*(1+v_f)}{k_m*(1+v_f)+k_f*(1-v_f)} \quad \text{(eqn. 2)}$$

In these equations;

kf, fiber heat conduction coefficient ,

km, matrix heat conduction coefficient,

vf, fiber volume ratio

Heat conduction equation with heat generation is given by Cengel (2002).

$$\frac{\partial}{\partial x}\left(\frac{k\partial T}{\partial x}\right) + \frac{\partial}{\partial y}\left(\frac{k\partial T}{\partial y}\right) + \frac{\partial}{\partial z}\left(\frac{k\partial T}{\partial z}\right) + egen = \rho Cp\ \partial T/\partial t \quad \text{(eqn. 3)}$$

2D and 3D heat transfer models have been studied in Fluent 6.3.26 environment and by in-house developed code. Finite volume method has been utilised by Fluent and finite difference method has been utilised by the in-house developed code.

2D and 3D plates have been subjected to convection coefficients that have been obtained from the wing CFD analyses obtained previously.

III. RESULTS AND DISCUSSION

1. 2D Isotropic Plate modelling

Heat generation is homogenously distributed in this configuration.

As illustrated by Jeong ve Myong (2022), nickel coated carbon composite laminates can satisfy this condition.

Boundary conditions:

- Top and bottom surfaces are subjected to thermal convection.
- Left and right surfaces are thermally insulated.

Table 2. Thermal model parameters for CFD solver

Heat convection coefficients, top and bottom edges	200-400 W/m^{2}K

Freestream temperature	267 K
Left and right edges	insulation
Heat generation	30 kW/m3
Density	2500 kg/m3
Specific heat (Cp)	990

Plate size is given by 1 m x0.1 m. In the solutions, a 100x100 mesh is utilized. The mesh density gets higher as the cells get closer to the walls.

Due to the stability and speed advantages compared to newer versions, solution has been performed in Fluent 6.3.26 environment. For the case where, non-isotropic materials are defined, this advantage can be clearly observed.

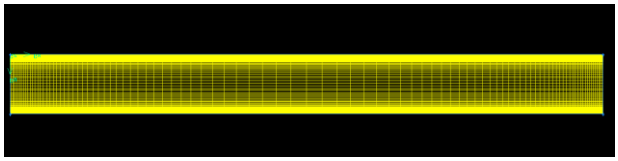

Figure 1. Solution domain, 2D plate

The mesh has been generated with gambit software. All quad elements have been used. In the solution domain, cells are smaller close to the walls where thermal gradients are higher. This is important for the accuracy of the results.

Heat conduction coefficient kx=ky=0.5 have been utilised. Temperature distributions are given in Figure 2, Figure 3, and Figure 4with varying heat generation rates.

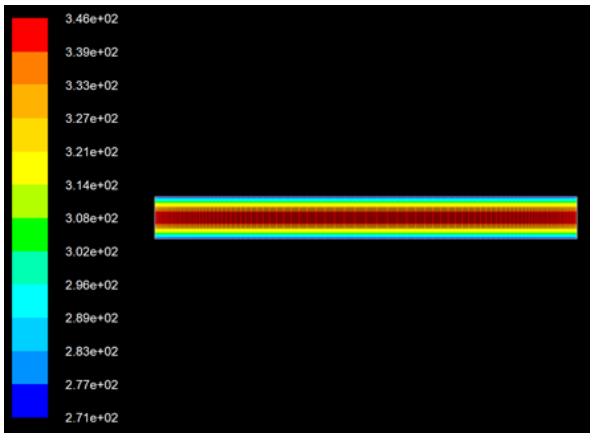

Figure 2.Temperature distribution (K), qgen=30 kw/m3, h=400 W/K m2

The convection coefficient was obtained from a 2D flow over airfoil case at Re=1.5 millions. As can be seen in the figures, despite very high convection coefficient, by means of heat generation, temperature can be kept at reasonable intervals. For wing structures, a similar strategy should be implemented.

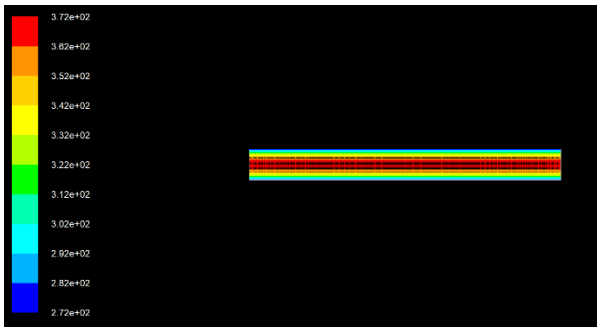

Figure 3. Temperature distribution (K), qgen=40 kw/m3, h=400 W/K m2

When the heat generation is further increased, temperatures increase undesirably. This situation is illustrated in Figure 4.

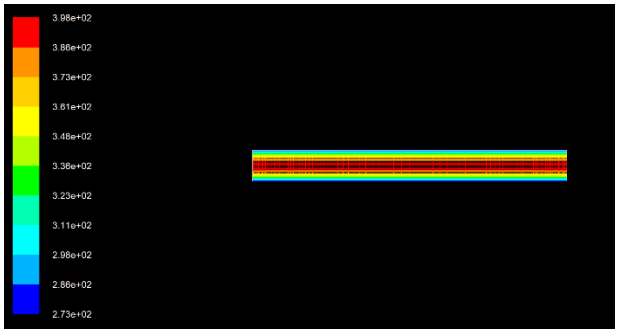

Figure 4. Temperature distribution (K), qgen=50 kw/m3, h=400 W/K m2

Plate is then subjected to a different convection coefficient and temperature field has been solved for 3 different heat generation rates (qgen=20,30 and 35 kW/m^3)

These solutions are illustrated in Figure 5, Figure 6 and Figure 7. Overall, no icing on the plate surface is expected. Temperature values increase as the heat generation increase.

Figure 5. Temperature distribution (K), qgen=20 kw/m3, h=200 W/K m2

Figure 6. Temperature distribution (K), qgen=30 kw/m3, h=200 W/K m2

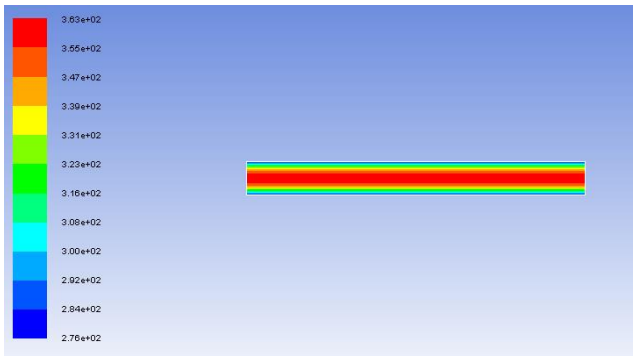

Figure 7. Temperature distribution (K), qgen=35 kw/m3, h=200 W/K m2

2. 2D Orthotropic Plate Modelling

Heat conduction coefficients have been calculated with the equation 1 and 2 given previously.

In the analyses, kx=0.8 and ky=0.5 values have been utilised.

When compared to the isotropic model, it can be seen in Figure 8 and Figure 9 that temperature values are lower, but they are still in the acceptable range.

Figure 8. Temperature distribution (K), orthotropic plate, qgen=30 kw/m3, h=400 W/K m2

Figure 9. Temperature distribution (K), orthotropic plate, qgen=20 kw/m3, h=400 W/K m2

When the heat generation rate is further lowered, temperature is reaching critical point for freezing. This situation is illustrated in Figure 10.

Figure 10. Temperature distribution (K), orthotropic plate, qgen=10 kw/m3, h=400 W/K m2

From the analyses performed, it can be seen that isotropic modelling should not be employed for composite plates as it will lower the safety margin.

3. 3D isotropic plate

Heat transfer analyses for a 3D plate has been performed in ANSYS Mechanical platform. On the top and bottom surfaces heat transfer by convection is specified. Inside the plate, there is a heat generation surface that generates heat. Due to the heat generation, plate temperatures are kept at reasonable levels despite very high convection heat transfer.

Table 3. Problem data for 3D isotropic plate case

Convection coefficient	400 W/K m^2
Ambient temperature	267 K
Plate heat conduction coefficient	0.5 W/mK
Heat generation inside plate	10E3 W/m^2
Plate initial temperature	283 K
Heat generating plate thickness	10 mm
Total plate thickness	100 mm
Overall plate dimensions	10E3 mm x 1E3 mm x 100 mm

Solution has been performed for the unsteady heat transfer problem.

In between the surfaces, there is temperature coupling The upper surface of the bottom part is coupled with lower surface of the part in the middle and are at the same temperature. The upper surface of the part in the middle is at the same temperature with the lower surface of the upper part.

Temperature distribution is given in Figure 11. Reasonable temperature values have been obtained. Under these conditions, no icing shall be observed. It has been observed that Depending on the heat generation rate, temperature values are changing significantly.

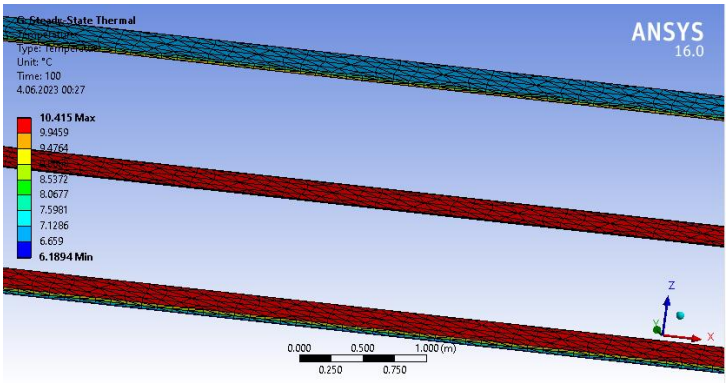

Figure 11. 3D isotropic plate temperature distribution

4. In-House Solver

After simulations with ANSYS, a 2D plate analysis has been performed where conductivity in different directions are different (kx,ky are not equal)based on an in-house developed solver. The analyses are based on the unsteady heat transfer.

The 2nd order central differencing and 1st order explicit time integration has been implemented. Other parameters utilised in the study are given in the table. Matlab high level language which is based on the C language has been utilised for the study.

Table 4. Thermal model parameters for in-house developed solver

Heat convection coefficients, top and bottom edges	200-400 W/m^2K
Freestream temperature	267 K
Left and right edges	insulation
Heat generation	30 kW/m3
Density	2500 kg/m3
Specific heat (Cp)	990
Geometry	1 m x0.1 m
dx	0.01 m
dy	0.01 m
kx	0.5 W/ mK
ky	0.5 W/ mK
Heater 2 dimensions	varying
Heat generation rate, heater 1	0-40 kw/m3
Heat generation rate, heater 2	0-40 kw/ m3
h	400 W/ m2K
Heater width	0-10 cm
Convergence criteria	(T-Told)/Tref<=2E-6

4.1 Homogenous Heat generation

In-house developed code has been compared with the Fluent solver. It is calculated that percent relative error in terms of

temperature is less than 2%. This can be validated visually by comparing Figure 2 with Figure 12.

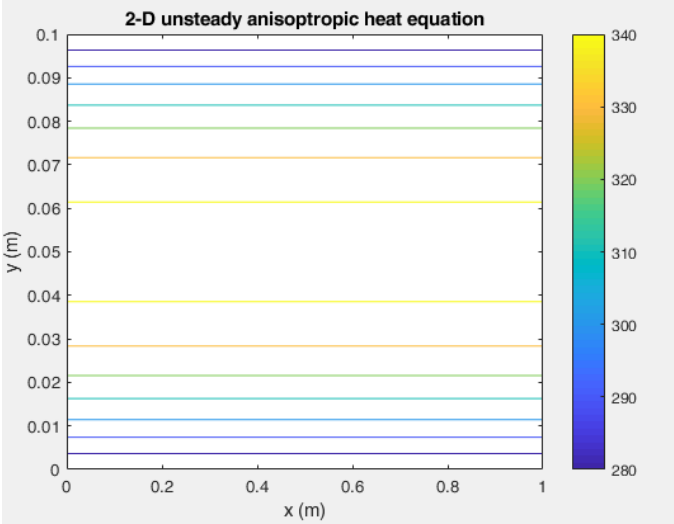

Figure 12. Temperature distribution for isotropic case, egen=30 kw/m^3, k=0.5W/mK, h=400 W/Km^2

Effect of heat generation rate on the maximum temperature (which is seen in the middle of the plate) is illustrated with the in-house developed code next.

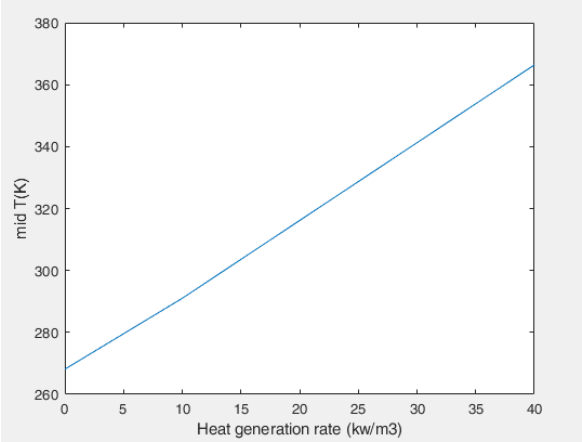

Figure 13. Temperature distribution, homogenous heat generation, h=400 W/Km^2

This graph hints that there should be an optimum value for the heat generation.

4.2 Inhomogenous Heat generation

Second, instead of an homogenous heat generation, local patches of heat generation surfaces are used. First, 1 patches of 0.98 m x 0.01 m band is inserted into the domain.

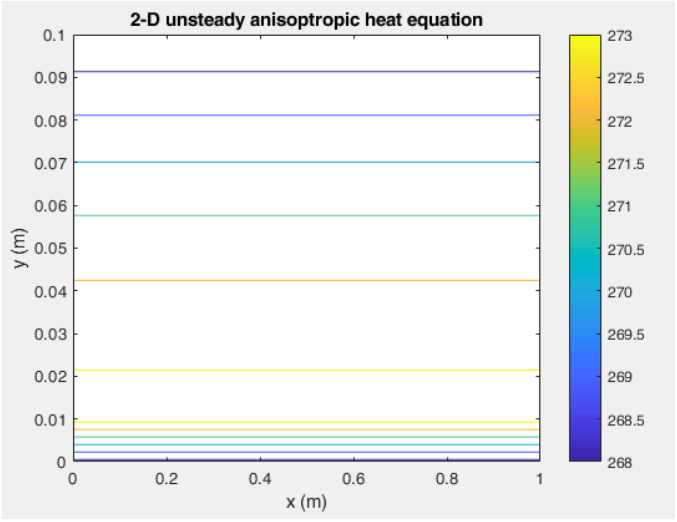

Figure 14. Temperature distribution for isotropic case, egen=30 kw/m^3(1 heating strip), k=0.5W/mK, h=400 W/Km^2

As seen in Figure 14, heating effect is prominent only in the region close to the heating strip.

Secondly, two heating strips can be utilised. (One close to the top wall, another close to the bottom wall) Th results are illustrated in Figure 15.

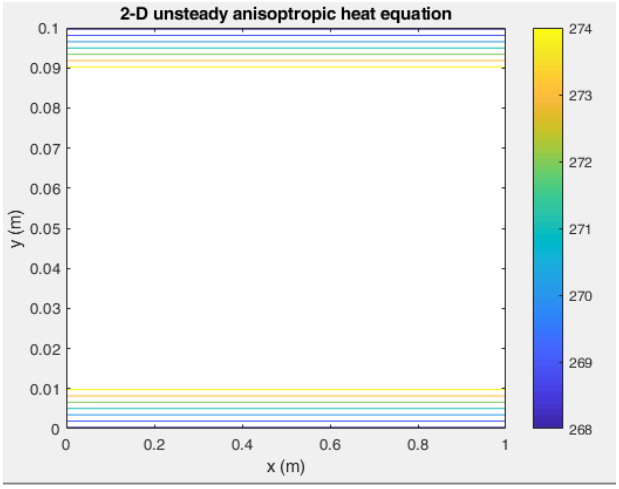

Figure 15. Temperature distribution for isotropic case, egen=30 kw/m3(2 heating strips, 1 cm width), k=0.5W/mK, h=400 W/Km2

It can be seen in Figure 14 and Figure 15 that temperature values inside the domain are still too low to be acceptable. To remedy this, width of the heating strips should be increased. So, 0.98 m x 0.2 m patches are utilized next. The results are illustrated in Figure 16.

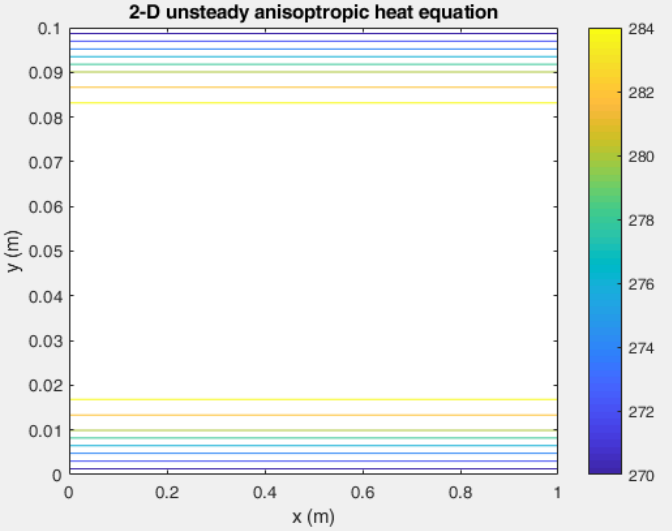

Figure 16. Temperature distribution for isotropic case, egen=30 kw/m3(2 heating strips, 2 cm width), k=0.5W/mK, h=400 W/Km2

As seen in Figure 16, temperature values are much more desirable compared to narrower case.

5. Optimization Studies

In the literature optimization studies for the heat transfer problems are abundant. For example, Kumar el al. (2019) has studied the optimization of the heat exchangers with a gradient based optimization routine. Barzi (2014) has performed optimization studies towards optimizing aircraft de icing systems. Habashi and Pourbagian (2015) have conducted an optimization study to lower the deicing time on aircraft wings.

In general, two basic optimization methods are available. In the first one, gradient information is calculated to obtain optimum values of the variables of interest. In the second method, evolutionary techniques are utilised that can skip over local minima and maxima much more easily, but with a slight lty higher computational cost.

Genetic algorithm is one of the basic methods of evolutionary optimization. For the optimization, Genetic Algorithm function of the MATLAB R2017b has been utilised.

Nonequal heat conduction coefficients, 2 heating strips (buckypaper), and coating material for high thermal conductivity has been included in the solution domain.

5 variables have been studied for the optimization.

Variable 1: Magnitude of heat generation
Variable 2: Size of the heat generating stirps
Variable 3: kx value for the composite plate structure
Variable 4: ky value for the composite plate structure
Variable 5: Heat conduction coefficient of the coating material on the convecting surfaces

Heat conduction coefficients are also taken as optimization variables since they can also be tailored to a degree in composite structures. The variable intervals are summarized in Table 5.

Table 5. Optimization variable intervals

Variable No	Lower Limit	Upper Limit
1	1 kw/m3	10 kw/m3
2	0.5 cm	2.5 cm
3	0.2 W/mK	0.5 W/mK
4	0.5 W/mK	1 W/mK
5	1 W/mK	20 W/mK

To help the solution process, first and second variables are restricted to integer values. To achieve this, a transformation has been applied on the 2nd variable.

Optimization parameters are summarized in Table 6.

Table 6. Optimization parameters

Population size	20
Number of generations	100
Elite member count	1

As per the optimization parameters, 20 solution has been performed for 100 generations. In each generation, the most successful member is preserved for the next generation.

The initial values given in Table 7 are utilised for the variables during start up phase of the optimization.

Table 7. Initial values used in optimization

Variable No	Value
1	2 kw/m3
2	15 cm
3	0.3 W/m·K
4	0.7 W/m·K
5	10 W/m·K

The boundary conditions used are summarized in Table 8.

Table 8. BCs used in the optimization study

Surface	BC
Uppersurface	(h=104, Tdış=263 K)
Lowersurface	(h=104, Tfreestream=263 K)
Left wall	273 K
Right wall	273 K
Heating strips	Heat generation

The value of h used here is taken from the plate analogy as given by Bahrami (2011) with Pr=0.71, Re=1e6 values used.

There are many possible form of the objective function, however with some critical thinking and trial and error, the following objective function has been utilised for the optimization.

Objective function=

$abs(T(ny,100)-277)^3$ + (term 1)
$abs(T(1,100)-277)^3$+ (term 2)
$energy^{0.5}$ + (term 3)
abs(max(T(:))) (term 4)

Objective function is being minimised as a result of the optimisation.

There are 4 terms in the objective function.

The first and second terms try to bring the upper and lower surface temperatures to 277 K, and for values below this rapidly produce penalty values. The exponent 3 is used fort his purpose.

The third term is incorporated to minimise the electrical power used. The reduction of electrical power used contributes to the minimisation of the objective function.

Finally, the fourth term is related to the minimisation of the maximum temperature reached inside the plate. Thanks to this term, excessive temperatures are prevented inside the plate structure.

As a result of the optimisation process, temperature field given in Figure 17 has been obtained. As shown in Figure 17, temperature is kept at reasonable levels both on the surface and inside the plate structure.

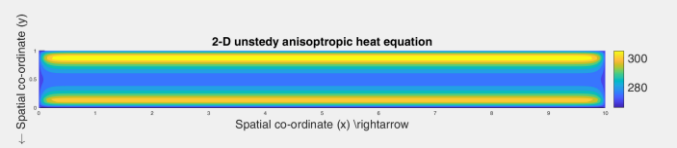

Figure 17. Optimum temperature field (Kelvin)

As a result of the optimisation study, the set of variables for the optimum performance have been obtained. These are given in Table 9.

In this study, an 8 core Intel Xeon W 2245 Cpu has been utilised. Calculation of population members in each generation has been done in parallel to the extent possible.

Table 9. Optimization results

Variable No	1	2	3	4	5
Value	5574 W/m3	25 cm	0.287 W/mk	0.98 W/mK	4.15 W/mK

In the future, it is planned that computer infrastructure which has more CPU cores shall be utilised for 3D optimizations activities. Furthermore, experimental validation activities shall be performed.

IV. CONCLUSION

The study is important in the field of aviation as it contributes to the efficiency and overall reliability of the UAVS. The studies in the literature use mostly convection coefficients based on 1D relations, however in this study, more realistic 2D and 3D results are incorporated to the overall design methodology. As part of the optimization studies, in addition to the location of the heating strips, number of heating strips, size, of the heating strips, current &heat flux parameters are studied in detail.

V. REFERENCES

[1] Bahrami, M., Lecture notes, Forced Convection Heat Transfer, ENSC 388, 2011
[2] Barzi, M. P. 2014. "Multidisciplinary Optimization of In-Flight Electro Thermal Ice Protection Systems", McGill University, PhD. Thesis, Canada.
[3] Cao L, Liu Y, Wang J, Pan Y, Zhang Y, Wang N, Chen J. Multi-Functional Properties of MWCNT/PVA Buckypapers Fabricated by Vacuum Filtration Combined with Hot Press: Thermal, Electrical and Electromagnetic Shielding. Nanomaterials (Basel). 2020 Dec 14;10(12):2503.
[4] Cengel, Y. Cengel, Y.A. (2002) Heat Transfer: A Practical Approach. 2nd Edition, McGraw-Hill, New York.
[5] Dag, Y., Stephen, A., Patrick., M. 2014. "Determination of convective heat transfer for subsonic flows over asymmetric airfoil NACA 4412", Proceedings of the 15th International Heat Transfer Conference, IHTC-15.
[6] Devi, P. V. Paulson, V. Madhanraj & Shah, D. A. 2017. "Heat transfer and temperature effects on a dimpled NACA0012 airfoil with various

angles of attack", International Journal of Ambient Energy Volume 39, 2018 - Issue 8, 783-786.
[7] Falzon, B. G., Robinson, P., Frenz, S., Gilbert, B. 2015. "Development and evaluation of a novel integrated anti-icing/de-icing technology for carbon fibre composite aerostructures using an electro-conductive textile", Composites Part A: Applied Science and Manufacturing, 68.
[8] Habashi, W. & Pourbagian, M. 2015. "Aero-thermal optimization of in-flight electro-thermal ice protection systems in transient de-icing mode", International Journal of Heat and Fluid Flow, 54.
[9] Ibrahim, Y. Kempers, R., Amirfazli, A. 2019. "3D printed electro-thermal anti- or de-icing system for composite panels" Cold Regions Science and Technology, 166, 102844.
[10] Kumar, T.A., Sharma, N., Mohammad, M.D. Pradeep, B.T., Saichand, U., Vamsi, N.M. 2019. "Optimization of spiral plate heat exchanger by gradient based optimizer", International Journal of Innovative Technology and Exploring Engineering, 8, 1819-1823.
[11] Kim, M. Sung, D. H., Kong, K. Kim, N., Kim, B., Park, H. W. 2016. Young-Bin Park, Jung, M., Lee, S. H., Kim. S. G., "Characterization of resistive heating and thermoelectric behavior of discontinuous carbon fiber-epoxy composites", Composites Part B: Engineering, 90, 37-44
[12] Laroche, A., 2017. "Comparative Evaluation of Embedded Heating Elements as Electrothermal Ice Protection Systems for Composite Structures", Msc. Thesis, Montreal, Canada.
[13] Mohseni, M., Amirfazli, A. 2013. A novel electro-thermal anti-icing system for fiber-reinforced polymer composite airfoils, Cold Regions Science and Technology, 87, 47-58.
[14] Mutnuri, B. 2006. "Thermal conductivity characterization of composite materials", West Virginia University.
[15] Rosa, D. F., & Esposito, A. 2012. "Electrically heated composite leading edges for aircraft anti-icing applications", Fluid Dynamics and Materials Processing, 8(1), 107-128
[16] Roy, R., Raj, L. P., Je-Hyun, J, Min-Young C., Jin-Hwe, K. Myong, R. S. 2021. "Multiphysics anti-icing simulation of a CFRP composite wing structure embedded with thin etched-foil electrothermal heating films in glaze ice conditions", Composite Structures, 276, 114441.
[17] Szymiczek, M.; Buła, D.; Koczwara, J. 2022. "Influence of the Reinforcement Structure on the Thermal Conductivity and Surface Resistivity of Vinyl Ester Composites Used on Explosion-Proof Enclosures of Electrical Equipment" Materials, 15, 5190.
[18] Zohary, Aideal & Asrar, Waqar & Aldheeb, Mohammed. 2021. "Numerical Investigation on the Pressure Drag of Some Low-Speed Airfoils for UAV Application" CFD Letters, 13, 29-48.

Controlled Discrete Chip Formation in Turning with CNC Programming

M. E. DURSUN[1] and S. KESRİKLİOGLU[1]

[1] Abdullah Gül University, Kayseri/Turkey, muhammedemin.dursun@agu.edu.tr
[1] Abdullah Gül University, Kayseri/ /Turkey, sinan.kesriklioglu@agu.edu.tr

***Abstract* – In machining operations, continuous chip formation has been a problem affecting the surface quality of machined parts, tool-life, cutting fluid performance and energy dissipation. Although the methods such as cutting parameter optimization, high-pressure coolants, chip breakers, chip-pullers, and modulation assisted machining (MAM) with piezo actuators has been used in the previous studies and practices, the problem still exist or requires expensive equipment. This study focuses on MAM which is quite complex, but effective method in chip management. The sinusoidal cutting path of the MAM was replicated by modulating the tool in the feed direction by computer numerical control (CNC) manipulation without using an expensive and/or complex system. A program was written in Matlab to create the G-codes based on MAM parameters so that the cutting tool completely disengages from the workpiece during each turning cycle, and it results in the disruption of the severe and continuous tool chip contact. This method enables the control of the chip sizes cost effectively without any external devices such as piezoelectric transducers and high-resolution sensors. To test the effectiveness of the method, cutting experiments were conducted under two different turning speeds with various MAM parameters on Al6061-T6 alloy. The results of the experiment indicate that while the cutting insert with chip brakers still creates continuous chips in the CNC turning operations of a ductile workpiece material, this method can be effectively used for controlling the chip length at different cutting and modulation frequencies.**

***Keywords* - Modulated assisted machining, continuous chip, Turning, CNC programming.**

I. INTRODUCTION

Continuous chip buildup has been an everlasting issue in manufacturing operations such as CNC turning, boring, and threading. Chip buildup refers to the accumulation of machining chips around the cutting tool or cutting area. It occurs due to the continuous engagement of the cutting tool with the workpiece and has many disadvantages. It accelerates the wear of cutting tools which can lead to an increase in machining forces [1], power consumption, and heat accumulation and poor surface finish [2]. Chip accumulation can also damage the cutting tool and prolong the machining time [3]. These problems which are caused by chip buildup, are intertwined with each other. For example, the wear of the cutting tool causes surface finish quality to be reduced while increasing the cutting resistance. This requires a higher force exertion from the cutting tool thus increasing the power consumption. When chips accumulate around the cutting tool, coolants cannot penetrate the cutting zone, thus, reduce the cooling and lubrication effects [2]. It can even pose a threat to workers' safety due to the manual intervention required to prevent chip accumulation [4]. Because of all these problems, the prevention of chip build-up plays an important role in machining operations to preserve workers' safety, low matching cost and high efficiency.

There are various methods being used to overcome chip build-up to increase the tool life, surface finish, and dimensional accuracy. These methods are based on the cutting parameter optimization, usage of high-pressure coolants, chip breakers, chip-pullers, and modulation assisted machining (MAM). While these methods work on preventing chip buildup to some extent, there are also shortcomings such as high cost, unsteady results, and health risks.

Utilization of high-pressure fluids in machining operations to prevent chip buildup may consist of up to one-fifth of the total machining cost [5]. Although high-pressure coolants can improve the tool life and surface quality of the machined parts, it requires expensive pumps and significantly increases the manufacturing costs. Moreover, it was found that the machining of Inconel 718 by turning under high-pressure coolant couldn't reduce the tool wear [6]. Depending on the workpiece material and cutting parameters, the predominant purpose of using high-pressure coolant might be solely chip control. This is an inefficient way of using high pressure coolants compared to their usage with the purpose of both chip control and prevention of heat accumulation. Furthermore, cutting fluids used in machining processes can contaminate the environment in addition to endangering the operators by causing health problems such as lung cancer or respiratory diseases [7]. Even though there are non-harmful alternatives such as vegetable oil-based cutting fluids, hazardous materials make up most of the cutting fluids used in machining and due to the environmental risk factors, safe and permitted disposal of these fluids can significantly increase the cost of production [8]. There are also problems with the disposal of coolants. Regulations on safe disposal of used coolants and filtering systems can increase the cost significantly [9]. In addition, coolants cause contamination of the chips which needs a costly cleaning process before recycling [10].

Chip-pulling is another method with proven effectiveness on chip management [11]. Contrary to other chip management methods that focus on chip-breaking, in the chip-pulling process a device pulls the continuous chip through a tunnel.

However, pulling forces and rollers used in pulling have to be controlled strictly to prevent chip breaking [12]. Another challenge is that the chip must be guided into the tunnel so it can be pulled. Depending on the cutting parameters and material properties, chip-pulling may require manual intervention which would slow down the machining process and increase the cost.

The chip breakers are the most widely used method to prevent continuous chip formation in turning operations [13]. Chip breakers are the obstacle or grooves on the rake face which causes continuous chips to bend and break. However, the effectiveness of the chip breaker depends on various cutting parameters such as rake angle, workpiece material, and breaker width [14]. It is reported that the temperature is lower in the machining processes were cutting tool's engagement gets constantly interrupted [15]. Compared to other methods with constant interruptions such as MAM, this is disadvantageous. Due to the continuous engagement between the cutting tool and the workpiece, heat accumulation would occur at the cutting edge.

MAM is one of the recent approaches to prevent continuous chip formation and it works by oscillating the cutting tool. As the cutting tool oscillates, it disengages from the workpiece, and continuous chip production gets obstructed. Previous studies on MAM proved that it could benefit the manufacturing process by decreasing the overall cutting tool temperature, extending the tool life, lowering the energy loss, controlling the discontinuous chip size, reducing the machining time, and enhancing the surface texture [16], [17].

However conventional MAM comes with its disadvantages. piezoelectric transducers/actuators have to be used to create vibrations. Also, the usage of high precision of the sensor significantly increases the cost of machining [18]. Similarly, ultrasonic assisted machining (UAM) was found to be very complex and bound due to the limitations of piezoelectric transducers [19]. Moreover, the chips are rewelded due to the high frequency modulation during the cutting process.

The objective of this work is to replicate the cutting behavior of MAM with G-code to prevent continuous chip production in turning operations. G-code will cause cutting tools to constantly engage and disengage from the workpiece thus preventing chip buildup. This can theoretically prevent excessive heat on the cutting tool which would increase the tool life and lower the machining cost. This method can enable MAM to be more accessible and easier to be used without any additional devices since conventional MAM needs high control and precise piezoelectric transducers/actuators to create consistent vibration.

II. Methodology

In order to replicate modulation assisted machining (MAM) with G-code, the time-dependent cutting tool path was determined. The cutting tool path was then simplified to positions and velocities in MATLAB to generate the G-code. Finally, the text files were created based on different cutting and modulation parameters to perform the turning experiments.

The time-dependent cutting tool path is described as:

$$Z = (f_w f_r)t + \left(\frac{A}{h_0} * f_r\right) \sin\left(\left(2\pi f_w * \frac{f_m}{f_w}\right)t\right) \quad (1)$$

where A, h_0 and t represent the tool oscillation amplitude, undeformed chip thickness (mm), and time(s), respectively. Other parameters such as f_r, f_m, and f_w, represent the feed rate (mm/rev), modulation frequency, and spindle speed (rps), respectively. In equation 1, the primary variables are the A/ h_0 and f_m/f_w. In conventional MAM, the chip production being continuous or discontinuous is solely determined by these two ratios. Hence, the formula above was put into a MATLAB code with the two primary variables in addition to feed rate and spindle speed.

The time-dependent tool path cannot be directly used without simplification since CNC machines cannot execute G-codes containing excessive data. For this reason, the tool path was simplified by keeping the velocity constant between sequential local maximum and local minimum positions. Figure 1 shows primary and simplified cutting tool paths which are important to verify the accuracy of the simplification. Finally, MATLAB script integrates the velocity and position values with G-code commands. The generated G-code is automatically entered into a txt file to be used in CNC turning operations.

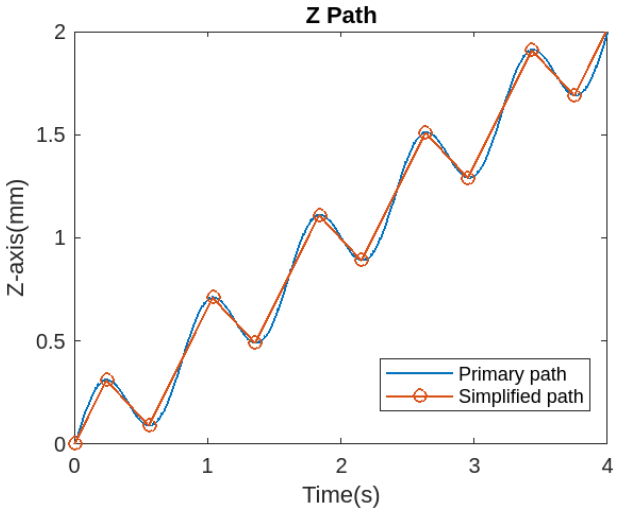

Figure 1: Simplified and Primary time-dependent cutting tool path (A/ h_0 and f_m/f_w are 1 and 0.5, respectively)

In order to test the performance and precision of MAM replication with G-code, different types of G-codes had to be used in the experiment. There are two primary parameters which are the A/ h_0 and f_m/f_w. In MAM, A/ h_0 determines the length of engagement and disengagement. The cutting tool will make a greater back and forth movement with its high values while decreasing the A/ h_0 value would cause a shorter back and forth movement. When the A/ h_0 is below 0.5, the cutting tool won't disengage from the workpiece which will prevent MAM from functioning. The value of the f_m/f_w affects the number of

disengagements in addition to the cutting tool pattern. Therefore, this parameter is the main factor in the controlling of chip size. When A/h_0 and f_m/f_w are combined, they determine whether the cutting tool path will be continuous or discontinuous. Figure 2 shows the discontinuous and continuous regions based on these two parameters.

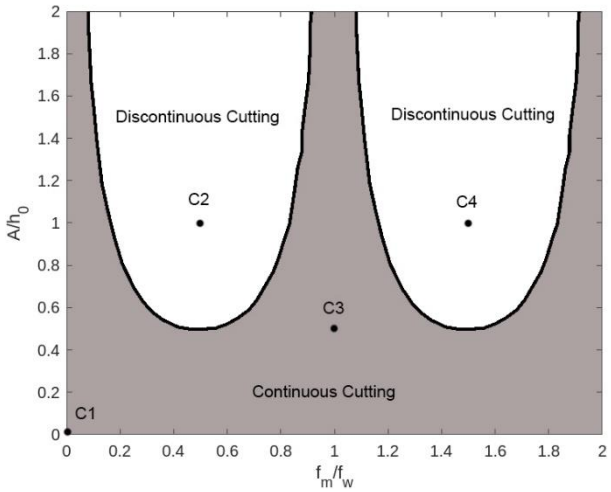

Figure 2: Continuous and discounting cutting regions

Various parameter combinations which have both continuous and discontinuous properties were used in order to test the performance and precision of G-codes. For this reason, four different parameter combinations of A/h_0 and f_m/f_w were chosen as shown in Figure 2. Out of the four parameter combinations, C2 and C4 are in the discontinuous cutting region while C1 and C3 are in the continuous region. At C1 continuous turning operation (without modulation) was used, and the feed rate was kept constant to prevent the cutting tool from going back and forth. At C2 discontinuous turning operation, A/h_0 and f_m/f_w were chosen as 0.5 and 1, respectively. At C3 continuous turning operation, A/h_0 and f_m/f_w were chosen as 1 and 0.5, respectively. At C4 discontinuous turning operation, A/h_0 and f_m/f_w were chosen as 1.5 and 1, respectively.

The attributes of the parameter combinations can be clearly observed from the theoretical cutting patterns. Table 1 shows the theoretical cutting patterns around the cylindrical surface for each parameter combination. When the cutting patterns of C1 and C3 are examined, it can be seen that the cutting trajectories do not intersect each other. This results in constant engagement of the cutting tool with the workpiece. The effect of f_m/f_w on chip size can be observed from the cutting patterns of C2 and C4. As shown in cutting patterns, the C4 has more trajectory intersections resulting in more disengagements per circumference. This will cause discrete chips to be smaller in size.

Table 1: Theoretical cutting tool patterns based on the parameter combinations used in the experiment.

	A/h_0	f_m/f_w	Cutting Type	Cutting Pattern
C1	0	0	Continuous	
C2	0.5	1	Discrete	
C3	1	0.5	Continuous	
C4	1.5	1	Discrete	

A more detailed theoretical cutting tool pattern is shown in Figure 3. These patterns were created in MATLAB where the feed rate and spindle speed were defined as 0.2 mm/rev and 500 rpm, respectively. As shown in Figure 3, the intersection between the trajectories is 0.2 mm in both parameter combinations, since the f_m/f_w is 1 in both C2 and C4. If the f_m/f_w was 0.5 and 1.5, the intersection length would have been 0 and 0.4 mm, respectively. As mentioned before, the A/h_0 determines the number of disengagements of the cutting tool from the workpiece, per revolution. At C2, since the A/h_0 is 0.5 there are 0.5 disengagements per revolution while there are 1.5 disengagements at C4.

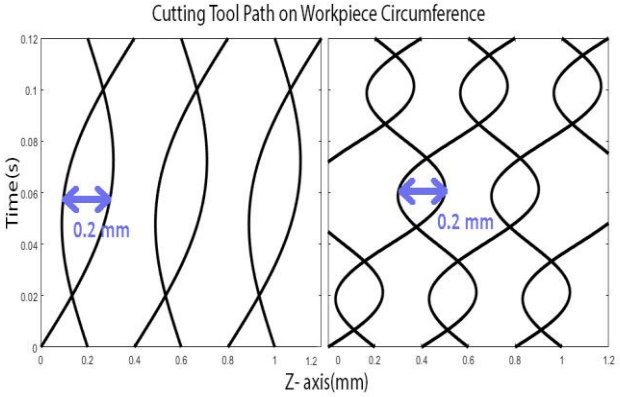

Figure 3: Cutting tool path on the cylindrical surface(C1, C2)

III. Results and Discussion

In the experiments, an Al6061-T6 round stock was machined with 4 different parameter combinations (C1, C2, C3 and, C4) under the rotational cutting speeds of 250 rpm and 500 rpm. In each machining process, a DCMT11T304-MP type coated insert with chip breaker was used. In these turning operations, the depth of cutting was 1 mm while the radius of the workpiece was 22 and 19 mm under 250 and 500 rpm, respectively. Before each turning operation, the metal bar was processed at 1000 rpm and 0.1 mm/rev to obtain a smooth surface finish. For each combination of parameters, a 10 mm length of the round bar

was machined and the machine was turned off to collect the chips for classification and comparison.

In the turning operation with a rotational cutting speed of 250 rpm, C2 and C4 were expected to produce discrete chips while C1 and C3 were expected to produce continuous chips. The result of this experiment is shown in Figure 4. In this experiment, C1, C2 and C3 showed consistent results with theoretical expectations, while C4 revealed a contradictory result compared to other parameter combinations. It is shown in Figure 4 that the chips of C1, C3 and C4 are continuous while the chips of C2 are discrete.

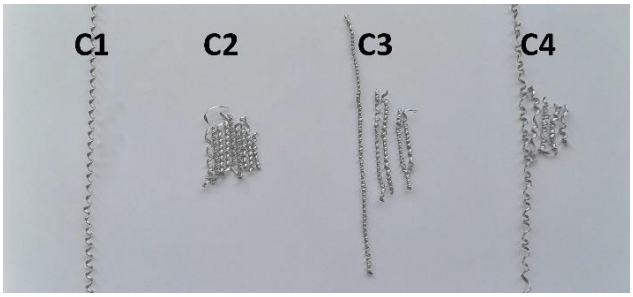

Figure 4: Chips from the 250-rpm turning processes.

Even though the results of the C4 didn't match the expectations, the G-code of C2 successfully prevented the continuous chip production that happened at C1. The continuous chips of C3 operation also show that the MAM parameters in the continuous region led to chip build-up. In addition, all the discrete chips at C2 have similar sizes, unlike chips of other parameter combinations. This is an indication of MAM replication working properly at C2. One possible reason for the continuous chips at C4 is the inaccuracies of CNC on executing the G-codes. The differences between G- code velocities and actual velocities is expected to be the main cause of this inconsistency at C4. Even though there must be similar differences of G-code and actual velocities in other parameters, it is likely that only at C4, error rates caused it show continuous cutting behavior.

Similar to the previous experiment, under 500 rpm, turning operation C2 and C4 were expected to produce discrete chips while C1 and C3 were expected to produce continuous chips. Discrete chips were successfully produced at C2 and C4 as shown in Figure 5. Even though C1, C2 and C4 are consistent with the expected results, the chips were not continuous in C3.

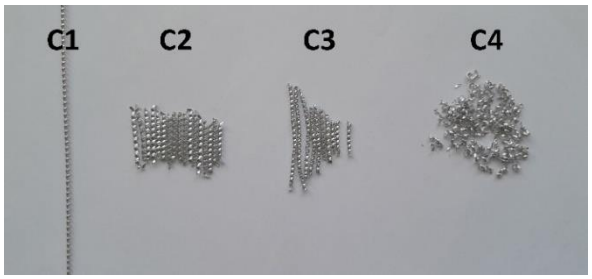

Figure 5: Chips from the 500-rpm turning processes.

While chips of C3 are not as long as the on in C1, the sizes of chips of C3 are still longer compared to C2. Compared to the previous experiment, MAM replication with G-code showed better results at 500-rpm turning operation. Both at C2 and C4, chips showed consistent sizes with each other. Especially, getting smaller discrete chips at C4 compared to C2 proves the effect of the f_m/f_w on chip size management.

The experimental surface finish was compared with the theoretical cutting tool path to determine the accuracy. Figure 6 shows the three-dimensional cutting tool path overlapped with the surface of the metal bar used in the experiment. The metal bar image was taken after 500 rpm turning operation while the red-colored theoretical cutting tool paths were created three-dimensionally for each parameter combinations in MATLAB.

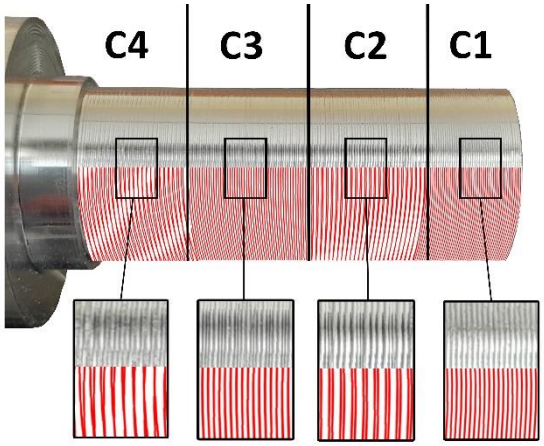

Figure 6: Theoretical and experimental cutting tool path on the cylindrical surface under 500 rpm turning operation

When the workpiece surfaces are compared with the theoretical patterns, similarities between the two can be observed clearly. Visual similarities prove that by changing the input parameters of the code, the surface finish can also be manipulated.

Theoretically, the turning process at C3 is supposed to produce continuous chips. Even though the 250 rpm C3 chips are continuous, 500 rpm C3 is discrete. This may be due to the chip breaker geometry of the insert used in the machining. Even though the same chip breakers were used in both experiments, it is possible that the feed rate and cutting forces of C3 created a different circumstance at 500 rpm, causing the chip breaker geometry to be effective. As can be seen from Figure 7, on multiple occasions, recordings of the cutting process show that the continuous chip hits the tailstocks before falling off which might be the primary reason for discontinuous chips.

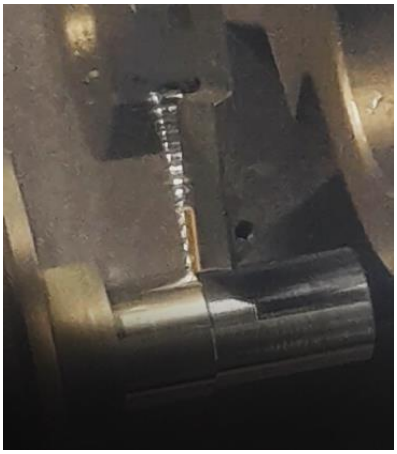

Figure 7: Continuous chip breaks due to the headstock

Another reason might be the continuous-discontinuous parameter regions in Figure 2, due to the shift based on the spindle speed and cutting tool speed. If the cutting tool cannot match up to the theoretical velocities in the G-code, it is expected that the cutting tool can move in a discontinuous pattern without disengaging from the workpiece. The primary reasons for this problem are expected to be the chip breaker geometry of the insert, vibration caused by the constant back and forward movement of the cutting tool in addition to the acceleration and deceleration causing unprecise cutting tool speed.

IV. Conclusion

Continuous chip-build up is a prevailing problem in machining operations and the effectiveness of MAM on this issue is well established. A new way of preventing chip buildup by utilizing the G-code to create pre-determined cutting patterns is examined in this paper. Results from the experiment indicate that this method can prevent chip buildup by creating discrete chips with consistent lengths in particular parameters. It can be expected that this method may have benefits like the MAM's such as tool life extension and controlled surface texture.

Since this method can be applied to machining operations without any equipment nor modification, it is easy and promising. Further research must be done on the cost-effectiveness, time efficiency and reliability of this method under different conditions to compare with MAM and other methods. Further research has to be done to examine the effectiveness of this method under different conditions and parameters.

Appendix

MatLab code for G-code generation:

```
clc; clear all; close all
% Inputs
spindle_speed = 500 ;          % rpm
global_feed =0.200 ;           % Fr mm/rev
length=40;                     % length of the workpiece that needs to
be machined (mm)
Fm_Fw = 1.5 ;                  % fm/fw
A_h0 = 1 ;                     % A/h0

%---------------------------------------
revolution_time=60/spindle_speed;        %time required per one
revolution of  the workpiece (s)
finishing_time=length/(global_feed/revolution_time); %total time
needed for entire machining (s)
time_array=0:0.0001:finishing_time;
z_axis_wave=(spindle_speed*global_feed/60)*time_array +
((A_h0*global_feed)*sin((2*pi*spindle_speed*Fm_Fw/60)*time_array));
% Z-axis MAM cutting tool path(mm)

%------------ local max and min--------------------
time_interval1= 89/((2*180*spindle_speed*Fm_Fw/60)); % determining
time intervals of the first local max&min of z axis wave
time_interval2= 300/((2*180*spindle_speed*Fm_Fw/60));%
determining time intervals of the first local max%min of z axis wave
time_interval=time_interval1:0.001:time_interval2; %time interval array
z_interval=(spindle_speed*global_feed/60)*time_interval +
((A_h0*global_feed)*sin((2*pi*spindle_speed*Fm_Fw/60)*time_interval
)); %mm

max_z_value=max(z_interval);             % finding the max value of Z
axis in the interval
max_z_index = find(z_axis_wave>=(max_z_value-0.00001), 1, 'first');
%index of the maximum Z value in the interval is found
z_max_value=z_axis_wave(max_z_index); %the Z value of the first
local maximum

min_z_value=min(z_interval); % finding the min value of Z axis in the
interval
min_z_index_values = find(z_axis_wave<=(min_z_value+0.000001));
min_z_index= min_z_index_values(
find(min_z_index_values>=max_z_index, 1, 'first'));
z_min_value=z_axis_wave(min_z_index);%the Z value of the first local
minimum
z_reduction=z_min_value-z_max_value; % value of reduction from
local Z max to local Z min
z_increment=2*z_max_value; % value of increment from local Z min to
local Z max
increment_time=2*time_array(max_z_index); %time passing during
each Z position increment
reduction_time=time_array(min_z_index)-time_array(max_z_index);
%time passing during each Z postion reduction
max_array_size=1+2*floor(finishing_time/(reduction_time+
increment_time)); % maximum number of array elements for feed rate
and time

%------------ Z AXIS POSITIONS--------------
Z_axis_positions(1)=0.000; %first Z position is 0
Z_axis_positions(2)=z_max_value;
i=3;
for a=3:1:(2*max_array_size)
Z_axis_positions(i)=Z_axis_positions(i-1)+z_reduction;
i=i+1;
Z_axis_positions(i)=Z_axis_positions(i-1)+z_increment;
i=i+1;
end
Z_axis_positions= Z_axis_positions* (-1);

%-------------- FEED RATES -------------
feed_rate_increment = 60*z_max_value/(increment_time/2); %
constant increment of the feed rate
feed_rate_reduction= -60*z_reduction/(reduction_time);% constant
reduction of the feed rate
Feed_Rate(1)=feed_rate_increment/2; %first feed rate value
f=2;
for c=2:1:(2*max_array_size) %rest of the feed rate values in an array
Feed_Rate(f)=feed_rate_reduction;
f=f+1;
Feed_Rate(f)=feed_rate_increment;
f=f+1;
end
```

```
%---------- G-CODE ARRAY----------
Z_axis_G_code(1)="G01 Z" + round(Z_axis_positions(1),3) + " F"+
round(Feed_Rate(1),3)+";";
for c=2:1:max_array_size
Z_axis_G_code(c)="Z" + round(Z_axis_positions(c),3) + " F"+
round(Feed_Rate(c),3) + ";";
end
Z_axis_G_code(max_array_size )="Z" + (-round(length,3)) + " F"+
round(Feed_Rate(max_array_size),3);

Z_axis_G_code2 = Z_axis_G_code.'; % horizontal G-codes lines
rearranged vertically
G_Code=table(Z_axis_G_code2); % G-codes turned into table so it
can be written to file
writetable(G_Code,'G_CODE.txt') % G-codes are written to the
"G_CODE.txt" file
disp(G_Code)
```

ACKNOWLEDGMENT

This work was partially supported by the Faculty of Engineering at Abdullah Gul University.

REFERENCES

[1] B. M. Lane, M. Shi, T. A. Dow, and R. Scattergood, "Diamond tool wear when machining Al6061 and 1215 steel," *Wear*, vol. 268, no. 11–12, pp. 1434–1441, May 2010, doi: 10.1016/j.wear.2010.02.019.

[2] B. Yılmaz, Ş. Karabulut, and A. Güllü, "A review of the chip breaking methods for continuous chips in turning," *Journal of Manufacturing Processes*, vol. 49. 2020. doi: 10.1016/j.jmapro.2019.10.026.

[3] R. Copenhaver, T. Schmitz, and S. Smith, "Stability analysis of modulated tool path turning," *CIRP Annals*, vol. 67, no. 1, 2018, doi: 10.1016/j.cirp.2018.03.010.

[4] L. Berglind and J. Ziegert, "Modulated Tool Path (MTP) Machining for Threading Applications," in *Procedia Manufacturing*, 2015. doi: 10.1016/j.promfg.2015.09.029.

[5] S. Kumar *et al*., "A comprehensive study on minimum quantity lubrication," *Mater Today Proc*, vol. 56, 2022, doi: 10.1016/j.matpr.2021.12.158.

[6] A. R. C. Sharman, J. I. Hughes, and K. Ridgway, "Surface integrity and tool life when turning Inconel 718 using ultra-high pressure and flood coolant systems," *Proc Inst Mech Eng B J Eng Manuf*, vol. 222, no. 6, 2008, doi: 10.1243/09544054JEM936.

[7] B. Ozcelik, E. Kuram, M. Huseyin Cetin, and E. Demirbas, "Experimental investigations of vegetable based cutting fluids with extreme pressure during turning of AISI 304L," *Tribol Int*, vol. 44, no. 12, pp. 1864–1871, Nov. 2011, doi: 10.1016/j.triboint.2011.07.012.

[8] S. Debnath, M. M. Reddy, and Q. S. Yi, "Environmental friendly cutting fluids and cooling techniques in machining: A review," *Journal of Cleaner Production*, vol. 83. 2014. doi: 10.1016/j.jclepro.2014.07.071.

[9] R. N. Callahan and K. M. Hubbard, "The development and analysis of an environment friendly machining fluid application system," *International Journal of Environmentally Conscious Design & Manufacturing*, vol. 12, no. 3, 2004.

[10] S. Anton, S. Andreas, and B. Friedrich, "Heat dissipation in turning operations by means of internal cooling," in *Procedia Engineering*, 2015. doi: 10.1016/j.proeng.2015.01.474.

[11] E. Shamoto, T. Aoki, B. Sencer, N. Suzuki, R. Hino, and T. Koide, "Control of chip flow with guide grooves for continuous chip disposal and chip-pulling turning," *CIRP Ann Manuf Technol*, vol. 60, no. 1, 2011, doi: 10.1016/j.cirp.2011.03.081.

[12] B. Sencer, T. Aoki, E. Shamoto, T. Hasegawa, and T. Koide, "Development of a chip pulling system for efficient turning," in *Procedia CIRP*, 2014. doi: 10.1016/j.procir.2014.03.092.

[13] H. Gurbuz, A. Kurt, I. Ciftci, and U. Seker, "The influence of chip breaker geometry on tool stresses in turning," *Strojniski Vestnik/Journal of Mechanical Engineering*, vol. 57, no. 2, 2011, doi: 10.5545/sv-jme.2009.191.

[14] J. Mahashar Ali and M. Murugan, "Influence of chip breaker location and angle on chip form in turning low carbon steel," *International Journal of Machining and Machinability of Materials*, vol. 5, no. 4, 2009, doi: 10.1504/IJMMM.2009.026903.

[15] D. A. Stephenson and A. Ali, "Tool temperatures in interrupted metal cutting," *Journal of Manufacturing Science and Engineering, Transactions of the ASME*, vol. 114, no. 2, 1992, doi: 10.1115/1.2899765.

[16] J. B. Mann, Y. Guo, C. Saldana, W. D. Compton, and S. Chandrasekar, "Enhancing material removal processes using modulation-assisted machining," *Tribol Int*, vol. 44, no. 10, 2011, doi: 10.1016/j.triboint.2011.05.023.

[17] B. Eren and B. Sencer, "Mechanistic cutting force model and specific cutting energy prediction for modulation assisted machining," 2020. doi: 10.1016/j.promfg.2020.05.071.

[18] L. Zheng, W. Chen, and D. Huo, "Review of vibration devices for vibration-assisted machining," *International Journal of Advanced Manufacturing Technology*, vol. 108, no. 5–6, 2020, doi: 10.1007/s00170-020-05483-8.

[19] H. Martins and H. Puga, "Ultrasonic Assisted Machining Overview: Accessing Feasibility and Overcoming Challenges for Milling Applications," *Metals*, vol. 13, no. 5. 2023. doi: 10.3390/met13050908.

Vehicle Crash System Design

A. DOGAN [1] and B. AYDEMIR [2]

[1] Marmara University, Engineering Faculty, Mechanical Eng., Istanbul/TURKIYE,
arifdogan@marrun.edu.tr, ORCID: 0009-0006-2992-5754

[2] TUBITAK UME, Gebze/Kocaeli/TURKIYE,
bulent.aydemir@tubitak.gov.tr, ORCID: 0000-0001-6848-2681

Abstract **- Crash tests are tests that evaluate how cars perform in various crash scenarios. These tests are performed to determine the safety level of vehicles and to ensure the protection of the driver and passengers in a possible accident. A large number of collision systems have been developed according to the axis of the collision or the types of colliding elements (vehicle-vehicle, vehicle-pedestrian, vehicle-barrier, etc.). The most basic type of crash testing is called frontal crash testing. This test simulates the front of the vehicle colliding with a fixed barrier or another vehicle. In this study, the system design, relevant standards and commonly used test procedures were examined and carried out through the Solidworks program in order to perform the front crash test. Although the design is based on the Japanese-NCAP frontal crash test procedure, it has been developed to be adaptable to different test procedures such as Euro-NCAP.**

Keywords **- Crash test system, NCAP, Frontal crash test**

I. INTRODUCTION

TODAY, the damages and losses caused by road traffic accidents are a major concern not only for individuals but also for the overall safety and economic stability of society. With the rapidly increasing number of vehicles, the issue of traffic safety has become more important than ever. In this context, vehicle crash test systems have formed the basis of the modern automotive industry's efforts to set and improve safety standards.

The history of the vehicle crash test system reflects the development of the automotive industry and the evolution of the understanding of safety. The tests, which started with simple observation and experimental approaches in the early periods (1930-1970), have become scientifically based over time. After 1970, the formation of NCAP organisations pioneered the standard crash tests and the sharing of the results with the public. While tests have become more sophisticated with the advancement of technology, environmentally friendly design has also gained importance.

Vehicle crash test systems generally aim at two important objectives. Firstly, these tests are designed to evaluate the safety performance of the vehicle in a crash. Simulating different scenarios, these tests aim to maximize the safety of drivers, passengers and pedestrians. Secondly, it provides guidance to vehicle manufacturers and engineers, providing feedback to continuously improve safety systems and designs. This process supports the automotive industry's goal of continuously raising safety standards and minimizing injuries and casualties caused by road traffic accidents. By raising awareness of car safety, vehicle crash test systems encourage manufacturers to design safer vehicles and play an important role in reducing the impact of road accidents.

II. CRASH TEST SYSTEM DESIGN

In order to determine the design of vehicle crash test systems, the type of crash must first be determined. We will focus on the design of the front barrier crash test, which is one of the vehicle-barrier crash types, which is now classic and has been used most widely for years with its general structure all over the world.

For the design of the test, firstly the test setup and obstacle mechanism are determined. The test area where the test will be performed should be of suitable dimensions and specially designed. In addition, the sensors and measuring devices to be used for the test are selected. Sensors and cameras are placed in the vehicle so that the forces can be measured and deformations can be analysed at the moment of impact.

Professional equipment and personnel are required to carry out the test. The area where the test will be carried out is kept under control by taking security measures.

After the test, the data obtained are analysed and the behaviour of the vehicle and its occupants is evaluated as a result of the collision. Factors such as deformations, forces, and passenger and driver safety are taken into consideration. The test results provide valuable information for improving vehicle design or developing safety systems.

The front barrier crash test is one of the most critical types of test for vehicle safety and occupant protection.

The test procedure we will use is the Japanese-NCAP H30-02 frontal crash safety performance test procedure available in the references section.

The vehicle for this test system shall have a maximum capacity of 9 passengers and a maximum weight of 2.8 tonnes. Adult male 50 per cent dummies shall be used to be placed on the front passenger seat. The front barrier crash test is a type of test in which the vehicle hits the front of the vehicle at a speed of 64.0 ± 1 km/h and an angle of 0^{o}.

This test is used to assess whether the front of the vehicle is designed to ensure the safety of the driver and passengers in a crash. In order to determine the test system design, we can

prepare many different test setups based on the requirements specified in international standards. For example, we can create unique systems on many subjects such as acceleration of the vehicle and the design of the crash wall.

A. Vehicle Acceleration

A carrier element connected to the rail system will be used to accelerate our vehicle. It is a lightweight element that can be produced by aluminum casting or machining. Since its only function is to accelerate the vehicle to the required speed, there is no need for excessive strength. With its detachable notched structure, it will lean against the rear axle of the vehicle and push the vehicle along the road. There is no permanent connection between the vehicle and the carrier element. The carrier element will accelerate from stationary state to 64 km/h (=17.78 m/s) with constant acceleration and will get stuck in the obstacle and stop 3 meters away. Since the vehicle will not get stuck on the obstacle, it will continue at constant speed and hit the wall. According to ISO 3784 standard, speed measurement should be done 0.2 seconds before with 1% accuracy. 0.2*17.78 = 3.556 meters before the vehicle can be released. For this reason, the obstacle that will separate the carrier element from the vehicle is placed 3 meters away from the wall.

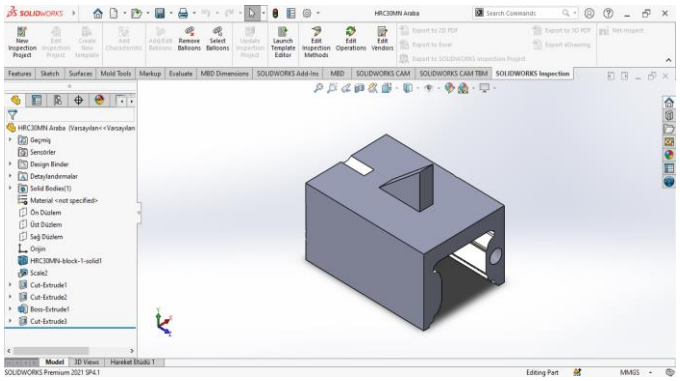

Figure 1 Rail carrier element design

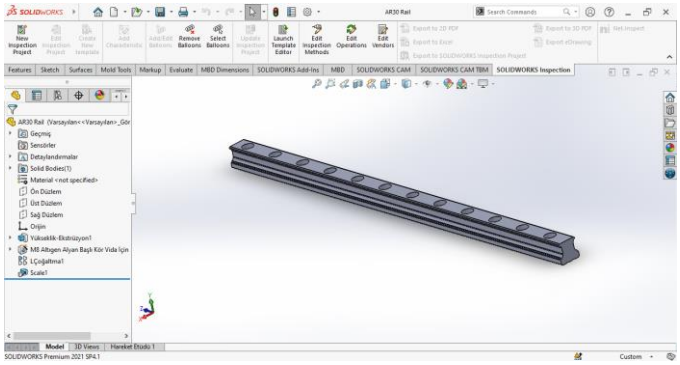

Figure 2 Rail design

B. Wall And Floor Design

The floor on which the test will be carried out must be dry and level. The wall to be hit by the vehicle must be greater than 70000 kg (see ISO 3560-4.2). We will choose a steel reinforced concrete block for our test system. Assuming that 1 m^3 of densely reinforced concrete weighs about 2500 kg, 28 m^3 of concrete will provide sufficient weight. It is sufficient for the wall to have a height of 3 meters, a depth of 2 meters and a width of ≥5 meters. The wall width is taken as 5 meters. The wall is buried half a meter below the ground level to prevent vibration and deformation.

Depending on the power of the electric motor and the mass of the vehicle, a sufficient length can be selected for the vehicle to reach the desired speed. The floor length is 60 meters. The rail length is selected as 50 meters. This selection is based on the 75 kW power of both engines, the cylinder shaft diameter to which the engine is connected and the vehicle weight.

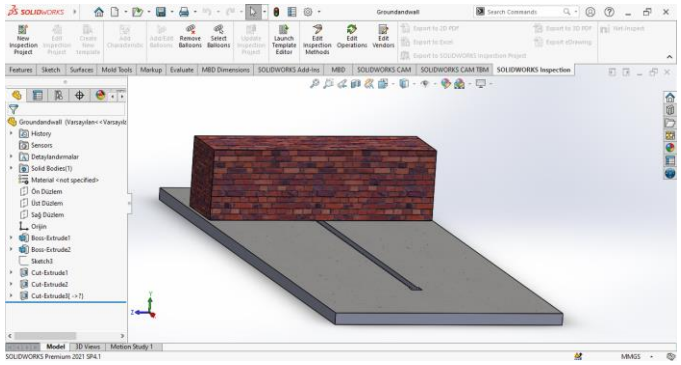

Figure 3 Wall and floor design

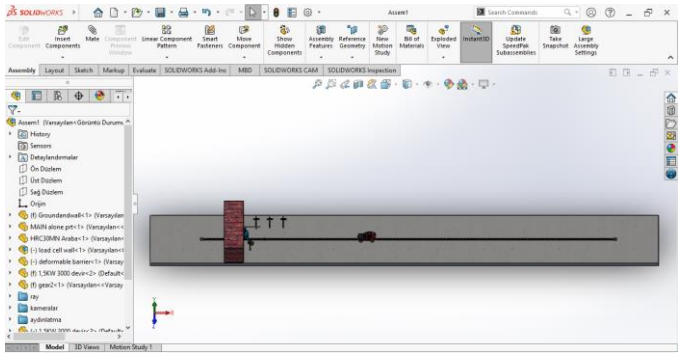

Figure 4 Vehicle acceleration distance ~50 meters

C. Barrier Design

Since the barrier that the vehicle will hit will be produced as specified in the standards, we do not have the possibility of modification.

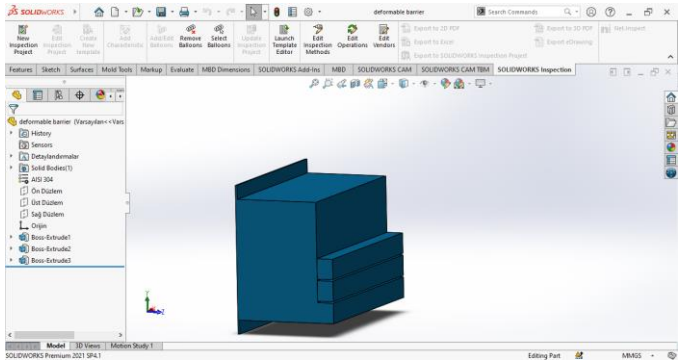

Figure 5 Barrier design (dimensioned according to standards)

D. Electric Motor Selection

The electric motor must have sufficient power and torque to accelerate the 2.8 tons weight from 0 km/h to 64 km/h. In the calculations made, it was seen that a high-volume industrial electric motor of 500 kW and above is required for the vehicle to reach sufficient speed at short distances (~30m).

As an alternative to this, considering the lack of space limitations, a 75 kW motor can be selected and the acceleration distance can be preferred as 100 meters. As a third alternative, the distance can be halved by synchronized operation of 2 electric motors. With 2 75 kW electric motors, the vehicle can reach a speed of 90 km/h at a distance of 50 meters. (64 km/h is sufficient for the designed test.) The reason for choosing the 3rd alternative is to provide advantages in terms of both high cost and maintenance and repair problems.

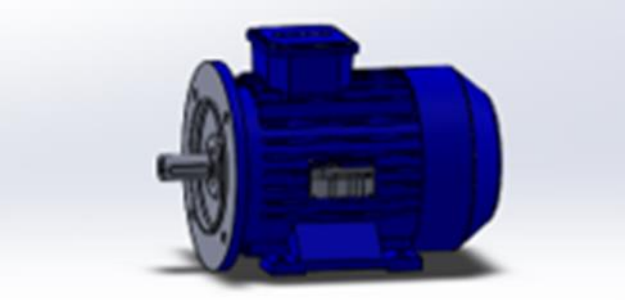

Figure 6 Electric motor design

E. Camera System

In order to obtain crash video recordings, we need a video recorder capable of taking a minimum of 500 frames per second. According to the test procedure, we need 6 high speed cameras, 4 from outside and 2 from inside. The camera angles are positioned in the appropriate position as shown in the figure 7.

Camera No.	Camera Angle
1	Movement of dummy in driver's seat and collapse of vehicle
2	Movement and collapse of vehicle (right side)
3	Movement of dummy in front seat Movement
4	of vehicle and collision position
5,6	Movement of dummy in rear seat (onboard)

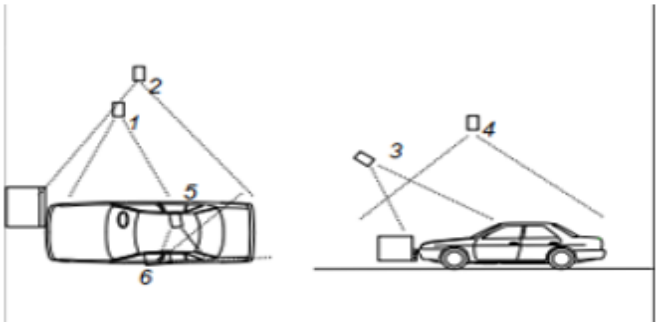

Figure 7 High-Speed camera covering range

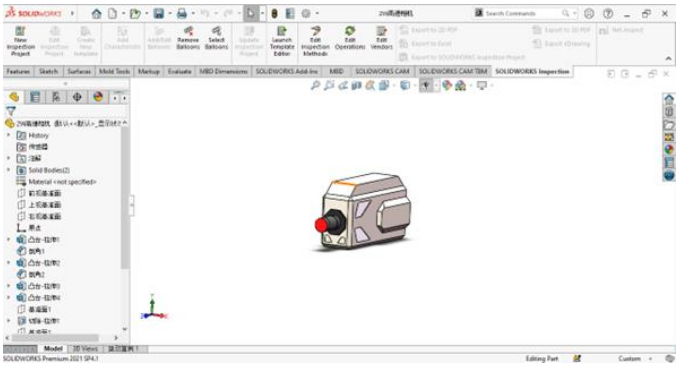

Figure 8 1000 fps Camera design

F. Load Cell Wall Design

In order to fully realize the effects of the collision, it is sufficient to use a 3-axis 400 kN capacity load cell. In classical mechanics, momentum or momentum (plural momenta; SI unit kg.m/s or equivalently, N.s) is the product of the mass and velocity of an object; (p = mv). If we take the safety coefficient ≥2, it can be seen that a 400 kN capacity load cell has a sufficient capacity. Two types are commonly used for the load cell wall, 8*8 or 8*16. In our design, we preferred 8*8 load cell wall design due to its sufficient length.

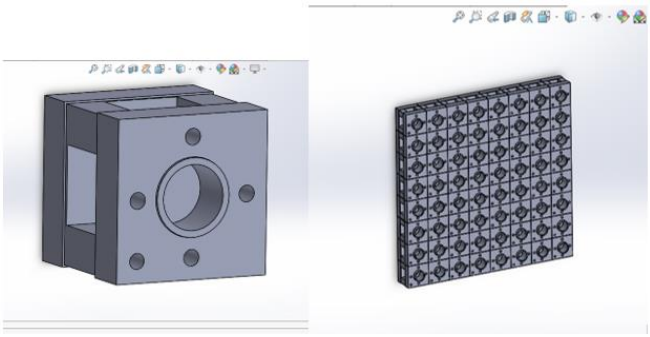

Figure 9 Load cell wall design

G. Other Equipment

Sensors on the test dummy are not mentioned. Lighting devices and other necessary sensors can be found in the related report [2].

The assembled version of the entire crash test system is shown in Figure 10.

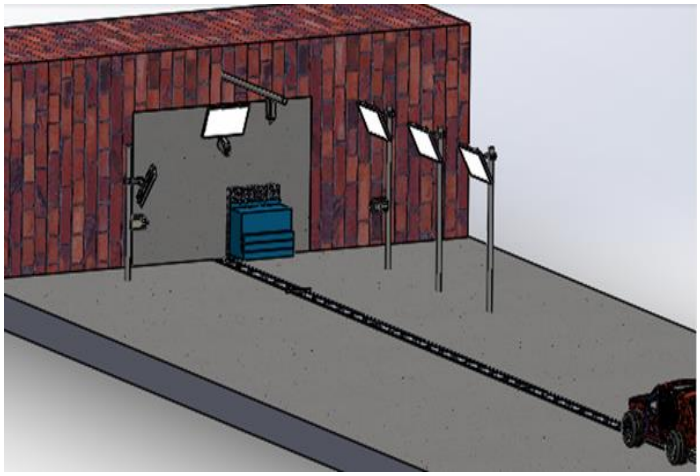

Figure 10 System view

III. CONCLUSION

In this study, important information and evaluations are presented about the importance and application of crash and impact tests, test procedures used worldwide, use and calibration of force measurement devices, and design and feasibility of the crash test system.

Crash and crash tests are one of the most important safety evaluation methods in the automobile industry. These tests are used to measure the safety performance of vehicles and design safer vehicles. In particular, international programs such as Euro NCAP (New Car Assessment Program) aim to increase consumer safety by evaluating the crash results of vehicles according to certain criteria. In this direction, Turkey NCAP requirement is in Turkey's automotive industry.

It is important in terms of contributing to the goals of locality, nationality, and independence. Supporting domestic automobile production and conducting safety assessments with domestic resources reduces foreign dependency and ensures the development of domestic technology capabilities. Additionally, it is important to evaluate and inform the safety performance of vehicles in terms of traffic safety and consumer awareness. Establishing a local and national NCAP organization in Turkey promotes vehicle safety, reduces risks from traffic accidents, and encourages automobile manufacturers to improve. Most importantly, it strengthens our self-sufficiency, that is, our independence.

REFERENCES

[1] Aydemir B., Kuvvet Kalibrasyon Rehberi, TÜBİTAK UME, September 2021
[2] Doğan, A., Araç çarpişma test sistemi tasarımı ve fizibilite etudu, TÜBİTAK UME, August 2023
[3] www.dekra.com/en/crash-testing/
[4] www.euroncap.com/en/for-engineers/protocols/general/
[5] www.iihs.org/
[6] www.iso.org/standards.html
[7] www.globalncap.org/resources
[8] www.ancap.com.au
[9] www.latinncap.com/en
[10] www.nasva.go.jp/mamoru/en
[11] www.ncap-cn.com/en
[12] www.ume.tubitak.gov.tr/en
[13] www.kistler.com/INT/en/
[14] www.messring.de/en/products/passive-safety/mwall/
[15] grabcad.com/
[16] www.nasva.go.jp/mamoru/en/download/H30-01_en.pdf
[17] www.nasva.go.jp/mamoru/en/download/H30-02_en.pdf
[18] www.nasva.go.jp/mamoru/en/download/H31-03_en.pdf
[19] Woon Kim, Impact of Speeds on Drivers and Vehicles – Results from Crash Tests

The Feasibility Study of a Vehicle Crash System

A. DOGAN [1] and B. AYDEMIR [2]

[1] Marmara University, Engineering Faculty, Mechanical Eng., Istanbul/TURKIYE,
arifdogan@marrun.edu.tr, ORCID: 0009-0006-2992-5754

[2] TUBITAK UME, Gebze/Kocaeli/TURKIYE,
bulent.aydemir@tubitak.gov.tr, ORCID: 0000-0001-6848-2681

***Abstract* -Crash tests are tests that evaluate how cars perform in various crash scenarios. These tests are carried out to determine the safety level of vehicles and to ensure the protection of drivers and passengers in a possible accident. A large number of crash systems have been developed according to the axis of collision or the types of colliding elements (vehicle-vehicle, vehicle-pedestrian, vehicle-barrier, etc.). The most basic type of crash test is called frontal crash test. This test simulates a collision of the front of the vehicle with a fixed barrier or another vehicle. In this study, the current market analysis of the vehicle crash test system prepared in accordance with the relevant standards and test procedures was carried out and a cost-oriented feasibility study was prepared.**

***Keywords* – Feasibility study, Crash test system NCAP, Frontal crash**

I. Introduction

TODAY, the damages and losses caused by road traffic accidents are a major concern not only for individuals but also for the overall safety and economic stability of society. With the rapidly increasing number of vehicles, the issue of traffic safety has become more important than ever. In this context, vehicle crash test systems have formed the basis of the modern automotive industry's efforts to set and improve safety standards.

The history of the vehicle crash test system reflects the development of the automotive industry and the evolution of the understanding of safety. The tests, which started with simple observation and experimental approaches in the early periods (1930-1970), have become scientifically based over time. After 1970, the formation of NCAP organizations pioneered the standard crash tests and the sharing of the results with the public. While tests have become more sophisticated with the advancement of technology, environmentally friendly design has also gained importance.

We wanted to demonstrate the feasibility and cost of the vehicle crash test system, which we had previously designed in accordance with the relevant standards and adaptable to different test procedures.

II. Vehicle Crash Test System Requirements

A. Load cells

The crash wall and standards, barrier height design and material specifications (UNECE Regulation No: 94*) are specified, as well as the frontal crash test protocol (offset-deformable-barrier-frontal-impact-test-protocol-v711*).

The average cost of the force sensor Kistler 9661B40 wall sensor or Kistler 9350B1Q01 X 64 ADET load cell to be used in the test system is approximately 1 million euro. A similar system is available at Messring. In addition to having a similar price, Messring's moving wall can be preferred due to its various functions.

M=WALL Full Frontal 2.000mm x 1.000	**814.000,00 €**
consisting of	
M=WALL - Load Cells - Mounting Plate - Backplane	
Peripheral Equipment - Gateways - Cables - Switch cabinet - Contol PC - Software	

Moveable Block	**1.036.000,00 €**

Figure 1 Messring movable block price

Figure 2 Messring movable block

Figure 3 Messring loadcell wall

B. Dummy

Dummy varies according to many standards and includes a wide variety of sensor types, so a company that produces in accordance with the specified standard will be selected without going into detail.

- Hybrid III Dummy Male 50th Percentile (Standard ATD 78051-218-H)
- Hybrid III Dummy Female 5th Percentile

(Code of Federal Regulations) Title 49, Part 572, subpart O)

№	Code	Description	Q'ty (Set)	Unit price(EURO) EX work Japan	Total Amount (EURO)
		ATD for Measurement Apparatus Anthropomorphic Test Devices HS-CODE(9031-90)			
1	78051-218T	Hybrid-III 50th Percentile, Non-Instrumented, Tested and Certified	1	EUR 53,180.00	EUR 53,180.00
2	PIII 50-218T	Hybrid-III 50th Percentile Pedestrian, Non-Instrumented, Tested and Certified	1	EUR 51,800.00	EUR 51,800.00
		For inquiries, please contact us at Email: info@jasti-europe.eu **And for inquiries, please provide us with your information, the type of dummy you need (are you requesting a sitting dummy[No1] or a standing dummy[No2]?), and when you need season[Year, month].**			
		EXW (Numazu, Shizuoka / Japan)			
		Total:			

Terms and Conditions:
1) Validity : This quotation is valid only for 30 days.
2) Payment : 100% full payment against your Purchase Order by T/T remittance
3) Duty & Taxes : All to be borne by Tübitak UME
4) Other costs : Freight, Insurance and transportation are extras. (ExWorks at Numazu, Japan)
5) Delivery :one dummy is 4 - 4.5 months after receipt after confirmation

JASTI CO., LTD.
K Futami

Figure 4 Dummy price

C. Barrier

Standard barrier price.

Barriers		Barrier 30°	42.400,00 €
ODB	14.900,00 €	Bumper Barrier RCAR	11.700,00 €
Small overlap barrier	87.700,00 €	Barrier 10° for RCAR frontal impact	15.100,00 €
Pole Barrier 10" diameter, 2.3m height	16.000,00 €	Underride Barrier	12.500,00 €

Figure 5 Barrier prices

D. Electric Motor Price

In the calculations made, it was seen that a high-volume industrial electric motor of 500 kW and above is required for the vehicle to reach sufficient speed at short distances (~30m). As an alternative to this, considering that we have no space limitations, the acceleration distance is preferred as 100 meters and a lower electric motor is preferred. Another alternative is to halve the distance by synchronized operation of 2 electric motors. With 2 75 kW electric motors, the vehicle can reach a speed of 90 km/h at a distance of 50 meters. (64 km/h is sufficient for the designed test.) The reason for choosing the 3rd alternative is to provide advantages in terms of both high cost and maintenance and repair problems. Instead of a very large engine volume and long distance cost, a 75kW electric motor to be placed at both ends can accelerate the carrier system to a sufficient speed at a length of about 45 meters. The preferred motor is Gamak 7kW 1500D/D 380V three-phase electric motor.

Figure 6 Electric motor price

E. Camera System

For camera selection, PHOTRON brand FASTCAM MH6 model, which has twice the number of second shots better than the ISO standard and is produced in accordance with ISO 12,500 monochrome and ISO 5,000 color standards, was selected. Nova R5 and R2 were selected outside the vehicle.

The desired number of shots per second is 500 fps, 10ms.

Specifications of the selected camera 1000 fps (at maximum resolution), 4ms.

The FASTCAM MH6

Specifically developed for on-board automotive safety testing and defense applications, the FASTCAM. MH6 can capture high-speed images in severely space constrained locations during impact.

FASTCAM NOVA R2
High-speed high-resolution imaging system. Providing 4 Megapixel image resolution (2048x2048 pixels) at frame rates up to 1,440fps and Full HD resolution (1920x1080 pixels) at 2,560fps. System comprises: 2048x2048 pixel CMOS sensor with 12bit output and Variable Region of Interest. Supplied as standard with automatic mechanical shutter for image calibration and interchangeable 'C' and Nikon lens fitting (compatible with both 'F' and 'G' type lenses), Canon EF lens adapter available as an option. 8GB recording memory (16GB, 32GB, 64GB or 128GB options), 1/10 GigaBit Ethernet. Optional FASTDrive for rapid download and archive of recording memory to large capacity SSD Media. 100-240VAC power adapter. Photron FASTCAM Viewer v4 system control software and support for MATLAB and LabVIEW. No video output

107238 FASTCAM NOVA R2 type 100K-C-64GB-NV € 47,400.00

Figure 7 Outside High- Speed camera features and price

Figure 8 Insight Camera picture

F. Other Equipment

- Light and Lighting Systems
- Thermometer Min: 0.1 with decimal notation
- Humidity meter Min: 1% accuracy
- Three Dimensional Measurement Device: It must have a minimum accuracy of 0.5 mm/m.

III. TOTAL COST CALCULATION

The prices of the required products are valid for July 2023 by contacting the relevant companies in the market. Cost is very crudely written and is for forecasting purposes only.

Table 1 Total Cost Estimation

Product	Piece	Price	Total cost
Fastcam Nova R5	1	~70.000E	70.000E
Fastcam Nova R2	4	~50,000E	200.000E
Fastcam M6	1	~130.000E	130.000E
Hybrid III Dummy Female 5th Percentile (with instrumented)	1	~100.000E	~100.000E
Hybrid III Dummy Male 50th Percentile (with instrumented)	1	~250.000E	~250.000E
Data Acquisition System	1	~10,000E	~10,000E
Cysts 9661B40 wall	1	~1,000,000E	~1,000,000E
Barriers(7 types)*	3	~200.000E	200.000E
Others Equipment and Sensors: Accelerometer, temperature, humidity meter, lighting … etc.	#	~30.000E	60.000E
Electric Motor and Rail System	1	~21.000E	21.000E
Test evaluation software. (x-crash)	1	~5.000E	~5.000E
		Grand Total Cost =>	1,646,000 Euros

*Disposable products

In the light of the researches, the estimated cost of the designed test system has been calculated as approximately 1 million 646 thousand Euros. This amount corresponds to 48 million 752 thousand TL in Turkish Lira. (In this calculation, the value of 1 Euro has been accepted as 29.68 Turkish Liras as of August 9, 2023.) The test system needs a minimum area of 800 square meters in order to be operational. However, considering that there should be room for the personnel who will perform the test in a similar area, it is foreseen that a total area of approximately 1600 square meters will be required. When the purchases and other operational costs are combined, it is thought that a cost of approximately 200 million Turkish Liras (TL) may arise for the test system facility. A total cost of 250 million TL can be envisaged for the test system and center. This cost includes several factors required for the system to operate effectively and produce high quality results.

IV. CONCLUSION

In this study, the necessary parts for vehicle crash test systems were selected by the desired features. Cost research of the chosen parts was carried out. As a result, a feasibility study was conducted to establish such a test system in our country.

In light of the research, the estimated cost of the designed test system is calculated approximately 1 million 646 thousand Euros. This amount corresponds to 48 million 752 thousand TL in Turkish Lira. (In this calculation, the value of 1 Euro is accepted as 29.68 Turkish Lira as of August 9, 2023.) The test system requires a minimum area of 800 square meters to be operational. However, considering that space needs to be made available for the personnel who will perform the test in a similar area, it is estimated that a total area of approximately 1600 square meters will be required. If we make an approximate evaluation, of the test center's personnel salaries, facility

installation, and equipment when purchases and other operational costs are combined, it is thought that a cost of approximately 200 million Turkish Liras may arise for the test system facility. A total cost of 250 million ₺ can be predicted for the test system and center. This cost includes various factors required for the system to operate effectively and produce high-quality results.

REFERENCES

[1] Doğan, A., Araç çarpişma test sistemi tasarımı ve fizibilite etudu, TÜBİTAK UME, August 2023
[2] www.dekra.com/en/crash-testing/
[3] www.euroncap.com/en/for-engineers/protocols/general/
[4] www.iihs.org/
[5] www.iso.org/standards.html
[6] www.globalncap.org/resources
[7] www.ancap.com.au
[8] www.latinncap.com/en
[9] www.nasva.go.jp/mamoru/en
[10] www.ncap-cn.com/en
[11] www.ume.tubitak.gov.tr/en
[12] www.aseancap.org
[13] https://webdosya.kosgeb.gov.tr/Content/Upload/Dosya/strateji-urun/
[14] www.kistler.com/INT/en/
[15] www.messring.de/en/products/passive-safety/mwall/
[16] https://grabcad.com/
[17] www.nasva.go.jp/mamoru/en/download/H30-01_en.pdf
[18] www.nasva.go.jp/mamoru/en/download/H30-02_en.pdf
[19] www.nasva.go.jp/mamoru/en/download/H31-03_en.pdf
[20] Woon Kim, Impact of Speeds on Drivers and Vehicles – Results from Crash Tests

Investigation of The Impact Behavior of Structural Steel Coated with Thermal Flame Spraying Method

BUKET ÇAKAR AÇIKGÖZ [1] and ŞERAFETTİN EKİNCİ[2]

[1] Department of Mechanical Engineering, Institute of Sciences, Selçuk University, Konya, Turkey
[2] Department of Mechanical Engineering, Faculty of Technology, Selçuk University, Konya, Turkey

Abstract **- Thermal spraying, also known as flame spraying or wire flame spraying, is a coating method applied to various metals with the aim of enhancing oxidation and corrosion resistance by creating a layer on the material surface. In this research, sandblasting was performed as a surface preparation technique to clean and prepare the material surface before coating. Coating processes were carried out using Zinc/Aluminum 85/15 wire on S355 steel at three different spraying distances and thicknesses. Low-velocity impact tests were conducted to quantitatively assess the impact resistance of the coated steel material. These tests involve subjecting the material to controlled low-velocity impacts and measuring its response, including deformation. During the low-velocity impact test, a coating defect known as a coating crack was observed in one of the coated samples, and the causes of this crack were investigated. As a result, it is presumed that one of the substrate materials had surface imperfections such as burrs prior to the coating process.**

Keywords **- Wire Flame Spray, Zinc/Aluminum 85/15 Wire, Drop Weight Test, Low Speed Impact, Coating Crack**

I. INTRODUCTION

AS technology rapidly advances, the performance of untreated metallic materials has become insufficient to meet the demands of progressively more challenging conditions [1]. ZnAl coatings, which consist of a combination of zinc and aluminum, function as protective coatings in diverse settings to safeguard components against corrosion. They are particularly prevalent in offshore applications, where the components face harsh environmental conditions, including exposure to saltwater, powerful winds, tidal movements, and ocean waves [2]. ZnAl coatings can also be used in the metallization of polymeric materials [3].

ZnAl coatings, which can be applied to various materials, have been applied to S355 (structural steel in this investigation. S355 (St 52) steel is used in automotive equipment, machine components, shafts, and many parts of manufacturing. It has a low carbon content [4].

Surface preparation is performed through sandblasting processes prior to thermal coatings [5]. Subsequent to the surface being readied, thermal spray coatings are accomplished by propelling particles that are either molten or partially melted, using high levels of heat and/or kinetic energy, onto a designated substrate material [6]. Coated samples can be examined using an optical microscope or a scanning electron microscope (SEM) [7]. These can be used for the analysis of the fracture morphologies of coated and uncoated samples [8]. Damage resulting from an impact in metals and metal alloys takes place on the surface that comes into contact with the impact [9].

The low-velocity impact test closely approximates real impact situations [10]. Numerous research efforts have explored tests and measurement techniques for assessing a material's resistance to impact. However, the prevailing literature suggests that the drop-weight test is the most commonly used method [11]. It is stated that most of the previous research on Zn-Al or Mg coatings in the literature primarily focuses on corrosion resistance and production techniques rather than the mechanical properties, cracking behavior, and formability performance of these coatings. There are limited studies that investigate impact and cracking mechanisms of the coatings. Various techniques can be employed to examine coating cracks, including microstructure and OIM analysis, nano indentation to determine local micro-mechanical properties, micro-digital image correlation (μ-DIC), and finite element analysis (FEA) [12].

II. MATERIALS AND METHODS

A. The Substrate Material for The Coating

S355 steel typically contains about 0.22% carbon, but the carbon content may vary depending on different manufacturers or specifications. S355 steel, in addition to carbon, also contains various other chemical elements. It is a structural steel class defined by European Standards (EN) and widely used in construction, mechanical engineering, transportation, and industrial applications. It has high tensile strength (355 MPa), yield strength (355 MPa), and impact resistance. Its chemical composition includes various elements, and it is suitable for welding. It does not require heat treatment, providing dimensional stability. S355 steel is preferred in many different applications due to its characteristics such as durability, weld ability, and impact resistance [13,14].

B. Coating Wire and Flame Spray Gun

For this investigation, a coating wire alloyed with 15% aluminum and 85% zinc was preferred. The diameter of the wire used in the study is 3.17 mm. The most crucial component

of the flame spraying device, the flame spray gun, involves the feeding of the wire into the nozzle, where it is melted and sprayed. For this investigation, an Amitech Henry 17E manual metal spray gun was used. In Figure 1, the wire flame spray process is schematically depicted.

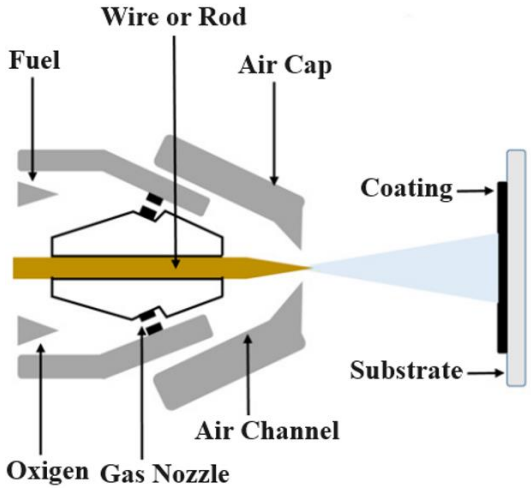

Figure 1: Wire Flame Spray [15]

An flame spray system fundamentally consists of gas supply, air supply, gas hoses, oxygen, fuel and air gas regulators, rotameters for gas flow control, a spray gun, and either powder or wire feeders [16].

C. Surface Preparation Before Coating

For the coating to adhere properly on the sprayed surface, it's essential to have a clean, rust-free, and roughened surface. Any remaining layer can act as a barrier between the coating and the base material. Effective surface preparation is key to establishing strong bonds. Techniques like creating rough surfaces, sandblasting, and grinding are commonly used for this purpose [17]. Adhesion properties on smooth and rough surfaces are depicted in Figure 2.

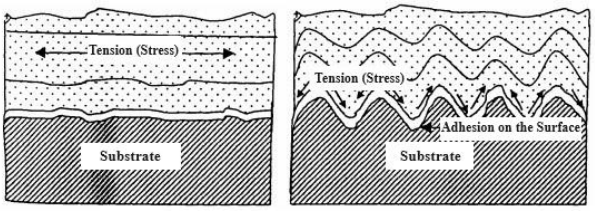

Figure 2: Adhesion Properties on Smooth and Rough Surfaces [18]

Sandblasting is the process of spraying various-sized materials onto the workpiece, which will erode the workpiece. The workpiece surface should be cleaned in a way that doesn't leave any residue. After the blasting process is completed, coating should commence as soon as possible, taking care to prevent the part from becoming dirty (preferably within 1-2 hours). This is because any dirt or oxide layer that forms on the surface of the part will hinder adhesion. When coated workpieces are rapidly cooled after the coating process, cracks can form due to material expansion and rapid cooling on the surface. Therefore, the parts should be allowed to cool slowly. Cracking also depends on the thickness of the coating layer and the coating material [18].

Obtaining a clean surface before any subsequent process or coating applied on the substrate material is crucial. In all types of metal coatings, it is largely true that early failure issues arise from incorrect or inadequate surface preparation [19].

D. Wire Flame Spray Coating Process

The cleaned steel samples, prepared by the sandblasting process, were coated within a maximum of 3 hours after the sandblasting was completed. After the samples were brought to the coating chamber, connections were made from the flame spraying machine to the spray gun, which included propane, oxygen, coating wire, and compressed air.

The ZnAl8515 coating wire to be sprayed was fed through the nozzle of the spray gun, and the coating material, which melted by a mixture of propane and oxygen gas as it passed through the nozzle, was atomized with the assistance of compressed air and deposited on the surface of the steel samples. During the coating process, the coating thickness was continuously monitored using a coating thickness measurement device, resulting in samples coated with average thicknesses of 80, 160, and 240 microns.

The coating thickness was determined by measuring five different points on the surface of the sample, both at the corners and in the middle. The average of these measurement values was considered as the coating thickness. Thickness measurements were continued until the desired thickness was achieved.

The coating process was repeated at application distances of 12 cm and 24 cm. Throughout the coating process, the spray angle was maintained at 70-80 °C, while the oxygen and propane pressures were in the range of 3-5 atm, and the air pressure was kept within the range of 4-6 bar.

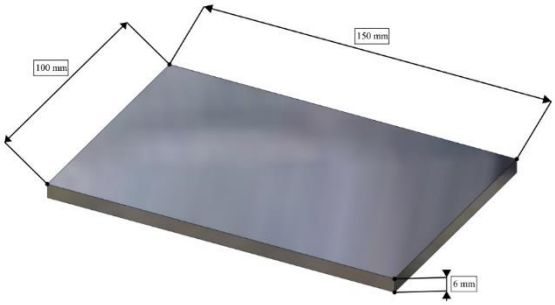

Figure 3: S355 Sample with Dimensions of 100x150x6 mm.

E. Low-Velocity Impact Test

Low-velocity impact tests were conducted in accordance with ASTM D7136 standard. The low-velocity impact test is based on the examination of the damage occurring on the sample due to the free fall of a certain weight part on the sample. Samples were prepared according to the dimensions given in Figure 3, as per ASTM D7136 standard.

Low speed impact tests have the ability to mimic real-world damage scenarios by closely replicating the impact loads that materials are subjected to. This testing method is based on the concept of dropping a specific weight onto the test specimen. In this particular research, a vertical weight drop impact testing apparatus located at Konya Technical University was

employed. The device is capable of conducting tests at an energy level of 5 J and an impact speed of 1.2549 m/s. It is equipped with a spherical tip measuring 20.5 mm in diameter and has a weight of 6.35 kg. Notably, the data for analysis only includes the impact values recorded after the first collision. The outcome of the impact tests resulted in the generation of graphs illustrating the changes in force over time, force relative to displacement, and the relationship between energy and time. In Table 1, the specimens used in impact tests are listed.

Table 1: Test Samples

Sample Name	Spraying Distance	Coating Thickness
S1	Uncoated Sample	
S2	12 cm	80 µ
S3	12 cm	160 µ
S4	12 cm	240 µ
S5	24 cm	80 µ
S6	24 cm	160 µ
S7	24 cm	240 µ

III. RESULTS

According to the force-displacement graphs, a closed curve graph was formed based on penetration in 6 coated and 1 uncoated steel plates as well.

In the force-displacement graphs, it is seen that the impact strength of all samples coated with different parameters does not have a negative effect compared to the uncoated steel sample.

The flame spray coating with ZnAl8515 wire is primarily applied for the purpose of corrosion protection. However, the decrease that may occur in the impact resistance of steel as a result of coating is often not desired. Table 2 lists the peak displacement values for all samples.

When the graphs are examined in terms of impact resistance (Figure 4-5-6-7-8-9-10), there is an average difference of 0.0002 mm between the peak displacement values. This peak displacement difference proves that the coating does not have a negative impact on impact resistance. Since ZnAl8515 coatings, which are generally used to protect against corrosion, do not have a negative effect on impact resistance, the flame spray coating method with ZnAl8515 coating wire can easily be preferred in places where impact resistance is required.

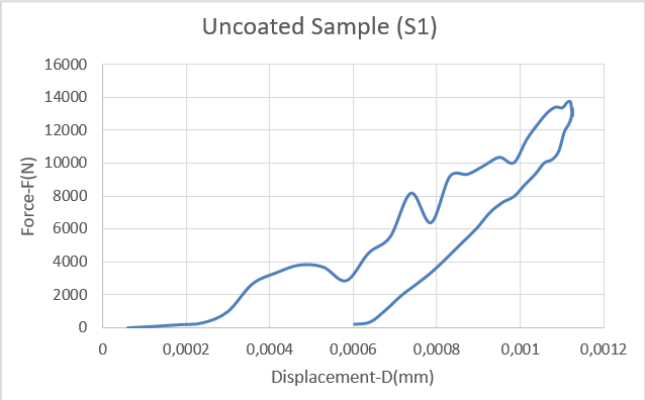

Figure 4: Sample S1 Force-Displacement Graph

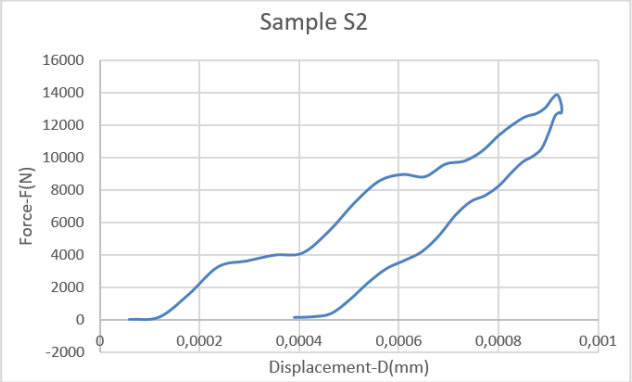

Figure 5: Sample S2 Force-Displacement Graph

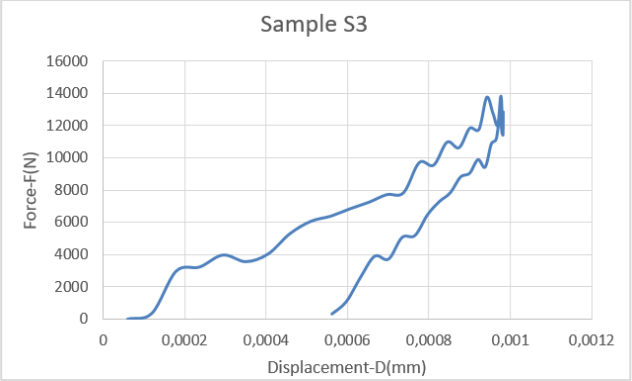

Figure 6: Sample S3 Force-Displacement Graph

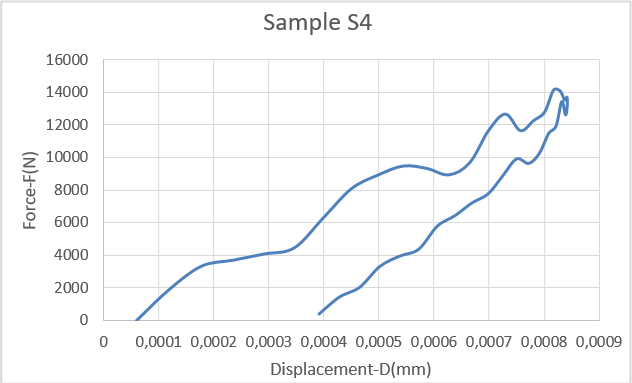

Figure 7: Sample S4 Force-Displacement Graph

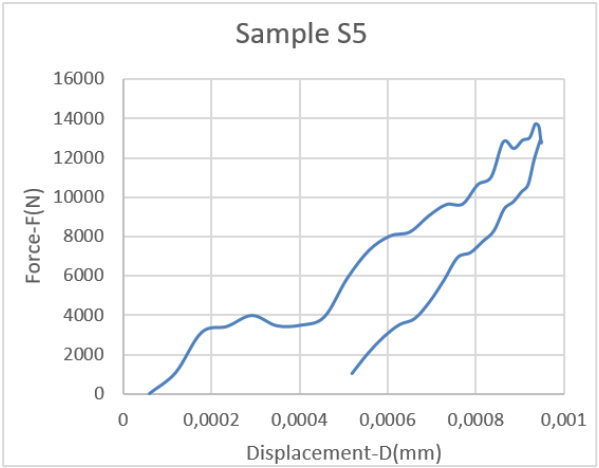

Figure 8: Sample S5 Force-Displacement Graph

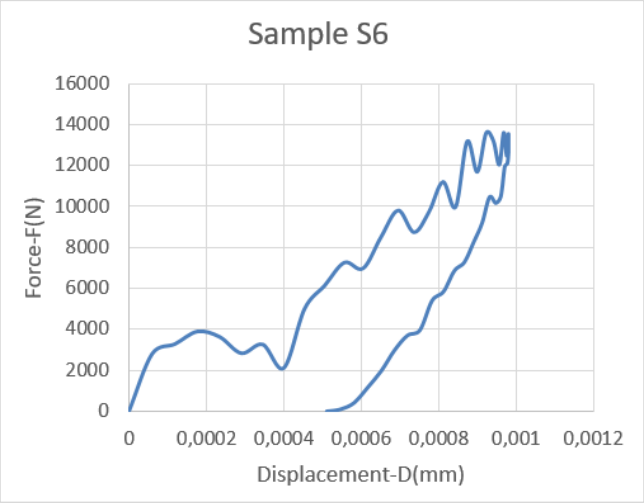

Figure 9: Sample S6 Force-Displacement Graph

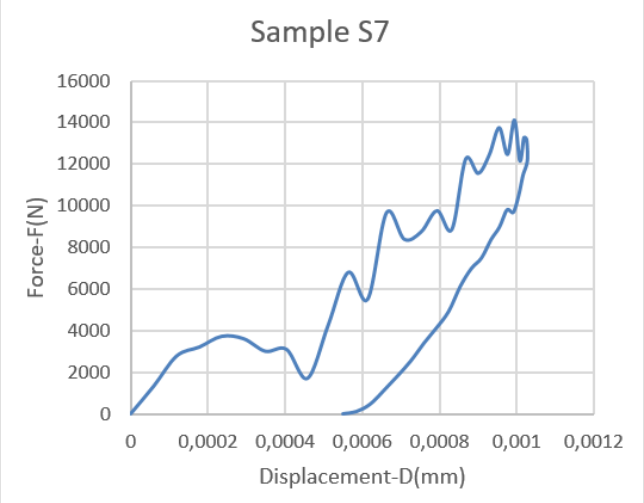

Figure 10: Sample S7 Force-Displacement Graph

Table 2: Impact Test Response According to Different Samples

Sample	Mass (kg)	Velocity (m/s)	Peak Force (N)	Time (s)	Peak Displacement (mm)
S1	5,6	1,5	13703,6	0,0019	0,0011
S2	5,6	1,5	13872,4	0,0018	0,0009
S3	5,6	1,5	13830,9	0,0017	0,0009
S4	5,6	1,5	14149,1	0,0016	0,0008
S5	5,6	1,5	13711,9	0,0017	0,0009
S6	5,6	1,5	13623,4	0,0018	0,0009
S7	5,6	1,5	14132,5	0,0018	0,001

In addition, during the low-speed impact test, an average straight crack of approximately 1cm in size occurred in sample S6, coated at a 24cm spraying distance with a thickness of 160 microns. The image of the crack formed on the surface examined with a microscope is shown in Figure 11.

Figure 11: Sample S6 Force-Displacement Graph

When the causes of coating cracks are examined; It was thought that there might be a thickness difference on the cracked surface and the coating thickness was checked. It was observed that all surfaces in the cracked sample were of the same thickness.

Since the coating crack occurred in only one sample (S6), it is thought that the crack that occurred during the impact test was caused by inadequate surface cleaning. It is thought that the dust or burr remaining on the sample surface during or after the sandblasting process prevents the coating from adhering well to the surface and ultimately causes coating cracks during the impact test.

IV. References

[1] S. Özel, "Thermal spray methods used on the surface coating processes," BEU Journal of Science, vol. 2, pp. 88-97, 2013.

[2] M. Milz, A.Wirtz, M. Abdulgader, D. Biermann, W. Tillmann, and F. Walther, "Influence of twin wire arc spraying and machine hammer peening on the corrosion fatigue of ZnAl4 coatings on S355 J2C + C substrate," Procedia Structural Integrity, vol. 42, pp. 830-837, 2022.

[3] D.G.A. Diaz, R.G.V. Navarro, N.O. Godoy, A.B. Pingarrón, J.R.G. Parra, J.J.O. Florez, M.T. Barragán, I.A. Moncaleano and C.A.O. Otalora, "Flame-sprayed Zn-Al coatings on ABS without chemical surface preparation," Materials Letters, vol.280: 128574, 2020.

[4] İ. Kırık, Z. Balalan, Y. Andan, and M. Yaz, "The Cladding of St52 Steel with WC-Reinforced Powder using TIG Welding Method," International Journal of Innovative Engineering Applications, vol. 3 (1), pp. 22-26, 2019.

[5] M. Schweda, T. Beck, J. Malzbender, and L. Singheiser, "Effect of support material creep on the delamination failure of air plasma sprayed thermal barrier coatings," Surface and Coatings Technology, vol. 259, pp. 543–550, 2014.

[6] A.C. Karaoğlanlı, A. Türk, F. Üstel, "Cold Gas Dynamic Spray (CGDS) Coating Technology and Methods," Academic Platform Journal of Engineering and Smart Systems, vol. 1(1), pp. 20-27, 2013.

[7] I. A. Gorlach, "A new method for thermal spraying of Zn–Al coatings," Thin Solid Films, vol. 517(17), pp. 5270–5273, 2009.

[8] Z. Wen, and K. Dejun, "Effects of laser thermal sprayed AlNiCr coating on fatigue performances of S355 structural steel," International Journal of Fatigue, vol. 131: 105359, 2019.

[9] M. Uyaner and S. Güvensoy, "Low-Velocity Impact Simulation of Open Ended Filament Wound Composite Tubes," Selçuk University Journal of Engineering, Science and Technology, vol. 26 (2), pp.55-66, 2011.

[10] A. U. Ude, A. K. Ariffin and C. H. Azhari, "An experimental investigation on the response of woven natural silk fiber/epoxy sandwich composite panels under low velocity impact," Fibers and Polymers, vol.14(1), pp. 127-132, 2013.

[11] M. Oltulu, and M. Altun, "The Drop Weight Test Method to Determine Impact Strength of Concrete and A Review of Research," Gümüşhane University Journal of Science, vol. 8 (1), pp.155-163, 2018.
[12] M. Ahmadi, B. Salgın, B. J. Kooi and Y. Pei, "Genesis and mechanism of microstructural scale deformation and cracking in ZnAlMg coatings," Materials & Design, vol.186:108364, 2020.
[13] A.Ç. Can, Materials Information Book for Designer Engineers, eBook, 2020.
[14] Erdemir Group: Erdemir Product Catalogue, 2015, Subb3c.
[15] Modified from J.R. Davis, "Introduction to thermal spray processing," In: Handbook of Thermal Spray Technology, ASM Innternational and Thermal Spray Society, pp.3–13, 2001.
[16] J.R. Davis, Handbook of Thermal Spray Technology, Ohio: ASM International, 2004.
[17] S. Anık, E. Anık, M.Vural, Welding Technology Handbook with 1000 Questions, İstanbul:Birsel Publisher, vol.1, 1993.
[18] Modified from Sulzer Metco (US) Inc. 1995., Sulzer Metco Catalog (US) Inc. New York.
[19] H.N. Samrat, G.L. Higgins, R.S. Hullcoop, S. Turgoose and W. Bullough, "Surface Pretreatment," Reference Module in Materials Science and Materials Engineering, 2017, doi:10.1016/b978-0-12-803581-8.09232-8.

Development of an Innovative Commercial Steam Peeling System for Various Vegetable Peels

Z. KAHRAMAN[1], M. HACI[1] and O. UGUR[1]

[1] Oztiryakiler Madeni Esya San. Ve Tic. A.S, Istanbul/Turkey, zkahraman@oztiryakiler.com.tr
[1]Oztiryakiler Madeni Esya San. Ve Tic. A.S, Istanbul/Turkey, mhaci@oztiryakiler.com.tr
[1]Oztiryakiler Madeni Esya San. Ve Tic. A.S, Istanbul/Turkey, ougur@oztiryakiler.com.tr

Abstract **- The United Nations Food and Agriculture Organization (FAO) emphasized the importance of increasing productivity in the food production sector by declaring that food production should increase by 60% until 2050 with the increase in the world population. In our company's portfolio, there is only a potato peeling machine for peeling various vegetable skins, and potatoes are peeled by hitting the silicon carbide-based emery surface with the effect of centrifugation. Vegetable losses up to 20% are experienced in this peeling process. The design and development of an innovative vegetable peeling machine that provides steam peeling for commercial kitchen applications for the elimination of losses and effective peeling of various vegetables (potatoes, celery, etc.) has been carried out with R&D activities. In addition to the development of an original designed prototype in accordance with the NSF / ANSI 8 standard, a 20% improvement in sound level was achieved compared to the existing product.**

Keywords **- Commercial steam peeling system, energy efficiency, reducing food losses, machine design.**

I. INTRODUCTION

IN commercial enterprises (restaurants, shopping malls, factories, etc.) where a large number of personnel consume food, various vegetables (potatoes, celery, etc.) need to be peeled before use in meals. There are many methods for peeling vegetables and fruits [1]. In case of using large amounts of vegetables, it is not possible to peel the skins by hand. For this reason, many different technological methods (infrared, ohmic, ultrasound, etc.) have been developed for peeling vegetable skins [1-25]. Some of these methods are not economical in terms of peeling large amounts of vegetable skins, as well as high investments in terms of application for businesses. For this reason, abrasive peeling systems are widely used in commercial kitchens because they are economical. However, these systems can cause high waste rates in vegetables due to their working principle.

Our company produces only potato peeling machines (3 different models /10, 20 and 30 Kg capacity) for peeling vegetables for commercial kitchens. The working principle of these machines is based on the principle of multiplying and peeling potatoes with the centrifugal effect on the silicon carbide-based sandpaper surface. However, these machines can create high wastage rates of up to 20% due to the differences in potato sizes and the working system principle in case of high working time. In addition, depending on the frequency of use of these machines, there is a need to replace the abrasives that provide abrasive peeling of potatoes on the inner surfaces of the machine. Therefore, additional costs are caused by the customer.

In addition, in the process of peeling potatoes of different sizes, unpeeled parts may remain on the surfaces of the potatoes. Against this problem, it is necessary to re-peel the potato surfaces with a knife by the kitchen staff. In addition, the existing sanded potato peeling machines used in commercial kitchens are among the machines that reach the highest noise levels. In line with the demands for systems that provide more efficient peeling of different vegetable peels received by our company for commercial kitchens, innovative peeling system development activities were carried out.

When the systems that provide steam peeling of various vegetable peels are examined, a low-capacity (10-30 Kg) and sized product for commercial kitchens was not found. It has been determined that the steam peeling systems are very large in size and have a high capacity for fabrication production. When large vegetable peeling systems using steam are evaluated in terms of capacity and size, they are not suitable for commercial kitchen needs in terms of usability and economy.

Within the scope of peeling different vegetable skins, infrared radiation heating [2-10], Pulsed Electric Fields (PEF) [11, 12], mechanical/abrasive [13], ohmic [14], lye [15], microwave [16], ultrasound [17], enzymatic [18-20], steam [21] etc. There are studies on methods. Various studies in this field are summarized below.

Since various peeling devices used in the industrial kitchen are commercial, literature studies specific to the scope of this study could not be determined.

Zhou and his study group evaluated various peeling methods for vegetables and fruits. For vegetables and fruits, peeling methods were collected into two main groups as conventional methods (lye, hot-water, steam, infrared radiation, ohmic heating, ultrasound) and novel methods (enzymatic, CO_2 laser drilling-assisted, freeze thaw, pulsed electric field). They evaluated the differences of these peeling methods according to various types of vegetables and fruits and their properties. They emphasized that peeling losses will vary depending on the application process and food

characteristics of peeling technologies. They explained that more environmentally friendly peeling methods should be used against the methods that use too much water and chemicals in the peeling processes. Peeling methods according to various vegetables and fruits are given in Figure 1 [1].

Figure 1: Peeling technologies for various fruits and vegetables [1].

Shen and his work group reported that the infrared radiation (IR) method could be an environmentally friendly alternative peeling method compared to the traditional soda water peeling process. They stated that when the hardness of the pears varies between 22 and 31 N, the peeling performance and the most suitable conditions for infrared radiation peeling at 450°C for 62 seconds depending on the product quality. Flow chart of peeling performance with infrared radiation (IR) method is given Figure 2 [2].

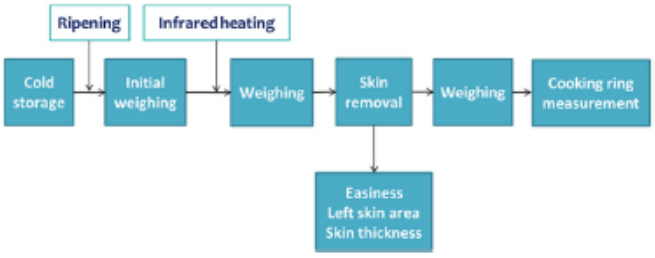

Figure 2: Flow chart of peeling performance with infrared radiation (IR) method [2].

Li and his study group evaluated the peeling of tomato skins by infrared radiation heating method. When this method is compared with traditional lye peeling, lower peeling loss and finer peeling firmer texture were obtained with infrared radiation heating method in 30 seconds and 75 seconds. The schematic representation of the system for the tomato peeling process is given in Figure 3 [4].

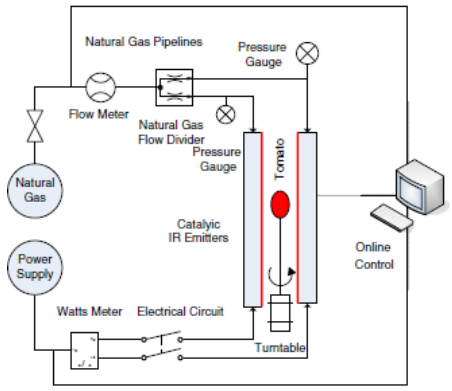

Figure 3: Schematic representation of the system for peeling tomatoes with infrared radiation heating method [4].

Li and his team studied the tomato peeling mechanism under infrared heating. They carried out studies on the theoretical and experimental development of an infrared heating system for tomato peeling. Infrared heating was applied by rotating the tomatoes for the tomato peeling mechanism. The changes on the tomato microstructure were examined using Scanning Electron Microscopy. In the infrared heating application of tomato peeling, the changes in temperature, internal pressure and tensions were investigated theoretically and experimentally [9].

Emadi and his study group examined the mechanical method of peeling pumpkin with two different abrasive surfaces. They reported that the mechanical peeling method is likely to create high peel losses but flattens the shape of products with surface irregularities. They obtained similar peeling results for concave and convex areas. They emphasized that the abrasive disc method can be used in industrial applications. They evaluated the peeling losses and the effects of concave and convex peeling of various parameters (shape, abrasion grade, angular velocity of pumpkin, angular velocity of peeler head and force) using abrasive discs. They reported that the mechanical method had more effects on peeling, especially abrasion grade, compared to other parameters (Figure 4). Three different grades (24, 46 and 60) were used in the study. They emphasized that while Grade 24 caused the most crustal removal, the other two grades showed similar features [13].

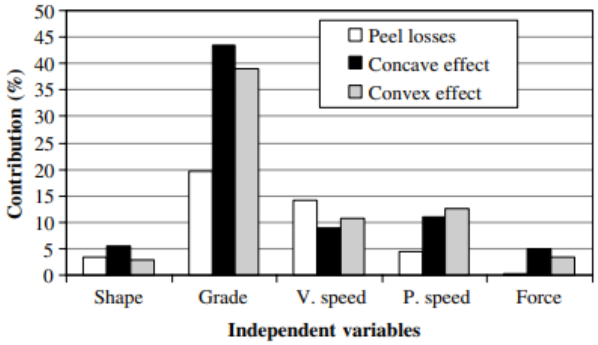

Figure 4: The effect of various independent variables on the peeling process in the use of abrasive discs [13].

Gavahian and Sastry studied the peeling of various fruits (tomato and pear) with the aid of ohmic. They reported that the Ohmic method is advantageous in terms of product quality and peeling efficiency compared to traditional peeling methods. However, they emphasized that it is important to choose the appropriate electrode material for continuous peeling application. The schematic representation of peeling tomato skin by ohmic method is given in Figure 5 [14].

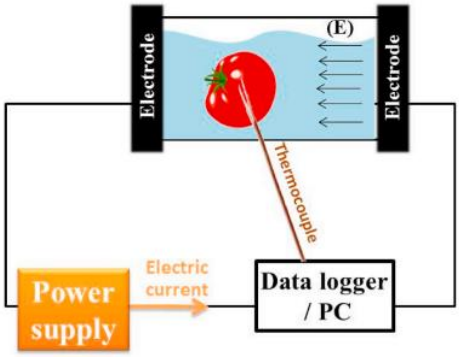

Figure 5: Schematic representation of the Ohmic peeling system. [14].

Summaries of various studies obtained within the scope of literature research on peeling potato skins with different peeling technologies are given below. However, there are no publications on the steam peeling process of vegetables in commercial kitchens.

Garrote and his team made various evaluations on the steam peeling process of potatoes and examined the effects of heating in the steam peeling process of potatoes. They reported that peeling losses and environmental pollution were reduced by the widespread use of sensitive temperature, time and pressure in electronically controlled, highly automated fabrication systems in steam peeling. At least 17 seconds in heat treatment application in steam peeling process. and reported the thermal weakening of the cell structure at 100°C. Thus, they reported that peeling can be done with the development of internal vapor pressure [21].

Ferraz and his study team conducted studies on mathematical modeling for cutting and peeling potatoes using the laser-based method. They reported that an innovative study was carried out for cutting various vegetables with the CO_2 laser. The laser system and hardware used in the study are shown schematically in Figure 6 [22].

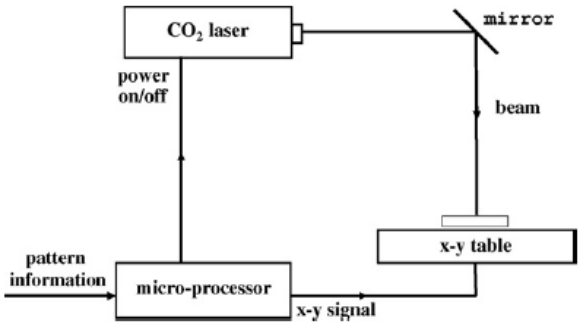

Figure 6: Schematic representation of the laser system and hardware [22].

Okonkwo and his work group evaluated the microwave assisted infrared method for beet peeling. They also made comparisons only with infrared and hot lye methods. In the infrared method, the effects of heating time and power levels on the peeling performance (ease of peeling, peeling loss, etc.) and quality characteristics (surface color change, etc.) of beet were examined. An illustration of the various peeling processes for beets is given in Figure 7 [23].

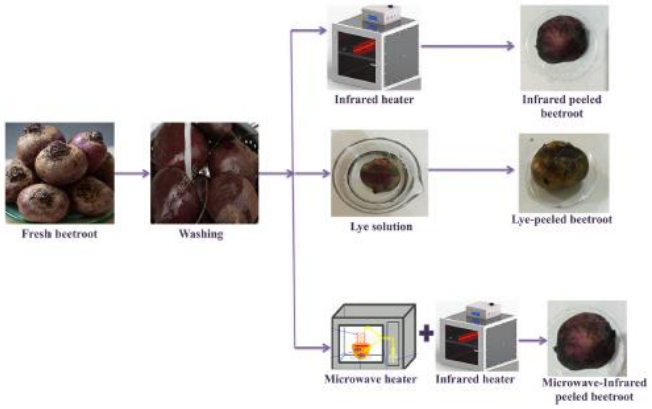

Figure 7: Various peeling methods for fresh beet root. [23].

Sampaio and his working group evaluated the reuse of potato skins in the food and pharmaceutical industries. They emphasized the importance of using potato skins as a value-added product in this regard. Various uses of potato skins in industry are shown in Figure 8 [24].

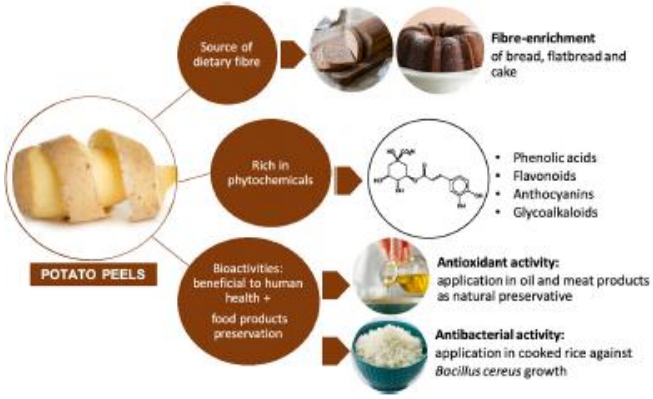

Figure 8: Various uses of potato peels in industry [24].

Zhou and his work group evaluated the use of high-humidity hot air impingement blanching (HHAIB) as an alternative method for peeling tomatoes, with the superior features of HHAIB heating technology, besides eliminating the use of chemicals and wastewater discharge. They emphasized that application temperature, relative humidity and processing time have significant effects on peeling performance. It has been reported that the most suitable process with this method is 40% relative humidity and 110 ◦C heating temperature with 75 seconds. Lower peel loss, loss of hardness and discoloration have been reported under these conditions [25].

II. METHOLOGY

Steam peeling technology was used for the first time, unlike our company's products with different capacities, which only perform abrasive potato peeling with centrifugal effect. Within the scope of this study, studies based on R&D systematics were carried out in order to reduce high peeling waste, comply with NSF / ANSI 8 standard, as well as reduce the noise level in the working environment.

III. EXPERIMENTAL PROCEDURE

After the original designs of the innovative steam peeling system prototype developed for commercial kitchens, its main body is made of stainless steel (AISI 304). A photograph of the innovative system for efficient peeling of various vegetable skins is given in Figure 9.

Figure 9: Photo of an innovative system prototype for steam peeling of various vegetable skins for commercial kitchens.

Inside view of the innovative steam peeling system (steam distribution pipe and resistances) is given Figure 10.

Figure 10: Inside view of the innovative steam peeling system (steam distribution pipe and resistances).

Electrical characteristics of the innovative steam peeling system is given Table 1.

Table 1. Electrical characteristics of the innovative steam peeling system.

Steam generator electrical power (kW)	*9*
Superheater electrical power (kW) [1st stage]	*7,5*
Superheater electrical power (kW) [2nd Stage]	*18,75*
Peeling unit Electric Motor (950 rpm 230V)	*0,37*
System Installed electrical power (kW)	*28,12*
System Electrical Supply (V AC)	*380*

In the testing and evaluation phase, peeling of potatoes and celery was investigated with the application of steam technology on the innovative prototype. The test and evaluation steps performed with potatoes is given below (Figure 11).

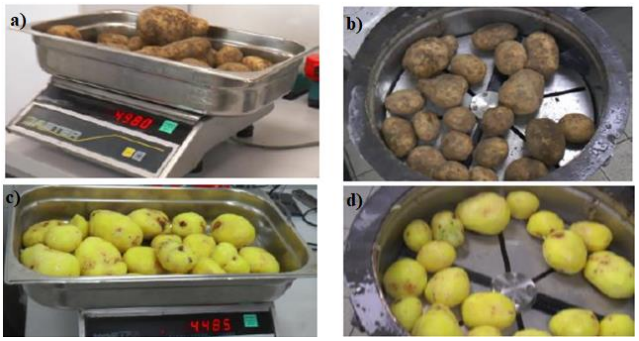

Figure 11: Photographs of potato peeling (before and after) on the innovative steam peeling system.

The potato weight, which was 4980 g at the beginning of the test, was weighed as 4485 g after the steam peeling process. On the innovative system, approximately 9.94% weight loss was determined after potato peeling. As can be seen in Fig. 12-d, all potatoes were peeled.

Evaluation of potato peeling on the innovative prototype is given Table 2.

Table 2. Evaluation of potato peeling on the innovative prototype.

Net weight before peeling (gr.)	*4980*
Net weight after peeling (gr)	*4485*
Weight difference (gr.)	*495*
Weight loss rate (%)	*9.94*

Photographs of the celery peeling process (before and after) in the innovative steam peeling system are given in Figure 12.

Figure 12 Photographs of celery peeling (before and after) on the innovative steam peeling system.

A difference of 10.75% was determined between the weight of celery at the beginning of the test (5025 gr.) and the weight after the test (4485 gr.). It was also ensured that all celery were peeled.

Evaluation of celery peeling on the innovative prototype is given Table 3.

Table 3. Evaluation of celery peeling on the innovative prototype.

Net weight before peeling (gr.)	5025
Net weight after peeling (gr)	4485
Weight difference (gr.)	540
Weight loss rate (%)	10.75

IV. Conclusion

The development of the system, which enables the efficient peeling of various vegetable peels in commercial kitchens, has been achieved through R&D activities.

With the innovative system, the waste rates related to the peeling process of the vegetable skins were reduced, as well as positive effects on the environment. At the same time, gains have been achieved in preventing food losses. The results obtained within the scope of the study are given below;

• Food losses (waste rates) in our current potato peeling machine are around 20%. In the innovative steam peeling system prototype, which provides efficient peeling of various vegetable peels for commercial kitchens, food losses are reduced to about 10% in the peeling process, with at least 50% reduction in food losses compared to the existing system.

• Our company's standard potato peeling machine, only silicon carbide-based sandpaper is used for peeling. However, in the prototype of the innovative steam peeling system, which provides efficient peeling of various vegetable peels, only the design-specific use of steam energy technology is ensured.

• An innovative steam peeling system has been developed for commercial kitchens that enables efficient peeling of at least two different vegetable skins (potato, celery, etc.).

• The designs of the innovative steam peeling system prototype were developed in accordance with the NSF/ANSI 8 standard.

• Our company's standard potato peeler (with abrasive system) operates at the highest noise level (95 dB) in commercial kitchens. With the innovative prototype, it has been achieved to reduce the working environment noise by at least 20% (at 75 dB levels).

Acknowledgment

This study was prepared from the project numbered 3160597 within the scope of TÜBİTAK-TEYDEB 1501 Industry R&D Projects Support Program. We would like to thank TÜBİTAK-TEYDEB Transport, Defense, Energy and Textile Technologies Group (USETEG) for their contribution to the project.

References

[1] Zhou, D.H., Vidyarthi, S.K., Yang, X.H., Duan, X., Liu, Z.L., Mujumdar, A.S., Xiao, H.W., Innovative Food Science and Emerging Technologies, vol. 77, 102961, 2022.
[2] Shen, Y., Khir, R., Wood, D., McHugh, T.H., Pan, Z., Innovative Food Science and Emerging Technologies, vol. 65, 102474, 2020.
[3] Wang, B., Venkitasamy, C., Zhang, F., Zhao, L., Khir, R., Pan, Z., LWT - Food Science and Technology, vol. 69, pp. 458-467, 2016.
[4] Li, X., Pan, Z., Atungulu, G.G., Zheng, X., Wood, D., Delwiche, M., McHugh, T.H., Innovative Food Science and Emerging Technologies, vol. 21, pp. 123-130, 2014.
[5] Qu, W., Liu, Y., Feng, Y., Ma, H., LWT - Food Science and Technology, vol. 163, 113542, 2022.
[6] Vidyarthi, S.K., Mashad, H.M.E., Khir, R., Zhang, R., McHugh, T.H., Pan, Z., Journal of Food Engineering, vol. 246, pp. 224-231, 2019.
[7] Kate, A.E., Sutar, P.P., Innovative Food Science & Emerging Technologies, vol. 48, pp. 111-121, 2018.
[8] Vidyarthi, S.K., Mashad, H.M.E., Khir, R., Zhang, R., Tiwari, R., Pan, Z., Biosystems Engineering, vol. 184, pp. 90-100, 2019.
[9] Li, X., Pan, Z., Atungulu, G.G., Wood, D., McHugh, T., Journal of Food Engineering, vol. 128, pp. 79–87, 2014.
[10] Mohammadi, Z., Kashaninejad, M., Ziaiifar, A.M., Ghorbani, M., LWT - Food Science and Technology, vol. 99, pp. 128-137, .2019.
[11] Koch, J., Witt, J., Lammerskitten, A., Siemer, C., Stefan Toepfl, S., Journal of Food Engineering, vol. 322, 110938, 2022.
[12] Zhang, C., Lyu, X., Arshad, R.N., Aadil, R.M., Tong, Y., Zhao, W., Yang, R., Food Chemistry, vol. 403, 134367, 2023.
[13] Gavahian, M., Sastry, S.K., Trends in Food Science & Technology, vol. 106, pp. 345-354, 2020.
[14] Emadi, B., Kosse, V., Yarlagadda, P.K.D.V., Journal of Food Engineering, vol. 79, pp. 647–656, 2007.
[15] Lavelli, V., Pompei, C., Casadei, M.A., Food Chemistry, vol. 115, pp. 1291–1298, 2009.
[16] Uthra, D., Sharma, M.P., Mendiratta, N., Materials Today: Proceedings, vol. 46, pp. 2183–2188, 2021.
[17] Gao, R., Ye, F., Lu, Z., Wang, J., Shen, X.L., Zhao, G., Ultrasonics – Sonochemistry, vol. 45, pp. 267-278, 2018.
[18] Toker, I., Bayindirli, A., LWT - Food Science and Technology, vol. 36, pp. 215-221, 2003.
[19] Barati, Z., Latif, S., Müller, J., Biocatalysis and Agricultural Biotechnology, vol. 20, 101247, 2019.
[20] Pagán, A., Conde, J., Ibarz, A., Pagán, J., Food and Bioproducts Processing, vol. 88, pp. 77-82, 2010.
[21] Garrote, R.L., Silva, E.R., Bertone, R.A., Journal of Food Engineering, vol. 45, pp. 67-76, 2000.
[22] Ferraz, A.C.O., Mittal, G.S., Bilanski, W.K., Abdullah, H.A., Biosystems, vol. 90, 3, pp. 602-613, 2007.
[23] Okonkwo, C.E., Ojediran, J.O., Baribefe, A.V., Ajao, F., Pan, Z., Arotile, A., Emmanuel, C.C., Ogomegbum, C.A., Innovative Food Science and Emerging Technologies, vol. 77, 102982, 2022.
[24] Sampaio, S.L., Petropoulos, S.A., Alexopoulos, A., Heleno, S.A., Buelga, C.S., Barros, L., Ferreira, I.C.F.R., Trends in Food Science & Technology, vol. 103, pp. 118–129, 2020.
[25] Zhou, Y.H., Sutar, P.P., Vidyarthi, S.K., Zhang, W.P., Xian-Yu, L., Li, X.Y., Bi, C., Xiao, H.W., Innovative Food Science and Emerging Technologies, vol. 77, 102987, 2022.

Development of Washer Disinfector Prototype for Various Glass Medical Products

Z. KAHRAMAN[1], M. HACI[1], S. GÜRCÜ and H.S. SOYHAN[2]

[1] Oztiryakiler Madeni Esya San. Ve Tic. A.S, Istanbul/Turkey, zkahraman@oztiryakiler.com.tr
[1]Oztiryakiler Madeni Esya San. Ve Tic. A.S, Istanbul/Turkey, mhaci@oztiryakiler.com.tr
[1]Oztiryakiler Madeni Esya San. Ve Tic. A.S, Istanbul/Turkey, sgurcu@oztiryakiler.com.tr
[2]Sakarya University, Sakarya/Turkey, hsoyhan@sakarya.edu.tr.tr

***Abstract* - In line with the constantly increasing need for all kinds of equipment in the medical field and technological developments, interest in products for the disinfection process is increasing, mainly to ensure the reuse of various products. Washer disinfector systems for cleaning and disinfecting various reused products (surgical instruments, respiratory equipment, glass tubes, etc.) are critical for efficiently using resources for medical applications (medicine, pharmacy, laboratory, etc.). Washer disinfectors are available in various models (under-counter, tunnel, etc.) with different operating systems (thermal, chemical, ultrasonic, etc.) and applications in various medical product groups. In addition, washer disinfectors stand out as technological products in a different category compared to commercial dishwashers with their structural models, purpose of use in the medical field and operating systems. Within the scope of this study, the cleaning and disinfection of medical glass materials (beakers, tubes, etc.) to be selected according to the manufacturer's declaration will be carried out in accordance with ISO 15883-1, IEC 61010-2-40, etc. It is aimed to develop an originally designed washer disinfector prototype that will meet international standards in cooperation with industry and university. While the innovative prototype was obtained, original designs were developed, and original simulation studies were carried out during the design verification phase. Different from our company's commercial dishwashers of various models and capacities (medical field application and working principle), the prototype developed through R&D activities and international standards have also been developed with disinfection and drying features, resulting in an innovative product that can be commercialized.**

***Keywords* - Washing disinfector, medical glass products, drying and cleaning technology.**

I. INTRODUCTION

Washer disinfectors stand out as medical products that provide cleaning and disinfection of various medical products that can be reused in medical enterprises [1-10]. Washer disinfectors are used to clean and disinfect loads containing various surgical instruments, anesthesia additional equipment, medical containers, instrument sets, glassware and similar materials.

Disinfection applications are generally carried out by two different methods: thermal and chemical. Thermal disinfection processes are easier to control compared to chemical applications. In addition, thermal disinfection and chemical disinfectants are used to prevent any dangers that may occur for personnel, patients and the environment. In case of use of chemical disinfectants, there is a possibility of corrosive damage to the system and the parts to be cleaned with various disinfectants [11]. In this regard, it is important to choose a disinfectant suitable for the characteristics of the parts to be cleaned. In addition, since the application and control process is more difficult and risky than the thermal disinfection process, in this context, the thermal disinfection method was preferred in the disinfection process of glass materials and it was aimed to obtain an innovative prototype that is more environmentally friendly in terms of the environment and the user.

Unlike the disinfection process carried out by washer disinfectors, sterilization should not be confused with each other. The disinfection process is defined as reducing the number of live microorganisms on a product to a predetermined level suitable for its intended use. Sterilization is the killing of microorganisms, including spores, on inanimate objects. Sterilization can be classified into three different categories (critical, semi-critical, non-critical) according to the risk group [12].

Various studies conducted in the medical field regarding washer-disinfectors are summarized below.

Deasy and his study group reported that the cleaning process after use of dental handpieces (DHP) with narrow channels is critical for medical applications. They evaluated the cleaning process of dental handpieces using a washer disinfector. Dental handpieces are reusable invasive medical devices that must be cleaned, decontaminated, lubricated, and steam sterilized after use. These instruments have a complex internal design with narrow channels whose contamination can compromise sterilization. Additionally, these tools are not designed for routine disassembly, cleaning/decontamination. They evaluated the direct effectiveness of the washer-disinfector in reducing microbial contamination, stating that there are very few studies on dental handpieces [1].

Collins and his study group reported that washer disinfectors are widely used to effectively clean many medical products, primarily in healthcare institutions. They made evaluations according to EN ISO 15883-1 and EN ISO 15883-3 standards in five different working programs in a commercial washer disinfector machine. They stated that a significant decrease in the amount of spores was achieved during the washing process with alkaline detergent [2].

Martin and his study group emphasized that the cleaning of endoscopes, among medical devices, is of critical importance due to their flexible structures and the high rate of exposure to hospital-acquired infections. The effectiveness of bacteria was evaluated by using peracetic acid and hydrogen peroxide, as well as chlorine dioxide, which has high disinfectant properties, in washer disinfectant. They also stated that although various microorganisms were exposed to high levels of disinfectants, they could not be completely destroyed [3].

Zuhlsdorf and his working group evaluated the cleaning process of endoscopes in washer-disinfectors at three different temperatures (43, 51 and 56ºC). They reported that endoscopes were chemo-thermally cleaned at approximately 56ºC in washer-disinfectors. During the 43ºC evaluation phase, they examined 87 endoscopes. They reported that it was not appropriate to make an effective evaluation regarding the low temperature (43ºC) as well as the low number of samples [4].

Zuhlsdorf and Martiny evaluated the cleaning effectiveness of flexible endoscope products in the washer-disinfector. They also emphasized that the relationship between protein detection and colony count densities should be investigated in future studies [5].

Washer disinfector systems may include different features and application systems for various medical product groups, as mentioned above. It is seen that washer disinfector systems stand out as technological products with their differences in usage area, structural, functional and operating features compared to commercial dishwashing systems.

The disinfectant application method appropriate to the characteristics of the parts to be cleaned must first be determined well. In addition, since the use of chemicals in the disinfection process of the innovative prototype is riskier and more difficult to control in terms of human health and the environment, the thermal disinfection method was preferred in the disinfection process of the laboratory glassware selected during the test phase, and it was aimed to obtain an innovative prototype that is more environmentally friendly in terms of the environment and the user.

II. METHOLOGY

The parts to be used in the innovative washer disinfector system prototype include the stainless steel (AISI 304) main body, boiler boiler, water transmission pipes, load basket, drying system, etc. for cleaning, drying and washing processes. Ergonomic technical drawings of the parts were first made.

By evaluating the positions of the innovative prototype parts, their connection elements and their effects on the working process, the parts that make up the innovative prototype are evaluated in different working conditions such as temperature, pressure, water flow, etc. Technical drawings were completed before prototype manufacturing according to the specifications and design verification data.

Examples of various simulation studies conducted for the original design of the innovative washer-disinfector system prototype within the scope of design verification activities are given below (Figure 1 and Figure 2).

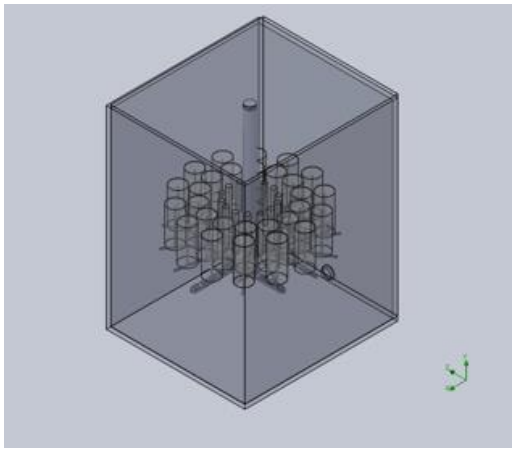

Figure 1: Design of innovative washer-disinfector system prototype.

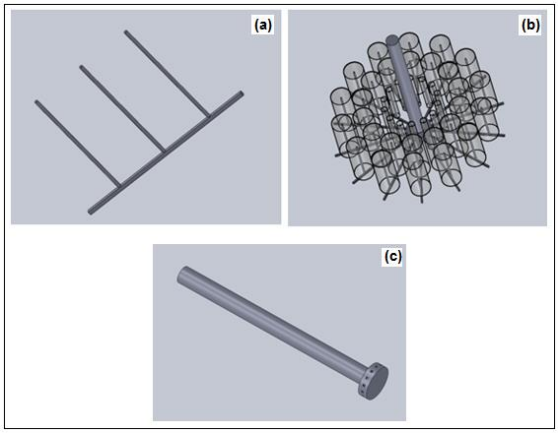

Figure 2: Spray arms and fittings of the innovative prototype.

The operating effects of the design-specific innovative washer-disinfector system prototype washer nozzles at different water pressures were evaluated by selecting 4 different pressures (25, 45, 55 and 65 PSI).

Simulation analyzes are given in Figure 3 for (a) 25 PSI and (b) 65 PSI pressures.

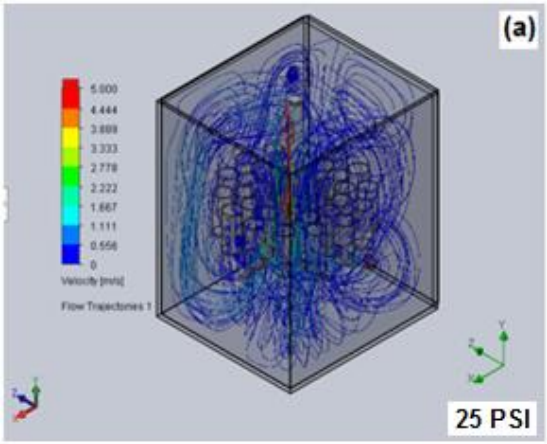

Figure 3.a: Simulations of the innovative prototype's spray arms at different water pressures (25 PSI).

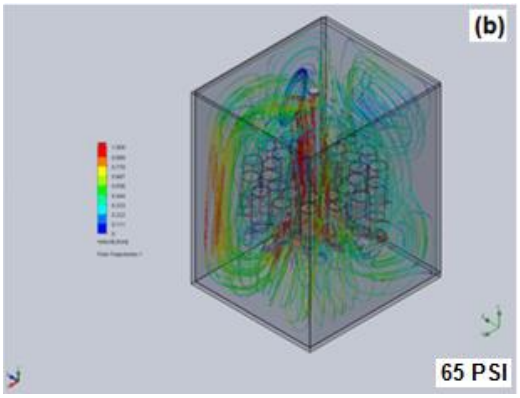

Figure 3.b: Simulations of the innovative prototype's spray arms at different water pressures (65 PSI).

During the placement made during the design verification phase, flow lines reach all the washing surfaces and contribute to effective cleaning. Pressure increase improves the cleaning rate from surfaces by changing the surface tension.

III. EXPERIMENTAL PROCEDURE

Following the prototype manufacturing of the innovative washer disinfector system, the testing and evaluation phase began. The photo of the innovation prototype used in the testing phase is given in Figure 4.

Figure 4: Photograph of the prototype of the innovative washer disinfector system that provides effective drying and cleaning (basket with a glass beaker).

The temperature control screen of the innovative washer disinfector system prototype is given in Figure 5.

Figure 5: Temperature control screen of the innovative washer disinfector system prototype.

The operation of the innovative washer-disinfector system prototype for disinfection of glass beakers is given in Figure 6.

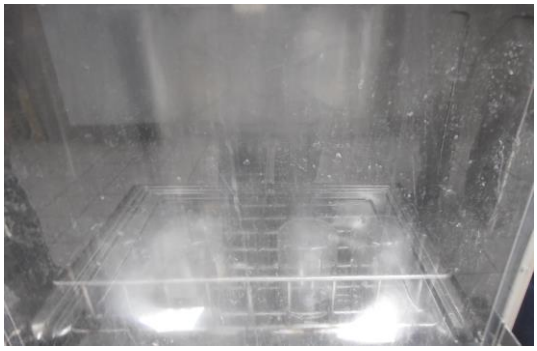

Figure 6: The operation of the innovative washer disinfector system prototype for disinfection of glass beakers.

A photo of the fan drying system (on the back side) of the innovative washer disinfector prototype is given in Figure 7.

Figure 7: A photo of the fan drying system (on the back side) of the innovative washer disinfector prototype.

Specific to this medical glass product, tests were carried out on glass beaker products washed in a washer-disinfector prototype according to three different application times (5, 10 and 15 minutes) and cleaning and disinfection cycle temperatures (70, 80 and 90ºC). Evaluations were made regarding the compliance of the developed washer-disinfector prototype with ISO 15883-1 and ISO 15883-2 international standards. In this context, it has been determined that up to 5 minutes of washing, disinfection and drying time for the glass beaker product is sufficient compared to other higher application times.

In addition, through tests and evaluations made according to three different cleaning and disinfection cycle temperatures, it was determined that 90-95ºC temperatures provide a more effective cleaning and disinfection cycle compared to other low temperature (70 and 80ºC) applications.

As a result, in the washer-disinfector prototype, in line with international standards, it was determined that the application time specific to this medical product was up to 5 minutes, and that the cleaning and disinfection cycle temperatures were 90-95°C.

IV. CONCLUSION

With studies based on R&D systematics, the design and prototype manufacturing of an innovative washer-disinfector system that provides effective cleaning and drying was carried out. By evaluating similar systems in this field, R&D gains have been achieved in obtaining an innovative prototype that is not in our company's product range.

In the washer-disinfector system prototype, for the effectiveness of the disinfection process, the temperature value and the cleaning and disinfection cycle were ensured to operate at 90-95°C (1-5 min.) in accordance with international standards.

In the innovative prototype, thermal disinfection was carried out by taking time and temperature as reference. By not applying the chemical disinfection process (chemical disinfectant concentration), a more environmentally friendly prototype (both for the user and the environment) has been achieved in providing thermal disinfection.

A uniquely designed effective drying system has been used to remove moisture from glass material surfaces (load surface) in accordance with international standards. Also medical/laboratory etc. It has been achieved to ensure compliance with various standards (ISO 15883-1 and ISO 15883-2, etc.) of the working process for glass materials used in fields (glass materials of various sizes specified in international standards / rimless test tube, short-shaped and slotted beaker, etc.).

With the R&D activities, the prototype manufacturing and testing and evaluation phases of the innovative washer-disinfector system with an original design for the medical field, unlike our company's existing commercial dishwashers, were carried out. In addition, innovative domestic products were introduced to the medical sector as high value-added products.

Following the testing and evaluation phase, the innovative washer-disinfector system prototype's effective operating performance of cleaning, drying, washing and disinfection processes in harmony with each other, in accordance with its intended use, was developed for the medical sector.

ACKNOWLEDGMENT

This study was prepared from the project study numbered 3170435 within the scope of TÜBİTAK-TEYDEB 1501 coded Industry Research Technology Development and Innovation Projects Support Programme. We would like to thank TÜBİTAK-TEYDEB Transport, Defense, Energy and Textile Technologies Group (USETEG) for their contribution to the project work.

REFERENCES

[1] Deasy, E.C., Scott, T.A., Swan, J.S., O'Donnell, M.J., Coleman, D.C., Journal of Hospital Infection, vol. 128, pp. 80-88, 2022.
[2] Collins, D.A., Carson, K.C., Riley, T.V., Infection, Disease & Health, vol. 24, pp. 208-211, 2019.
[3] Martin, D.J.H., Denyer, S.P., McDonnell, G., Maillard, J.Y., Journal of Hospital Infection, vol. 69, pp. 377-383, 2008.
[4] Zuhlsdorf, B., Winkler, A., Dietze, B., Floss, H., Martiny, H., Journal of Hospital Infection, vol. 55, pp. 276–282, 2003.
[5] Zuhlsdorf, B., Martiny, H., Journal of Hospital Infection, vol. 59, pp. 286–291, 2005.
[6] Offner, D., Brisset, L., Musset, A-M., Journal of Hospital Infection, vol. 103, pp. e73-e80, 2019.
[7] Howlin, R.P., Khammo, N., Secker, T., McDonnell, G., Keevil, C.W., Journal of Hospital Infection, vol. 75, pp. 66–71, 2010.
[8] Hatt, S., Schindler, B., Bach, D., Greene, C., American Journal of Infection Control, vol. 48, pp. 761−764, 2020.
[9] Zuhlsdorf, B., Kampf, G., Floss, H., Martiny, H., Journal of Hospital Infection, vol. 61, pp. 46–52, 2005.
[10] Kremer, T.A., Bancroft, R., Patel, Z., Owen, M., McDonnell, G., Journal of Hospital Infection, vol. 126, pp. 52-55, 2022.
[11] Lewis S. and McIndoe A.K., 2004, Cleaning, disinfection and sterilization of equipment, Anaesthesia & Intensive Care Medicine, 5, 11, 360-363.
[12] Solon J.G. and Killeen S., 2015, Decontamination and sterilization, Surgery (Oxford), 33, 11, 572-578.

Determination of tool wear, surface roughness and cutting temperature parameters in milling ST37 steel

Ünal DEĞİRMENCİ[1], Üsame Ali USCA[1] and Serhat ŞAP[1]

[1] Bingöl University, Bingöl/Turkey, udegirmenci@bingol.edu.tr
[1] Bingöl University, Bingöl /Turkey, ausca@bingol.edu.tr
[1] Bingöl University, Bingöl /Turkey, ssap@bingol.edu.tr

***Abstract* – This research focuses on the machining properties of St37 low-carbon steel, which is commonly used in the metal industry, under different milling conditions, specifically dry and compressed air environments. The milling process was carried out using a single feed rate of 0.05 mm/rev and three different cutting speeds (125-150-175 m/min) under both dry and compressed air conditions, while maintaining a cutting depth of 0.75 mm. The experiments were conducted using a computer-controlled CNC milling machine. Following the milling operations, analyses were performed to assess tool wear, surface roughness, and cutting temperatures. The results of the study clearly demonstrate the superiority of the compressed air environment over the dry environment in terms of reducing tool wear, improving surface roughness, and lowering cutting temperatures. In the compressed air environment, tool wear, surface roughness, and cutting temperatures decreased by approximately 19%, 24%, and 13%, respectively, when compared to the dry environment. Furthermore, the impact of cutting speed on machinability parameters was also examined.**

***Keywords* – St37 steel, milling, tool wear, surface roughness, cutting temperature.**

I. INTRODUCTION

Low-carbon steels are frequently used in many manufacturing industries such as drilling, turning, and milling. St37 is preferred as structural steel in the construction, automotive, machinery, pipe manufacturing, and energy sectors. St37, which has a yield strength of 235 MPa, is a material that can be easily shaped. St37 steel is classified as low-carbon structural steel and stands out with its easy machinability.

Machining constitutes an important part of the manufacturing sector. Machining is a manufacturing method used to shape or machine metal, wood, plastic, and other materials [1]. This process is based on removing fine particles called chips from the material to obtain the desired shape and size of the material [2]. Machining is generally preferred for the production of precision and customized parts [3]. Machining is used in many industries and plays an important role in engineering, automotive, aerospace, defense, medical device manufacturing, and more [4]. This process provides high precision, repeatability, and customizability, which is especially important in prototype production and custom parts production. Milling of low-carbon steels is a commonly used process for machining these materials. Low carbon steels are steels that typically have a carbon content ranging from 0.05% to 0.30% and are therefore sufficiently hard and durable, but also easy to machine. Accurate selection of cutting parameters, such as cutting speed and feed rate, is crucial in the milling process. The values of these factors may vary based on the material qualities of the workpiece, the specific cutting tool used, and the diameter of the procedure [5].

Machining is a production method used in industrial processes such as metal processing. It is common for metal parts processed during these processes to operate at high temperatures. Therefore, the importance of using a cooling medium becomes evident. It reduces wear on cutting tools working at high temperatures [6]. Cooling extends tool life and reduces machining costs. Cooling improves the surface quality of the metal part being machined. Keeping the temperatures occurring during the process under control reduces surface roughness and increases the precision of the workpiece. Cooling helps keep chips and chips under control during the process. This prevents chips formed during the process from damaging the workpiece and the machine. Machines operating at high temperatures may pose a worker safety risk. Cooling reduces the likelihood of workers being exposed to heat-related risks. Cooling can improve process efficiency. It allows working at higher speeds and feed rates, which shortens processing times. Metal parts processed at high temperatures may change their dimensions. Cooling helps keep the dimensions of the workpiece stable. In some metalworking processes, temperature control prevents undesirable hardening of the workpiece. In machining, cooling plays an important role in controlling the temperatures generated during the process and preserving the life of the workpiece and tool. By choosing the right cooling method and fluids, process efficiency can be increased and the quality of the workpiece improved [7].

There is a plethora of research in the existing body of literature that examine the machinability of steels. Bouacha et al. [8] performed a statistical analysis of surface roughness and cutting forces in the hard turning of AISI 52100 steel. They used the CBN tool and employed response surface

approach. Ekinovic et al. [9] investigated the machinability parameters of carbon steel St52 in a minimum quantity lubrication (MQL) environment. Correia and Davim [10] turned AISI 1045 carbon steel, which is frequently used in the manufacturing industry, using wiper inserts. As a result, they proved that surface quality can be achieved on the workpiece with mechanical precision without the need for cylindrical grinding operations. Hadad and Sadeghi [11] conducted research on turning AISI 4140 steel under minimum quantity lubrication. Muaz and Choudhury [12] conducted an experimental study on the MQL-assisted milling technique to finish AISI 4340 steel. According to their findings, the use of low-viscosity liquids yielded superior outcomes during the application of minimum quantity lubrication (MQL). Salur et al. [13] investigated the effects of AISI 1040 steel on the MQL and machinability parameters of milling in dry environments. Consequently, they observed that the MQL system offers superior performance in comparison to dry milling by mitigating tool wear, lowering cutting temperature, and minimizing power usage.

In this study, we focused on the milling of St37 steel, frequently used in the industry, in dry and compressed air environments. For this purpose, a single feed rate (0.05 mm/rev) and three cutting speeds (125-150-175 m/min) were used as cutting parameters. The cutting depth was determined as 0.75 mm. Following the milling process, studies were conducted to assess tool wear, surface roughness, and cutting temperature. There is a scarcity of research on the process of milling St37 steel. It is believed that this will enhance the uniqueness of the research and provide a valuable contribution to the literature.

II. Material and Method

In this study, St37 steel, which is frequently used in industry and is easily available commercially, was used as the workpiece. The sample dimensions are a 50x50x5 mm plate. Table 1 provides an analysis of the chemical components that make up the workpiece.

Table 1: The elemental makeup of St37 (wt%) [14].

Steel	C	Si	Mn	P	S	Cr	Ni
St37	0.11	0.03	0.56	0.007	0.005	0.07	0.03

Tests to assess machinability were conducted using a numerically controlled milling machine known as Dahlih MCV-860. AlTiN-coated tools were used as cutting edges in the experiments. Three cutting speeds (125-150-175 m/min) and a single feed rate (0.05 mm/rev) were selected as cutting parameters. The cutting depth was determined as 0.75 mm. The recommendations provided by the manufacturer were used to determine the cutting parameters. Dry and compressed air environments were chosen to control the temperature of the cutting zone. Air cooling is done with the help of a compressor connected to the machine tool. After the experiment, the amount of wear and images of the cutting tool were determined with the help of the INSIZE ISM-PM200SA digital microscope. During the tests, temperatures in the cutting zone were measured by a thermal imager (Testo 871). To get an idea of the surface integrity of the processed material, a TIME3200 model surface roughness measuring device was chosen. Figure 1 shows the equipment and processing center used in the experiments. The full experimental design is given in Table 2. Additionally, samples can be seen in Figure 2.

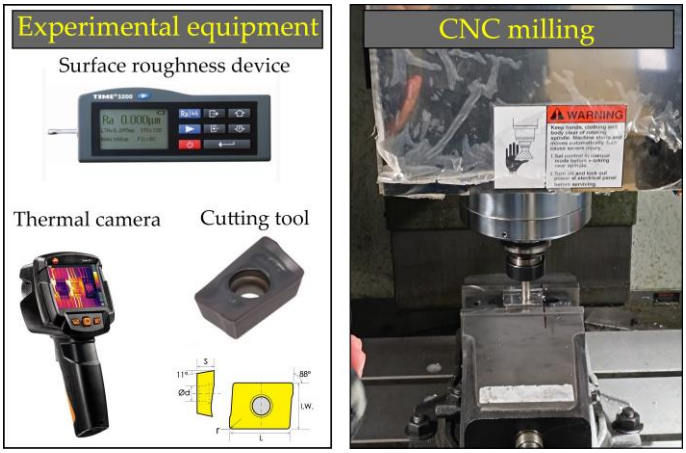

Figure 1: Experimental setup.

Table 2: Full experiment design

Milling parameters	Unit	Levels		
		1	2	3
Cooling conditions	-	Dry	Air	-
Cutting speed, (V_c)	m/min	125	150	175
Feed rate, (f_n)	mm/rev	0.05	-	-
Cutting depth (a_p)	mm	0.75	-	-

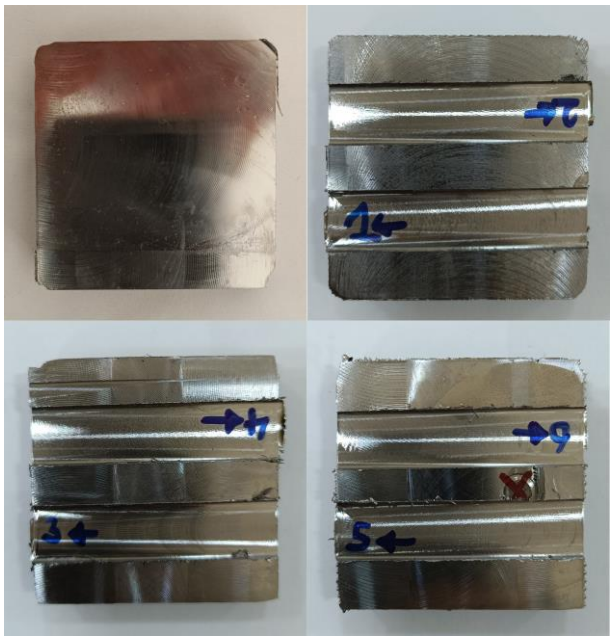

Figure 2: Samples used in experiments.

III. RESULT AND DISCUSSIONS

A. *Tool wear analysis*

Tool wear is an important parameter related to machinability parameters. It can be very effective in ensuring tool life and surface integrity [15]. Figure 3 depicts a graph illustrating the impact of various cooling environment and cutting rates on flank wear. It is seen that flank wear values decrease in machining in a compressed air environment. It has been determined that flank wear decreases by approximately 19% in a compressed-air environment compared to a dry environment. Furthermore, it was noted that the occurrence of flank wear escalated when the cutting speed was raised.

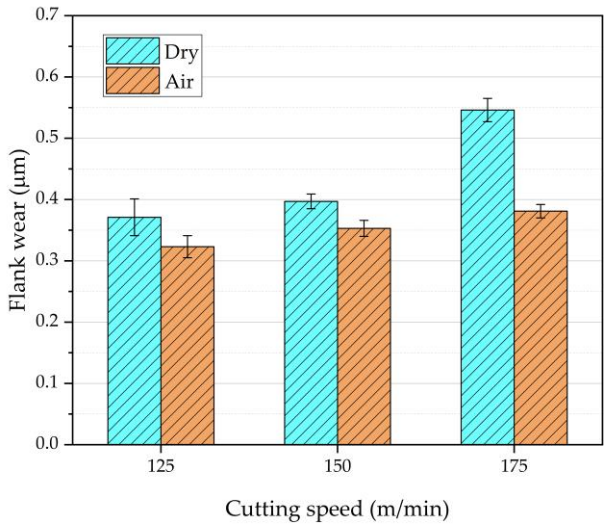

Figure 3: The impact of varying cutting speeds and cooling settings on the development of flank wear.

Flank wear has significant significance in machining, particularly in metalworking procedures. Flank wear refers to the gradual erosion of the lateral surfaces of the cutting tool. Wear has a substantial impact on the cutting tool's efficiency, the workpiece's quality, and the expenses associated with the operation. Flank wear is a determining element that restricts the operational lifespan of the cutting tool. Excessive wear on the lateral surfaces of the cutting tool necessitates more frequent replacement of the tool. This might result in frequent interruptions of transaction procedures and heightened operational expenses. Flank wear may have a negative impact on the surface integrity of the workpiece. As the cutting tool wears down, its accuracy may decrease and the workpiece's surface roughness may rise. This might result in a suboptimal quality of the workpiece. Flank wear may result in elevated cutting forces and contribute to heightened heat production. This may lead to higher energy consumption during the machining process and accelerated heating of the cutting tool. This may result in accelerated tool deterioration and diminished operational effectiveness. Regularly replacing the cutting tool might lead to higher operational expenses. Moreover, heightened energy consumption and personnel demands during operation might further escalate transaction costs. The presence of wear on the lateral surfaces of the cutting tool poses a potential risk to the safety of workers. An excessively used tool might lead to unforeseen complications during the cutting procedure and jeopardize the safety of personnel. Consequently, the occurrence of flank wear has significant significance in the process of machining. Hence, it is important to constantly assess the levels of wear on the instrument and implement required measures accordingly. Regular maintenance and regular replacement of the tool may enhance process efficiency and enhance the quality of the workpiece.

High temperatures occurring at the tool-chip interface during machining in a dry environment may cause plastic deformation. Increasing plastic deformation may cause a decrease in tool life. Figure 4 and Figure 5 depict the optical images illustrating the alterations in the cutting tool caused by machining in both dry and compressed air settings. Flank wear on the cutting tool can be seen in the optical images. Additionally, Built-up edge (BUE) formation was detected in the cutting tool during machining in a compressed air environment.

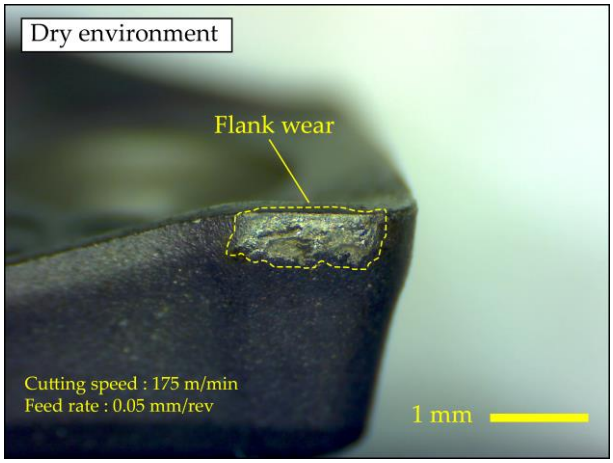

Figure 4: Optical image of the cutting tool machined in a dry environment.

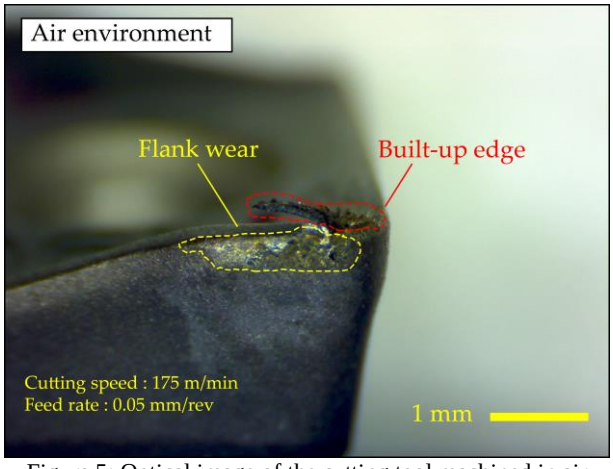

Figure 5: Optical image of the cutting tool machined in air environment.

B. *Surface roughness analysis*

The roughness of the machined surface during machining is affected by several factors and this roughness is closely related to the process parameters, the milling tool used, and the properties of the steel being processed [16]. The choice of

milling tool has a direct impact on the surface roughness of the material being processed. Factors such as the cutting speed of the cutting tool, cutting angle, and compatibility with the material are important. The cutting speed dictates the velocity at which the cutting tool moves over the workpiece. Increased cutting speeds may lead to reduced roughness, yet excessively high cutting rates might elevate the workpiece temperature and accelerate tool deterioration [17].

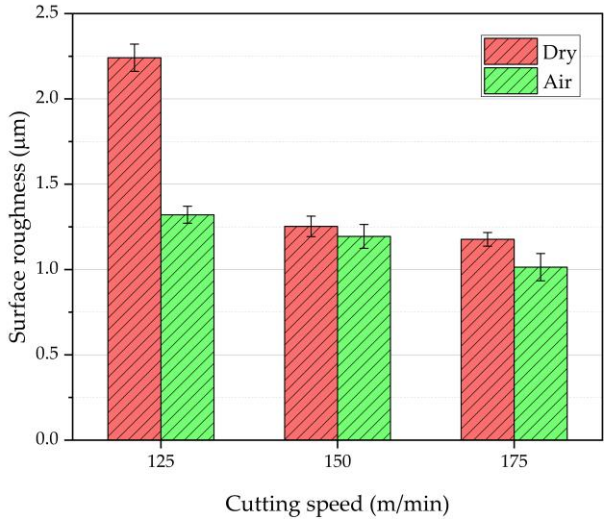

Figure 6: The impact of varying cutting speeds and diverse cooling conditions on surface roughness.

Applying enough cooling throughout the cutting process may decrease the level of roughness on the machined surface. Implementing cooling techniques may effectively mitigate tool wear and provide precise temperature regulation. In addition, the test material also affects roughness. Different types of steel have different mechanical properties and machinability, so the properties of the steel being processed can affect the roughness of the processing result. Figure 6 shows the effects of different cooling environments and different cutting speeds on flank wear. Surface roughness values decreased during machining in a compressed air environment. The improvement in surface quality may be ascribed to the decrease in temperatures inside the cutting zone. It was determined that the surface roughness decreased by approximately 24% in the compressed air environment compared to the dry environment. It is clearly seen that the surface roughness decreases with increasing cutting speeds.

C. Cutting temperature analysis

The milling process is greatly influenced by the cutting temperature, which plays a vital role in determining the efficiency of machining, the surface quality of the workpiece, and the lifespan of the cutting tool. The cutting temperature refers to the temperature that arises at the point of contact between the cutting tool and the steel being treated during the operation. This temperature affects the thermal effects on the material during processing and cutting efficiency [18]. Cutting temperature affects the softness and plasticity of the material during processing. Lower cutting temperatures provide better cutting efficiency because the material becomes harder and brittle. High cutting temperatures increase the plasticity of the material, facilitating chip formation, but may also cause tool wear. The temperature at which something is sliced has an effect on how long it will last. High cutting temperatures can cause tool wear and shorten its life. Therefore, it is important to control the cutting temperature and reduce tool wear by using appropriate cooling and lubrication methods [19]. Cutting temperature affects the quality of the machined surface. High cutting temperatures can cause thermal deformations and chip adhesion on the machined surface, which can increase surface roughness. Lower cutting temperatures tend to produce smoother surfaces. Controlling and optimizing the cutting temperature is important to improve process efficiency and surface quality during milling. This can be done with appropriate cutting speeds, cooling and lubrication methods, and tool selection. Regulating the cutting temperature might also prolong the lifespan of the tool and diminish the expenses associated with the operation. The influence that a variety of cooling chemicals and cutting velocities have on the temperature of the cut is shown graphically in Figure 7, which is a graph. When dry and compressed air environments are compared, it is seen that the compressed air environment reduces the cutting temperature. It has been determined that cutting temperatures decrease by approximately 13% in a compressed air environment compared to a dry environment. It may be said that higher cutting speeds lead to elevated cutting temperatures.

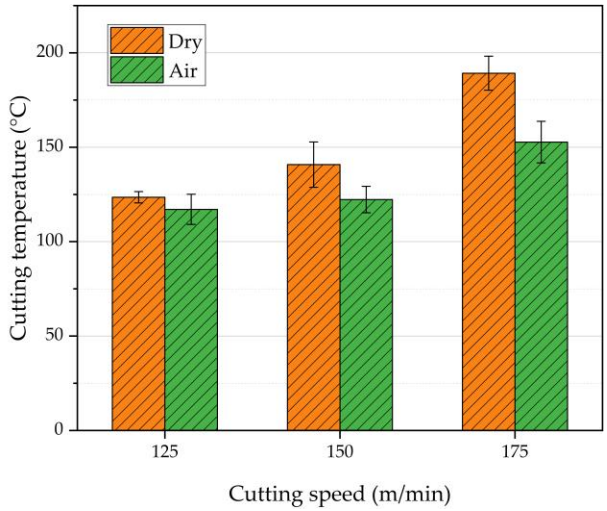

Figure 7: Effects of different cutting speeds and different cooling environments on cutting temperature.

IV. CONCLUSION

This study focused on milling St37 steel in different cooling environments and different cutting speeds. In this context, flank wear, surface roughness, and cutting temperature analyses were performed. The results are given below.

- It is seen that flank wear values decrease in machining in a compressed air environment. It has been

determined that flank wear decreases by approximately 19% in a compressed-air environment compared to a dry environment. Furthermore, it was noted that there was a direct correlation between the cutting speed and the rise in flank wear.

- The study found that the surface roughness reduced by about 24% in the compressed air environment in comparison to the dry environment. Surface roughness decreased with increasing cutting speeds.
- When dry and compressed air environments are compared, it has been determined that the compressed air environment reduces the cutting temperature. The study revealed that cutting temperatures saw a reduction of about 13% in a compressed air setting as compared to a dry setting. The increase in cutting speed increases cutting temperatures.

REFERENCES

[1] H. Sohrabpoor, S. P. Khanghah, and R. Teimouri, "Investigation of lubricant condition and machining parameters while turning of AISI 4340," *Int. J. Adv. Manuf. Technol.*, vol. 76, no. 9, pp. 2099-2116, 2015/02/01 2015, doi: 10.1007/s00170-014-6395-1.

[2] G. Singh *et al.*, "Investigations of Machining Characteristics in the Upgraded MQL-Assisted Turning of Pure Titanium Alloys Using Evolutionary Algorithms," *Materials*, vol. 12, no. 6, p. 999, 2019, doi: https://doi.org/10.3390/ma12060999.

[3] Ü. Değirmenci, Ü. A. Usca, and S. Şap, "Machining characterization and optimization under different cooling/lubrication conditions of Al-4Gr hybrid composites fabricated by vacuum sintering," *Vacuum*, vol. 208, p. 111741, 2023/02/01/ 2023, doi: https://doi.org/10.1016/j.vacuum.2022.111741.

[4] M. Abdul Hadi, J. A. Ghani, C. H. Che Haron, and M. S. Kasim, "Effect of cutting speed on the carbide cutting tool in milling Inconel 718 alloy," *J. Mater. Res.*, vol. 31, no. 13, pp. 1885-1892, 2016/07/01 2016, doi: 10.1557/jmr.2015.380.

[5] Ş. Serhat, "Effects on Machinability of Minimum Quantity Lubrication Strategy during Milling of ST52 Steel," *Türk Doğa ve Fen Dergisi,* vol. 12, no. 1, pp. 82-90, 2023.

[6] Ş. Şirin, Ç. V. Yıldırım, T. Kıvak, and M. Sarıkaya, "Performance of cryogenically treated carbide inserts under sustainable cryo-lubrication assisted milling of Inconel X750 alloy," *SM&T*, vol. 29, p. e00314, 2021, doi: https://doi.org/10.1016/j.susmat.2021.e00314.

[7] E. Şap, U. A. Usca, M. K. Gupta, and M. Kuntoğlu, "Tool wear and machinability investigations in dry turning of Cu/Mo-SiCp hybrid composites," *Int. J. Adv. Manuf. Technol.*, vol. 114, no. 1, pp. 379-396, 2021.

[8] K. Bouacha, M. A. Yallese, T. Mabrouki, and J.-F. Rigal, "Statistical analysis of surface roughness and cutting forces using response surface methodology in hard turning of AISI 52100 bearing steel with CBN tool," *Int. J. Refract. Hard Met.*, vol. 28, no. 3, pp. 349-361, 2010/05/01/ 2010, doi: https://doi.org/10.1016/j.ijrmhm.2009.11.011.

[9] S. Ekinovic, H. Prcanovic, and E. Begovic, "Investigation of Influence of MQL Machining Parameters on Cutting Forces During MQL Turning of Carbon Steel St52-3," *Procedia Eng.*, vol. 132, pp. 608-614, 2015/01/01/ 2015, doi: https://doi.org/10.1016/j.proeng.2015.12.538.

[10] A. Esteves Correia and J. Paulo Davim, "Surface roughness measurement in turning carbon steel AISI 1045 using wiper inserts," *Measurement*, vol. 44, no. 5, pp. 1000-1005, 2011/06/01/ 2011, doi: https://doi.org/10.1016/j.measurement.2011.01.018.

[11] M. Hadad and B. Sadeghi, "Minimum quantity lubrication-MQL turning of AISI 4140 steel alloy," *J. Clean. Prod.*, vol. 54, pp. 332-343, 2013/09/01/ 2013, doi: https://doi.org/10.1016/j.jclepro.2013.05.011.

[12] M. Muaz and S. K. Choudhury, "Experimental investigations and multi-objective optimization of MQL-assisted milling process for finishing of AISI 4340 steel," *Measurement*, vol. 138, pp. 557-569, 2019/05/01/ 2019, doi: https://doi.org/10.1016/j.measurement.2019.02.048.

[13] E. Salur, M. Kuntoğlu, A. Aslan, and D. Y. Pimenov, "The Effects of MQL and Dry Environments on Tool Wear, Cutting Temperature, and Power Consumption during End Milling of AISI 1040 Steel," *Metals*, vol. 11, no. 11, p. 1674, 2021, doi: https://doi.org/10.3390/met11111674.

[14] M. Jafarzadegan, A. Abdollah-zadeh, A. H. Feng, T. Saeid, J. Shen, and H. Assadi, "Microstructure and Mechanical Properties of a Dissimilar Friction Stir Weld between Austenitic Stainless Steel and Low Carbon Steel," *Journal of Materials Science & Technology*, vol. 29, no. 4, pp. 367-372, 2013/04/01/ 2013, doi: https://doi.org/10.1016/j.jmst.2013.02.008.

[15] S. Şap, Ü. A. Usca, M. Uzun, M. Kuntoğlu, and E. Salur, "Performance evaluation of AlTiN coated carbide tools during machining of ceramic reinforced Cu-based hybrid composites under cryogenic, pure-minimum quantity lubrication and dry regimes," *J. Compos. Mater.*, vol. 56, no. 22, pp. 3401-3421, 2022/09/01 2022, doi: https://10.1177/00219983221115846.

[16] M. A. Xavior and M. Adithan, "Determining the influence of cutting fluids on tool wear and surface roughness during turning of AISI 304 austenitic stainless steel," *J. Mater. Process. Technol.*, vol. 209, no. 2, pp. 900-909, 2009/01/19/ 2009, doi: https://doi.org/10.1016/j.jmatprotec.2008.02.068.

[17] Ü. A. Usca, S. Şap, and M. Uzun, "Evaluation of Machinability of Cu Matrix Composite Materials by Computer Numerical Control Milling under Cryogenic LN2 and Minimum Quantity Lubrication," *J. Mater. Eng. Perform.*, vol. 32, pp. 2417-2431, 2022/08/29 2023, doi: https://doi.org/10.1007/s11665-022-07262-w.

[18] A. Wagih, A. Fathy, and A. Kabeel, "Optimum milling parameters for production of highly uniform metal-matrix nanocomposites with improved mechanical properties," *Adv. Powder Technol.*, vol. 29, no. 10, pp. 2527-2537, 2018.

[19] Ü. A. Usca, M. Uzun, S. Şap, K. Giasin, D. Y. Pimenov, and C. Prakash, "Determination of machinability metrics of AISI 5140 steel for gear manufacturing using different cooling/lubrication conditions," *J. Mater. Res. Technol.*, vol. 21, pp. 893-904, 2022/11/01/ 2022, doi: https://doi.org/10.1016/j.jmrt.2022.09.067.

SYSTEM HEAT TRANSFER OF USING ALUMINUM HONEYCOMB AS THERMAL RESISTANCE EXPERIMENTAL INVESTIGATION OF ITS EFFECTS ON

Cuma Ali YILMAZ[1] and Adnan BERBER[2]

[1] Selcuk University, Konya/Turkey, Cumaali_yilmaz@hotmail.com
[2]Selcuk University, Konya/Turkey, aberber@selcuk.edu.tr

Abstract **- In this study, the effects of using a honeycomb core made of aluminum alloy 3005 as thermal resistance on the system heat transfer have been investigated. The convective heat transfer, friction factor, and performance evaluation criteria of the aluminum honeycomb on internal flow have been experimentally examined. In the study, air was used as the fluid. The experiments were conducted with air flow rates of 10 m/s and 15 m/s, and for each flow rate, current values of 50, 100, 150, 175, 200, 225, and 250 Amperes were applied. The experiments were carried out as combinations of variable parameters. The cell diameter of the honeycomb used as thermal resistance is 5.2 mm, and its dimensions are 8x250x250 mm.**

The results show that the thermal resistance of the honeycomb in the rectangular channel heats the incoming cold air by 7.21°C at a speed of 10 m/s and a power of 250 Amperes. As the air flow rate from the fan increases, the heating of the air passing through the honeycomb decreases. The Nusselt number increases linearly with the flow rate and decreases with the increase in the electrical power supplied to the honeycomb. When the graphs of the experimental results are examined, a constant increase in temperature is observed as the current value increases.

Keywords - **Aluminum, Aluminum Honeycomb, Thermal Resistance, Heat Transfer**

I. INTRODUCTION

In today's context, the rise in energy costs and increases in material prices have led to the necessity of saving on initial investment costs and achieving better heat transfer per unit area in conducted studies. The interest in enhancing heat transfer is increasing in line with industrial developments.

Aluminum honeycombs are materials typically composed of hexagonal cells. Aluminum, being a lightweight metal, makes honeycomb structures well-known for their lightweight properties. Additionally, aluminum is durable due to its high strength characteristics. Aluminum honeycombs provide effective heat transfer. This feature makes them popular in applications such as heat exchangers, radiators, and cooling systems. Aluminum is a recyclable material, making honeycomb structures an environmentally friendly option. Aluminum honeycomb structures can be used for a variety of industrial applications, including automotive, aerospace, energy transfer systems, heat exchange systems, and more.

The heat transfer of the systems considered in the name of energy efficiency is very important. Therefore, many numerical and experimental studies are carried out in the field of heat transfer. Various methods were tried to increase heat transfer and minimize losse [1, 2], fins [3, 4]. Honeycomb structures allow for natural airflow, which can enhance heat transfer. In recent years, many passive techniques such as, winglets [5] have been utilized in various thermal engineering applications by researchers.

In this study, heat transfer through convection in a horizontal channel with heat sources extended by surfaces of 10 PPI aluminum foam absorbers was experimentally investigated. Heat transfer coefficients and Nusselt number distributions were obtained for different Reynolds, Grashof, and Richardson numbers for laminar and turbulent flows. When using aluminum foam absorbers, it was observed that approximately 36% to 70% more heat transfer was achieved compared to the results obtained without the use of foam absorbers [6].

In this study, the linear thermal conduction of aluminum, an exemplary material, was experimentally and numerically examined. A constant heat flux was applied to an aluminum plate, and temperatures at different points on the plate were measured. Using experimental data, the thermal conductivity coefficient of aluminum was calculated. Additionally, the thermal conduction equation of the aluminum plate was numerically solved, and the temperature distribution was obtained. Numerical results were compared with experimental results, showing good agreement [7].

This study investigates adsorption cooling, a cooling technology based on a principle different from traditional cooling methods. This technology provides an environmentally friendly cooling solution that does not harm the ozone layer and has a low global warming potential (Adsorption cooling is a cooling technology that involves a material (usually called an adsorbent) adsorbing a gas or vapor onto its surface and using this adsorption process to absorb heat and perform the cooling process). A hexagonal honeycomb adsorption reactor was numerically investigated. Specific Cooling Power (SCP) and Coefficient of Performance (COP) were quantified for various geometric and operational parameters. The aluminum heat exchanger was found to provide 7.7% higher COP than copper [8].

In this study, to enhance the performance of a solar air collector, an aluminum absorber plate with a honeycomb geometry was used. HAD analyses of central and edge air-flow solar air collectors were conducted under varying radiation and mass flow rate conditions to determine the optimum operating ranges of the system, and the designs of central and edge air-flow collectors were compared. The highest thermal efficiencies for both configurations were found to be

approximately 45% for the edge-flow collector and 42% for the central-flow collector under 600 W/m² radiation and 0.015 kg/s mass flow rate [9].

Experimental results were obtained by operating rod resistances with powers of 1 kW, 1.5 kW, and 2 kW, placed inside aluminum plates. It was observed that the aluminum plate positioned under the AISI 304 stainless steel body uniformly heated water through convection in heat transfer. The results obtained from the experiments were compared based on the specified parameters, revealing that the 2 kW rod resistance reached the desired temperature in a shorter time [10].

This article experimentally and numerically examines two-dimensional heat transfer in the form of a heat exchanger using open-cell aluminum foams. Aluminum foams with different pore densities formed the fins of the heat exchanger for a constant heat flux. Heat transfer parameters such as temperature distribution, pressure drop, and Nusselt number were calculated. Numerical results showed good agreement with experimental results [11].

In this study, a prototype of an mPCM honeycomb wallboard was created by combining building construction practice, microencapsulated phase change materials (mPCM), and aluminum honeycomb structures. The results showed that the aluminum honeycomb used in the structure rapidly transferred heat flux into the mPCM, providing approximately 36% to 70% more heat transfer compared to results obtained without using foam absorbers [12].

The efficiency of microcell aluminum honeycombs in augmenting heat transfer in compact heat exchangers was evaluated using analytical models. For convective cooling, an open channel designed with an aluminum honeycomb core was found to elevate the overall heat transfer rate by approximately two orders of magnitude. The performance was comparable to that achieved by using open-celled aluminum foams but attributed to different mechanisms. The overall heat transfer rate of the heat sink was maximized when the cell morphology of the honeycomb was optimized [13].

This study highlights the promising flow and transfer characteristics of hexagonal channels, considering them as prospective structured catalyst carriers. While transfer intensity in long channels is rather moderate, it may be greatly enhanced by channel shortening. The heat transfer in honeycomb structures composed of short hexagonal channels was experimentally studied, and the results were found to be in good agreement with literature solutions [14].

This paper presents a detailed physics-based model for the pressure drop through a honeycomb substrate. The model, valid for various channel shapes and void fractions, uses a computational model of a single channel based on CFD to study the pressure drop when flow enters, passes through, and leaves the substrate. A wide set of 3D computational experiments covering square, hexagonal, and triangular channel cross-sections, void fractions from 0.39 to 0.84, and channel Reynolds numbers from 95 to 1284 was utilized [15].

II. EXPERIMENTAL METHODOLOGY

The experimental setup used in the study consists of a rectangular channel, as schematically shown in Figure 1. The experimental arrangement consists of the inlet, test, and outlet sections. A rectangular channel with dimensions of 250×250 mm and a length of 400 mm was designed and manufactured from aluminum alloy 5754 for the flow channel. Additionally, the experimental setup includes a fan, thermocouples, a differential pressure gauge, a data recording device, and a flow velocity measurement anemometer in sequence. Here, a honeycomb made of aluminum alloy 3005, used as the thermal resistance, is employed (Figure 2). Table 1 provides information on the materials used in the experiment and the properties of the fluid material. The air flow was forced through the rectangular channel at varying speeds by a blower. The top of the channel is designed with a cover, and the insertion of the honeycomb into the channel is performed by opening this cover (Detailed view of the rectangular channel is shown in Figure 3). The power input to the test section was obtained from a calibrated power transformer. PT100 type thermocouples were used to measure the surface temperatures of the test channel. A total of 29 thermocouples were used in the experimental setup. Among these, 3 measured the outlet temperature, 2 measured the ambient temperature, 1 measured the inlet temperature of the channel, and 23 were used to measure the surface temperatures of the test channel. Experiments were conducted with variable air flow rates and variable current values. Thermophysical properties of air for overall temperature were obtained. It was expected to achieve a steady state by making the fluid and wall temperatures, along with the pressure difference, stationary to ensure the hydrodynamic and thermal development of the air flow. This period is approximately 1.5–2 hours. Therefore, all experiments were conducted under steady-state conditions. Temperature measurements inside the rectangular channel, at the channel inlet and outlet, were made using thermocouples, as shown in Figure 4. The pressure difference in the channel throughout the airflow was determined by a digital pressure manometer connected to pressure points at the inlet and outlet of the test section. Additionally, the velocity of the airflow passing through the test section was measured with an anemometer placed in the outlet section.

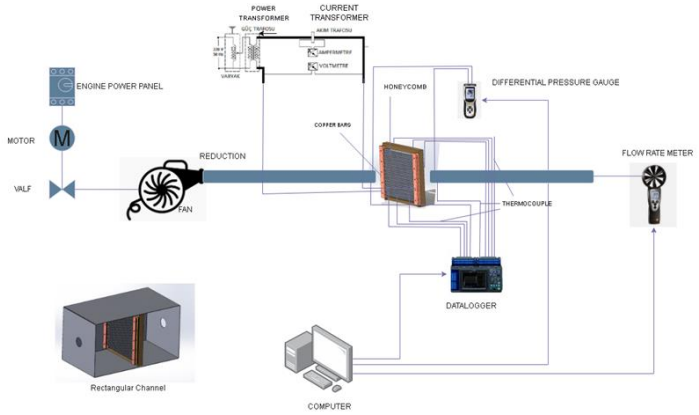

Figure 1. Schematic view of the experimental setup

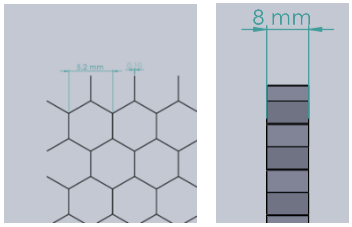

Figure 2. Properties of aluminum honeycomb

Table 1. Thermophysical specification of aluminum 3005, aluminum 5754 and air [16-17].

Properties	Aluminum 3005	Aluminum 5754	air
ρ(kg/m3)	2800	2660	1.184
k (W/mK)	160	120	0.025
cp (J/kgK)	900	900	1007

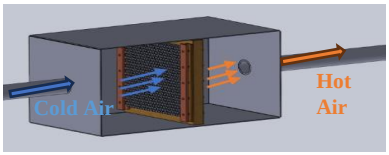

Figure 3. Detail view of rectangular channel

The inlet and outlet temperatures of the channel with the use of aluminum honeycomb as thermal resistance were measured using PT100 type thermocouples (the locations of the thermocouples are shown in Figures 4, 5, 6, and 7).

Thermocouple connections; Connections 1 and 2 measure the ambient temperature.

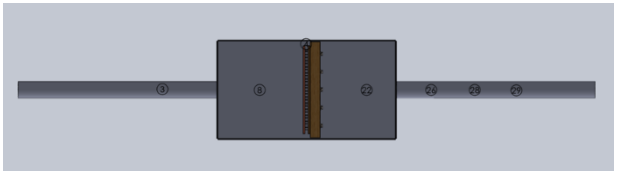

Figure 4. Experimental setup, thermocouple connections

- Thermocouple wire number 3 measures the incoming air temperature.
- Thermocouple wire number 8 measures the temperature of the entrance wall inside the channel (opposite wall to number 7).
- Thermocouple wire number 4 measures the ambient temperature inside the channel.
- Thermocouple wire number 22 measures the temperature of the exit wall inside the channel (opposite wall to number 21).
- Thermocouple wires numbered 26, 28, and 29 measure the outgoing air temperature.

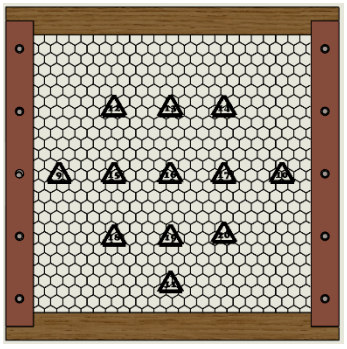

Figure 5. Honeycomb detail view of the experimental setup, thermocouple connections

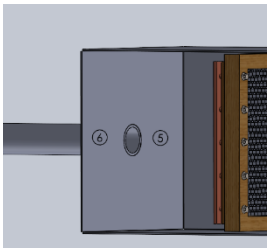

Figure 6. Experimental setup, channel entrance section view, thermocouple connections

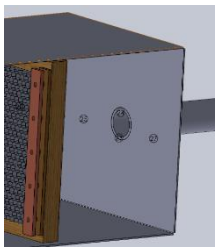

Figure 7. Experimental setup, channel outlet section view, thermocouple connections

The graph of the values read on the data logger of the experimental setup is shown in Figure 8 below. Additionally, thermocouple connections are shown in figure 9 and the values read on the datalogger are shown in figure 10.

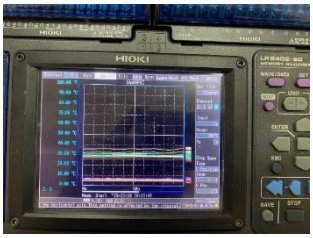

Figure 8. Graphs of temperature values in the data logger device

Figure 9. Visualization of the connection of thermocouples to the in-channel test setup with thermocouple connections of the data logger

Figure 10. Temperature values read on the display of the data logger

III. ANALYTICAL CALCULATION

In this study, experimental findings in the way of heat transfer coefficient, Nusselt number, friction factor and Reynolds number can be calculated as follows:

The heating method of the system was done with a transformer using electrical energy. Current and voltage values were used to calculate how much power was consumed. Thus, the total heater power will be calculated from equation 1 [18].

$$P_t = VI \quad (1)$$

To calculate the net heater power, the amount of heat lost from the system (equation 2) must be determined.

$$Q' = 1{,}24\pi D' L\left(\overline{T}' - T_\infty\right)^{\frac{4}{3}} \quad (2)$$

Net heater power is calculated by subtracting the amount of heat lost (equation 3) from the total heater power.

$$P = P_t - Q' \quad (3)$$

The outer surfaces of the rectangular ducts and flow pipes are covered with glass wool insulation material to prevent heat exchange between the indoor temperature and the outdoor temperature. The rectangular channel cross-section is shown in figure 11)

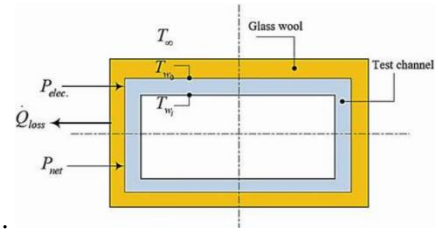

Figure 11. Test channel cross-sectional view

It is calculated by the heat flux on the test pipe surface (equation 4).

$$q_\omega = \frac{P}{2\pi LRw_i} \quad (4)$$

Internal heat production amount (equation 5)

$$\dot{q} = \frac{p}{2\pi L(r_{w_o}^2 - r_{w_i}^2)} \quad (5)$$

Volumetric flow rate (equation 6)

$$U_m = \frac{\dot{v}}{A_i} \quad (6)$$

K factor (equation 7)

$$K = \left(r_{w_0}\right)^2 \left[ln\frac{r_{w_0}}{r_{w_i}} - \frac{1}{2}\left(1 - \frac{\left(r_{w_i}\right)^2}{\left(r_{w_0}\right)^2}\right)\right] \quad (7)$$

Pipe outer surface temperature is measured by thermocouples and is expressed as $Twox$.

Inner surface temperature (equation 8)

$$T_{w_{i_x}} = T_{w_{o_x}} K\dot{q} \quad (8)$$

Bulk temperatures vary linearly along the test pipe axis. Therefore, the bulk temperature (equation 9) at each point x is determined.

$$T_{b_x} = T_{b_i} + \frac{P(x/L)}{\rho C_p \dot{V}} \quad (9)$$

Convection coefficient at point X (equation 10)

$$h_x = \frac{q_w}{T_{\omega_{i_x}} - T_{b_x}} \quad (10)$$

Nusselt number at point x (equation 11)

$$N_{u_x} = \frac{2h_x r_{w_i}}{k} \quad (11)$$

The experimentally determined overall heat transfer coefficients in terms of Nusselt numbers for fully developed turbulent flow in the smooth rectangular duct are compared with the most common empirical correlation referred to in the literature [19]. This correlation is the so-called Dittus–Boelter correlation given as (equation 12)

$$N_U = \frac{hD_h}{k} = 0.023R_e^{0,8}P_\Gamma^{0,4} \quad (12)$$

where k is the thermal conductivity of the air in the channel, D_H is hydraulic diameter and hx is the local heat transfer coefficient. The Reynolds number can be calculated as follows (equation 13)

$$R_e = \frac{\rho \cdot v_{avg} D_H}{\mu} = \frac{VL}{\vartheta} \quad (13)$$

Pressure drop (equation 14)

$$\Delta P = P_1 - P_2 = \frac{8\mu L u_{avg}}{R^2} \quad (14)$$

where Vavg is the average fluid velocity, ρis the density of the fluid based on the bulk temperature and ρ is dynamic

viscosity of the fluid. Friction factor along the channel using the channel length, density, average fluid velocity and pressure drop is calculated as follows (equation 15)

$$f = \frac{2D_H \Delta p}{\rho v_{avg}^2 L} \quad (15)$$

IV. APENDIX

The calculated values of the thermophysical properties of air are given in table 2 for a speed of 10 m/s and in table 3 for a speed of 15 m/s. Table 2. Thermophysical properties of air for a speed of 10 m/s

Table 2. Thermophysical properties of air for 10 m/s velocity

Velocity (m/s)	Ampere (A)	Outlet Temperature (°C)	Kinematic Viscosity of Air (m^2/s)	Reynolds
10	50	25,90	0,001590	6289,31
	100	26,50	0,001610	6211,18
	150	26,80	0,001620	6172,84
	175	27,80	0,001660	6024,10
	200	28,85	0,001690	5917,16
	225	30,30	0,001740	5747,13
	250	31,70	0,001790	5586,59

Table 3. Thermophysical properties of air for a speed of 15 m/s

Velocity (m/s)	Ampere (A)	Outlet Temperature (°C)	Kinematic Viscosity of Air (m^2/s)	Reynolds
15	50	25,00	0,001562	6402,05
	100	25,40	0,001580	6329,11
	150	25,60	0,001580	6329,11
	175	26,85	0,001620	6172,84
	200	28,15	0,001670	5988,02
	225	29,50	0,001710	5847,95
	250	30,80	0,001760	5681,82

Uncertainty analysis and measurement accuracy

The accuracy of findings is very important in experimental studies. Therefore, uncertainty analysis of dimensionless parameters such as Nusselt number, friction factor and Reynolds number was performed according to the ANSI/ASME measurement standard [20, 21]. The uncertainties of the specified dimensionless parameters were obtained using some dimensional parameters in the measurement methodology [22]. The uncertainties of Reynolds number, Nusselt number and friction factor were obtained as ±5.5%, ±6.1% and ±4.5%, respectively. Additionally, in this experimental study, the accuracy of the parameters and maximum errors are introduced.

Table 4. Accuracy and error values of measurement variables.

Variable	Accuracy error%
Temperature	±0.1°C ±0.3
Current	±0.1 A ± 5
Voltage	±0.15 V ± 2
Flow rate	±0.2 m/s ± 2
Pressure	±0.1 Pa ±5

Since the measurement parameters and the accuracy of the instruments are different, repeating the experiments for the same Reynolds is important for the accuracy of the results. For this reason, the experiments were repeated twice for each Reynolds number under the same operating conditions and it was determined that the deviation in the Nusselt number was at most 6.4%. For this reason, it was determined that the repeatability gave good results in the experiments.

The purpose of this experimental study is to determine how much the honeycomb used as thermal resistance heats the fluid air passing through it at different air flow speed values in rectangular ducts.

The results obtained according to these test input values are as in the graphs below.

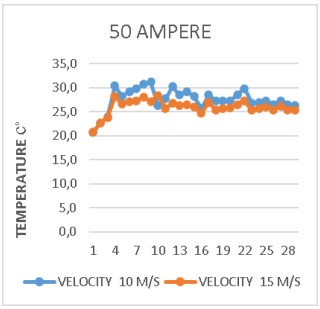

a

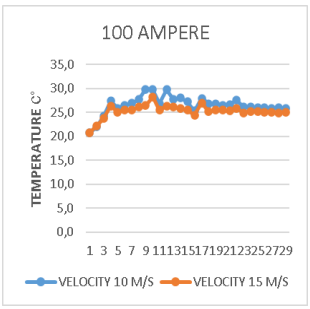

b

a) 50 amp power value temperature chart according to speed
b) 100 amp power value temperature chart according to speed

As seen in the graph above, the temperature difference occurs as the current increases.

At a speed of 10 m/s, the temperature difference at 50 amperes is 1.70 °c, i.e. the cold air entering is heated by 1.70 degrees.

At 100 amperes, the temperature difference is 2.13°c, that is, the cold air entering is 2.13 degrees warmer.

At a speed of 15 m/s, the temperature difference at 50 ampere power is 1.23 °c, i.e. the cold air entering is heated by 1.23 degrees

At 100 ampere power, the temperature difference is 1.58°c, i.e. the cold air entering is heated by 1.58 degrees.

The graphs are similar to each other. Here, as the flow rate increases, the temperature of the air decreases.

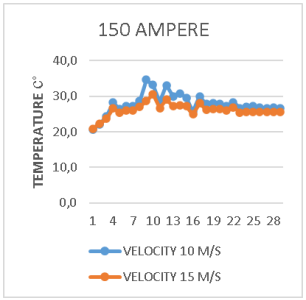

c

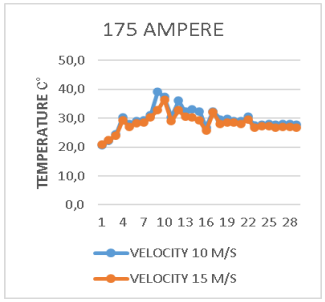

d

c) 150 amp power value temperature chart according to speed
d) 175 amp power value temperature chart according to speed

At a speed of 10 m/s, the temperature difference at 150 ampere power is 2.39 °c, that is, the cold air entering is 2.39 degrees warmer.

At 175 amperes, the temperature difference is 3.49°c, that is, the cold air entering is 3.49 degrees warmer.

At 15 m / s speed value; The temperature difference at 150 ampere power is 1.86 ° c, that is, the cold air entering is heated by 1.86 degrees.

At 175 ampere power, the temperature difference is 3.04°c, i.e. the cold air entering is 3.04 degrees warmer.

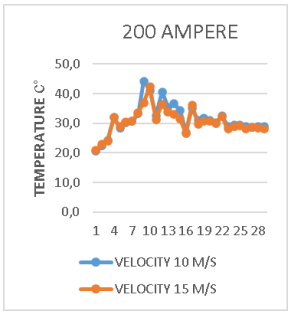

e

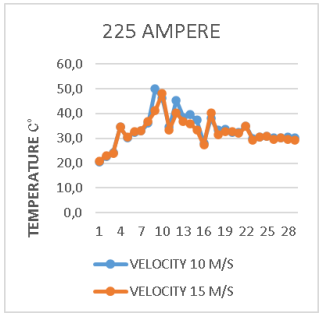

f

e) 200 amp power value temperature chart according to speed
f) 225 amp power value temperature chart according to speed

At a speed of 10 m/s, the temperature difference at 200 ampere power is 4.49 °c, that is, the cold air entering is 4.49 degrees warmer.

At 225 amperes, the temperature difference is 5.91°c, i.e. the cold air entering is 5.91 deg-rees warmer.

At 15 m / s speed value; The temperature difference at 200 ampere power is 4.21 ° c, that is, the incoming cold air is heated by 4.21 degrees.

At 225 ampere power, the temperature difference is 5.39°c, i.e. the cold air entering is heated by 5.39 degrees.

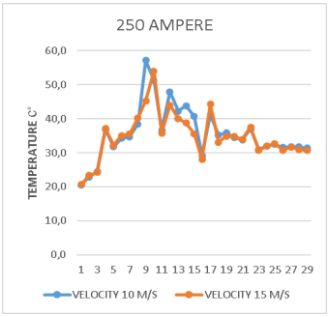

At 10 m / s speed value; At 250 ampere power, the temperature difference is 7.21 °c, that is, the cold air entering is 7.21 degrees warmer.

At a speed of 15 m/s, the temperature difference at 250 ampere power is 6.57 °c, i.e. the cold air entering is 6.57 degrees warmer.

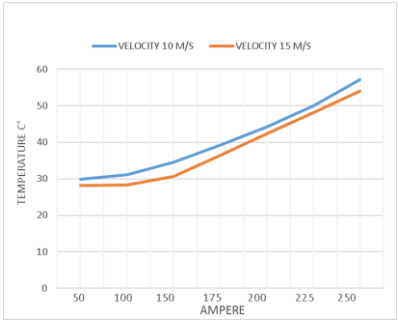

Figure 19. Channel output temperature graph according to amperage value

In the graph above, the graph of the maximum temperature value at which the air is heated according to each ammeter value is given.

It can be seen from the graph that the heating value of the air increases linearly with the increase in the current value.

V. CONCLUSION

By using the aluminum honeycomb as a thermal resistance, it has been observed that it heats the incoming cold air by drawing power.

According to the data obtained in the results of this experimental study, the parameter that heats the cold air the highest is the maximum current power at the minimum speed value. In other words, it heated the cold air by 7.21°C at a speed of 10 m/s and a power of 250 amps.

The aim of this study is to determine how much the honeycomb can heat the cold air by using it as thermal resistance, which we think is lacking in the literature, and to bring it to the literature.

As a result of the test, a linear graph was obtained in the current and temperature relati-onship with the readings. In this case, the accuracy of the experiment is considered to be high. No deviation was observed in the test data.

NOMENCLATURE

A: surface area of heat transfer (m^2)
Dh: hydraulic diameter of duct (m)
f: friction factor
h: heat transfer coefficient (W/m^2K)
I: electric current (amp)
k: thermal conductivity (W/mK)
L: length of test channel (m)
Nu: Nusselt number
Pnet: net electrical power
ΔP: pressure drop (Pa)
Re: Reynolds number
ϑ: kinematic viscosity of a fluid (m^2/s)
Q: heat transfer rate (W)
q": heat flux (W/m^2)
T: temperature (K)
U: flow rate (m/s)
V_{avg}: average velocity (m/s)
ΔV: electric voltage (volt)

ACKNOWLEDGMENT

I would like to thank Mr. Mevlüt ÇATLI, General Manager of "Altıgen Aviation and Space Ship Construction Panel Industry Trade Limited Company" for his support in the production of the materials used in this study. I would also like to thank Mr. Adnan BERBER for his support in design.

REFERENCES

[1] A. H. Altun, M. Gürdal, and A. Berber, "Effects of sinusoidal strip element with different amplitudes on heat transfer and flow characteristics of circular channels," *Heat Transf. Res*., vol. 50, pp. 6, 2019.
[2] A. H. Altun, M. Gurdal, and A. Berber, "Effects of sinusoidal turbulator in cylindrical channel on heat transfer and flow characteristics," *Maejo Int. J. Sci. Technol*., vol. 14, pp. 27–42, 2020.
[3] A. Berber, M. Gürdal, and K. Bağırsakçı, "Prediction of heat transfer in a circular tube with aluminum and Cr-Ni alloy pins using artificial neural network," *Exp. Heat Transf*., 2020.
[4] A. Berber, K. Bagirsakci, and M. Gurdal, "Investigation of effects on heat transfer and flow characteristics of Cr-Ni alloy and aluminum pins placed in AISI 304 tube," *Therm. Sci*., vol. 24, pp. 1999–2011, 2020.
[5] Berber A., Gürdal M., Yetimoğlu M. Experimental study on the heat transfer enhancement in a rectangular channel with curved winglets, *Experimental Heat Transfer*, pp. 797-817, 2021.
[6] Doğan A., Öney B., "Experimental Investigation of Convection Heat Transfer through Aluminum Foam Heat Sinks", *Gazi Univ. Eng. Arch. Fac. Journal*, vol. 29, pp. 71-78, 2014.
[7] Özcelik G. et al, "Experimental and Numerical Investigation of Linear Heat Conduction in a Sample Material", *Istanbul Arel University 13th National Installation Engineering Congress*, vol. 13, 2017.
[8] Papakokkinos G., Castro J., Oliet C., Olica A., "Computational investigation of a hexagonal honeycomb adsorption reactor for cooling applications", *Applied Thermal Engineering*, vol. 202, 2022.
[9] Eyyublu S., Buker M.S., "CFD Analysis of a Solar Air Collector with Aluminum Honeycomb Absorber Surface", *European science and technology journal*, vol 32, pp. 484 – 490, 2021.
[10] Basmacı G., Butgül İ., "An experimental study on the design of a blade sterilizer used in meat processing plants", *Journal of Mehmet Akif Ersoy University Graduate School of Natural and Applied Sciences*, vol 12, pp. 313-320, 2021,
[11] Temiz A.et al, "Theoretical Analysis of Compact Heat Exchanger with Hexagonal Honeycomb Metal Foam Fins", *14th International Combustion Sysmposium* ,2018.
[12] Lai C., Hokoi S., "Thermal performance of an aluminum honeycomb wallboard incorporating microencapsulated PCM", *Energy and Buildings*, vol. 73, pp. 37–47, 2014.
[13] Lu T.J., "Heat transfer efficiency of metal honeycombs", *International Journal of Heat and Mass Transfer*, vol. 42, pp. 2031-2040, 1999.
[14] Iwaniszyn M. et al, "Entrance effects on forced convective heat transfer in laminar flow through short hexagonal channels", Experimental and CFD study, *Chemical Engineering Journal, vol.* 405, 2021.
[15] Cornejo I., Nikrityuk P., Hayes R.E., "The influence of channel geometry on the pressure drop in automotive catalytic converters: Model development and validation", *Chemical Engineering Science*, vol. 212, 2020.
[16] Makeitfrom, "Aluminum 5754 properties and aluminum 3005 properties". [access date: 25/11/2023], https://www.makeitfrom.com/
[17] Rsrenerji, "Havanın Özkütlesi" [access date: 25/11/2023], https://rsrenerji.com/blog/havanin-ozkutlesi
[18] Özen K et al, "Experimental Investigation of Heat Transfer on Finned Surfaces at Different Speeds and Heat Fluxes" *Necmettin Erbakan Üniversitesi Seydişehir Ahmet Cengiz Mühendislik Fakültesi*, 2019
[19] B. Sunden Introduction to Heat Transfer WIT Press, UK (2012)
[20] R. B. Abernethy, R. P. Benedict, and R. B. Dowdell, "ASME measurement uncertainty," 1985.
[21] A. T. Wijayanta, I. Yaningsih, W. E. Juwana, M. Aziz, and T. Miyazaki, "Effect of wing-pitch ratio of double-sided delta-wing tape insert on the improvement of convective heat transfer," *Int. J. Therm. Sci*., vol. 151, 2020.
[22] L. Kirkup and R. B. Frenkel. "An Introduction to Uncertainty in Measurement: Using the GUM (Guide to the Expression of Uncertainty in Measurement)". *Cambridge University Press*, 2006

Investigation of Torsional and Soft Storey Behavior of a Reinforced Concrete Building in Adana Province According to Turkey Building Earthquake Code 2018.

D.ERTÜRKMEN[1]

[1] Mersin University, Mersin/Turkey, derturkmen@mersin.edu.tr

Abstract **- Earthquakes are an important reality in our lives. Turkey is located on many active fault lines and a large part of Turkey is always in danger of earthquakes. The recent earthquakes, which took place simultaneously in Kahramanmaraş and Hatay and affected 11 provinces, have painfully revealed the extent of this danger. By the earthquake, many lives and property were lost in a large area. When the collapsed structures are examined, it is observed that the structures are not suitable for the soil they are located on and the current earthquake regulations. This bad result proved once again how important earthquake-resistant building design is for human life. Adana was one of the most damaged cities in the recent earthquakes. For this reason, this research is focused on the seismic response of structures in Adana. The earthquake analysis of L'shaped ten-story buildings with five and seven spans in x directions are performed, respectively. Five different districts of Adana city are chosen to carry out the comparison between different locations. The equivalent seismic load method is used based on the Turkey Building Earthquake Code-2018 (TBEC-2018). In the earthquake analysis for the considered building models, the SAP2000 structural analysis program is used to investigate the torsional and soft storey irregularities that may arise in the structure. As a result of the analysis, by increasing the number of spans in the x-direction of the building the irregularity in the plan also increases. It is carried out that there is an increase in the torsional irregularity values calculated especially in the y direction. In the building models examined within the scope of the study, it was also observed that the soft storey irregularity was within acceptable limits.**

Keywords **- Torsional irregularity, Soft storey irregularity, Turkey Building Earthquake Code 2018, Earthquake analysis, Irregular buildings.**

I. Introduction

TURKEY is located on many active fault lines. Among these fault lines, the most important and dangerous ones in terms of earthquake-producing capacity are: North Anatolia, East Anatolia and West Anatolia fault lines. A large number of major earthquakes have occurred on these fault lines to date, and a large number of lives and property have been lost in these earthquakes.

There have been 22 earthquakes with a magnitude of 6.5 and above in Turkey in the last century, which have caused significant damage and loss of life. As a result of the 7.7 and 7.6 magnitude earthquakes recently experienced in Turkey, the epicenter of which is Kahramanmaraş, 11 provinces, including our province of Adana, have been greatly affected. Due to the both architectural and engineering errors in the provinces affected by the earthquake, many structures collapsed and a large number of citizens lost their lives. In the examinations carried out in the affected areas after the earthquake, it was observed that a large number of structures with various structural irregularities collapsed, while those that were able to survive received moderate and severe damage.

Structural irregularities that should be taken into account in the design and control of irregular buildings are defined in the TBDY (Turkey Building Earthquake Code) 2018 under two main headings: "States of Irregularity in the Plan" and "States of Irregularity in the Vertical Direction". Structural irregularities significantly reduce the seismic performance of structures under the influence of earthquakes. Buildings with structural irregularities are exposed to various structural damages by causing excessive torsion according to the type of irregularity, soft storey irregularity due to the decrease in horizontal displacement rigidity, and uneven distribution of internal forces with the increase in relative storey displacements [6].

This research is focused on the seismic response of structures in Adana. The earthquake analysis of L'shaped ten-story buildings with five and seven spans in x directions are performed, respectively. Five different districts of Adana city are chosen to carry out the comparison between different locations. The equivalent seismic load method is used based on the Turkey Building Earthquake Code-2018 (TBEC-2018) [9]. In the earthquake analysis for the considered building models, the SAP2000 structural analysis program is used to investigate the torsional and soft storey irregularities that may arise in the structure [11]. As a result of the analysis, by increasing the number of spans in the x-direction of the building the irregularity in the plan also increases.

II. Structure Damages and Causes of Damage

The 7.7 and 7.6 magnitude earthquakes that occurred in Turkey on 6 February 2023, with the epicenter in

Kahramanmaraş, were effective in a wide area across the country. Due to these earthquakes, a large number of lives and property losses have been experienced in 11 provinces, including Adana province. In the examinations carried out in the region after the earthquakes, it was seen that a large number of houses, public buildings, many mosques, various historical monuments and road structures were heavily damaged and became unusable. When the damaged structures were examined, it was concluded that the majority of the damages were caused by structural irregularities, and the most destructive structure damages occurred in structures that were not designed in accordance with the ground on which they were located.

If we give the causes of damage observed in the examined structures under the headings:

- Removal of the filling walls on the ground floor of the buildings and the use of these floors as shops,
- The height of the ground floor in buildings is higher than other floors,
- Formation of short columns in basement floors,
- Cutting of the some columns for some reasons,
- Failure to perform sufficient tightening at the column-beam joints,
- The use of low strength concrete,
- Not carrying out a ground survey on the ground where the buildings will be built,
- Failure to ensure continuity of vertical load-bearing elements between floors and sudden stiffness change,
- Construction of structures that do not have regular geometry in plan and are subject to torsion.

In this section, examples of buildings damaged in the recent earthquakes in Adana province and the causes of damage will be discussed. Figure 1, shows images of some building examples that were damaged due to various irregularities occurring as a result of the Kahramanmaraş earthquakes.

a) Soft storey irregularity-Column rupture (Kahramanmaraş)

b) Soft storey irregularity (Kahramanmaraş)

c) Torsional and soft storey irregularities (Gaziantep)

d) Torsional irregularity (Adana)

Figure 1(a-d): Examples of damaged buildings due to Kahramanmaraş earthquakes

III. Analysis Model and Method

In this study, a ten-storey reinforced concrete building model with an L-shaped geometry with five and seven spans in x directions were analyzed with the SAP2000 structural analysis program using the Equivalent Earthquake Load Method in TBEC-2018. It is assumed that the model is located in 5 different districts of Adana province and the earthquake parameters taken into account in the method were obtained using AFAD Turkey Earthquake Hazard Maps [12]. In the analysis, ZC type soil class was accepted for all districts selected as locations.

The location information selected on the map in the districts taken into consideration within the scope of the analysis and the earthquake spectrum parameters taken from https://tdth.afad.gov.tr according to the ZC class soil type in the relevant locations are given in Table 1. In the analysis, the rare earthquake ground motion level called DD-2 Earthquake Ground Motion was taken into account. The plan and 3D view of the building model used in the study are given in Figure 2.

Table 1: Latitude-longitude information of the building model and earthquake spectrum parameters obtained from the map

Districts	Latitude	Longitude	ZC			
			S_{DS}	S_{D1}	T_A(s)	T_B(s)
Seyhan	36.994°	35.322°	0.673	0.195	0.058	0.290
Çukurova	37.049°	35.301°	0.655	0.191	0.058	0.292
Ceyhan	37.031°	35.822°	0.800	0.245	0.061	0.306
Aladağ	37.577°	35.355°	0.598	0.180	0.060	0.301
Saimbeyli	37.586°	36.089°	0.657	0.205	0.062	0.312

Column dimensions (50 cm x 50 cm), beam dimensions (30 cm x 50 cm), slab height 15 cm, floor height 3 m and concrete

class C30 were selected in modeling. The weight of the building was calculated manually, and the weight of the elements was not taken into account in SAP2000 structural analysis program. The slabs in the program were modeled as shell elements and the loads were defined on the slabs directly. The equivalent earthquake load values were calculated according to TBEC-2018 and affected by applying ±0.05 eccentricity value to the center of mass of the structure in both (x-y) earthquake directions. Equivalent earthquake loads acting on the floors were calculated using equations (1) and (2).

$$V_{tE}(X) = m_t S_{aR}(T_p(X)) \geq 0.04 m_t I S_{DS} g \quad (1)$$

$$V_{tE}(Y) = m_t S_{aR}(T_p(Y)) \geq 0.04 m_t I S_{DS} g \quad (2)$$

After the analysis, the displacement values at the corner points of the building were read and the necessary structural irregularities were checked according to TBEC-2018. The building models discussed in this study were examined especially in terms of torsional and soft storey irregularities formation. Equation 3 was used for torsional irregularity values, and equation 4 was used for soft storey irregularity values.

$$\eta_{bi} = (\Delta_i)_{\max} / (\Delta_i)_{ort} > 1.2 \quad (3)$$

$$\eta_{ki} = (\Delta_i / h_i)_{ort} / (\Delta_{i+1} / h_{i+1})_{ort} > 2.0 \quad \text{or} \quad (4)$$
$$\eta_{ki} = (\Delta_i / h_i)_{ort} / (\Delta_{i-1} / h_{i-1})_{ort} > 2.0$$

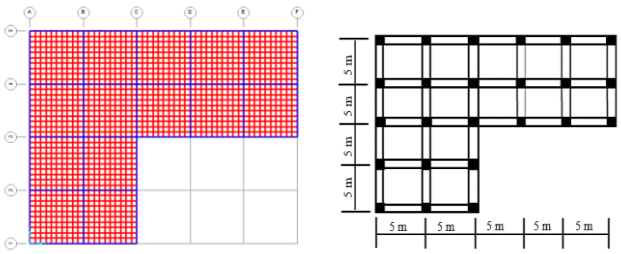

a) xy view for five spans model in x direction

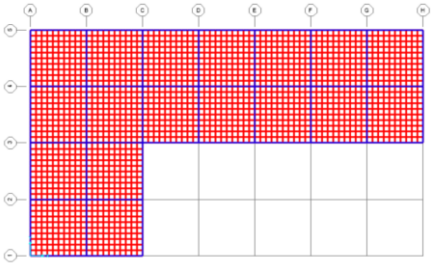

b) xy view for seven spans model in x direction

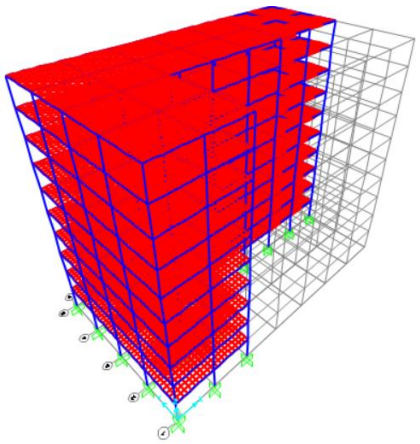

c) 3D view for seven spans model

Figure 2(a-c): The plan and 3D view of the building model

IV. Analysis Results

When the analysis results were examined, it was seen that the equivalent earthquake loads obtained in both earthquake directions had the same values. Table 2 shows the equivalent earthquake loads in X and Y earthquake direction for five and seven spans building model. It was seen from the table that as the number of spans of the building model increased, the equivalent earthquake loads and base shear force values increased.

Table 2: Equivalent earthquake loads in X and Y earthquake direction for five and seven spans building model

Equivalent Earthquake Loads (kN) -X and Y					
Five spans model					
Floor No	**Seyhan**	**Çukurova**	**Ceyhan**	**Aladağ**	**Saimbeyli**
10	185.03	180.08	219.94	164.41	180.63
9	141.63	137.84	168.36	125.85	138.27
8	125.90	122.53	149.65	111.87	122.90
7	110.16	107.21	130.95	97.88	107.54
6	94.42	91.90	112.24	83.90	92.18
5	78.68	76.58	93.53	69.92	76.81
4	62.95	61.26	74.83	55.93	61.45
3	47.21	45.95	56.12	41.95	46.09
2	31.47	30.63	37.41	27.97	30.73
1	15.74	15.32	18.71	13.98	15.36
ΣV(T)	**893.19**	**869.30**	**1061.74**	**793.65**	**871.96**
Seven spans model					
Floor No	**Seyhan**	**Çukurova**	**Ceyhan**	**Aladağ**	**Saimbeyli**
10	235.96	229.65	280.49	209.66	230.35
9	180.41	175.58	214.45	160.30	176.12
8	160.36	156.07	190.62	142.49	156.55
7	140.32	136.56	166.79	124.68	136.98
6	120.27	117.05	142.97	106.87	117.41
5	100.23	97.54	119.14	89.06	97.84
4	80.18	78.04	95.31	71.24	78.27
3	60.14	58.53	71.48	53.43	58.71
2	40.09	39.02	47.66	35.62	39.14
1	20.05	19.51	23.83	17.81	19.57
ΣV(T)	**1137.98**	**1107.55**	**1352.73**	**1011.17**	**1110.93**

As a result of the analysis performed by entering the equivalent earthquake loads into the program, various structural irregularities specified in the TBEC-2018 were checked by reading the displacement values formed at critical corners in the building models. The results obtained in terms of torsional irregularity are given in Table 3 and Table 4.

Table 3: Torsional irregularity values in X earthquake direction for five and seven spans building model

Torsional irregularity values -X					
Five spans model					
Floor No	**Seyhan**	**Çukurova**	**Ceyhan**	**Aladağ**	**Saimbeyli**
10	1.05	1.06	1.06	1.06	1.05
9	1.07	1.07	1.07	1.07	1.07
8	1.07	1.07	1.07	1.07	1.07
7	1.08	1.07	1.08	1.08	1.07
6	1.07	1.08	1.08	1.08	1.08
5	1.08	1.08	1.08	1.08	1.08
4	1.08	1.08	1.08	1.08	1.08
3	1.08	1.08	1.08	1.08	1.08
2	1.09	1.09	1.09	1.09	1.09
1	1.09	1.09	1.09	1.09	1.09
Seven spans model					
Floor No	**Seyhan**	**Çukurova**	**Ceyhan**	**Aladağ**	**Saimbeyli**
10	1.00	1.00	1.00	1.00	1.00
9	1.01	1.01	1.01	1.01	1.01
8	1.01	1.01	1.01	1.01	1.01
7	1.01	1.01	1.01	1.01	1.01
6	1.01	1.01	1.01	1.01	1.01
5	1.01	1.01	1.01	1.01	1.01
4	1.01	1.01	1.01	1.01	1.01
3	1.02	1.01	1.02	1.02	1.02
2	1.02	1.02	1.02	1.02	1.02
1	1.02	1.02	1.02	1.02	1.02
<1.20					

Table 4: Torsional irregularity values in Y earthquake direction for five and seven spans building model

Torsional irregularity values -Y					
Five spans model					
Floor No	**Seyhan**	**Çukurova**	**Ceyhan**	**Aladağ**	**Saimbeyli**
10	1.18	1.18	1.18	1.18	1.18
9	1.17	1.17	1.17	1.17	1.17
8	1.16	1.16	1.16	1.16	1.16
7	1.16	1.16	1.16	1.16	1.16
6	1.16	1.16	1.17	1.16	1.16
5	1.16	1.16	1.15	1.16	1.16
4	1.16	1.16	1.16	1.16	1.16
3	1.15	1.15	1.15	1.15	1.15
2	1.15	1.15	1.15	1.15	1.15
1	1.14	1.14	1.14	1.14	1.14
<1.20					
Seven spans model					
Floor No	**Seyhan**	**Çukurova**	**Ceyhan**	**Aladağ**	**Saimbeyli**
10	1.18	1.18	1.18	1.17	1.18
9	1.20	1.20	1.20	1.20	1.20
8	1.21	1.21	1.21	1.21	1.21
7	1.22	1.22	1.22	1.22	1.22
6	1.22	1.22	1.22	1.22	1.22
5	1.22	1.22	1.22	1.22	1.22
4	1.23	1.23	1.23	1.23	1.23
3	1.23	1.23	1.23	1.23	1.23
2	1.24	1.24	1.24	1.24	1.24
1	1.26	1.26	1.26	1.26	1.26
>1.20					

When the results obtained in terms of torsional irregularity were examined, it was seen that the torsional irregularity values calculated in the X earthquake direction remained within normal limits for both building models. At the same time it was observed that the earthquake direction with the highest torsion was the +Y direction, and with the increase in the number of spans, it was determined that the torsional irregularity values exceeded the limit value that specified in the building code 2018. So when Table 4 and Figure 3 are examined, it can be said that torsional irregularity occurs in the seven spans building model.

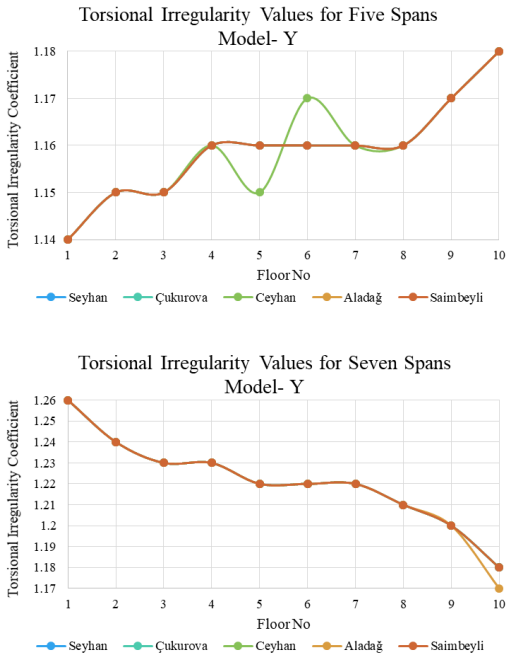

Figure 3: Torsional irregularity values for five and seven spans building model in Y direction

The results obtained in terms of soft storey irregularity are given in Table 5 and Table 6. In the case of soft storey irregularity, it was observed that the values increased more in the +Y earthquake direction. However, since the calculated soft storey irregularity values are below the limit value specified in the building code 2018, it has been concluded that there is no soft storey irregularity in the building models.

Table 5: Soft storey irregularity values in X earthquake direction for five and seven spans building model

Soft storey irregularity values -X										
Five spans model										
F. No	**Seyhan**		**Çukurova**		**Ceyhan**		**Aladağ**		**Saimbeyli**	
10	-	0.65	-	0.64	-	0.65	-	0.65	-	0.65
9	1.55	0.74	1.55	0.74	1.54	0.74	1.54	0.74	1.55	0.74
8	1.35	0.81	1.35	0.81	1.35	0.81	1.36	0.81	1.35	0.81
7	1.23	0.86	1.23	0.86	1.23	0.86	1.23	0.86	1.24	0.86
6	1.16	0.90	1.16	0.89	1.16	0.90	1.16	0.90	1.16	0.90
5	1.11	0.93	1.12	0.93	1.11	0.93	1.11	0.93	1.11	0.93
4	1.07	0.98	1.07	0.97	1.08	0.98	1.07	0.98	1.07	0.97
3	1.02	1.09	1.03	1.09	1.02	1.09	1.02	1.09	1.03	1.09
2	0.92	1.82	0.92	1.83	0.92	1.83	0.92	1.82	0.92	1.82
1	0.55	-	0.55	-	0.55	-	0.55	-	0.55	-
Seven spans model										
F. No	**Seyhan**		**Çukurova**		**Ceyhan**		**Aladağ**		**Saimbeyli**	
10	-	0.64	-	0.64	-	0.64	-	0.64	-	0.64
9	1.57	0.74	1.56	0.74	1.56	0.74	1.56	0.74	1.57	0.74
8	1.35	0.81	1.36	0.81	1.36	0.81	1.36	0.81	1.36	0.81
7	1.23	0.86	1.23	0.86	1.24	0.86	1.24	0.86	1.23	0.86
6	1.16	0.90	1.17	0.90	1.16	0.90	1.16	0.89	1.16	0.90
5	1.12	0.93	1.11	0.93	1.12	0.93	1.12	0.93	1.11	0.93
4	1.07	0.97	1.07	0.97	1.08	0.98	1.07	0.97	1.07	0.97
3	1.03	1.08	1.03	1.08	1.03	1.08	1.03	1.08	1.03	1.08
2	0.92	1.82	0.92	1.82	0.92	1.81	0.92	1.81	0.92	1.82
1	0.55	-	0.55	-	0.55	-	0.55	-	0.55	-
<2.00										

Table 6: Soft storey irregularity values in Y earthquake direction for five and seven spans building model

Soft storey irregularity values -Y										
Five spans model										
F. No	**Seyhan**		**Çukurova**		**Ceyhan**		**Aladağ**		**Saimbeyli**	
10	-	0.66	-	0.66	-	0.66	-	0.66	-	0.66
9	1.52	0.74	1.52	0.74	1.52	0.74	1.52	0.74	1.52	0.74

8	1.35	0.81	1.35	0.81	1.35	0.81	1.35	0.81	1.35	0.81
7	1.23	0.86	1.23	0.86	1.23	0.86	1.23	0.86	1.23	0.86
6	1.16	0.90	1.16	0.90	1.17	0.91	1.16	0.90	1.16	0.90
5	1.11	0.93	1.11	0.93	1.09	0.93	1.11	0.93	1.11	0.93
4	1.07	0.98	1.07	0.98	1.08	0.98	1.07	0.98	1.07	0.98
3	1.02	1.09	1.02	1.09	1.02	1.09	1.02	1.09	1.02	1.09
2	0.92	1.85	0.91	1.84	0.92	1.85	0.92	1.85	0.91	1.85
1	0.54	-	0.54	-	0.54	-	0.54	-	0.54	-
Seven spans model										
F. No	**Seyhan**		**Çukurova**		**Ceyhan**		**Aladağ**		**Saimbeyli**	
10	-	0.65	-	0.66	-	0.66	-	0.66	-	0.66
9	1.53	0.74	1.52	0.74	1.52	0.74	1.52	0.75	1.52	0.75
8	1.34	0.82	1.35	0.81	1.35	0.81	1.34	0.81	1.34	0.81
7	1.23	0.86	1.23	0.86	1.23	0.86	1.23	0.86	1.23	0.86
6	1.16	0.90	1.16	0.90	1.16	0.90	1.16	0.90	1.16	0.90
5	1.11	0.93	1.11	0.94	1.11	0.93	1.11	0.94	1.11	0.93
4	1.07	0.98	1.07	0.98	1.07	0.98	1.07	0.98	1.07	0.98
3	1.02	1.09	1.02	1.09	1.02	1.09	1.02	1.09	1.02	1.09
2	0.92	1.84	0.92	1.84	0.92	1.84	0.91	1.85	0.91	1.84
1	0.54	-	0.54	-	0.54	-	0.54	-	0.54	-
<2.00										

V. CONCLUSION

Eleven of our provinces have been affected to a great extent by the recent simultaneous earthquakes centered in Kahramanmaraş. Adana was one of the provinces most affected by the earthquakes. For this reason, the building model analyzed in this study is assumed to be located in Adana province. At the same time, five different districts of Adana city are chosen to carry out the comparison between different locations.

In the earthquake analysis, L-shaped ten-storey buildings with five and seven spans in x direction were considered respectively. The SAP2000 structural analysis program was used to investigate the irregularities especially the torsional and soft storey irregularities in the structure.

According to the results obtained from the analysis;

- In the seven-span building model, it was observed that the torsional irregularity values in the Y earthquake direction exceeded the limit value specified in TBEC-2018.
- It was observed that the results obtained from the analysis did not change too much for the different locations considered in the study.
- No torsional irregularity occurred in the X earthquake direction for both five and seven span building models.
- Torsional irregularity occurred only in the Y earthquake direction and in the seven-span building model.
- By increasing the number of spans in the x direction, the building has become more irregular in plan. Thus, since the center of mass of the building and the center of rigidity of the vertical structural elements moved away from each other, the unwanted torsional effects occurred in the building.
- It was observed that the soft story irregularity values obtained in both earthquake directions for both five- and seven-span building models did not exceed the limit value specified in TBEC-2018. Therefore, no soft storey irregularity was found for the building models selected for analysis.

REFERENCES

[1] A. Akbaş, and Ö. Çalışkan, "Deprem etkisinde hasar alan betonarme yapıların düzensizlik türleri yönü ile incelenmesi," International Conference on Scientific and Academic Research. Vol. 1, pp. 428-435, Konya, Turkey, March, 2023.

[2] H. Erdem, "Burulma düzensizliğinin betonarme kirişler ve kolonlar üzerine etkileri," Nigde University Journal of Engineering Sciences, 5, 2, pp. 148-156, 2016.

[3] L. E. Firar, and İ. B. Günaydın, "Analysis and comparison of reinforced concrete structures with different package programs." Sciennovation 3.1, pp. 15-38, 2021.

[4] G. Özmen, "Plan Geometrisinin Burulma Düzensizliği Etkisi", Türkiye Mühendislik Haberleri, 410, pp. 37-41, 2000.

[5] T. İnan, and K. Korkmaz, "Düşey doğrultudaki yapı düzensizliklerinin incelenmesi." Erciyes Üniversitesi Fen Bilimleri Enstitüsü Fen Bilimleri Dergisi 28.3, pp. 240-248, 2012.

[6] H. Kasap, H. Qamarzadah, and N. Mert, "L tipi planlı betonarme yapılarda perdelerin plandaki konumlarının değişiminin binaların yapısal davranışına etkisinin incelenmesi," Ege 2. Uluslararası Uygulamalı Bilimler Kongresi, ISBN: 978-625-7341-18-9, pp. 76-95, İzmir, 2021.

[7] G. Özmen, K. Girgin, and Y. Durgun, "Torsional irregularity in multi-story structures," International Journal of Advanced Structural Engineering, 6, pp. 121–131, 2014.

[8] Ö. Çavdar, and A. Yolcu, "Mevcut bir okul binasının Türk Bina Deprem Yönetmeliği 2018'e göre yapısal düzensizliklerinin incelenmesi, " Ordu University Journal of Science and Technology, 8(2), pp. 153-164, 2018.

[9] TBDY (2018). Türkiye Bina Deprem Yönetmeliği, Deprem Etkisi Altında Binaların Tasarımı İçin Kurallar, Çevre ve Şehircilik Bakanlığı, Ankara.

[10] TS500, (2000). Betonarme Yapıların Hesap ve Yapım Kuralları. Türk Standartları Enstitüsü, Ankara.

[11] SAP2000, (2022). SAP 2000 (Structural Analysis Programme), ver 22, Computers and Structures Inc. Berkeley, USA.

[12] AFAD, Afet ve Acil Durum Yönetimi Başkanlığı, Türkiye Deprem Tehlike Haritası. https://tdth.afad.gov.tr/ (Erişim tarihi: 07.06.2023)

Estimation of the Unconfined Compressive Strength of Cement Stabilized Clay Using Artificial Neural Networks (ANN)

Z. ALMAHMODI[1], S. KHATRUSH[1], M. MEHMETOĞLU[1]

[1] Istanbul Gelisim University, Turkey, zainab25razaq@gmail.com*
[1] Istanbul Gelisim University, Turkey, sasmohamed@gelisim.edu.tr
[1] Istanbul Gelisim University, Turkey, Mashhadani@gelisim.edu.tr

Abstract **- Stabilization of clay soils is necessary in many civil engineering projects in order to increase strength, reduce settlement and also for other special purposes, especially when weak soils do exist. Soil treatment with cement is one of the most commonly used method, it is proved to be an efficient and effective chemical stabilization method due to its economic advantages and ease of use. In this research, Test data sets with a wide range of parameters were implemented in an Artificial Neural Networks (ANN) program in order to evaluate the unconfined compressive strength of cementations clay soils. The data were collected from the selected published laboratory experimental investigations conducted by many researchers to study the effect of various parameters on the strength improvement of cement treated clay. The selected data were chosen to represent a wide range of clayey soils obtained from different places around the world. The predictive model was developed using the artificial neural network tools in MATLAB software. The artificial neural network (ANN) technique was applied using the Levenberg-Marquardt algorithm to develop a model that predicts the unconfined compressive strength of cement treated clayey soils. The number of data sets for this study were (429) collected from (16) previous research studies. Eight input parameters were chosen as follows: Liquid limit (LL)%, Plasticity index (PI)%, Clay fraction (CF)%, Sand (S)%, silt (M)%, water content (Wc) % , curing time (Tm) in days and cement content (Cc)% The unconfined compressive strength (UCS) was chosen as one output parameter, then the data was normalized using the min-max method. In order to evaluate the performance of the predictive model developed in this study, the statistical analysis of the model was performed using regression (R2), mean square error (MSE), root mean square error (RMSE), and coefficient of efficiency (CE). Good correlation was obtained with regression (R2) of 0.897. Sensitivity analysis indicate that the cement content is mostly affecting the resulting soil strength (UCS) followed by water content, curing time and liquid limit. The rest of the variables show relatively lower impact.**

Keywords **- Artificial Neural Networks (ANN), cement stabilization, unconfined compressive strength, clay soil.**

I. INTRODUCTION

Fine grained soils especially Soft clay is considered as one of the problematic soils that requires attention during construction of any civil engineering project. This type of soils is commonly associated with a change in water content that leads to a reduction in shear strength and hence low bearing capacity. The behavior usually associated with a volume change that causes swelling, shrinkage and settlement which can cause severe damage to buildings and infrastructures [1]. Most of the constructions especially of buildings and roads are preferably build on the soil that is strong and stable. Nevertheless, in practice, it sometimes difficult to find natural soil that provided the desired strength and acceptable stiffness. Such less competent soils need a kind of treatment in order to improve their strength and stiffness. However, several types of soil stabilization have been widely practiced [2]. Soil stabilization is a method of improving soil properties and engineering performance by adding special cementing material, or other chemicals to natural soil to improve one or more of its geotechnical properties such as compressibility, strength, permeability, and durability [3]. The stabilization techniques that have been used over the years for soil remediation include physical, mechanical and chemical stabilization processes. Chemical stabilization is the process of soil stabilization by improving the engineering properties of the soil by adding a chemical additive to the soil, which changes the physical and chemical properties of the soil to be stabilized [4,5]. Cement is one of the oldest bonding agents used since the invention of the soil stabilization technique, which is the bonding of soil particles resulting from the interaction of cement particles with water, and they grow into crystals that can intervene with each other, which gives a high compressive strength [6]. There exist in the research literature large amount of experimental work previously conducted to improve the strength of clay soils by adding cement as a stabilizing agent. The results of many researches have demonstrated that the cement stabilization technique is improving the resulting strength of clay soils [7,8,9,10,11,12,13,14,15,16,17,18,19,20,21,22]. Their work covers a wide range of fine grained soils (i.e. silt and clay) from different places around the world using ordinary Portland cement (OPC). It is aimed in this study to apply a reliable technique in order to investigate the link between the several parameters which have a significant effect on the resulting strength of cement treated clayey soils generated from the large amount of data in the literature. Artificial neural network

(ANN) is a form of artificial intelligence that is a machine learning technology that can simulate the mechanism of the human brain. ANNs have been successfully applied to almost all aspects of geotechnical engineering problems and have shown predictive ability when compared to traditional methods [8]. The ANN technique is therefore applied to develop a strength prediction model in terms of the unconfined compressive strength (UCS) for different data samples collected from several previous studies involved the stabilization of clay soils using ordinary Portland cement.

A. Factors Affecting the Clay Stabilization with Cement

The purpose of chemical stabilization is to enhance soil stability by increasing the grain size of the soil material, reducing the plasticity index, swelling and shrinking potential, and provide cementation [23].The type of stabilizer used depends on the type of soil to be treated (plasticity, particle size distribution, clay content and minerals) mainly, properties of the soil to be improved, strength and durability required for the soil to be improved, cost and environmental conditions [10].Cement is one of the commonly used binders for soil stabilization since the invention of soil stabilization techniques in the sixties of the last century [2]. The strength of the soil increases when it is fixed with cement due to the occurrence of the same pozzolanic reaction. Cement soil stabilization process can be affected by several factors, including water-cement ratio, curing conditions [24,22,15,25]. In order to obtain a good bond, the cement particles should cover most of the soil particles to provide good contact between the cement particles and the soil and thus stabilize the soil effectively. The soil-cement mixture becomes a solid and strong substance when the cement is hydrated as the cement reacts with water and becomes hard [26,27]. Other factors also important such as the sample preparation method used for the cement treated clay which reflects the initial condition of the material to be stabilized and their water content. [15,25].

B. Artificial Neural Networks (ANN)

Artificial neural networks provide a way to describe artificial neurons to solve complex problems in the same way as the human brain [28]. In multilayer artificial neural networks, there are neurons that are laid out in a manner similar to human brain cells. Where each neuron is connected to other neurons with certain parameters, during the training process, information is distributed to these connection points so that the network can be recognized [29]. In artificial neural networks, the learning process is an important behavior for network training. The learning process is a technique for introducing network experience in this field to help them acquire decision-making skills based on real data and the knowledge gained. Thus, the artificial neural network will build a predictive model that can solve a specific problem by taking advantage of the learning ability it has previously acquired [30]. A multi-layer artificial neural network consists of three layers known as input, output, and hidden layers. The transmission of the signal from the input units to the output units. The intermediate layer between the input and output layers is the hidden layer in which all computations are performed during the network training process [31]. Using weights, the nodes are connected to each other, and the size of the weight determines the effect of the input variables on the output values [32]. Recently, the use of artificial neural networks (ANNs) has increased widely in many fields of engineering, especially geotechnical engineering [33]. Classification and prediction are the most common applications of supervised learning artificial neural networks. In supervised learning, both the actual input and output values are provided. After completing the training process, the output of the model will be compared with the desired output to reduce the difference between them. The classification focuses on determining which group the data belongs to, while prediction attempts to estimate a specific value based on the real data [31]. Nabeel S. Juwaied,(2018) [34]stated that Neural networks have a number of important properties for modeling a complex mechanical behavior: good generalization capability, universal function approximation capability, resistance to noisy or missing data, and accommodation of multiple nonlinear variables for unknown interactions. The ANN technique was applied in the field of geotechnical engineering for modelling problems related to Site characterization, Soil properties and behavior, foundations, slope stability, Earth retaining structures, soil liquefaction and other geotechnical engineering applications [35]. It is also stated that the use of ANN model may work as a simple and reliable predictive tool for deriving many geotechnical parameters of soil at the site without the need for excessive field tests [36]. Furthermore, it was concluded that the ANN model allows the development of a highly efficient predictive model by reducing the costs and time required to conduct laboratory or field tests [37]. Moreover, it was demonstrated that using the GMDH-type NN is an efficient method in obtaining a new empirical mathematical model to provide a reliable prediction of the strength parameters of soils [38]. Sarat Kumar Das et.al (2010) [39] has developed an artificial neural network model to predict the unconfined compressive strength (UCS) of cement-stabilized soils. The input parameters were liquid limit (LL), plasticity index (PI), clay fraction (CF)%, sand (S)%, gravel Gr (%), moisture content (MC), cement content (Ce), and compressive strength value unconfined compressive strength as an output parameter. The value of the correlation coefficient was (R2) = 0.851, while the value of coefficient of efficiency CE = 0.73. Van-Ngoc Pham [40] developed an ANN model to predict compressive strength in cement-treated sandy soil. The results of the statistical analysis showed that the proposed model developed in this study is accurate and reliable with a high correlation coefficient and low root mean square errors. It also demonstrated that the UCS prediction model met external criteria well; Hence it demonstrates the great potential of the predictive ability of ANN technique for geotechnical parameters.

II MATERIALS and METHODS

A. *Soil Data Collection*

This study uses the Levenberg-Marquardt algorithm (LMNN) to develop a predictive model for unconfined compressive strength (UCS). Prior to the development of this model, data for this study were collected from previous scientific research on clay soil samples treated in the laboratory with cement, as shown in Table 1. Where the number of samples reached 429 samples from 16 scientific researches for several varieties of clay soil taken from several regions around the world. Soil parameters that are expected to have the greatest effect on unconfined compressive strength were identified as observed from the literature review.

B. *Datasets*

The unconfined compressive strength (UCS) is the output Parameters required to be predicted in this study using artificial neural networks, and to obtain good and accurate prediction results, the input parameters must be chosen correctly and closely related to the output parameter. This study was conducted using the results of UCS considered as an output parameter. 8 input parameters were selected, liquid limit (LL)% , plasticity index (PI)% , clay fraction (CF)%, sand (S)%, silt (M) %, water content (Wc) % , curing time (Tm) in days and cement content (Cc)% . In Table 2, a statistical description of the data parameters of this study is presented. Statistical analysis can be performed by various methods to measure and evaluate the performance of prediction models. In this study, the value of regression (R2), mean squared error (MSE), root mean squared error (RMSE), and coefficient of efficiency (CE) of the predicted parameters were calculated in evaluating the performance of regression models.

C. Pre-Processing

In machine learning systems, data quality is often a major concern. In order to build a decent and widely applicable prediction model as possible, the independent variables must be normalized and unified within a certain range, in addition to eliminating the dependence of the variables on unity [38]. Therefore, normalization is performed, which is the method of transforming the data and limiting it within a certain range, and it is especially useful in neural networks, where once the data is normalized, the type of unit used will not affect the result [39]. Normalization is done using the min – max method in normalizing variables, due to its ability to ensure that all features are scaled in the same range and receive equal attention while training the artificial neural network. All data values are independent of their units [39]. Data were normalized using the following formula:

$$X_{norm} = \frac{x - min(x)}{max(x) - min(x)} \quad (1)$$

Where x and X_{norm} represent data value and normalized data, respectively.

III NEURAL NETWORK MODEL DEVELOPMENT

A. *Data Division*

The data were divided after normalization into two groups, training and testing. The proportion of the data was determined using the trial and error method in this work. The best ratio was chosen based on the performance of the resulting neural network, where the ratio that gives the lowest value of the mean squared error (MSE) and the highest correlation coefficient R2 in addition to the highest equivalence coefficient CE was taken as the best ratio for training neural networks. It was found that the ratio of 75% (320 data sets) and 25% (109 data sets) is the best ratio for training and testing, respectively.

B. *Define Neural Network Architecture*

A two-layer feed-forward network structure was used, one hidden layer of 10 neurons and one output layer. The input layer is not calculated because no calculations are performed in this layer. In a frontal neural network, there is no backward transmission of information, information is transmitted only in the forward pathway to the neurons of the next layer.

C. *Neural Network Training*

The MATLAB neural network toolkit was used to build the prediction model. As a first step both the corresponding input and output values were provided while training the neural network. One hidden layer was used as it gives better results, as shown in Figure 1. In addition to the feeding network, the standard Evenberg-Marquardt backpropagation algorithm was used to adjust the weights and bias, thus reducing the potential error. ' Trainlm ' is often used as the fastest back propagation algorithm and is suggested as a first choice learning algorithm. Although this training function is more memory consuming than other methods, it was chosen because of its fast computing power. For the transfer function we used the tangential sigmoid transfer function (TANSIG), which is the most common function.

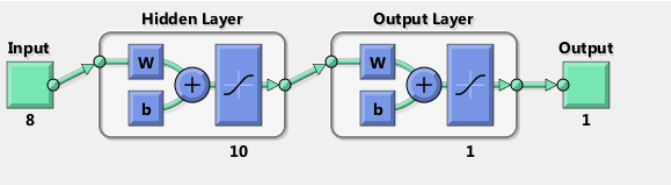

Figure 1: Implementation of FFBP ANN Model using MATLAB

D. *Model Performance Evaluation*

To evaluate the performance of the artificial neural network model developed in this study, the values of regression (R2), mean squared error (MSE), root mean squared error (RMSE), and coefficient of efficiency (CE) were calculated for the estimated and actual target parameters in evaluating the performance of the regression models. Where the values of (R2), (MSE), (RMSE), and (CE) are mathematically calculated as follows:

$$R^2 = 1 - \frac{\sum_{i=1}^{N}(y_{mea} - y_{pre})^2}{\sum_{i=1}^{N}(y_{mea} - y_m)^2} \quad (2)$$

$$MSE = \frac{\sum_{i=1}^{N}(y - y_{pre})^2}{N} \quad (3)$$

$$RMSE = \sqrt{\frac{\sum_{i=1}^{N}(y-y_{pre})^2}{N}} \quad (4)$$

$$CE = 1 - \frac{\sum_{i=1}^{N}(y_m-y_{pre})^2}{\sum_{i=1}^{N}(y_{pre}-y_{mea})^2} \quad (5)$$

Where:

y_m : actual output value .

y_{pre} : estimated output value .

y_{mea} : the average of actual output value .

N : represents the total number of data.

Table 1: Sources of research studies from which data were collected

Reference	Study area	Soil Classification
Uddin K. et.al (1997) [7]	Bangkok	Soft clay
Tugba E. (2015) [8]	Turkey	Soft clay
Jafer H. M. et.al (2016) [9]	UK	Silty clay
Chew S. H. et al (2004) [10]	Singapore	Marine clay
Obaid Q. J. et al (2019) [11]	India	Silty soil
Majeed Q. G. et.al (2021) [12]	Iraq	Soft clay
Yan-Jun Du et.al (2013) [13]	China	Kaolin clay
Preetham H. K. and Nayak S. (2019) [14]	India.	Marine clay
Rahman M. M. et al (2012) [15]	Bangladesh	Silty clay
Al-Jabban W. et al (2019) [16]	Sweden.	Sandy clayey silt
Mohammed O. A. et al (2017) [17]	(USA)	Silty clay
Narendra B.S. et al (2006) [18]	India	Sandy clayey + Silty clay
Alkiki I. M. et al (2021) [19]	Iraq	Silty clay
Verástegui Flores R. D. and Emidio Di G. (2010) [20]	U K	Kaolin clay
Thomas G. and Rangaswamy K. (2019) [21]	India	Silty clay
Lorenzo G. A. and Bergado D. T (2004) [22]	Bangkok	Silty clay

Table 2: Descriptive statistics of parameters.

Variable	Min	Max	Mean	Stand. Dev.
Liquid limit (L.L)%	33	105	65 .7	25.1
plasticity index (PI)%	8	62	37.6	18.1
Water content (Wc) %	11	250	90.7	59.8
clay fraction (CF)%	12	73	48.0	16.2
Silt (M) %	11	85	38.6	13.1
Sand (S) %	0	40	13.2	11.5
curing time (Tm) days	0	90	30.2	27.3
cement content (Cc)%	0	33.3	9.3	6.8
Unconfined Compressive Strength (UCS) (kpa)	5	1842	300.7	310.6

IV RESULTS AND DISCUSTIONS

The lowest prediction error and maximum correlation coefficient was obtained from the network with 10 hidden layer nodes. Figure 2 shows predictive capability of developed ANN model by plot of measured against predicted normalized unconfined compressive strength UCS, for the testing data sets. As seen, most of the predicted UCS are around the middle, showing good distribution of the results, indicating that the model has R2 of 0.897, MSE of 0.0024, RMSE of 0.049 and CE of 0.887 values. However, the predictive study model can be considered highly efficient after obtaining these values for the statistical analysis of the performance of the model, as the mean square error MSE value was low. Furthermore, values of R2 and CE indicates a highly efficient model. A minor deviation from the line of perfect equality shown in Figure 2 is an indication of a good relationship between the actual and predicted values of unconfined compressive strength UCS.

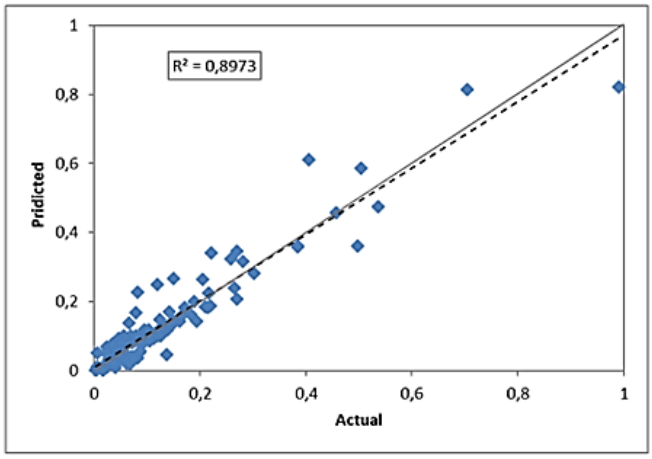

Figure 2: Regression relationship between the actual and predicted UCS data.

The adopted method of sensitivity analysis of the input variable is implemented based on the method described by (Barbara Mrzygłód, 2020) [41]after the network training process is completed and the network error is determined. The level of significance of input variables can be assessed by a way of eliminating them one at the time from the network input, re-implementing the training process and determining a new network error *Ei*. However, when a certain amount of data is rejected, an increase in the network error should be expected. Therefore, the basic measure of network sensitivity is the quotient W of the error obtained at the network startup for a data set without one variable *Ei* and the error obtained

for a dataset with all the variables *E*.

$$W = Ei / E \quad (6)$$

The quotient W is considered to represent the significant of each parameter as presented in Figure 3. It is clearly seen that the cement content Cc, have the a highly significant effect on the predicted UCS with a value equals to 43.73 followed by the effect of water content Wc of 12.71, curing time Tm of 9.49 and liquid limit LL of 7.96. The other variables PI, CF, M & S have relatively low effects ranging between 4.41 To 6.27 It is also seen that none of the implemented variables can be considered as completely insignificant.

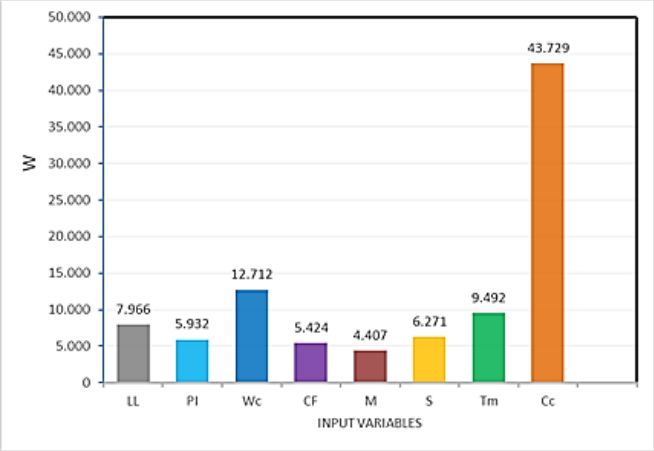

Figure 3: Results of sensitivity analysis presenting the relative importance of input variables

V CONCLUSIONS

A back-propagation neural network was used to demonstrate the feasibility of ANN to predict the unconfined compressive strength UCS of a cement treated clay based on 429 collected datasets from the literature used for development of the model. A feed-forward network with the Levenberg-Marquardt algorithm was used in the training stage. The optimal network was found to be 8 inputs, one hidden layer of 10 neurons, and one output. The results obtained in this study indicate that the model has ability to predict the unconfined compressive strength UCS with a highly acceptable degree of accuracy (R2 = 0.897). A sensitivity analysis was also carried out to study the relative importance of the factors, affecting lateral spreading. The sensitivity analysis indicates that the cement content is the most significant factor affecting the predicted UCS while water content and curing time have respectively moderate effect and the other factors have relatively lower impact.

REFERENCES

[1] S. Abdulkareem, & J. Abbas, " Effect of Adding Metakaolin Based Geopolymer to Improve Soft Clay Under Different Conditions," *in CONF. REC. 2021 IOP Conference Series: Earth and Environmental Science, pp. 2-3.*

[2] H. Hamzah, M. Abdullah, H. Yong , M. Zainol, & K. Hussin, "Review of Soil Stabilization Techniques : Geopolymerization Method One of the New Technique," *Trans Tech Publications.Key Engineering Materials, 298-299. (2015).*

[3] H. Afrin, "A Review on Different Types Soil Stabilization Techniques" . *International Journal of Transportation Engineering and Technology, Vol. 3, No. 2, 2017, pp. 19-24. July 2017.*

[4] A. Zahri, A. Zainorabidin, "An overview of traditional and non traditional stabilizer for soft soil" . *in CONF. REC. 2021 IOP Conference Series: Materials Science and Engineering, pp. 1-6. (2019).*

[5] G. Archibong , E.Sunday, J.Akudike and O.Okeke ,"A REVIEW OF THE PRINCIPLES AND METHODS OF SOIL STABILIZATION," *International Journal of Advanced Academic Research, pp.89-113. (2020).*

[6] H.Solihu ,"Cement soil stabilization as an improvement technique for rail track subgrade, and highway subbase and base courses: A review." *Journal of Civil and Environmental Engineering 10.3 : PP. 1-8, June (2020).*

[7] K.Uddin, A.S.Balasubramaniam, and D.T.Bergado. "Engineering behavior of cement-treated Bangkok soft clay," *Geotechnical Engineering 28 :pp. 89-119 (1997).*

[8] T. Eskisar, "Influence of cement treatment on unconfined compressive strength and compressibility of lean clay with medium plasticity." *Arabian Journal for Science and Engineering 40: 763-772. (2015).*

[9] H.M. Jafer, K. Hashim, W. Atherton and A. Alattabi, "A Statistical Model for the Geotechnical Parameters of Cement-Stabilised Hightown's Soft Soil: A Case Study of Liverpool, UK." *International Journal of Civil, Environmental, Structural, Construction and Architectural Engineering 10.7 : 885-890.(2016)*

[10] S.H. Chew, A.H.M. Kamruzzaman , and F. H. Lee. "Physicochemical and engineering behavior of cement treated clays." *Journal of geotechnical and geoenvironmental engineering 130.7 : 696-706 July(2004).*

[11] O.Q.Jan, and S. Raj. "Strength Behavior of Cement Stabilized Karewa Soil." *Springer, pp. 273-281, 2019.*

[12] Q.G. Majeed, A.M. Shihab , J.M. Abbas and S. SH. Sammen, "Improving the Characteristics of a Soft Clay Soil Using Cement Activated Low-Calcium Fly Ash." *Diyala Journal of Engineering Sciences Vol (14)n=No 3: pp. 8-22 (2021).*

[13] Y. Du, N. Jiang , S. Liu , F Jin , D. Singh and A. Puppala , "Engineering properties and microstructural characteristics of cement-stabilized zinc-contaminated kaolin." *Canadian Geotechnical Journal pp. 289-302, (2014).*

[14] H. K. Preetham and S. Nayak. "Geotechnical investigations on marine clay stabilized using granulated blast furnace slag and cement." *International Journal of Geosynthetics and Ground Engineering , pp. 1-12.(2019).*

[15] M. M. Rahman, A. Siddique, and M. K. Uddin , "Clay-water/cement ratio is the prime parameter for fine grained soil improvement at high water content" . *DUET Journal, Vol.1 Issue 3 , June 2012.*

[16] W. Al-Jabban, J. Laue , S. Knutsson and N. Al-ansari, "A comparative evaluation of cement and by-product petrit T in soil stabilization." *Applied Sciences 9.23 : 5238 (2019).*

[17] M.O.A Bazne , F. Vahedifard, and I. L. Howard. "Effects of light cement stabilization on properties of fine grained dredged soils." *Geotechnical Testing Journal (2018).*

[18] B.S. Narendra, P.V. Sivapullaiah, S. Suresh and S.N. Omkar " Prediction of unconfined compressive strength of soft grounds using computational intelligence techniques: A comparative study " *Elsever : Computers and Geotechnics 33(3):196-208 April 2006*

[19] I.M. Alkiki, M. D. Abdulnafaa and A. Aldaood "Geotechnical and other characteristics of cement-treated low plasticity clay" *Soils and Rocks journal 44(1):1-13 March 2021*

[20] R. D. V. Flores , G. D. Emidio and W.F.V Impe "Small-Strain Shear Modulus and Strength Increase of Cement-Treated Clay" *Geotechnical Testing Journal January 33(1):62 2010.*

[21] A. G. Thomas & B. K. Rangaswamy, "Strength behavior of enzymatic cement treated clay," *International Journal of Geotechnical Engineering, 2-15(2019).*

[22] G. A. Lorenzo and D. T. Bergado, "Fundamental Parameters of Cement-Admixed Clay—New Approach" *Journal of Geotechnical and Geoenvironmental Engineering 130(10) October 2004.*

[23] A. A. Fondjo, , E. Theron, and R. P. Ray. "Stabilization of expansive soils using mechanical and chemical methods: a comprehensive review." *Civil Engineering and Architecture 9(5) :pp. 1295-1308 (2021).*

[24] S. Sasanian, T.A.Newson, ~Basic parameters governing the behavior of cement-treated clay 'Soils and Foundations2014;54(2):209–224

[25] G. Kang , Y. Kim , J. Kang ," Predictive strength model of cement-treated fine-grained soils using key parameters: Consideration of the total water/cement and soil/cement ratios" *Case Studies in Construction Materials 18 (2023).*

[26] CH.M.Geiman, . "Stabilization of soft clay subgrades in Virginia phase I laboratory study. Diss." *master dissertation, Dept. Civil Eng. Virginia Univ. Blacksburg , 2005.*

[27] S. D.Rafalko, G.M.Filz , T.L. Brandon and J.K. Mitchell "Rapid chemical stabilization of soft clay soils." *Transportation research record 2026.1 : pp. 39-46(2007).*

[28] Y. Huang "Advances in artificial neural networks–methodological development and application." *MDPI journal : Algorithms 2.3 : pp. 973-1007(2009).*

[29] M.M. Mijwel "Artificial neural networks advantages and disadvantages." *Researchgate Jan. (2018).*

[30] S. Karsoliya, "Approximating number of hidden layer neurons in multiple hidden layer BPNN architecture." *International Journal of Engineering Trends and Technology VOL.3 ISSUE.6 :PP. 714-717(2012).*

[31] A.Abraham, "Artificial neural networks." *Handbook of measuring system design (2005).*

[32] Ph.Kim, "Matlab deep learning." With machine learning, neural networks and artificial intelligence *130.21 (2017).*

[33] M.A.Shahin, M. B. Jaksa, and H. R. Maier. "Artificial neural network applications in geotechnical engineering." *Australian geomechanics 36.1 :PP. 49-62 (2001).*

[34] N.S. Juwaied," APPLICATIONS OF ARTIFICIAL INTELLIGENCE IN GEOTECHNICAL ENGINEERING" *ARPN JOURNAL OF ENGINEERING AND APPLIED SCIENCES , VOL. 13, NO. 8, APRIL 2018.*

[35] M. Kim, O. Okuyucu , E. Ordu , S. Ordu , Ö.Arslan and J.Ko, "Prediction of Undrained Shear Strength by the GMDH-Type Neural Network Using SPT-Value and Soil Physical Properties." *MDPI journal : Materials pp. 15.18 : 6385(2022).*

[36] S. K. Das , P. Samui, and A. K. Sabat. "Application of artificial intelligence to maximum dry density and unconfined compressive strength of cement stabilized soil." *Geotechnical and Geological Engineering 29: 329-342 (2011).*

[37] V. Pham, H.Do , E. Oh and D. Ong "Prediction of unconfined compressive strength of cement-stabilized sandy soil in Vietnam using artificial neural networks (ANNs) model." *International Journal of Geotechnical Engineering 15.9 : 1177-1187(2021).*

[38] B.Mrzygłód , M. Hawryluk , M.Janik , I.Olejarczyk-Wożeńska "Sensitivity analysis of the artificial neural networks in a system for durability prediction of forging tools to forgings made of C45 steel" *The International Journal of Advanced Manufacturing Technology 109:pp.1385–1395(2020)* .

Steady State Seepage Analysis of Dam Foundation Made of Different Layers

T. A. ASLAN[1] and B. TEMEL[1]

[1] Cukurova University, Adana/Turkey, taslan@cu.edu.tr
[1] Cukurova University, Adana/Turkey, btemel@cu.edu.tr

***Abstract* - In this study, the steady-state seepage problem of dam foundations made of different layers has been investigated. Equations obtained by using Darcy's law and continuity equations are solved by finite element method (FEM) based on Galerkin's method. A program written in the Fortran programming language has been utilized for the solution process. The paper presents the determination of hydraulic head, pore water pressure values, uplift pressure beneath the dam, and seepage quantities for dam foundations with different layers. To verify and ensure the accuracy of the written programs, the suggested method results are compared with those obtained from SEEP/W, a finite element CAD software.**

Keywords - Steady-state seepage, Galerkin method, Fortran program, Uplift pressure, Seep/w program.

I. INTRODUCTION

Dams are crucial engineering structures. Seepage can lead to stability issues in dams, which may ultimately result in their collapse. Therefore, seepage in dams is of great significance and is extensively studied by numerous researchers.

Mesci [1] examined the methods applied to find the seepage quantity in the dam body in his thesis. In addition, flow lines and equipotential lines were calculated and assessed graphically. El-Jumaily and Al-Bakry [2] investigated the seepage problem in dams with heterogeneous foundations using the finite volumes method. Moharrami et al. [3] centered on a numerical approach to assessing the effectiveness of cutoff wall systems in addressing uplift pressure and piping issues. Çalamak et al. [4] reviewed the effects of blanket, chimney, and toe drains on seepage in dams, assessing their performance in separate cases for different material types and geometric characteristics. Ullah et al. [5] utilized SEEP/W software to model the seepage quantity at the Baz Ali small dam. For the 2D steady-state seepage flow problem of water through the soil beneath an impermeable dam the singular function boundary integral method (SFBIM) was implemented by Elliotis [6]. Arshad et al. [7] used SEEP/W to develop a finite element model for a non-homogeneous earth dam in their study. Chouireb and Djehiche [8] modeled seepage flows in earth dams equipped with a vertical drainage system and compared the results with observed data (case study: Harreza Dam, Algeria). Zhang et al. [9] aimed to solve the seepage analysis of a concrete dam foundation consisting of different soil layers using the flow network method. Norouzi et al. [10] conducted a study considering various parameters to examine the seepage phenomenon at the foundation of Sabalan Dam. Wang et al. [11] suggested the FE-Meshfree method for performing steady-state seepage analysis. The seepage analyses for the dam body and foundation were conducted by Çoşkun [12] using the Steady State Groundwater module within the Slide program. Polater [13] aimed to perform seepage analysis for embankment dams using different impermeable materials. Farhadian et al. [14] examined the seepage analysis of the Peygham-Chay Dam using the SEEP program and investigated the effect of Cutoff Walls on seepage. Chen et al. [15] established a three-dimensional finite element model of a typical earth dam with a polymer cutoff wall using numerical simulation technology to analyze the impact of the number, location, and random defects in the wall on the seepage characteristics. Abokwiek et al. [16] investigated the seepage event occurring at the dam foundation, taking into account various parameters such as dam dimensions like width and depth, reservoir water level, soil permeability, and ambient temperature. Charrak et al. [17] studied the seepage beneath the Sidi Abdelli earth dam, considering various parameters such as discharge seepage, exit gradient, and uplift pressure.

As a result of the investigations carried out by the researchers, many studies have been encountered that examined the steady-state seepage phenomenon occurring in dams with different methods and programs. However, no study has been found that examines the seepage problem occurring in dams with foundations consisting of layers using the FEM based on the Galerkin method.

II. MATHEMATICAL FORMULATIONS

The 2D steady-state seepage within a permeable, anisotropic soil is mathematically represented through the subsequent partial differential equation, employing Darcy's principle and continuity equations, as referenced in [18].

$$K_x(\partial^2 h)/(\partial x^2) + K_z(\partial^2 h)/(\partial z^2) = 0 \quad (1)$$

In this context, K_x and K_z represent the hydraulic conductivity coefficients in the x and z directions, while h signifies the total hydraulic head.

The total hydraulic head value is expressed as the sum of the elevation head and the pressure head, as the velocity head is neglected due to the very slow movement of water in the ground.

$$h = z + p/\gamma_w \quad (2)$$

The partial differential form of eq. (1) is transformed into integral form by employing the weighted residuals method as depicted below:

$$\int\int_{A_e} \psi\left(K_x(\partial^2 h)/(\partial x^2) + K_z(\partial^2 h)/(\partial z^2)\right) dA = 0 \tag{3}$$

Eq. (4) is derived by applying partial integration to eq. (3).

$$\int\int_{A_e} \left(K_x(\partial\psi/\partial x)(\partial h)/(\partial x) + K_z(\partial\psi/\partial z)(\partial h)/(\partial z)\right) dxdz - \int_{\Gamma} \psi\left((\partial h/\partial x)n_x + (\partial h/\partial z)n_z\right) d\sigma = 0 \tag{4}$$

Here, the second part of the equation specifies the boundary conditions. In the Galerkin formulation, the variation of the hydraulic load is taken as weight functions.

$$\psi = \delta h \tag{5}$$

After substituting the weight functions, the element integral form is transformed into matrix form.

$$\int\int_{A_e} \left(K_x(\partial(\delta h)/\partial x)(\partial h)/(\partial x) + K_z(\partial(\delta h)/\partial z)(\partial h)/(\partial z)\right) dxdz - \int_{\Gamma} (\delta h) q d\sigma = 0 \tag{6}$$

The FEM stands as a highly efficient numerical technique. It entails dividing the problem domain into multiple elements of restricted dimensions and offering approximations for the system's nodes. In this particular investigation, an isoparametric 8-noded serendipity element is utilized in the formulation. Eq. (7) furnishes the hydraulic head values at any location within the element.

$$\{h\} = \begin{bmatrix} N_1 N_2 N_3 N_4 N_5 N_6 N_7 N_8 \end{bmatrix} \begin{Bmatrix} h_1 \\ h_2 \\ h_3 \\ h_4 \\ h_5 \\ h_6 \\ h_7 \\ h_8 \end{Bmatrix} = [N]\{h\} \tag{7}$$

here, *[N]* denotes the matrix of shape functions, and *{h}* represents the vector of element hydraulic heads. The coordinates of any point inside the quadratic element are determined according to the shape functions

$$x = \sum_{i=1}^{8} N_i x_i \qquad z = \sum_{i=1}^{8} N_i z_i \tag{8}$$

here x_i and z_i are the coordinates of a node. For the chosen isoparametric element, the geometric shape functions are the same as the interpolation shape functions. Therefore, the hydraulic load at any point within the element is calculated from the element node loads based on the shape functions.

$$h(\xi,\eta) = \sum_{i=1}^{8} N_i(\xi,\eta) h_i \tag{9}$$

Substituting Eq. (7) into Eq. (6) the element integral form takes the following equation form.

$$\int\int_{A_e} (\partial(\delta h)/\partial x) \begin{pmatrix} K_x(\partial[N]\{h\})/(\partial x) \\ +(\partial(\delta h)/\partial z) K_y(\partial[N]\{h\})/(\partial z) \end{pmatrix} dxdz - \int_{\Gamma} (\delta h) q d\sigma = 0 \tag{10}$$

Eq.(10) is based on the hydraulic head gradient vector. This vector can be calculated through the *[B]* matrix, which includes the derivatives of the interpolation functions.

$$\{gv\} = \begin{Bmatrix} \partial h/\partial x \\ \partial h/\partial z \end{Bmatrix} = \begin{bmatrix} \partial[N]/\partial x \\ \partial[N]/\partial z \end{bmatrix} \{h\} = [B]\{h\} \tag{11}$$

Accordingly, the variations of the hydraulic load are as in eq. 12.

$$\delta h = N\{\delta h\} \qquad \delta h^T = N\{\delta h\}^T \tag{12}$$

Substituting of eqs. (11-12) into eq. (10). It results in

$$\int\int_{A_e} (\partial(\delta h)/\partial x) \begin{pmatrix} K_x(\partial[N]\{h\})/(\partial x) \\ +(\partial(\delta h)/\partial z) K_z(\partial[N]\{h\})/(\partial z) \end{pmatrix} dxdy - \int_{\Gamma} (\delta h) q d\sigma = 0 \tag{13}$$

The eq. (13) is presented in its simplified form as follows:

$$\{\delta\Delta\}^T \left(\int\int_{A_e} \left([B]^T [K][B]\right) dA \{h\} \right) - \int_{\Gamma} [N]^T q d\sigma = 0 \tag{14}$$

where $[K]$ is defined as the conductivity matrix. The element seepage matrix, $[g_e]$, and the element applied flux vector, $\{f_s\}$ are:

$$[g_e]_{(8*8)} = \int\int_{A_e} \left([B]^T [K][B]\right) dA \; ; \; \{f_s\}_{(8*1)} \int_{\Gamma} [N]^T q d\sigma \tag{15}$$

The typical expression of the finite element equation used in the analysis of steady-state seepage is

$$[g_e]\{h\} = \{f_s\} \quad (16)$$

For the analyzed flow region, with the help of the coding technique, the contributions of the elements are taken to create the system conductance matrix and system load vector.

$$[G]\{H\} = \{F\} \quad (17)$$

where *[G]* is the global seepage matrix, $\{H\}$ is the system hydraulic head vector and {F} is the system load vector for all nodes. By performing a numerical solution under specified boundary conditions, the total hydraulic head at nodal points is determined. Subsequently, the Seepage rate per unit width and pressures value can be readily.

III. Numerical Examples and Discussion

In this section, the steady-state seepage problem in dams consisting of layered foundations has been investigated with FEM based on Galerkin method and SEEP/W [19] program. Additionally, seepage rate per unit width, hydraulic head, pore water pressure values, and uplift pressure beneath the dam have been determined using the suggested method and provided in tabular form.

In this study, the seepage phenomenon occurring at the foundation of the dam geometry provided in Fig. 1 ([20]) has been investigated. Various layer conditions have been considered in the seepage analysis, which encompasses four different cases (Fig. 2).

The material and geometric properties of various soil layers in the dam foundation are presented in Table 1.

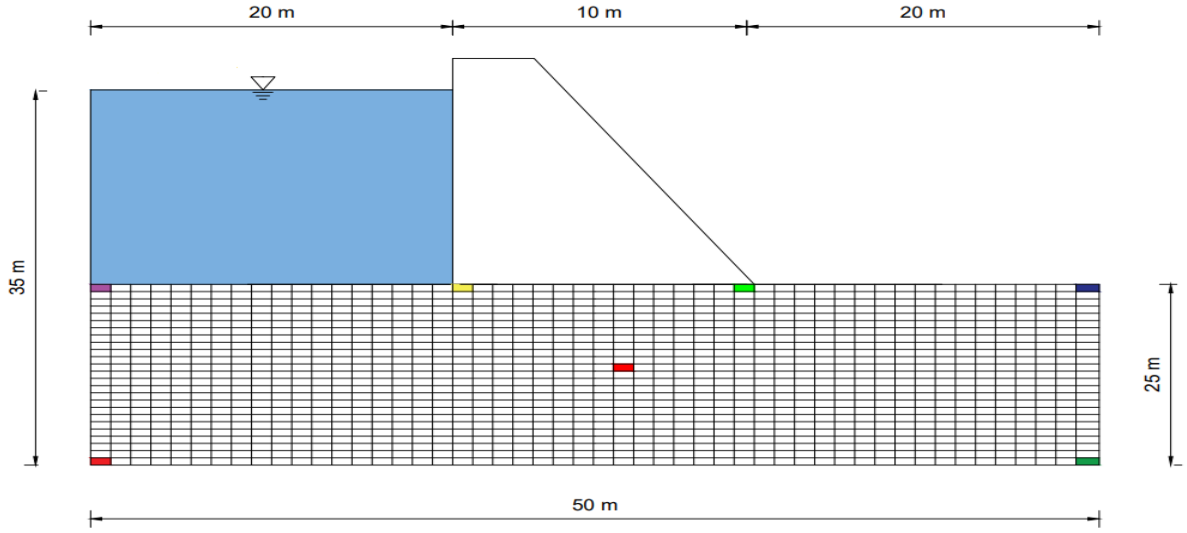

Fig.1 Geometric properties of the dam foundation.

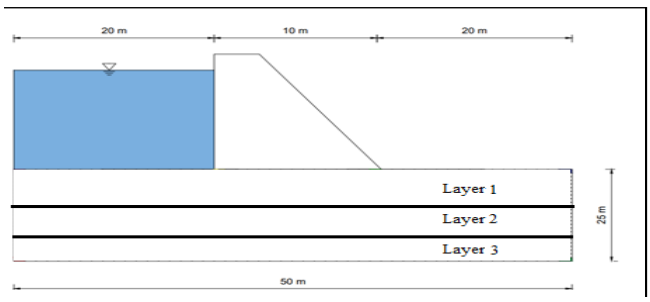

Case A

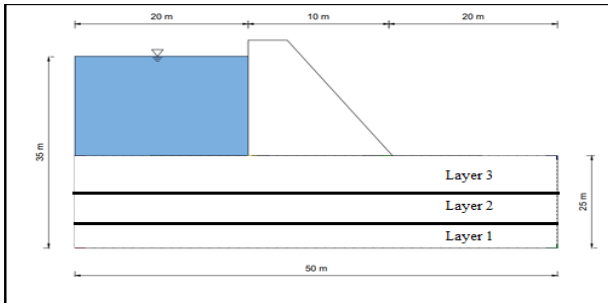

Case B

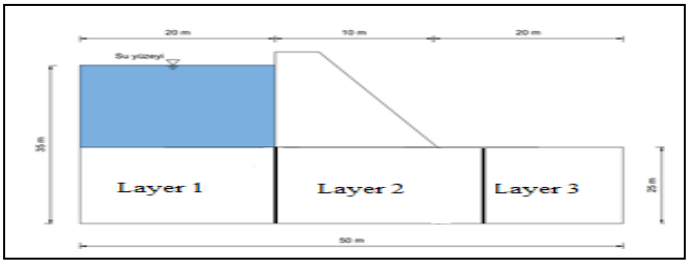

Case C

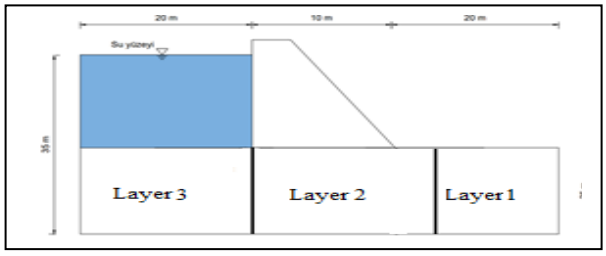

Case D

Fig. 2 Geometry and material properties of the dam for different case

The Seepage rate per unit width of the dam foundation, calculated by FEM based on the Galerkin method, is given in Table 2 with the results obtained from the SEEP/W program.

It can be seen clearly in Table 2 that the proposed method results are in excellent agreement with SEEP/w. Additionally, from Table 2 it can be observed that the highest seepage rate occurs in Case D.

Table 1. Materials and geometry properties of dam foundation different soil layers.

		Case A		Case B		Case C		Case D	
Layer	**Permeability Coefficient K_x, K_z (m/s)**	**Height (m)**	**Length (m)**	**Height (m)**	**Length (m)**	**Height (m)**	**Length (m)**	**Height (m)**	**Length (m)**
1	10^{-7}	10	50	5	50	25	20	25	10
2	10^{-6}	10	50	10	50	25	20	25	20
3	10^{-5}	5	50	10	50	25	10	25	20

Table 2. Calculation results of Seepage rate per unit width of different soil layers. ($m^3/s/m$)

	Seep/W[13]	**Present Study**
Case A	1.220 E-06	1.212 E-06
Case B	5.630 E-06	5.627 E-06
Case C	3.885 E-06	3.898 E-06
Case D	9.481 E-06	9.478E-06

The hydraulic head and pressure values of the dam have been computed and are presented in Table 3 for the locations at the ends and the midpoint of the foundation (1, 50, 1200, 1250), as well as for the two elements (1221, 1231) situated beneath the downstream and upstream areas of the structure.

One of the most critical factors related to the safety and stability of hydraulic structures is uplift force. Uplift pressure beneath hydraulic structures applies an upward force against dam foundations due to seepage beneath the hydraulic structure. This uplift pressure, which exerts forces upward against the structure's foundations, is known as the uplift force. If the uplift force cannot be balanced with the weight of the soil, it can lead to stability issues. Therefore, by calculating the uplift pressure, the uplift force acting on the structure is determined and presented in Fig.3 and Table 4.

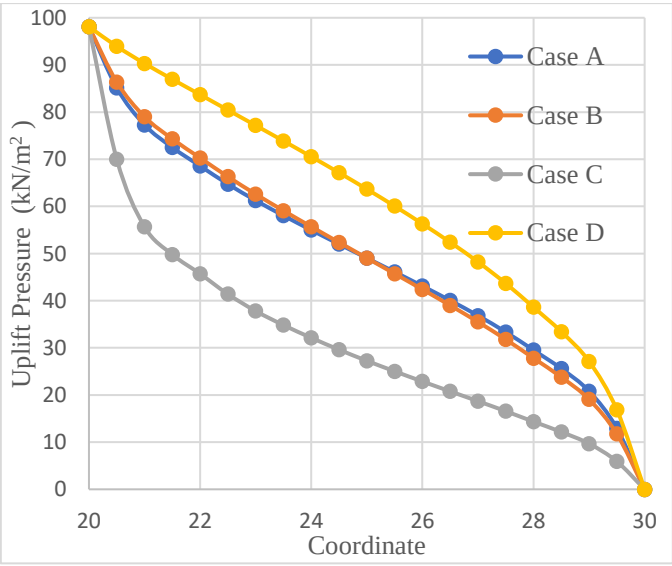

Fig. 3 The uplift force acting on the dam

As mentioned earlier, when designing a hydraulic structure, it is essential to consider the seepage issue and ensure that the uplift force is balanced with the structure's weight.

CONCLUSIONS

In this study, 2D steady-state seepage analysis in the dam foundation consisting of different soil layers has been carried out using the FEM based on the Galerkin approach. Moreover, For dam foundations with different layers, hydraulic head, pore water pressure values, uplift pressure beneath the dam, and seepage quantities have been determined and presented in tabular form. The prepared Fortran program has demonstrated that it can be easily and effectively applied to layered environments.

REFERENCES

[1] S.B. Mesci. Dolgu baraj gövdelerindeki sızmaların ve freatik hattın incelenmesi: Seferihisar barajı uygulaması. Yüksek Lisans Tezi, İstanbul Teknik Üniversitesi, 2006.

[2] K.K. El-Jumaily, and J.M.H. Al-bakry, Seepage analysis through and under hydraulic structures applying finite volume method, *Eng. Tech.J.*. 9, 1719-1731, 2013.

[3] A. Moharrami, G. Moradi, M.H. Bonab, J. Katebi, G. Moharrami performance of cutoff walls under hydraulic structures against uplift pressure and piping phenomenon, *Geotech Geol. Eng.* 33, 95–103, 2015.

[4] M., Çalamak, A.N. Yılmaz, A.M. Yanmaz, Performance evaluation of ınternal drains of earthen dams, *J. Perform. Constr. Facil.*,32(6): 04018085, 2018.

[5] A. Ullah, A. Kassım. I. Alam, M. Junaıd, I.Z. Ahmad. Efficiency analysis of seepage of Baz Ali small dam, Kurram Agency using clay blanket and cut-off wall with sand filter. Bulletin of the Geological Society of Malaysia, 67, 113 – 118, 2019.

[6] M.C. Elliotis A mathematical model for a steady-state seepage flow of groundwater under a reinforced concrete damApplied Computing and Geosciences 1 (2019) 100003

[7] I. Arshad, M.M. Babar, C.A.E. Vallejera, Computation of seepage and exit gradient through a non-homogeneous earth dam without cut-off walls by using geo-slope (seep/w) software, *PSM Biol. Res.* 4(1), 40-50, 2019.

[8] M. Chouireb, A. Djehiche, Simulation of seepage flow through an earthen dam with vertical drain and comparison of results with observations data (case study: Harreza Dam-Algeria), *Arabian Journal of Geosciences.* 12, 406, 2019.

[9] M. Zhang, D. Yao, H. Lu. and H. Wang. Solution of seepage field in different soil layers of concrete dam foundation by flow net method. IOP Conf. Series: Earth and Environmental Science 546 (2020) 052053.

[10] R. Norouzi, F. Salmasi, H. Arvanaghi, Uplift pressure and hydraulic gradient in Sabalan Dam, *Applied Water Science*. 10:111, 2020.

[11] B. Wang, J. Li, G. Jiang, Y. Yang, X.T. Feng, 2020.An improved Fe-meshfree method for solving steady seepage problems, *Computers and Geotechnics*. 119:103223, 2020.

[12] K. Çoşkun, *Dolgu barajlarda gövde stabilitesi ve Çukurca barajı örneği*, Yüksek Lisans Tezi, Karabük Üniversitesi, 2021.
[10] Polater Ö, 2021. Dolgu Barajların Farklı Geçirimsiz Malzemeler Kullanılarak Sızma Analizi.. Lisans Tezi, Bitlis Eren Üniversitesi, 53 s.
[14] H. Farhadian, Z. Maleki, S. A. Eslaminezhad, Assessment of the optimum depth of sealing cutoff walls in the clay core of Peygham-Chay dam, *J. Hydraul. Struct*.. 7(1), 59 -76, 2021.
[15] Y. Chen, B. Xue, S. Zhang, X. Du, M. Shi, . Seepage characteristics analysis on earth dams considering polymer cutoff wall with construction defects, *Sustainability*. 14, 11879, 2022.
[16] R. Abokwiek, M. Al Sharabati, R. Hawileh, J.A. Abdalla, R. Sabouni, G.A. Husseini, A finite element model for the analysis of seepage flow of water under concrete dams, *Geotech Geol Eng*.. 40, 2823–2841, 2022.
[17] Charrak, Hicham, Nadia Smail, and Bouchrit Rouissat. "Influence of combination of the cutoff wall and horizontal drainage on seepage characterization in earth dam foundations." Indian Geotechnical Journal (2023): 1-16.
[18] A.E.Harr, *Groundwater and Seepage*, McGraw-Hill B Company, 1962.
[19] Seepage Modeling with SEEP/W An Engineering Methodology July 2012 Edition GEO-SLOPE International Ltd. Calgary, Alberta, Canada.
[20] T. A. Aslan, B. Temel. Finite element analysis of the seepage problem in the dam body and foundation based on Galerkin's approach. European Mechanical Science (2022), 6(2): 143-151.

Table 3. Hydraulic head and pressure load values of the dam with different soil layers

			Case A		Case B		Case C		Case D	
NODE	**X (m)**	**Y (m)**	**Hydraulic Head (m)**	**Pressure Head (m)**	**Hydraulic Head (m)**	**Pressure Head (m)**	**Hydraulic Head (m)**	**Pressure Head (m)**	**Hydraulic Head (m)**	**Pressure Head (m)**
1	0.0	0.0	30.178	30.178	33.808	33.808	29.757	29.757	34.618	34.618
2	0.5	0.0	30.178	30.178	33.807	33.807	29.755	29.755	34.618	34.618
3	1.0	0.0	30.178	30.178	33.802	33.802	29.748	29.748	34.617	34.617
99	49.0	0.0	29.822	29.822	26.198	26.198	25.232	25.232	30.432	30.432
100	49.5	0.0	29.822	29.822	26.193	26.193	25.232	25.232	30.425	30.425
101	50.0	0.0	29.822	29.822	26.192	26.192	25.232	25.232	30.422	30.422
102	0.0	0.5	30.178	29.678	33.81	33.31	29.759	29.259	34.618	34.118
103	1.0	0.5	30.178	29.678	33.804	33.304	29.751	29.251	34.617	34.117
151	49	0.5	29.822	29.322	26.196	25.696	25.232	24.732	30.429	29.929
152	50	0.5	29.822	29.322	26.19	25.69	25.232	24.732	30.42	29.92
153	0.0	1.0	30.179	29.179	33.815	32.815	29.766	28.766	34.618	33.618
154	0.5	1.0	30.179	29.179	33.813	32.813	29.764	28.764	34.618	33.618
155	1.0	1.0	30.178	29.178	33.808	32.808	29.757	28.757	34.618	33.618
251	49.0	1.0	29.822	28.822	26.192	25.192	25.232	24.232	30.422	29.422
252	49.5	1.0	29.822	28.822	26.187	25.187	25.231	24.231	30.416	29.416
253	50.0	1.0	29.821	28.821	26.185	25.185	25.231	24.231	30.413	29.413
1873	24.0	12.0	30.035	18.035	30.343	18.343	26.755	14.755	33.119	21.119
1874	24.5	12.0	30.017	18.017	30.172	18.172	26.713	14.713	32.961	20.961
1875	25.0	12.0	30	18	30	18	26.668	14.668	32.805	20.805
1950	24.0	12.5	30.037	17.537	30.353	17.853	26.79	14.29	33.087	20.587
1951	25.0	12.5	30	17.5	30	17.5	26.699	14.199	32.763	20.263
2025	24.0	13.0	30.039	17.039	30.363	17.363	26.827	13.827	33.054	20.054
2026	24.5	13.0	30.019	17.019	30.182	17.182	26.78	13.78	32.886	19.886
2027	25.0	13.0	30	17	30	17	26.731	13.731	32.72	19.72

Table 3. Hydraulic head and pressure load values of the dam with different soil layers

			Case A		Case B		Case C		Case D	
NODE	**X (m)**	**Y (m)**	**Hydraulic Head (m)**	**Pressure Head (m)**	**Hydraulic Head (m)**	**Pressure Head (m)**	**Hydraulic Head (m)**	**Pressure Head (m)**	**Hydraulic Head (m)**	**Pressure Head (m)**
3649	0.0	24.0	34.553	10.553	34.942	10.942	34.641	10.641	34.974	10.974
3650	0.5	24.0	34.553	10.553	34.942	10.942	34.64	10.64	34.974	10.974
3651	1.0	24.0	34.553	10.553	34.942	10.942	34.64	10.64	34.974	10.974
3689	20	24.0	33.497	9.497	33.7	9.7	30.89	6.89	34.847	10.847
3690	20.5	24	33.151	9.151	33.357	9.357	30.826	6.826	34.52	10.52
3691	21.0	24	32.659	8.659	32.876	8.876	30.217	6.217	34.182	10.182
3710	30.5	24	26.162	2.162	25.968	1.968	25.468	1.468	26.485	2.485
3711	31.0	24	25.984	1.984	25.787	1.787	25.375	1.375	26.245	2.245
3747	49.0	24	25.447	1.447	25.058	1.058	25.016	1.016	25.37	1.37
3748	49.5	24	25.447	1.447	25.058	1.058	25.016	1.016	25.369	1.369
3749	50.0	24	25.447	1.447	25.058	1.058	25.016	1.016	25.368	1.368
3750	0.0	24.5	34.777	10.277	34.971	10.471	34.82	10.32	34.987	10.487
3751	1.0	24.5	34.777	10.277	34.971	10.471	34.82	10.32	34.987	10.487
3770	20.0	24.5	34.065	9.565	34.181	9.681	32.274	7.774	34.91	10.41
3771	21.0	24.5	32.877	8.377	33.057	8.557	30.731	6.231	34.204	9.704
3780	30.0	24.5	25.935	1.435	25.819	1.319	25.405	0.905	26.208	1.708
3781	31.0	24.5	25.499	0.999	25.4	0.9	25.191	0.691	25.631	1.131
3799	49.0	24.5	25.223	0.723	25.029	0.529	25.008	0.508	25.185	0.685
3800	50.0	24.5	25.223	0.723	25.029	0.529	25.008	0.508	25.184	0.684
3801	0.0.	25	35	10	35	10	35	10	35	10
3802	0.5	25	35	10	35	10	35	10	35	10
3803	1.0	25	35	10	35	10	35	10	35	10
3841	20.0	25	35	10	35	10	35	10	35	10
3842	20.5	25	33.68	8.68	33.803	8.803	32.137	7.137	34.576	9.576
3843	21.0	25	32.878	7.878	33.054	8.054	30.676	5.676	34.206	9.206
3861	30.0	25	25	0	25	0	25	0	25	0
3862	30.5	25	25	0	25	0	25	0	25	0
3863	31.0	25	25	0	25	0	25	0	25	0
3899	49.0	25	25	0	25	0	25	0	25	0
3900	49.5	25	25	0	25	0	25	0	25	0
3901	50.0	25	25	0	25	0	25	0	25	0

Table 4. The Uplift Force Acting on the Dam

		Case A			**Case B**			**Case C**			**Case D**		
X (m)	Y (m)	Hydraulic Head (m)	Pressure Head (m)	Uplift Pressure (kN/m^2)	Hydraulic Head (m)	Pressure Head (m)	Uplift Pressure (kN/m^2)	Hydraulic Head (m)	Pressure Head (m)	Uplift Pressure (kN/m^2)	Hydraulic Head (m)	Pressure Head (m)	Uplift Pressure (kN/m^2)
20	25	35	10	98.100	35	10	98.100	35	10	98.100	35	10	98.100
20.5	25	33.68	8.68	85.151	33.803	8.803	86.357	32.137	7.137	70.014	34.576	9.576	93.941
21	25	32.878	7.878	77.283	33.054	8.054	79.010	30.676	5.676	55.682	34.206	9.206	90.311
21.5	25	32.391	7.391	72.506	32.575	7.575	74.311	30.076	5.076	49.796	33.865	8.865	86.966
22	25	31.99	6.99	68.572	32.165	7.165	70.289	29.659	4.659	45.705	33.532	8.532	83.699
22.5	25	31.599	6.599	64.736	31.759	6.759	66.306	29.22	4.22	41.398	33.199	8.199	80.432
23	25	31.244	6.244	61.254	31.381	6.381	62.598	28.854	3.854	37.808	32.866	7.866	77.165
23.5	25	30.917	5.917	58.046	31.024	6.024	59.095	28.55	3.55	34.826	32.531	7.531	73.879
24	25	30.605	5.605	54.985	30.678	5.678	55.701	28.276	3.276	32.138	32.191	7.191	70.544
24.5	25	30.3	5.3	51.993	30.338	5.338	52.366	28.019	3.019	29.616	31.845	6.845	67.149
25	25	30	5	49.050	30	5	49.050	27.779	2.779	27.262	31.49	6.49	63.667
25.5	25	29.7	4.7	46.107	29.662	4.662	45.734	27.552	2.552	25.035	31.123	6.123	60.067
26	25	29.395	4.395	43.115	29.322	4.322	42.399	27.332	2.332	22.877	30.74	5.74	56.309
26.5	25	29.083	4.083	40.054	28.976	3.976	39.005	27.118	2.118	20.778	30.341	5.341	52.395
27	25	28.756	3.756	36.846	28.619	3.619	35.502	26.906	1.906	18.698	29.917	4.917	48.236
27.5	25	28.401	3.401	33.364	28.241	3.241	31.794	26.689	1.689	16.569	29.452	4.452	43.674
28	25	28.01	3.01	29.528	27.835	2.835	27.811	26.463	1.463	14.352	28.937	3.937	38.622
28.5	25	27.609	2.609	25.594	27.425	2.425	23.789	26.24	1.24	12.164	28.408	3.408	33.432
29	25	27.122	2.122	20.817	26.946	1.946	19.090	25.987	0.987	9.682	27.766	2.766	27.134
29.5	25	26.32	1.32	12.949	26.197	1.197	11.743	25.603	0.603	5.915	26.718	1.718	16.854
30	25	25	0	0.000	25	0	0.000	25	0	0	25	0	0.000

Investigation on Fresh Properties of Geopolymer Mortar

A.KARSLIOĞLU KAYA[1] and M.İ.ONUR[1]

[1]Eskisehir Technical University, Eskişehir/Türkiye, asenakarslioglukaya@gmail.com
[1]Eskisehir Technical University, Eskişehir/Türkiye, mionur@eskisehir.edu.tr

Abstract **- Waste recycling is a significant concern in the contemporary world from both economic and environmental perspectives. Cement-based industries have shown an increasing interest in researching the properties and potential applications of waste-incorporated geopolymer building materials due to their sustainability benefits. The incorporation of various waste materials instead of cement has a vital impact in advancing the improvement of sustainable construction materials. Geopolymer mortar is a type of mortar created by combining sand and geopolymer made from raw materials opulent in aluminum and silicon activated with an alkaline solution. This research examines the fresh performance of geopolymer mortars. The findings from this study suggest that geopolymer mortar has the potential to be utilized as an eco-friendly and sustainable building and construction material, making it a viable alternative to traditional cement mortar in the coming years.**

Keywords **– Boron waste, Silica fume, Geopolymer, Taguchi optimization, Workability.**

I. INTRODUCTION

CEMENT, while a widely used construction material, presents several disadvantages from a sustainability perspective. First and foremost, the manufacture of cement is energy-intensive and promotes significantly to carbon dioxide (CO_2) emissions. The process involves heating limestone and clay at extremely high temperatures in kilns, releasing substantial amounts of CO_2 into the atmosphere [1, 2]. This carbon footprint makes cement production a major contributor to climate change. Another issue with cement is that it relies on depleting natural resources, particularly limestone and clay. The extraction of these raw materials can result in habitat destruction, soil erosion, and water pollution, leading to adverse environmental impacts. Moreover, cement-based materials tend to have a relatively short lifespan, requiring maintenance and replacement over time. This not only increases construction costs but also generates additional waste, contributing to landfill problems.

In contrast, geopolymer mortar offers several sustainability advantages [2]. Firstly, geopolymer production typically requires lower temperatures, reducing energy consumption and associated emissions. Geopolymers are made from abundant industrial by-products like fly ash (FA) and blast furnace slag (YFC), which divert these materials from landfills and reduce the need for resource-intensive extraction. Furthermore, geopolymer mortars exhibit excellent durability, often outlasting traditional cement-based materials. This longevity reduces the need for frequent repairs or replacements, resulting in reduced construction and maintenance costs. Additionally, geopolymers can be formulated to have a lower carbon footprint, making them a more environmentally friendly choice. They can even be engineered to capture and store CO_2, contributing to carbon sequestration efforts.

In conclusion, while cement has long been the conventional choice in construction, its disadvantages in terms of energy consumption, greenhouse gas emissions, resource over-use, and limited lifespan make it less sustainable. Geopolymer mortar, on the other hand, offers a promising alternative due to its lower environmental impact, utilization of waste materials, longer lifespan, and potential for carbon capture. Considering these factors, geopolymer mortar should be seriously considered as a more sustainable option for construction in the modern world.

II. LITERATURE REVIEW

Nath and Sarker (2014), the characteristics of fly ash geopolymer, including its workability and setting time properties, were investigated. They explored the effect of replacing a portion of the FA with YFC under normal environmental conditions. They activated the mixture using a combination of sodium hydroxide (NaOH) and sodium silicate (Na_2SiO_3). It's worth noting that the workability of geopolymer differs from that of cement, primarily because of the higher viscosity of the alkaline activator. Interestingly, a rise in YFC content resulted in decreased workability and setting time but led to an increase in compressive strength [3].

Kotwal et al. (2015) investigated the temperature of fresh geopolymer mortar was assessed utilizing a digital stem-type thermometer. Their results showed that it varied between 32 and 54^0C. Furthermore, it was observed that the temperature raised with higher amounts of NaOH and Na_2SiO_3. Conversely, there was a declining propensity to in temperature as the fine aggregate/FA ratio content was raised [4].

Topark-Ngarm et al. (2015), the elevated calcium content in FA was connected with the manufacture of geopolymer construction material characterized by high strength, along with a setting time ranging from 28 to 58 minutes [5].

Al-Majidi et al. (2016) findings indicated that increase in YFC content reduced the flow ability and setting times of geopolymer mortars were substantially affected [6]. In another

study, it was determined that the flow ability of geopolymer mortar included high calcium FA was greatly influenced by the NaOH concentration [7].

Samantasinghar and Singh (2019) found that fly ash-slag blended geopolymer mortar exhibited consistency and setting times similar to ordinary Portland cement mortar. It has also been noted that both FA and YFC show excellent resistance to expansion and contraction [8].

III. Materials and Method

A. Materials

In the context of this research, we formulated 16 types of alkali-activated mortar employing boron waste (BA), silica fume (SD), F type FA (F-FA), YFC, CEN standard sand, NaOH, and Na_2SiO_3, as per existing literature. Additionally, a conventional cement mortar was manufactured as the reference sample.

Figure 1: Binder materials (**a**) BA, (**b**) SD, (**c**) F-FA, (**d**) YFC, (**e**) CEN standard sand, and (**f**) alkaline activator.

B. Mixture design with Taguchi optimization

Taguchi optimization, named after Japanese engineer and statistician Genichi Taguchi, is a powerful methodology used in the field of robust design and quality improvement. It is particularly valuable in industries were minimizing variation and achieving consistent, high-quality results are critical, such as manufacturing and product development. Taguchi optimization employs a systematic and structured approach to optimize processes and products by identifying key factors that influence performance and quality. It involves the design of experiments (DOE) to efficiently explore a wide range of factors and their interactions with a limited number of experimental runs. By doing so, it helps in determining the optimal combination of factors and settings that lead to improved performance, reduced variation, and enhanced quality while also making processes more robust against external factors and noise. Taguchi optimization is widely used for its ability to deliver cost-effective and reliable solutions for quality enhancement and process improvement.

In this research, five parameters involving usage of boron waste, usage of silica fume, sodium (Na) concentration, oven curing temperature, and oven curing time were taken into account shown in Table 1. The minimum number of experiments needed has been established by considering the quantity of process variables and their respective levels. Following the principles of Taguchi's DOE, the experimental trials for the L16 orthogonal array are elaborated in Table 2. The amount of binding material (F-FA, BA and SD) is 450 g. Moreover, 60 g of YFC was added to ensure hardening at room temperature.

Table 1: Parameters used in the Taguchi experimental design.

Level	BA (%)	SD (%)	Na (%)	T (^{0})	Hour
1	0	0	6	40	12
2	5	5	8	60	24
3	10	10	10	80	48
4	15	15	12	100	72

Table 2: Types of samples produced.

Sample	UK (g)	BA (g)	SD (g)	Na (%)
S1	450.0	0	0	6
S2	427.5	0	22.5	8
S3	405.0	0	45.0	10
S4	382.5	0	67.5	12
S5	427.5	22.5	0	8
S6	405.0	22.5	22.5	6
S7	382.5	22.5	45.0	12
S8	360.0	22.5	67.5	10
S9	405.0	45.0	0	10
S10	382.5	45.0	22.5	12
S11	360.0	45.0	45.0	6
S12	337.5	45.0	67.5	8
S13	382.5	67.5	0	12
S14	360.0	67.5	22.5	10
S15	337.5	67.5	45.0	8
S16	315.0	67.5	67.5	6

Moreover, 450 grams of cement (CEM I 42.5 R), 225 grams of water and 1350 grams of standard sand were used in the production of the reference sample (S0).

C. Method

In this research, the flow test was performed according to TS EN 1015-3 [9]. Test for setting times were carried out using the Vicat needle apparatus, according to ASTM C 807 [10]. Moreover, the temperature of the fresh geopolymer mortar was tested in adapted for ASTM C 1064 [11].

IV. RESULTS AND DISCUSSION

A. Workability

The workability of fresh geopolymer mortar is a crucial characteristic as it directly influences the properties of the hardened geopolymer mortar [12]. While the flow table test results are given in Figure 2, the fresh unit volume weight results are given in Figure 3. As the amount of SD and Na% increased, the flow value decreased. The lowest fresh unit volume weight value was determined in S9 mortar.

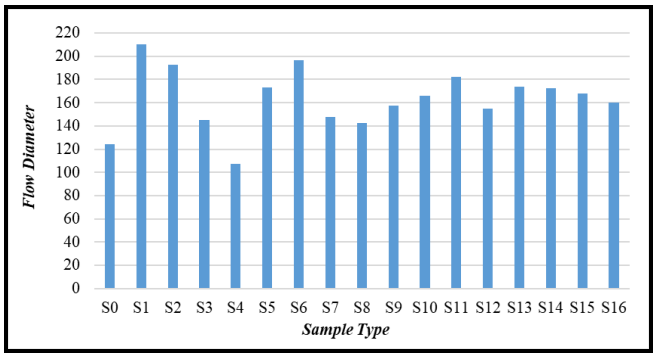

Figure 2: Results of flow table test of fresh geopolymer mortar

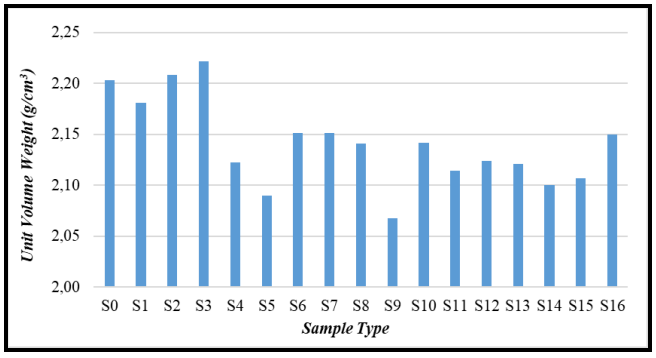

Figure 3: Results of unit volume weight of fresh geopolymer mortar

B. Setting time

In practical terms, the setting duration of the fresh mortar holds immense importance, as it dictates the allowable time for transporting, pouring, and compacting the mortar [12]. The initial and final setting time results are shown in Figure 4. The setting times decreased with increasing Na% ratio, however it increased with increasing BA and SD amounts. It is thought that the reason for this is the high amount of boric acid (B2O3) in BA. Additively, adding YFC to geopolymer mortar mixtures caused the mortars to set earlier than normal conditions.

C. Temperature

While preparing the geopolymer mortar, it's noteworthy that the temperature of the fresh geopolymer mixture is considerably higher compared to traditional cement mortar. This disparity is attributed to the more intricate chemical reactions involved in geopolymerization, which generate heat [13]. The temperature results are given in Figure 5. It was determined that as Na% increased, the temperature of the fresh mortar increased.

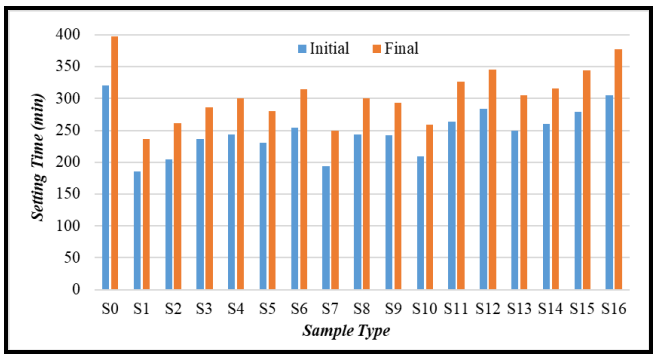

Figure 4: Results of setting times of geopolymer mortars

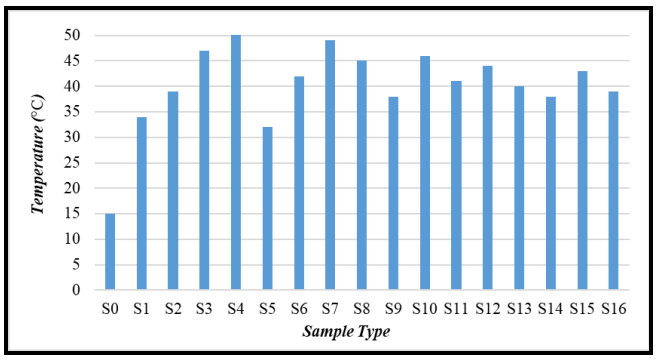

Figure 5: Results of temperature of fresh geopolymer mortar

V. CONCLUSION

The workability, setting time and temperature of fresh geopolymer mortars created using the Taguchi method were investigated within the scope of this study. The general conclusions that can be drawn are:

- The cement industry's substantial role in CO_2 emissions, a major concern for environmentalists in light of global warming, underscores the need to explore alternative industrial by-products as raw materials to reduce energy demands in cement production. Therefore, the effectiveness of resources and their consequences could serve as the foundation for the implementation of geopolymer applications at the national level.
- Moreover, based on this research and literature, it is envisaged that geopolymer mortar can be used instead of conventional cement mortar in the future. However, achieving this transition demands a substantial feasibility assessment and an in-depth study.

ACKNOWLEDGMENT

This study was carried out considering the priority field vision of YÖK 100/2000 doctoral project "Building, Building Materials and Building Management". Asena KARSLIOĞLU KAYA would like to thank those concerned for their support with Tübitak Bideb 2211-A General Domestic Doctoral Scholarship and YÖK 100/2000 Doctoral Scholarship. This study was supported by Eskişehir Technical University Scientific Research Projects Commission within the scope of the project numbered 22DRP202.

REFERENCES

[1] J. He, G. Zhang. Geopolymerization of red mud and rice husk ash and potentials of the resulting geopolymeric products for civil infrastructure applications. Developments in Strategic Materials and Computational Design II: Ceramic Engineering and Science Proceedings, 2011, 32: 45-52.

[2] M. Sumesh, U.J. Alengaram, M.Z. Jumaat, K.H. Mo & M.F. Alnahhal. Incorporation of nano-materials in cement composite and geopolymer based paste and mortar–A review. Construction and Building Materials, 2017, 148: 62-84.

[3] P. Nath, P.K. Sarker. Effect of GGBFS on setting, workability and early strength properties of fly ash geopolymer concrete cured in ambient condition. Construction and Building materials, 2014, 66: 163-171.

[4] A.R. Kotwal, Y.J. Kim, J. Hu, V. Sriraman, Characterization and early age physical properties of ambient cured geopolymer mortar based on class C fly ash, International Journal of Concrete Structures and Materials 9 (1) (2015) 35-43.

[5] P. Topark-Ngarm, P. Chindaprasirt &V. Sata. Setting time, strength, and bond of high-calcium fly ash geopolymer concrete. Journal of materials in civil engineering, 2015, 27(7), 04014198.

[6] M.H. Al-Majidi, A. Lampropoulos, A. Cundy, S. Meikle, Development of geopolymer mortar under ambient temperature for in situ applications, Construction and Building Materials 120 (2016) 198-211.

[7] A.B. Malkawi, M.F. Nuruddin, A. Fauzi, H. Almattarneh, B.S. Mohammed, Effects of alkaline solution on properties of the HCFA geopolymer mortars, Procedia Engineering 148 (2016) 710-717.

[8] S. Samantasinghar, & S.P. Singh. Fresh and hardened properties of fly ash–slag blended geopolymer paste and mortar. International Journal of Concrete Structures and Materials, 2019, 13, 1-12.

[9] TS EN 1015-3, 2000. Kagir Harcı- Deney Metotları- Bölüm 3: Taze Harç Kıvamının Tayini (Yayılma Tablası İle), Türk Standartları Enstitüsü, Ankara.

[10] ASTM C 807-13, Standard Test Methods for Time of Setting of Hydraulic Cement Mortar by Modified Vicat Needle, ASTM, International, West Conshohocken, PA, 2008.

[11] ASTM C 1064, Standard Test Methods for Temperature of Freshly Mixed Hydraulic-cement concrete, ASTM, International, West Conshohocken, PA, 2011.

[12] Zhang, P., Zheng, Y., Wang, K., & Zhang, J. (2018). A review on properties of fresh and hardened geopolymer mortar. Composites Part B: Engineering, 152, 79-95.

[13] J. Davidovits, Geopolymer: inorganics polymeric new materials, Journal of Thermal Analysis 37 (1991) 1633-1656.

Challenges Encountered in Column Tests Under Eccentric Axial Load and Proposed Solutions

Ahmet Özbayrak

Erciyes University, Engineering Faculty, Department of Civil Engineering, Kayseri, Türkiye

ozbayrak@erciyes.edu.tr

***Abstract* – The difficulties encountered in experimental research cause loss of time and money. For this reason, both the sample production process and the experimental setup design are extremely important. In this study, the difficulties encountered in column tests under uniaxial bending and the solution of the problem are presented. For the solution, the structure of the end regions of the columns and the design of the support plates of the experimental setup are revised and the expected column buckling behavior is obtained. The unreinforced concrete cover in the end zones of the columns breaks suddenly due to bending effect as a result of eccentric axial compressive loading and the expected collapse behavior in the middle zone does not occur. In order to solve the problem, firstly, modifications were made to increase the support stiffness in the experimental setup. Then, in order to provide sufficient improvement, the 25 mm concrete cover formed during production at the ends of the columns was cut. In fact, column longitudinal reinforcements should be welded directly to the metal plates to be formed in the end cross-section of the column during fabrication without mitring. Thus, in this way, no concrete cover is left in the end regions of the column, preserving its slenderness without reducing the effective length of the column, and preventing fracture from occurring at the end region.**

***Keywords* - Column test, uniaxial bending, experimental difficulties, longitudinal reinforcements, test setup.**

I. INTRODUCTION

IN order for civil engineers to overcome the difficulties in their experimental work, comprehensive approaches including detailed planning, correct equipment selection, data collection and analysis, and safety measures are required. Furthermore, environmental variability and weather conditions, cost overheads and time constraints affect the feasibility and process of experiments. Scaling in the laboratory should also not lead to behavioral differences. Many research topics have either remained in the background due to experimental difficulties or have been concluded only by means of numerical models.

There are challenging stages in a study in terms of design, fabrication, and experimental set-up. In the aforementioned research, slab irregularity was investigated by creating slab openings at different ratios on a one-storey ½ scale structure with two openings in both directions. For this purpose, an axial compressive load of 10% of the bearing capacity was applied to nine columns in the structure and the performance of the structure under horizontal load was analyzed. Under laboratory conditions, an axial compressive force of 200 kN from a single hydraulic jack was distributed to the columns of the structure in the calculated ratio using a steel test rig [1]. Another study states that it is very difficult to perform short column tests and that the aspect ratio should be very low to capture the behavior. It is reported that this situation, which causes an increase in the lateral load level, leads to the production of faulty columns and in most studies these columns are treated as control specimens [2]. In another study it was noted that the deflection results of the second-floor slab were not considered. The reason was that the measurement range was completely different than expected [3]. It is noted that steel-reinforced natural rubber bearings, which are widely used in bridges, have rarely been investigated in previous experiments due to the complexity and experimental difficulties [4]. Similarly, it has been suggested that the analysis of cylindrical shells with different boundary conditions has rarely been investigated in the literature due to experimental difficulties [5]. To overcome such experimental difficulties, finite element analysis has been used to determine the mechanical properties of isotropic short fibre SRPP composites with varying strand lengths [6]. Concrete toughness is better determined by uniaxial tensile testing. However, due to the experimental challenges associated with these tests, several code developers have suggested flexural tests (with three- or four-point loading) as an alternative [7]. Different standards are used in different countries around the world for the design and testing of prestressed concrete railway sleepers. (TS) EN 13230-2 is one of the most widely used prestressed concrete railway sleeper standards in the world and is actively applied by some 73 members of the International Union of Railways (UIC). Several sleeper tests are mentioned in this standard. The most important are the "positive moment capacity of the rail seat" and the "negative moment capacity of the center" tests. These tests are designed to determine several different parameters. The most important of these parameters are the "first elastic (re-closing) crack initiation loads" (Frr for rail seat positive moment tests and Fcr for center negative moment tests). The detection of these cracks in prestressed concrete sleepers can often be misleading because these cracks remain at the micro level due to the effect of prestressing compression. Therefore,

the standard test procedure in EN 13230-2 is often not satisfactory and results in much higher Frr loads than the actual values. Therefore, the authors of the cited studies [8-10] used "acetone spray" to overcome the test result deviations. During testing, a fine mist of acetone spray is applied to the prestressed concrete sleepers under load and this chemical, which evaporates rapidly from undamaged surfaces, is used to detect cracks. Once a crack has started, some of the chemical can penetrate into the crack and, due to its slower evaporation in these areas, can assist in the rapid detection of cracks, even at the micron level. As a result, the Frr load values are more accurate, and the results show less variation and high repeatability.

II. MATERIAL AND METHOD

The problems that cause experimental difficulties arise from both the reinforced concrete column and the experimental setup. In order to solve the problem, the experimental setup was first revised and when it was not sufficient, it was necessary to make changes on the reinforced concrete column specimens.

Reinforced concrete columns have been designed with a cross-section of 200 x 200 mm and a height of 1500 mm. A reinforced concrete column with a compressive strength of 45 MPa has an approximate axial load-bearing capacity exceeding 2000 kN. Therefore, considering laboratory capabilities, the maximum dimensions for column sections that can be produced have been set at 200 mm (Fig.1).

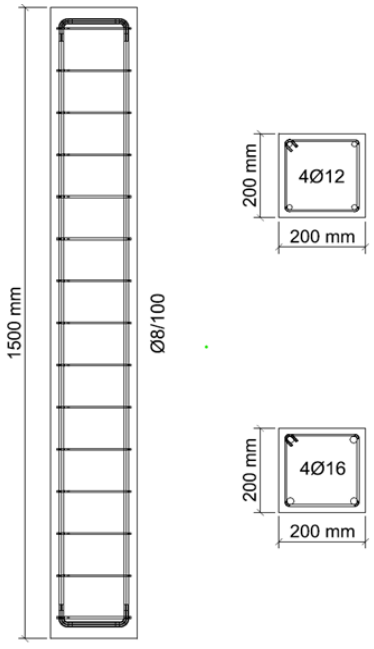

Figure 1: Column reinforcement and geometric properties

The longitudinal reinforcement ratio of the column is approximately 0.01 (4Ø12) and 0.02 (4Ø16). In columns, the axial load is expected to be carried more by the concrete section rather than the reinforcement. Therefore, longitudinal reinforcement diameters have been determined according to the most commonly preferred minimum reinforcement spacing in practice. To prevent sudden and brittle collapse in columns, shear reinforcement has been placed along the section at a constant interval (Ø8/100). This arrangement aims to induce column failure through uniaxial bending under the axial compressive effect in experimental conditions.

The plates on the upper and lower heads where the columns are supported have been designed to accommodate eccentric axial loading. They also act as pinned support, allowing the column to experience uniaxial bending. The column is placed into a 220 x 220 mm and 50 mm deep socket and secured using plates in Figure 2.

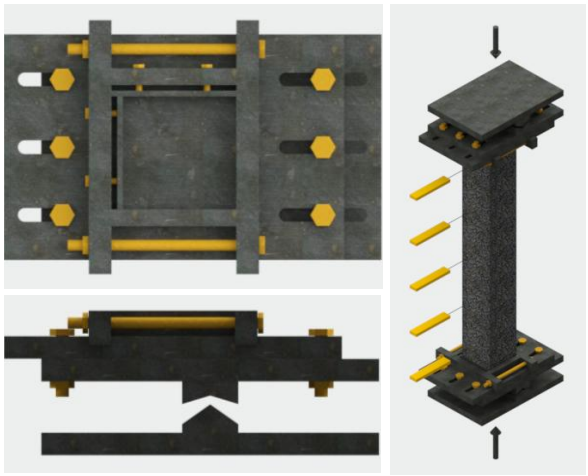

Figure 2: Column lower and upper supports

The column support plates are 40 mm thick and the upper and lower supports consist of 3 plates each. Plate dimensions are 400 x 600 mm. The first two plates provide rotation with male and female adapters. The second and third plates have large oval hole bolt connections to provide eccentricity. Eccentric connection is made with 6 M24 bolts. After the column was placed, 10 mm thick removable plates were placed on the column surface and fixed to the support by tightening with M12 bolts from the outside (Figure 2).

After the reinforced concrete columns were placed in the steel loading setup, displacement readings were taken with a total station between load controlled increments of 30 kN. During the experiments, 63 mm eccentric axial pressure loading was applied to the columns. For horizontal displacement readings, 5 potentiometric rulers were also used along the column height. Two LVDTs were used to read the shortening and elongation on the compression and tension faces, and one LVDT was used to control the deflections outside the bending plane. Finally, one LVDT was installed to measure the shortening of the column length (Figure 3).

Figure 3: Taking measurements from the experimental setup

During load-controlled loading, collapse occurred when the load suddenly dropped after reaching a specific level. Therefore, since fracture occurred with the transition to the plastic stage, the experiments were terminated without the need for a displacement-controlled loading as in beams.

III. EXPERIMENTAL CHALLANGES

During the experiments, instead of the anticipated failure occurring within the column body, damage in the support region led to premature termination of the experiments before reaching the column's load-carrying capacity, and the desired column collapse behavior could not be achieved. The desired failure mode was eventually achieved after a series of experiments. For this purpose, various improvements were implemented after each experiment, and the issue was resolved after a total of 5 experiments.

Table 1: The failure loads of the column specimens.

Sample Name	Longitudinal Reinforcement	M_{max} (kNm)	F_{max} (kN)
Test1	4Ø12	52	713
Test 2	4Ø12	37	508
Test 3	4Ø16	40	570
Test 4	4Ø16	44	592
Test 5	4Ø12	46	615

The upper and lower support plates, where the ends of the reinforced concrete column are connected, have rotational freedom. This allows the column body to bend (in a C-shape) due to eccentric axial loading, resulting in the expected form of failure. In the first test, the column fractured from the lower support region. The fractured part consists of plain concrete where the longitudinal reinforcement mitred, and where only concrete cover was left at the column end zones. As the axial load increased during the experiment, the concrete on the compression side of the column was crushed in the support regions. Subsequently, due to the moment effect and the absence of longitudinal reinforcements at the column ends, the concrete cover in the end zone ruptured, leading to the end of the experiment (Figure 4).

Figure 4. End of Test1

After the investigation, it was concluded that the problem could potentially be resolved by cutting the average 25 mm thick concrete cover that had detached from the bottom column end. However, due to the initial lack of equipment for cutting, alternative solutions were explored. As a second approach, experiments were conducted by placing the column freely between the support plates in the test setup, without compressing the column ends. This approach aimed to prevent stress concentrations at the column ends by allowing the column to rotate on the plate surfaces, in addition to the rotational freedom provided by the support plates (Figure 5).

Figure 5. End of Test2

The issue of longitudinally reinforcing bars being mitred at the column end and concrete cover being placed perpendicular to the column cross-section revealed a production planning error. To address this, a third solution was implemented: the slot depth in the support plates where the column is placed was increased to 100 mm in the bending direction. This modification was intended to allow the tensile effect resulting

from the bending moment to be effectively resisted by the longitudinal reinforcements situated at levels higher than the lower end. Similar to the previous experiment, the column end was left free on the support plates without compression (Figure 6).

Figure 6. End of Test3

The increase in the slot depth in the support plates of the experimental setup has shifted the point of failure slightly higher. However, it was still unable to prevent the rupture of the concrete cover at the bottom end of the column. As a fourth solution, it was decided to confine the column within the slot using plates in a direction perpendicular to the bending plane, with a height of 100 mm. Despite the decrease in column slenderness due to the confinement of the column ends within a 100 mm deep slot instead of the previous 50 mm, it was assumed that this arrangement would allow for more effective performance of the longitudinal reinforcements along the column length (Figure 7).

Figure 7. End of Test4

Finally, the only remaining option was to proceed with the initial plan of cutting the concrete cover at the column ends. For this purpose, the process of purchasing and procuring the necessary machinery has begun. After obtaining the machine, the columns were cut by 25 mm from both ends, reducing the column length to 1450 mm (Figure 8). This allowed the longitudinal reinforcements to extend up to the top and bottom cross-sectional faces of the column.

Figure 8. Concrete cutting

As a result of both the improvements made in the steel plates on which the column ends were supported and the cutting of the reinforced concrete column ends, the experiment was successful. Although the column slenderness decreased slightly, the fracture occurred in the center of the column due to bending. The column reached its full load carrying capacity and more accurate data were obtained for the evaluations to be made (Figure 9).

Longitudinal reinforcements that will meet the bending moment effect occurring in the end regions of the column should extend to these regions without mitring. Additionally, the slot depth in the bottom and top loading plates, where the column is supported in the experimental setup, should be increased to limit the bending effect in the end regions. Mitred longitudinal reinforcements in the column end zones and leaving 25 mm concrete cover causes the problem.

Figure 9. End of Test5

IV. SOLUTION PROPOSALS

After a series of experiments, a solution was found. However, in order to avoid this difficult and troublesome process again, two important issues should be taken into consideration in the tests of axial pressure loaded columns

under uniaxial bending effect. Firstly, longitudinal reinforcements should be welded by extending up to the sheet plates to be formed at the ends of the column. No concrete cover should be left at the ends of the column in the direction perpendicular to the cross-sectional area. Secondly, attention should be paid to the steel test apparatus on which the upper and lower ends of the column are supported. In this setup, the depth of the slot in which the column will be placed and fixed in the bending plane should be at least 100 mm. If these two aspects are taken into consideration, the expected collapse behavior would occur as intended, with the column body bending and fracturing.

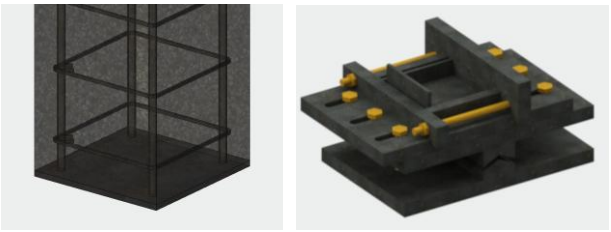

Figure 10. Improvements

V. CONCLUSION

In order to simulate the structural behavior in a laboratory environment and establish the support conditions for the test specimen, various steel testing setups are designed. However, if the produced specimens and designed equipment fail to fulfill their intended functions, it can lead to increased costs, wasted time, and efforts going in vain. Therefore, in order to avoid encountering problems that are difficult to rectify, meticulous planning is crucial during the initial stages.

In some cases, unforeseen issues might arise despite thorough planning. To mitigate such situations, the experience and knowledge gained from previous endeavors are of paramount importance. This information helps in preventing and addressing unexpected challenges, ensuring a smoother execution of the testing process and achieving accurate and reliable results.

In eccentric axial load tests on columns, slenderness is a crucial factor. Firstly, the columns designed should not be short but instead, they should be slender and flexible. In a two-hinged testing setup, the columns are expected to buckle and fail at their midsection due to the combined axial force and bending moment. At the points where the column connects to the steel setup for load transfer, maximum rigidity should be ensured. For this purpose, a robust reinforced concrete design should be implemented at the column ends, and the connection between the column and the steel setup should have sufficient depth to facilitate a reliable transfer of forces.

ACKNOWLEDGMENT

This research was supported by TUBITAK (The Scientific and Technological Research Council of Turkey) under grant number 121M236.

REFERENCES

[1] Özbayrak, A., & Altun, F., (2018). Experimental Difficulties and Solution Proposals in a Three-Dimensional Reinforced Concrete Frame. 13th International Congress on Advances in Civil Engineering (pp.56). İzmir, Turkey.

[2] Dirikgil, T., Altun, F., & Düğenci, O., (2018). Experimental Investigation of Performance of Externally Collared Reinforced Concrete Short Columns. The 2018 Structures Congress_Structures18, Incheon, South Korea

[3] Pacheco, J., De Brito, J., Ferreira, J., & Soares, D. (2015). Flexural load tests of full-scale recycled aggregates concrete structures. Construction and Building Materials, 101, 65-71.

[4] Maghsoudi-Barmi, A., Khaloo, A., & Moeini, M. E. (2021, August). Experimental investigation of unbonded ordinary steel reinforced elastomeric bearings as an isolation system in bridges. In Structures (Vol. 32, pp. 604-616). Elsevier.

[5] Temami, O., Ayoub, A., Hamadi, D., & Bennoui, I. (2019). Effect of boundary conditions on the behavior of stiffened and un-stiffened cylindrical shells. International Journal of Steel Structures, 19, 867-878.

[6] Goutianos, S., Cabrera, N. O., Alcock, B., Reynolds, N., & Peijs, T. (2020). Self-Reinforced polypropylene composites based on discontinuous tapes-an experimental and numerical study of the influence of tape length. Applied Composite Materials, 27(6), 767-793.

[7] Carpinteri, A., Aledda, L., & Accornero, F. Ductile-to-brittle transition in fiber-reinforced materials: Effects of dimensional scale and fiber volume ratio.

[8] Çeçen, F., Aktaş, B., (2021). Incremental LUR tests of new LCR concrete railway sleepers. *Engineering Failure Analysis*, Cilt: 130 (105793). doi: https://doi.org/10.1016/j.engfailanal.2021.105793

[9] Çeçen, F., Aktaş, B., Öztürk, H., Öztürk, İ. Ş., Navdar, M. B., (2022). Comparison of new LCR and ordinary prestressed concrete railway sleepers with LUR tests. *Construction and Building Materials*, Cilt: 321. Doi: https://doi.org/10.1016/j.conbuildmat.2022.126414

[10] Çeçen, F., Aktaş, B., Özbayrak, A., (2023). Decarbonization of the concrete railway sleeper production: bringing the low-dosage pozzolanic cement usage in the sleeper production via novel laminated CFRPU reinforcement technique. *Materials Today Sustainability*, Cilt: 23, ID: 100455. doi: https://doi.org/10.1016/j.mtsust.2023.100455

Vehicle Detection and Counting in Traffic Videos using Deep Learning

A. BATTAL[1], Y.E. AVCI[2], and A. TUNCER[3]

[1]Yalova University, Institute of Graduate Studies, Yalova/Türkiye, battalahsen@gmail.com
[2]Arizona State University, Civil, Environmental and Sustainable Engineering, Arizona/USA, yavci@asu.edu
[3]Yalova University, Department of Computer Engineering, Yalova/Türkiye, adem.tuncer@yalova.edu.tr

***Abstract* - Nowadays, many factors such as population growth and urban growth lead to the emergence of traffic-related problems such as traffic accidents and traffic congestion. Artificial intelligence technologies, which have gained momentum in recent years and have been used effectively in addressing a wide range of problems, have also found a place in traffic applications. By using artificial intelligence-based algorithms on traffic videos, the type of vehicles passing through the specified regions can be determined and the number of vehicles can be calculated. In this study, vehicle detection and classification were carried out using YOLOv5 (You Only Look Once), a deep learning method, in flowing traffic videos. The accuracy rate of the model developed for the detection of five different classes, namely cars, motorcycles, trucks, buses, and bicycles is 88% on average. After the detection of the vehicles, the SORT algorithm was used to calculate the number of passing vehicles. The model produced an average accuracy rate of 85% in counting vehicles. Experimental results show that vehicle detection, classification, and counting are successfully achieved using YOLOv5 and SORT algorithms.**

***Keywords* – Vehicle Detection, Traffic, Deep Learning, YOLOv5, SORT**

I. INTRODUCTION

Traffic management and safety is of great importance due to the ever-increasing population and rising rate of urbanization. Because with economic growth and urbanization, more and more vehicles are on the roads every year, which increases traffic accidents and traffic congestion. In order to overcome these situations, it has become inevitable to implement applications such as smart traffic monitoring and parking lot management. In this context, studies such as automatic detection of vehicles, determining which class (car, bus, etc.) they belong to and calculating the number of vehicles passing through a certain area have an important position in optimizing traffic management processes and increasing traffic safety.

Detection of vehicles in a video or image can be performed using computer vision techniques. In addition to standard image processing techniques, artificial intelligence-based deep learning algorithms have been frequently used in object detection in recent years. In the literature, there are studies on vehicle detection using different object detection algorithms. There are studies in which a single object detection model is used in the object detection phase and studies in which more than one object detection model is used and their performances are compared.

To tackle the problem of false detection and missed detection resulting from complex scenes and large differences in target scales, an enhanced vehicle recognition technique based on YOLOv5s was proposed by Xiaomeng et al. [1]. In the study carried out by Wang [2] for vehicle class detection, the YOLOv3 model was improved, and the performance of the developed model was compared with the YOLOv2 and YOLOv3 models. In another study [3], an improved vehicle detection method based on the YOLOv3 model was proposed and the model was compared with SSD and YOLOv2 models.

To determine traffic intensity and congestion, in addition to detecting and classifying vehicles, it is also important to count the number of vehicles passing through a certain area. Counting vehicles has a role that can contribute to reducing traffic congestion and accidents. Therefore, this is of great importance for traffic management and safety. There are various studies on automatic vehicle counting systems in the literature. In the study carried out by Anil et al. [4], five different vehicle (car, bus, truck, motorbike, and bicycle) classes were detected with YOLOv3 and vehicle tracking and counting was carried out using the SORT algorithm. In the study, it was stated that the accuracy rate of the vehicle counting process was 85.45%. Another study on counting vehicles was also proposed by Algiriyage et al. [5]. In the study, YOLOv4 was used to detect five different vehicles and SORT algorithm was used for counting. In a different study [6], the YOLOv4 model was used for vehicle detection, and the DeepSORT algorithm was employed for counting. It was reported that the model used for the detection of four different vehicle classes (car, motorcycle, bus, and truck) achieved an accuracy rate of 82.08%.

In addition to object detection algorithms such as YOLO, there are some studies that use background subtraction technique to detect objects in videos. In a study proposed by Seenouvong et al. [7], a background subtraction technique was used and then was performed vehicle counting using a virtual detection region. In another study [8] used the method based on a computer vision approach which utilized background modeling and Kalman filter.

This study aims to develop a system that enables automatic detection, classification and counting of vehicles in traffic. Vehicle detection, classification and counting with traditional methods involves a complex and time-consuming process, and human errors are inevitable in methods based on manual intervention. The study aimed to find a solution that makes

traffic management processes more efficient and reliable by using deep learning algorithms on traffic camera images. YOLOv5 [9] model was used to detect 5 different vehicles (car, motorcycle, truck, bus, and bicycle) and SORT [10] algorithm was used to count the detected vehicles.

The rest of the paper is organized as follows: the methodology, including YOLO and SORT algorithm, dataset and evaluation criteria was given in section 2. Section 3 presents experimental results, and the conclusion was presented in section 4.

II. METHODOLOGY

Figure 1 shows the block diagram of the system designed for vehicle detection and counting. First, a model is trained to detect five different vehicle classes (car, motorcycle, truck, bus, bicycle). Then, the relevant region in the video under study is determined, and the vehicles within that region are detected and classified using the trained model. Once the class is identified, an ID is assigned, and the vehicle counting process is carried out.

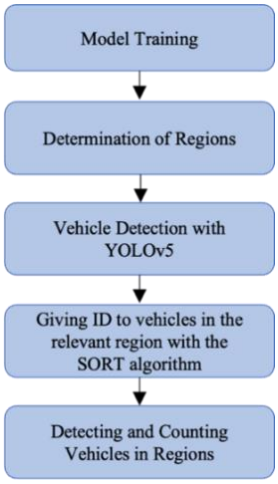

Figure 1: The block diagram of the vehicle detection and counting.

A. You Only Look Once (YOLO)

Widely used for object detection, YOLO is a real-time object detection algorithm that uses a single Convolutional Neural Network (CNN) to detect objects in an image. YOLO worked with Darknet frameworks in its versions up to YOLOv5. However, YOLOv5 runs on the PyTorch framework. It has four different models as *s*, *m*, *l*, and *x*.

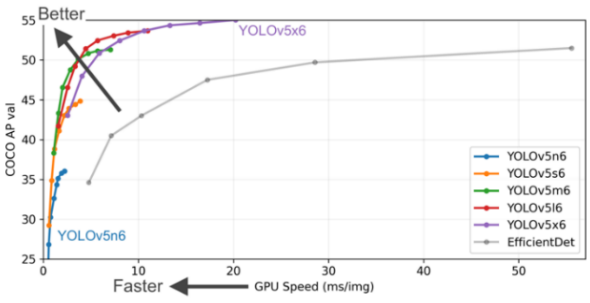

Figure 2: Performance graph of YOLO models [9].

As can be seen in Figure 2, each model has different accuracy and performance. YOLOv5m6 was preferred in this study.

Figure 3 shows the architecture of YOLOv5. When its architecture is examined, it can be seen that it consists of three parts: Backbone, Neck and Head. CNN is used in the backbone. It extracts the feature map from the backbone by dividing the input image into smaller pieces. It creates feature maps used for object detection and classification in the head. This section includes converting feature maps into binding boxes, classifying, and predicting the location of objects.

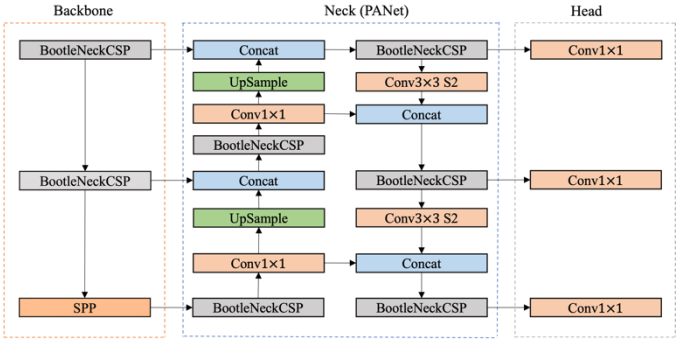

Figure 3: The architecture of YOLOv5 [11].

B. Simple Online and Realtime Tracking (SORT)

The SORT [10] algorithm is used in the multi-object tracking and counting process. It uses techniques such as Kalman Filter and Hungarian Algorithm.

C. Dataset

The vehicle detection dataset used in the study was obtained from GitHub [12]. Out of the 1258 images in the dataset, 1141 were used for training, and the remaining 117 were used for testing. An additional dataset containing truck images from Kaggle [13] was added because there are not enough truck images in the dataset. Figure 4 illustrates an example from the dataset used for model training.

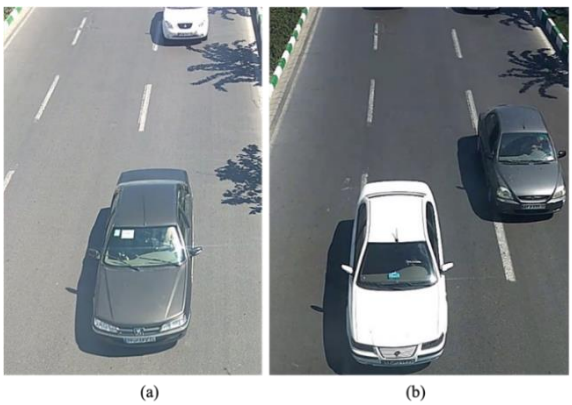

Figure 4: An example from the dataset.

D. Evaluation Criteria

Precision, recall, and mean average precision (mAP) values are employed in the evaluation phase of the model obtained through YOLOv5 training. Precision is computed by dividing the true positive (TP) values by the total positive values, and the precision calculation is depicted in equation (1).

$$precision = \frac{True\ Positive}{True\ Positive + False\ Positive} \quad (1)$$

Recall is the ratio of true positive values to positive predicted values. The calculation of recall is displayed in equation (2).

$$recall = \frac{True\ Positive}{True\ Positive + False\ Negative} \quad (2)$$

mAP is calculated in several steps. First, object detection is performed to assess how accurately objects are detected. Then, precise recall curves are generated for each class at different precision thresholds. The areas under these curves are then calculated for each class, and the average of these areas provides the overall mAP value, representing the model's performance across all classes. When calculating the accuracy of the system during the vehicle counting stage [14], the error rate is initially computed (equation 3). Then, this error rate is subtracted from 100 to determine the system's accuracy rate (equation 4).

$$Error\ (\%) = \frac{|\text{Estimated Number} - \text{True Number}|}{\text{True Number}} \times 100 \quad (3)$$

$$Accuracy\ (\%) = 100 - \text{Error}(\%) \quad (4)$$

III. EXPERIMENTAL RESULTS

The YOLOv5m6 model was used in the study to detect the vehicles and determine their class. In addition to the dataset obtained from GitHub, the training process was carried out by adding truck images in the data set from Kaggle to the dataset. The training process was carried out with 30, 50, 70, and 150 epochs, respectively. The steps of the training phase are illustrated in Figure 5.

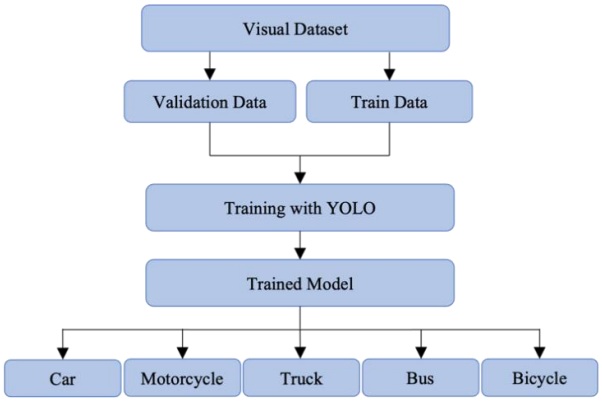

Figure 5: Steps of the training phase.

The precision, recall, mAP@50 and mAP@50-95 score values obtained as a result of the training are shown in Table 1. Figure 6 shows the precision-recall graph.

Table 1: Performance results obtained as a result of training.

Epoch	Precision	Recall	mAP@50	mAP@50-95
30	0.84	0.81	0.85	0.66
50	0.81	0.84	0.88	0.69
70	0.80	0.81	0.86	0.68
150	0.89	0.75	0.87	0.67

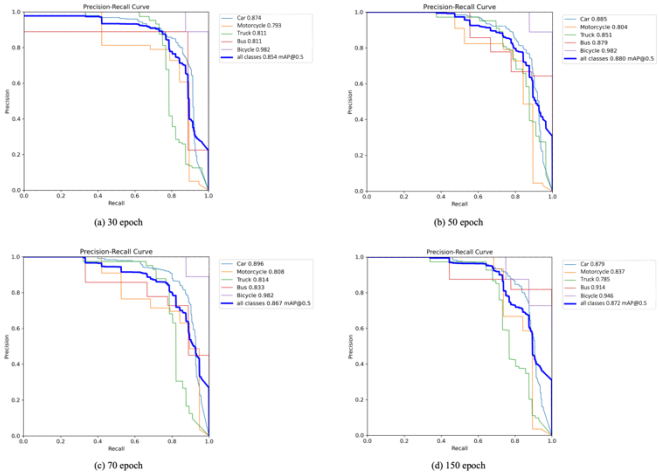

Figure 6: The precision-recall graph of model.

As seen in Table 2, as a result of the tests performed on four different videos, it was observed that the model reached an average accuracy rate of 88% in vehicle detection and classification.

Table 2: Test results for vehicle detection and classification.

Video	Accuracy
Video 1	0.88
Video 2	0.90
Video 3	0.85
Video 4	0.90
Average	0.88

After detecting and classifying vehicles, the area in the video to monitor was determined and the vehicles entering and exiting this area were counted. Using the SORT algorithm for vehicle counting, each vehicle was given a unique ID and the total number of vehicles passing through the designated area was calculated. In order to test the model, counting of the vehicles in the video footage captured by ourselves in Figure 7 was performed. As seen in the figure, the area for vehicle counting was defined with lines, and the vehicles entering this area were counted. The experimental results of the videos with frame rates of 29 and 30 fps used in the testing phase are shown in Table 3. As a result of the testing conducted on four different videos, it is observed that the model achieved an average accuracy rate of 85% for vehicle counting.

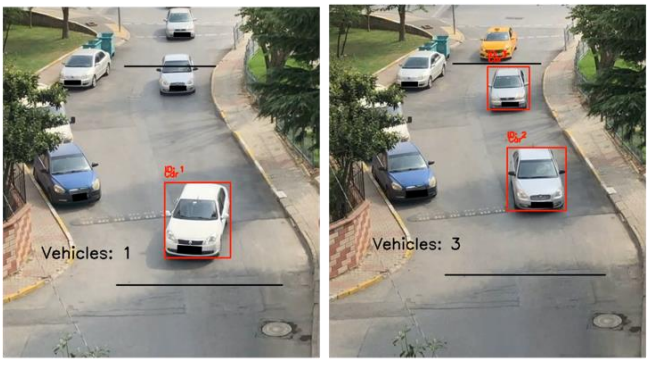

Figure 7: Test phase of vehicle counting.

Table 3: Test results for vehicle counting.

Video	Accuracy
Video 1	0.96
Video 2	0.90
Video 3	0.75
Video 4	0.82
Average	0.85

IV. CONCLUSION

Traffic-related issues, including accidents and congestion, are becoming increasingly common these days due to a variety of factors, such as population growth and urbanization. Applications for traffic management have also benefited from the recent surge in popularity of artificial intelligence technologies, which prove useful in addressing a range of issues. The type of vehicles traveling through designated areas and their quantity can be determined by leveraging artificial deep learning algorithms on traffic videos. In this study, we used flowing traffic videos to train the deep learning model YOLOv5m6 for vehicle detection and classification. The model, designed to detect five distinct classes—car, motorbike, truck, bus, and bicycle—achieved an average accuracy rate of 88%. After the vehicles were detected, the number of passing vehicles was determined using the SORT method. For counting vehicles, the model demonstrated an average accuracy rate of 85%. The results of the experiments illustrate the effectiveness of the YOLOv5m6 and SORT algorithms in achieving vehicle detection, categorization, and counting.

ACKNOWLEDGMENT

This study was supported by the Research Fund of Yalova University (Project Number: 2023/AP/0002).

REFERENCES

[1] L. Xiaomeng, F. Jun., and C. Peng, "Vehicle detection in traffic monitoring scenes based on improved YOLOV5s," in *Conf. Rec. 2022 Int. Conf. on Computer Engineering and Artificial Intelligence*, pp. 467-471.

[2] A. Wang, "Vehicle recognition algorithm based on improved YOLOV3," in *Conf. Rec. 2020 IEEE 9th Joint International Information Technology and Artificial Intelligence Conference*, pp. 2301-2305.

[3] X. Sung, Q. Huang, Y. Li, and Y. Huang, "An improved vehicle detection algorithm based on YOLOV3," in *Conf. Rec. 2019 IEEE Intl Conf on Parallel & Distributed Processing with Applications, Big Data & Cloud Computing, Sustainable Computing & Communications, Social Computing & Networking*, pp. 1445-1450.

[4] J. M. Anil, L. Mathews, R. Renji, R. M. Jose, and S. Thomas, "Vehicle Counting based on Convolution Neural Network," in *Conf. Rec. 2023 7th International Conference on Intelligent Computing and Control Systems*, pp. 695-699.

[5] N. Algiriyage, R. Prasanna, E. E. Doyle, K. Stock, D. Johnston, M. Punchihewa, and S. Jayawardhana, "Towards Real-time Traffic Flow Estimation using YOLO and SORT from Surveillance Video Footage," in *Conf. Rec. Proceedings of the 18th International Conference on Information Systems for Crisis Response and Management, Blacksburg, VA, USA*, pp. 23-26.

[6] M. A. B. Zuraimi, and F. H. K. Zaman, "Vehicle detection and tracking using YOLO and DeepSORT," *In 2021 IEEE 11th IEEE Symposium on Computer Applications & Industrial Electronics (ISCAIE)*, pp. 23-29, April 2021.

[7] N. Seenouvong, U. Watchareeruetai, C. Nuthong, K. Khongsomboon, and N. Ohnishi, "A computer vision-based vehicle detection and counting system," In *Conf. Rec. 2016 8th International conference on knowledge and smart technology*, pp. 224-227.

[8] V. Shaweddy, and W. Wahyono, "Vehicle Counting Framework for Intelligent Traffic Monitoring System," In *Conf. Rec. 2019 5th international conference on science and technology (ICST)*, pp. 1-5.

[9] Ultralytics. YOLOv5. Available: https://github.com/ultralytics/yolov5 (accessed on 10 February 2023).

[10] A. Bewley, Z. Ge, L. Ott, F. Ramos, and B. Upcroft, "Simple online and realtime tracking," In *Conf. Rec. 2016 IEEE international conference on image processing*, pp. 3464-3468.

[11] J. Zhao, X. Zhang, J. Yan, X.Qiu, X. Yao, Y. Tian, Y.Zhu, and W. Cao, "A wheat spike detection method in UAV images based on improved YOLOv5," *Remote Sensing*, 13(16), 3095, 2021.

[12] Vehicle Detection. https://github.com/MaryamBoneh/Vehicle-Detection/tree/main/Dataset (accessed on 12 February 2023).

[13] Images Dataset. https://www.kaggle.com/datasets/lyensoetanto/vehicle-images-dataset (accessed on 21 February 2023).

[14] A. M. Santos, C. J. A. Bastos-Filho, A. M. A. Maciel, E. Lima, "Counting vehicle with high-precision in Brazilian roads using yolov3 and deep sort," In *Conf. Rec. 2020 33rd SIBGRAPI Conference on Graphics, Patterns and Images*, pp. 69-76.

Analysis of Surface Roughness in Machining of Al-Si Based Alloys: An Experimental Study

Cem ALPARSLAN[1], Şenol BAYRAKTAR [1*]
[1]*Department of Mechanical Engineering/ Faculty of Engineering and Architecture, Recep Tayyip Erdoğan University, Zihni Derin Campus, 53100, TURKIYE*

**(senol.bayraktar@erdogan.edu.tr)*

Abstract *- In this study, Al-7Si-Mg and Al-7Si-0.6Mg alloys were produced by permanent mold casting method and their microstructural, mechanical and machinability properties were analyzed. While the microstructures were examined with an optical microscope, Brinell hardness measurement and tensile tests were performed for mechanical properties. Machining tests were conducted using 6 mm diameter two-fluted uncoated carbide end mill, different cutting speed (V: 50, 80 and 110 m/min), feed rate (f: 0.08; 0.16 and 0.24 mm/rev) and constant depth of cut (1 mm) in CNC vertical machining center. The microstructure of the Al-7Si-Mg alloy comprised of α-Al, primary Si, eutectic Al-Si, Mg_2Si, β-Al_5FeSi and π-AlSiMgFe phases. Al-7Si-0.6Mg alloy exhibited higher mechanical properties than Al-7Si-Mg alloy. Machining tests showed that the SR (Surface roughness), BUL (Built –up layer) and BUE (Built-up edge) reduced with raising V and raised with raising f. Al-7Si-0.6Mg alloy exhibited better mechanical and machinability properties.*

Keywords *- Al-Si based alloy, Microstructure, Hardness, Mechanical properties, Cutting, Surface roughness*

I. INTRODUCTION

Aluminum-Silicon (Al-Si) based alloys are generally used in sectors such as automotive and aviation owing to their high specific strength, lightweight nature, weldability, high fluidity, and low shrinkage characteristics [1,2]. These alloys have become particularly important in the automotive sector, aiming to enhance fuel efficiency, reduce greenhouse gas emissions, and decrease material weights [3]. It is also preferred in the industrial production of components whose engine blocks, pistons and cylinder heads are exposed to high stresses and temperatures [4, 5]. The addition of magnesium (Mg) in Al-Si based alloys contributes to the enhancement of mechanical properties. Additionally, it improves the thermal stability of mechanical components at high operating temperatures, thereby enhancing their performance [6]. Al-Si-Mg alloys are widely produced by casting method in order to be produced at low cost in mass production. In order to use the alloy materials produced by casting as mechanical components, the application of machining processes is significant in terms of dimensional stability and machined surface quality. The machined SR must be kept to a minimum in order for the mechanical components in contact with each other to work precisely. SR is the most significant parameter indicating the microstructural geometric defects on the surface of the parts [7]. During machining operations, friction between the the machined surface and cutting tool, plastic deformation and high-frequency vibration during chip separation cause changes in SR [8]. Furthermore, the resulting SR increases the stress concentration of the machined surface. Great influence on the fatigue life of engineering parts to the stress concentration of the machined surface. When stress concentration is higher, the parts tend to have a shorter fatigue life. [9]. In other words, SR can cause notch effect during the operation of the workpieces and negatively affect the service life of these parts. Due to the increase in production costs with low service life, it becomes difficult for enterprises to compete in the global market. Therefore, it is necessary to control the cutting conditions for the desired surface quality of the workpieces produced during machining operations. In the literature, it has been seen that some researches have been carried out on the machinability properties of Al-Si based alloys. In these studies; Braga et al. reported that BUE occurred in drilling Al-Si alloy (A356) with minimum quantity lubricant at high f using diamond-coated drills and that uncoated carbide cutters exhibited better machinability performance compared to diamond-coated cutters [10]. Basavakumar et al. observed that during machining of Al-12Si and Al-12Si-3Cu alloys, polished CVD diamond-coated cutters exhibited lower SR and BUE formation compared to uncoated and PVD-coated cutters. They also determined that the SR increased with the raise in the size of soft and eutectic components in the microstructure [11]. Bayraktar and Hekimoğlu reported that SR and BUE formation reduced with raising V and raised with raising f in turning Al-12Si-0.1Sr alloy with PVD-TiAlN/TiN coated carbide [12]. Wain et al. observed that in dry drilling of Al-Si-Cu (A319) alloy using low friction Dymon-iC, Graphit-iC, MoST and MoS2 based coatings, Graphit-iC coated cutters exhibited better tool life and minimum BUE formation [13]. Steininger et al. found that, in the screw drilling of AlSi9Cu3 alloy with uncoated, TiCN, CrN, SCiL-TiCN, TiB2 and DLC coated cutters, better surface quality was obtained with DLC coated carbide cutters and BUE formation and cutting torque decreased with increasing V [14]. Barooah et al. found that BUE and abrasive wear mechanisms are effective on the cutting tool in the screwdriving process of Al-12Si alloy manufactured by die casting method with uncoated HSS and that hard silicon particles in the Al phase cause abrasive wear [15]. Hekimoğlu and Bayraktar determined that the addition of Sr to Al-9Si alloy raised the SR and BUE formation in the turning

operations, while it reduced with the addition of Mg [16]. Gai et al., in the turning of ZL109 Al-Si piston alloy with PCD (Polycrystalline Diamond) cutting tools under varied *V* (150, 200, 250 and 300 m/min), *f* (0.05; 0.1; 0.15 and 0.2 mm/rev) and depth of cut (0.1; 0.2; 0.3 and 0. 4 mm) conditions, they found that vibration and SR raised with raising cutting depth due to cutting tool-chip effect and that SR can be minimized by using 200-250 m/min *V* range, low cutting depth and *f* values [17]. Razin et al. examined the impact of different cutting parameters and Si ratios on the surface quality of Al-Si based automotive alloys using HSS (High speed steel) tools. They found that the SR reduced with increasing *V* and depth of cut. In addition, they stated that the high Si ratio of the alloys exhibited lower elongation properties and improved machinability by facilitating fracture [18, 19]. Kumaran et al. AlSi7Cu4 alloy using cemented carbide insert for different *V* (8000, 8500 and 9000 rpm), *f* (0.6125; 0.634 and 0.645 mm/rev), depth of cut (0.4; 0.6 and 0.8 mm) and insert radius (0.5; 0.75 and 1 mm) parameters for minimum SR, using the TOPSIS method (Technique of Order Preference Similarity to the Ideal Solution), optimum cutting conditions are determined at a *V* of 8000 rpm, 0.6125 mm/rev *f*, 0.5 mm depth of cut and 0.5 mm tip Radius [20]. In the literature, it has been observed that there are researches on the machinability properties of Al-Si based alloys, but there is no detailed research on the machinability properties of Al-Si-Mg alloys. In this study, the structural and mechanical properties of Al-7Si-Mg and Al-7Si-0.6Mg alloys manufactured by the permanent mold casting technique will be revealed. In addition, it is purposed to investigate the impacts of varied *V* and *f* parameters on SR, BUL and BUE formation in milling process.

II. Material And Method

Al-7Si-Mg and Al-7Si-0.6Mg alloys were melted at 775 ±5 ^{o}C using a melting furnace (induction) and solidified by pouring into a permanent mold at room conditions. As a result of this process, casting samples of 140x100x16 mm were obtained. The chemical percent composition ratios of the cast samples are given in the study in [21]. These samples were prepared by machining operations to determine structural (Fig. 1a), mechanical (Fig. 1a and b) and machinability (Fig. 1c) properties using band saws, universal turning and milling machines.

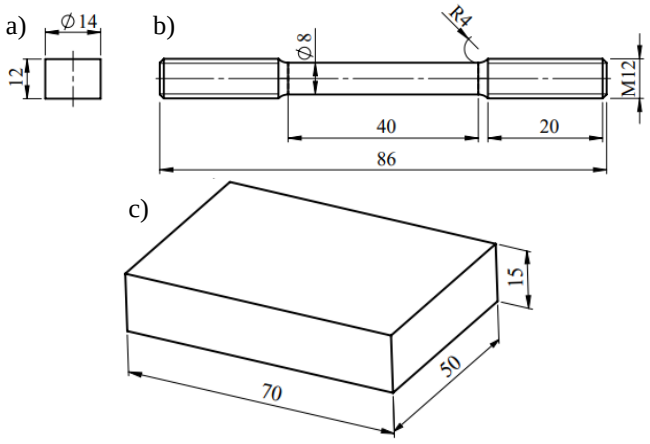

Figure 1. Technical details of specimens, a) Specimen for microstructural and hardness examination, b) Tensile test specimen and c) Specimen for milling test (Dimensions in mm)

For tests, the microstructures of the samples prepared as in Fig.1a were prepared by metallographic methods and examined under an optical microscope. Mechanical tests were carried out under the conditions of 0.25 mm s^{-1} fixed jaw and $5.9x10^{-3}$ s^{-1} average deformation rate with tensile specimens prepared as in Fig. 1b in dimensions in accordance with ASTM E8 standard. Brinell hardness measurement method was used to determine the hardness values of the alloys. Three samples were produced from each alloy in the microstructural examination and mechanical tests. In determining the mechanical properties, the arithmetic average of the measured values from these samples was taken and the final results were obtained as in [21].

Milling tests were using CNC vertical machining center at different *V* (50, 80 and 110 m/min), *f* (0.08; 0.16 and 0.24 mm/rev), constant cutting depth (1 mm) parameters [22, 23]. Two flute uncoated carbide end mills with Ø6 mm diameter were used in the tests. Each test was made with a new cutting tool and a total of eighteen tests were carried out considering the cutting parameters and alloy material conditions. While the milling tests, the roughness values of the machined surface were measured with a Mahr Perthometer tracer device (using ISO 4287). Average SR is calculated based on the expression $Ra = \frac{1}{L}\int_0^L |y(x)|dx$. Here L is the measuring length, y is the measured value and Ra is the arithmetic mean of the y coordinates [24]. The measurements were repeated five times for each machined surface. Then, were determined to arithmetic average of these measurements. Final SR values were obtained.

III. Result and Discussion

The microstructure of Al-7Si-Mg and Al-7Si-0.6Mg casting alloys is mainly composed of α-Al, primary Si and eutectic Si (Al-Si) phase with coral-like morphology. Many plate and β-Al_5FeSi and script-like π-Al-SiMgFe intermetallic particles were observed along the dendritic boundaries (Fig. 2 and 3). It

was observed that there was no significant difference between α-Al and eutectic Si phase morphologies in the microstructure of Al-7Si-0.6Mg alloy with the raise of Mg content. However, it was determined that the size and fraction of Fe-rich intermetallics raised significantly (Fig. 3).

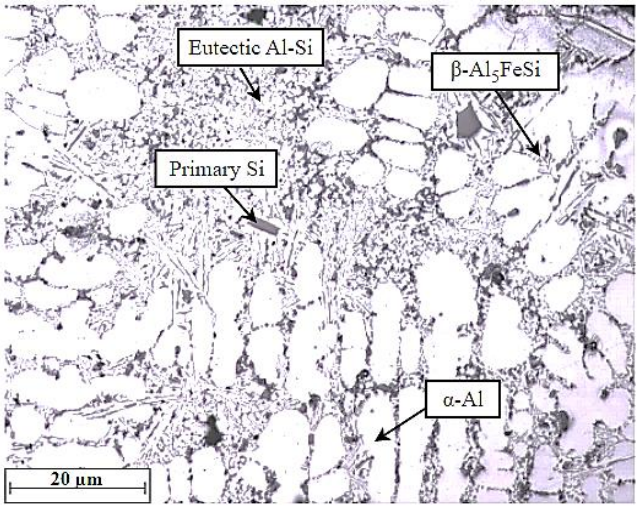

Figure 2. Microstructure image of Al-7Si-Mg alloy (10X)

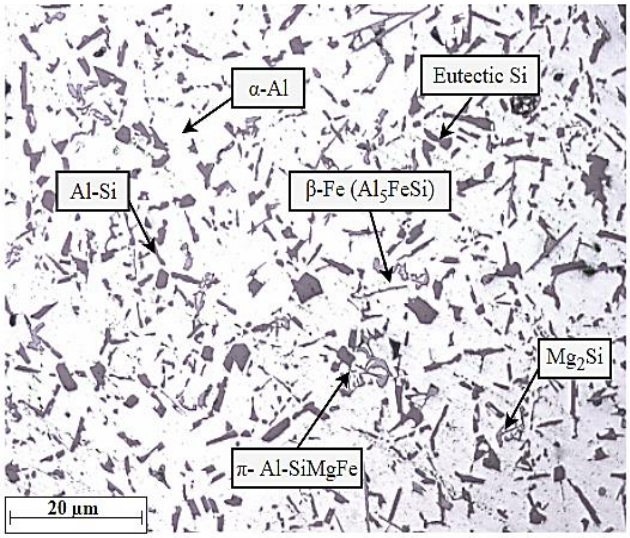

Figure 3. Microstructure image of Al-7Si-0.6Mg alloy (10X)

It was determined that the Mg content in the Fe-rich intermetallic phases increased with the increase of Mg content in the alloy structure. With the decrease in temperature during the solidification process, a triple eutectic reaction occurs with Al, Si and β-Al_5FeSi phases in the microstructure. Furthermore, the π-AlSiMgFe phase is formed as a result of the semi-peritectic reaction of the β phase. The π-Fe phase, which has a needle-like morphology in the microstructure, transforms into intermetallics with a high Fe content, forming triple eutectic structures of Al, Si and Mg_2Si (Fig. 3) [25]. In their previous work on mechanical tests, the authors [21] found that the hardness, yield and tensile strength values of Al-7Si-0.6Mg alloy were higher than Al-7Si-Mg alloy, while the elongation to fracture values were lower. It is thought that this situation is because of the formation and distribution of more precipitates due to the raise in the ratio of Mg in the α-Al phase in the microstructure of the alloy [26, 27].

It was noticed that the SR raised with the raise of *f* in the milling of both alloys under constant *V* conditions (Fig. 4a). It is thought that the increase in SR is due to the raise in the chip volume removed per unit time during cutting and the raise in the cutting tool/chip interface contact area [26, 28]. As it can be understood from the expression $Ra=f^2/32r$ (r: cutting edge radius), it was seen that the SR will increase with the raise in *f* [29]. It was observed that the SR reduced with raising *V* at constant *f* (Fig. 4b). This situation can be attributed that decrease in the yield strength of the material as a result of the increase in the tool/chip interface temperature during cutting, the plastic deformation becomes easier and the tool/chip contact surface area decreases [30].

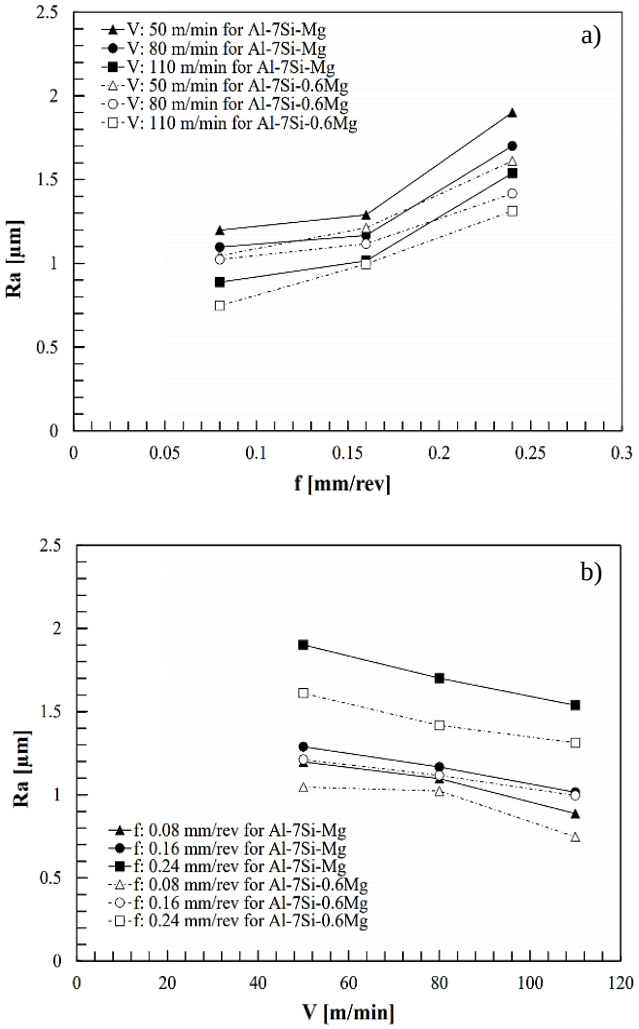

Figure 4. SR graph of Al-7Si-Mg and Al-7Si-0.6Mg alloys, a) f-Ra relationship at constant *V* and b) V-Ra relationship at constant *f*

It was observed that the Al-7Si-0.6Mg alloy exhibited the lowest SR among the machined alloys. It's thought that this situation is due to the reduce in elongation to fracture due to the increasing Mg ratio of the alloy and the improvement of the machinability properties of the chip by breaking easily

during the cutting process [26, 31]. The images of the surface conditions formed during the processing of the alloys are given in Fig. 5.

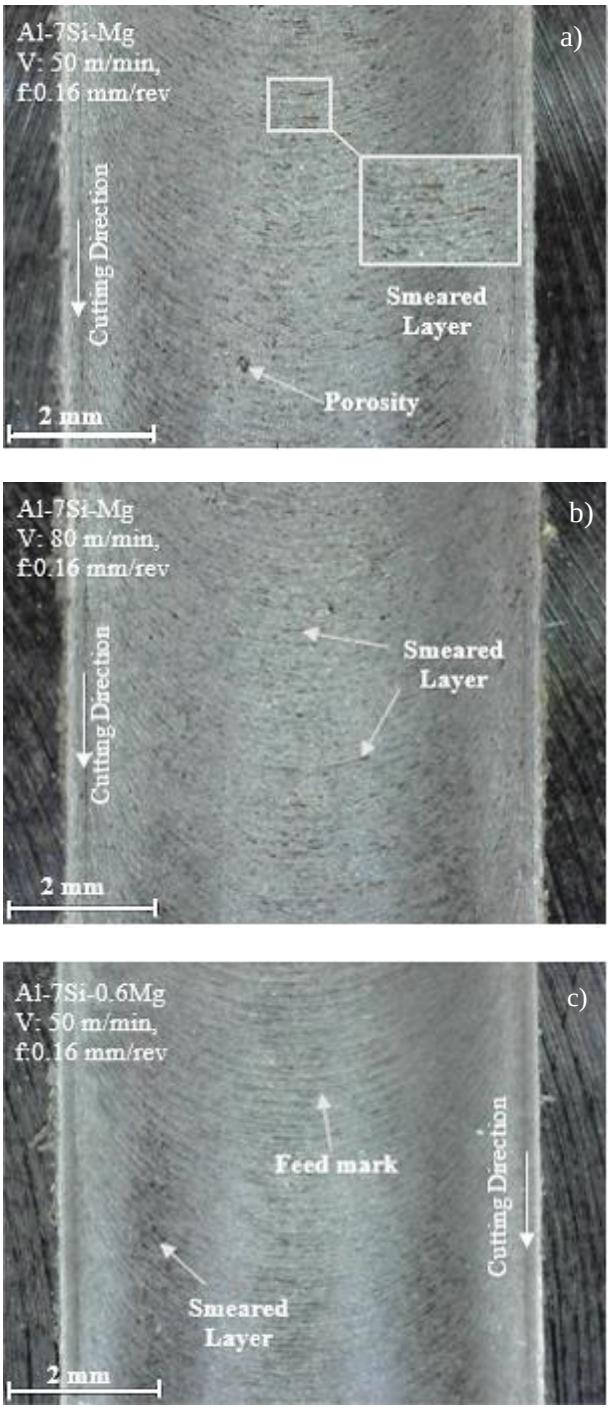

Figure 5. Machined surface images at different cutting parameters, a and b) Al-7Si-Mg and c and d) Al-7Si-0.6Mg

When milling the Al-7Si-Mg alloy under the same cutting conditions, it was observed that more smeared layers were formed on the machined surface compared to the Al-7Si-0.6Mg alloy. It is thought that this is due to the fact that the ductile α-Al phase in the microstructure is smearing layer on the machined surface owing to the higher elongation to fracture of the Al-7Si-Mg alloy. In addition, the reduction in elongation to fracture at Al-7Si-0.6Mg alloy facilitates the removal of chips formed during cutting and the irregularities on the cutting surface are minimized. Thus, the quality of the machined surface is improved [32]. It was determined that the formation of smeared layer decreased in both alloys with the raise in *V*. It is thought that this situation is due to the reduce in the elongation to fracture of the material and the facilitation of plastic deformation owing to the raise in *V*. In this way, a more stable machined surface quality is obtained by reducing the smearing layer [26, 31].

IV. Conclusion

The results finding from the study can be listed as follows;

- The microstructure of both alloys consisted of α-Al, primary Si, eutectic Al-Si, Mg_2Si, β-Al_5FeSi and π-AlSiMgFe phases.
- While the SR increased with the increase in the *f* in the machining of alloys, it decreased with the increase in the *V*.
- It was established that the Al-7Si-0.6Mg alloy exhibited the lowest SR measurements.
- It was observed that smeared layer and feed mark were formed on the machined surfaces. It has been determined that the formation of smeared layer is less due to the low elongation to fracture in the machining of Al-7Si-0.6Mg alloy.

REFERENCES

[1] S. Santhi, and S. Sundarrajan, ''Shrinkage estimation of cast Al–Si alloys through process simulation,'' *Metallofiz Noveishie Tekhnology*, vol. 39 (7), pp. 959-81, 2017.

[2] S. Samavedam, and S. Sundarrajan, ''Al-Si and Al-Si-Mg cast alloys shrinkage porosity estimation,'' *Archives of Foundry Engineering*, vol. 16(1), pp. 61-68, 2016.

[3] R. Molina, P. Amalberto, and M. Rosso, ''Mechanical characterization of aluminium alloys for high temperature applications Part1: Al-Si-Cu alloys,'' *Metallurgical Science and Technology,* vol. 29 (1), pp. 5-15, 2011.

[4] M. H. Abdelaziz, A. M. Samuel, H. W. Doty, S. Valtierra, and F. H. Samuel, ''Effect of additives on the microstructure and tensile properties of Al–Si alloys,'' *Journal of Materials Research and Technology*, vol. *8*(2), pp. 2255-68, 2019.

[5] P. Huter, P. Renhart, S. Oberfrank, M. Schwab, F. Grün, and Stauder B, ''High- and low-cycle fatigue influence of silicon, copper, strontium and iron on hypo-eutectic Al–Si–Cu and Al–Si–Mg cast alloys used in cylinder heads'' *International Journal of Fatigue*, vol. 82(3), pp. 599-601, 2016.

[6] S. Beroual, Z. Boumerzoug, P. Paillard, and Y. Borjon-Piron, ''Effects of heat treatment and addition of small amounts of Cu and Mg on the microstructure and mechanical properties of Al-Si-Cu and Al-Si-Mg cast alloys,'' *Journal of Alloys and Compounds*, vol. 784, pp. 1026-35, 2019.

[7] D. Zhang, and X. Pei, ''Effects of machining processes on surface roughness and fatigue life,'' *China Mechanical Engineering,* vol. 14(16), pp. 1374–77, 2003.

[8] S. Andrews, H. Sehitoglu, ''Computer model for fatigue crack growth from rough surfaces,'' *International Journal of Fatigue,* vol. 22(7), pp. 619–30, 2000.

[9] D. Arola, and C. L. Williams, ''Estimating the fatigue stress concentration factor of machined surfaces,'' *International Journal of Fatigue,* vol. 24(9), pp. 923–30, 2002.

[10] D. U. Braga, A. E. Diniz, G. W. Miranda, and N. L. Coppini, ''Using a minimum quantity of lubricant (MQL) and a diamond coated tool in the drilling of aluminum–silicon alloys,'' *Journal of Materials Processing Technology,* vol. 122(1), pp. 127-38, 2002.

[11] K. G. Basavakumar, P. G. Mukunda, and M. Chakraborty, ''Influence of melt treatments and turning inserts on cutting force and surface integrity in turning of Al–12Si and Al–12Si–3Cu cast alloys,'' *Surface and Coating Technology,* vol. 201(8), pp. 4757–66, 2007.

[12] Ş. Bayraktar, and A. P. Hekimoğlu, ''Al-12Si-0.1Sr alaşımının PVD-TiAlN/TiN kaplamalı kesici ile işlenmesinde işlenebilirlik özellikleri üzerine deneysel araştırma,'' *5. Internatinonal Conference on Materials Science, Mechanical and Automotive Engineerings and Technology*, Nevşehir, Türkiye, 2022.

[13] N. Wain, N. R. Thomas, S. Hickman, J. Wallbank, and D. G. Teer, ''Performance of Low-Friction Coatings in the Dry Drilling of Automotive Al–Si Alloys,'' *Surface and Coatings Technology*, vol. 200, pp. 1885-92, 2005.

[14] A. Steininger, A. Siller, and F. Bleicher, ''Investigations Regarding Process Stability Aspects in Thread Tapping Al-Si Alloys,'' *Procedia Engineering,* vol. 100, pp. 1124-32, 2015.

[15] R. K. Barooah, A. F. M. Arif, J. M. Paiva, S. Oomen-Hurst, and S. C. Veldhuis, ''Wear of Form Taps in Threading of Al-Si Alloy Parts: Mechanisms and Measurements,'' *Wear,* vol. 442, 203153, 2020.

[16] A. P. Hekimoğlu, and Ş. Bayraktar, ''Experimental research on machinability characteristics of Al-9Si alloy: Effect of Sr and Mg additives,'' *Proceedings of the Institution of Mechanical Engineers Part B-Journal of Engineering Manufacture*, vol. 236(13), pp. 1807-16, 2022(a).

[17] S. Gai, A. Li, J. Liu, Z. Gong, and J. Zhao, ''Effect of surface roughness on stress concentration factor of machined surface and cutting parameter optimization in boring of Al-Si piston alloy,'' *The International Journal of Advanced Manufacturing Technology*, vol. 121(5-6), pp. 4129-40, 2022.

[18] A. A. Razin, D. S. Ahammed, M. A. Nur, and M. S. Kaiser, ''Role of Si on machined surfaces of Al-based automotive alloys under varying machining parameters,'' *Journal of Mechanical and Energy Engineering,* vol. 6(1), pp. 43-52, 2022.

[19] H. De O. Santos, F. M. dos Reis, C. T. Kunioshi, J. L. Rossi, and I. Costa, ''Corrosion performance of Al-Si-Cu hypereutectic alloys in a synthetic condensed automotive solution,'' *Materials Research*, vol. 8(2), pp. 155–159, 2005.

[20] D. Kumaran, S. S. S. S. Paramasivam, and H. Natarajan, ''Optimization of High Speed Machining Cutting Parameters for End Milling of AlSi7Cu4 Using Taguchi Based Technique of Order Preference Similarity to the Ideal Solution,'' *Materials Today: Proceedings,* vol. 47, pp. 6799-804, 2021.

[21] C. Alparslan, and Ş. Bayraktar, ''Comparison of Machinability Performances in Milling of Al-7Si-Mg and Al-7Si-0.6Mg Alloys''. *5th In International Conference on Engineering, Natural and Social Sciences (ICAENS-2023),* vol. 1, pp. 977-83, 2023.

[22] T. O. Sadiq, B. A. Hameed, J. Idris, O. Olaoye, S. Nursyaza, Z. H. Samsudin, and M. I. Hasnan, ''Effect of different machining parameters on surface roughness of aluminium alloys based on Si and Mg content,'' *Journal of the Brazilian Society of Mechanical Sciences and Engineering*, vol. 41(10), pp. 1-11, 2019.

[23] M. Sekmen, M. Günay, and U. Şeker, ''Alüminyum Alaşımlarının İşlenmesinde Kesme Hızı ve Talaş Açısının Yüzey Pürüzlülüğü, Yığıntı Talaş ve Yığıntı Katmanı Oluşumu Üzerine Etkisi,'' *Politeknik Dergisi*, vol. 18, pp. 141-48, 2015.

[24] A. P. Hekimoğlu, & Ş. Bayraktar, ''Experimental research on machinability characteristics of Al-9Si alloy: Effect of Sr and Mg additives,'' *Proceedings of the Institution of Mechanical Engineers, Part B: Journal of Engineering Manufacture*, 236(13), 1807-1816, 2022.

[25] X. Wu, H. Zhang, Z. Ma, T. Tao, J. Gui, J, Song, W, and Zhang, H, ''Interactions between Fe-rich intermetallics and Mg-Si phase in Al-7Si-xMg alloys,'' *Journal of Alloys and Compounds*, vol. 786, pp. 205-14, 2019.

[26] Ş. Bayraktar, and O. Demir, ''Processing of T6 heat-treated Al-12Si-0.6 Mg alloy,'' Materials and Manufacturing Processes, vol. 35(3), pp. 354-362, 2020.]

[27] K. P. S. Chauhan, '' Influence of heat treatment on the mechanical properties of aluminium alloys (6xxx series): a literature review,'' *International Journal of Engineering Research and Technology*, vol. 6 (3), pp. 386-389, 2017.

[28] T. D. Hoang, N. T. Nguyen, D. Q. Tran, V. T. and Nguyen, ''Cutting forces and surface roughness in face-milling of SKD61 hard steel,'' *Strojniski Vestnik/Journal of Mechanical Engineering*, vol 65(6). pp. 375-85, 2019.

[29] R. K. Bhushan, S. Kumar, and S. Das, ''Effect of machining parameters on surface roughness and tool wear for 7075 Al alloy SiC composite,'' *The International Journal of Advanced Manufacturing Technology*, vol. 50, pp. 459-69, 2010.

[30] Ş. Bayraktar, Ç. Çamkerten, and N. Salihoğlu, "Bakır ve Silisyum İlavelerinin Al-25Zn Alaşımının CVD Al2O3 Kaplamalı Takımlarla Tornalanmasında İşlenebilirliğe Etkisinin İncelenmesi," *Gazi University Journal of Science Part C: Design and Technology*, vol. 8 (1), pp. 79-93, 2020.

[31] A. P. Hekimoğlu, and Ş. Bayraktar, ''Kokil kalıba Döküm Yöntemi ile Üretilmiş Al-12Si-(0,02-1) Sr Alaşımlarının CVD-TiCN/Al_2O_3/TiN Kaplamalı Kesici Uç ile Tornalanmasında Kesme Kuvveti ve Yüzey Pürüzlülüğü Üzerine Deneysel Çalışma,'' *Gazi Üniversitesi Fen Bilimleri Dergisi Part C: Tasarım ve Teknoloji*, vol. *10*(1), pp. 50-62, 2022.

[32] Ş. Bayraktar, and A. P. Hekimoğlu, ''Effect of zinc content and cutting tool coating on the machinability of the Al-(5–35) Zn alloys,'' *Metals and Materials International*, vol. *26*, pp. 477-90, 2020.

Biomedical Engineering

Computer Engineering

Electrical and Electronics Engineering

Mechanical Engineering

Mechatronic Engineering

Metallurgical and Materials Engineering

Civil Engineering

ICENTE'23

INTERNATIONAL CONFERENCE ON ENGINEERING TECHNOLOGIES

November 23-25, 2023

Konya/TURKEY

icente.selcuk.edu.tr